

ISSN 0015-5659
eISSN 1644-3284
Impact Factor: 1.195

POLISH ANATOMICAL SOCIETY

FOLIA **MORPHOLOGICA**



Vol. 82 *2023* *No. 2*


VIA MEDICA

https://journals.viamedica.pl/folia_morphologica

FOLIA MORPHOLOGICA

An international multidisciplinary journal devoted to fundamental research in the morphological sciences

Official Journal of the Polish Anatomical Society

(a Constituent Member of European Federation for Experimental Morphology — EFEM)

EDITOR-IN-CHIEF

Janusz Moryś

Department of Normal Anatomy,
Pomeranian Medical University, Szczecin, Poland

https://journals.viamedica.pl/fovia_morphologica

*See our website for information on manuscript status, aims and scope,
instructions for authors as well as editorial board.*

Folia Morphologica

Publishing, Subscription and Advertising Office:
VM Media Group sp. z o.o., Grupa Via Medica
ul. Świętokrzyska 73, 80–180 Gdańsk, Poland
tel. (+48 58) 320 94 94, fax (+48 58) 320 94 60

Managing editor

Joanna Niezgodna

e-mail: fm.journals@viamedica.pl

Cover designer

Sylvia Scisłowska

The journal is published at: https://journals.viamedica.pl/fovia_morphologica in one volume per year consisting of four numbers.

Subscription rates: Paper subscription, 4 issues incl. package and postage institutional — 210 euro. The above prices are inclusive of regular postage costs. Payment should be made to: VM Media Group sp. z o.o., Grupa Via Medica, BNP Paribas Bank Polska SA account number: 15 1600 1303 0004 1007 1035 9021; SWIFT: PPABPLPK. Single issues, subscriptions orders and requests for sample copies should be send to e-mail: prenumerata@viamedica.pl. Electronic orders option available at: https://journals.viamedica.pl/fovia_morphologica. The publisher must be notified of a cancellation of access to electronic version not later than two months before the end of a calendar year. After that date electronic access will be automatically prolonged for another year.

Advertising. For details on media opportunities within this electronic version of journal please contact the advertising sales department, ul. Świętokrzyska 73, 80–180 Gdańsk, Poland, tel: (+48 58) 320 94 94, e-mail: viamedica@viamedica.pl

The editors accept no responsibility for advertisement contents.

Folia Morphologica is the official journal of the Polish Anatomical Society. For information about the Society, please contact: Prof. Janusz Moryś, Department of Normal Anatomy, Pomeranian Medical University, Al. Powstańców Wielkopolskich 72, 70–111 Szczecin, Poland, tel. (+48 91) 466 15 43, e-mail: jmorys@pum.edu.pl

All rights reserved, including translation into foreign languages. No part of this periodical, either text or illustration, may be used in any form whatsoever. It is particularly forbidden for any part of this material to be copied or translated into a mechanical or electronic language and also to be recorded in whatever form, stored in any kind of retrieval system or transmitted, whether in an electronic or mechanical form or with the aid of photocopying, microfilm, recording, scanning or in any other form, without the prior written permission of the publisher. The rights of the publisher are protected by national copyright laws and by international conventions, and their violation will be punishable by penal sanctions.

Editorial policies and author guidelines are published on journal website: https://journals.viamedica.pl/fovia_morphologica

Legal note: https://journals.viamedica.pl/fovia_morphologica/about/legalNote

Folia Morphologica is indexed by: BIOSIS Previews, CAS, CINAHL, CrossRef, Dental Abstracts, EBSCO, Elsevier BIOBASE, EMBIOLOGY, FMJ, Google Scholar, Index Copernicus (159.83), Index Medicus/MEDLINE, Index Scholar, Polish Ministry of Education and Science (70), NCBI/National Center for Biotechnology Information, Polish Medical Bibliography, Scopus, SJR, Thomson Reuters, Thomson Scientific Products — Biological Abstracts, Ulrich's Periodicals Directory, Veterinary Bulletin, WorldCat and Zoological Record. Position in Index Copernicus ranking systems is available at: www.indexcopernicus.com. Current Impact Factor of Folia Morphologica (2021) is 1.195.



FOLIA MORPHOLOGICA

Editor-in-Chief
JANUSZ MORYŚ

Department of Normal Anatomy, Pomeranian Medical University
Al. Powstańców Wielkopolskich 72, 70-111 Szczecin, Poland
tel. (+48 91) 466 15 43, e-mail: jmorys@pum.edu.pl

EDITORIAL ADVISORY BOARD

Rafael BOSCOLO-BERTO, *Department of Neuroscience, University of Padova, Italy*

Franciszek BURDAN, *Experimental Teratology Unit of the Human Anatomy Department, Medical University of Lublin, Poland*

Małgorzata BRUSKA, *Department of Anatomy, University Medical School, Poznań, Poland*

Mafalda CACCIOTTOLO, *USC Leonard Davis School of Gerontology, University of Southern California, Los Angeles, United States*

Stephen W. CARMICHAEL, *Department of Anatomy, Mayo Clinic, Rochester, United States*

Bogdan CISZEK, *Department of Human Anatomy, Medical University of Warsaw, Poland*

Om Prakash CHOUDHARY, *Department of Veterinary Anatomy, Guru Angad Dev Veterinary and Animal Sciences University, Bathinda, Punjab, India*

Carla D'AGOSTINO, *Neuromuscular Center, University of Southern California, Los Angeles, CA, United States*

Halina DOBRZYŃSKI, *Cardiovascular Sciences, Faculty of Biology, Medicine and Health, University of Manchester, United Kingdom*

Zygmund Antoni DOMAGAŁA, *Department of Anatomy, Medical University of Wrocław, Poland*

Rastislav DRUGA, *Department of Functional Anatomy, 2nd Medical Faculty Charles University, Prague, Czech Republic*

Sergio Domenico GADAU, *Department of Veterinary Medicine, University of Sassari, Italy*

Marek GRZYBIAK, *Elblag University of Humanities and Economics, Elblag, Poland*

Hans Jorgen GUNDERSEN, *Stereological Research Laboratory, University of Aarhus, Denmark*

Kazimierz JĘDRZEJEWSKI, *Department of Anatomy, Medical University of Łódź, Poland*

Leszek KACZMAREK, *Department of Molecular Cell Neurobiology, Nencki Institute, Warsaw, Poland*

Ilona KLEJBOR, *Department of Anatomy, Jan Kochanowski University of Kielce, Poland*

Zbigniew KMIEĆ, *Department of Histology, Medical University of Gdańsk, Poland*

Henryk KOBRYŃ, *Department of Morphological Sciences, Warsaw, Agricultural University, Poland*

Przemysław KOWIAŃSKI, *Department of Human Anatomy and Physiology, Pomeranian University in Słupsk, Poland*

Marios LOUKAS, *Department of Anatomical Sciences, School of Medicine, St. George's University, Grenada, West Indies*

Andrzej ŁUKASZYK, *Department of Histology and Embryology, University Medical School, Poznań, Poland*

Alexander J. McDONALD, *Department of Cell Biology and Neuroscience, USC School of Medicine, Columbia, United States*

Stanisław MOSKALEWSKI, *Department of Histology and Embryology, Medical University of Warsaw, Poland*

Łukasz OLEWNIK, *Department of Normal and Clinical Anatomy, Medical University of Łódź, Poland*

Orlando PACIELLO, *Dipartimento di Patologia e Sanità animale, Univesita degli Studi di Napoli Federico II, Napoli, Italy*

Asla PITKÄNEN, *Department of Neurobiology, A.I. Virtanen Institute, University of Kuopio, Finland*

Michał POLGUJ, *Department of Angiology, Medical University of Łódź, Poland*

Marcin SADOWSKI, *Department of Anatomy, Jan Kochanowski University of Kielce, Poland*

Michał K. STACHOWIAK, *Department of Molecular and Structural Neurobiology and Gene Therapy, State University of New York, Buffalo, United States*

Paweł SYSA, *Department of Histology and Embryology, Warsaw University of Life Sciences, Poland*

Michał SZPINDA, *Department of Anatomy, Nicolaus Copernicus University in Toruń, Collegium Medicum in Bydgoszcz, Poland*

Edyta SZUROWSKA, *2nd Department of Radiology, Medical University, Gdańsk, Poland*

Jean-Pierre TIMMERMANS, *Laboratory of Cell Biology and Histology/Central Core Facility for Microscopic Imaging, Department of Veterinary Sciences, University of Antwerp, Belgium*

Mirosław TOPOL, *Department of Angiology, Medical University of Łódź, Poland*

Mehmet Cudi TUNCER, *Department of Anatomy, University of Dicle, Medical School, Diyarbakir, Turkey*

Krzysztof TURLEJSKI, *Department of Biochemistry and Cell Biology, Cardinal Stefan Wyszyński University, Warsaw, Poland*

Jiro USUKURA, *Structural Biology Research Center, Nagoya, Japan*

Jerzy WALOCHA, *Department of Anatomy, Jagiellonian University, Collegium Medicum, Kraków, Poland*

Mark J. WEST, *Department of Neurobiology, Institute of Anatomy, Aarhus University, Denmark*

Sławomir WÓJCİK, *Department of Anatomy and Neurobiology, Medical University of Gdańsk, Poland*

Maciej ZABEL, *Collegium Medicum University of Zielona Gora, Poland*

Marco ZEDDA, *Department of Veterinary Medicine, University of Sassari, Italy*

Variations in the branching pattern of tibial nerve in foot: a review of literature and relevant clinical anatomy

A. Priya¹, S.K. Ghosh¹, J.A. Walocha², R.S. Tubbs^{3–8}, J. Iwanaga^{3, 4, 9, 10}

¹Department of Anatomy, All India Institute of Medical Sciences, Phulwarisharif, Patna, India

²Department of Anatomy, Jagiellonian University, Krakow, Poland

³Department of Neurosurgery, Tulane Centre for Clinical Neurosciences, Tulane University School of Medicine, New Orleans, LA, United States

⁴Department of Neurology, Tulane Centre for Clinical Neurosciences, Tulane University School of Medicine, New Orleans, LA, United States

⁵Department of Anatomical Sciences, St. George's University, St. George's, Grenada, West Indies

⁶Department of Structural and Cellular Biology, Tulane Centre for Clinical Neurosciences, Tulane University School of Medicine, New Orleans, LA, United States

⁷Department of Neurosurgery and Ochsner Neuroscience Institute, Ochsner Health System, New Orleans, LA, United States

⁸Department of Surgery, Tulane Centre for Clinical Neurosciences, Tulane University School of Medicine, New Orleans, LA, United States

⁹Dental and Oral Medical Centre, Kurume University School of Medicine, Kurume, Fukuoka, Japan

¹⁰Division of Gross and Clinical Anatomy, Department of Anatomy, Kurume University School of Medicine, Kurume, Fukuoka, Japan

[Received: 1 March 2022; Accepted: 31 March 2022; Early publication date: 20 April 2022]

Considerable variations have been reported regarding the branching pattern of tibial nerve (TN) close to its termination in foot. In order to comprehend the clinical anatomy of heel pain awareness of all the possible variations in relation to terminal branching pattern of TN (close to the tarsal tunnel) is essential. The present study was conducted to undertake a comprehensive review of the variations in TN branches in foot with particular emphasis on the implications for sensory distribution of these branches. Articles were searched in major online indexed databases using relevant key words. The pattern of termination of TN was noted as either trifurcation or bifurcation. Bifurcation pattern was more commonly observed and is associated with the medial calcaneal nerve (MCN) either arising high or low relative to the tarsal tunnel. The most commonly noted type of bifurcation was proximal to malleolar-calcaneal axis but within the tarsal tunnel. Across all five types of bifurcation reported in literature, the termination points of TN ranged from 3 cm proximal to 3 cm distal to malleolar-calcaneal axis and, therefore, the area beyond this region can be considered as safe zone for performing invasive procedures. MCN showed considerable variations in its origin both in trifurcation and bifurcation pattern pertaining to number of branches (one/two/three) at the point of origin. The origin of inferior calcaneal nerve was observed to be relatively less variable as it mostly arose as a branch of lateral plantar nerve and sometimes as a direct branch from TN before termination. The frequent variation of MCN

Address for correspondence: Prof. J. Walocha, Department of Anatomy, Jagiellonian University, ul. Kopernika 12, 31–034 Kraków, Poland, e-mail: jwalocha@cm-uj.krakow.pl

This article is available in open access under Creative Common Attribution-Non-Commercial-No Derivatives 4.0 International (CC BY-NC-ND 4.0) license, allowing to download articles and share them with others as long as they credit the authors and the publisher, but without permission to change them in any way or use them commercially.

in the tarsal tunnel should be kept in mind while undertaking decompression measures in medial ankle region. (Folia Morphol 2023; 82, 2: 231–241)

Key words: tibial nerve, tarsal tunnel, heel pain, plantar nerves, medial calcaneal nerve, inferior calcaneal nerve

INTRODUCTION

The classical trifurcation of the tibial nerve (TN) deep to the flexor retinaculum of the foot (laciniat ligament) was reported by Horwitz in 1938 [34]. This pattern corresponds to the medial plantar nerve (MPN), lateral plantar nerve (LPN) and medial calcaneal nerve (MCN) arising as terminal branches of the tibial nerve within the tarsal tunnel (TT) (Fig. 1) [25]. Over the years, researchers have reported several variations in the origins of the terminal branches of tibial nerve in this region [18, 28, 31, 46]. In most cases the variation involves the origin of the MCN. When the classical trifurcation is not reported, the MCN arises either proximal to the TT (here the TN terminates as the MPN and LPN, thus showing a bifurcation pattern) or as a branch of one of the plantar nerves, more commonly the LPN [20, 21, 30]. Several authors have viewed the variations in the level of bifurcation of the TN in relation to the TT and the malleolar-calcanal axis (MCA). Many have also classified the bifurcation into types (Fig. 2) [7, 15, 20, 27, 32, 35, 36, 41, 52, 54, 62, 73, 78]. The TT is an osseo-fibrous tunnel that houses the aforesaid terminal branches of the TN, which frequently undergo compression, causing an entrapment neuropathy known as TT syndrome [25, 49]. Thus, for clinicians to comprehend the surgical anatomy of TT syndrome, awareness of all the possible variations of the TN and its branches in the TT is essential.

The TN can also give rise to the inferior calcaneal nerve (ICN) as a branch close to its termination [34]. The ICN is reported to arise as a branch of LPN at the level of the medial malleolus in most cases, so it is often referred to as the first branch of the LPN [13, 16, 65]. Incidentally the "ICN" is also known eponymously in the literature as the 'Nerve of Baxter' [28, 65]. It can arise as a direct branch of the TN or as a branch of the LPN, but its origin is always distal to that of the MCN the origin of MCN as per published literature [30].

As discussed above, the terminal branches of the TN are involved in the sensory supply to the foot [6, 9]. The MPN is involved in the cutaneous supply

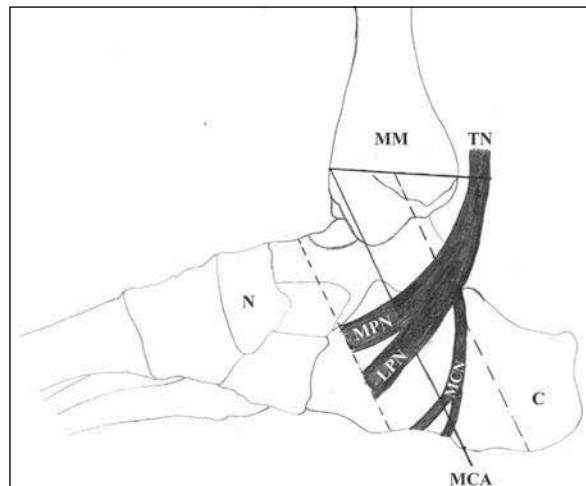


Figure 1. Lateral scheme of the ankle region showing trifurcation of the tibial nerve (TN) in the tarsal tunnel (TT). The horizontal dotted line is an imaginary line marking the beginning of the TT. The dotted oblique lines show the extent of the TT proximo-distally. The plane oblique line is the malleolar-calcanal axis (details of the malleolar-calcanal axis [MCA] are found in the Results section); MM — medial malleolus; N — navicular; MPN — medial plantar nerve; LPN — lateral plantar nerve; MCN — medial calcaneal nerve; C — calcaneus.

of the medial aspect of the sole and adjacent sides of the great, second and third toes and the medial side of the fourth toe. The cutaneous branch of the LPN supplies the lateral side of the sole and the lateral side of the fourth toe along with adjacent sides of the little toe. The MCN provides sensory innervation to the heel pad and to the superficial tissues overlying the inferior aspect of the calcaneus (Fig. 3). ICN provides sensory innervations to the anterior aspect of the calcaneus (Fig. 3) [68]. In accordance with their sensory distribution, compression of these nerves, which is particularly common within the tarsal tunnel, is associated with pain around the heel and along the sole [9].

In view of the foregoing, it can be inferred that variations in the branching pattern of the TN close to its termination in the foot are clinically significant because the sensory distribution of these nerves encompasses the heel and the sole. Hence it was hypothesized that exploring the reported variations in

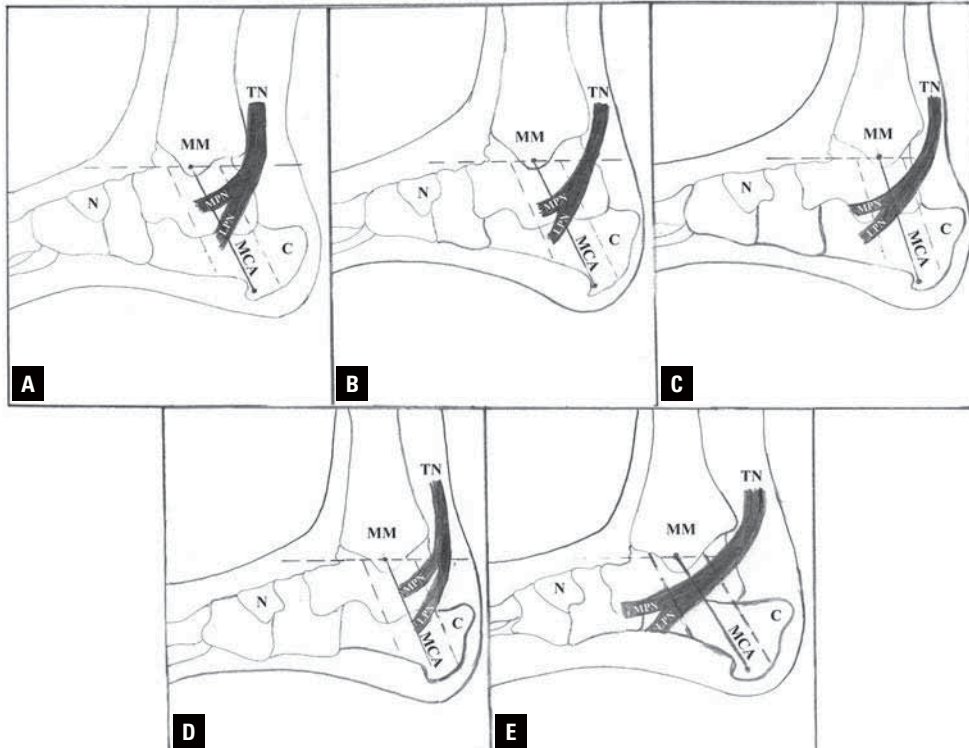


Figure 2. Schematic representation of types of bifurcation of tibial nerve with reference to the malleolar-calcaenal axis and tarsal tunnel (TT). The dotted oblique lines showing the extent of the TT proximo-distally. The plane oblique line is the malleolar-calcaenal axis (details of malleolar-calcaenal axis [MCA] are found in the Results section); **A.** Type I: the bifurcation was proximal to the axis and inside the TT; **B.** Type II: the tibial nerve (TN) bifurcated at the axis; **C.** Type III: the bifurcation was distal to the axis and inside the TT; **D.** Type IV: the bifurcation was proximal to the axis and outside the TT; **E.** Type V: the bifurcation was distal to the axis and outside the tunnel; MM — medial malleolus; N — navicular; MPN — medial plantar nerve; LPN — lateral plantar nerve; MCN — medial calcaneal nerve; C — calcaneus.

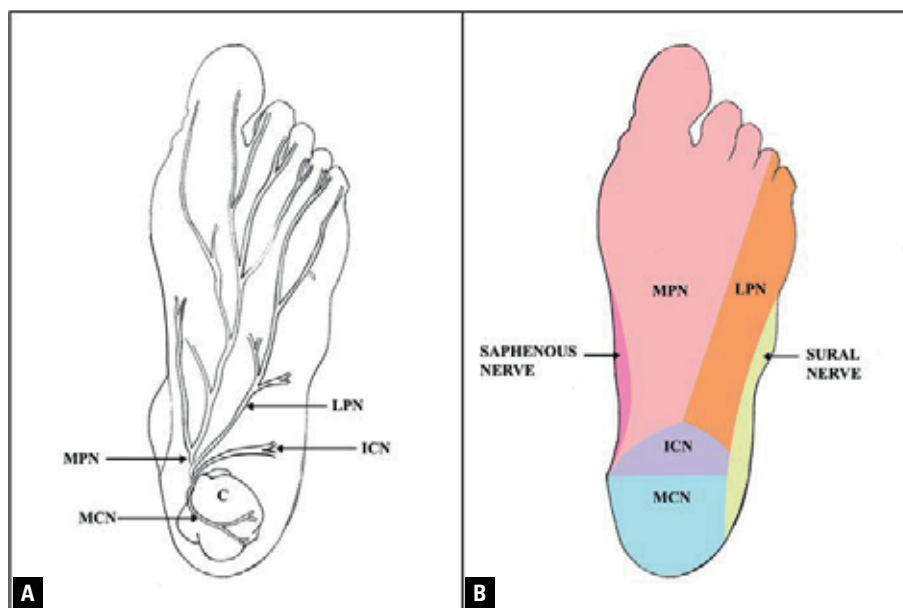


Figure 3. A. Illustration of branching pattern of medial plantar nerve (MPN), lateral plantar nerve (LPN), medial calcaneal nerve (MCN), and inferior calcaneal nerve (ICN) in the plantar aspect of the foot; **B.** Sensory innervation of MPN, LPN, MCN, and ICN in the plantar aspect of the foot.

the available literature and analysing the findings both anatomically and clinically. Accordingly, the present study was conducted to review the variations in the TN branches in the foot comprehensively. A brief account of the commonly reported pattern of termination of the TN in the foot (trifurcation/bifurcation) will be followed by details of variations in the origin, number, and classification of the MCN and ICN. The article will also present a short discussion of the clinical implications of variations in the TN branches in the foot in relation to the sensory distribution of these nerves.

METHODS

The study was conducted between January 2021 and October 2021. An extensive literature search was undertaken from the following indexed databases:

- Medline and PubMed (United States National Library of Medicine, Bethesda, MD);
- Scopus (Elsevier, Amsterdam, The Netherlands);
- Embase (Ovid Technologies, Inc., New York, NY);
- CINAHL Plus (EBSCO Information Services, Ipswich, MA);
- Web of Science (Clarivate Analytics, Philadelphia, PA);
- Google Scholar (Google, Inc., Mountain View, CA).

The literature search was based on key terms relevant to anatomical details of variations in the branches of the TN in the foot: “tibial nerve branches in foot”, “variations in tibial nerve branches in foot”, “terminal branches of tibial nerve”, “variations in origin of plantar nerves” and “variations in origin of calcaneal nerves”. The literature search was limited to studies with relevant information. After searching almost 80 articles and meticulously inspecting the references in each, we acknowledged a further 42 related articles, detailed analysis of which directed us to 35 highly relevant studies. In the present study, the literature was reported in accordance with the PRISMA statement and established guidelines were followed [51, 56]. All the authors searched the literature independently and they were blinded to each other’s findings. After the search was completed, the authors’ findings were compiled and final observations were prepared.

RESULTS

Variations in branching patterns of the TN and its terminal branches were noted, especially at the level of the tarsal tunnel. The sequential research history of these variations is represented in Figure 4. Trifurcation

of the TN was reported by Horwitz [34], Kim et al. [45], and Yang et al. [78] (Fig. 1). We also observed that the origin of the MCN was highly variable. The MCN has been reported to branch inside the TT [20, 23, 27, 30, 34, 41, 52, 62, 77], or proximal to it [18, 20, 57, 73, 77].

When the MCN arises proximal to the tarsal tunnel, the TN terminates in a bifurcation. Variations in the level of this bifurcation in relation to the TT (Table 1) [3, 7, 8, 15, 18, 20, 27, 31, 32, 34–36, 41, 42, 52, 54, 61, 62, 71, 73, 78] and MCA (Table 2) [3, 7, 18, 31, 52, 78] have also been documented in previous studies. Dellon and Mackinnon [20] first proposed the term MCA in 1984 as the guideline for locating the point of bifurcation of the TN. MCA is a line passing from the tip of the medial malleolus to the medial tubercle of the calcaneus. The TT was defined as extending 2 cm proximal and distal to the MCA, shown as oblique dotted lines in Figure 1.

Classification of tibial nerve bifurcation

The classification was first proposed by Bilge et al. [15] and extended by Torres and Ferreira [73] and Inthasan et al. [36]. Five types of bifurcation of the TN are distinguished on the basis of its relationship to the MCA and the TT (Fig. 2): type I — the bifurcation is proximal to the axis and inside the TT; type II — the TN bifurcates at the axis; type III — the bifurcation is distal to the axis and inside the TT; type IV — the bifurcation is proximal to the axis and outside the TT; type V — the bifurcation is distal to the axis and outside the TT. We collected data on the prevalence of the different types of bifurcation described in several studies (Table 3) [7, 15, 20, 27, 31, 32, 35, 36, 41, 52, 54, 62, 71, 73, 78].

Variations of the MCN and ICN

The more frequent variations in the mode of origin and number of branches of the MCN and ICN are tabulated (Table 4) [5, 18, 20, 21, 23, 27, 30, 31, 34–36, 41, 45, 52, 54, 57, 62, 66, 69, 71, 73, 77, 78]. The most common variant origin of the MCN is from the LPN in form of two branches. In contrast, Dellon and Mackinnon [20], Havel et al. [31], and Davis and Schon [18], concluded that the MCN arises from the MPN.

Classification of the MCN and ICN

However, very few studies on the classification of the MCN and ICN are available. Havel et al. [31], Dellon and Mackinnon [20], and Yang et al. [78] found 9, 17,

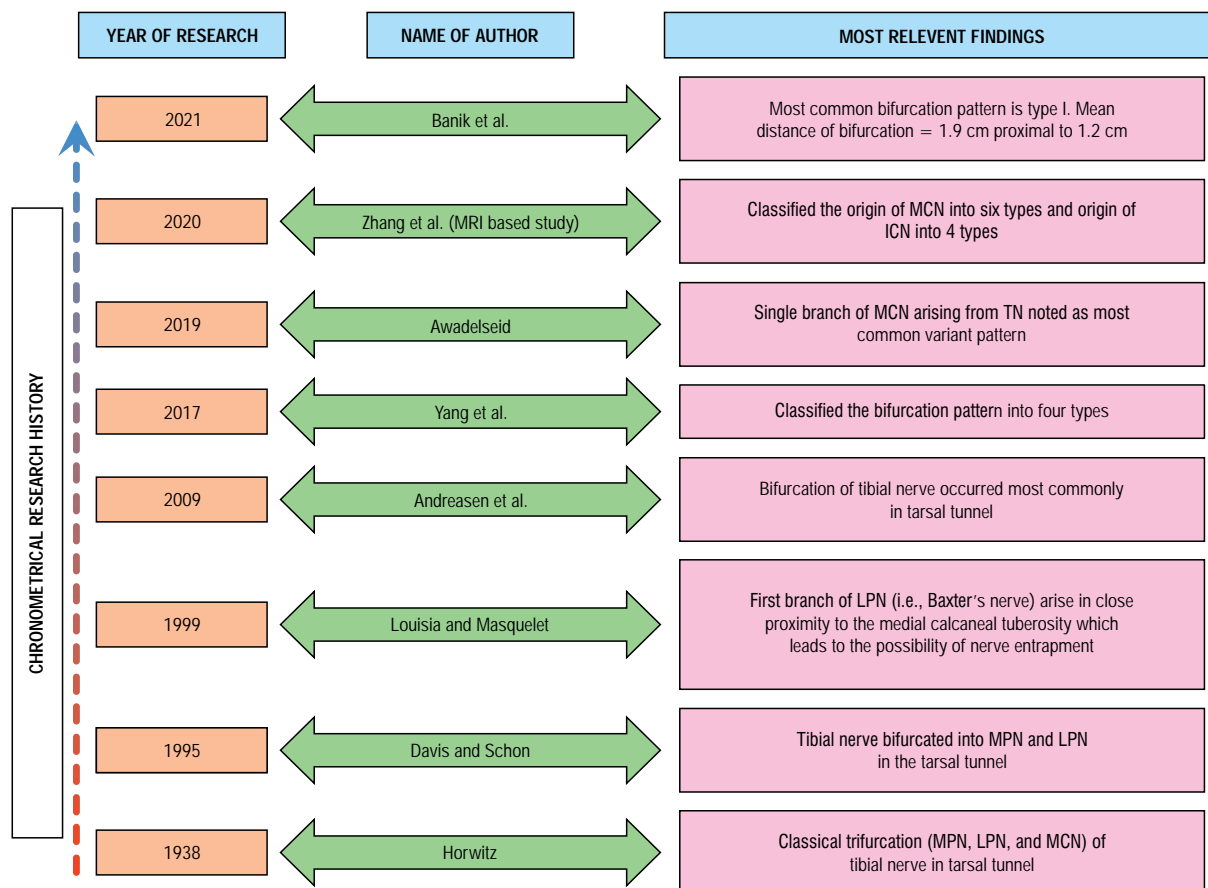


Figure 4. A timeline representation of the research history of the variations reported on branching on branching of tibial nerve (TN) in foot in a sequential manner based on chronology; ICN — inferior calcaneal nerve; LPN — lateral plantar nerve; MCN — medial calcaneal nerve; MPN — medial plantar nerve; MRI — magnetic resonance imaging.

and 21 branching patterns of the MCN respectively [20, 77, 78]. Govsa et al. [30], classified the MCN into eight types and the ICN into four types. Zhang et al. [79], used multiplanar reconstruction to obtain three-dimensional datasets of variations in the branching pattern of the MCN and ICN. Accordingly, they classified the MCN and ICN into six and three types, respectively. Classification of the MCN: type I — one MCN originating from the TN; type II — one MCN originating from the LPN; type III — two MCNs, one from the TN, and the other from the LPN; type IV — two MCNs, both originating from the TN; type V — two MCNs, with a common origin from the TN; type VI — three MCNs, one from the TN and two from the LPN. Classification of the ICN: type I — origin of ICN from the TN; type II — origin of the ICN from the bifurcation of the LPN; type III — origin of the ICN from the TN.

DISCUSSION

The pattern of termination of the TN in the foot has been well described in the literature. As well as

the usual trifurcation of the TN (i.e. MPN, LPN, and MCN) [25, 33, 43, 75], a bifurcation pattern (i.e. MPN and LPN) has also been noted if the origin of the MCN is very high or low [20, 21, 30, 75]. Authors have classified the bifurcation of TN into five types, of which type I (bifurcation proximal to the MCA but in the TT) is most frequent [7, 15, 32, 35, 36, 41, 52, 54, 71, 77, 78]. Some have also measured the distance of the bifurcation from the MCA and found it usually to be within 2 cm proximal to the axis [7, 18, 52, 77]. Research on this topic has gained momentum and some recent studies have classified variant origins of the MCN and ICN [30, 78, 79], emphasizing the risk of symptomatic nerve entrapment if they lie near the TT or the medial calcaneal tuberosity, respectively. All these variations in the termination of the TN in the foot are crucial to making the best treatment decision for intractable heel pain (especially medial and inferior aspects of the heel), which is very commonly reported these days.

Table 1. A chronological representation of the point of bifurcation of the tibial nerve in relation to the tarsal tunnel as reported in published literature

Author, year [reference]	Type and no. of sample	Bifurcation proximal to the tarsal tunnel (%)	Bifurcation in the tarsal tunnel (%)	Bifurcation distal to the tarsal tunnel (%)
Horwitz, 1938 [34]	100 feet	4	96	–
Dellon and Mackinnon, 1984 [20]	31 feet	6	94	–
Heimkes et al., 1987 [32]	60 feet	–	100	–
Havel et al., 1988 [31]	68 feet	7	93	–
Nagoaka, 1990 [61]	62 feet	15	85	–
Bareither et al., 1990 [8]	126 feet	31	69	–
Davis and Schon, 1995 [18]	20 feet	10	90	–
Louisia and Masquelet, 1999 [52]	15 feet	27	73	–
Bilge et al., 2003 [15]	50 feet	–	96	4
Ndiaye et al., 2003 [62]	20 feet	10	90	–
Fernandes et al., 2006 [27]	30 feet	10	86.7	3.3
Joshi et al., 2006 [41]	112 feet	–	99.9	0.89
Andreasen Struijk et al., 2010 [3]	10 feet	10	80	10
Torres and Ferreira, 2012 [73]	50 feet	12	88	–
Malar, 2016 [54]	20 feet	–	100	–
Tamang et al., 2016 [71]	30 feet	–	100	–
Kalpana and Komala, 2017 [42]	50 lower limbs	92	6	2
Yang et al., 2017 [78]	60 cases	18	82	–
Iborra et al., 2018 [35]	12 feet	8.3	91.7	–
Inthasan et al., 2020 [36]	40 legs	50	50	–
Banik and Guria, 2021 [7]	10 lower limbs	–	100	–

Table 2. A chronological representation of the distance of bifurcation of the tibial nerve from the malleolar-calcaneal axis as reported in published literature

Author, year [reference]	Type and no. of sample	Mean distance of bifurcation of tibial nerve from malleolar-calcaneal axis				
		Proximal to the axis		At the axis	Distal to the axis	
		≤ 2 cm	> 2 cm		≤ 2 cm	> 2 cm
Havel et al., 1988 [31]	68 feet	45.5	7.3	38.2	8.8	–
Davis and Schon, 1995 [18]	20 feet	90	10	–	–	–
Louisia and Masquelet, 1999 [52]	15 feet	33.3	26.7	33.3	6.7	–
Andreasen et al., 2010 [3]	10 feet	–	10	80	–	10
Yang et al., 2017 [78]	60 cases					
Banik and Guria, 2021 [7]	20 lower limbs	55	–	30	15	–

Values are presented as percentages.

Clinical presentation of heel pain due to plantar nerve (MPN and/or LPN) compression

The origin of MPN as one of the terminal branches of the TN within the TT (both in trifurcation and bifurcation pattern of TN termination) has been uniformly reported in published literature [11, 20, 25, 28, 77]. The MPN can be compressed deep to the flexor retinaculum, adjacent to the crossover point of the flexor

digitorum longus and flexor hallucis longus tendons (master knot of Henry) [19, 53]. The MPN can be compressed by regular and repetitive eversion of the foot, common among runners. The condition presents as pain along the medial side of the sole (medial plantar neuropraxia) and around the navicular tuberosity (Jogger's foot) [26, 59]. Entrapment of the MPN in a clinical setting is popularly referred to as "Jogger's

Table 3. A chronological representation of the findings of various studies regarding classification of bifurcation into types as reported in published literature

Author, year [reference]	Type I	Type II	Type III	Type IV	Type V
Dellon and Mackinnon, 1984 [20]	22.58	54.84	16.13	6.45	–
Heimkes et al., 1987 [32]	100	–	–	–	–
Havel et al., 1988 [31]	45.59	38.24	8.82	7.35	–
Louisia and Masquelet, 1999 [52]	37.7	28.6	7.1	28.6	–
Ndiaye et al., 2003 [62]	–	–	90	10	–
Bilge et al., 2003 [15]	84	12	–	–	–
Joshi et al., 2006 [41]	85.2	14.7	0.89	–	–
Fernandes et al., 2006 [27]	23.34	33.33	30	10	3.33
Torres and Ferreira, 2012 [73]	52	14	22	12	–
Malar, 2016 [54]	85	10	5	–	–
Tamang et al., 2016 [71]	90	10	–	–	–
Yang et al., 2017 [78]	70	7	–	18	–
Iborra et al., 2018 [35]	91.7	–	–	8.3	–
Inthasan et al., 2020 [36]	50	–	–	50	–
Banik and Guria, 2021 [7]	55	30	15	–	–

Values are presented as percentages. For description of the types mentioned in the table, please refer to Results section of the text, subheading: classification of tibial nerve bifurcation

foot” [17, 26, 59]. This condition is characterized by chronic pain along the middle portion of the plantar surface of the foot (typically the pain radiates along the medial longitudinal arch), a burning sensation in the heel and tenderness over the area corresponding to the site of nerve compression (proximal part of the medial longitudinal arch beneath the navicular bone) [22, 48, 70]. All these clinical manifestations are attributed to the sensory distribution of the MPN in the foot (Fig. 3) [68]. The clinical condition (Jogger’s foot) is typically reported among joggers and long distance and marathon runners. As such, marathon training and average weekly running of over 20 km increase the risk of developing the condition [76]. A person with a flat foot is particularly predisposed to it because the risk of nerve injury/compression is greater when the foot touches the ground with force [12, 26, 53].

Isolated compression of the LPN or its branches is uncommon (apart from Baxter neuropathy) because, as with the MPN, the origin of the LPN as a terminal branch of the TN shows little or no variation (in both the trifurcation and bifurcation patterns of TN termination) according to published reports [11, 20, 25, 28, 77]. The LPN is usually compressed along with the MPN in tarsal tunnel syndrome, mostly following trauma (ankle sprain/fracture) in and around the ankle region. The condition presents clinically

as paraesthesia along the sole [63]. In other words any compression of the LPN is usually associated with compression of the MPN [26, 50]. A tendency to overpronate during walking or running whereby the foot rolls to a considerable extent, is associated with an increased risk of LPN compression [2]. As the symptoms overlap with plantar nerve compression, a reliable method for identifying LPN compression is to elicit the associated area of tenderness. In LPN entrapment there is palpable tenderness along the medial side of the heel over the plantar surface and the area corresponding to the abductor hallucis muscle. In a clinical setting, it is important to differentiate plantar nerve compression (MPN and/or LPN) from plantar fasciitis and TT syndrome [2, 14, 70]. Plantar fasciitis, although common among runners but may also affect person with sedentary lifestyle [33]. It is a self-limiting condition and is associated with heel pain that is aggravated by activity (weight bearing) after episodes of rest [29]. On the other hand heel pain in MPN/LPN compression is constant, with or without weight bearing [29]. Tarsal tunnel syndrome is a rare condition with diagnosis seldom established. The condition is more commonly reported in females and can involve any age group [44]. The Tinel sign, which is characteristic of TT syndrome is commonly used in the clinical setting to differentiate the condition from plantar nerve compression [37, 38].

Table 4. A chronological representation of the most frequent origin and the number of branches of the calcaneal nerves (MCN and ICN) as reported in published literature

Author, year [reference]	Most frequent pattern			
	MPN		ICN	
	Origin	No. of branches	Origin	No. of branches
Horwitz, 1938 [34]	LPN	–	–	–
Dellon and Mackinnon, 1984 [20]	LPN	2 branches	–	–
Rondhuis and Hudson, 1986 [66]	TN	1 branch	–	–
Didia et al., 1990 [23]	TN	2 branches	–	–
Davis and Schon, 1995 [18]	TN	2–3 branches	LPN	–
Havel et al., 1988 [31]	TN	1 branch	–	–
Louisia and Masquelet, 1999 [52]	TN	2 branches	LPN	2 branches
Moraes Filho et al., 2000 [57]	TN	1 branch	–	–
Fernandes et al., 2006 [27]	TN	2 branches	–	–
Dellon et al., 2002 [21]	TN	2 branches	–	–
Ndiaye et al., 2003 [62]	TN	1 branch	–	–
Joshi et al., 2006 [41]	TN	1–2 branches	–	–
Govsa et al., 2006 [30]	TN	2 branches	TN	1 branch
Torres and Ferreira, 2012 [73]	TN	1 branch	LPN	1 branch
Kim et al., 2015 [45]	TN	2 branches	LPN	1 branch
Sharma et al., 2015 [69]	TN	2 branches	–	–
Malar, 2016 [54]	TN	2 branches	–	–
Tamang et al., 2016 [71]	LPN	2 branches	–	–
Yang et al., 2017 [78]	LPN	2 branches	–	–
Iborra et al., 2018 [35]	–	–	LPN	–
Awadelseid, 2019 [5]	TN	1 branch	–	–
Inthasan et al., 2020 [36]	TN	3 branches	LPN	1 branch
Warchol et al., 2021 [77]	TN	1 branch	–	–

ICN — inferior calcaneal nerve; LPN — lateral plantar nerve; MPN — medial plantar nerve; TN — tibial nerve

The risk of compression of the calcaneal nerves (MCN/ICN) and the clinical presentation of heel pain in such condition

Variations in the origin of MCN have been reported, but the nerve commonly arises as a branch of the TN [11, 20, 25, 28, 77]. The proximity of the origin of the MCN to the TT determines the risk of entrapment and subsequent compression of the nerve [10, 24, 28]. In other words, the risk of compression of the MCN is greater in the trifurcation pattern of TN termination. Entrapment and compression of the MCN is associated with over-pronation during walking or sustained pressure from ill-fitting shoes. The condition presents as heel pain, exaggerated after running or standing for long periods, and mimics “Jogger’s foot” to an extent [67, 74]. Chronic heel pain due to compression of the MCN can present with symptoms overlapping those of plantar fasciitis and Jogger’s

foot [10, 47]. It can present among runners/joggers with a prolonged history of ill-fitting shoes [2, 43]. As with Jogger’s foot, patient often complains of pain radiating along the sole to the medial arch of the foot [1, 72]. However, heel pain due to MCN compression is aggravated by activity. i.e. running/walking (unlike Jogger’s foot but similar to plantar fasciitis) [29, 40]. MCN compression can be differentiated from plantar fasciitis by eliciting palpable tenderness over the medial malleolus [55].

The origin of the ICN is very variable as reported in research articles [11, 20, 25, 28, 77]. However, this nerve is at maximum risk of compression when it arises as a branch of the LPN (first branch of LPN/Baxter’s nerve) [4, 79]. The ICN can be compressed secondary to micro trauma (calcaneal spur/ internal foot derangement) or to plantar fasciitis [58]. The increased risk can be attributed to the proximity of

the flexor retinaculum or TT in the foot and the compression of this nerve presents as pain around the anterior aspect of the calcaneus (heel pain) and the condition is known as Baxter neuropathy [52, 58]. The patient presents with heel pain that radiates along the inner aspect of the calcaneus to the medial arch of foot [26, 60]. The diagnosis is established by eliciting tenderness of the nerve on the inside of the heel and a positive Tinel's sign [10, 39, 64].

The plantar aspect of the foot particularly on the medial side is very relevant in terms of clinical anatomy of pain experienced in the area due to a number of pathological conditions. Clinical examination along with sound knowledge of anatomical details are key elements in ensuring a proper diagnosis. Therefore, the authors are hopeful that the cumulative data concerning these variations will serve as a guide to preventing misdiagnosis of several conditions (Jogger's foot/Plantar fasciitis/neuroma) that present as heel pain.

Limitations of the study

We concede that the present study is a narrative review and, therefore, has its limitations. We have tried to present comprehensive data on this research topic, but a further evidence based meta-analysis which be clinically beneficial.

CONCLUSIONS

The commonest pattern of termination of the TN in the foot is bifurcation. The most frequent type of bifurcation type I, entails an increased risk of nerve entrapment in the TT. As the distance of the specific bifurcation point ranged from 3 cm proximal to 3 cm distal to the MCA, a point outside this region was assumed to be relatively safe for invasive procedures in the medial aspect of the ankle.

The MCN has invariably been observed to originate from the LPN as two branches. This fact should be considered during decompression surgeries for TT syndrome and when selecting the injection site for therapeutic TN block for chronic heel pain.

Although ICN is not involved in direct sensory innervation of the calcaneal region, variations in its origin of ICN should be kept in mind because its compression can cause pain and difficulty in walking. It also causes the patient to assume the antalgic position of foot while walking, increasing the risk of injury. Therefore, looking at the complexity of the branches of the TN in foot, clinicians should re-evaluate plan-

tar fasciitis patients and deem the MCN and ICN the probable causes of refractory heel pain.

Acknowledgements

The authors would like to mention that the studies included in this review are based on findings from dissection of precious human tissues. Therefore, we as authors of this review article are equally grateful to those who donated their bodies to science so that anatomical research could be performed. Results from such research can potentially increase mankind's overall knowledge that can then improve patient care. Therefore, these donors and their families deserve our highest gratitude [37].

Conflict of interest: None declared

REFERENCES

1. Aldridge T. Diagnosing heel pain in adults. *Am Fam Physician*. 2004; 70(2): 332–338, indexed in Pubmed: [15291091](#).
2. Alshami AM, Souvlis T, Coppieters MW. A review of plantar heel pain of neural origin: differential diagnosis and management. *Man Ther*. 2008; 13(2): 103–111, doi: [10.1016/j.math.2007.01.014](#), indexed in Pubmed: [17400020](#).
3. Andreasen Struijk LNS, Birn H, Teglbjaerg PS, et al. Size and separability of the calcaneal and the medial and lateral plantar nerves in the distal tibial nerve. *Anat Sci Int*. 2010; 85(1): 13–22, doi: [10.1007/s12565-009-0045-y](#), indexed in Pubmed: [19449089](#).
4. Arbab D, Bouillon B, Lüring C, et al. [Plantar fascia release and decompression of the first branch of the lateral plantar nerve (Baxter's nerve)]. *Oper Orthop Traumatol*. 2021; 33(6): 517–524, doi: [10.1007/s00064-021-00720-z](#), indexed in Pubmed: [34255092](#).
5. Awadelseid K. Branching pattern of the medial calcaneal neurovascular bundle in porta pedis of the human foot. *Int J Hum Anatom*. 2019; 1(4): 2–12, doi: [10.14302/issn.2577-2279.ijha-19-3013](#).
6. Bailie D, Kelikian A. Tarsal tunnel syndrome: diagnosis, surgical technique, and functional outcome. *Foot Ankle Int*. 2016; 19(2): 65–72, doi: [10.1177/107110079801900203](#).
7. Banik S, Guria LR. Variable branching pattern of tibial nerve in the tarsal tunnel: a gross anatomical study with clinical implications. *Cureus*. 2021; 13(3): e13729, doi: [10.7759/cureus.13729](#), indexed in Pubmed: [33717767](#).
8. Bareither DJ, Genau JM, Massaro JC. Variation in the division of the tibial nerve: application to nerve blocks. *J Foot Surg*. 1990; 29(6): 581–583, indexed in Pubmed: [2292650](#).
9. Barrett SL. A guide to neurogenic etiologies of heel pain. *Podiatry Today*. 2005; 18: 36–44.
10. Barrett SL, Reese MM, Tassone J, et al. The use of low-energy radial shockwave in the treatment of entrapment neuropathy of the medial calcaneal nerve: a pilot study. *Foot Ankle Spec*. 2008; 1(4): 231–242, doi: [10.1177/1938640008320930](#), indexed in Pubmed: [19825723](#).
11. Barrett SL, Sohani S, DuCasse S, et al. Midarch foot pain: entrapment neuropathy of the distal medial plantar nerve and its branches. *J Am Podiatr Med Assoc*. 2021; 111(2), doi: [10.7547/19-036](#), indexed in Pubmed: [33872364](#).

12. Baxter DE, Zingas C. The foot in running. *J Am Acad Orthop Surg.* 1995; 3(3): 136–145, doi: [10.5435/00124635-199505000-00003](https://doi.org/10.5435/00124635-199505000-00003), indexed in Pubmed: [10790662](https://pubmed.ncbi.nlm.nih.gov/10790662/).
13. Baxter DE, Pfeffer GB. Treatment of chronic heel pain by surgical release of the first branch of the lateral plantar nerve. *Clin Orthop Relat Res.* 1992(279): 229–236, indexed in Pubmed: [1600660](https://pubmed.ncbi.nlm.nih.gov/1600660/).
14. Bhatti UN, Khan SHm, Zubairy AI. Managing the patient with heel pain. *Br J Hosp Med (Lond).* 2019; 80(4): 196–200, doi: [10.12968/hmed.2019.80.4.196](https://doi.org/10.12968/hmed.2019.80.4.196), indexed in Pubmed: [30951414](https://pubmed.ncbi.nlm.nih.gov/30951414/).
15. Bilge O, Ozer MA, Govsa F. Neurovascular branching in the tarsal tunnel. *Neuroanatomy.* 2003; 2: 39–41.
16. Chundru U, Liebeskind A, Seidelmann F, et al. Plantar fasciitis and calcaneal spur formation are associated with abductor digiti minimi atrophy on MRI of the foot. *Skeletal Radiol.* 2008; 37(6): 505–510, doi: [10.1007/s00256-008-0455-2](https://doi.org/10.1007/s00256-008-0455-2), indexed in Pubmed: [18286281](https://pubmed.ncbi.nlm.nih.gov/18286281/).
17. Collins MS, Tiegs-Heiden CA, Frick MA. MRI appearance of jogger's foot. *Skeletal Radiol.* 2020; 49(12): 1957–1963, doi: [10.1007/s00256-020-03494-w](https://doi.org/10.1007/s00256-020-03494-w), indexed in Pubmed: [32556951](https://pubmed.ncbi.nlm.nih.gov/32556951/).
18. Davis TJ, Schon LC. Branches of the tibial nerve: anatomic variations. *Foot Ankle Int.* 1995; 16(1): 21–29, doi: [10.1177/107110079501600105](https://doi.org/10.1177/107110079501600105), indexed in Pubmed: [7697149](https://pubmed.ncbi.nlm.nih.gov/7697149/).
19. Delfaut EM, Demondion X, Bieganski A, et al. Imaging of foot and ankle nerve entrapment syndromes: from well-demonstrated to unfamiliar sites. *Radiographics.* 2003; 23(3): 613–623, doi: [10.1148/rg.233025053](https://doi.org/10.1148/rg.233025053), indexed in Pubmed: [12740464](https://pubmed.ncbi.nlm.nih.gov/12740464/).
20. Dellon AL, Mackinnon SE. Tibial nerve branching in the tarsal tunnel. *Arch Neurol.* 1984; 41(6): 645–646, doi: [10.1001/archneur.1984.04210080053013](https://doi.org/10.1001/archneur.1984.04210080053013), indexed in Pubmed: [6721738](https://pubmed.ncbi.nlm.nih.gov/6721738/).
21. Dellon AL, Kim J, Spaulding CM. Variations in the origin of the medial calcaneal nerve. *J Am Podiatr Med Assoc.* 2002; 92(2): 97–101, doi: [10.7547/87507315-92-2-97](https://doi.org/10.7547/87507315-92-2-97), indexed in Pubmed: [11847261](https://pubmed.ncbi.nlm.nih.gov/11847261/).
22. Dellon AL. The four medial ankle tunnels: a critical review of perceptions of tarsal tunnel syndrome and neuropathy. *Neurosurg Clin N Am.* 2008; 19(4): 629–648, doi: [10.1016/j.nec.2008.07.003](https://doi.org/10.1016/j.nec.2008.07.003), indexed in Pubmed: [19010287](https://pubmed.ncbi.nlm.nih.gov/19010287/).
23. Didia BC, Horsefall AU. Medial calcaneal nerve. An anatomical study. *J Am Podiatr Med Assoc.* 1990; 80(3): 115–119, doi: [10.7547/87507315-80-3-115](https://doi.org/10.7547/87507315-80-3-115), indexed in Pubmed: [2332828](https://pubmed.ncbi.nlm.nih.gov/2332828/).
24. Diers DJ. Medial calcaneal nerve entrapment as a cause for chronic heel pain. *Physiother Theory Pract.* 2008; 24(4): 291–298, doi: [10.1080/09593980701738392](https://doi.org/10.1080/09593980701738392), indexed in Pubmed: [18574754](https://pubmed.ncbi.nlm.nih.gov/18574754/).
25. Erickson SJ, Quinn SF, Kneeland JB, et al. MR imaging of the tarsal tunnel and related spaces: normal and abnormal findings with anatomic correlation. *AJR Am J Roentgenol.* 1990; 155(2): 323–328, doi: [10.2214/ajr.155.2.2115260](https://doi.org/10.2214/ajr.155.2.2115260), indexed in Pubmed: [2115260](https://pubmed.ncbi.nlm.nih.gov/2115260/).
26. Ferkel E, Davis WH, Ellington JK. Entrapment neuropathies of the foot and ankle. *Clin Sports Med.* 2015; 34(4): 791–801, doi: [10.1016/j.csm.2015.06.002](https://doi.org/10.1016/j.csm.2015.06.002), indexed in Pubmed: [26409596](https://pubmed.ncbi.nlm.nih.gov/26409596/).
27. Fernandes RMP, Mozella A, Dias M, et al. Anatomical study of the tibial nerve in the tarso-tunnel. *Rev Bras Ortop.* 2006; 41(7): 272–277.
28. Ghosh SK, Raheja S, Tuli A. Potential sites of compression of tibial nerve branches in foot: a cadaveric and imaging study. *Clin Anat.* 2013; 26(6): 768–779, doi: [10.1002/ca.22203](https://doi.org/10.1002/ca.22203), indexed in Pubmed: [23255292](https://pubmed.ncbi.nlm.nih.gov/23255292/).
29. Goff JD, Crawford R. Diagnosis and treatment of plantar fasciitis. *Am Fam Physician.* 2011; 84(6): 676–682, indexed in Pubmed: [21916393](https://pubmed.ncbi.nlm.nih.gov/21916393/).
30. Govsa F, Bilge O, Ozer MA. Variations in the origin of the medial and inferior calcaneal nerves. *Arch Orthop Trauma Surg.* 2006; 126(1): 6–14, doi: [10.1007/s00402-005-0088-z](https://doi.org/10.1007/s00402-005-0088-z), indexed in Pubmed: [16333630](https://pubmed.ncbi.nlm.nih.gov/16333630/).
31. Havel PE, Ebraheim NA, Clark SE, et al. Tibial nerve branching in the tarsal tunnel. *Foot Ankle.* 1988; 9(3): 117–119, doi: [10.1177/107110078800900304](https://doi.org/10.1177/107110078800900304), indexed in Pubmed: [2852629](https://pubmed.ncbi.nlm.nih.gov/2852629/).
32. Heimkes B, Posel P, Stotz S, et al. The proximal and distal tarsal tunnel syndromes. An anatomical study. *Int Orthop.* 1987; 11(3): 193–196, doi: [10.1007/BF00271447](https://doi.org/10.1007/BF00271447), indexed in Pubmed: [3623755](https://pubmed.ncbi.nlm.nih.gov/3623755/).
33. Horobin L. Diagnosis and treatment of jogger's heel. *Emerg Nurse.* 2015; 22(9): 18–23, doi: [10.7748/en.22.9.18.e1401](https://doi.org/10.7748/en.22.9.18.e1401), indexed in Pubmed: [25659794](https://pubmed.ncbi.nlm.nih.gov/25659794/).
34. Horwitz M. Normal anatomy and variations of the peripheral nerves of the leg and foot. *Arch Surg.* 1938; 36(4): 626, doi: [10.1001/archsurg.1938.01190220068005](https://doi.org/10.1001/archsurg.1938.01190220068005).
35. Iborra A, Villanueva M, Barrett SL, et al. Anatomic delineation of tarsal tunnel innervation via ultrasonography. *J Ultrasound Med.* 2018; 37(6): 1325–1334, doi: [10.1002/jum.14499](https://doi.org/10.1002/jum.14499), indexed in Pubmed: [29205431](https://pubmed.ncbi.nlm.nih.gov/29205431/).
36. Inthasan C, Vaseenon T, Mahakkanukrauh P. Anatomical study and branching point of neurovascular structures at the medial side of the ankle. *Anat Cell Biol.* 2020; 53(4): 422–434, doi: [10.5115/acb.20.087](https://doi.org/10.5115/acb.20.087), indexed in Pubmed: [32814704](https://pubmed.ncbi.nlm.nih.gov/32814704/).
37. Iwanaga J, Singh V, Ohtsuka A, et al. Acknowledging the use of human cadaveric tissues in research papers: Recommendations from anatomical journal editors. *Clin Anat.* 2021; 34(1): 2–4, doi: [10.1002/ca.23671](https://doi.org/10.1002/ca.23671), indexed in Pubmed: [32808702](https://pubmed.ncbi.nlm.nih.gov/32808702/).
38. Jabre JF, Dillard JW, Salzsieder BT, et al. The use of multiple Tinel's sign in the identification of patients with peripheral neuropathy. *Electromyogr Clin Neurophysiol.* 1995; 35(3): 131–136, indexed in Pubmed: [7649059](https://pubmed.ncbi.nlm.nih.gov/7649059/).
39. Jaring MRF, Khan AZ, Livingstone JA, et al. A case of bilateral Baxter's neuropathy secondary to plantar fasciitis. *J Foot Ankle Surg.* 2019; 58(4): 771–774, doi: [10.1053/j.jfas.2018.11.010](https://doi.org/10.1053/j.jfas.2018.11.010), indexed in Pubmed: [31027970](https://pubmed.ncbi.nlm.nih.gov/31027970/).
40. Jeswani T, Morlese J, McNally EG. Getting to the heel of the problem: plantar fascia lesions. *Clin Radiol.* 2009; 64(9): 931–939, doi: [10.1016/j.crad.2009.02.020](https://doi.org/10.1016/j.crad.2009.02.020), indexed in Pubmed: [19664484](https://pubmed.ncbi.nlm.nih.gov/19664484/).
41. Joshi SS, Joshi SD, Athavale AS. Anatomy of tarsal tunnel and its applied significance. *J Anat Soc India.* 2006; 55(1): 52–56.
42. Kalpana R, Komala N. Branching pattern of tibial nerve in the tarsal tunnel: a cadaveric study. *Nat J Clin Anat.* 2017; 6(2): 120–125, doi: [10.1055/s-0039-1700734](https://doi.org/10.1055/s-0039-1700734).
43. Khan MN, Jacobs BC, Ashbaugh S. Considerations in footwear and orthotics. *Prim Care.* 2013; 40(4): 1001–1012, doi: [10.1016/j.pop.2013.08.013](https://doi.org/10.1016/j.pop.2013.08.013), indexed in Pubmed: [24209730](https://pubmed.ncbi.nlm.nih.gov/24209730/).
44. Khedr EM, Fawi G, Abbas MAA, et al. Prevalence of common types of compression neuropathies in qena governorate/egypt: a population-based survey. *Neuroepidemiology.* 2016; 46(4): 253–260, doi: [10.1159/000444641](https://doi.org/10.1159/000444641), indexed in Pubmed: [26974980](https://pubmed.ncbi.nlm.nih.gov/26974980/).
45. Kim DI, Kim YS, Han SH. Topography of human ankle joint: focused on posterior tibial artery and tibial nerve. *Anat Cell Biol.* 2015; 48(2): 130–137, doi: [10.5115/acb.2015.48.2.130](https://doi.org/10.5115/acb.2015.48.2.130), indexed in Pubmed: [26140224](https://pubmed.ncbi.nlm.nih.gov/26140224/).
46. Kosinski C. The course, mutual relations and distribution of the cutaneous nerves of the metatarsal region of leg

- and foot. *J Anat.* 1926; 60(Pt 3): 274–297, indexed in Pubmed: [17104102](#).
47. Kuran B, Aydoğ T, Erçalık C, et al. Medial calcaneal neuropathy: A rare cause of prolonged heel pain. *Agri.* 2017; 29(1): 43–46, doi: [10.5505/agri.2015.13540](#), indexed in Pubmed: [28467569](#).
 48. Kushner S, Reid DC. Medial tarsal tunnel syndrome: a review. *J Orthop Sports Phys Ther.* 1984; 6(1): 39–45, doi: [10.2519/jospt.1984.6.1.39](#), indexed in Pubmed: [18806381](#).
 49. Lam SJ. A tarsal-tunnel syndrome. *Lancet.* 1962; 2(7270): 1354–1355, doi: [10.1016/s0140-6736\(62\)91024-3](#), indexed in Pubmed: [13928212](#).
 50. Lareau CR, Sawyer GA, Wang JH, et al. Plantar and medial heel pain: diagnosis and management. *J Am Acad Orthop Surg.* 2014; 22(6): 372–380, doi: [10.5435/JAAOS-22-06-372](#), indexed in Pubmed: [24860133](#).
 51. Liberati A, Altman DG, Tetzlaff J, et al. The PRISMA statement for reporting systematic reviews and meta-analyses of studies that evaluate health care interventions: explanation and elaboration. *PLoS Med.* 2009; 6(7): e1000100, doi: [10.1371/journal.pmed.1000100](#), indexed in Pubmed: [19621070](#).
 52. Louisiana S, Masquelet AC. The medial and inferior calcaneal nerves: an anatomic study. *Surg Radiol Anat.* 1999; 21(3): 169–173, doi: [10.1007/BF01630895](#), indexed in Pubmed: [10431329](#).
 53. Maeseneer M, Madani H, Lenchik L, et al. Normal anatomy and compression areas of nerves of the foot and ankle: US and MR imaging with anatomic correlation. *Radiographics.* 2015; 35(5): 1469–1482, doi: [10.1148/rg.2015150028](#), indexed in Pubmed: [26284303](#).
 54. Malar D. A study of tibial nerve bifurcation and branching pattern of calcaneal nerve in the tarsal tunnel. *Int J Anat Res.* 2016; 4(1): 2034–2036, doi: [10.16965/ijar.2016.139](#).
 55. McClinton SM, Flynn TW, Heiderscheid BC, et al. Comparison of usual podiatric care and early physical therapy intervention for plantar heel pain: study protocol for a parallel-group randomized clinical trial. *Trials.* 2013; 14: 414, doi: [10.1186/1745-6215-14-414](#), indexed in Pubmed: [24299257](#).
 56. Moher D, Liberati A, Tetzlaff J, et al. PRISMA Group. Preferred reporting items for systematic reviews and meta-analyses: the PRISMA Statement. *Open Med.* 2009; 3(3): e123–e130, indexed in Pubmed: [21603045](#).
 57. Moraes Filho DC, Galbiatti JA, Fialho HAS. Avaliação anatômica do túnel do tarso. *Rev Bras de Ortop.* 2000; 35(8): 282–289.
 58. Moroni S, Zwierzina M, Starke V, et al. Clinical-anatomic mapping of the tarsal tunnel with regard to Baxter's neuropathy in recalcitrant heel pain syndrome: part I. *Surg Radiol Anat.* 2019; 41(1): 29–41, doi: [10.1007/s00276-018-2124-z](#), indexed in Pubmed: [30368565](#).
 59. Murphy PC, Baxter DE. Nerve entrapment of the foot and ankle in runners. *Clin Sports Med.* 1985; 4(4): 753–763, indexed in Pubmed: [4053199](#).
 60. Nakano H, Shima H, Tei K, et al. Ultrasound-assisted near nerve method in nerve conduction study for the diagnosis of tarsal tunnel syndrome. A case report. *Clin Neurophysiol Pract.* 2020; 5: 135–138, doi: [10.1016/j.cnp.2020.06.002](#), indexed in Pubmed: [32715164](#).
 61. Nagaoka M. [An anatomical study of tarsal tunnel]. *Nihon Seikeigeka Gakkai Zasshi.* 1990; 64(4): 208–216, indexed in Pubmed: [2380586](#).
 62. Ndiaye A, Dia A, Konate I, et al. Topographic anatomy of the tibial nerve in the medial malleolus: application to the effect of nerve block anesthesia. *Morphologie.* 2003; 87(277): 25–27.
 63. Oh SJ, Kwon KH, Hah JS, et al. Lateral plantar neuropathy. *Muscle Nerve.* 1999; 22(9): 1234–1238, doi: [10.1002/\(sici\)1097-4598\(199909\)22:9<1234::aid-mus10>3.0.co;2-3](#), indexed in Pubmed: [10454719](#).
 64. Park TA, Del Toro DR. Isolated inferior calcaneal neuropathy. *Muscle Nerve.* 1996; 19(1): 106–108, doi: [10.1002/\(SICI\)1097-4598\(199601\)19:1<106::AID-MUS18>3.0.CO;2-U](#), indexed in Pubmed: [8538658](#).
 65. Przylucki H, Jones CL. Entrapment neuropathy of muscle branch of lateral plantar nerve: a cause of heel pain. *J Am Podiatry Assoc.* 1981; 71(3): 119–124, doi: [10.7547/87507315-71-3-119](#), indexed in Pubmed: [7204858](#).
 66. Rondhuis JJ, Huson A. The first branch of the lateral plantar nerve and heel pain. *Acta Morphol Neerl Scand.* 1986; 24(4): 269–279, indexed in Pubmed: [3425404](#).
 67. Rose JD, Malay DS, Sorrento DL. Neurosensory testing of the medial calcaneal and medial plantar nerves in patients with plantar heel pain. *J Foot Ankle Surg.* 2003; 42(4): 173–177, doi: [10.1016/s1067-2516\(03\)70025-8](#), indexed in Pubmed: [12907926](#).
 68. Standring S. *Gray's Anatomy: The anatomical basis of clinical practice.* 42nd Ed. Elsevier, London 2020.
 69. Sharma S, Khullar M, Bhardwaj S. Variations in the Origin and Number of Medial Calcaneal Nerve. *Int J Med Dent Sci.* 2015; 4(2): 842, doi: [10.19056/ijmdsjssmes/2015/v4i2/79814](#).
 70. Singh G, Kumar VP. Neuroanatomical basis for the tarsal tunnel syndrome. *Foot Ankle Int.* 2012; 33(6): 513–518, doi: [10.3113/FAI.2012.0513](#), indexed in Pubmed: [22735326](#).
 71. Tamang B, Sinha P, Bhutia K, et al. Neurovascular relation and origin of medial calcaneal nerve in the tarsal tunnel in embalmed cadavers of eastern india. *Ann Int Med Dent Res.* 2016; 2(6): 19–22, doi: [10.21276/aimdr.2016.2.6.at5](#).
 72. Thomas JL, Christensen JC, Kravitz SR, et al. American College of Foot and Ankle Surgeons heel pain committee. The diagnosis and treatment of heel pain: a clinical practice guideline-revision 2010. *J Foot Ankle Surg.* 2010; 49(3 Suppl): S1–19, doi: [10.1053/j.jfas.2010.01.001](#), indexed in Pubmed: [20439021](#).
 73. Torres AL, Ferreira MC. Study of the anatomy of the tibial nerve and its branches in the distal medial leg. *Acta Ortop Bras.* 2012; 20(3): 157–164, doi: [10.1590/S1413-78522012000300005](#), indexed in Pubmed: [24453596](#).
 74. Tu P. Heel pain: diagnosis and management. *Am Fam Physician.* 2018; 97: 86–93.
 75. Ulcay T, Uzun A, Ziyilan T. The origin and branching of medial calcaneal nerve in newborn fetuses. *J Anat Soc India.* 2014; 63: S1–S5.
 76. Vasiliadis AV, Kazas C, Tsalidou M, et al. Plantar injuries in runners: is there an association with weekly running volume? *Cureus.* 2021; 13(8): e17537, doi: [10.7759/cureus.17537](#), indexed in Pubmed: [34646594](#).
 77. Warchol Ł, Walocha JA, Mizia E, et al. Ultrasound-guided topographic anatomy of the medial calcaneal branches of the tibial nerve. *Folia Morphol.* 2021; 80(2): 267–274, doi: [10.5603/FM.a2020.0062](#), indexed in Pubmed: [32488855](#).
 78. Yang Y, Du ML, Fu YS, et al. Fine dissection of the tarsal tunnel in 60 cases. *Sci Rep.* 2017; 7(1): 46351, doi: [10.1038/srep46351](#), indexed in Pubmed: [28398291](#).
 79. Zhang Y, He X, Li J, et al. An MRI study of the tibial nerve in the ankle canal and its branches: a method of multiplanar reformation with 3D-FIESTA-C sequences. *BMC Med Imaging.* 2021; 21(1): 51, doi: [10.1186/s12880-021-00582-8](#), indexed in Pubmed: [33731040](#).

Pneumatization of the articular eminence in cone-beam computed tomography: prevalence and characteristics — literature review

M. Wrzosek¹, K. Wilczek¹, J. Tusiewicz¹, M. Piskórz² , I. Różyło-Kalinowska² 

¹Student Research Group at the Department of Dental and Maxillofacial Radiodiagnostics, Medical University of Lublin, Poland

²Department of Dental and Maxillofacial Radiodiagnostics, Medical University of Lublin, Poland

[Received: 20 October 2021; Accepted: 20 January 2022; Early publication date: 8 March 2022]

Background: The articular tubercle is a site prone to pneumatization within the cranial bones. Knowledge of the anatomical variations of pneumatization adjacent to the temporomandibular joint (TMJ) is an important issue. Air cells exhibit decreased resistance to trauma, facilitate the spread of various pathologies in the TMJ, such as inflammation, tumours or fractures. Articular tubercle pneumatization may cause complications during TMJ surgery. Information of possible location allows to detect and conduct differential diagnosis of pneumatization of the articular tubercle (PAT) during cone-beam computed tomography (CBCT) examinations. The aim of this study is to determine the prevalence and characteristics of PAT, with respect to age, gender, location and type through assessment in CBCT images.

Materials and methods: Articles were selected through database search (PubMed, Scopus, Google Scholar), in which the main objective was to assess the prevalence of articular tubercle pneumatization using CBCT. Search strategies included the following keywords: “pneumatized articular eminence” and “CBCT”, “pneumatized articular tubercle” and “CBCT” and “zygomatic air cell defect” and “CBCT”. A meta-analysis of prevalence using a random effects model was performed.

Results: Fifteen studies met the selection criteria. The results showed that an overall prevalence of articular tubercle pneumatization was 25.22% ($n = 6393$; 95% confidence interval [CI] 15.84–35.94). The occurrence of PAT in females was 25.14% ($n = 3064$; 95% CI 14.96–36.94). The frequency of PAT in males was 25.81% ($n = 2671$; 95% CI 15.30–37.99).

Conclusions: There was no correlation between the frequency, location or type of PAT with age and gender. (Folia Morphol 2023; 82, 2: 242–247)

Key words: articular tubercle, pneumatization, air cells, zygomatic air cell defect, pneumatized articular tubercle, pneumatized articular eminence, cone-beam computed tomography

INTRODUCTION

The skull is a bone containing many air-filled cavities. This phenomenon is defined as pneumatization

[12]. One of the pneumatized bones is the temporal bone. It contains ten aerated sites, including the zygomatic process of the temporal bone, in which,

Address for correspondence: Dr. M. Piskórz, Department of Dental and Maxillofacial Radiodiagnostics, Medical University of Lublin, ul. Chodzki 6, 20–093 Lublin, Poland, tel: +48 81502 1800, e-mail: magdalena.piskorz@umlub.pl

This article is available in open access under Creative Common Attribution-Non-Commercial-No Derivatives 4.0 International (CC BY-NC-ND 4.0) license, allowing to download articles and share them with others as long as they credit the authors and the publisher, but without permission to change them in any way or use them commercially.

depending on the location, pneumatization of the articular eminence (PAT) or pneumatization of the roof of the glenoid fossa is classified [3, 17, 23].

The term PAT was first used in 1985 by Tyndall and Matteson [24] to describe an asymptomatic, radiolucent, non-expansive defect in the zygomatic process of the temporal bone and articular process that does not extend beyond the zygomatic-temporal suture and does not destroy the cortical layer of the bone. Pneumatization can occur unilaterally or bilaterally as a single (unicellular) or divided by thin septa (multicellular) radiolucency [24].

Knowledge of the anatomical dissimilarity of the air cells adjacent to the temporomandibular joint is an important issue. The pneumatized articular eminence, by creating less bone resistance, can be a complication during surgical procedures and can lead to unintentional penetration, dura mater rupture and cerebrospinal fluid leakage [13, 17, 22]. In addition, air cells can be an obstacle to surgical procedures in the temporomandibular joint, such as eminectomy or insertion of miniplates [8]. The presence of air cells may facilitate the spread of inflammation, tumours, infections, fractures or other pathological processes deep into the bone and consequently cause fractures of the associated bone or ankylosis of the temporomandibular joint [8, 12, 17, 22]. The development of temporomandibular joint ankylosis at a young age leads to secondary effects in mandibular growth such as malocclusion, facial asymmetry and mandibular retraction [7, 14, 16].

Pneumatization of the articular eminence can be observed on panoramic radiographs obtained during dental examinations. However, the anatomical complexity of the area and overlap of adjacent structures may prevent accurate assessment of the location and dimensions of the pneumatization [17]. Cone-beam computed tomography (CBCT) may lead to a more accurate diagnosis and better visualization of areas affected by pneumatization [18]. It is a relatively safe imaging modality widely used in dentistry characterised by low radiation exposure compared to computed tomography (CT), precise three-dimensional imaging of the jaws without magnification or distortion [12].

The aim of the study was to conduct the meta-analysis concerning the PAT based on CBCT examinations.

MATERIALS AND METHODS

A systematic literature review was conducted, using electronic databases: PubMed, Scopus and Google

Scholar. Search strategies in databases included the following keywords: “pneumatized articular eminence” and “CBCT”, “pneumatized articular tubercle” and “CBCT” and “zygomatic air cell defect” and “CBCT”. Reference lists of selected articles were searched in an attempt to identify any additional references.

Inclusion criteria

The article selection process was two-phased. In the first phase three authors independently reviewed the titles and abstracts of all publications identified through database searches. Studies, in which the main objective was to assess the prevalence of articular tubercle pneumatization using CBCT were selected. Articles unrelated to this topic were rejected. In the second phase full-text resources were independently reviewed using the following exclusion criteria: (1) reviews, case reports, book excerpts; (2) studies in which the sample included patients with craniofacial deformities, malformations or any maxillofacial fracture history; (3) papers, that did not independently assess the occurrence of PAT and pneumatization of the roof of the glenoid fossa; (4) papers published exclusively in university journals. Finally, 15 papers met the inclusion criteria.

Data synthesis

A meta-analysis of prevalence was performed using MedCalc software, with significance level set at 5%, using a random effects model due to the high heterogeneity of studies included in the meta-analysis. MedCalc 19.8 is a statistical software package for biomedical research, compatible with contemporary Windows desktop editions. It was chosen because of its fully-featured meta-analysis module, which allows for: easy input of individual studies, heterogeneity tests such as Cochran’s Q test with I^2 statistic, fixed and random effects model calculations and visualization of statistical data using multiple plots and graphs. A forest plot was selected as a method of displaying results.

RESULTS

From the 369 originally identified articles, 20 remained after the first selection phase. After the second phase 15 studies remained and were included in the meta-analysis. A diagram of the selection process can be found in Figure 1.

Research papers included in the review were conducted in five different countries: India, Turkey, Iran, Brazil, and Egypt. All papers except one [2] were

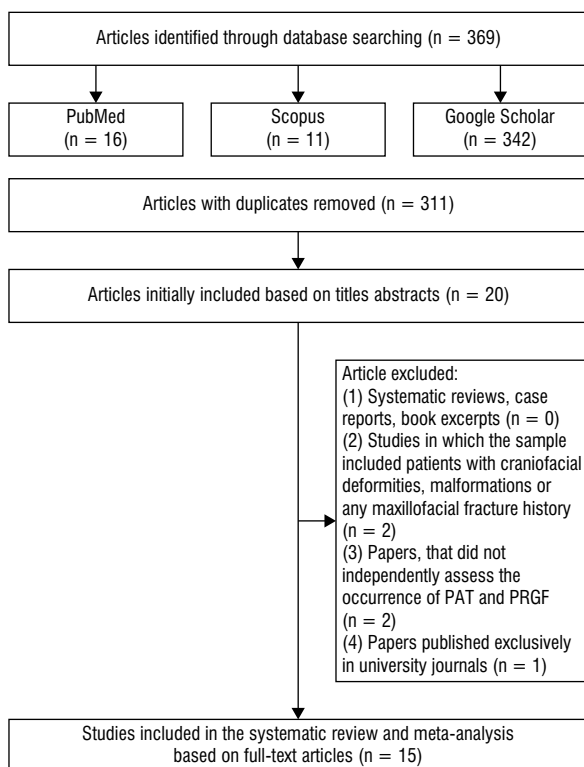


Figure 1. PRISMA diagram for the search strategy and selected studies; PAT — pneumatization of the articular eminence; PRGF — pneumatization of the roof of the glenoid fossa.

published in English. Sample sizes ranged from 111 [12] to 1000 [6, 20] CBCT images. All studies included in the meta-analysis assessed the presence of articular tubercle pneumatization using CBCT. Most studies showed no statistically significant differences in the incidence of PAT between males and females [2, 4–6, 9–11, 15, 17–22]. One study [12] showed a statistically significant difference between the incidence of PAT in females (73.6%) and males (51.3%; $p < 0.05$).

Results of the meta-analysis showed that the overall prevalence of articular tubercle pneumatization was 25.22% ($n = 6393$; 95% confidence interval [CI] 15.84–35.94). The prevalence of PAT in females was 25.14% ($n = 3064$; 95% CI 14.96–36.94). The prevalence of PAT in males was 25.81% ($n = 2671$; 95% CI 15.30–37.99) (Table 1, Fig. 2).

Most of the studies [2, 5, 6, 9, 11, 12, 15, 17–22] did not have clearly defined sampling criteria; moreover, most authors used convenience sampling instead of random sampling, thus the samples may not represent the overall population prevalence.

DISCUSSION

The development of air cells within the temporal bone is the result of physiologic periosteal activity [10].

Table 1. Summary of studies included in the meta-analysis

Study	Country	Sample size	Patients, n		Patients with PAT present, n	Patients with PAT present, n		Age of patients	Laterality		Prevalence
			M	F		M	F		Unilateral	Bilateral	
Bhalchim et al. (2018) [4]	India	200	138	62	25	17	8	10–73	11	14	12.5%
Şallı et al. (2019) [20]	Turkey	1000	489	511	147	74	73	16–77	85	62	14.7%
Khojastepour et al. (2017) [15]	Iran	327	177	150	251	139	112	7–65	76	175	76.7%
Miloglu et al. (2010) [18]	Turkey	514	216	298	41	16	25	4–85	31	10	8%
İlgüy et al. (2015) [12]	Turkey	111	39	72	73	20	53	17–81	31	42	65.8%
Buyuk et al. (2018) [6]	Turkey	1000	423	577	391	165	226	18–86	215	176	39.1%
Ladeira et al. (2012) [17]	Brazil	658	257	401	140	–	–	11–85	76	64	21.3%
Mosavat and Ahmadi (2015) [19]	Iran	239	111	128	51	25	26	18–81	35	16	21.3%
Shokri (2015) [22]	Iran	377	183	194	59	27	32	8–73	41	18	15.6%
Shekhawat et al. (2020) [21]	India	106	50	56	50	24	26	18–80	44	14	56%
Demirel et al. (2014) [10]	Turkey	250	127	123	45	23	22	15–82	29	16	18%
Borahan et al. (2018) [5]	Turkey	300	134	166	98	55	43	18–85	56	42	32%
ElBeshlawy (2020) [11]	Egypt	210	74	136	40	20	20	5–65	20	20	19.1%
Delilbasi et al. (2013) [9]	Turkey	825	377	448	21	11	10	18–91	14	7	2.54%
Adisen and Misirlioglu (2018) [2]	Turkey	276	133	143	39	17	22	12–85	22	17	14.1%

F — female; M — male; PAT — pneumatization of the articular tubercle

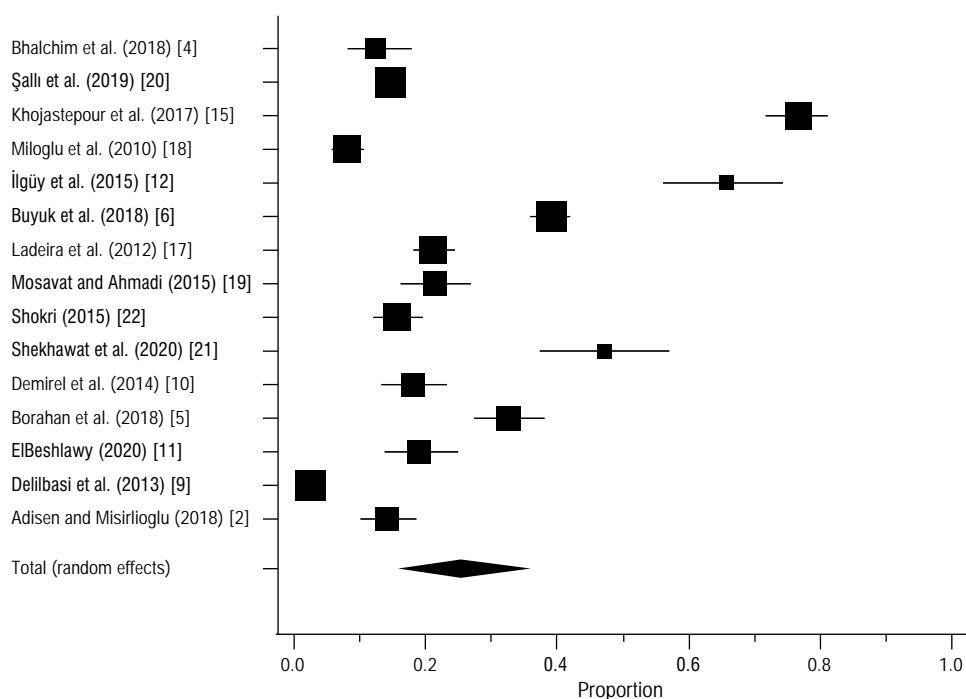


Figure 2. Forest plot of 15 prevalence studies and pooled prevalence using random effects model.

Classification of temporal bone pneumatization is a complex topic. The sites where it occurs include the middle ear, mastoid process, peri-labyrinth, and the apex of the temporal bone pyramid. However, many accessory air-cells can be localised within it, particularly in the region of the squamous area, the styloid process and the zygomatic process, from which it spreads toward the articular tubercle [4, 18].

Pneumatization of the articular tubercle is completely asymptomatic and is usually diagnosed incidentally on radiographs [11] as a well-demarcated translucency within the zygomatic process and the articular tubercle that does not extend beyond the zygomaticotemporal region [18]. Nowadays, three-dimensional imaging methods, such as CT and CBCT, are considered the gold standard for the evaluation of pneumatized cranial air spaces because they provide valuable information for better understanding the nature and character of these rare lesions [11]. These modalities decrease the problem of overlapping structures that is inherent in conventional panoramic radiographs, however this X-ray may be the first to take clinician's notice of the problem of PAT because of the high prevalence of these examinations in dental practice [18].

Pneumatization of the articular tubercle may predispose to the spread of inflammatory processes along the temporomandibular joint, as well as cause

complications of surgical procedures in this region and pathological fractures of the bones [18]. Therefore, the ability to diagnose and differentiate these lesions is an important aspect. PAT may resemble some pathological conditions such as aneurysmal bone cyst, vascular malformations, acidophilic granuloma, cancer metastasis, early type of fibrous dysplasia. To facilitate differentiation, clinical and radiographic signs of bone destruction by the above-mentioned lesions should be considered in comparison to asymptomatic pneumatization [11].

Treatment of PAT is not recommended. If a detected pneumatization is not accompanied by any signs and symptoms only follow-up is recommended. The presence of PAT may be a contraindication to eminectomy or articular tubercle plastic surgery for the treatment of recurrent chronic mandibular dislocation [18].

Tyndall and Matteson [24] distinguished three types of articular tubercle pneumatization — unilocular, multilocular and trabecular [18, 24]. In the studies on PAT included in this systematic review, most authors distinguished between two types: unilocular and multilocular [4–6, 11, 12, 15, 17–22]. Demirel et al. [10] did not differentiate between the pneumatization types in their study. In the vast majority of authors who included Tyndall and Matteson's division, the multilocular type occurred more often than the unilocular type

[4, 6, 11, 12, 15, 17–20, 22]. Only in two studies the unilocular type was more prevalent [5, 21].

In the study by ElBeshlawy [11], out of 40 CBCT scans with diagnosed pneumatization, 20 PATs were unilateral (50%) (8 on the right side and 12 on the left side) and 20 (50%) cases had bilateral PATs (1:1 ratio). There was no statistically significant difference between unilateral and bilateral or right/left incidence. Many of the previous studies using CBCT have shown that unilateral pneumatization of the articular tubercle is more common than bilateral [12, 17, 20]. In a study by Miloglu et al. [18], unilateral PAT was observed in 75.6% of cases, while bilateral PAT was found in only 24.4% of cases. Shokri et al. [22] also showed that unilateral lesions were significantly more common than bilateral lesions. Mosavat and Ahmadi [19] described unilateral PAT in 68.6% of cases. On the other hand, three authors, Bhalchim et al. [4], Khojastepour et al. [15] and İlgüy et al. [12], reported a higher incidence of bilateral PAT. The cited literature did not clearly identify the determinants of unilateral or bilateral articular tubercle pneumatization.

In 7 of the 15 studies reviewed, PAT was found more often in women [2, 6, 12, 18, 19, 21, 22] while in 6 men [4, 5, 9, 10, 15, 20]. The authors of one of the studies included in the current review did not include the gender of the subjects as a factor determining the possibility of PAT [17]. In ElBeshlawy's study [11], PAT occurred in an equal number of female and male subjects.

In a study by Adisen and Misirlioglu [2] conducted on 276 patients aged 12–85 years, pneumatization was most commonly observed in subjects aged 20–29 years, with the lowest in the age range 50–59 years. Similarly, in a study of ElBeshlawy [11] conducted on 210 patients between 5, and 65 years of age, the highest percentage of PAT cases occurred in subjects aged 10–20 years (10.5%), and the lowest in the age range 60–70 years (0%).

Bhalchim et al. [4], whose study included 200 subjects in the age range of 10–73 had the highest rate of pneumatization of the articular eminence in subjects aged 21–30 years. Delilbasi et al. [9] conducted a study on 825 individuals, among which the highest percentage of positive findings is observed in individuals between the ages of 20–29. A similar result was obtained by Miloglu et al. [18] where among the 514 individuals studied, the highest percentage of positive findings was in individuals between the ages of 21–40. Şallı et al. [20] in their study included

1000 CBCT scans, where PAT was confirmed in 147 individuals and the highest prevalence was in patients between the ages of 30–39. On the other hand, in a study conducted by Borahan et al. [5] on 300 patients, as many as 103 or 34.3% were over the age of 55. The quoted authors did not clearly demonstrate a relationship between age and the incidence of PAT in the patients studied [2, 4–6, 9–12, 15, 17–22].

CONCLUSIONS

The articular eminence is a predisposed site for pneumatization within the cranial bone. Knowledge of the possible location of this anatomical variation allows to detect and differentiate PAT during evaluation CBCT examinations. In the reviewed studies, no correlation was found between the frequency, location, as well as type of PAT and age and gender.

Conflict of interest: None declared

REFERENCES

1. Abramovitch K, Rice DD. Basic principles of cone beam computed tomography. *Dent Clin North Am.* 2014; 58(3): 463–484, doi: [10.1016/j.cden.2014.03.002](https://doi.org/10.1016/j.cden.2014.03.002), indexed in Pubmed: [24993919](https://pubmed.ncbi.nlm.nih.gov/24993919/).
2. Adisen M, Misirlioglu M. Konik ışınılı bilgisayarlı tomografi görüntülerinde pnömatisize artiküler tüberkül prevalansı ve karakteristik özelliklerinin değerlendirilmesi. *Turkish J Clin Laboratory.* 2018, doi: [10.18663/tjcl.336158](https://doi.org/10.18663/tjcl.336158).
3. Allam AF. Pneumatization of the temporal bone. *Ann Otol Rhinol Laryngol.* 1969; 78(1): 49–64, doi: [10.1177/000348946907800105](https://doi.org/10.1177/000348946907800105), indexed in Pubmed: [5763190](https://pubmed.ncbi.nlm.nih.gov/5763190/).
4. Bhalchim SG, Jugade SC, Ramaswami E, et al. Prevalence of pneumatized articular tubercle using panoramic radiography and cone beam-computed tomography: a retrospective study. *Contemp Clin Dent.* 2018; 9(Suppl 2): S221–S226, doi: [10.4103/ccd.ccd_64_18](https://doi.org/10.4103/ccd.ccd_64_18), indexed in Pubmed: [30294148](https://pubmed.ncbi.nlm.nih.gov/30294148/).
5. Borahan M, Sadıkoğlu AY, Ulay G, et al. A preliminary study of prevalence and characteristics of pneumatization of articular eminence on cone beam computed tomography. *Marmara Dental Journal.* 2018; 2(1): 1–6, doi: [10.12990/mdj.2018.11](https://doi.org/10.12990/mdj.2018.11).
6. Buyuk C, Gunduz K, Avsever H. Prevalence and characteristics of pneumatizations of the articular eminence and roof of the glenoid fossa on cone-beam computed tomography. *Oral Radiol.* 2019; 35(2): 171–176, doi: [10.1007/s11282-018-0334-z](https://doi.org/10.1007/s11282-018-0334-z), indexed in Pubmed: [30484191](https://pubmed.ncbi.nlm.nih.gov/30484191/).
7. Chidzonga MM. Temporomandibular joint ankylosis: review of thirty-two cases. *Br J Oral Maxillofac Surg.* 1999; 37(2): 123–126, doi: [10.1054/bjom.1997.0089](https://doi.org/10.1054/bjom.1997.0089), indexed in Pubmed: [10371317](https://pubmed.ncbi.nlm.nih.gov/10371317/).
8. da Costa Ribeiro R, dos Santos BJ, Provenzano N, et al. Dautrey's procedure: an alternative for the treatment of recurrent mandibular dislocation in patients with pneumatization of the articular eminence. *Int J Oral Maxillofac Surg.*

- 2014; 43(4): 465–469, doi: [10.1016/j.ijom.2013.10.007](https://doi.org/10.1016/j.ijom.2013.10.007), indexed in Pubmed: [24239140](https://pubmed.ncbi.nlm.nih.gov/24239140/).
9. Delilbaşı BÇ, Orhan K, İçen M, et al. Evaluation of articular eminence pneumatization using cone beam computed tomography. *Minerva Stomatologica*. 2013; 62(10): 349–354.
 10. Demirel O, Kaya E, Üçok C. Evaluation of mastoid pneumatization using cone-beam computed tomography. *Oral Radiol*. 2013; 30(1): 92–97, doi: [10.1007/s11282-013-0150-4](https://doi.org/10.1007/s11282-013-0150-4).
 11. ElBeshlawy D. CBCT assessment of pneumatization of the articular tubercle and the roof of the glenoid fossa: a retrospective study. *Egyptian Dental J*. 2020; 66(3): 1553–1562, doi: [10.21608/edj.2020.27346.1098](https://doi.org/10.21608/edj.2020.27346.1098).
 12. İlgüy M, Dölekoğlu S, Fişekçioğlu E, et al. Evaluation of pneumatization in the articular eminence and roof of the glenoid fossa with cone-beam computed tomography. *Balkan Med J*. 2015; 32(1): 64–68, doi: [10.5152/balkan-medj.2015.15193](https://doi.org/10.5152/balkan-medj.2015.15193), indexed in Pubmed: [25759774](https://pubmed.ncbi.nlm.nih.gov/25759774/).
 13. Jadhav AB, Fellows D, Hand AR, et al. Classification and volumetric analysis of temporal bone pneumatization using cone beam computed tomography. *Oral Surg Oral Med Oral Pathol Oral Radiol*. 2014; 117(3): 376–384, doi: [10.1016/j.oooo.2013.12.398](https://doi.org/10.1016/j.oooo.2013.12.398), indexed in Pubmed: [24528795](https://pubmed.ncbi.nlm.nih.gov/24528795/).
 14. Kaban LB, Perrott DH, Fisher K. A protocol for management of temporomandibular joint ankylosis. *J Oral Maxillofac Surg*. 1990; 48(11): 1145–1152, doi: [10.1016/0278-2391\(90\)90529-b](https://doi.org/10.1016/0278-2391(90)90529-b), indexed in Pubmed: [2213309](https://pubmed.ncbi.nlm.nih.gov/2213309/).
 15. Khojastepour L, Paknahad M, Abdalipur V, et al. Prevalence and characteristics of articular eminence pneumatization: a cone-beam computed tomographic study. *J Maxillofac Oral Surg*. 2018; 17(3): 339–344, doi: [10.1007/s12663-017-1033-8](https://doi.org/10.1007/s12663-017-1033-8), indexed in Pubmed: [30034152](https://pubmed.ncbi.nlm.nih.gov/30034152/).
 16. Kumar R, Hota A, Sikka K, et al. Temporomandibular joint ankylosis consequent to ear suppuration. *Indian J Otolaryngol Head Neck Surg*. 2013; 65(Suppl 3): 627–630, doi: [10.1007/s12070-013-0666-2](https://doi.org/10.1007/s12070-013-0666-2), indexed in Pubmed: [24427727](https://pubmed.ncbi.nlm.nih.gov/24427727/).
 17. Ladeira DBS, Barbosa GLR, Nascimento MCC, et al. Prevalence and characteristics of pneumatization of the temporal bone evaluated by cone beam computed tomography. *Int J Oral Maxillofac Surg*. 2013; 42(6): 771–775, doi: [10.1016/j.ijom.2012.12.001](https://doi.org/10.1016/j.ijom.2012.12.001), indexed in Pubmed: [23290566](https://pubmed.ncbi.nlm.nih.gov/23290566/).
 18. Miloglu O, Yilmaz AB, Yildirim E, et al. Pneumatization of the articular eminence on cone beam computed tomography: prevalence, characteristics and a review of the literature. *Dentomaxillofac Radiol*. 2011; 40(2): 110–114, doi: [10.1259/dmfr/75842018](https://doi.org/10.1259/dmfr/75842018), indexed in Pubmed: [21239574](https://pubmed.ncbi.nlm.nih.gov/21239574/).
 19. Mosavat F, Ahmadi A. Pneumatized articular tubercle and pneumatized roof of glenoid fossa on cone beam computed tomography: prevalence and characteristics in selected iranian population. *J Dentomaxillofac Radiol, Pathol Surg*. 2015; 4(3): 10–14, doi: [10.18869/acadpub.3dj.4.3.10](https://doi.org/10.18869/acadpub.3dj.4.3.10).
 20. Şallı GA, Özcan İ, Pekiner FN. Prevalence of pneumatization of the articular eminence and glenoid fossa viewed on cone-beam computed tomography examinations in a Turkish sample. *Oral Radiol*. 2020; 36(1): 40–46, doi: [10.1007/s11282-019-00378-1](https://doi.org/10.1007/s11282-019-00378-1), indexed in Pubmed: [30796675](https://pubmed.ncbi.nlm.nih.gov/30796675/).
 21. Shekhawat C, Sobti G, Sundaragiri KS, et al. Evaluation of Pneumatization in Articular Tubercle and Roof of the Glenoid Fossa with Cone-Beam Computed Tomography. *RUHS J Health Sci*. 2020; 5(2), doi: [10.37821/ruhsjhs.5.2.2020.255](https://doi.org/10.37821/ruhsjhs.5.2.2020.255).
 22. Shokri A, Noruzi-Gangachin M, Baharvand M, et al. Prevalence and characteristics of pneumatized articular tubercle: First large series in Iranian people. *Imaging Sci Dent*. 2013; 43(4): 283–287, doi: [10.5624/isd.2013.43.4.283](https://doi.org/10.5624/isd.2013.43.4.283), indexed in Pubmed: [24380068](https://pubmed.ncbi.nlm.nih.gov/24380068/).
 23. Tremble GE. Pneumatization of the temporal bone. *Arch Otolaryngol - Head and Neck Surgery*. 1934; 19(2): 172–182, doi: [10.1001/archotol.1934.03790020018002](https://doi.org/10.1001/archotol.1934.03790020018002).
 24. Tyndall DA, Matteson SR. Radiographic appearance and population distribution of the pneumatized articular eminence of the temporal bone. *J Oral Maxillofac Surg*. 1985; 43(7): 493–497, doi: [10.1016/s0278-2391\(85\)80026-4](https://doi.org/10.1016/s0278-2391(85)80026-4), indexed in Pubmed: [3859592](https://pubmed.ncbi.nlm.nih.gov/3859592/).

Propofol protects rats against intra-cerebroventricular streptozotocin-induced cognitive dysfunction and neuronal damage

L. Sun , X. Dou , W. Yang 

Department of Anaesthesiology, Weifang People's Hospital, Weifang, Shandong, China

[Received: 15 January 2022; Accepted: 9 February 2022; Early publication date: 22 March 2022]

Background: Cognitive dysfunction is a severe issue of Alzheimer's disease. Thus, the present study was conducted to enumerate the protective effect of propofol (PPL) in rats against intra-cerebroventricular streptozotocin (STZ)-induced cognitive dysfunction and neuronal damage.

Materials and methods: The effect of PPL was investigated to evaluate behavioural changes in STZ-induced cognitive dysfunction in Wistar rats using Object Recognition Task (ORT) for nonspatial, Morris Water Maze (MWM) for spatial and locomotor activity. The effect of PPL was also investigated on acetylcholine (ACh) esterase (AChE) activity and oxidative stress markers, e.g., nitrite, malonaldehyde (MDA), superoxide dismutase (SOD), and glutathione (GSH). The level of pro-inflammatory cytokines, e.g., tumour necrosis factor (TNF)- α , interleukin (IL)-1 β , and IL-6, was also studied in the PPL-treated group. The effect of PPL on the level of neurotransmitters, e.g., dopamine (DA), serotonin (5-HT), and norepinephrine (NE) and their metabolites 3,4-dihydroxyphenylacetic acid (DOPAC), 5-hydroxyindoleacetic acid (5-HIAA), and homovanillic acid (HVA) levels were also estimated in frozen hippocampal tissues by high-performance liquid chromatography. Histopathology analysis of neurons in the hippocampus of rats was performed using haematoxylin and eosin (H&E) staining.

Results: Propofol showed significant improvement in the spatial and nonspatial memory deficit of rats in the MWM test and ORT in rats. It also causes improvement in locomotor activity of rats by preserving ACh via inhibition of AChE. It also potentiates the expression of DA, 5-HT, and NE with a simultaneous reduction in the level of metabolites (DOPAC, HVA, and 5-HIAA). PPL showed a reduction of oxidative stress in rats by restoring the level of nitrite, SOD, MDA, and GSH near to normal. In the PPL-treated group, the level of TNF- α , IL-1 β , and IL-6 was found reduced in a dose-dependent manner. In histopathology analysis of neurons in the hippocampus of the STZ rats, PPL causes dose-dependent reduction of pyknosis in the nucleus, which confirmed the protective effect of PPL.

Conclusions: The present study demonstrated that PPL could significantly attenuate cognitive dysfunction and neuronal damage in STZ-induced rats. (Folia Morphol 2023; 82, 2: 248–255)

Key words: propofol, cognitive deficit, oxidative stress, inflammation

Address for correspondence: Dr. W. Yang, Department of Anaesthesiology, Weifang People's Hospital, Weifang, Shandong, China, 261000, tel/fax: +86-05362603756, e-mail: sdwei1982@163.com

This article is available in open access under Creative Common Attribution-Non-Commercial-No Derivatives 4.0 International (CC BY-NC-ND 4.0) license, allowing to download articles and share them with others as long as they credit the authors and the publisher, but without permission to change them in any way or use them commercially.

INTRODUCTION

Current advances in therapeutics and diagnostics for cognitive dysfunction significantly impacted the lives of human well-being. It increases the mean life expectancy of individuals across the globe. It exposes the older people to many non-infectious diseases, such as cognitive dysfunction, osteoporosis, type 2 diabetes, cardiovascular diseases, cataracts, and cancer. Dementia is a cognitive disorder where the affected individual loses the ability to perform daily tasks due to reduced memory and disability [1, 8, 21].

Alzheimer's disease (AD) is a sub-type of dementia and is considered an irreversible, chronic progressive neurodegenerative brain disease due to the necrosis of brain cells. It mainly affects older people aged over 60 years and older. It is considered as both a structural and an inflammatory condition. The characteristic hallmark is the presence of extracellular amyloid plaques and intracellular neurofibrillary tangles (NFTs) in the brain, with abnormally folded amyloid- β 42 (A β 42) and tau proteins of AD. Studies have shown that cellular homeostasis and mitochondrial function are altered in AD patients due to oxidative stress induced by abnormal amyloid- β proteins, hence partially explaining the high prevalence of AD in the elderly [3, 10, 12]. In a study, institutionalized elderly patients showed a high level of oxidative stress and elevated concentration of pro-inflammatory cytokines, which is considered an underlying cause for their cognitive dysfunction. Thus, many current drugs target oxidative stress and inflammation to treat/control AD mainly [14, 16]. However, the current therapeutic option provides modest benefits against AD, necessitating discovering newer agents.

Propofol (PPL), which is commonly used as an anaesthetic agent, showed a protective effect against many ailments, such as ischaemic reperfusion injury of heart, liver, and kidney, ionising radiation-induced haematopoietic system damage mice, and lung injury via strong radical scavenging effect [17, 23, 24]. Considering the importance of free radicals in the pathogenesis of AD, and the strong radical scavenging effect of PPL, in the present manuscript, we intended to examine whether PPL has a protective effect against AD or not.

Experimental

Chemical

The chemicals used in the study were obtained from Sigma Aldrich, USA and used without further purification unless otherwise stated.

Animals

Male Wistar rats (220–260 g) were obtained from the institutional animal house and kept in strict hygienic conditions. The rats were supplied with food and water ad-libitum and accommodated in an alternate day and night cycles of 12 h. The study has been approved by Animal Ethical Board for Biomedical Experiments of Weifang People's Hospital (WPH/2020/00237).

Experimental induction of cognitive dysfunction

The anaesthesia was induced in the rats by intramuscular injection of ketamine/xylazine (90:10 mg/kg) and then fixed on the stable platform. The head of the rats was shaved to expose the skull for creating a sagittal midline incision. The streptozotocin (STZ) was diluted in freshly prepared citrate buffer (pH 4.4) before the injection and injected into the brain's exposed lateral cerebral ventricle. The animals were then further divided into five groups containing ten animals each.

- Group 1: control (received surgery with no treatment);
- Group 2: injected bilaterally with STZ (5 mg/kg) in a volume of 4 μ L to each ventricle on day 1 and 3; In the PPL-treated group, the PPL was administered to rats after 1 h of STZ administration (peroral) at the indicated dose for 21 days.
- Group 3: STZ + PPL (5 mg/kg, p.o.);
- Group 4: STZ + PPL (10 mg/kg, p.o.);
- Group 5: STZ + PPL (20 mg/kg, p.o.).

Behavioural assessment

Object Recognition Test

The Object Recognition Task (ORT) was performed using a wooden open box apparatus as per the previously reported procedure. The discrimination index to identify rats' ability between the novel and familiar item was estimated using $D = N - F/N + F$ (F — familiar, N — novel).

Morris Water Maze test

The rats' spatial memory was estimated using the Morris Water Maze (MWM) test, per the reported procedure elsewhere. The apparatus consisted of a circular water tank with a depth of 50 cm to a depth, and skimmed milk powder was added to make the floor invisible. The time used up in the marked quadrant showed the extent of memory retention which had taken place after the acquisition trial.

Locomotor activity determination

Actophotometer was used to define the effect on the locomotor activity. Each animal was tested and observed over 10 min in a square closed arena (30 × 30 cm²) equipped with infrared light-sensitive photocells using a digital actophotometer. The rats were examined for crossing light beam using infrared light-sensitive photocells.

Assessment of hippocampal catecholamines using HPLC

Catecholamines such as dopamine (DA), serotonin (5-HT) and norepinephrine (NE) and their metabolites 3,4-dihydroxyphenylacetic acid (DOPAC), 5-hydroxyindoleacetic acid (5-HIAA), and homovanillic acid (HVA) levels were estimated by high-performance liquid chromatography (HPLC) using the electrochemical detector. Frozen hippocampal tissues were homogenized in 0.2 M perchloric acid, and samples were centrifuged at 12,000 g for 5 min. The supernatant was filtered through 0.22 mm nylon filters before injecting in the HPLC sample injector, and separation was carried out at a flow rate of 0.8 mL/min at 0.75 V. The concentration of neurotransmitters and their metabolites were calculated from the standard curve generated by using standard in the concentration range of 10–100 ng/mL.

Acetylcholine esterase activity

The acetylcholine (ACh) esterase (AChE) activity was determined using DTNB (Ellman reagent) as described by Ellman et al. [5] with minor modification [5, 25]. The assay mixture contained 0.05 mL of tissue supernatant, 0.10 mL of acetylthiocholine iodide, 3 mL of 0.01 M sodium phosphate buffer (pH 8), and 0.10 mL of DTNB (5,5'-dithiobis-(2-nitrobenzoic acid), Ellman's Reagent). The change in absorbance was measured spectrophotometrically immediately at zero and one minute at 412 nm.

Estimation of anti-oxidant biomarkers

The anti-oxidant biomarkers (malonaldehyde [MDA], superoxide dismutase [SOD], glutathione [GSH]) were studied using commercially available ELISA kits (Cayman Kits) as per the manufacturer's instructions. Briefly, after removing the brain, the rat hippocampal tissues were then homogenised with ice-cold 0.1 M phosphate buffer (pH 7.4) in a volume 10 times the weight of the tissue. The brain tissue homogenate pellets obtained after centrifugation at 10,000 g for 15 min (4°C) were suspended to the

desired concentration with phosphate buffered saline (PBS) (pH 7.4) and plated at 30 µL/well in Immulon 2HB plates (Thermo Scientific Waltham, MA). Plates were incubated for 2 h at room temperature (RT). The liquid was gently removed from wells and plates were either allowed to air dry or fixed by adding 50 µL/well fixative (1% paraformaldehyde, 3% glutaraldehyde, or methanol). Plates were then blocked with PBS + 1% bovine serum albumin (BSA) (50 µL/well) for 1 h at RT. Primary antibodies were diluted with PBS + 1% BSA, added to the respective wells (50 µL/well), and plates were incubated for 2 h at RT. Unbound antibodies were removed by washing the plates 3 times with PBS. Secondary antibodies were diluted with PBS + 1% BSA (1:200) and added to each well (50 µL/well) for 1 h at RT. Plates were then washed with PBS were read on a SpectraMax M2 plate reader (Molecular Devices, Sunnyvale, CA) at 630 nm absorption.

Enzyme-linked immunosorbent assay (ELISA)

The determination of tumour necrosis factor alpha (TNF-α), interleukin 1beta (IL-1β), and interleukin 6 (IL-6) was performed using commercially available ELISA kits as per the manufacturer's instructions. Briefly, after removing the brain, the rat hippocampal tissues were then homogenized with ice-cold 0.1 M phosphate buffer (pH 7.4) in a volume 10 times the weight of the tissue. The brain tissue homogenate pellets obtained after centrifugation at 10,000 g for 15 min (4°C) were suspended to the desired concentration with PBS (pH 7.4) and plated at 30 µL/well in Immulon 2HB plates (Thermo Scientific Waltham, MA). Plates were incubated for 2 h at RT. The liquid was gently removed from wells, and plates were either allowed to air dry or fixed by adding 50 µL/well fixative (1% paraformaldehyde, 3% glutaraldehyde, or methanol). Plates were then blocked with PBS + 1% BSA (50 µL/well) for 1 h at RT. Primary antibodies were diluted with PBS + 1% BSA, added to the respective wells (50 µL/well), and plates were incubated for 2 h at RT. Unbound antibodies were removed by washing the plates 3 times with PBS. Secondary antibodies were diluted with PBS + 1% BSA (1:200) and added to each well (50 µL/well) for 1 h at RT. Plates were then washed with PBS were read on a SpectraMax M2 plate reader (Molecular Devices, Sunnyvale, CA) at 630 nm absorption.

Haematoxylin and eosin staining

The harvested brains were fixed in 4% paraformaldehyde for 2 days and paraffin-embedded after gra-

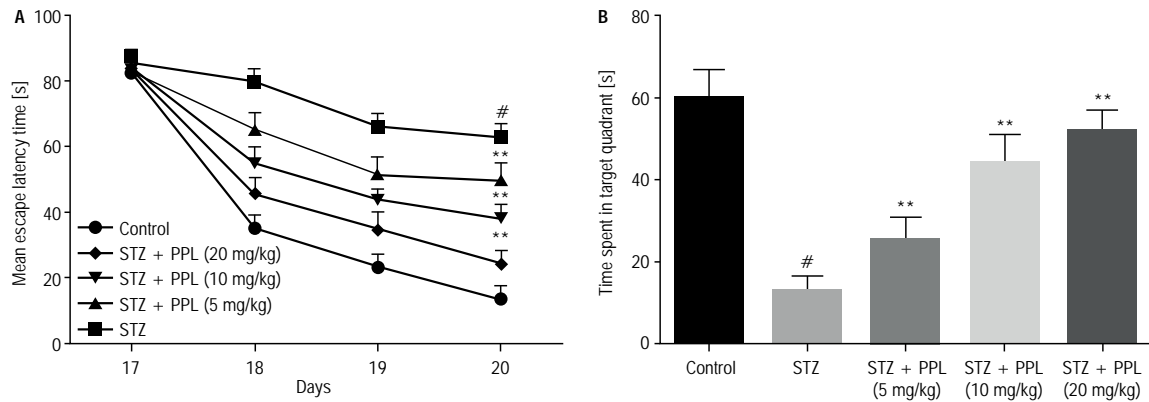


Figure 1. Effect of propofol (PPL) on the neuronal deficit; # $P < 0.05$ vs. control and ** $P < 0.01$ vs. streptozotocin (STZ) group. Data are presented as means \pm standard error of the mean.

Table 1. Effect of propofol (PPL) on the exploration and latency of streptozotocin (STZ) rats

Group	Total exploration time [s]		Total exploration time [s]		Discrimination Index (DI)
	F01	F02	Familiar	Novel	
Control	10.66 \pm 1.96	11.31 \pm 2.32	4.76	15.26	0.52
STZ	9.73 \pm 1.03 [#]	8.8 \pm 0.98 [#]	3.97 [#]	3.99 [#]	0.0025 [#]
STZ + PPL (5 mg/kg)	9.03 \pm 1.23 ^{**}	9.43 \pm 1.12 ^{**}	4.44 ^{**}	7.76 ^{**}	0.27 ^{**}
STZ + PPL (10 mg/kg)	9.41 \pm 1.34 ^{**}	10.16 \pm 1.63 ^{**}	4.45 ^{**}	10.28 ^{**}	0.39 ^{**}
STZ + PPL (20 mg/kg)	10.14 \pm 1.04 ^{**}	10.36 \pm 1.20 ^{**}	4.61 ^{**}	12.9 ^{**}	0.47 ^{**}

[#] $P < 0.05$ vs. control and ^{**} $P < 0.01$ vs. STZ group. Data are presented as means \pm standard error of the mean. The DI was calculated using $D = N - F/N + F$ (F—familiar, N—novel).

dent alcohol dehydration. The wax blocks were sectioned (4- μ m thick) on a paraffin slicer and stained with haematoxylin and eosin (H&E). Brain histopathological changes were observed under a light microscope.

Statistical analysis

The data were expressed as mean \pm standard deviation (SD). Statistical analysis was executed using ANOVA pursued by Bonferroni *post hoc* multiple comparison test using GraphPad Prism 5.0 (California, USA). The p -value < 0.05 was measured as statistically significant.

RESULTS

Effect of PPL on the spatial memory deficit of rats

Initially, the effect of PPL was investigated on the memory deficit of rats. As shown in Figure 1, in the MWM test, the STZ rats showed a significant reduction in memory as they were not acquainted during acquisition and maintenance trials. The entire treated animals were guided for 5 days from the 17th day of STZ infusion in MWM. On the first training day, no significant variation was observed in mean latencies among the tested groups. The STZ rats showed significant memory deficits on the 2nd and 3rd day of the training compared

to the control. Conversely, the PPL treated group considerably inhibited STZ-provoked memory deficit.

Effect of PPL on nonspatial memory deficit in rats

The effect of PPL was also investigated on the nonspatial memory deficit in rats, and results are presented in Table 1. After the 14th day of 1st STZ administration, the rats were exposed to ORT. In ORT, both items were alike. On the 15th day, the animals were open to both familiar and novel items. It has been observed that STZ-treated rats showed an inability to differentiate between the novel and familiar item compared to control. However, the PPL-treated rats showed dose-dependent improvement in differentiating between the novel and familiar items compared to STZ-rats.

Effect of STZ on the locomotor activity of rats

As shown in Table 1, no significant difference was observed among the treated and non-treated groups in spontaneous locomotor activity on the 16th day.

Effect of PPL on AChE activity in rats

The effect of PPL was investigated on the AChE level in brain homogenate of rats, and results are

Table 2. Effect of propofol (PPL) on the locomotor activity, acetylcholine esterase (AChE) activity, neurotransmitter level, and neurotransmitter metabolite level in the streptozotocin (STZ) rats

Group	Activity count/ /10 min	AChE activity (nmol/min/mg protein)	% Change in neurotransmitter level (ng/mg of tissue sample)			% Change in neurotransmitter metabolite level (ng/mg of tissue sample)		
			Dopamine	Norepinephrine	5-HT	DOPAC	HVA	5-HIAA
Control	250.34 ± 23.34	110.67 ± 32.26	98.02 ± 3.56	99.45 ± 5.23	99.32 ± 6.43	100.02 ± 4.56	99.45 ± 3.43	99.32 ± 3.26
STZ	226.02 ± 12.32 [#]	423.12 ± 25.04 [#]	26.54 ± 6.32 [#]	44.63 ± 4.45 [#]	30.45 ± 3.45 [#]	233.50 ± 40.22 [#]	274.51 ± 43.73 [#]	265.52 ± 43.21 [#]
STZ + PPL (5 mg/kg)	245.73 ± 9.03 ^{**}	350.43 ± 21.42 ^{**}	39.34 ± 3.27 ^{**}	50.73 ± 3.42 ^{**}	45.62 ± 4.53 ^{**}	200.45 ± 37.27 ^{**}	220.66 ± 36.54 ^{**}	211.37 ± 34.62 ^{**}
STZ + PPL (10 mg/kg)	248.05 ± 10.23 ^{**}	267.22 ± 20.15 ^{**}	47.62 ± 4.44 ^{**}	66.21 ± 3.78 ^{**}	55.45 ± 4.37 ^{**}	175.28 ± 34.81 ^{**}	175.59 ± 35.52 ^{**}	168.23 ± 37.06 ^{**}
STZ + PPL (20 mg/kg)	251.26 ± 8.45 ^{**}	176.30 ± 22.25 ^{**}	65.52 ± 4.51 ^{**}	75.03 ± 5.34 ^{**}	63.32 ± 3.83 ^{**}	148.63 ± 22.37 ^{**}	134.58 ± 25.43 ^{**}	120.45 ± 26.57 ^{**}

[#]P < 0.05 vs. control and ^{**}P < 0.01 vs. STZ group. Data are presented as means ± standard error of the mean; 5-HT — serotonin; DOPAC — 3,4-dihydroxyphenylacetic acid; 5-HIAA — 5-hydroxyindoleacetic acid; HVA — homovanillic acid

Table 3. Effect of propofol (PPL) on the oxidative and nitrosative activity in streptozotocin (STZ) rats

Group	Nitrite [μ Mol/mg prot.]	MDA [nMol/mg prot.]	SOD [μ Mol/mg prot.]	GSH [μ Mol/mg prot.]
Control	122.41 ± 20.48	2.41 ± 0.37	8.28 ± 1.26	9.63 ± 1.59
STZ	352.26 ± 35.40 ^{##}	4.53 ± 0.58 ^{##}	3.21 ± 0.45 ^{##}	4.11 ± 0.73 ^{##}
STZ + PPL (5 mg/kg)	303.17 ± 34.71 ^{**}	4.02 ± 0.65 ^{**}	4.07 ± 0.85 ^{**}	5.89 ± 0.84 ^{**}
STZ + PPL (10 mg/kg)	256.48 ± 28.36 ^{**}	3.68 ± 0.61 ^{**}	5.32 ± 0.97 ^{**}	7.26 ± 1.43 ^{**}
STZ + PPL (20 mg/kg)	188.27 ± 24.42 ^{**}	3.03 ± 0.56 ^{**}	7.18 ± 1.14 ^{**}	8.06 ± 1.51 ^{**}

^{##}P < 0.05 vs. control and ^{**}P < 0.05 vs. STZ group. Data are presented as means ± standard error of the mean; MDA — malonaldehyde; SOD — superoxide dismutase; GSH — glutathione

presented in Table 2. The STZ-treated rats showed a significant increase in the level of AChE in the brain homogenate of rats compared with the control. On the contrary, the PPL-treated rats showed a dose-dependent reduction in the elevated level of AChE as compared to STZ-treated rats.

Effect of PPL on the level of neurotransmitters and metabolites

The effect of PPL was investigated on the level of numerous neurotransmitters and metabolites in the rat brain homogenate. As shown in Table 2, STZ-infusion significantly decreased DA, 5-HT, and NE compared to control. Moreover, the level of metabolites (DOPAC, HVA, and 5-HIAA) was significantly enhanced in the STZ treated group compared to the control. The PPL treated group significantly restored this tested neurotransmitter and metabolites near normal in a dose-dependent manner.

Effect of PPL on oxidative-nitrosative stress

The effect of PPL was investigated on the oxidative-nitrosative stress level in rats. As shown in Table 3,

nitrite and MDA level was found to significantly increase, with a reduced level of SOD and GSH in STZ-treated rats compared to control ($p < 0.05$). However, PPL administration causes significant restoration of these biomarkers near to normal compared to STZ treated rats.

Effect of PPL on the pro-inflammatory cytokines

As shown in Table 4, the level of tested cytokines (TNF- α , IL-1 β , and IL-6) was found significantly elevated after administration of STZ to the rats compared to control. However, PPL causes a dose-dependent reduction in the level of these cytokines near to normal compared to STZ-treated rats.

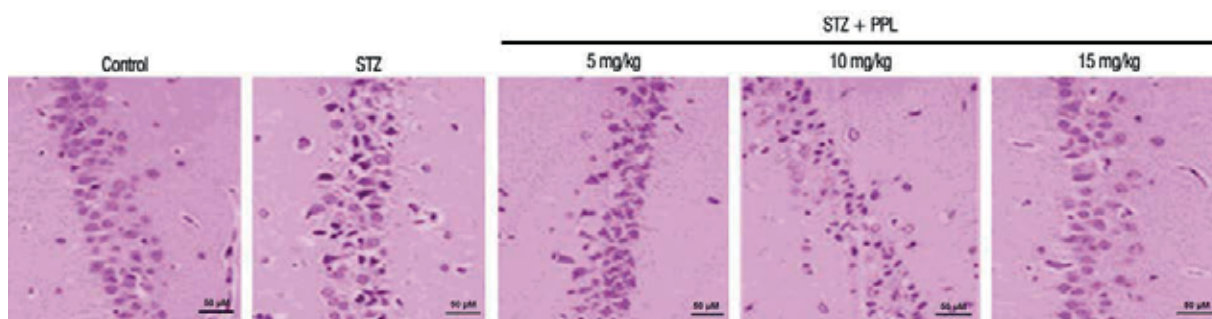
Effect of PPL on the histopathology of neurons in the hippocampus of rats

In the subsequent study, we examine the morphology of neurons in the hippocampus of rats following the administration of STZ and PPL. As shown in Figure 2, the rats in the STZ group showed a higher level of altered morphology with pyknosis in the nucleus with irregular arrangements than the control-treated

Table 4. Effect of propofol (PPL) on the inflammatory cytokines in streptozotocin (STZ) rats

Group	TNF- α [pg/mL]	IL-1 β [pg/mL]	IL-6 [pg/mL]
Control	185.52 \pm 76.20	15.35 \pm 2.34	16.45 \pm 2.05
STZ	502.28 \pm 136.47 [#]	233.82 \pm 62.82 [#]	178.92 \pm 52.37 [#]
STZ + PPL (5 mg/kg)	423.42 \pm 112.28 ^{**}	173.76 \pm 56.38 ^{**}	140.82 \pm 30.72 ^{**}
STZ + PPL (10 mg/kg)	336.72 \pm 89.34 ^{**}	103.51 \pm 35.71 ^{**}	110.34 \pm 23.58 ^{**}
STZ + PPL (20 mg/kg)	250.35 \pm 67.06 ^{**}	65.72 \pm 23.37 ^{**}	85.15 \pm 19.42 ^{**}

[#]P < 0.05 vs. control and ^{**}P < 0.05 vs. STZ group. Data are presented as means \pm standard error of the mean; TNF- α — tumour necrosis factor alpha; IL-1 β — interleukin 1beta; IL-6 — interleukin 6

**Figure 2.** Effect of propofol (PPL) on the neurons in hippocampus of the streptozotocin (STZ) rats (\times 400).

group. In the PPL-treated group, these morphological features were improved and restored near to normal compared to STZ-treated rats. This result suggests the protective role of PPL against the neuronal damage in STZ-induced cognitive deficit in rats.

DISCUSSION

Cognitive impairment/dysfunction is a critical ailment for aged people and compromises their quality of life. The increased life expectancy has amplified the number of older people who experience mild to severe cognitive dysfunction after 60 years of age. It is considered a characteristic hallmark of AD, a type of degenerative brain disorder [6, 10]. According to a study, people with cognitive dysfunction have 3-fold more hospital stays than people hospitalised for any other causes. This has put significant demand for more in-home or institutional care and unpaid assistance by family and friends, causing a huge economic burden [15, 19]. Thus, an effective therapeutic agent is urgently needed to provide beneficial effects against cognitive dysfunction and associated neuronal damage. Anaesthetics agents are considered the main cause of cognitive dysfunction in elderly patients in the post-operative recovery phase; for instance, midazolam causes a serious cognitive deficit in patients after 1-week of operation [13]. In the

present study, we have shown a strong protective effect of PPL against cognitive dysfunction in STZ-induced rats. The present study showed no mortality of rats during the duration of the study. The effect of PPL was investigated on the cognitive impairment in STZ infused rats by MWM and ORT to define spatial and nonspatial learning parameters. The MWM test is the most widely used behavioural procedure used in rodents to study drugs' psychological processes and effects. In this test, the distal cue is used to steer from the start spot in the boundary region of an open swimming ring to find a sunken escape platform. Spatial learning is calculated transversely frequent trials, and reference memory is assessed by an inclination for the platform area when the platform is missing. Reversal and shift trials increase the recognition of spatial impairments [11, 20]. On the other hand, the ORT tries to evaluate cognition, particularly recognition memory, in rodents. In this, the mouse is offered two similar items in the first session, and then one of the two items is restored by a new item during a second session. The total time to discover the new item affords an index of recognition memory. In this test, STZ treated rats showed significant spatial and nonspatial memory impairment, which is in line with previous studies. However, the PPL administration causes significant improvement in spatial and non-

spatial memory with improved ability to discriminate between different items and has increased latency. The results were found in agreement with a previous study where PPL showed the least impact on cognitive function of patients after 1 week of surgery [13]. The PPL-treated rats also showed no significant effect on the locomotor activity of the rats. Acetylcholine, a cholinergic neurotransmitter essential for processing memory and learning, is reduced in concentration and function in patients with AD. The over-activation of AChE is an important enzyme responsible for catalysing the degradation of ACh into acetic acid and choline. Thus, inhibition of AChE causes an increase in the total extracellular concentration of ACh and improves the cognitive dysfunction and other symptoms of AD [7, 18, 22]. In the present study, PPL-treated rats showed a reduction in AChE level compared to STZ-rats, which was highly elevated. Besides cholinergic neurotransmitters, monoaminergic and glutamatergic neurotransmitters also have a significant role in AD's pathogenesis. In AD patients, the level of these neurotransmitters was found significantly reduced, and studies have warranted the significance of restoring the deficit of these neurotransmitters in providing benefit against AD [9]. Thus, in the present study, we have determined the level of DA, NE, and 5-HT and their metabolite (DOPAC, HVA, and 5-HIAA) in rats. These neurotransmitters were found significantly reduced in STZ-treated rats with an increased level of metabolites and provoke cognitive decline, possibly by increased metabolic deactivation. However, the PPL-treated rats significantly reduced the generation of these metabolites, which restored the level of neurotransmitters near to normal. This modulation is suggested to be the probable mechanism behind the protective effect of PPL against cognitive dysfunction. Numerous studies have suggested the significance of oxidative stress and neuroinflammation in the pathogenesis of AD, which causes a reduction of neuronal viability. AD patients have a high level of oxidative stress, which arises due to the reduction of endogenous anti-oxidants, like GSH and SOD. It induces lipid peroxidation (MDA, a biomarker for lipid peroxidation). The flawed anti-oxidant system also leads to the production of peroxynitrite and nitrotyrosine, which causes cell injury and induces neuronal death [2, 4]. In the present study, STZ rats showed impaired anti-oxidant defence as evidenced by the low level of SOD and GSH, which results in a high concentration of MDA and nitrite. However, the

PPL-treated rats showed improvement in anti-oxidant status by restoring the SOD and GSH, which caused a reduction in MDA and nitrite levels. The level of pro-inflammatory (TNF- α , IL-1 β , and IL-6) cytokines was also found significantly reduced in PPL treated compared to control. The study's findings were consistent with previous results where PPL showed anti-oxidant activity and prevented the generation of pro-inflammatory cytokines. These observations suggest that PPL might abrogate cognitive dysfunction induced by STZ, possibly by strong anti-oxidant and anti-inflammatory effects. A similar trend was also observed in the histopathology of neurons in the hippocampus of rats. The STZ rats showed pyknotic nuclei and were found loosely and irregularly arranged. However, the PPL-treated rats showed an ameliorative effect on these morphological characteristics and improved nuclei morphology.

CONCLUSIONS

The present work demonstrated that PPL could significantly attenuate the cognitive dysfunction and neuronal damage in the STZ-induced rats, possibly by reducing oxidative stress and inflammation and restoring the level of vital neurotransmitters. It also prevented neuronal damage and provided significant benefits against the cognitive deficit in rats. This study has limitations, and future studies are warranted to explore the possible effect of PPL on microglial activation and Amygdala-dependent learning behaviour. However, the clinical applicability of PPL has been limited due to various disadvantages, such as emulsion instability, hyperlipidaemia, pain upon injection, microbial contamination, and PPL infusion syndrome. These disadvantages could be easily overcome by changing the dosage form, such as nano-formulation of PPL which improves anaesthetic, pharmacokinetic, hemocompatibility, safety, and permeation profile.

Conflict of interest: None declared

REFERENCES

1. Bloom DE, Cafiero E, Jané-Llopis E, et al. The global economic burden of noncommunicable diseases. *World Econ Forum*. 2011; 1–46.
2. Cai Z, Zhao B, Ratka A. Oxidative stress and β -amyloid protein in Alzheimer's disease. *Neuromolecular Med*. 2011; 13(4): 223–250, doi: [10.1007/s12017-011-8155-9](https://doi.org/10.1007/s12017-011-8155-9), indexed in Pubmed: [21901428](https://pubmed.ncbi.nlm.nih.gov/21901428/).
3. Chen Z, Trapp BD. Microglia and neuroprotection. *J Neurochem*. 2016; 136 Suppl 1: 10–17, doi: [10.1111/jnc.13062](https://doi.org/10.1111/jnc.13062), indexed in Pubmed: [25693054](https://pubmed.ncbi.nlm.nih.gov/25693054/).

4. De la Monte SM, Tong M. Brain metabolic dysfunction at the core of Alzheimer's disease. *Biochem Pharmacol.* 2014; 88(4): 548–559, doi: [10.1016/j.bcp.2013.12.012](https://doi.org/10.1016/j.bcp.2013.12.012), indexed in Pubmed: [24380887](https://pubmed.ncbi.nlm.nih.gov/24380887/).
5. Ellman GL, Courtney KD, Andres V, et al. A new and rapid colorimetric determination of acetylcholinesterase activity. *Biochem Pharmacol.* 1961; 7: 88–95, doi: [10.1016/0006-2952\(61\)90145-9](https://doi.org/10.1016/0006-2952(61)90145-9), indexed in Pubmed: [13726518](https://pubmed.ncbi.nlm.nih.gov/13726518/).
6. Farkas E, Luiten PG. Cerebral microvascular pathology in aging and Alzheimer's disease. *Prog Neurobiol.* 2001; 64(6): 575–611, doi: [10.1016/s0301-0082\(00\)00068-x](https://doi.org/10.1016/s0301-0082(00)00068-x), indexed in Pubmed: [11311463](https://pubmed.ncbi.nlm.nih.gov/11311463/).
7. Gallagher M, Colombo PJ. Ageing: the cholinergic hypothesis of cognitive decline. *Curr Opin Neurobiol.* 1995; 5(2): 161–168, doi: [10.1016/0959-4388\(95\)80022-0](https://doi.org/10.1016/0959-4388(95)80022-0), indexed in Pubmed: [7620303](https://pubmed.ncbi.nlm.nih.gov/7620303/).
8. Hyder A, Wunderlich C, Puvanachandra P, et al. The impact of traumatic brain injuries: A global perspective. *NeuroRehabilitation.* 2007; 22(5): 341–353, doi: [10.3233/nre-2007-22502](https://doi.org/10.3233/nre-2007-22502).
9. Kandimalla R, Reddy PH. Therapeutics of neurotransmitters in Alzheimer's disease. *J Alzheimers Dis.* 2017; 57(4): 1049–1069, doi: [10.3233/JAD-161118](https://doi.org/10.3233/JAD-161118), indexed in Pubmed: [28211810](https://pubmed.ncbi.nlm.nih.gov/28211810/).
10. Korczyn AD, Vakhapova V, Grinberg LT. Vascular dementia. *J Neurol Sci.* 2012; 322(1-2): 2–10, doi: [10.1016/j.jns.2012.03.027](https://doi.org/10.1016/j.jns.2012.03.027), indexed in Pubmed: [22575403](https://pubmed.ncbi.nlm.nih.gov/22575403/).
11. Kumaran D, Hassabis D, Spiers HJ, et al. Impaired spatial and non-spatial configural learning in patients with hippocampal pathology. *Neuropsychologia.* 2007; 45(12): 2699–2711, doi: [10.1016/j.neuropsychologia.2007.04.007](https://doi.org/10.1016/j.neuropsychologia.2007.04.007), indexed in Pubmed: [17507060](https://pubmed.ncbi.nlm.nih.gov/17507060/).
12. Lee CY, Landreth GE. The role of microglia in amyloid clearance from the AD brain. *J Neural Transm (Vienna).* 2010; 117(8): 949–960, doi: [10.1007/s00702-010-0433-4](https://doi.org/10.1007/s00702-010-0433-4), indexed in Pubmed: [20552234](https://pubmed.ncbi.nlm.nih.gov/20552234/).
13. Li WX, Luo RY, Chen C, et al. Effects of propofol, dexmedetomidine, and midazolam on postoperative cognitive dysfunction in elderly patients: a randomized controlled preliminary trial. *Chin Med J (Engl).* 2019; 132(4): 437–445, doi: [10.1097/CM9.000000000000098](https://doi.org/10.1097/CM9.000000000000098), indexed in Pubmed: [30707179](https://pubmed.ncbi.nlm.nih.gov/30707179/).
14. Liu H, Zhang J. Cerebral hypoperfusion and cognitive impairment: the pathogenic role of vascular oxidative stress. *Int J Neurosci.* 2012; 122(9): 494–499, doi: [10.3109/00207179.2012.686543](https://doi.org/10.3109/00207179.2012.686543), indexed in Pubmed: [22519891](https://pubmed.ncbi.nlm.nih.gov/22519891/).
15. O'Brien JT, Thomas A. Vascular dementia. *Lancet.* 2015; 386(10004): 1698–1706, doi: [10.1016/S0140-6736\(15\)00463-8](https://doi.org/10.1016/S0140-6736(15)00463-8), indexed in Pubmed: [26595643](https://pubmed.ncbi.nlm.nih.gov/26595643/).
16. Przedborski S. Neurodegeneration. *Neuroimmune Pharmacology.* 2016: 345–354, doi: [10.1007/978-3-319-44022-4_22](https://doi.org/10.1007/978-3-319-44022-4_22).
17. Razavi BM, Fazly Bazzaz BS. A review and new insights to antimicrobial action of local anesthetics. *Eur J Clin Microbiol Infect Dis.* 2019; 38(6): 991–1002, doi: [10.1007/s10096-018-03460-4](https://doi.org/10.1007/s10096-018-03460-4), indexed in Pubmed: [30680564](https://pubmed.ncbi.nlm.nih.gov/30680564/).
18. Schliebs R, Arendt T. The cholinergic system in aging and neuronal degeneration. *Behav Brain Res.* 2011; 221(2): 555–563, doi: [10.1016/j.bbr.2010.11.058](https://doi.org/10.1016/j.bbr.2010.11.058), indexed in Pubmed: [21145918](https://pubmed.ncbi.nlm.nih.gov/21145918/).
19. Tenner AJ. Complement in Alzheimer's disease: opportunities for modulating protective and pathogenic events. *Neurobiol Aging.* 2001; 22(6): 849–861, doi: [10.1016/S0197-4580\(01\)00301-3](https://doi.org/10.1016/S0197-4580(01)00301-3), indexed in Pubmed: [11754992](https://pubmed.ncbi.nlm.nih.gov/11754992/).
20. Threlkeld SW, Hill CA, Szalkowski CE, et al. Effects of test experience and neocortical microgyria on spatial and non-spatial learning in rats. *Behav Brain Res.* 2012; 235(2): 130–135, doi: [10.1016/j.bbr.2012.07.031](https://doi.org/10.1016/j.bbr.2012.07.031), indexed in Pubmed: [22884828](https://pubmed.ncbi.nlm.nih.gov/22884828/).
21. Truelsen T, Begg S, Mathers C. The global burden of cerebrovascular disease. *Glob Burd Dis.* 2000: 1–67.
22. Van Beek AH, Claassen JA. The cerebrovascular role of the cholinergic neural system in Alzheimer's disease. *Behav Brain Res.* 2011; 221(2): 537–542, doi: [10.1016/j.bbr.2009.12.047](https://doi.org/10.1016/j.bbr.2009.12.047), indexed in Pubmed: [20060023](https://pubmed.ncbi.nlm.nih.gov/20060023/).
23. Wang B, Shrivah J, Luo H, et al. Propofol protects against hydrogen peroxide-induced injury in cardiac H9c2 cells via Akt activation and Bcl-2 up-regulation. *Biochem Biophys Res Commun.* 2009; 389(1): 105–111, doi: [10.1016/j.bbrc.2009.08.097](https://doi.org/10.1016/j.bbrc.2009.08.097), indexed in Pubmed: [19703415](https://pubmed.ncbi.nlm.nih.gov/19703415/).
24. Yuzer H, Yuzbasioglu MF, Ciralik H, et al. Effects of intravenous anesthetics on renal ischemia/reperfusion injury. *Ren Fail.* 2009; 31(4): 290–296, doi: [10.1080/08860220902779962](https://doi.org/10.1080/08860220902779962), indexed in Pubmed: [19462278](https://pubmed.ncbi.nlm.nih.gov/19462278/).
25. Zhao T, Ding Km, Zhang L, et al. Acetylcholinesterase and butyrylcholinesterase inhibitory activities of β -carboline and quinoline alkaloids derivatives from the plants of genus *peganum*. *J Chem.* 2013; 2013: 1–6, doi: [10.1155/2013/717232](https://doi.org/10.1155/2013/717232).

The spinal accessory nerve and its entry point into the posterior triangle of the neck

S. Ellis¹, C. Brassett, N. Glibbery, J. Cheema, S. Madenlidou

Human Anatomy Centre, Department of Physiology, Development and Neuroscience, University of Cambridge, United Kingdom

[Received: 3 November 2021; Accepted: 2 February 2022; Early publication date: 17 February 2022]

Background: The course of the spinal accessory nerve in the neck is long and superficial rendering it at high risk of injury during procedures performed in the posterior triangle. The majority of spinal accessory nerve injuries are iatrogenic in nature. This is associated with significant morbidity including reduction in shoulder movements, drooping of the shoulder, winging of the scapula and neuropathic pain. Knowledge of the nerve anatomy reduces the risk of intra-operative nerve injury. Traditional teaching describes the point of entry into the posterior triangle as the intersection between the upper and middle third of the posterior border of sternocleidomastoid. The aim of this study was to determine whether this is in fact the case and if so, whether this landmark can reliably be used to identify the spinal accessory nerve in order to improve patient outcomes.

Materials and methods: The spinal accessory nerve was identified unilaterally in 26 cadavers. The total length of sternocleidomastoid was measured as well as the length along the posterior border from the inferior aspect of the mastoid process to the point at which the accessory nerve enters the posterior triangle of the neck. These measurements were used to calculate the ratio of the entry point of the nerve into the posterior triangle along the length of the posterior border of sternocleidomastoid from its superior insertion point. The mean ratio was 0.35 with 95% confidence intervals of 0.33 to 0.36.

Results and Conclusions: Our findings confirm the traditional description of the entry point of the spinal accessory nerve into the posterior triangle of the neck. We describe a so-called ‘safe zone’ inferior to the midpoint of the posterior border of sternocleidomastoid within which the spinal accessory nerve is unlikely to be found, thereby reducing the risk of iatrogenic injury. (Folia Morphol 2023; 82, 2: 256–260)

Key words: spinal accessory nerve, anatomy, posterior triangle, iatrogenic injury

INTRODUCTION

The accessory nerve is the 11th cranial nerve and is derived from two roots: a spinal root and a cranial root [7]. The spinal accessory nerve exits the cranium via the jugular foramen, coursing through the neck,

to provide motor supply to the sternocleidomastoid and trapezius muscles [1, 7]. Its long and superficial course renders it at high risk of injury during procedures performed in the posterior triangle of the neck [1, 10].

Address for correspondence: S. Ellis, BSc(Hons), MBChB, MRCS(ENT), Human Anatomy Centre, Department of Physiology, Development and Neuroscience, University of Cambridge, Downing Street, CB2 3EG Cambridge, United Kingdom, tel: 07967 642 841, e-mail: sarah.ellis@doctors.org.uk

This article is available in open access under Creative Common Attribution-Non-Commercial-No Derivatives 4.0 International (CC BY-NC-ND 4.0) license, allowing to download articles and share them with others as long as they credit the authors and the publisher, but without permission to change them in any way or use them commercially.

Most spinal accessory nerve injuries are iatrogenic in nature [6]. The literature demonstrates that it is one of the most commonly injured nerves during surgery across all specialties [20]. The anatomy of the nerve puts it at risk during otolaryngological surgery involving the lateral skull base, superior neck and posterior triangle [7, 15]. This includes cervical lymph node biopsy, sebaceous cyst excision and neck dissection procedures [15]. Whilst the spinal accessory nerve is intentionally resected during a radical neck dissection, both modified-radical and selective neck dissections with nerve preservation are still associated with significant nerve morbidity [1, 5, 18]. Injury to the spinal accessory nerve results in the so-called 'Shoulder Syndrome' [16], characterised by paralysis of the trapezius muscle [10, 13, 17]. Clinical sequelae include reduction in shoulder movements, drooping of the shoulder, winging of the scapula and neuropathic pain [10, 13, 17]. This morbidity, secondary to unintentional iatrogenic injury, has significant medicolegal repercussions as a source of malpractice litigation [15].

Detailed anatomical knowledge of the course of the spinal accessory nerve is fundamental to a reduction in the rate of iatrogenic injury. The nerve arises from the spinal nucleus at the levels C1–6 of the spinal cord [7, 22]. These fibres merge to enter the posterior cranial fossa via the foramen magnum, after which the spinal root combines with the fibres of the cranial root to form a single common accessory nerve trunk [7, 22]. The accessory nerve then exits the cranium via the jugular foramen, in close proximity to the internal jugular vein, before dividing again into a spinal and a cranial portion, with fibres from the latter running with the vagus nerve [7, 22]. The spinal accessory nerve typically descends laterally to the internal jugular vein, then anterior to the transverse process of the atlas before passing medial to the styloid process, the stylohyoid and digastric muscles [7, 17, 22]. The nerve then enters or continues deep to the sternocleidomastoid muscle [17, 22], before exiting from its posterior border to enter the posterior triangle of the neck, where it lies superficially [7, 17, 22]. The nerve then has a tortuous course as it continues to descend inferolaterally before exiting the posterior triangle by passing deep to the anterior border of trapezius [7, 17, 22].

Traditional anatomical teaching describes the point of entry of the spinal accessory nerve into the posterior triangle as the intersection between the su-

perior one-third and inferior two-thirds of the length of the posterior border of sternocleidomastoid muscle [14, 19]. The aim of this study was to determine the veracity of this statement and if so, whether this landmark can reliably be used to identify the spinal accessory nerve intra-operatively, in order to improve patient outcomes through avoidance of iatrogenic injury and associated morbidity.

MATERIALS AND METHODS

Unilateral neck dissections were performed on 26 embalmed cadavers at the Human Anatomy Centre, Department of Physiology, Development and Neuroscience, University of Cambridge. All donors had provided consent before decease for the use of their bodies for anatomical research, in compliance with the Human Tissue Act 2004. The side of the neck where the common carotid artery had not been used for vascular embalming was selected for dissection. The cadavers were placed in a supine position with a shoulder roll in order to extend the neck. The head was also rotated 45 degrees to the contralateral side. A standardised post-auricular skin incision was made. This was extended along the inferior aspect of the mandible, inferiorly at the midline of the anterior neck and along the clavicle laterally to the acromion. The skin flap was reflected laterally to expose the anterior triangle, the sternocleidomastoid muscle, the tip of the mastoid process and the posterior triangle of the neck. The sternocleidomastoid was cleared along its length to allow identification of insertion points, as was the anterior border of trapezius. Meticulous dissection of the posterior triangle allowed for identification of the accessory nerve and its entry and exit points along the sternocleidomastoid and trapezius muscles. The following measurements were taken:

- Length of posterior border of sternocleidomastoid (from the mastoid process superiorly to its attachment inferiorly onto the clavicle);
- Length along posterior border of sternocleidomastoid from its superior insertion point to the point at which the accessory nerve emerged to enter the posterior triangle;
- Length of the anterior border of trapezius (from the clavicle inferiorly to its insertion at the superior nuchal line);
- Length along the anterior border of trapezius from the clavicle inferiorly to the point at which the accessory nerve exits the posterior triangle.

Table 1. Measurements taken and entry point of spinal accessory nerve (SAN) into the posterior triangle

Measurement	Mean	Standard deviation	Range
Length posterior border of sternocleidomastoid	210 mm	23.3 mm	171–260 mm
Length from superior insertion point sternocleidomastoid to entry point of SAN into posterior triangle	73 mm	9.6 mm	51–90 mm
Ratio of entry point SAN into posterior triangle along length of posterior border sternocleidomastoid	0.35	0.04	0.27–0.43

In order to reduce the risk of variability between measurements taken by differing researchers, the insertion points of sternocleidomastoid and trapezius were identified and marked by a single researcher using pins. String measurements were then taken. This was performed independently, and confirmed by two further researchers.

Having obtained the above measurements, the mean length and standard deviations were calculated for each measurement as well as the ratio of the entry point of the accessory nerve into the posterior triangle along the length of the posterior border of sternocleidomastoid from its superior insertion point. The Pearson's correlation coefficient was also calculated in order to determine whether there was any significant relationship between this ratio and the height of the donor.

RESULTS

The spinal accessory nerve was identified unilaterally in 26 cadavers (14 male, 12 female). The median age was 83 years with a range of 67–100 years. The average height and weight were 1.68 m and 63.0 kg, respectively. Seventeen neck dissections were performed on the left and 9 on the right.

The mean length of the posterior border of sternocleidomastoid was 210 mm \pm 23.2 mm standard deviation (SD) with a range of 171–260 mm. The mean length from the superior insertion point to the entry point of the spinal accessory nerve into the posterior triangle, along the posterior border of sternocleidomastoid, was 73 mm \pm 9.6 mm SD.

The ratio of the entry point of the accessory nerve into the posterior triangle along the length of the posterior border of sternocleidomastoid from its superior insertion point ranged from 0.27 to 0.43, with a mean of 0.35 \pm 0.04 SD and 95% confidence intervals of 0.33 to 0.36 (Table 1).

Correlation studies were also performed to investigate the relationship between the height of the donor and the ratio of the entry point of the nerve into the posterior triangle from the superior insertion of sternocleidomastoid. The Pearson's correlation coefficient

was -0.29 ($p < 0.05$). This weak but significant correlation demonstrates that the entry point ratio does not alter with height. The mean entry point ratio was also calculated for male and female specimens; in males this was 0.34 and females it was 0.35.

The mean exit point of the nerve from the posterior triangle was 39 mm along the anterior border of trapezius from the clavicle inferiorly.

DISCUSSION

The aims of this study were to determine if the entry point of the spinal accessory nerve into the posterior triangle of the neck conformed to traditional anatomical teaching, and whether this would be a reliable landmark for intra-operative identification of the nerve. Our findings corroborate traditional teaching which describes the point of entry of the spinal accessory nerve into the posterior triangle as the intersection between the superior one-third and inferior two-thirds of the length of the posterior border of sternocleidomastoid muscle (33% of its length) [14, 19]. In this study, the mean entry point of the nerve into the posterior triangle was 35% of the total length of the posterior border of sternocleidomastoid from its superior insertion. With regards to whether this landmark should be used for intra-operative identification of the spinal accessory nerve, this study has demonstrated, with 95% confidence intervals, that the ratio of the entry point of the accessory nerve into the posterior triangle along the border of sternocleidomastoid lies consistently between 33% and 36% of its length from the superior insertion point, and that this is independent of height and sex.

There have been many attempts within the literature to describe the course of the spinal accessory nerve and to define its point of entry into the posterior triangle of the neck in relation to surrounding structures [8]. This includes distance from the clavicle [8, 9], the mastoid process [3, 4, 8, 11, 12, 23], the angle of the mandible [23], the greater auricular nerve [21] as well as, similar to this study, the distance along the posterior border of sternocleidomastoid from its superior insertion point [1, 2, 13, 21, 22]. This study

found the ratio of the entry point of the accessory nerve into the posterior triangle along the length of the posterior border of sternocleidomastoid from its superior insertion point to be between 0.27 to 0.43 of the total length. Our findings suggest that iatrogenic injury to the spinal accessory nerve may be avoided in the majority of cases by limiting dissection inferior to half way along the posterior border of sternocleidomastoid. These findings are in keeping with those reported within the literature. Symes and Ellis (2005) [22] found that in a cadaveric study of 50 spinal accessory nerves, this ratio was between 0.28 and 0.44 with a mean entry point of 0.36. Similarly, Abakay et al. (2020) [1] found that this ratio was between 0.25 and 0.40 in 87 out of 100 specimens. Soo et al. (1986) [21] reported that in 31 of 32 cadaveric specimens the spinal accessory nerve entered the posterior triangle within the superior half of the border of sternocleidomastoid with the nerve only entering outside of this in area 3% of cases. As such, we can conclude that the majority of iatrogenic injuries to the spinal accessory nerve may be avoided by limiting dissection to the inferior half of sternocleidomastoid and cautious dissection superiorly.

There are methodological limitations to this study including a small sample size of only 26 nerves and the potential for variation in the points between which measurements were taken, for example, when identifying the insertion point of sternocleidomastoid and trapezius muscles. In an attempt to overcome inter-rater variability, a single researcher identified these points with pins for all specimens and two researchers subsequently took all the measurements which were then compared and repeated. However, in order to replicate the clinical environment, we ensured standard positioning with shoulder roll and neck rotated 45 degrees to the contralateral side.

CONCLUSIONS

The principal aim of this study was to determine whether the entry point of the spinal accessory nerve into the posterior triangle is, as described in traditional anatomical teaching, at the intersection between the superior one-third and inferior two-thirds of the length of the posterior border of sternocleidomastoid muscle [14,19]; our findings do confirm this description. In addition, we describe a so-called 'safe zone' of the posterior triangle of the neck, inferior to the midpoint of the posterior border of sternocleidomastoid, within which the spinal accessory nerve

is unlikely to be found, thereby reducing the risk of iatrogenic injury.

Acknowledgements

Donors and their families without whom this study would not have been possible as well as the Dissection Room technical staff at the Human Anatomy Centre, Department of Physiology, Development and Neuroscience, University of Cambridge.

Conflict of interest: None declared

REFERENCES

1. Abakay MA, Güneş S, Küçük C, et al. Accessory nerve anatomy in anterior and posterior cervical triangle: a fresh cadaveric study. *Turk Arch Otorhinolaryngol.* 2020; 58(3): 149–154, doi: [10.5152/tao.2020.5263](https://doi.org/10.5152/tao.2020.5263), indexed in Pubmed: [33145498](https://pubmed.ncbi.nlm.nih.gov/33145498/).
2. Amuti TM, Butt F, Otieno BO, et al. The relation of the extracranial spinal accessory nerve to the sternocleidomastoid muscle and the internal jugular vein. *Craniofac Trauma Reconstr.* 2019; 12(2): 108–111, doi: [10.1055/s-0038-1641171](https://doi.org/10.1055/s-0038-1641171), indexed in Pubmed: [31073359](https://pubmed.ncbi.nlm.nih.gov/31073359/).
3. Canella C, Demondion X, Abreu E, et al. Anatomical study of spinal accessory nerve using ultrasonography. *Eur J Radiol.* 2013; 82(1): 56–61, doi: [10.1016/j.ejrad.2011.04.038](https://doi.org/10.1016/j.ejrad.2011.04.038), indexed in Pubmed: [21596503](https://pubmed.ncbi.nlm.nih.gov/21596503/).
4. Dailiana ZH, Mehdian H, Gilbert A. Surgical anatomy of spinal accessory nerve: is trapezius functional deficit inevitable after division of the nerve? *J Hand Surg Br.* 2001; 26(2): 137–141, doi: [10.1054/jhsb.2000.0487](https://doi.org/10.1054/jhsb.2000.0487), indexed in Pubmed: [11281665](https://pubmed.ncbi.nlm.nih.gov/11281665/).
5. Goldstein DP, Ringash J, Bissada E, et al. Scoping review of the literature on shoulder impairments and disability after neck dissection. *Head Neck.* 2014; 36(2): 299–308, doi: [10.1002/hed.23243](https://doi.org/10.1002/hed.23243), indexed in Pubmed: [23554002](https://pubmed.ncbi.nlm.nih.gov/23554002/).
6. Grossman JAI, Ruchelsman DE, Schwarzkopf R. Iatrogenic spinal accessory nerve injury in children. *J Pediatr Surg.* 2008; 43(9): 1732–1735, doi: [10.1016/j.jpedsurg.2008.04.029](https://doi.org/10.1016/j.jpedsurg.2008.04.029), indexed in Pubmed: [18779017](https://pubmed.ncbi.nlm.nih.gov/18779017/).
7. Johal J, Iwanaga J, Tubbs K, et al. The accessory nerve: a comprehensive review of its anatomy, development, variations, landmarks and clinical considerations. *Anat Rec (Hoboken).* 2019; 302(4): 620–629, doi: [10.1002/ar.23823](https://doi.org/10.1002/ar.23823), indexed in Pubmed: [29659160](https://pubmed.ncbi.nlm.nih.gov/29659160/).
8. Khavanin N, Carl HM, Yang R, et al. Surgical "safe zone": rapid anatomical identification of the lesser occipital nerve. *J Reconstr Microsurg.* 2019; 35(5): 341–345, doi: [10.1055/s-0038-1676601](https://doi.org/10.1055/s-0038-1676601), indexed in Pubmed: [30562799](https://pubmed.ncbi.nlm.nih.gov/30562799/).
9. Kierner AC, Zelenka I, Heller S, et al. Surgical anatomy of the spinal accessory nerve and the trapezius branches of the cervical plexus. *Arch Surg.* 2000; 135(12): 1428–1431, doi: [10.1001/archsurg.135.12.1428](https://doi.org/10.1001/archsurg.135.12.1428), indexed in Pubmed: [11115348](https://pubmed.ncbi.nlm.nih.gov/11115348/).
10. London J, London NJ, Kay SP. Iatrogenic accessory nerve injury. *Ann R Coll Surg Engl.* 1996; 78(2): 146–150, indexed in Pubmed: [8678450](https://pubmed.ncbi.nlm.nih.gov/8678450/).
11. Lu L, Haman SP, Ebraheim NA. Vulnerability of the spinal accessory nerve in the posterior triangle of the neck:

- a cadaveric study. *Orthopedics*. 2002; 25(1): 71–74, doi: [10.3928/0147-7447-20020101-20](https://doi.org/10.3928/0147-7447-20020101-20), indexed in Pubmed: [11811246](https://pubmed.ncbi.nlm.nih.gov/11811246/).
12. Lloyd S. Accessory nerve: anatomy and surgical identification. *J Laryngol Otol*. 2007; 121(12): 1118–1125, doi: [10.1017/S0022215107000461](https://doi.org/10.1017/S0022215107000461), indexed in Pubmed: [17892604](https://pubmed.ncbi.nlm.nih.gov/17892604/).
 13. Mirjalili SA, Muirhead JC, Stringer MD. Ultrasound visualization of the spinal accessory nerve in vivo. *J Surg Res*. 2012; 175(1): e11–e16, doi: [10.1016/j.jss.2011.10.046](https://doi.org/10.1016/j.jss.2011.10.046), indexed in Pubmed: [22261590](https://pubmed.ncbi.nlm.nih.gov/22261590/).
 14. Moore KL, Dalley AF. Clinically orientated anatomy. 3rd ed. Lippincott Williams and Wilkins, Philadelphia 1992.
 15. Morris LGT, Ziff DJS, DeLacure MD. Malpractice litigation after surgical injury of the spinal accessory nerve: an evidence-based analysis. *Arch Otolaryngol Head Neck Surg*. 2008; 134(1): 102–107, doi: [10.1001/archotol.134.1.102](https://doi.org/10.1001/archotol.134.1.102), indexed in Pubmed: [18209145](https://pubmed.ncbi.nlm.nih.gov/18209145/).
 16. Nahum AM, Mullally W, Marmor L. A syndrome resulting from radical neck dissection. *Arch Otolaryngol*. 1961; 74: 424–428, doi: [10.1001/archotol.1961.00740030433011](https://doi.org/10.1001/archotol.1961.00740030433011), indexed in Pubmed: [14477989](https://pubmed.ncbi.nlm.nih.gov/14477989/).
 17. Overland J, Hodge JC, Breik O, et al. Surgical anatomy of the spinal accessory nerve: review of the literature and case report of a rare anatomical variant. *J Laryngol Otol*. 2016; 130(10): 969–972, doi: [10.1017/S0022215116008148](https://doi.org/10.1017/S0022215116008148), indexed in Pubmed: [27268496](https://pubmed.ncbi.nlm.nih.gov/27268496/).
 18. Popovski V, Benedetti A, Popovic-Monevska D, et al. Spinal accessory nerve preservation in modified neck dissections: surgical and functional outcomes. *Acta Otorhinolaryngol Ital*. 2017; 37(5): 368–374, doi: [10.14639/0392-100X-844](https://doi.org/10.14639/0392-100X-844), indexed in Pubmed: [29165431](https://pubmed.ncbi.nlm.nih.gov/29165431/).
 19. Romanes GF, Cunningham DJ. Cunningham's textbook of anatomy, 12th ed. Oxford University Press, Oxford 1981.
 20. Sharp E, Roberts M, Żurada-Zielińska A, et al. The most commonly injured nerves at surgery: A comprehensive review. *Clin Anat*. 2021; 34(2): 244–262, doi: [10.1002/ca.23696](https://doi.org/10.1002/ca.23696), indexed in Pubmed: [33090551](https://pubmed.ncbi.nlm.nih.gov/33090551/).
 21. Soo KC, Hamlyn PJ, Pegington J, et al. Anatomy of the accessory nerve and its cervical contributions in the neck. *Head Neck Surg*. 1986; 9(2): 111–115, doi: [10.1002/hed.2890090207](https://doi.org/10.1002/hed.2890090207), indexed in Pubmed: [3623936](https://pubmed.ncbi.nlm.nih.gov/3623936/).
 22. Symes A, Ellis H. Variations in the surface anatomy of the spinal accessory nerve in the posterior triangle. *Surg Radiol Anat*. 2005; 27(5): 404–408, doi: [10.1007/s00276-005-0004-9](https://doi.org/10.1007/s00276-005-0004-9), indexed in Pubmed: [16132192](https://pubmed.ncbi.nlm.nih.gov/16132192/).
 23. Tubbs RS, Salter EG, Wellons JC, et al. Superficial landmarks for the spinal accessory nerve within the posterior cervical triangle. *J Neurosurg Spine*. 2005; 3(5): 375–378, doi: [10.3171/spi.2005.3.5.0375](https://doi.org/10.3171/spi.2005.3.5.0375), indexed in Pubmed: [16302632](https://pubmed.ncbi.nlm.nih.gov/16302632/).

The structure of the rostral epidural rete mirabile and caudal epidural rete mirabile of the domestic pig

S. Graczyk¹, M. Zdun¹

Department of Basic and Preclinical Sciences, Institute of Veterinary Medicine, Nicolaus Copernicus University in Torun, Poland

[Received: 15 November 2021; Accepted: 17 January 2022; Early publication date: 31 January 2022]

Background: *The rostral epidural rete mirabile in the domestic pig has been studied by many scientists; however, the caudal epidural rete mirabile has been poorly understood and is rarely mentioned in the literature in domestic pig species. Based on the role of the rostral epidural rete mirabile in retrograde transfer of neurotransmitters and its localisation and structure, we hypothesize that the caudal rete may also play an important role in this process.*

Materials and methods: *The study was conducted on 80 domestic pigs (*Sus scrofa domestica*) of the Suidae family, including 60 piglets aged 0–20 days and 20 adult animals aged 5–9 months.*

Results: *The rostral epidural rete mirabile is an even well-developed structure consisting of dozens of anastomosing arterioles embedded in the cavernous sinus, formed by the maxillary and external ocular artery branches, which are extensions of the external carotid artery, and a thick branch to the rostral epidural rete mirabile. However, the caudal epidural rete mirabile is a structure made up of several interlacing arterioles consisting of the vertebral, condylar and occipital arteries on the caudal side, while on the rostral side it is made up of the middle meningeal artery branching off the inner surface of the temporal bone.*

Conclusions: *The whole caudal epidural rete mirabile is embedded in the basilar and occipital sinuses, which led us to hypothesize that in these sinuses a retrograde transfer of neurotransmitters may take place analogous to the rostral epidural rete mirabile. (Folia Morphol 2023; 82, 2: 261–268)*

Key words: cavernous sinus, swine, retrograde transfer of neurotransmitters, rete mirabile

INTRODUCTION

The rostral epidural rete mirabile (*rete mirabile epidurale rostrale*) and the caudal epidural rete mirabile (*rete mirabile epidurale caudale*) are the main sources of arterial blood supplied to the encephalon of the domestic pig. The presence of both retia in this species was mentioned by Daniel et al. [5], Getty and

Sisson [14], and Tandler [45], but the researchers did not describe their structure in detail. The available studies (publications) provide information about the location of both retia and their general characteristics [6, 23, 31, 50]. The structure of the rostral epidural rete mirabile is closely related to its function. It plays an important role in selective cooling of the brain

Address for correspondence: Dr. S. Graczyk, Department of Basic and Preclinical Sciences Institute of Veterinary Medicine, Nicolaus Copernicus University in Torun, ul. Lwowska 1, 87–100 Toruń, Poland, e-mail: graczyk72@gmail.com

This article is available in open access under Creative Common Attribution-Non-Commercial-No Derivatives 4.0 International (CC BY-NC-ND 4.0) license, allowing to download articles and share them with others as long as they credit the authors and the publisher, but without permission to change them in any way or use them commercially.

[3, 19, 43], the water-saving mechanism in the body [20] and in the retrograde transfer of neurotransmitters [27, 28]. However, there have been no studies on the function of the caudal epidural rete mirabile. This study provides an analysis of the location of both retia, their structure and relations with the venous system. The aim of the study was to pose hypotheses about the potential role of the caudal epidural rete mirabile and to provide information which may be used in future physiological research in this area.

MATERIALS AND METHODS

The study was conducted on 80 domestic pigs (*Sus scrofa domestica*) of the Suidae family, including 60 piglets aged 0–20 days and 20 adult animals aged 5–9 months. All the animals were provided by private breeders.

Twenty-five (21 piglets, 4 adults) specimens were prepared by injecting red self-curing DURACRYL® PLUS (SporaDental) into the bilateral common carotid arteries. Blue DURACRYL® PLUS was also injected into the venous system of 15 (13 piglets, 2 adult) specimens, i.e. into the venous sinus of the eye. Fifteen piglets were injected only by blue DURACRYL® PLUS into the venous sinus of the eye. When the specimens had cured after about 20 min, the material was enzymatically macerated with Persil powder (Henkel) at 42°C for about 1 month. The procedure resulted in corrosion casts of blood vessels on the bone scaffold. The remaining 25 (15 piglets, 10 adults) specimens were prepared by injecting liquid red LBS 3060 latex into the bilateral common arteries. Blue LBS 3060 latex was also injected into the external jugular vein of 15 (11 piglets, 4 adults) specimens. In addition, 15 piglets were only injected with blue LBS 3060 latex into the external jugular vein. Next, the material was immersed in a 5% formalin solution for 14 days to harden. Then the arteries were dissected with surgical instruments to obtain images of the blood vessels on the animals' tissues. The names of the anatomical structures were standardised according to the *Nomina Anatomica Veterinaria* (2017).

Ethics approval

All applicable international, national, and institutional guidelines for the care and use of animals were followed.

RESULTS

The rostral epidural rete mirabile of the domestic pig is mainly formed by the ramus to the rostral epi-

dural rete mirabile (*ramus ad rete mirabile epidurale rostrale*), which is an extension of the internal carotid artery (*arteria carotis interna*). Blood is also supplied to the rete by arteries, which are an extension of the external carotid artery (*arteria carotis externa*). This is the maxillary artery (*arteria maxillaris*) through its rami to the rostral epidural rete mirabile, which is formed by two vessels merging just before the rete. Apart from that, the maxillary artery branches into the external ophthalmic artery (*arteria ophthalmica externa*), whose rami go to the rostral epidural rete mirabile. The rami to the rostral epidural rete mirabile extending from the maxillary and external ophthalmic arteries do not play a significant role in supplying arterial blood to the encephalon because their lumens are too small. The intracranial segment of the internal carotid artery emerges from the rostral epidural rete mirabile. It contributes to the formation of the cerebral arterial circle (*circulus arteriosus cerebri*) in the form of paired rostral cerebral arteries (*arteriae cerebri rostrales*) and paired caudal communicating arteries (*arteriae communicans caudales*).

The rostral epidural rete mirabile is a well-developed, paired structure composed of numerous tiny anastomosing arteries. It enters the cranial cavity through the foramen lacerum and bends at its rostral edge. The intracranial part comprises 60% of the rete, whereas the extracranial part comprises 40%. Due to the course of the arteries the rostral epidural rete mirabile is shaped like an inverted saddle placed on the basisphenoid bone (Fig. 1). In a cross-sectional view the rostral epidural rete mirabile has a circular outline. All arteries in the rete were of the same thickness. Their number varied depending on the age of the animal. On average, the piglets had 103 arteries in the left rete, with a standard deviation of 18, and 120 arteries in the right rete, with a standard deviation of 20. The adult animals had on average 132 vessels in the left rete, with a standard deviation of 20, and in 147 vessels in the right rete with a standard deviation of 19. The cross section of this rete showed that newborn piglets had one vessel with a much larger diameter than the other vessels in the rete. However, this feature disappeared shortly after birth. The bilateral retia were connected by 35–40 small arterioles in the anterior segment, regardless of the age of the animal. As for the length of the rete in piglets, its average was 9.45 mm with a standard deviation of 3.65 mm. The same value in adults was 24.51 mm with a standard deviation of 2.08 mm. The

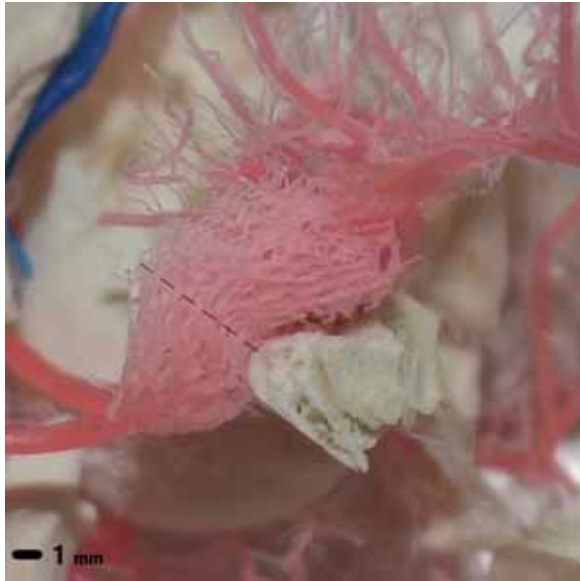


Figure 1. Domestic pig (*Sus scrofa domestica*). Rostral epidural rete mirabile (lateral view). Dashed line — entry point to the cranial cavity. Corrosive preparation.

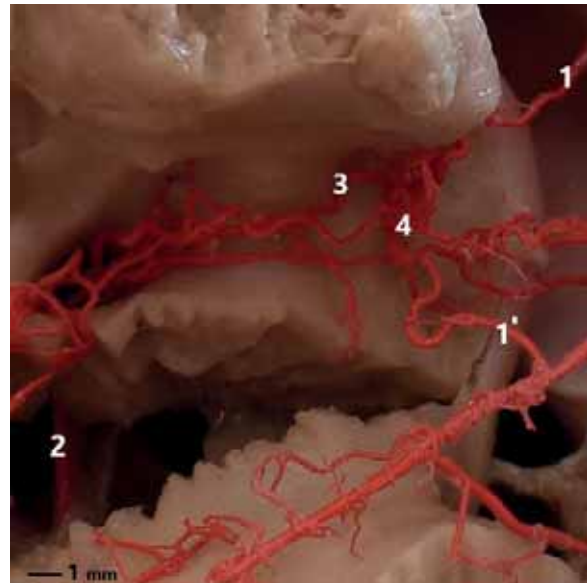


Figure 2. Domestic pig (*Sus scrofa domestica*). Caudal epidural rete mirabile — posterior side (dorsal view); 1 — vertebral artery; 1' — extension of vertebral artery; 2 — condylar artery; 3 — occipital artery; 4 — caudal epidural rete mirabile. Latex preparation.

diameters of the arterioles present in the rete in both study groups were also measured. In the piglet group, the mean value of the arterioles diameter of the rete was 0.26 mm with a standard deviation of 0.03. In the adult pig group, this size was equal to 0.45 mm with a standard deviation of 0.05 mm.

The posterior side of the caudal epidural rete mirabile is formed by the vertebral artery (*arteria vertebralis*), which is joined by the occipital artery (*arteria occipitalis*) before the rete. The posterior side of the rete is also formed by the condylar artery, which reaches the rete through the foramen alare of the atlas (Fig. 2). Meningeal branch (*ramus meningeus*) of the condylar artery is another tributary to the rete on the rostral side. It branches into 6–8 arterioles running dorsally in a triangular shape along the inner surface of the lateral part of the occipital bone. Next, these arterioles extend to supply blood to the meninges. The caudal epidural rete mirabile is connected to the cerebral arterial circle through the basilar artery (*arteria basillaris*), which is formed by the bilateral vertebral arteries.

The caudal part of the rete is situated on the border of the atlas and the occipital bone, just before the entrance to the foramen magnum, whereas the rostral part adjoins the inner surface of the lateral part of the occipital bone. It is a flat structure, extending on one plane. The number of arteries in the rete does not change during ontogenesis. However,

the course of the arterioles supplying blood to the meninges, i.e. the rostral part of the rete, changes with the age of the animal. The arterial vessels run straight in young animals, but their course becomes more tortuous as animals grow older. There was no direct connection between the rostral and caudal epidural retia mirabilia.

The cavernous sinus enters the cranial cavity through the foramen lacerum and fills most of it. It is seated on the presphenoid bone just below the surface of the meninges. In the central part of this sinus there is a fragment connecting the bilateral sinuses. It is the intercavernous sinus (*sinus intercavernosus*), situated rostrally from the sella turcica. The rostral segment of the caudal epidural rete mirabile with the meningeal branch from the condylar artery is completely covered by the occipital sinus, which extends over the entire inner surface of the lateral part of the occipital bone. This sinus is in direct contact with the basilar sinus, which is an extension of the cavernous sinus in the caudal direction. It runs along the border between the basisphenoid bone and the petrous part of the temporal bone up to the inner surface of the alae of the atlas, where it extends into the ventral vertebral venous plexus, which runs on both sides of the spinal canal. Apart from that, at the caudal fragment of the rete, i.e. on the border between the foramen magnum and the vertebral foramen of the atlas, a segment connecting the bilateral basilar

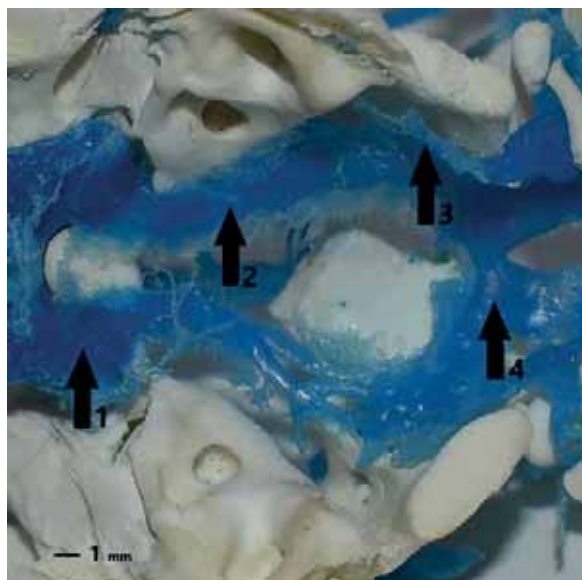


Figure 3. Domestic pig (*Sus scrofa domestica*); 1 — cavernous sinus; 2 — basilar sinus; 3 — occipital sinus; 4 — interbasilar sinus. Corrosive preparation.

sinuses, i.e. the interbasilar sinus (*sinus interbasilaris*), was found. The cavernous sinus together with the basilar and occipital sinuses form a system which completely covers the rostral and caudal retia (Fig. 3). The material from the arterial system was not mixed with the material injected into the veins. This fact shows that the blood returning from the cephalic region does not mix with the oxygenated blood from the lungs. An intracranial segment of the internal carotid artery emerges from the rostral epidural rete mirabile embedded in the cavernous sinus and forms the cerebral arterial circle. Part of the occipital sinus surrounds numerous meningeal arteries supplying arterial blood to the meninges, whereas the basilar sinus surrounds the bilateral vertebral arteries, which contribute to the formation of the basilar artery.

DISCUSSION

A paired epidural rete mirabile can be found not only in the domestic pig but also in other even-toed ungulates of the Atriodyctyla order, i.e. Antilopinae [11], Moschidae [10], Bovinae [7, 13, 37, 47], Giraffidae [15, 33], Caprinae [1, 38], Camelidae [22, 34, 47], Cervidae [25, 51, 53], and Antilocapridae [4]. The only exception is mouse-deer of the Tragulidae family, which do not have a rostral epidural rete mirabile. The components of their cerebral arterial circle are formed by the internal carotid artery [9, 32]. The rostral epidural rete mirabile in animals of the Bovidae family is

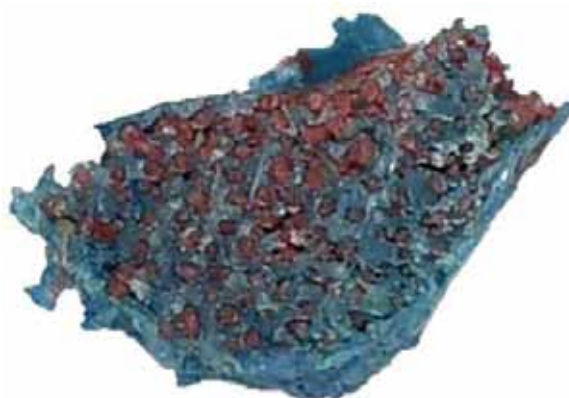


Figure 4. Domestic pig (*Sus scrofa domestica*). Relationships of the arterioles of the rostral epidural rete mirabile to the cavernous sinus. Cross-section. Corrosive preparation.

formed by the rostral branches and the caudal ramus to the rostral epidural rete mirabile [51, 52]. Apart from the aforementioned tributaries, blood to the rete is also supplied by the condylar artery, which is characteristic of the Cervidae and Giraffidae families [12, 16, 26]. Kieltycka-Kurc et al. [26] observed that the rostral epidural rete mirabile in animals of the Camelidae family was formed by branches running from the maxillary artery and the external ophthalmic artery. The internal carotid artery is the third tributary, which becomes obliterated during the ontogenesis of animals of the Suidae family [15, 49].

The caudal epidural rete mirabile can also be found in animals of the Bovini tribe, where it is an extension of the condylar artery. In contrast to animals of the Suidae family, the caudal epidural rete mirabile in representatives of the Bovini tribe is directly connected to the rostral epidural rete mirabile and it is not a paired structure [52].

Simoens et al. [38] distinguished two types of the rostral epidural rete mirabile, i.e. the fascicular type, with the intraretial segment of the internal carotid artery, which has a much greater lumen than other arterioles, this situation is observed in newborn piglets, and the bipolar type, where all vessels in the rete have similar diameters, which can be seen in a cross-sectional view. The change in rete type from fascicular to bipolar occurs shortly after birth (Fig. 4).

The physiology of the epidural rete mirabile seems to significantly affect the regulation of the processes taking place in the body. For centuries this structure has been researched by scientists specialising in anatomy and physiology. Apart from the mechanisms of selective cooling of the brain [42, 46], which have already been

investigated [19], the retrograde transfer of neurotransmitters in the rete also seems to be very important.

Krzymowski et al. [27] were the first to describe the phenomenon of neuropeptide exchange (Lh-Rh, progesterone, and beta-endorphin) in the cavernous sinus and the rostral epidural rete mirabile. This process is possible due to the specific structure of the entire complex of the rete and the cavernous sinus. The rete vessels and the sinus have a common adventitia, which ensures a direct connection, whereas the lamina muscularis mucosae of the arterial vessels in the rete itself has 3–5 layers [24]. Additionally, the arterial vessels of the rete exhibit fenestrations [23], whose diameters change depending on the phase of the cycle. This fact may be of key importance in the retrograde exchange of hormones between the venous blood returning to the sinus from the brain, pituitary gland, part of the ear and the eye, and the arterial blood in the rete. Krzymowski et al. [29] found the following cranial nerves in the cavernous sinus: the oculomotor nerve (III), trochlear nerve (IV), branches of the trigeminal nerve (V), i.e. the optic nerve (V₁) and maxillary nerve (V₂), and the abducens nerve (VI) between the arterial vessels of the rete. However, the potential role of the nerves passing through the cavernous sinus has not been investigated yet. Grzegorzewski et al. [17, 18] conducted a study on 37 sows' heads, in which they observed that when radiolabelled oxytocin and gonadoliberin were injected into the angular vein of the eye, there was countercurrent exchange of this hormone in the cavernous sinus exactly 2 days after ovulation, and then also between the 12th and 14th day of the cycle, in the late luteal phase. The authors of later studies observed a positive reaction after the injection of labelled dopamine in sheep [41] or testosterone and androstenol in isolated sows' heads [39, 44]. There was no evidence of the countercurrent exchange of prolactin (PRL) and luteinising hormone (LH), most likely due to the mass of these substances, i.e. 23 kDa (PRL) and 30 kDa (LH). These values were greater than the mass of the aforementioned hormones, which ranged from 0.19 kDa to 3.4 kDa [40]. Oren [35] indicated a very important function of carbon monoxide (CO), which is synthesised on the retina thanks to the action of light rays in the phototransduction mechanism. According to the researcher, CO may regulate the activity of various areas of the brain, thanks to the countercurrent exchange mechanism through the blood flowing from the ophthalmic re-

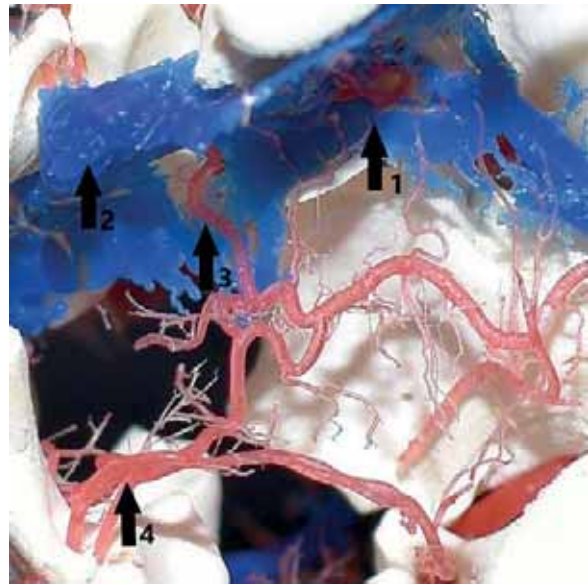


Figure 5. Domestic pig (*Sus scrofa domestica*); 1 — rostral part of caudal epidural rete mirabile (excised section of the occipital sinus to show the rete arterioles); 2 — occipital sinus; 3 — vertebral artery; 4 — caudal part of caudal epidural rete mirabile. Corrosive preparation.

gion, including the retina, to the cavernous sinus and the exchange of this substance from the venous blood into the arterial blood of the rete. Kozirowski et al. [30] confirmed Oren's hypothesis. They also found CO in the suprachiasmatic nucleus and suggested that it may change the expression of the *per* and *cry* genes, which regulate the circadian and seasonal rhythms, and thus it may significantly affect the daily activity of these animals. The presence of CO synthesised on the retina, as well as the presence of the aforementioned neurotransmitters in various areas of the brain, indicates the superior function of these substances in the regulation of processes occurring in the bodies of animals and humans, and points to the existence of an internal self-regulation system [28].

As far as the caudal epidural rete mirabile is concerned (Fig. 5), the key role seems to be played by the effect of one of the oestrogens, i.e. 17-beta-estradiol, which by means of the mechanism of countercurrent exchange can get from the blood returning from the brain to the vessels of this rete and reciprocally affect the cerebellum through the basilar artery. This hormone, after penetrating the cell membrane, binds to specific ER-alpha and ER-beta receptors, which, after binding to appropriate ligands, form dimers and in the form of oestrogen response elements bind to promoters for oestrogen genes, finally leading to mod-

ifications in the transcription of a specific gene [8]. Apart from the fact that oestradiol has been recognised as an important regulator in the physiology of reproduction through its influence on the hypothalamic-pituitary-ovarian system, there is another, crucial function of this hormone, which is its participation in the development of the central nervous system, and particularly in the formation of motor and cognitive functions [2, 21]. The same study [21] demonstrated high levels of ER-beta receptors during the early growth of granule cell axons and dendrites of cerebellar Purkinje cells. Expression of these receptors remained high during the growth and development of Purkinje cell dendrites and continued into adulthood. In later adulthood, high levels of ER-beta receptors were also shown in basket cells, stellate cells as well as glial cells, suggesting that these receptors may contribute significantly to cerebellar cell development and their synaptic connections [36] in a study performed in rats demonstrated a close relationship between prostaglandin E2 (PGE2), which activates oestradiol for aromatase synthesis, and microglia cells, which have phagocytic properties during cerebellar maturation. When inhibitors for oestradiol and PGE2 were used, the levels of phagocytic microglia cells in the cerebellar vermis and both cerebellar hemispheres were measured using the universal marker Iba1. After aromatase inhibition, a slight decrease in phagocytic cells was demonstrated in the cerebellar vermis, while no significant change in the number of these cells was observed in the cerebellar hemispheres. However, the authors of the text emphasised that when the animal was treated exogenously, oestradiol and PGE2 had little effect on the activity and number of phagocytic cells of microglia, whereas the same substances of endogenous origin were crucial for this process and were essential for its proper functioning. The reason could be the maximum threshold of these substances in the cerebellum, which was already reached by those of endogenous origin. Thus, in view of the above facts, we believe that in the area of the occipital sinus there may be an exchange of these substances between the venous blood returning from the head and the arterial blood of the caudal epidural rete mirabile, and thus the maintenance of a constant level of them in the area of the maturing cerebellum which contributes into its correct development.

These mechanisms may significantly affect the processes taking place in the animal's body, especially

those occurring in the reproductive system, diseases, development and the oestrus cycle. Detailed analysis, knowledge, understanding, and skilful use of the principle of operation of this system will improve the productivity of animals and enable economical management of the herd by minimising reproductive losses. It is likely that these phenomena may play an even greater role in domestic pigs, because the paired caudal epidural rete mirabile is completely embedded in the occipital and basilar sinuses. In consequence, the process of penetration can only be improved and the amount of these substances returning to the brain can be multiplied. By demonstrating the precise relationship between the caudal epidural rete mirabile and the occipital and basilar sinuses, we believe that this study will form the basis for further research into the retrograde transfer of neurotransmitters within the caudal epidural rete mirabile, similar to the rostral epidural rete mirabile.

CONCLUSIONS

The rostral epidural rete mirabile is a paired structure composed of small embedded anastomosing arteries, located on the rostral edge of the foramen ovale and shaped like an inverted saddle.

The caudal epidural rete mirabile is a paired structure composed of the caudal and rostral parts. The caudal part, which includes the condylar, vertebral, and occipital arteries, is located on the border between the alae of the apical vertebra and the occipital bone. The rostral part, which is directly connected with the caudal part, is located on the inner surface of the lateral part of the occipital bone, which extends into the meningeal arteries.

The rostral epidural rete mirabile is embedded in the cavernous sinus. Both parts of the caudal epidural rete mirabile are embedded in the occipital sinus.

There was no direct connection between the rostral and caudal epidural retia mirabilia.

The number of arteries in the rostral epidural rete mirabile increases with the age of the animal.

Conflict of interest: None declared

REFERENCES

1. Alsafy MA, Kamal B, Elgendy SA. Morphological configuration of the brain arterial supply of the goat (*Capra hircus*). *J Appl Biol.* 2017; 11: 39–43.
2. Beyer C. Estrogen and the developing mammalian brain. *Anat Embryol (Berl).* 1999; 199(5): 379–390, doi: [10.1007/s004290050236](https://doi.org/10.1007/s004290050236), indexed in Pubmed: [10221449](https://pubmed.ncbi.nlm.nih.gov/10221449/).

3. Caputa M. The mechanisms of brain protection against overheating in human and some other species of mammals. Dissertation. Uniwersytet Mikołaja Kopernika, Toruń 1982.
4. Carlton C, McKean T. The carotid and orbital retia of the pronghorn, deer and elk. *Anat Rec.* 1977; 189(1): 91–107, doi: [10.1002/ar.1091890107](https://doi.org/10.1002/ar.1091890107), indexed in Pubmed: [907206](https://pubmed.ncbi.nlm.nih.gov/907206/).
5. Daniel PM, Dawes JDK, Prichard MML. Studies of the carotid rete and its associated arteries. *Philos Trans R Soc Lond B Biol Sci.* 1997; 237(645): 173–208, doi: [10.1098/rstb.1953.0003](https://doi.org/10.1098/rstb.1953.0003).
6. de Lima EMM, Severino RS, Carneiro FO, et al. Artérias da base do encéfalo em suínos (*Sus scrofa domestica* - Linnaeus, 1758) da linhagem Camborough 22. *J Biosci.* 2005; 21: 137–147, doi: [10.14393/ufu.di.2002.24](https://doi.org/10.14393/ufu.di.2002.24).
7. Ding Y, Shao B, Wang J. The arterial supply to the brain of the yak (*Bos grunniens*). *Ann Anat.* 2007; 189(1): 31–38, doi: [10.1016/j.aanat.2006.07.011](https://doi.org/10.1016/j.aanat.2006.07.011), indexed in Pubmed: [17319606](https://pubmed.ncbi.nlm.nih.gov/17319606/).
8. Edwards DP. The role of coactivators and corepressors in the biology and mechanism of action of steroid hormone receptors. *J Mammary Gland Biol Neoplasia.* 2000; 5(3): 307–324, doi: [10.1023/a:1009503029176](https://doi.org/10.1023/a:1009503029176), indexed in Pubmed: [14973393](https://pubmed.ncbi.nlm.nih.gov/14973393/).
9. Fukuta K, Kudo H, Sasaki M, et al. Absence of carotid rete mirabile in small tropical ruminants: implications for the evolution of the arterial system in artiodactyls. *J Anat.* 2007; 210(1): 112–116, doi: [10.1111/j.1469-7580.2006.00667.x](https://doi.org/10.1111/j.1469-7580.2006.00667.x), indexed in Pubmed: [17229288](https://pubmed.ncbi.nlm.nih.gov/17229288/).
10. Frąckowiak H. Magistrale tętnicze głowy u niektórych rzędów ssaków. *Rocz AR.* 2003; 336: 5–80.
11. Frąckowiak H, Dębiński D, Komosa M, et al. The arterial circle of the brain, its branches and connections in selected representatives of the antilopinae. *J Morphol.* 2015; 276(7): 766–771, doi: [10.1002/jmor.20377](https://doi.org/10.1002/jmor.20377), indexed in Pubmed: [25694115](https://pubmed.ncbi.nlm.nih.gov/25694115/).
12. Frąckowiak H, Jakubowski H. Arterial vascularization in the giraffe brain. *Ann Zool Fenn.* 2008; 45(4): 353–359, doi: [10.5735/086.045.0418](https://doi.org/10.5735/086.045.0418).
13. Frąckowiak H, Zdun M, Kowalczyk K, et al. Comparison of cerebral base arteries in antelopes of *Tragelaphus*, *Taurotragus* and *Boselaphus* genera. *Zoomorphology.* 2014; 133(3): 351–357, doi: [10.1007/s00435-014-0229-4](https://doi.org/10.1007/s00435-014-0229-4).
14. Getty R, Sisson S. Sisson and Grossman's the Anatomy of the Domestic Animals. Saunders, Philadelphia 1975.
15. Godynicki S, Frackowiak H. Arterial branches supplying the rostral and caudal retia mirabilia in artiodactyls. *Folia Morphol.* 1979; 38(4): 505–510, indexed in Pubmed: [317588](https://pubmed.ncbi.nlm.nih.gov/317588/).
16. Graczyk S, Zdun M. The structure of the rostral epidural rete mirabile in selected representatives of the Cervidae and Bovidae families. *Acta Zool.* 2021; 102(4): 496–501, doi: [10.1111/azo.12391](https://doi.org/10.1111/azo.12391).
17. Grzegorzewski W, Skipor J, Wasowska B, et al. Counter current transfer of oxytocin from the venous blood of the perihypophyseal cavernous sinus to the arterial blood of carotid rete supplying the hypophysis and brain depends on the phase of the estrous cycle in pigs. *Biol Reprod.* 1995; 52(1): 139–144, doi: [10.1095/biolreprod52.1.139](https://doi.org/10.1095/biolreprod52.1.139), indexed in Pubmed: [7711172](https://pubmed.ncbi.nlm.nih.gov/7711172/).
18. Grzegorzewski WJ, Skipor J, Wasowska B, et al. Counter-current transfer of 125I-LHRH in the perihypophyseal cavernous sinus-carotid rete vascular complex, demonstrated on isolated pig heads perfused with autologous blood. *Domest Anim Endocrinol.* 1997; 14(3): 149–160, doi: [10.1016/S0739-7240\(97\)00004-0](https://doi.org/10.1016/S0739-7240(97)00004-0), indexed in Pubmed: [9171973](https://pubmed.ncbi.nlm.nih.gov/9171973/).
19. Hayward JN, Baker MA. A comparative study of the role of the cerebral arterial blood in the regulation of brain temperature in five mammals. *Brain Res.* 1969; 16(2): 417–440, doi: [10.1016/0006-8993\(69\)90236-4](https://doi.org/10.1016/0006-8993(69)90236-4), indexed in Pubmed: [4311724](https://pubmed.ncbi.nlm.nih.gov/4311724/).
20. Hetem RS, Strauss WM, Fick LG, et al. Selective brain cooling in Arabian oryx (*Oryx leucoryx*): a physiological mechanism for coping with aridity? *J Exp Biol.* 2012; 215(Pt 22): 3917–3924, doi: [10.1242/jeb.074666](https://doi.org/10.1242/jeb.074666), indexed in Pubmed: [22899527](https://pubmed.ncbi.nlm.nih.gov/22899527/).
21. Jakab R, Wong J, Belcher S. Estrogen receptor? immunoreactivity in differentiating cells of the developing rat cerebellum. *J Comp Neurol.* 2001; 430(3): 396–409, doi: [10.1002/1096-9861\(20010212\)430:3<396::aid-cne1039>3.0.co;2-0](https://doi.org/10.1002/1096-9861(20010212)430:3<396::aid-cne1039>3.0.co;2-0).
22. Jerbi H, Khaldi S, Pérez W. Morphometric study of the rostral epidural rete mirabile in the dromedary (*Camelus dromedarius*, Linnaeus 1758). *Int J Morphol.* 2016; 34(4): 1429–1435, doi: [10.4067/s0717-95022016000400042](https://doi.org/10.4067/s0717-95022016000400042).
23. Khamas WA, Ghoshal NG. Gross and scanning electron microscopy of the carotid rete--cavernous sinus complex of the sheep (*Ovis aries*). *Anat Anz.* 1985; 159(1-5): 173–179, indexed in Pubmed: [4096396](https://pubmed.ncbi.nlm.nih.gov/4096396/).
24. Khamas WA, Ghoshal NG, Bal HS. Histomorphologic structure of the carotid rete-cavernous sinus complex and its functional importance in sheep (*Ovis aries*). *Am J Vet Res.* 1984; 45(1): 156–158, indexed in Pubmed: [6703449](https://pubmed.ncbi.nlm.nih.gov/6703449/).
25. Kiełtyka-Kurc A, Frąckowiak H, Brudnicki W. The arteries of brain base in species of the cervid family. *Anat Rec (Hoboken).* 2015; 298(4): 735–740, doi: [10.1002/ar.23096](https://doi.org/10.1002/ar.23096), indexed in Pubmed: [25399744](https://pubmed.ncbi.nlm.nih.gov/25399744/).
26. Kiełtyka-Kurc A, Frąckowiak H, Zdun M, et al. The arteries on the base of the brain in the camelids (Camelidae). *Ital J Zool.* 2014; 81(2): 215–220, doi: [10.1080/11250003.2014.901428](https://doi.org/10.1080/11250003.2014.901428).
27. Krzymowski T, Skipor J, Grzegorzewski W. Cavernous sinus and carotid rete of sheep and sows as a possible place for countercurrent exchange of some neuropeptides and steroid hormones. *Anim Reprod Sci.* 1992; 29(3-4): 225–240, doi: [10.1016/0378-4320\(92\)90036-d](https://doi.org/10.1016/0378-4320(92)90036-d).
28. Krzymowski T, Stefańczyk-Krzybowska S. Local retrograde and destination transfer of physiological regulators as an important regulatory system and its role. Facts and hypothesis. *J Physiol Pharmacol.* 2012; 63(1): 3–16, indexed in Pubmed: [22460455](https://pubmed.ncbi.nlm.nih.gov/22460455/).
29. Krzymowski T, Stefańczyk-Krzybowska S, Muszak J, et al. Cavernous sinus and its mysterious physiological functions: facts and hypotheses. *Acta Biol Crac Ser Zool.* 2014; 55(56): 7–15.
30. Koziorowski M, Stefańczyk-Krzybowska S, Tabecka-Lonczyńska A, et al. The gaseous messenger carbon monoxide is released from the eye into the ophthalmic venous blood depending on the intensity of sunlight. *J Biol Regul Homeost Agents.* 2012; 26(1): 111–118, indexed in Pubmed: [22475102](https://pubmed.ncbi.nlm.nih.gov/22475102/).
31. McGrath P. Observations on the intra-cranial carotid rete and the hypophysis in the mature female pig and sheep. *J Anat.* 1977; 124: 689–699, indexed in Pubmed: [604338](https://pubmed.ncbi.nlm.nih.gov/604338/).

32. O'Brien HD. Cranial arterial pattern of the Sri Lankan spotted chevrotain, *Moschiola memmina*, and comparative basicranial osteology of the Tragulidae. *PeerJ*. 2015; 3: e1451, doi: [10.7717/peerj.1451](https://doi.org/10.7717/peerj.1451), indexed in Pubmed: [26644983](https://pubmed.ncbi.nlm.nih.gov/26644983/).
33. O'Brien HD, Gignac PM, Hieronymus TL, et al. A comparison of postnatal arterial patterns in a growth series of giraffe (*Artiodactyla: Giraffa camelopardalis*). *PeerJ*. 2016; 4: e1696, doi: [10.7717/peerj.1696](https://doi.org/10.7717/peerj.1696), indexed in Pubmed: [26925324](https://pubmed.ncbi.nlm.nih.gov/26925324/).
34. Ocal MK, Erden H, Ogut I, et al. A quantitative study on the retial arteries in one-humped camels. *Ann Anat*. 1998; 180(4): 369–371, doi: [10.1016/S0940-9602\(98\)80046-0](https://doi.org/10.1016/S0940-9602(98)80046-0), indexed in Pubmed: [9728280](https://pubmed.ncbi.nlm.nih.gov/9728280/).
35. Oren D. Humoral phototransduction: blood is a messenger. *Neuroscientist*. 2016; 2(4): 207–210, doi: [10.1177/107385849600200408](https://doi.org/10.1177/107385849600200408).
36. Perez-Pouchoulen M, Yu SJ, Roby CR, et al. Regulatory control of microglial phagocytosis by estradiol and prostaglandin E2 in the developing rat cerebellum. *Cerebellum*. 2019; 18(5): 882–895, doi: [10.1007/s12311-019-01071-z](https://doi.org/10.1007/s12311-019-01071-z), indexed in Pubmed: [31435854](https://pubmed.ncbi.nlm.nih.gov/31435854/).
37. Rao KT, Dayalu K, Puttannaiyah GB. A comparison of the circulus arteriosus of *Bos indicus* and *Bos bubalis*. *Mysore J Agric Sci*. 1968; 2: 35–37.
38. Simoens P, Lauwers H, De Geest JP, et al. Functional morphology of the cranial retia mirabilia in the domestic mammals. *Schweiz Arch Tierheilkd*. 1987; 129(6): 295–307, indexed in Pubmed: [3616596](https://pubmed.ncbi.nlm.nih.gov/3616596/).
39. Skipor J, Grzegorzewski W, Krzymowski T, et al. Local transport of testosterone from the nasal mucosa to the carotid blood and the brain in the pig. *Pol J Vet Sci*. 2000; 3: 19–22.
40. Skipor J, Grzegorzewski W, Wasowska B, et al. Luteinizing hormone and prolactin are not retrogradely transferred in perihypophyseal vascular complex in ewes. *Reprod Biol*. 2004; 4: 195–201.
41. Skipor J, Wasowska B, Grzegorzewski W, et al. Transfer of dopamine by counter-current mechanism in the ewes changes with endocrine stage. *Biog Amines*. 2001; 16: 431–445.
42. Strauss WM, Hetem RS, Mitchell D, et al. Selective brain cooling reduces water turnover in dehydrated sheep. *PLoS One*. 2015; 10(2): e0115514, doi: [10.1371/journal.pone.0115514](https://doi.org/10.1371/journal.pone.0115514), indexed in Pubmed: [25675092](https://pubmed.ncbi.nlm.nih.gov/25675092/).
43. Strauss WM, Hetem RS, Mitchell D, et al. Body water conservation through selective brain cooling by the carotid rete: a physiological feature for surviving climate change? *Conserv Physiol*. 2017; 5(1): cow078, doi: [10.1093/conphys/cow078](https://doi.org/10.1093/conphys/cow078), indexed in Pubmed: [29383253](https://pubmed.ncbi.nlm.nih.gov/29383253/).
44. Stefańczyk-Krzyszowska S, Krzymowski T, Grzegorzewski W, et al. Humoral pathway for local transfer of the priming pheromone androstenol from the nasal cavity to the brain and hypophysis in anaesthetized gilts. *Exp Physiol*. 2000; 85(6): 801–809, doi: [10.1111/j.1469-445x.2000.02056.x](https://doi.org/10.1111/j.1469-445x.2000.02056.x), indexed in Pubmed: [11187974](https://pubmed.ncbi.nlm.nih.gov/11187974/).
45. Tandler J. Über Ein Corpus Caverosum Tympanicum Beim Seehnd. *Monatschr*. 1899; 33: 437–440.
46. Taylor CR, Lyman CP. Heat storage in running antelopes: independence of brain and body temperatures. *Am J Physiol*. 1972; 222(1): 114–117, doi: [10.1152/ajplegacy.1972.222.1.114](https://doi.org/10.1152/ajplegacy.1972.222.1.114), indexed in Pubmed: [5060212](https://pubmed.ncbi.nlm.nih.gov/5060212/).
47. Wang XR, Liu Y, Zhang LP, et al. Comparative anatomical study of the epidural retia mirabilia in the yak and cattle. *Asian J Anim Vet Adv*. 2012; 7(9): 884–890, doi: [10.3923/ajava.2012.884.890](https://doi.org/10.3923/ajava.2012.884.890).
48. Weihua W. The carotid rete of the camel (*Bactrianus Camelus*). *Chin J Anim Vet Sci*. 1989.
49. Wible JR. The ontogeny and phylogeny of the mammalian cranial arterial pattern (internal carotid artery). Doctoral dissertation. Duke University 1984.
50. Yaoxing C, Weizhou L, Zixu W, et al. The morphological study on the epidural rete mirabile of the miniature swine. 1994.
51. Zdun M, Frąckowiak H. Specyfika zaopatrzenia w krew mózgowia przeżuwaczy. *Med Wet*. 2019; 75: 389–393.
52. Zdun M, Frąckowiak H, Kiełtyka-Kurc A, et al. The arteries of brain base in species of Bovini tribe. *Anat Rec (Hoboken)*. 2013; 296(11): 1677–1682, doi: [10.1002/ar.22784](https://doi.org/10.1002/ar.22784), indexed in Pubmed: [24106047](https://pubmed.ncbi.nlm.nih.gov/24106047/).
53. Zdun M, Jabłoński R, Dębiński D, et al. The Eurasian Elk's (*Alces alces*) Brain Base Arteries in View of Vascular Variation. *Anat Rec (Hoboken)*. 2019; 302(2): 339–345, doi: [10.1002/ar.23968](https://doi.org/10.1002/ar.23968), indexed in Pubmed: [30312526](https://pubmed.ncbi.nlm.nih.gov/30312526/).

The relationship between the aggrecan VNTR polymorphism and its content in lumbar intervertebral discs

P. Pękala¹, D. Felkle², K. Dykas², A. Jarosz³, P. Elnazir¹, T. Konopka⁴, J.A. Walocha¹, J. Dulinska-Litewka²

¹Department of Anatomy, Jagiellonian University Medical College, Krakow, Poland

²Department of Biochemistry, Jagiellonian University Medical College, Krakow, Poland

³Malopolska Centre of Biotechnology, Jagiellonian University, Krakow, Poland

⁴Department of Forensic Medicine, Jagiellonian University Medical College, Krakow, Poland

[Received: 7 February 2022; Accepted: 9 February 2022; Early publication date: 28 February 2022]

Background: There is a specific polymorphism of the ACAN gene called the variable number of tandem repeats (VNTR), which is particularly interesting in the light of the development of intervertebral disc pathology and associated low back pain.

Materials and methods: The nucleus pulposus specimens were harvested from the L5/S1 intervertebral discs. The aggrecan content was determined using enzyme-linked immunosorbent assay (ELISA). Moreover, the VNTR polymorphism in the ACAN gene was evaluated.

Results: The genotyping of VNTR polymorphism in ACAN gene was successful in 94 tissue samples (48 homozygotes and 46 heterozygotes). The alleles were divided into four groups, in accordance with the number of tandem repeats in the ACAN gene. No difference between groups in the mean aggrecan mass nor in the mean degree of tissue moisture was observed.

Conclusions: No relationship between the ACAN gene VNTR polymorphism and the aggrecan content was observed in studied Caucasian cadavers. Such a relationship may be a more complex phenomenon and exists in other populations. (Folia Morphol 2023; 82, 2: 269–273)

Key words: aggrecan, intervertebral disc, morphology, risk factor

INTRODUCTION

Low back pain is a common problem, which will eventually affect almost everyone in the population [2, 9]. It is diagnosed in patients across a variety of countries of differing socioeconomic status, profession and age groups [7]. While mechanical factors related to trauma and/or occupation such as heavy lifting may result in morphological damage to the intervertebral discs (IVDs) or contiguous soft tissues, many other risk factors of low back pain have been hypothesized; these

include age, body mass index, chronic diseases as well as genetic predisposition [2, 17]. Many studies have explored the significance of genetic polymorphisms in the pathogenesis of intervertebral disc degeneration (IDD) [3, 13]. One of the possible candidates is the ACAN gene (encoding aggrecan core protein). Its product constitutes the major proteoglycan of IVDs and the articular cartilage. The content of the aggrecan in IVDs has been shown to be crucial to their function [15]. A dense network of this proteoglycan forms aggre-

Address for correspondence: Dr. P. Pękala, Department of Anatomy, Jagiellonian University Medical College, ul. Kopernika 12, 31–034 Kraków, Poland, e-mail: pekala.pa@gmail.com

This article is available in open access under Creative Common Attribution-Non-Commercial-No Derivatives 4.0 International (CC BY-NC-ND 4.0) license, allowing to download articles and share them with others as long as they credit the authors and the publisher, but without permission to change them in any way or use them commercially.

gates which are osmotically active to draw water into the IVDs and cause an increase in the osmotic pressure of the tissue to allow for movement and the weight bearing functions of the spine [16]. It was reported that loss of this proteoglycan may play a role in the development of osteoarthritis and degenerative IVD disease [11]. There is a specific polymorphism of the *ACAN* gene called the variable number of tandem repeats (VNTR), which is particularly interesting. Precisely the humans were described to have between 11 to 33 repetitions of a specific 57 nucleotide sequence [6].

In a systematic study, Cong et al. [4, 6] suggested an interaction between obesity and this polymorphism in the development of IVD pathology in individuals of Han Chinese ethnicity, whilst another study by the same research group suggested a similar multiplicative relationship between VNTR, smoking and IDD. Therefore, the presence of this polymorphism may indeed impact the robust, weight-bearing functions of the spine. Moreover, the meta-analysis performed by Gu et al. [8] suggested the increased risk of IDD related to presence of shorter (13–25 repetitions) compared with the normal, longer alleles in the *ACAN* gene. Such a relationship was found only in Asian populations, however not in Europeans [8]. Therefore, the aim of this study was to attempt to investigate the possible relationship between the VNTR polymorphism in the gene encoding aggrecan and its content within the Caucasian donor's IVDs using accurate molecular methods.

MATERIALS AND METHODS

Sample preparation

The specimens were harvested from the L5/S1 IVDs collected from the 100 male cadaveric donors of age between 18 and 80. Additionally, the following exclusion criteria were used: ankylosing spondylitis, visible injury or/and surgery to the spine or such history. The mean age of the donors was 42.09 ± 12.29 (all male Caucasian cadavers) [14].

After harvesting, all tissue samples were shattered manually using a scalpel into pieces of size ≈ 1 mm in every dimension. Then, the specimens were transferred to test tubes which were then weighed. Sample masses were calculated using the equation: weight of tube with sample – weight of empty tube = weight of sample.

Solubilisation

The solution of 4 M guanidine hydrochloride (Sigma-Aldrich, G3272-100G), 1 M sodium acetate (Sigma-Aldrich, S2889-250G), Triton 2% (Sig-

ma-Aldrich, X100-1L) and protease inhibitor cocktail (Sigma-Aldrich, P8340-1ML) was added to the tissue samples homogenized as described above. Then specimens were processed at 4°C overnight on the laboratory shaker which was set on gentle shaking. After the solubilisation, test tubes were centrifuged at 3000 rpm for 10 min to obtain a supernatant which was transferred to new test tubes and was stored at –20°C.

Enzyme-linked immunosorbent assay (ELISA)

The temperature of the supernatant was raised to $\approx 20^\circ\text{C}$. Then, the solutions were diluted (2–10 times) in fresh tubes with deionized water (Milli-Q Millipore device) to acquire concentrations in the range of detection of the method. ELISA was performed in accordance with the protocol provided by the manufacturer (RayBiotech, ELH-ACAN-1). Then, the absorbance was assessed at 450 nm using plate reader (Bio-TEK Synergy HT). The aggrecan concentration was established based on the mean of two separate measurements according to the standard curve constructed for each plate.

Genetic polymorphism in *ACAN* gene

DNA was extracted from samples using Xpure Genomic Mini kit (A&A Biotechnology, Gdansk) according to the protocol recommended by the manufacturer. Purity of obtained DNA isolates was assessed using NanoDrop spectrophotometer (Thermo Scientific, Waltham, MA) and DNA concentration was measured with Qubit fluorometer (Thermo Scientific, Waltham, MA). Polymerase chain reaction (PCR) amplification of the CS1 domain in aggrecan gene was performed using the specific primers (sense primer: 5'-TAGAGGGCTCTGCCTCTGGAGTTG-3' and anti-sense primer: 5'-AGGTCCCCTACCGCAGAGGTAGAA-3'). PCR reaction mixture consisted of: 1X Gold Buffer, 1.5 mM MgCl₂, 0.25 mM of dNTPs, 0.6 μM of each primer, 50 ng of DNA, 1 U of AmpliTaq Gold DNA Polymerase (Applied Biosystems, Foster City, CA) and DNase-free water up to 25 μL . PCR was performed on C1000 Touch Thermal Cycler (Bio-Rad Laboratories, Hercules, CA) using following temperature profile: 95°C for 4 min, 33 cycles of 30 s at 95°C, 30 s at 63°C, 2 min at 72°C, and final extension at 72°C for 10 min. PCR products were analysed for their size on 2100 Bioanalyzer (Agilent) utilizing High Sensitivity DNA Assay. Number of repeats in the VNTR region was determined by comparison of the amplicon length. The alleles were divided into four groups, in accordance with the number of tandem repeats in the *ACAN* gene (I: A11–25; II: A26–27; III: A28–30; IV: A31–33).

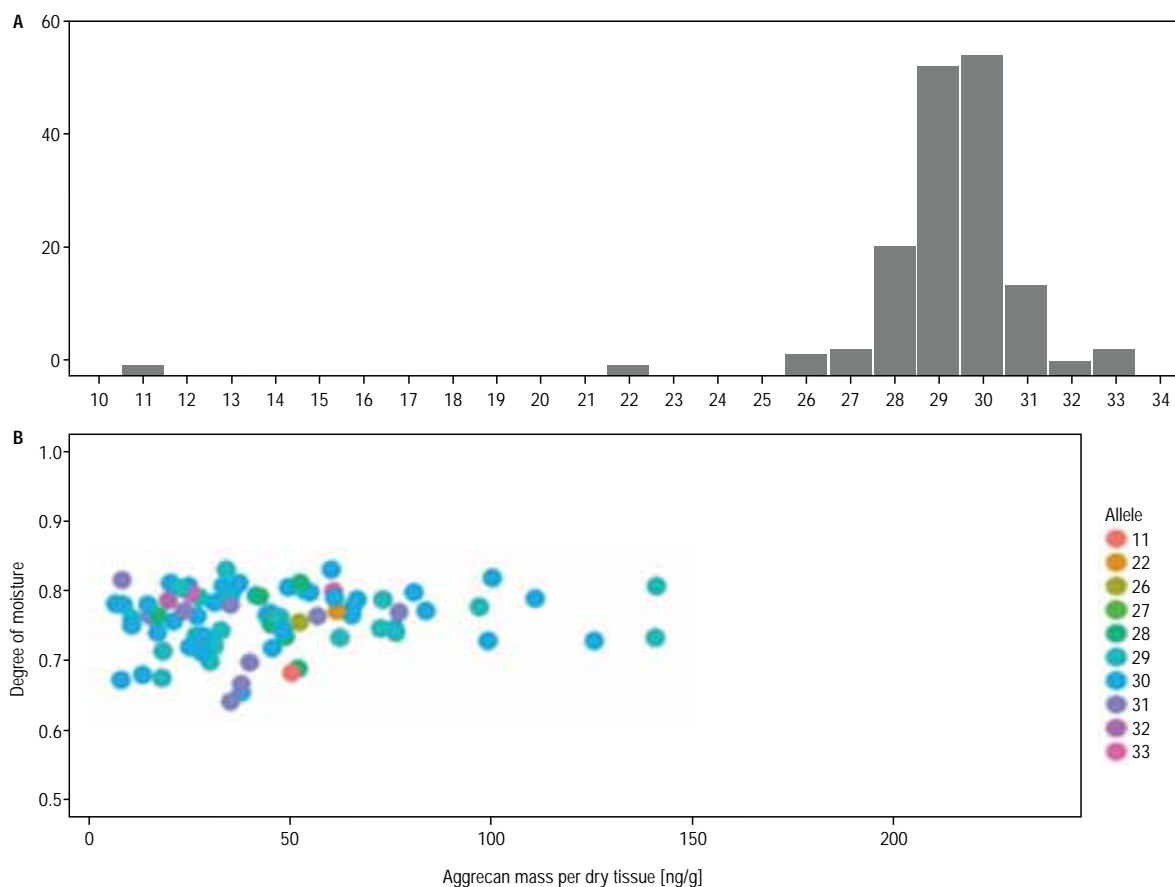


Figure 1. A. The histogram of allele frequencies; **B.** The distribution of aggrecan mass, considering the degree of moisture and allele type.

Table 1. Mean aggrecan mass per dry tissue and mean degree of moisture by number of tandem repeats in the *ACAN* gene

Alleles	Mean aggrecan mass per dry tissue [ng/g] (SD)	P-value*	Mean degree of moisture (SD)	P-value*
A11–25	55.83 (6.56)	0.1515	0.73 (0.05)	0.6264
A26–27	41.60 (17.96)		0.77 (0.04)	
A28–30	51.76 (38.18)		0.76 (0.04)	
A31–33	35.12 (17.94)		0.75 (0.05)	

*Kruskal-Wallis test; SD — standard deviation

Statistical analysis

Statistical analysis and data visualization were conducted using R Software (version 1.2.5042). For group comparison performance, Kruskal-Wallis test was applied, according to its assumptions. The correlation between variables was computed using Spearman's method. The significance level was set to 0.05.

Ethics

The study protocol was accepted by the local bioethical committee. This study was performed in accordance with the principles of the Declaration of Helsinki and its later amendments.

RESULTS

In this study, the genotyping of VNTR polymorphism in *ACAN* gene was successful in 94 tissue samples (48 homozygotes and 46 heterozygotes). The distribution of the VNTR alleles was in accordance with the Hardy-Weinberg equilibrium (Fig. 1A). No difference between allele groups in the mean aggrecan mass nor in the mean degree of tissue moisture was observed (Table 1). Consistently, no correlation between aggrecan mass and the water content (p -value = 0.173) was found. The distribution of aggrecan mass, considering the degree of moisture and allele type is shown in Figure 1B.

DISCUSSION

To the best of the authors knowledge, it was the first human study analysing the influence of the VNTR polymorphism in *ACAN* gene on the concentration of the aggrecan in the IVDs nucleus pulposus in Caucasian sample. The main goal was to investigate this hypothesized relationship using objective and accurate molecular methods.

Noteworthy is the fact that many case-control studies on VNTR polymorphism in *ACAN* gene and the IDD have been performed in the past, reporting frequently contradicting results [4, 6, 8]. Although they brought a plethora of valuable data, the significant bias likely existed due to uncontrolled factors contributing to the final development of the IDD, which was the main outcome based on what the cases and controls were allocated. It is well-known that the low back pain symptoms are related not only to the pathology of the IVD, but also to morphological changes in the surrounding tissues such as lumbar facet joints, etc. [10]. Therefore, as it was shown in the literature that aggrecan concentration decreases in IVD with degeneration and aging, in this study it was decided to analyse this objective and isolated outcome, which is also the most logical causative result of the *ACAN* gene altered expression [1, 12].

The results of this study showed no relationship between the presence of short alleles and the aggrecan concentration in the nucleus pulposus of the L5/S1 IVDs. Interestingly, the meta-analysis performed by Gu et al. [8], found a relationship between the IDD and the presence of the shorter alleles of the *ACAN* gene in Asian population, but reached no statistical significance pooling European samples. Together with our observations it is likely that such phenomenon may be ethnic specific and/or other cofactors may play a significant role.

Moreover, the recent systematic study performed by Cong et al. [5] found that the A21 allele (with 21 repetitions of a specific 57 nucleotide sequence) in *ACAN* gene is overexpressed in patients with IDD in their pooled sample. Interestingly, such a relationship was not identified for the rest of shorter and any other alleles [5]. However, in our study this allele had no representation among studied individuals. One must remember that considering our sample size, prevalence of particular alleles is relatively low and such comparisons require testing on numerous populations.

Interestingly, the specimens from donors with the shortest alleles (A11–A25) were found to have

lower water content than the IVDs from the other three groups (72.7% vs. 76.0%); however, this difference was not significant. This observation may suggest that despite the VNTR in the *ACAN* gene does not influence the aggrecan dry mass in the nucleus pulposus of the lumbar IVD, it may alter its water attracting function. However, such a hypothesis cannot be confirmed by this study and requires further well-designed research.

Our study is limited by the uniform sex and ethnicity of the donors. However, it was designed to establish possible association in the Caucasian male population. Further, large studies on different populations are required in the future. The other limitation is a number of specimens included. However, it is challenging to perform larger cadaveric studies, and it is important that the results of this study can be pooled in systematic studies in the future to obtain more statistical power.

CONCLUSIONS

In summary, no relationship between the *ACAN* gene VNTR polymorphism and the aggrecan content was observed in studied Caucasian cadavers. Such a relationship may be a more complex phenomenon and exist in other populations.

Acknowledgements

We would like to acknowledge all the donors and their families, whose contribution allowed us to conduct this research. This research was supported by governmental funds for research in 2016–2021 (Polish Ministry of Science and Higher Education, Diamond Grant).

Conflict of interest: None declared

REFERENCES

1. Antoniou J, Steffen T, Nelson F, et al. The human lumbar intervertebral disc: evidence for changes in the biosynthesis and denaturation of the extracellular matrix with growth, maturation, ageing, and degeneration. *J Clin Invest.* 1996; 98(4): 996–1003, doi: [10.1172/JCI118884](https://doi.org/10.1172/JCI118884), indexed in Pubmed: [8770872](https://pubmed.ncbi.nlm.nih.gov/8770872/).
2. Balagué F, Mannion AF, Pellisé F, et al. Non-specific low back pain. *Lancet.* 2012; 379(9814): 482–491, doi: [10.1016/S0140-6736\(11\)60610-7](https://doi.org/10.1016/S0140-6736(11)60610-7), indexed in Pubmed: [21982256](https://pubmed.ncbi.nlm.nih.gov/21982256/).
3. Biczko A, Szita J, McCall I, et al. Genodisc Consortium. Association of vitamin D receptor gene polymorphisms with disc degeneration. *Eur Spine J.* 2020; 29(3): 596–604, doi: [10.1007/s00586-019-06215-7](https://doi.org/10.1007/s00586-019-06215-7), indexed in Pubmed: [31768839](https://pubmed.ncbi.nlm.nih.gov/31768839/).

4. Cong L, Pang H, Xuan D, et al. The interaction between aggrecan gene VNTR polymorphism and cigarette smoking in predicting incident symptomatic intervertebral disc degeneration. *Connect Tissue Res.* 2010; 51(5): 397–403, doi: [10.3109/03008200903564455](https://doi.org/10.3109/03008200903564455), indexed in Pubmed: [20367118](https://pubmed.ncbi.nlm.nih.gov/20367118/).
5. Cong L, Tu G, Liang D. A systematic review of the relationship between the distributions of aggrecan gene VNTR polymorphism and degenerative disc disease/osteoarthritis. *Bone Joint Res.* 2018; 7(4): 308–317, doi: [10.1302/2046-3758.74.BJR-2017-0207.R1](https://doi.org/10.1302/2046-3758.74.BJR-2017-0207.R1), indexed in Pubmed: [29922449](https://pubmed.ncbi.nlm.nih.gov/29922449/).
6. Cong L, Zhu Y, Pang H, et al. The interaction between aggrecan gene VNTR polymorphism and obesity in predicting incident symptomatic lumbar disc herniation. *Connect Tissue Res.* 2014; 55(5-6): 384–390, doi: [10.3109/03008207.2014.959117](https://doi.org/10.3109/03008207.2014.959117), indexed in Pubmed: [25188217](https://pubmed.ncbi.nlm.nih.gov/25188217/).
7. Gleinert-Rożek MŁ, Kosiński A, Kaczyńska A, et al. Metric analysis of the lumbar region of human vertebral column. *Folia Morphol.* 2020; 79(4): 655–661, doi: [10.5603/FM.a2020.0008](https://doi.org/10.5603/FM.a2020.0008), indexed in Pubmed: [32020579](https://pubmed.ncbi.nlm.nih.gov/32020579/).
8. Gu J, Guan F, Guan G, et al. Aggrecan variable number of tandem repeat polymorphism and lumbar disc degeneration: a meta-analysis. *Spine (Phila Pa 1976).* 2013; 38(25): E1600–E1607, doi: [10.1097/BRS.0000000000000012](https://doi.org/10.1097/BRS.0000000000000012), indexed in Pubmed: [24296484](https://pubmed.ncbi.nlm.nih.gov/24296484/).
9. Hoy D, Brooks P, Blyth F, et al. The Epidemiology of low back pain. *Best Pract Res Clin Rheumatol.* 2010; 24(6): 769–781, doi: [10.1016/j.berh.2010.10.002](https://doi.org/10.1016/j.berh.2010.10.002), indexed in Pubmed: [21665125](https://pubmed.ncbi.nlm.nih.gov/21665125/).
10. Kapetanakis S, Gkantsinikoudis N. Anatomy of lumbar facet joint: a comprehensive review. *Folia Morphol.* 2021; 80(4): 799–805, doi: [10.5603/FM.a2020.0122](https://doi.org/10.5603/FM.a2020.0122), indexed in Pubmed: [33084010](https://pubmed.ncbi.nlm.nih.gov/33084010/).
11. Maldonado M, Nam J. The role of changes in extracellular matrix of cartilage in the presence of inflammation on the pathology of osteoarthritis. *Biomed Res Int.* 2013; 2013: 284873, doi: [10.1155/2013/284873](https://doi.org/10.1155/2013/284873), indexed in Pubmed: [24069595](https://pubmed.ncbi.nlm.nih.gov/24069595/).
12. Pearce RH, Thompson P, Bebault GM, et al. Magnetic resonance imaging reflects changes of ageing degeneration in the human intervertebral disc. *J Rheumatol.* 1991; 18(Suppl. 27): 42–43.
13. Pękala PA, Henry BM, Tattera D, et al. FokI as a genetic factor of intervertebral disc degeneration: A PRISMA-compliant systematic review of overlapping meta-analyses. *J Clin Neurosci.* 2019; 60: 36–43, doi: [10.1016/j.jocn.2018.09.028](https://doi.org/10.1016/j.jocn.2018.09.028), indexed in Pubmed: [30309807](https://pubmed.ncbi.nlm.nih.gov/30309807/).
14. Pękala P, Tattera D, Krupa K, et al. Correlation of morphological and radiological characteristics of degenerative disc disease in lumbar spine: a cadaveric study. *Folia Morphol.* 2022; 81(2): 503–509, doi: [10.5603/FM.a2021.0040](https://doi.org/10.5603/FM.a2021.0040), indexed in Pubmed: [33899206](https://pubmed.ncbi.nlm.nih.gov/33899206/).
15. Roughley P, Martens D, Rantakokko J, et al. The involvement of aggrecan polymorphism in degeneration of human intervertebral disc and articular cartilage. *Eur Cell Mater.* 2006; 11: 1–7, doi: [10.22203/ecm.v011a01](https://doi.org/10.22203/ecm.v011a01).
16. Urban JPG, Roberts S. Degeneration of the intervertebral disc. *Arthritis Res Ther.* 2003; 5(3): 120–130, doi: [10.1186/ar629](https://doi.org/10.1186/ar629), indexed in Pubmed: [12723977](https://pubmed.ncbi.nlm.nih.gov/12723977/).
17. Will JS, Bury DC, Miller JA. Mechanical low back pain. *Am Fam Physician.* 2018; 98(7): 421–428, indexed in Pubmed: [30252425](https://pubmed.ncbi.nlm.nih.gov/30252425/).

Multidetector computed tomography evaluation of origin, V2 segment variations and morphology of vertebral artery

R. Tasdemir¹ , O.F. Cihan² 

¹Department of Anatomy, Faculty of Medicine, Gaziantep Islam Science and Technology University, Gaziantep, Turkey

²Department of Anatomy, Faculty of Medicine, Gaziantep University, Gaziantep, Turkey

[Received: 26 January 2022; Accepted: 14 January 2022; Early publication date: 22 March August 2022]

Background: The current study aimed to determine the origin of vertebral artery (VA) on both sides and the levels of entry into respective foramen transversarium (FT), to evaluate possible effects of sex on the entry levels, and to investigate the frequency of VA dominance and VA hypoplasia based on the VA V2 segment.

Materials and methods: For this study, archived images of patients undergoing multidetector computed tomography (MDCT) examination of the chest and head-neck for various reasons at Gaziantep University Medical Faculty Hospital were reviewed retrospectively. Three-dimensional reconstructions were performed for a total of 644 VA images from 322 patients using Horos software, and VA origin, the level of entry to FT and transverse diameters of both VA and FT were measured at the point of entry.

Results: It was found that, among males, the VA originated from the truncus brachiocephalicus on the right side in only 1 patient and from the aortic arch in 2 patients on the left side. Left VA emerging from the aortic arch was observed in 2 females. The right VA was found to enter the FT at C3 in 1 male, at C4 in 6 patients (5 males, 1 female), at C5 in 19 patients (3 males, 16 females), and at C6 in 300 patients (141 males, 159 females). The left artery entered the FT at C5 in 23 patients (9 males, 14 females) and at C6 in 298 patients (141 males, 157 females). Looking at the relationship between variations of VA origin and the levels of entry to the FT, it was observed that only one of the left VAs originating from the arcus aorta entered the FT at C6 and at C5 in all others. On the right side, there was only one VA originating from the truncus brachiocephalicus, which entered the FT at C3. Of the remaining 248 VAs originating from the subclavian artery, 5 VAs entered the FT at C4, 14 VAs at C5 and 229 VAs at C6. The measurements of VA diameters showed right VA hypoplasia in 14 patients and left VA hypoplasia in 17 patients. Also, the right VA dominance was found in 110 patients and the left VA dominance in 128 patients. A moderate, positive correlation was observed between VA and FT diameters in both sides. A regression analysis showed that a 1 mm change in the right VA diameter was associated with a 75% change in the FT diameter and a 1 mm change in the left VA diameter caused a 72% change in the FT diameter.

Address for correspondence: R. Tasdemir, Assistant Professor, Department of Anatomy, Faculty of Medicine, Gaziantep Islam Science and Technology University, Gaziantep, Turkey, tel: +90 5058548754, e-mail: rabiatsdmr@gmail.com

This article is available in open access under Creative Common Attribution-Non-Commercial-No Derivatives 4.0 International (CC BY-NC-ND 4.0) license, allowing to download articles and share them with others as long as they credit the authors and the publisher, but without permission to change them in any way or use them commercially.

Conclusions: An understanding of VA variations and FT morphometry is crucial for informed clinical practice. This will clearly affect the success rates of physicians in the diagnosis and treatment of pathologies involving cervical region. The presence of any VA variation in a patient should be investigated on computed tomography or magnetic resonance imaging images prior to surgery. (Folia Morphol 2023; 82, 2: 274–281)

Key words: multidetector computed tomography, morphometry, vertebral artery, foramen transversarium

INTRODUCTION

In classical anatomy knowledge, vertebral artery (VA) is divided into 4 segments, and the second segment, which we studied, is the region between the C6 and C2 foramen transversarium (FT) [15]. The VA accounts for 28% of the blood supply to the brain [32]. Therefore, any changes in the haemodynamics of the VAs may result in severe disorders in the cerebellum, brain stem, inner ear and spinal cord. The VA is the primary source of posterior circulation. Posterior circulation strokes represent about 20% of all ischaemic strokes [9, 22], making the VA very important clinically [16]. Also, considering many functions of the hindbrain, blood flow is vital, and the VAs are among the most important medium-sized arteries that supply the hindbrain centres controlling cardiac and respiratory functions and balance [19].

Although rare, injury to the VA leads to severe consequences when it occurs. Traumatic VA injury poses a clinical challenge because it is difficult to diagnose and there are no established guidelines for its diagnosis and management [7]. In their study examining blunt cerebrovascular injuries, Sticco et al. (2021) [26] reported that blunt VA injuries accounted for 1.1% of all trauma admissions, and ischaemic stroke developed in only 0.71% of these patients. In another study, Cothren and Moore [6] reported that 25% of blunt VA injuries resulted in stroke, and through a survey of cervical spine surgeons, Lunardini et al. (2014) [14] found that VA injuries occurred in 0.07–1.4% of surgeries, and 10% of these injuries were associated with neurologic sequelae or death. Thus, VA anomalies along the V2 segment require careful evaluation of computed tomography (CT) and magnetic resonance imaging (MRI) images prior to cervical spine surgery [25, 33].

The current study aimed to determine the origin of VA on both sides and the levels of entry into respective FT, to evaluate possible effects of sex on

the entry levels, and to investigate the frequency of VA dominance and VA hypoplasia based on the VA V2 segment.

MATERIALS AND METHODS

For this study, archived images of patients undergoing multidetector computed tomography (MDCT) examination of the chest and head-neck for various reasons between 2015 and 2020 at Gaziantep University Medical Faculty Hospital were reviewed retrospectively. Of ~4000 patient scans identified through archive screening, 504 images suitable for the study purposes were selected.

The exclusion criteria were poor image quality due to motion artefacts or insufficient distribution of the contrast agent within the VA, patients with a tumour in or injury to the craniocervical junction, patients with a history of surgery and/or interventional procedure to the chest or head-neck region, images where VA segments were not covered in the field of view and patients aged under 18 or over 80 years of age. Ultimately, a total of 644 VA images from 322 patients satisfactory MDCT images from 171 females and 151 males were included in the study. The mean age of the patients was 52.14 ± 16.52 years. All measurements were obtained by a single investigator. The data were anonymised to avoid identification of the patients.

Image acquisition and processing: Patient images were acquired with a 64-detector MDCT (Light Speed VCT XTe; General Electric, Milwaukee, USA). In our study, 120 mL of non-ionic contrast agent with an iodine concentration of 300 mgI/mL was injected into the right or left antecubital vein with the help of an automated injector (Covidien LF OptiVantage DH, Ohio, USA) as a bolus at a rate of 4 mL/s, followed by 40 mL of saline at a rate of 4 mL/s. The following parameters were used for all scans — collimation: 40 mm (64×0.625); tube rotation time: 0.35 s; pitch value: 1; X-ray tube operating at 100–120 kV and

150–600 milliamperere; detector thickness: 0.625 mm; reconstruction interval: 0.625 mm.

Three-dimensional (3D) reconstructions of two-dimensional MDCT images were done using the open-source Horos v.4.0.0 software (<https://horosproject.org/>). On the Horos software, the origin of VA (right and left) and the level of VA entry into the FT were identified, and the transverse diameters of both VA and FT were measured on the right and left at the level where VA enters the FT (Fig. 1). Hypoplasia was defined as a VA diameter of less than 2 cm [10, 20]. A difference of 0.3 mm or greater between the right and left VA diameters was considered as the criterion for VA dominance, and VA diameters were assumed to be equal in the case of a difference of less than 0.3 mm [10, 21].

Ethics approval

Ethics approval for the study was obtained from the Ethics Committee for Non-Interventional Clinical Trials of Gaziantep Islam Science and Technology University on July 13, 2021 (No. 2021/37).

Statistical analysis

Statistical analysis of the study data was performed using SPSS for Windows (23.0.0; SPSS Inc., Chicago, IL, USA). Percentage values were derived from the frequencies of the parameters. Chi-square test was used to analyse the relationship between sex and the level of entry of the VAs into the FT. The normality of data distribution was checked using Kolmogorov-Smirnov test. Pearson correlation analysis was used to investigate whether there was a correlation between VA and FT diameters. Regression analysis was employed to model the relationship between the diameters. A *p* value less than 0.05 was considered statistically significant.

RESULTS

A total of 322 patients (171 females, 151 males) were included in the study and stratified into age groups of 18–44 years (115 subjects), 45–64 years (118 subjects) and 65–80 years (89 subjects). The parameters for the right and left VAs were measured for each patient individually and a total of 644 VAs were examined (Table 1).

The origin of the VA could be evaluated on the right side for 249 patients and on the left side for 241 patients. The right VA originated from the right subclavian artery in all patients (118 males, 130 females),

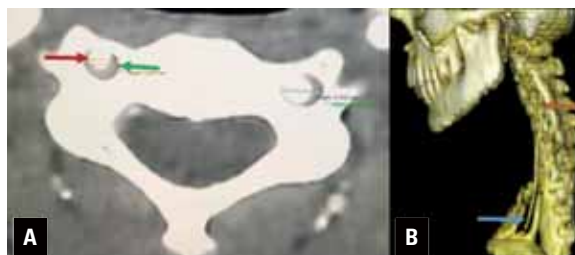


Figure 1. **A.** The green arrow shows the transverse diameter of the foramen transversarium, and the red arrow shows the transverse diameter of the vertebral artery; **B.** The blue arrow indicates the origin of the vertebral artery, the red arrow the level at which it enters the foramen vertebrae.

Table 1. Distribution of multidetector computed tomography images by age and sex

	Female	Male	Total
Group 1 (18–44 years)	71	44	115
Group 2 (45–64 years)	61	53	114
Group 3 (65–80 years)	35	54	89
Total	171	151	322

except for 1 (0.8%) male patient in whom the VA originated from the truncus brachiocephalicus. The left VA originated from the arcus aorta in 2 (1.7%) male patients and in 5 (4%) female patients. In the remaining patients, the left VA was found to originate from the left subclavian artery as usual (115 males, 98.3%; 119 females, 96%) (Table 2, Fig. 2).

When we examined the level of entry of the VAs into respective foramen vertebrae in males, the right VA entered the FT at C3 in 1 (0.7%) patient, C4 in 5 (3.3%) patients, C5 in 3 (2%) patients and C6 in 141 (94%) patients. In females, it was observed that the right VA entered the FT at C4 in 1 (0.6%) patient, C5 in 16 (9.4%) patients and C6 in 154 (90.1%) patients. A significant difference was observed between sexes in terms of the entry of the VA to the FT at C4, which was more common in males than in females ($p < 0.05$). Likewise, there was a significant difference between the sexes in the entry of the VA at C5, which was more common in females than in males ($p < 0.05$). On the left side, the VA entered the FT at C5 in 23 patients (9 males, 14 females) and C6 in 298 patients (141 males, 157 females) (Table 3, Fig. 3).

Looking at the relationship between variations of VA origin and the levels of entry to the FT, it was determined that only 1 (14.29%) of the left VAs originating from the arcus aorta entered the FT at C6

Table 2. Distribution of the origins of vertebral artery (VA)

	Right VA		Left VA		Total
	Female	Male	Female	Male	
Subclavian artery	130	118	119	115	482
Aortic arch	-	-	5	2	7
Brachiocephalic trunk	-	1	-	-	1
Total	130	119	124	117	490



Figure 2. **A.** Left vertebral artery originating from the left subclavian artery; **B.** Right vertebral artery originating from the right subclavian artery; **C.** Right vertebral artery originating from the aortic arch are shown.

Table 3. Distribution of the entry levels of the vertebral artery (VA) to foramen transversarium

		C3	C4	C5	C6	C7
Right VA	Female	-	1	16	154	-
	Male	1	5	3	141	-
Left VA	Female	-	-	14	157	-
	Male	-	-	9	141	-
Total		1	6	42	593	-

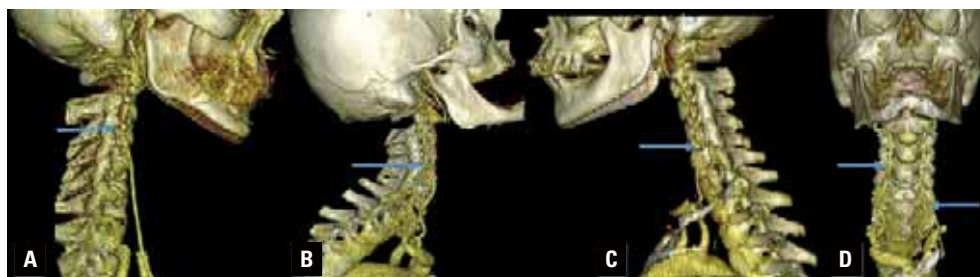


Figure 3. The entrances of the right vertebral artery through the foramen of the 3rd cervical vertebrae (**A**); the right vertebral artery through the foramen of the 4th cervical vertebra (**B**); the left vertebral artery through the foramen of the 5th cervical vertebra (**C**); the right vertebral artery through the foramen of the 4th cervical vertebra, and the left vertebral artery through the 6th cervical vertebra are shown (**D**).

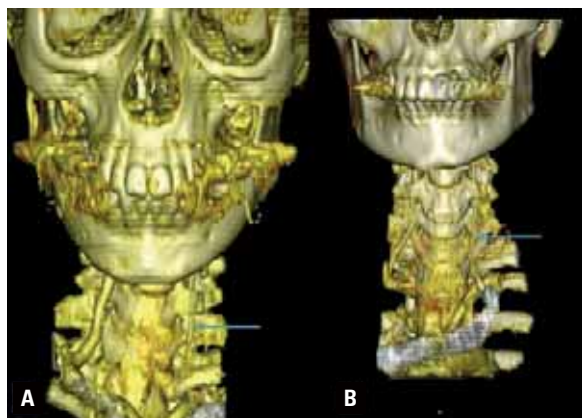


Figure 4. A, B. Left-sided hypoplastic vertebral artery from different patients is shown.

Table 4. Frequencies of vertebral artery (VA) hypoplasia and dominance

	Right VA	Left VA	Total
VA hypoplasia	14 (4.35%)	17 (5.28%)	31 (9.63%)
VA dominance	42 (13%)	58 (18%)	100 (31%)

and at C5 in all others (85.71%). On the right side, there was only 1 VA originating from the truncus brachiocephalicus, which was found to enter the FT at C3. Of the remaining 248 VAs originating from the subclavian artery, 5 (2%) VAs entered the FT at C4, 14 (5.65%) VAs at C5 and 229 (92.3%) VAs at C6.

The measurements of VA diameters showed hypoplasia of the right VA in 14 (4.35%) patients and hypoplasia of the left VA in 17 (5.28%) patients (Fig. 4). Based on the difference between the right and left VA diameters, the right VA dominance was found in 110 (34.2%) patients and the left VA dominance in 128 (39.8%) patients. The right and left VA diameters were equal in 84 (26.1%) patients (Table 4).

When we examined the relationship between the VA and FT diameters, a moderate, positive correlation was observed in both sides. A regression analysis of the relationship between the VA and FT diameters showed that a 1 mm change in the right VA diameter was associated with a 75% change in the FT diameter and a 1 mm change in the left VA diameter caused a 72% change in the FT diameter.

DISCUSSION

In our study, we have chosen to evaluate the parameters related to the VA and FT on MDCT images since we considered that such an approach would

provide more reliable data than measurements obtained from cadavers and also to achieve a larger sample size.

As the prevertebral segment of the VA originating from the aortic arch is less protected by bone, it is more vulnerable to injury and carries a high risk for tear during surgery [29]. Knowledge of the origin of the VA is important in planning vascular or cardiothoracic surgery. Anomaly of VA origin may result in disruption of cerebral haemodynamics, dissection or aneurysm formation due to congenital structural defect in the artery wall [11]. Therefore, screening of patients with anomalous VA origin for aneurysm may be considered, which may allow for endovascular treatment before subarachnoid haemorrhage or any other devastating event occurs, and reduce morbidity and/or mortality [24]. Data from separate studies indicate that anomalous origins of the left VA most commonly include those emerging from the aortic arch, with incidence rates ranging from 2.4% to 5.8% [1, 2, 12, 13, 29, 31]. In a study on cadavers, Woraputtaporn et al. (2019) [29] did not observe any variations in the right VA origin, and Canyigit et al. [2] and Yuan [31] reported a rare incidence of such variations. In our study, we observed that the left VA originated from the aortic arch on 5.7% of the images among those we could examine the VA origin. On the right side, the VA originating from the truncus brachiocephalicus was detected in only 1 out of 249 images (0.4%).

It has been reported that anomalies of the cervical vertebra and VA variations may also cause VA compression along its trajectory. Since cerebral haemodynamics will be impaired in the case of VA compression, this may lead to problems in the short and long-term such as aneurysm formation, risk of thrombosis, occlusion, dissection and atherosclerosis [5, 19]. Zhang et al. (2020) [33] examined the incidence of anomalies of the V2 segment of the VA and reported that variations occurred mostly at C5, with a higher incidence (70.3% in total) compared to previous studies. Woraputtaporn et al. (2019) [29] investigated the variations of VA entrance to the FT and observed that most of the left VAs entered the FT at C5 (4.1%), whereas the right VA entered at C4 and C5 in only 1 case each, and 99.2% of the right VAs entered the FT at C6. In a study on 515 cadavers, Yamaki et al. (2006) [30] examined VA variations and found that most of the variations occurred at the C5 level on both the right (8.8%) and left (49.9%) sides,

followed by C7, C4 and C3 respectively bilaterally. In a large-scale study involving both patients and cadavers, it was reported that 43% of the left VAs entered the FT at C5, and 21.3% of the right VAs at C7 [31]. Consistently, in the current study, most of the VA variations at both sides were seen at the FT of C5, with rates of 73.1% on the right side (among variations) and 100% on the left side (because entry at C5 was detected only for the left VAs).

In our study, among all cases studied, 8.1% of the right VAs and 7.2% of the left VAs entered the FT at C5 level. Although our results were in line with the literature in terms of the most common entry level variation, we observed a very low rate for variations in VA entry level on the left side.

When we examined the relationship between variations in the origin of the VA and the levels of entry to the FT, it was observed that only 1 (14.29%) of the left VAs emerging from the aortic arch entered the FT of the 6th cervical vertebra and others (85.71%) entered at the 5th cervical vertebra. In 1 study (2015), Melovitz-Vasan et al. [18] reported that the left VA of aortic origin entered the FT at the 6th cervical vertebra; however, in Meila et al.'s study (2012) [17], the left VAs were found to enter the FT at 4th or 5th cervical vertebra. Regarding the right side, there was only 1 VA originating from the truncus brachiocephalicus among all cases, which entered the FT at 3rd cervical vertebra in our study. Of the remaining 248 VAs originating from the subclavian artery, 5 (2%) entered the FT at 4th cervical vertebra, 14 (5.65%) at the 5th cervical vertebra, and 229 (92.3%) at the 6th cervical vertebra. Uchino et al. (2013) [27] found that the left VAs emerging from the aortic arch entered the FT at C4, C5 or C7, the right VAs originating from the subclavian artery entered the FT at C5, C4 or C3, whereas an abnormal right VA entered at C7. A study examining the entry levels of the VAs to FT on MDCT images reported that while the left VA entered the FT at C7 in only 2 cases, at C5 in 30 cases, at C4 in 7 cases, and at C6 in 421 cases, the right VA entered the FT at C5 in 15 cases, at C4 in 10 cases and at C6 in 434 cases [25].

There is still no clear consensus on the VA diameter to be defined as hypoplastic. Although a VA diameter of 2 mm or less was defined as hypoplastic in many studies and atretic in others, it was considered as a variation in some other studies [3, 4, 28]. In the literature, the reported frequency of hypoplastic VA which has been associated with pathologies

such as migraine and stroke ranges from 2% to 6% [3, 23]. In clinical practice, it is important to distinguish between VA hypoplasia and its stenosis or occlusion [10]. In a study investigating the relationship between VA hypoplasia and ischaemic stroke, the authors detected unilateral and bilateral VA hypoplasia in 26.5% and 1.6% of healthy individuals, respectively. Among the patients with ischaemic stroke, 19.3% had right VA hypoplasia, 12.5% had left VA hypoplasia and 3.4% had bilateral VA hypoplasia, and therefore, a significantly higher frequency of hypoplastic VA was reported in patients with ischaemic stroke [23]. To identify the role of hypoplastic VA in stroke, Chuang et al. (2006) [3] evaluated 191 patients with acute ischaemic stroke using magnetic resonance angiography within 72 hours of stroke onset, and reported a unilateral hypoplastic VA incidence of 11.51%. They stated that this rate was higher especially in patients with brainstem/cerebellar infarction [20, 34]. In a study (2004) examining VA hypoplasia and asymmetry, Jeng and Yip [10] found right VA hypoplasia in 7.8% and left VA hypoplasia in 3.8% of the patients. In the present study, 5.28% of the left VAs and 4.35% of the right VAs were hypoplastic. Thus, our findings are consistent with the literature.

Knowledge of the FT morphology is important in surgery to confirm whether screw fixation can be performed safely [20]. Because of many morphometric anatomic variations found in different ethnicities, it is our belief that such surgical procedures should be performed with utmost care without relying solely on information from previous studies.

Moreira and Herrero (2020) [20] observed that the diameter of FT was likely to be increased with advancing age [34]. In another study, Zibis et al. (2016) [34] found a strong correlation between the vertebral artery and the FT and suggested that variations of VA may lead to variations in FT [20]. Similarly, we observed a moderate positive correlation between FT diameters and VA diameters bilaterally in this study using 644 CT images. However, only a weak positive correlation was found between age and left FT diameter in our study.

El-Dwairi et al. (2021) [8] examined 329 CT scans of a Jordanian sample to generate a database of FT dimensions, and reported mean FT diameters of 4.62 ± 0.52 mm on the right side and 4.76 ± 0.51 mm on the left side. The authors also reported larger FT size in males than in females, and FT diameters were found to increase with increasing age. In our study,

the mean right FT diameter was 6.39 ± 0.93 mm and the left FT diameter was 6.25 ± 0.91 mm. We consider that this difference may be related to the differences in the mean age or ethnicity of the samples studied. Our findings are in line with those of previous studies with respect to sex and age. We suggest that the increase in FT diameter with age may be attributed to morphological degeneration.

CONCLUSIONS

Extraforaminal variations are important considerations in planning cervical spine surgeries. An understanding of VA variations and FT morphometry is crucial for informed clinical practice. It is our belief that this will affect the success rates of physicians in the diagnosis and treatment of pathologies involving cervical region. We think that the presence of any VA variation in a patient should be investigated on CT or MRI images prior to surgery.

Conflict of interest: None declared

REFERENCES

- Al-Okaili R, Schwartz ED. Bilateral aortic origins of the vertebral arteries with right vertebral artery arising distal to left subclavian artery: case report. *Surg Neurol.* 2007; 67(2): 174–176, doi: [10.1016/j.surneu.2006.02.045](https://doi.org/10.1016/j.surneu.2006.02.045), indexed in Pubmed: [17254881](https://pubmed.ncbi.nlm.nih.gov/17254881/).
- Canyigit M, Akgoz A, Koksal A, et al. Aberrant right vertebral artery: a rare aortic arch anomaly. *Br J Radiol.* 2009; 82(981): 789–791, doi: [10.1259/bjr/17139421](https://doi.org/10.1259/bjr/17139421), indexed in Pubmed: [19729552](https://pubmed.ncbi.nlm.nih.gov/19729552/).
- Chuang YM, Huang YC, Hu HH, et al. Toward a further elucidation: role of vertebral artery hypoplasia in acute ischemic stroke. *Eur Neurol.* 2006; 55(4): 193–197, doi: [10.1159/000093868](https://doi.org/10.1159/000093868), indexed in Pubmed: [16772715](https://pubmed.ncbi.nlm.nih.gov/16772715/).
- Cloud GC, Markus HS. Diagnosis and management of vertebral artery stenosis. *QJM.* 2003; 96(1): 27–54, doi: [10.1093/qjmed/hcg003](https://doi.org/10.1093/qjmed/hcg003), indexed in Pubmed: [12509646](https://pubmed.ncbi.nlm.nih.gov/12509646/).
- Cornelius JF, Pop R, Fricia M, et al. Compression syndromes of the vertebral artery at the craniocervical junction. *Acta Neurochir Suppl.* 2019; 125: 151–158, doi: [10.1007/978-3-319-62515-7_22](https://doi.org/10.1007/978-3-319-62515-7_22), indexed in Pubmed: [30610316](https://pubmed.ncbi.nlm.nih.gov/30610316/).
- Cothren CC, Moore EE. Blunt cerebrovascular injuries. *Clinics (Sao Paulo).* 2005; 60(6): 489–496, doi: [10.1590/s1807-59322005000600011](https://doi.org/10.1590/s1807-59322005000600011), indexed in Pubmed: [16358140](https://pubmed.ncbi.nlm.nih.gov/16358140/).
- Desouza RM, Crocker MJ, Haliasos N, et al. Blunt traumatic vertebral artery injury: a clinical review. *Eur Spine J.* 2011; 20(9): 1405–1416, doi: [10.1007/s00586-011-1862-y](https://doi.org/10.1007/s00586-011-1862-y), indexed in Pubmed: [21674212](https://pubmed.ncbi.nlm.nih.gov/21674212/).
- El-Dwairi QA, Ghaidi JH, Isa HM, et al. Morphometric study of foramina transversaria in Jordanian population using cross-sectional computed tomography. *Anat Sci Int.* 2021; 96(1): 70–78, doi: [10.1007/s12565-020-00559-7](https://doi.org/10.1007/s12565-020-00559-7), indexed in Pubmed: [32783119](https://pubmed.ncbi.nlm.nih.gov/32783119/).
- Gulli G, Marquardt L, Rothwell PM, et al. Stroke risk after posterior circulation stroke/transient ischemic attack and its relationship to site of vertebrobasilar stenosis: pooled data analysis from prospective studies. *Stroke.* 2013; 44(3): 598–604, doi: [10.1161/STROKEAHA.112.669929](https://doi.org/10.1161/STROKEAHA.112.669929), indexed in Pubmed: [23386676](https://pubmed.ncbi.nlm.nih.gov/23386676/).
- Jeng JS, Yip PK. Evaluation of vertebral artery hypoplasia and asymmetry by color-coded duplex ultrasonography. *Ultrasound Med Biol.* 2004; 30(5): 605–609, doi: [10.1016/j.ultrasmedbio.2004.03.004](https://doi.org/10.1016/j.ultrasmedbio.2004.03.004), indexed in Pubmed: [15183225](https://pubmed.ncbi.nlm.nih.gov/15183225/).
- Komiyama M, Morikawa T, Nakajima H, et al. High incidence of arterial dissection associated with left vertebral artery of aortic origin. *Neurol Med Chir (Tokyo).* 2001; 41(1): 8–11, doi: [10.2176/nmc.41.8](https://doi.org/10.2176/nmc.41.8), indexed in Pubmed: [11218642](https://pubmed.ncbi.nlm.nih.gov/11218642/).
- Lazaridis N, Piagkou M, Loukas M, et al. A systematic classification of the vertebral artery variable origin: clinical and surgical implications. *Surg Radiol Anat.* 2018; 40(7): 779–797, doi: [10.1007/s00276-018-1987-3](https://doi.org/10.1007/s00276-018-1987-3), indexed in Pubmed: [29459992](https://pubmed.ncbi.nlm.nih.gov/29459992/).
- Lemke AJ, Benndorf G, Liebig T, et al. Anomalous origin of the right vertebral artery: review of the literature and case report of right vertebral artery origin distal to the left subclavian artery. *AJNR Am J Neuroradiol.* 1999; 20: 1318–1321.
- Lunardini DJ, Eskander MS, Even JL, et al. Vertebral artery injuries in cervical spine surgery. *Spine J.* 2014; 14(8): 1520–1525, doi: [10.1016/j.spinee.2013.09.016](https://doi.org/10.1016/j.spinee.2013.09.016), indexed in Pubmed: [24411832](https://pubmed.ncbi.nlm.nih.gov/24411832/).
- Magklara EP, Pantelia ET, Solia E, et al. Vertebral artery variations revised: origin, course, branches and embryonic development. *Folia Morphol.* 2021; 80(1): 1–12, doi: [10.5603/FM.a2020.0022](https://doi.org/10.5603/FM.a2020.0022), indexed in Pubmed: [32073130](https://pubmed.ncbi.nlm.nih.gov/32073130/).
- Markus HS, Larsson SC, Dennis J, et al. Vertebral artery stenting to prevent recurrent stroke in symptomatic vertebral artery stenosis: the VIST RCT. *Health Technol Assess.* 2019; 23(41): 1–30, doi: [10.3310/hta23410](https://doi.org/10.3310/hta23410), indexed in Pubmed: [31422789](https://pubmed.ncbi.nlm.nih.gov/31422789/).
- Meila D, Tysiac M, Petersen M, et al. Origin and course of the extracranial vertebral artery: CTA findings and embryologic considerations. *Clin Neuroradiol.* 2012; 22(4): 327–333, doi: [10.1007/s00062-012-0171-0](https://doi.org/10.1007/s00062-012-0171-0), indexed in Pubmed: [22941252](https://pubmed.ncbi.nlm.nih.gov/22941252/).
- Melovitz-Vasan C, Varricchio P, Defouw D, et al. Atypical vertebral artery: embryological explanation and implications in neck surgery. *Int J Anat Variations.* 2015; 8: 1–3.
- Mitchell J. The vertebral artery: a review of anatomical, histopathological and functional factors influencing blood flow to the hindbrain. *Physiother Theory Pract.* 2005; 21(1): 23–36, doi: [10.1080/09593980590911570](https://doi.org/10.1080/09593980590911570), indexed in Pubmed: [16385941](https://pubmed.ncbi.nlm.nih.gov/16385941/).
- Moreira JJ, Herrero CF. Anatomical variations and morphometric features of the foramen transversarium in the cervical vertebrae of a latin american population: a Brazilian study. *World Neurosurg.* 2020; 137: e18–e26, doi: [10.1016/j.wneu.2019.11.040](https://doi.org/10.1016/j.wneu.2019.11.040), indexed in Pubmed: [31911157](https://pubmed.ncbi.nlm.nih.gov/31911157/).
- Ngo MT, Kwak HS, Chung GHo. Change in basilar artery length and bending according to aging and vertebral artery dominance: A longitudinal study. *Sci Rep.* 2020;

- 10(1): 8904, doi: [10.1038/s41598-020-65682-x](https://doi.org/10.1038/s41598-020-65682-x), indexed in Pubmed: [32483170](https://pubmed.ncbi.nlm.nih.gov/32483170/).
22. Nouh A, Remke J, Ruland S. Ischemic posterior circulation stroke: a review of anatomy, clinical presentations, diagnosis, and current management. *Front Neurol.* 2014; 5: 30, doi: [10.3389/fneur.2014.00030](https://doi.org/10.3389/fneur.2014.00030), indexed in Pubmed: [24778625](https://pubmed.ncbi.nlm.nih.gov/24778625/).
 23. Park JH, Kim JM, Roh JK. Hypoplastic vertebral artery: frequency and associations with ischaemic stroke territory. *J Neurol Neurosurg Psychiatry.* 2007; 78(9): 954–958, doi: [10.1136/jnnp.2006.105767](https://doi.org/10.1136/jnnp.2006.105767), indexed in Pubmed: [17098838](https://pubmed.ncbi.nlm.nih.gov/17098838/).
 24. Satti SR, Cerniglia CA, Koenigsberg RA. Cervical vertebral artery variations: an anatomic study. *AJNR Am J Neuroradiol.* 2007; 28(5): 976–980, indexed in Pubmed: [17494682](https://pubmed.ncbi.nlm.nih.gov/17494682/).
 25. Shin HY, Park JiK, Park SK, et al. Variations in entrance of vertebral artery in korean cervical spine: MDCT-based analysis. *Korean J Pain.* 2014; 27(3): 266–270, doi: [10.3344/kjp.2014.27.3.266](https://doi.org/10.3344/kjp.2014.27.3.266), indexed in Pubmed: [25031813](https://pubmed.ncbi.nlm.nih.gov/25031813/).
 26. Sticco A, Gandhi SS, Knoedler B, et al. Current outcomes of blunt vertebral artery injuries. *Ann Vasc Surg.* 2021; 70: 252–257, doi: [10.1016/j.avsg.2020.07.045](https://doi.org/10.1016/j.avsg.2020.07.045), indexed in Pubmed: [32768545](https://pubmed.ncbi.nlm.nih.gov/32768545/).
 27. Uchino A, Saito N, Takahashi M, et al. Variations in the origin of the vertebral artery and its level of entry into the transverse foramen diagnosed by CT angiography. *Neuroradiology.* 2013; 55(5): 585–594, doi: [10.1007/s00234-013-1142-0](https://doi.org/10.1007/s00234-013-1142-0), indexed in Pubmed: [23344682](https://pubmed.ncbi.nlm.nih.gov/23344682/).
 28. Vilimas A, Barkauskas E, Vilionskis A, et al. Vertebral artery hypoplasia: importance for stroke development, the role of posterior communicating artery, possibility for surgical and conservative treatment. *Acta Medica Lituanica.* 2003; 10: 110–114.
 29. Woraputtaporn W, Ananteerakul T, Iamsaard S, et al. Incidence of vertebral artery of aortic arch origin, its level of entry into transverse foramen, length, diameter and clinical significance. *Anat Sci Int.* 2019; 94(4): 275–279, doi: [10.1007/s12565-019-00482-6](https://doi.org/10.1007/s12565-019-00482-6), indexed in Pubmed: [30806941](https://pubmed.ncbi.nlm.nih.gov/30806941/).
 30. Yamaki Ki, Saga T, Hirata T, et al. Anatomical study of the vertebral artery in Japanese adults. *Anat Sci Int.* 2006; 81(2): 100–106, doi: [10.1111/j.1447-073x.2006.00133.x](https://doi.org/10.1111/j.1447-073x.2006.00133.x), indexed in Pubmed: [16800294](https://pubmed.ncbi.nlm.nih.gov/16800294/).
 31. Yuan SM. Aberrant origin of vertebral artery and its clinical implications. *Braz J Cardiovasc Surg.* 2016; 31(1): 52–59, doi: [10.5935/1678-9741.20150071](https://doi.org/10.5935/1678-9741.20150071), indexed in Pubmed: [27074275](https://pubmed.ncbi.nlm.nih.gov/27074275/).
 32. Zarrinkoob L, Ambarki K, Wählin A, et al. Blood flow distribution in cerebral arteries. *J Cereb Blood Flow Metab.* 2015; 35(4): 648–654, doi: [10.1038/jcbfm.2014.241](https://doi.org/10.1038/jcbfm.2014.241), indexed in Pubmed: [25564234](https://pubmed.ncbi.nlm.nih.gov/25564234/).
 33. Zhang M, Dayani F, Purger DA, et al. Extraforaminal vertebral artery anomalies and their associated surgical implications: an epidemiologic and anatomic report on 1000 patients. *World Neurosurg.* 2020; 141: e971–e975, doi: [10.1016/j.wneu.2020.06.110](https://doi.org/10.1016/j.wneu.2020.06.110), indexed in Pubmed: [32585381](https://pubmed.ncbi.nlm.nih.gov/32585381/).
 34. Zibis AH, Mitrousias V, Baxevanidou K, et al. Anatomical variations of the foramen transversarium in cervical vertebrae: findings, review of the literature, and clinical significance during cervical spine surgery. *Eur Spine J.* 2016; 25(12): 4132–4139, doi: [10.1007/s00586-016-4738-3](https://doi.org/10.1007/s00586-016-4738-3), indexed in Pubmed: [27554348](https://pubmed.ncbi.nlm.nih.gov/27554348/).

Variations of coronary sinus tributaries among patients undergoing cardiac resynchronisation therapy

B. Gach-Kuniewicz¹, G. Goncerz¹, D. Ali¹, M. Kacprzyk², M. Zarzecki¹, M. Loukas^{3, 4}, J. Walocha¹, E. Mizia¹

¹Department of Anatomy, Jagiellonian University Medical College, Krakow, Poland

²Department of Electrocardiology, Institute of Cardiology, Jagiellonian University Medical College, Krakow, Poland

³Department of Anatomical Sciences, St. George's University, Grenada, West Indies

⁴Department of Anatomy, Varmia and Mazury University, Olsztyn, Poland

[Received: 19 February 2022; Accepted: 7 April 2022; Early publication date: 28 April 2022]

Background: In cardiac resynchronisation therapy (CRT), the coronary venous system is used for left ventricular pacing electrode placement. Despite the well-known anatomy of the coronary sinus and its tributaries, heart failure patients' remodelled and enlarged left ventricles may impede the successful lead placement because of acquired anatomical obstacles.

Materials and methods: Fifty-five patients qualified for CRT treatment were divided into ischaemic and non-ischaemic cardiomyopathy. Forty-four control groups without heart failure underwent dual-source computed tomography (CT). Rendered reconstructions of cardiac coronary systems were compared.

Results: The presence of main tributaries was comparable in all groups. The left marginal vein, small cardiac vein, and oblique vein of the left atrium were present in 63%, 60%, and 51% of the hearts in all the groups. CRT referred CTs had significantly longer distances between posterior and lateral cardiac veins over the left ventricle ($p < 0.05$), wider angles of tributaries ($p = 0.03$), and smaller lumen of coronary sinus ($p = 0.03$). In the non-ischaemic group, the posterior interventricular and great cardiac veins are more extensive than in the control group. Age-related analysis of vessel size shows a moderate correlation between age and diminishing mean vessel size in all the groups studied.

Conclusions: The general structure of the coronary heart system is consistent in patients with and without heart failure. The variance of the general structure, or the presence of adequate veins, is an individual variation. The use of CT and analysis of the coronary veins allow better planning of the CRT-D implantation procedure and may reduce the risk of ineffective left ventricular electrode implantation. (Folia Morphol 2023; 82, 2: 282–290)

Key words: coronary sinus, resynchronization therapy, heart failure

Address for correspondence: B. Gach-Kuniewicz, MD, Department of Anatomy, Jagiellonian University Medical College, ul. Kopernika 12, 31–034 Kraków, Poland, tel/fax: +48 12 422 95 11, e-mail: bgkuniewicz@gmail.com

This article is available in open access under Creative Common Attribution-Non-Commercial-No Derivatives 4.0 International (CC BY-NC-ND 4.0) license, allowing to download articles and share them with others as long as they credit the authors and the publisher, but without permission to change them in any way or use them commercially.

INTRODUCTION

The coronary venous system consisting of the coronary sinus (CS) and its tributaries contributes to most venous drainage from the heart muscle. The great cardiac vein (GCV), middle cardiac vein (MCV)/posterior interventricular vein (PIV), and small cardiac vein (SCV), in addition to the left marginal vein (LMV), the posterior vein of the left ventricle (PVLV), and oblique vein of the left atrium (OVLA), also known as the vein of Marshall (VoM), constitute the most constant tributaries of the CS [8, 13, 18, 20, 21, 24, 27].

The coronary system is often used during invasive transcatheter procedures, such as radiofrequency ablation, biventricular pacing, retrograde cardioplegia administration, or mitral annuloplasty. Furthermore, the CS and GCV are relevant in almost every electrophysiology procedure and are often used as landmarks for safe transseptal punctures [11]. In addition, consideration is given to the use of the MCV for the placement of left ventricular leads and ablation of posterior epicardial accessory pathways or the treatment of epicardial ventricular arrhythmias. Meanwhile, the PVLV or LMV, both of which drain the lateral wall of the left ventricle (LV), are often the target for left ventricular or biventricular pacing [6, 10, 19].

Cardiac resynchronisation therapy (CRT) is a well-established treatment for patients with dilation and systolic dysfunction of the LV, and electrocardiographic evidence of intraventricular conduction delay. The reason for left ventricular dilation may be advanced ischaemic heart disease or there may be non-ischaemic reasons. Resynchronisation therapy requires the insertion of right and left ventricular leads to resynchronise ventricular contraction. For the successful pacing of the LV and the success of epicardial pacing, the use of one of the posterolateral tributaries of the CS is imperative [1, 4, 8, 21]. Unfortunately, 30–40% of patients do not respond adequately to CRT [17]. Trespassing through the Thebesian and Vieussens valve is one of the determinants of this response [14, 32].

The successful left ventricular pacing depends on the coronary system constitution and the highly variable anatomy of the CS and its tributaries. The important fact is that CRT is required for selected patients obtaining physical and imaging requirements for heart failure (HF) improvements without aetiology differentiation. We believe that blood flow reduction in ischaemic aetiology reduces the volume of coronary

veins, impeding successful electrode placement. In contrast, non-ischaemic aetiology will change only the architecture of the coronary system.

Clinical experience, manual skills, and knowledge of the coronary venous system anatomy are necessary for successful CS cannulation and reaching the desirable vein. Although CS anatomy is well-known, hearts with LV enlargement and cardiomyopathy anatomically differ from general anatomy. Remodelling the LV myocardial scar may change the size of the CS tributaries, angulations, constrict or close the existing vessels, and impede the invasive procedure, making it more challenging or even impossible to perform [25]. Therefore, this study aims to evaluate the CS tributaries anatomy in ischaemic and non-ischaemic cardiomyopathy vs. non-HF venous anatomy.

MATERIALS AND METHODS

This study was approved by the local ethics committee [NB.060.1.26.2021]. The study protocol conformed to the ethical guidelines of the 1975 Declaration of Helsinki. The methods were executed per the approved guidelines.

Study populations

This study included 55 consecutive patients (mean age 65 ± 12 [35–82] years, 11 women [20%]) with HF, considered to CRT treatment, who underwent dual-source computed tomography (CT).

The designation of patients from the HF group, according to aetiology, was 29 (52%) to ischaemic cardiomyopathy (ischaemic HF) and 26 (48%) to non-ischaemic cardiomyopathy (non-ischaemic-HF). From the non-ischaemic HF group, 22 were idiopathic dilated cardiomyopathy, 1 hypertrophic, 1 post-infectious, 2 tachy-cardiomyopathy. Five patients from the HF group had implantable cardioverter-defibrillator and 2 had pacemakers.

For more accurate anatomical comparison we included 44 non-HF patients from the control group (mean age 61.9 ± 13.7 years [20–91] 24 women [54.5%]), who underwent CT evaluation of coronary artery disease ($n = 20$) and pulmonary veins before cryoballoon ablation ($n = 24$).

Descriptions of further clinical details of patients from each group are shown in Table 1.

CT-protocol

Before each cardiac CT examination, every patient had a pulse check. If a patient's heart rate was over

Table 1. Characteristics of the study population

	Ischaemic-HF (n = 29)	Non-ischaemic-HF (n = 26)	Non-HF (n = 44)
Sex: female	3 (10.3%)	9 (34.6%)	24 (54.5%)
Age (\pm SD) [year]	66.23 \pm 10.72 (35–82)	62.2 \pm 12.97 (31–81)	61.9 \pm 13.7 (20–91)
Ejection fraction [%]	24.55 \pm 6.47 (35–10)	24.88 \pm 7.14 (35–15)	54.2 \pm 9.1 (44–72)
NYHA	II–III	II–III	I
QRS duration [ms]	140 \pm 23 (120–160)	146 \pm 36 (124–174)	91 \pm 15 (80–110)
Hypertension	25 (86.2%)	18 (69.2%)	36 (81%)
Diabetes type 2	12 (41.4%)	6 (23.1%)	12 (27%)
Hypercholesterolaemia	28 (96.5%)	13 (50%)	26 (59%)
Chest pain	18 (62.1%)	10 (38.5%)	30 (68%)
Dyspnoea	24 (82.8%)	19 (73.1%)	30 (68%)
Atrial fibrillation	10 (34.5%)	7 (26.9%)	24 (54.5%)
Atrio-ventricular block	3 (10.3%)	4 (15.4%)	0 (0%)

HF — heart failure; NYHA — New York Heart Association; SD — standard deviation

70 bpm, 10 mg or 40 mg of propranolol or 40 mg verapamil was administered, according to medical indications. A dual-source CT scanner (Somatom Definition, Siemens, Erlangen, Germany) and the contrast-enhanced electrocardiogram (ECG)-retrospectively gated image acquisitions were performed during an inspiratory breath-hold. The imaging parameters for the dual-source CT were a tube voltage of 100–120 kV and an effective tube current of 350–400 mA. The collimation and temporal resolution revealed $2 \times 32 \times 0.6$ mm and 165 ms. Determination of the arrival time of the contrast agent to the ascending aorta at the level of the carina employed the use of the test bolus method (volume of 15 mL contrast agent, followed by 20 mL saline). The procedure works by injecting the contrast agent at the dose of 1.0 mL/kg and a rate of 5.5 mL/s followed by a 40 mL saline chaser at the same rate range. The acquisition delay was the time of maximum density of the ascending aorta in the test bolus with an additional 6 s of delay. Image reconstruction using B26f and B46f kernel and an image matrix of 512×512 pixels allowed for an assessment of the best quality image reconstructions after the multiphase reconstruction (from 10% to 100%). Uses of a dedicated workstation (Aquarius, TeraRecon, San Mateo, United States) by an experienced radiologist allowed for the performance of post-processing and study evaluation. Multiplanar (MPR) and volume-rendered technique (VRT) reconstructions allowed identification of CS ostium in Ludinghausen modifications, number, and variety of veins over LV, distances, and angles between branches of CS.

Anatomic observation

The anatomy of the CS and its tributaries was studied and identified on the volume-rendered reconstructions, and the course of the veins was evaluated in three orthogonal planes using multiplanar reformatting [7]. The categorization of each heart used one of the three types proposed by Von Ludinghausen [26].

First, the ostium of the sinus was identified from the right atrium, using multiplanar reformatting for measurements in two directions [28]. The subsequent examination considered the presence of each CS tributary (SCV, MCV, PVLV, LMV, VoM, and AIV). In addition to the assessments of the 5.1 F (1.7 mm) and LV-electrode cannulation of each tributary, the verification of the presence of the Vieussens valve and the distance between the ventricular tributaries was measured on volume-rendered reconstructions (Fig. 1).

Statistical analysis

The presentation of data is as follows: (1) mean values with the corresponding standard deviations and ranges; and/or (2) determining percentages. To verify a relative homogeneity of variance, we performed Levene's tests. The Student's t-tests and the Mann-Whitney U tests were used for statistical comparisons. Additionally, qualitative variables were compared using χ^2 tests of proportions for categorical variables. Statistical analyses using StatSoft STATISTICA 13.1 software for Windows (StatSoft Inc., Tulsa, OK, USA) enable the detection of a moderate correlation ($r = 0.4$), for 80% power with a 5% significance level (two-tailed; $\alpha = 0.05$; $\beta = 0.2$). The statistical significance was set at a p-value lower than 0.05.

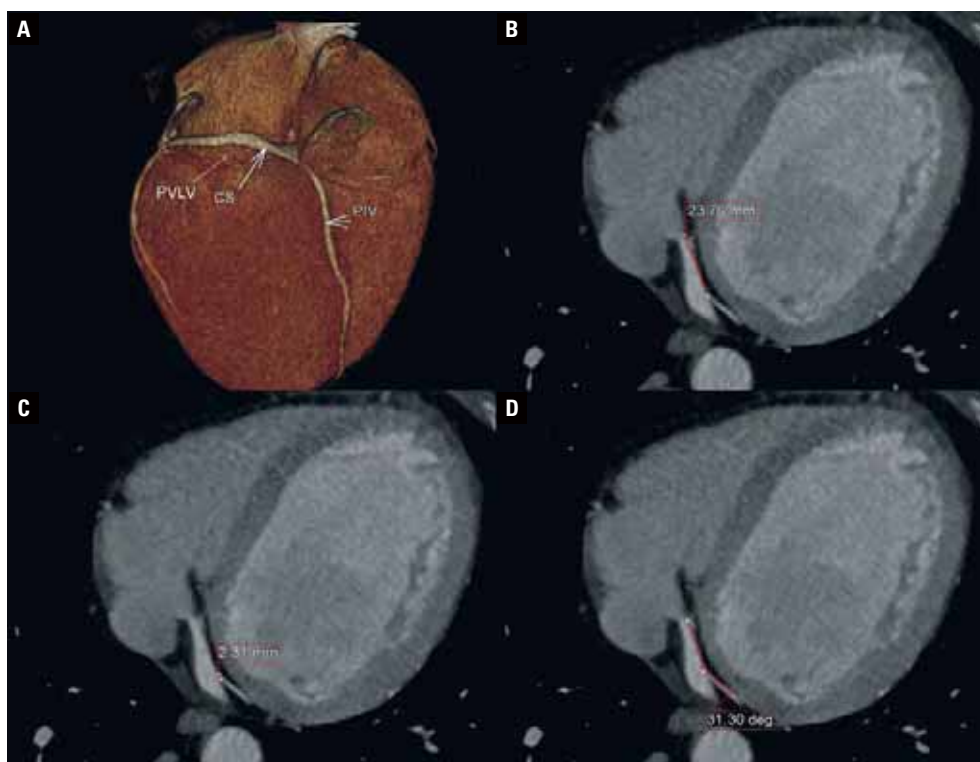


Figure 1. Coronary veins anatomy (A) and quantitative analysis of distance from coronary sinus (CS) ostium (B), diameter (C), angle (D) of insertion using multiplanar and volume rendered technique reconstructions; PVLV — posterior vein of the left ventricle; PIV — posterior interventricular vein.

RESULTS

Study population

The imaging studies to visualise the cardiac venous system were performed in all patients in all groups. The CS, PIV, PVLV, and AIV were present in all patients. There is an observation of the LMV, in ischaemic-HF/nonischaemic-HF/control group in the 21, 15 and 26 (72.4%, 57.7%, 59.1%) hearts, OVLA in the 10, 11 and 30 (34.5%, 42.3%, 68.2%) hearts, and SCV in the 15, 19 and 25 (51.7%, 73.1%, 56.8%) hearts, respectively.

Anatomical variants (proposed by Von Ludwighausen) vary between the groups. In ischaemic-HF most common variant was with SCV continuity into CS (variant 1) (58.6% $p < 0.05$). In non-ischaemic-HF and non-HF with separate SCV presented with PIV connected to the crus-cordis (variant 2). The third variant with PIV disconnected to the CS was the rarest, with a presence from 6.9% in ischaemic-HF to 11.4%, 11.5% in non-HF, and non-ischaemic-HF.

The OVLA (vein of Marshall) was distinguishable in 12/44 (27.3%) in the non-HF ($p = 0.18$) group compared to 4/29 (13.8%) and 6/26 (19.2%) in both HF

groups. A rare appearance of the Vieusens valve appears in approximately 20% of all the groups. Table 2 summarizes detailed information of anatomical observations.

Quantitative data

The distances between the main tributaries draining venous blood from LV, angles, and diameters of specific branches demonstrate observable differentials. While most values are not statistically significant between the groups in general summaries, some measurements conduct important differences. PVLV-LMV interspace and angle of PIV in both HF vs. non-HF groups ($p < 0.005$) reveal essential discrepancies between the distances. The mean distance in the non-HF group was 35.67 ± 13.53 mm, while in non-ischaemic-HF, 46.56 ± 17.15 to 47.54 ± 10.98 mm ($p = 0.002$) in the ischaemic-HF group. The angle of PIV entering CS in HF hearts was significantly bigger — $110.74 \pm 22.42^\circ$ ($p = 0.03$) in ischaemic-HF and $116.1 \pm 21.38^\circ$ ($p = 0.03$) in non-ischaemic-HF vs. non-HF group $98.4 \pm 22.94^\circ$. Figure 2 presents a summary of vessel displacement.

Table 2. Anatomic observations. Quantitative analysis of coronary sinus anatomy and its tributaries

	Ischaemic-HF (n = 29)	Non-ischaemic-HF (n = 26)	Non-HF (n = 44)
Coronary sinus:			
Type 1*	17 (58.6%)	4 (15.4%)	12 (27.3%)
Type 2*	10 (34.5%)	19 (73.1%)	27 (61.4%)
Type 3*	2 (6.9%)	3 (11.5%)	5 (11.4%)
Small cardiac vein	15 (51.7%)	19 (73.1%)	25 (56.8%)
Posterior interventricular vein:			
Posterior vein of left ventricle	S: 4 (14%) M: 25 (86%)	S: 3 (12%) M: 23 (88%)	S: 8 (18%) M: 36 (82%)
Left marginal vein	21 (72.4%)	15 (57.7%)	26 (59.1%)
Vein of Marshall	4 (13.8%)	5 (19.2%)	12 (27.3%)
Viessens valve	6 (20.1%)	4 (15.4%)	8 (18.2%)
Anterior interventricular vein	29 (100%)	26 (100%)	44 (100%)

*Types refer to von Ludinghausen classification; HF — heart failure; S — single; M — multiple

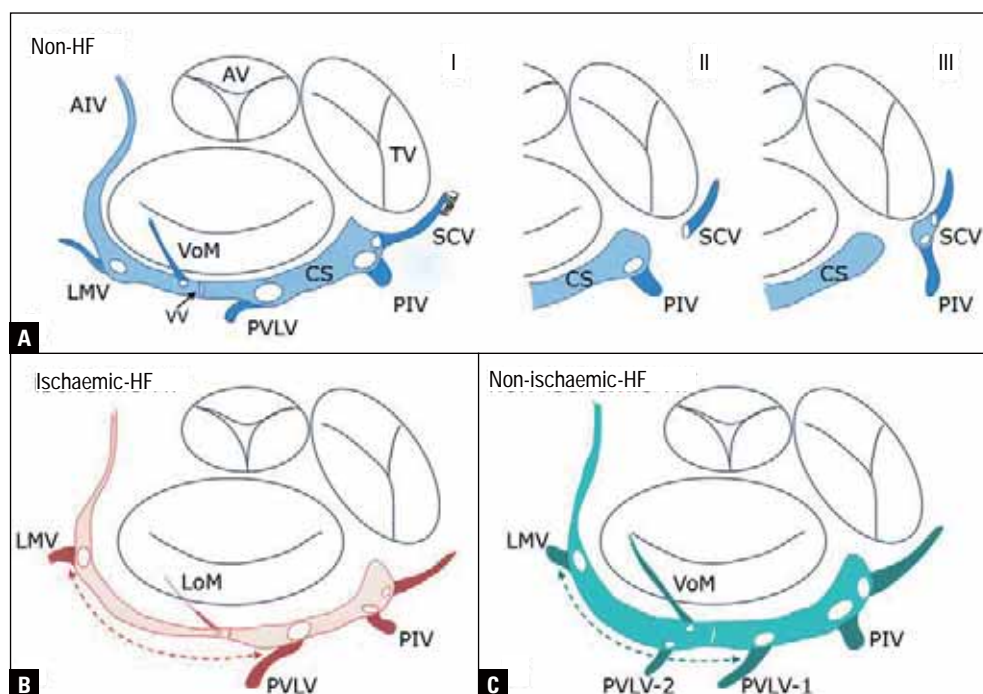


Figure 2. Schematic picture of differences between non-HF (blue) group (A) and ischaemic-HF (red) group (B) and non-ischaemic-HF (C); Panel A represents three types of von Ludinghausen modifications I, II and III; AIV — anterior interventricular vein; AV — aortic valve; CS — coronary sinus; HF — heart failure; LMV — left marginal vein; LoM — ligament of Marshall; PIV — posterior interventricular vein; PVLV — posterior vein of left ventricle; SCV — small cardiac vein; TV — tricuspid valve; VoM — vein of Marshall; VV — Viessens valve.

Then, the separate consideration of differences for each group. In ischaemic-HF vs. non-HF (control group), vessel diameters are generally smaller with statistical significance in AIV diameter (2.64 vs. 3.18 mm, $p = 0.01$). Also, the CS diameter (6.82 vs. 7.84 mm, $p = 0.03$) and CS ostium ($p = 0.03$) are smaller. Such significances do not appear in non-ischaemic-HF

vs. non-HF groups. In non-ischaemic-HF, the differences are opposite. PVI diameter (5.43 vs. 3.9 mm, $p = 0.01$) was significantly larger than non-HF groups, while the CS diameter was bigger, approximately 5 mm. However, this is without statistical significance ($p = 0.8$).

Comparing HF groups, PIV diameter is significantly broader in nonischaemic-HF vs. ischaemic (5.43 vs.

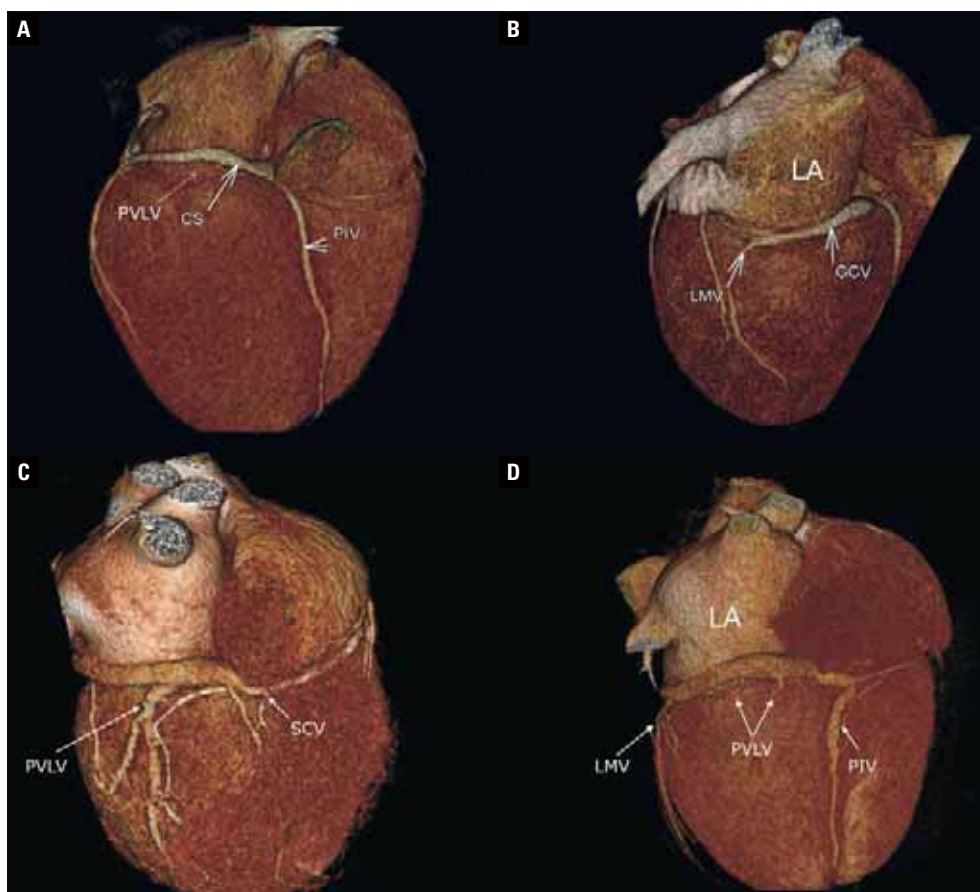


Figure 3. Rendered reconstructions of coronary sinus (CS) with tributaries; **A, B.** In ischaemic heart failure; **C, D.** In non-ischaemic heart failure; GCV — great cardiac vein; LA — left atrium; LMV — left marginal vein; PIV — posterior interventricular vein; PVLV — posterior vein of left ventricle; SCV — small cardiac vein.

4.33 mm, $p = 0.04$), as is the CS diameter (8.3 vs. 6.82 mm, $p = 0.03$). The presentation of differentials for each HF group is on the volume-rendered reconstructions (Fig. 3).

Results demonstrate moderate correlations between the patient's age and AIV diameter in ischaemic-HF ($r = 0.56$, $p = 0.21$) and PIV angle in non-ischaemic-HF ($r = 0.40$, $p = 0.6$). Furthermore, correlations with left ventricular ejection fraction (LVEF) only present in ischaemic-HF between SCV diameter ($r = 0.55$, $p = 0.8$) and LMV angle ($r = 0.43$, $p = 0.5$). None from correlations because sample size reached statistical significance.

Finally, the attainable vessels were counted for possible LV lead placement. For accessible vessels for the CRT, the size of 5.1 F (1.7 mm) and angle is less than 60° [2] are considered. The size over 1.7 mm was found in 23/26 PVLV and 10/15 LMV in non-ischaemic-HF and 28/29 and 16/21 in ischaemic-HF. The tributaries' ostium angles less than 60° advanc-

ing cannulation were found in 13/26 PVLV and 10/15 LMV in nonischaemic-HF and 14/29 and 11/21 in ischaemic-HF. The only correlation in the χ^2 test was found in PVLV diameter for ischaemic-HF favouring implantation $p = 0.02$.

Table 3 summarizes the quantitative data.

DISCUSSION

Cardiac resynchronisation therapy provides HF improvement and an effective increase in LVEF only in 70% of the patients. For years, the statement that nearly one-third of CRT patients do not respond to resynchronization therapy has become general knowledge. It is discussed and partially accepted without questioning the reasons [2]. Besides optimal programming of the CRT device, the anatomical structure of the coronary system plays the crucial role. Remodelled heart muscle with venous drainage may differ from a healthy one, and the aim of that study emphasizes such discrepancies.

Table 3. Anatomic observations. Qualitative analysis of diameters, distances and angles of coronary sinus and its tributaries

	Ischaemic-HF (n = 29)	Non-ischaemic-HF (n = 26)	Non-HF (n = 44)
Ostium CS antero-posterior diameter	9.26 ± 4.02	9.8 ± 4.25	11 ± 4.3
Ostium CS superior-inferior diameter	14.94 ± 5.6 (p = 0.03)*	16.24 ± 6	18.36 ± 7.74
SCV diameter [mm]	1.37 ± 0.65	2.19 ± 1.3	1.5 ± 0.75
PIV diameter [mm]	4.33 ± 1.88 (p = 0.04)**	5.43 ± 2.03 (p = 0.01)*	3.9 ± 1.78
PVLV diameter [mm]	3.35 ± 1.17	3.15 ± 1.17	3.1 ± 1.46
LMV diameter [mm]	2.3 ± 1.04	2.62 ± 1.04	2.72 ± 1.27
GCV diameter [mm]	6.82 ± 1.46 (p = 0.03)*	8.3 ± 3.14 (p = 0.03)**	7.84 ± 2.49
AIV diameter [mm]	2.64 ± 0.83 (p = 0.02)**	2.86 ± 1.45	3.17 ± 0.98
CS ostium PIV distance [mm]	4.21 ± 2.68	3.12 ± 2.46	3.25 ± 3.32
PIV–PVLV distance [mm]	24.33 ± 10.43	27.4 ± 15.75	28.32 ± 15.31
PVLV–LMV distance [mm]	47.54 ± 10.98 (p = 0.002)*	46.56 ± 17.15 (p = 0.005)	35.67 ± 13.53
PIV angle [°]	110.74 ± 22.42 (p = 0.03)*	116.1 ± 21.38 (p = 0.03)*	98.4 ± 22.94
PVLV angle [°]	54.56 ± 22.87	61.46 ± 26.04 (p = 0.04)*	50.82 ± 26.94
LMV angle [°]	62 ± 33.54	50.25 ± 20.14	55.39 ± 37.92

*Statistical significance to control group (non-HF), **statistical significance between ischaemic to non-ischaemic HF; AIV — anterior interventricular vein; CS — coronary sinus; GCV — great cardiac vein; HF — heart failure; LMV — left marginal vein; PIV — posterior interventricular vein; PVLV — posterior vein of the left ventricle; SCV — short cardiac vein

The general structure of the coronary heart system is consistent in patients with and without HF [9, 12, 30]. The variance of the general structure, or the presence of particular veins, is an individual variation [3, 13, 20, 22, 23]. It refers mainly to the prevalence of LMV (from 72.4–57.7%) in all groups. As in VoM, where the occurrence variability is high, and the detection ability is low [15, 33]. When VoM is not visible the structure which is present is the ligament of Marshall (LoM) (Fig. 2C).

Besides the individual arrangement of veins, ventricular remodelling affects the coronary system in HF patients. When analysing individual subgroups, the most significant difference between the coronary system in HF and the control group (non-HF) is the substantial change in the distance between PVLV and LMV (Fig. 2B, C). The average elongation of these distances ranges 12 mm. Apart from the PVLV outlet is variable and often multi-vessel (Fig. 3D). Vein displacement also changes the outlet angles. PIV shifts from the CS outlet further affect the outlet angles. While the distance appears to be statistically insignificant, the change in vessel angle from 98.4° to 110.7° (p = 0.03) indicates a shift in the vessel's outlet relative to the mitral ring. An interesting observation is a change in the diameters of individual vessels — ischaemic-HF heart coronary sinuses demonstrate a reduction in vein diameter (GCV, AIV, CS outlets) when compared with non-HF (p = 0.01). Inversely, these vessels in the nonischaemic-HF group are more extensive

than in the study group, mainly PIV and GCV (p = 0.01). Performing an age-related correlation analysis of vessel size — we found a moderate correlation between the age and mean vessel size in all the groups studied. The Mazur et al. [13] study demonstrates similar observations. Finally, the CS outlet also differs between groups. Assuming application of the S-I (superior–inferior) and A-P (anterior–posterior) dimensions to the ellipse area, it turns out that the CS opening in the ischaemic-HF is significantly smaller than in the control group. It relates to the ischaemic-HF group, in which there was a less frequent observation of the presence of the Thebesian valve [31]. Nevertheless, the coronary venous system is fragmentary stenosed in patients with ischaemic-HF, while significantly widened in individual segments in nonischaemic-HF concerning the control group — non-HF.

The observed qualitative differences result from changes in the architecture of the heart muscle itself, which cause vessel displacement and changes in ostium angles [5]. Left ventricle dilation determines the displacement change in HF patients. Analysing the possibility of LV electrode placement in PVLV or LMV veins with a 5.1 F LV electrode is likely to be highly successful. According to the lumen size, the possible cannulation ranges from 66–96%; however, the anatomy of the coronary system is not the only determinant of the final location of the electrode. It also depends on the resynchronization response of the LV assessed by the ECG and echocardiography

[16, 20, 29]. Access to the vessels due to the angular departure makes 50% of the vessels easily accessible. Additionally, the change of vessel angles in HF vs. non-HF facilitates cannulation by reducing the departure angles ($p = 0.02$). The use of CT and analysis of the coronary veins allow better planning of the CRT-D implantation procedure and may reduce the risk of ineffective left ventricular electrode implantation.

CONCLUSIONS

The general structure of the coronary heart system is consistent in patients with and without HF.

The substantial change between HF vs. non-HF hearts is the distance elongation between outlets of veins draining the LV.

In ischaemic-HF hearts the volume of the CS is generally smaller, while in non-ischaemic-HF broader to control group.

The change of vessel angles in HF vs. non-HF facilitates cannulation by reducing the departure angles.

Conflict of interest: None declared

REFERENCES

1. Becker M, Hoffmann R, Schmitz F, et al. Relation of optimal lead positioning as defined by three-dimensional echocardiography to long-term benefit of cardiac resynchronization. *Am J Cardiol.* 2007; 100(11): 1671–1676, doi: [10.1016/j.amjcard.2007.07.019](https://doi.org/10.1016/j.amjcard.2007.07.019), indexed in Pubmed: [18036367](https://pubmed.ncbi.nlm.nih.gov/18036367/).
2. Butter C, Georgi C, Stockburger M. Optimal CRT implantation—where and how to place the left-ventricular lead? *Curr Heart Fail Rep.* 2021; 18(5): 329–344, doi: [10.1007/s11897-021-00528-9](https://doi.org/10.1007/s11897-021-00528-9), indexed in Pubmed: [34495452](https://pubmed.ncbi.nlm.nih.gov/34495452/).
3. Cendrowska-Pinkosz M. The variability of the small cardiac vein in the adult human heart. *Folia Morphol.* 2004; 63(2): 159–162, indexed in Pubmed: [15232770](https://pubmed.ncbi.nlm.nih.gov/15232770/).
4. Gold MR, Auricchio A, Hummel JD, et al. Comparison of stimulation sites within left ventricular veins on the acute hemodynamic effects of cardiac resynchronization therapy. *Heart Rhythm.* 2005; 2(4): 376–381, doi: [10.1016/j.hrthm.2004.12.025](https://doi.org/10.1016/j.hrthm.2004.12.025), indexed in Pubmed: [15851339](https://pubmed.ncbi.nlm.nih.gov/15851339/).
5. Gold MR, Thébault C, Linde C, et al. Effect of QRS duration and morphology on cardiac resynchronization therapy outcomes in mild heart failure: results from the Resynchronization Reverses Remodeling in Systolic Left Ventricular Dysfunction (REVERSE) study. *Circulation.* 2012; 126(7): 822–829, doi: [10.1161/CIRCULATIONAHA.112.097709](https://doi.org/10.1161/CIRCULATIONAHA.112.097709), indexed in Pubmed: [22781424](https://pubmed.ncbi.nlm.nih.gov/22781424/).
6. Habib A, Lachman N, Christensen KN, et al. The anatomy of the coronary sinus venous system for the cardiac electrophysiologist. *Europace.* 2009; 11 (Suppl 5): v15–v21, doi: [10.1093/europace/eup270](https://doi.org/10.1093/europace/eup270), indexed in Pubmed: [19861386](https://pubmed.ncbi.nlm.nih.gov/19861386/).
7. Jongbloed MRM, Lamb HJ, Bax JJ, et al. Noninvasive visualization of the cardiac venous system using multislice computed tomography. *J Am Coll Cardiol.* 2005; 45(5): 749–753, doi: [10.1016/j.jacc.2004.11.035](https://doi.org/10.1016/j.jacc.2004.11.035), indexed in Pubmed: [15734621](https://pubmed.ncbi.nlm.nih.gov/15734621/).
8. Kassem M, Lake S, Roberts W, et al. Cardiac veins, an anatomical review. *Transl Res Anat.* 2021; 23: 100096, doi: [10.1016/j.tria.2020.100096](https://doi.org/10.1016/j.tria.2020.100096).
9. Khan FZ, Virdee MS, Gopalan D, et al. Characterization of the suitability of coronary venous anatomy for targeting left ventricular lead placement in patients undergoing cardiac resynchronization therapy. *Europace.* 2009; 11(11): 1491–1495, doi: [10.1093/europace/eup292](https://doi.org/10.1093/europace/eup292), indexed in Pubmed: [19880411](https://pubmed.ncbi.nlm.nih.gov/19880411/).
10. Kozłowski D, Koźluk E, Piatkowska A, et al. The middle cardiac vein as a key for “posteroseptal” space: a morphological point of view. *Folia Morphol.* 2001; 60(4): 293–296, indexed in Pubmed: [11770339](https://pubmed.ncbi.nlm.nih.gov/11770339/).
11. Manolis AS. Transeptal access to the left atrium: tips and tricks to keep it safe derived from single operator experience and review of the literature. *Curr Cardiol Rev.* 2017; 13(4): 305–318, doi: [10.2174/1573403X13666170927122036](https://doi.org/10.2174/1573403X13666170927122036), indexed in Pubmed: [28969539](https://pubmed.ncbi.nlm.nih.gov/28969539/).
12. Markstad H, Bakos Z, Ostenfeld E, et al. Preoperative CT of cardiac veins for planning left ventricular lead placement in cardiac resynchronization therapy. *Acta Radiol.* 2019; 60(7): 859–865, doi: [10.1177/0284185118803796](https://doi.org/10.1177/0284185118803796), indexed in Pubmed: [30304945](https://pubmed.ncbi.nlm.nih.gov/30304945/).
13. Mazur M, Hołda M, Koziej M, et al. Morphology of tributaries of coronary sinus in humans — corrosion casting study. *Folia Med Cracov.* 2015; 55(2): 5–13, indexed in Pubmed: [26839238](https://pubmed.ncbi.nlm.nih.gov/26839238/).
14. Mazur M, Tomaszewska R, Pasternak A, et al. The Thebesian valve and its significance for electrophysiologists. *Folia Morphol.* 2014; 73(3): 298–301, doi: [10.5603/FM.2014.0047](https://doi.org/10.5603/FM.2014.0047), indexed in Pubmed: [25242157](https://pubmed.ncbi.nlm.nih.gov/25242157/).
15. Młynarski R, Młynarska A, Gołba KS, et al. Visualisation of the oblique vein of the left atrium (vein of Marshall) using cardiac computed tomography: is the game worth the candle? *Kardiol Pol.* 2018; 76(9): 1344–1349, doi: [10.5603/KP.a2018.0131](https://doi.org/10.5603/KP.a2018.0131), indexed in Pubmed: [30251241](https://pubmed.ncbi.nlm.nih.gov/30251241/).
16. Noheria A, Sodhi S, Orme GJ. The evolving role of electrocardiography in cardiac resynchronization therapy. *Curr Treat Options Cardiovasc Med.* 2019; 21(12): 91, doi: [10.1007/s11936-019-0784-6](https://doi.org/10.1007/s11936-019-0784-6), indexed in Pubmed: [31828564](https://pubmed.ncbi.nlm.nih.gov/31828564/).
17. Ojo A, Tariq S, Harikrishnan P, et al. Cardiac resynchronization therapy for heart failure. *Interv Cardiol Clin.* 2017; 6(3): 417–426, doi: [10.1016/j.iccl.2017.03.010](https://doi.org/10.1016/j.iccl.2017.03.010), indexed in Pubmed: [28600094](https://pubmed.ncbi.nlm.nih.gov/28600094/).
18. Ortale JR, Gabriel EA, Iost C, et al. The anatomy of the coronary sinus and its tributaries. *Surg Radiol Anat.* 2001; 23(1): 15–21, doi: [10.1007/s00276-001-0015-0](https://doi.org/10.1007/s00276-001-0015-0), indexed in Pubmed: [11370136](https://pubmed.ncbi.nlm.nih.gov/11370136/).
19. Rad MM, Blaauw Y, Dinh T, et al. Left ventricular lead placement in the latest activated region guided by coronary venous electroanatomic mapping. *Europace.* 2015; 17(1): 84–93, doi: [10.1093/europace/euu221](https://doi.org/10.1093/europace/euu221), indexed in Pubmed: [25186457](https://pubmed.ncbi.nlm.nih.gov/25186457/).
20. Roberts W, Salandy S, Mandal G, et al. Across the centuries: piecing together the anatomy of the heart. *Transl Res Anat.* 2019; 17: 100051, doi: [10.1016/j.tria.2019.100051](https://doi.org/10.1016/j.tria.2019.100051).

21. Saremi F, Muresian H, Sánchez-Quintana D. Coronary veins: comprehensive CT-anatomic classification and review of variants and clinical implications. *Radiographics*. 2012; 32(1): E1–32, doi: [10.1148/rg.321115014](https://doi.org/10.1148/rg.321115014), indexed in Pubmed: [22236907](https://pubmed.ncbi.nlm.nih.gov/22236907/).
22. Shah SS, Teague SD, Lu JC, et al. Imaging of the coronary sinus: normal anatomy and congenital abnormalities. *Radiographics*. 2012; 32(4): 991–1008, doi: [10.1148/rg.324105220](https://doi.org/10.1148/rg.324105220), indexed in Pubmed: [22786990](https://pubmed.ncbi.nlm.nih.gov/22786990/).
23. Sinha M, Pandey NN, Sharma A. Anomalies of the coronary sinus and its tributaries: evaluation on multidetector computed tomography angiography. *J Thorac Imaging*. 2020; 35(2): W60–W67, doi: [10.1097/RTI.0000000000000456](https://doi.org/10.1097/RTI.0000000000000456), indexed in Pubmed: [31688460](https://pubmed.ncbi.nlm.nih.gov/31688460/).
24. Sirajuddin A, Chen MY, White CS, et al. Coronary venous anatomy and anomalies. *J Cardiovasc Comput Tomogr*. 2020; 14(1): 80–86, doi: [10.1016/j.jcct.2019.08.006](https://doi.org/10.1016/j.jcct.2019.08.006), indexed in Pubmed: [31444098](https://pubmed.ncbi.nlm.nih.gov/31444098/).
25. Sommer A, Kronborg MB, Nørgaard BL, et al. Left and right ventricular lead positions are imprecisely determined by fluoroscopy in cardiac resynchronization therapy: a comparison with cardiac computed tomography. *Europace*. 2014; 16(9): 1334–1341, doi: [10.1093/europace/euu056](https://doi.org/10.1093/europace/euu056), indexed in Pubmed: [24687965](https://pubmed.ncbi.nlm.nih.gov/24687965/).
26. von Lüdinghausen M. The venous drainage of the human myocardium. *Adv Anat Embryol Cell Biol*. 2003; 168: I–VIII, 1, doi: [10.1007/978-3-642-55623-4](https://doi.org/10.1007/978-3-642-55623-4), indexed in Pubmed: [12645157](https://pubmed.ncbi.nlm.nih.gov/12645157/).
27. von Lüdinghausen M. Clinical anatomy of cardiac veins, Vv. cardiaca. *Surg Radiol Anat*. 1987; 9(2): 159–168, doi: [10.1007/BF02086601](https://doi.org/10.1007/BF02086601), indexed in Pubmed: [3120334](https://pubmed.ncbi.nlm.nih.gov/3120334/).
28. Whiteman S, Saker E, Courant V, et al. An anatomical review of the left atrium. *Transl Res Anat*. 2019; 17: 100052, doi: [10.1016/j.tria.2019.100052](https://doi.org/10.1016/j.tria.2019.100052).
29. Wouters PC, van Everdingen WM, Vernooij K, et al. Does mechanical dyssynchrony in addition to QRS area ensure sustained response to cardiac resynchronization therapy? *Eur Heart J Cardiovasc Imaging*. 2022; 23(12): 1628–1635, doi: [10.1093/ehjci/jeab264](https://doi.org/10.1093/ehjci/jeab264), indexed in Pubmed: [34871385](https://pubmed.ncbi.nlm.nih.gov/34871385/).
30. Yaminisharif A, Davoodi G, Kazemisaeid A, et al. Characterization of suitability of coronary venous anatomy for targeting left ventricular lead placement in patients undergoing cardiac resynchronization therapy. *J Tehran Heart Cent*. 2012; 7(1): 10–14, indexed in Pubmed: [23074628](https://pubmed.ncbi.nlm.nih.gov/23074628/).
31. Żabówka A, Hołda J, Strona M, et al. Morphology of the Vieussens valve and its imaging in cardiac multislice computed tomography. *J Cardiovasc Electrophysiol*. 2019; 30(8): 1325–1329, doi: [10.1111/jce.14018](https://doi.org/10.1111/jce.14018), indexed in Pubmed: [31187551](https://pubmed.ncbi.nlm.nih.gov/31187551/).
32. Żabówka A, Jakiel M, Bolechała F, et al. Topography of the oblique vein of the left atrium (vein of Marshall). *Kardiol Pol*. 2020; 78(7-8): 688–693, doi: [10.33963/KP.15318](https://doi.org/10.33963/KP.15318), indexed in Pubmed: [32347083](https://pubmed.ncbi.nlm.nih.gov/32347083/).
33. Zhivadinovik J, Papazova M, Matveeva N, et al. Anatomy of coronary sinus ostium. *Folia Morphol*. 2016; 75(2): 264–267, doi: [10.5603/FM.a2015.0089](https://doi.org/10.5603/FM.a2015.0089), indexed in Pubmed: [26431050](https://pubmed.ncbi.nlm.nih.gov/26431050/).

Topographical anatomy of the left ventricular summit: implications for invasive procedures

M. Kuniewicz^{1,2} , M. Krupiński³ , M. Urbańczyk-Zawadzka³, M.K. Hołda^{4,5} ,
R. DeFonseka¹, T. Wadhwa¹, N. Cholewa¹, A. Matuszyk¹ , J. Walocha¹, H. Dobrzynski^{1,5}

¹Department of Anatomy, Jagiellonian University Medical College, Krakow, Poland

²Department of Electrophysiology, Institute of Cardiology, John Paul II Hospital, Jagiellonian University Medical College, Krakow, Poland

³Department of Radiology and Diagnostic Imaging, John Paul II Hospital, Krakow, Poland

⁴HEART — Heart Embryology and Anatomy Research Team, Department of Anatomy, Jagiellonian University Medical College, Krakow, Poland

⁵Division of Cardiovascular Sciences, The University of Manchester, United Kingdom

[Received: 7 September 2022; Accepted: 31 October 2022; Early publication date: 28 November 2022]

Background: Recent clinical reports have emphasized the clinical significance of the left ventricular summit (LVS), a specific triangular epicardial area, as the source of ventricular arrhythmias where radiofrequency ablation is of great difficulty.

Materials and methods: The macroscopic morphology of the LVS has been assessed in 80 autopsied and 48 angio-computed tomography (CT) human hearts. According to Yamada's equation, the size was calculated based on the distance to the first, most prominent septal perforator.

Results: The size of the LVS varies from 33.69 to 792.2 mm², is highly variable, and does not correlate with body mass index, sex, or age in general. The mean size of the LVS was 287.38 ± 144.95 mm² in autopsied and angio-CT ($p = 0.44$). LVS is mostly disproportionately bisected by cardiac coronary veins to superior-inaccessible and inferior-accessible areas. The superior aspect dominates over the inferior in both groups ($p = 0.04$). The relation between superior and inferior groups determines three possible arrangements: the most common type is superior domination (50.2%), then inferior domination (26.6%), and finally, equal distribution (17.2%). In 10.9%, the inferior aspect is absent. Only 16.4% of the LVS were empty, without additional trespassing coronary arteries.

Conclusions: The difference in size and content of the LVS is significant, with no correlation to any variable. The size depends on the anatomy of the most prominent septal perforator artery. The superior, inaccessible aspect dominates, and the LVS is seldom free from additional coronary vessels, thus making this region hazardous for electrophysiological procedures. (Folia Morphol 2023; 82, 2: 291–299)

Key words: left ventricular summit, septal summit, ventricular arrhythmias

INTRODUCTION

The left ventricular summit (LVS) is a triangular area located at the base of the left ventricle, at the

most superior portion of the left epicardial ventricular region. It comprises the apex, septal margin, mitral margin, and base [15, 17, 27]. Enclosed in the left

Address for correspondence: M. Kuniewicz, MD, PhD, Department of Anatomy, Jagiellonian University Medical College, ul. Kopernika 12, 31–034 Kraków, Poland, tel: +48 12 4229511, e-mail: kuniewicz@gmail.com

This article is available in open access under Creative Commons Attribution-Non-Commercial-No Derivatives 4.0 International (CC BY-NC-ND 4.0) license, allowing to download articles and share them with others as long as they credit the authors and the publisher, but without permission to change them in any way or use them commercially.

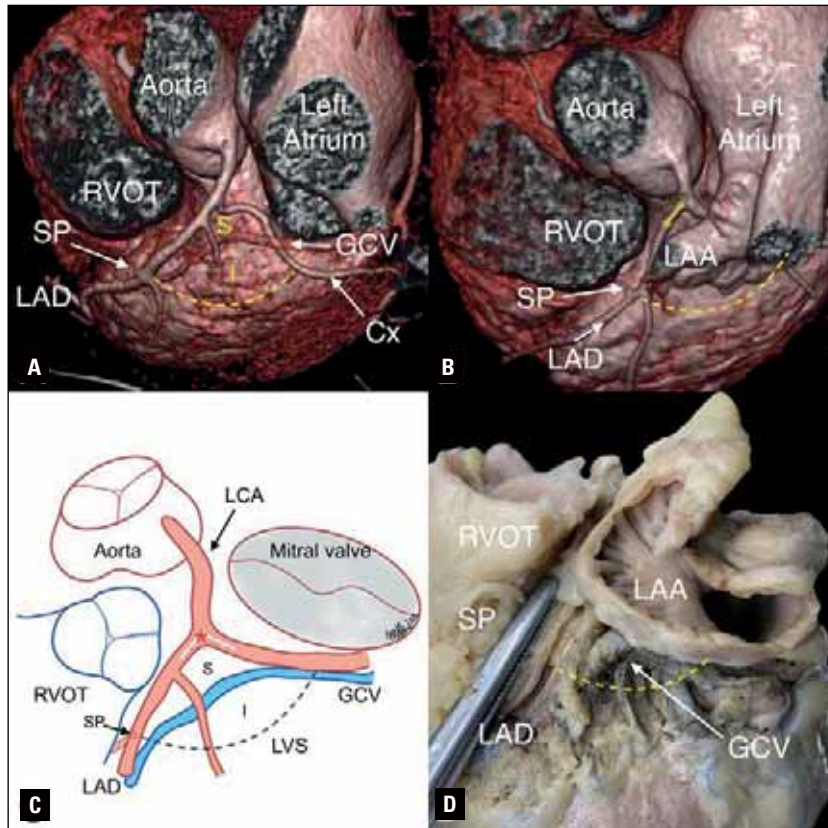


Figure 1. Left ventricular summit (LVS) — views from the lateral and superior aspects; **A.** Computed tomography (CT) rendered image showing the LVS region without overlapping left atrial appendage (LAA); **B.** Rendered CT image of the LVS region covered by LAA; **C.** Schematic picture of presented structures; red asterisks indicate the point of left coronary artery (LCA) bifurcation with arms of the angle; S — superior area of the LVS; I — inferior area; **D.** Cadaveric heart with LVS region covered by an open LAA. The yellow/blue dotted line delineates the inferior border of the LVS; Cx — circumflex artery; GCV — great cardiac vein; LAD — left anterior descending artery; LCA — left coronary artery; RVOT — right ventricular outflow tract; SP — septal perforator.

coronary artery bifurcation was firstly described by McAlpine in 1975 [21] and 35 years later revisited by Yamada because of the arrhythmic importance [14, 33]. Because of its location, this heart region is complex to approach for electrophysiology procedures, which is why it is also known as the Bermuda triangle [1]. The great cardiac vein divides the LVS into a superior area (named the inaccessible area) and an inferior area (named the accessible area) (Fig. 1A, C) [20, 30]. Epicardially, the LVS is overlapped by the left atrial appendage (LAA) covering more than 50% of the LVS area (Fig. 1B, D) [16, 18, 25].

There are various approaches to reaching arrhythmias arising from the LVS, but precise targeting of the arrhythmia source may be troublesome [4, 6]. Extensive epicardial area and delicate anatomical structures may complicate these approaches [33]. A detailed understanding of the anatomical structure of the LVS and surrounding structures may help in

planning and performing ablation procedures within this area. Therefore, this study aimed to analyse morphometrically the cadaveric heart specimens and angio-computed tomography (CT) images to provide a more detailed description of the LVS region.

MATERIALS AND METHODS

This study was approved by the Bioethical Committee of Jagiellonian University (1072.6120.131.2018) and the Hospital Scientific Board approval (NB.060.1.015.2021). The study protocol conformed to the ethical guidelines of the 1975 Declaration of Helsinki. The methods were carried out in accordance with the approved guidelines.

Study population

We examined 128 human hearts (88 male and 40 female) in two methods: autopsy and angio-CT examination.

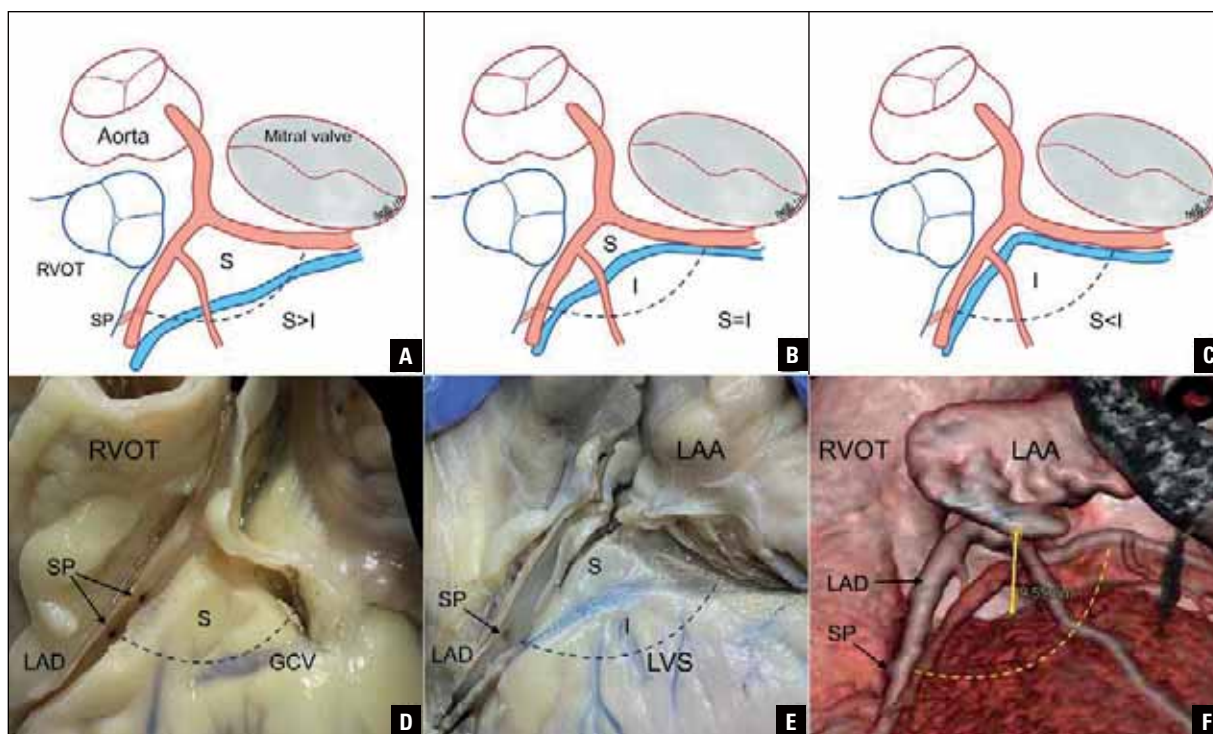


Figure 2. Left ventricular summit (LVS) schematic and study variations figures; **A.** Superior aspect dominance ($S>I$); **B.** Equipoise between superior and inferior aspect ($S=I$); **C.** Inferior aspect dominance ($S<I$); **D, E.** Cadaveric hearts studies complementary to panels A and B; **F.** Angio-computed tomography rendered image with compliance to panel C; GCV — great cardiac vein; I — inferior area; LAA — left atrium appendage; LAD — left anterior descending artery; RVOT — right ventricular outflow tract; S — superior area; SP — septal perforator; blue/yellow dotted line — delineates the inferior border of the LVS.

The first method analysed 80 randomly selected human cadaveric hearts (68 male and 12 female) dissected from donors who died of noncardiac causes. The organs were collected during routine forensic medical autopsies. All hearts were dissected from adults who were on average 44.4 ± 15.5 years old. The average body mass index (BMI) was 26.1 kg/m^2 , and the mean heart weight was $442.0 \pm 91.2 \text{ g}$. The leading causes of death of the studied subjects were suicide, murder, and traffic/home accidents. Donors with known severe anatomic defects, past cardiac surgeries/interventions, or vascular or cardiac pathologies discovered during the autopsy were excluded from this study.

Additionally, contrast-enhanced electrocardiogram-gated cardiac computed tomography scans from randomly selected 48 patients (20 male and 28 female) were evaluated. Cardiac computed tomography scans were performed for various clinical reasons in patients who were on average 57.9 ± 11.6 years old and with an average BMI of 28.1 kg/m^2 . Only patients with no severe anatomic heart defects and no past cardiac surgeries/interventions were included.

Cadaveric dissections

Hearts were dissected routinely and then placed in 10% paraformaldehyde solution for 2 months until further observations. Next, the anterior surface of the LVS was exposed by uplifting the LAA (Fig. 2D, E). The left coronary artery was open from the ostium to bifurcation and along the left anterior descending artery (LAD) to expose the septal perforators. The coronary sinus was cannulated with a haemodynamic guidewire, and the great cardiac/anterior interventricular cardiac vein was revealed from the epicardial adipose tissue. Then, measurements were collected with hearts held in their anatomical position using 0.03-mm precision electronic callipers (YATO, YT-7201, Poland).

Cardiac computed tomography protocol

The CT examinations were performed using a 64-row dual-source scanner (Somatom Definition, Siemens, Erlangen, Germany). The contrast-enhanced acquisitions were performed during inspiratory breath hold with the collimation of 0.75 mm. An iodinated contrast agent was injected with an injection rate of

5 mL/s [18]. Images were reconstructed with an image matrix of 512×512 pixels. The post-processing and study evaluation was performed using a dedicated workstation (Syngovia, Siemens, Erlangen, Germany). Analyses of coronary vessel course over the left ventricle were done by volume rendered reconstructions as well as sagittal, coronal, and transverse presentations. Virtual callipers were used to measure dimensions.

Observations and measurements

First, the left coronary artery bifurcation pattern was noted, and the angle of bifurcation was measured. Next, the course of the great cardiac/anterior interventricular cardiac vein was studied. The first dominant septal perforator was chosen to encircle the LVS area. The septal margin, mitral margin, and base were established. The following distances were measured: distance from the left coronary artery ostium to bifurcation and distance from bifurcation to the first dominant septal perforator (LVS margin) (Fig. 1C). Yamada's equation was used to calculate the LVS surface area by multiplying the bifurcation angle and distance to the septal perforator [18, 33]. Next, the surface area of the LVS superior region (named the inaccessible area) and an inferior region (named the accessible area) were calculated using Sketchandcalc® (iCalc Inc) computer software after precise calibration.

Statistical analysis

The results are presented as mean values with corresponding standard deviations or percentages. The Shapiro-Wilk test was used to determine if the quantitative data were normally distributed, and Levene's test was performed to verify a relative homogeneity of variance. A χ^2 test was used to evaluate the difference in dichotomous data. The t-test or Mann-Whitney was used to evaluate the differences in diameters, angles, and volumes between study groups. Statistical analyses were conducted using STATISTICA v13.3 software for Windows (StatSoft Inc., Tulsa, OK, USA). Results were considered statistically significant when the p-value was less than 0.05.

RESULTS

The mean size of the LVS combined in cadaveric and CT reached 287.38 ± 144.95 mm². For autopsied hearts 270.46 ± 160.21 mm² (33.69–792.2 mm²), for CT 291.58 ± 115.5 mm² (Table 1). No statistical differentiation was found between both study groups

($p = 0.44$). The superior aspect of the LVS, with 145.62 ± 84.35 mm² (6.74–429.12 mm²), outperforms the inferior aspect, 121.69 ± 94.38 mm² (8.96–431.13 mm²). In 13 hearts, 6 (7.5%) cadaveric and 7 (14.6%) CT, there was no inferior aspect (Fig. 2D). Statistically, the superior aspect is notably more extensive than the inferior ($p = 0.04$); however, no difference was found between both study groups ($p = 0.18$ for the superior and $p = 0.35$ for the inferior aspect).

Analysing the LVS size to gender — the female summit size of 244.71 ± 119.92 mm² was significantly smaller than the male 293.68 ± 152.3 mm² ($p = 0.05$). Also, in the female subgroup, the inferior aspect is significantly smaller than in the male ($p < 0.01$), while no difference was found between superior aspects to the male gender ($p = 0.07$). Providing a Pearson coefficient, we have found a mailed correlation of the LVS calculations to BMI in the female group ($r = 0.32$, $p = 0.18$), while in men, not ($r = 0.03$, $p = 0.92$). Detailed data are shown in Table 2.

Analysing a combination of the superior to inferior aspects, we determined three main types of LVS. With superior aspect domination, equal distribution, and inferior aspect domination. We established no more than 10% of the difference between the areas as equal distribution. The most common pattern of the LVS (50.2%) is the dominance of the superior aspect (Fig. 2A, D). In 26.6% of the hearts, the inferior aspect dominates (Fig. 2C, F), while in 17.2% of the hearts, the superior and inferior aspects are equipoise (Fig. 2B, E). Analysing the subgroups, the distribution between studies and genders was similar.

The second exciting observation was coronary vessel distribution inside LVS. Only 21 (16.4%) hearts were out of additional coronary branches. Majority of summits contain at least 1 (51%), 2 (32%) to 3 (17%) additional vessels trespassing LVS. We found almost equal distribution from the LAD and circumflex branch of the left coronary artery. In 30 (23.4%) hearts, the LVS contains ramus intermedius exiting directly from the trunk of the left coronary artery. More often, female LVS were freer from additional coronary artery branches than males ($p = 0.02$) (Table 2).

The venous distribution draining into great cardiac vein-anterior interventricular vein (GCV-AIV) from the inferior aspect, known as anterior cardiac veins, and tiny veins draining into the right atrium from the superior was not analysed because of lack of visualization in the CT. In 17 (21.3%) cadaveric hearts, we noticed the conus vein connecting the great cardiac

Table 1 Morphometric characteristics of the left ventricular summit (LVS) in cadaveric (n = 80) and computed tomography (CT) (n = 48) samples

Parameter [number form Fig. 1C]	Combined data	Cadaveric (n = 80)	Angio-CT (n = 48)	P-value
LCA ostium bifurcation [mm] (min-max)	9.59 ± 4.14 (1.61–21.6)	9.02 ± 4.04 (1.61–21.6)	10.54 ± 4.18 (3–21)	0.05
LAD bifurcation – SP [mm] (min-max)	18.92 ± 5.19 (7.25–33.08)	18.2 ± 5.55 (7.25–33.08)	20.06 ± 4.47 (10–28)	0.05
Angle of LCA bifurcation [°] (min-max)	85.46 ± 15.94 (48–125)	87.41 ± 13.61 (55–124)	82.21 ± 18.91 (48–125)	0.09
LVS from formula [mm ²] (min-max)	287.38 ± 144.95 (33.69–792.2)	270.46 ± 160.21 (33.69–792.2)	291.58 ± 115.5 (91.58–556.04)	0.44
LVS superior aspect [mm ²] (min-max)	145.62 ± 84.35 (6.74–429.12)	152.92 ± 90.19 (6.74–429.12)	133.42 ± 72.89 (39.11–322.8)	0.18
LVS inferior aspect [mm ²] (min-max)	121.69 ± 94.38 (8.96–431.13) (n = 13 [10.9%] with no inferior aspect)	127.07 ± 106.98 (19.29–431.13) (n = 6 [7.5%] with no inferior aspect)	112.01 ± 65.72 (8.96–253.78) (n = 7 [14.6%] with no inferior aspect)	0.20
LVS distribution — superior to inferior relation [%]*	Superior > Inferior 59/115 [50.2%] Superior < Inferior 34/115 [26.6%] Superior = Inferior 22/115 [17.2%]	Superior > Inferior 39/74 [52.7%] Superior < Inferior 20/74 [27%] Superior = Inferior 15/74 [20.3%]	Superior > Inferior 20/41 [48.8%] Superior < Inferior 14/41 [34.1%] Superior = Inferior 7/41 [17.1%]	0.69 0.43 0.68
Coronary vessels trespassing through LVS	RI [30] Dx1 [58]	RI [16] Dx1 [44]	RI [14] Dx1 [14]	0.23 0.03
Parity of distribution [n] — number of coronary branches**	Dx2 [9] Mg1 [53] Mg2 [3]	Dx2 [6] Mg1 [33] Mg2 [3]	Dx2 [3] Mg1 [20] Mg2 [0]	0.96
	LAD > Cx 32/107 [29.9%] LAD < Cx 35/107 [32.7%] LAD = Cx 40/107 [37.4%]	LAD > Cx 24/71 [33.8%] LAD < Cx 22/71 [31%] LAD = Cx 25/71 [35.2%]	LAD > Cx 8/36 [22.2%] LAD < Cx 13/36 [36.1%] LAD = Cx 15/36 [41.7%]	0.22 0.59 0.51
Blank LVS***	N = 21/128 16.4%	N = 9/80 11.25%	N = 12/48 25%	0.04
Type of LAA overlapping LVS	C: 44 (33.4%) CW: 41 (32%) AH: 43 (33.6%)	C: 28 (35%) CW: 23 (28.7%) AH: 29 (26.3%)	C: 16 (33.3%) CW: 18 (47.5%) AH: 14 (29.2%)	0.85 0.3 0.41
LVS to LAA distance [mm] (min-max)	5.45 ± 2.51 (1.5–12.2)	6.3 ± 2.55 (2.8–12.2)	5.14 ± 2.47 (1.5–10)	0.04

*from evaluation of the LVS, pattern samples without inferior area have been excluded. **from evaluation of the LVS pattern samples without additional coronary branches have been excluded; ***without coronary vessels; AH — arrowhead; C — cauliflower; CW — chicken wing; Cx — circumflex branch; Dx — diagonal branch; Mg — marginal branch; LAA — left atrial appendage; LCA — left coronary artery; LAD — left anterior descending; SP — septal perforator; RI — ramus intermedius

Table 2. Morphometric characteristics of the left ventricular summit (LVS) in female (n = 40) and male (n = 88) samples

Parameter	Combined data	Female (n = 40)	Male (n = 88)	P-value
LVS from formula [mm ²] (min-max)	287.38 ± 144.95	244.71 ± 119.92	293.68 ± 152.3	0.05
LVS superior aspect [mm ²] (min-max)	145.62 ± 84.35	127.8 ± 67.16	153.71 ± 89.78	0.07
LVS inferior aspect [mm ²] (min-max)	121.69 ± 94.38 (n = 13 [10.9%] with no inferior aspect)	81.58 ± 55.61 (n = 6 [7.5%] with no inferior aspect)	138.53 ± 101.57 (n = 7 [14.6%] with no inferior aspect)	< 0.01 0.3
LVS distribution — superior to inferior relation [%]*	Superior > Inferior 59/115 [50.2%] Superior < Inferior 34/115 [26.6%] Superior = Inferior 22/115 [17.2%]	Superior > Inferior 20/34 [58.8%] Superior < Inferior 7/34 [20.6%] Superior = Inferior 7/34 [20.6%]	Superior > Inferior 39/81 [48.2%] Superior < Inferior 27/81 [33.3%] Superior = Inferior 15/81 [18.5%]	0.3 0.17 0.8
Blank LVS**	N = 21/128 16.4%	N = 11/40 27.5%	N = 10/88 11.4%	0.02
LVS to LAA distance [mm]	5.45 ± 2.51	5.92 ± 2.6	5.11 ± 2.04	0.05

*from evaluation of the LVS pattern samples without inferior area has been excluded; **without coronary vessels abbreviations; LAA — left atrial appendage

vein and the right atrium below the trunk of the left coronary artery.

The LAA over LVS has been morphologically assessed based on a new simplified shape-based classification [11, 28]. The morphology in cadaveric/CT samples was cauliflower 28/16 (34.4%), then chicken wing 23/18 (32%), and arrowhead 29/14 (33.6%) with no statistical difference in distribution. The average distance between the LAA to the LVS surface was 5.45 ± 2.51 mm, in subgroups 6.3 ± 2.55 mm (2.8–12.2 mm) for cadaveric and 5.14 ± 2.47 mm (1.4–10 mm) for CT samples (Fig. 2F). The distance difference between methods was statistically significant ($p = 0.04$). Notably, the distance in the female group was greater, reaching 5.92 ± 2.6 mm vs. 5.11 ± 2.04 mm in male hearts ($p = 0.05$).

Interestingly almost all measurements of the LVS from cadaveric dissections are not statistically different from those from angio-CT (Table 1). However, the differences in the vessel's calculations differ in both methods. The mean length of the main trunk of the left coronary artery in the cadaveric heart was 9.02 ± 4.04 mm and is shorter than the CT control group 10.54 ± 4.18 mm ($p = 0.05$). Same with the septal perforator, 18.2 ± 5.55 mm vs. 20.06 ± 4.47 mm ($p = 0.05$).

DISCUSSION

The LVS is not a relatively small region, reminding a minefield because of its content. In this study, we conducted two approaches for a macroscopic morphology assessment of the LVS using cadaveric hearts and CT images of the beating hearts. The general anatomy of LVS is established; nevertheless, precise measurements and calculations have not been provided yet. The size of the LVS varies from 33.69 to 792.2 mm² and does not correlate with BMI, sex, or age in general; however, a mild correlation with BMI was noticed in the female group ($r = 0.32$, $p = 0.18$). Its size depends on the random exit of the first dominant septal perforator and the angle of bifurcation of the left coronary artery [13, 21, 33].

The LVS, divided by a great cardiac vein, comprises superior and inferior aspects. In 10.9%, an unusual combination of the septal perforator exit with the course of GCV-AIV may abolish an inferior aspect (Fig. 2D). Other almost 90% of the LVS are arranged into three patterns. With superior aspect domination at 50.2%, inferior aspect domination at 26.6%, and equal distribution of aspects at 17.2%. The inferior aspect is significantly smaller than the superior ($p = 0.01$).

In the female subgroup, the difference between areas is even more significant ($p < 0.001$).

The content of the LVS with additional coronary branches (diagonal or marginal) trespassing through is also variable. Only 11% (cadaveric) and 25% (CT) of the LVS were without additional accessory coronary arteries. The percentage of blank LVS is higher in the female group ($p = 0.02$), reaching almost 30% possibly, because of smaller area defined. The distribution of trespassing coronary vessels is equal from the left anterior descending and circumflex branch from the left coronary artery. More than 50% of the LVS contain at least one additional coronary artery, while 17% contain three branches, thus making this region hazardous for potential arterial dissection during epicardial or intravenous cardiology procedures.

From this perspective, coronarography is inevitable before arrhythmia abolishing [29]. The venous system intersects coronary vessels more often deeply than superficially in a 3/4 to 1/4 ratio, respectively (Fig. 1A, D). The relationships between the GCV-AIV and the coronary arteries in the LVS region were noticed before [5, 8, 20, 30].

An interesting observation was found in counting branches exiting from the LAD. More first diagonal branches were found during cadaveric dissections than in CT image analysis ($p = 0.03$). Counting arterial branches from open, dissected LAD in cadaveric hearts is far more precise than angio-CT acquisition.

Because the LVS is not a small structure and may reach almost 8 cm², a precise electro-anatomical mapping is necessary where ventricular arrhythmia has the earliest activation [2, 3]. The transcatheter approach is limited by transmural mapping via ventricular outflow tracts, pulmonary trunk, aorta, or coronary sinus. That is why the LVS located between them is known as the Bermuda triangle [1]. The epicardial approach (through the pericardial sac) allows mapping only inferior-accessible areas. Recently proposed access via the LAA is promising; however, on average, only half of the LVS is covered by this structure [15, 16]. Another critical issue is that variability of morphology and distance between the LAA, and the surface of the LVS (1.5–12.5 mm) may impede successful arrhythmia localization and annihilation [24]. In this study, the most common type of LAA overlapping the LVS was Arrowhead (33.6%), followed by Cauliflower (33.4%) and ChickenWing (32%), with almost equal distribution without statistical significance between the type of the study.

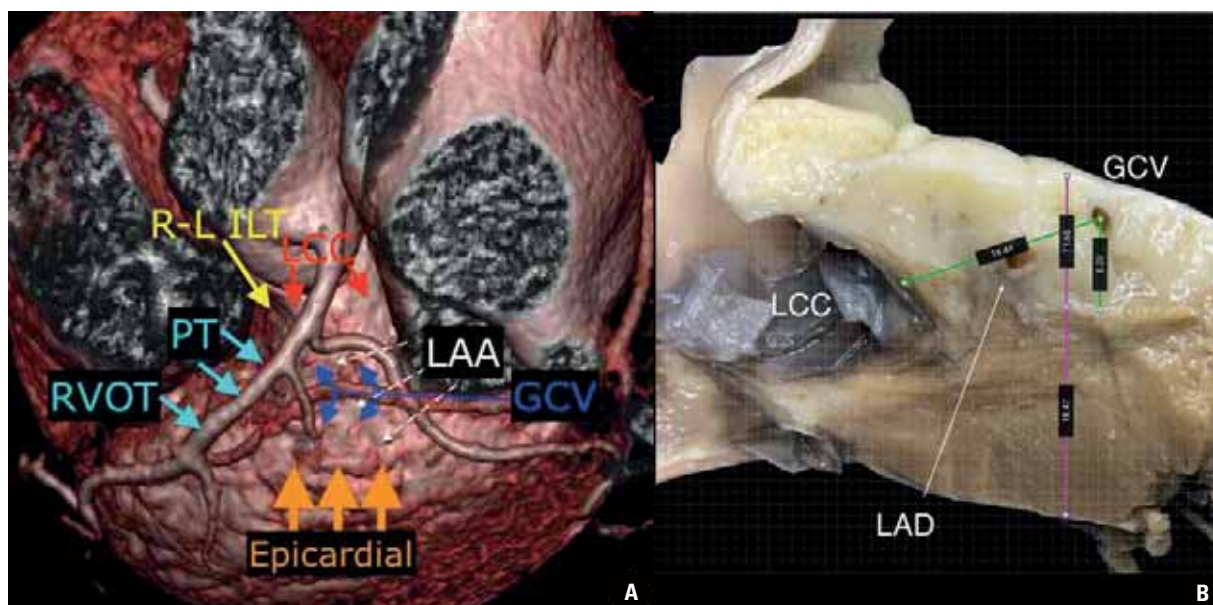


Figure 3. A. Angio-computed tomography rendered image with suggested approach to the certain left ventricular summit (LVS) regions, follow the description in the text; **B.** Cut through the LVS from right-left interleaflet trigon (R-L ILT) through the LVS; GCV — great cardiac vein; LAA — left atrium appendage; LAD — left anterior descending artery; LCC — aortic left coronary cusp; PT — pulmonary trunk; RVOT — right ventricular outflow tract.

Implication for electrophysiology procedures

The ventricular arrhythmias arising from the LVS apex or septal summit are capable from the left coronary cusp (Fig. 3A, red arrows) of the aortic valve or right-left inter leaflet triangle (Fig. 3A, yellow arrow) [4, 17, 19]. The lower septal summit arrhythmias or located on the right aspect of the LVS are reachable from the right ventricular outflow tract, the right coronary cusp of the pulmonic valve, pulmonary trunk, or even pulmonary artery (Fig. 3A, light blue arrow) [14]. The left margin is accessible from LAA (Fig. 3A, white arrows) or coronary venous system (Fig. 3A, dark blue arrow) [16, 31, 32]. A central aspect of the LVS is attainable from the venous system or LAA [11, 12, 16, 18, 22]. Hence the possible approach from the venous system (via a great cardiac vein) might be promising but also challenging because of the cardiac venous system's complex anatomy [5, 10, 23].

Arrhythmias located in the LVS need to be mapped from a different approach. Once the location is established, the most adjacent structure must be used for radiofrequency (RF) application. If necessary, a bipolar with double RF applicators should be on the course of the arrhythmia.

Approach from the endocardial region of the left ventricle is impossible because of the heart muscle thickness (Fig. 3B) unless using a bipolar radiofrequency catheter ablation (RFCA) [7].

The direct approach to the LVS provides access through the pericardial sac (Fig. 3A, orange arrows) and may abolish only arrhythmias located in the inferior aspect of the LVS. A critical remark is that access to the pericardial sac with a substernal approach is possible only among patients without previous open chest surgery [9, 26].

Limitations of the study

The first limitation was the difference in methods used to compare the size of the LVS. Beating hearts in a biological environment have different spaces between the LAA and the surface of the ventricle. The thickness of the epicardial adipose tissue and the heart muscle also in post-mortem studies were greater.

Choosing the proper septal perforator in a post-mortem study was troublesome. While in the CT study, the perforator looks like a single vessel, in cadaveric sections, we observe not one but two or even three septal perforators at a close distance (Fig. 2D). We acknowledge that the most apparent size will set the inferior border of the LVS. The same problem was with depicting diagonal branches in cadaveric specimens. We found statistically more branches in the post-mortem study than in the angio-CT images. We acknowledge that the angio-CT acquisition can depict the minimum 1 mm size vessels, smaller

septal perforators visible in cadaveric samples, and small additional coronary branches may differ in the calculations.

CONCLUSIONS

This study provided a comprehensive anatomical description of the LVS region. The rapid development of RFCA procedures requires a better understanding of access, distance, diameter, and potential risks of the LVS to terminate arrhythmias. We found that the LVS region is a highly variable anatomical structure. We claim that the most dominant septal perforator in the proximal aspect of LAD (comparing the CT hearts and postmortem) should represent the LVS definition. The LVS is seldom an empty structure and in 90% of the hearts investigated consists of additional coronary vessels with a variable origin. Therefore, each ablation procedure in this region should have a coronarography before RFCA.

Conflict of interest: None declared

REFERENCES

1. Altmann DR, Knecht S, Sticherling C, et al. Ventricular tachycardia originating from the "Bermuda Triangle". *Cardiovascular Medicine*. 2013; 16(0708): 208–210, doi: [10.4414/cvm.2013.00170](https://doi.org/10.4414/cvm.2013.00170).
2. Anderson RH, Boyett MR, Dobrzynski H, et al. The anatomy of the conduction system: implications for the clinical cardiologist. *J Cardiovasc Transl Res*. 2013; 6(2): 187–196, doi: [10.1007/s12265-012-9433-0](https://doi.org/10.1007/s12265-012-9433-0), indexed in Pubmed: [23242580](https://pubmed.ncbi.nlm.nih.gov/23242580/).
3. Daniels DV, Lu YY, Morton JB, et al. Idiopathic epicardial left ventricular tachycardia originating remote from the sinus of Valsalva: electrophysiological characteristics, catheter ablation, and identification from the 12-lead electrocardiogram. *Circulation*. 2006; 113(13): 1659–1666, doi: [10.1161/CIRCULATIONAHA.105.611640](https://doi.org/10.1161/CIRCULATIONAHA.105.611640), indexed in Pubmed: [16567566](https://pubmed.ncbi.nlm.nih.gov/16567566/).
4. Enriquez A, Malavassi F, Saenz LC, et al. How to map and ablate left ventricular summit arrhythmias. *Heart Rhythm*. 2017; 14(1): 141–148, doi: [10.1016/j.hrthm.2016.09.018](https://doi.org/10.1016/j.hrthm.2016.09.018), indexed in Pubmed: [27664373](https://pubmed.ncbi.nlm.nih.gov/27664373/).
5. Gach-Kuniewicz B, Goncerz G, Ali D, et al. Variations of coronary sinus tributaries among patients undergoing cardiac resynchronization therapy. *Folia Morphol*. 2022 [Epub ahead of print], doi: [10.5603/FM.a2022.0044](https://doi.org/10.5603/FM.a2022.0044), indexed in Pubmed: [35607878](https://pubmed.ncbi.nlm.nih.gov/35607878/).
6. Hayashi T, Santangeli P, Pathak RK, et al. Outcomes of catheter ablation of idiopathic outflow tract ventricular arrhythmias with an R wave pattern break in lead V2: a distinct clinical entity. *J Cardiovasc Electrophysiol*. 2017; 28(5): 504–514, doi: [10.1111/jce.13183](https://doi.org/10.1111/jce.13183), indexed in Pubmed: [28233951](https://pubmed.ncbi.nlm.nih.gov/28233951/).
7. Igarashi M, Nogami A, Fukamizu S, et al. Acute and long-term results of bipolar radiofrequency catheter ablation of refractory ventricular arrhythmias of deep intramural origin. *Heart Rhythm*. 2020; 17(9): 1500–1507, doi: [10.1016/j.hrthm.2020.04.028](https://doi.org/10.1016/j.hrthm.2020.04.028), indexed in Pubmed: [32353585](https://pubmed.ncbi.nlm.nih.gov/32353585/).
8. Ishizawa A, Fumon M, Zhou M, et al. Intersection patterns of human coronary veins and arteries. *Anat Sci Int*. 2008; 83(1): 26–30, doi: [10.1111/j.1447-073X.2007.00200.x](https://doi.org/10.1111/j.1447-073X.2007.00200.x), indexed in Pubmed: [18402085](https://pubmed.ncbi.nlm.nih.gov/18402085/).
9. Aly I, Rizvi A, Roberts W, et al. Cardiac ultrasound: an anatomical and clinical review. *Transl Res Anat*. 2021; 22: 100083, doi: [10.1016/j.tria.2020.100083](https://doi.org/10.1016/j.tria.2020.100083).
10. Ito S, Tada H, Naito S, et al. Development and validation of an ECG algorithm for identifying the optimal ablation site for idiopathic ventricular outflow tract tachycardia. *J Cardiovasc Electrophysiol*. 2003; 14(12): 1280–1286, doi: [10.1046/j.1540-8167.2003.03211.x](https://doi.org/10.1046/j.1540-8167.2003.03211.x), indexed in Pubmed: [14678101](https://pubmed.ncbi.nlm.nih.gov/14678101/).
11. Kimura T, Takatsuki S, Inagawa K, et al. Anatomical characteristics of the left atrial appendage in cardiogenic stroke with low CHADS2 scores. *Heart Rhythm*. 2013; 10(6): 921–925, doi: [10.1016/j.hrthm.2013.01.036](https://doi.org/10.1016/j.hrthm.2013.01.036), indexed in Pubmed: [23384894](https://pubmed.ncbi.nlm.nih.gov/23384894/).
12. Komatsu Y, Nogami A, Shinoda Y, et al. Idiopathic ventricular arrhythmias originating from the vicinity of the communicating vein of cardiac venous systems at the left ventricular summit. *Circ Arrhythm Electrophysiol*. 2018; 11(1): e005386, doi: [10.1161/CIRCEP.117.005386](https://doi.org/10.1161/CIRCEP.117.005386), indexed in Pubmed: [29326128](https://pubmed.ncbi.nlm.nih.gov/29326128/).
13. Kosiński A, Grzybiak M, Skwarek M, et al. Distribution of muscular bridges in the adult human heart. *Folia Morphol*. 2004; 63(4): 491–498, indexed in Pubmed: [15712149](https://pubmed.ncbi.nlm.nih.gov/15712149/).
14. Kumagai K. Idiopathic ventricular arrhythmias arising from the left ventricular outflow tract: Tips and tricks. *J Arrhythmia*. 2014; 30(4): 211–221, doi: [10.1016/j.joa.2014.03.002](https://doi.org/10.1016/j.joa.2014.03.002).
15. Kuniewicz M, Baszko A, Ali D, et al. Left ventricular summit-concept, anatomical structure and clinical significance. *Diagnostics (Basel)*. 2021; 11(8), doi: [10.3390/diagnostics11081423](https://doi.org/10.3390/diagnostics11081423), indexed in Pubmed: [34441357](https://pubmed.ncbi.nlm.nih.gov/34441357/).
16. Kuniewicz M, Budnicka K, Dusza M, et al. Gross anatomic relationship between the human left atrial appendage and the left ventricular summit region: implications for catheter ablation of ventricular arrhythmias originating from the left ventricular summit. *J Interv Card Electrophysiol*. 2023; 66(2): 301–310, doi: [10.1007/s10840-022-01172-6](https://doi.org/10.1007/s10840-022-01172-6), indexed in Pubmed: [35262858](https://pubmed.ncbi.nlm.nih.gov/35262858/).
17. Kuniewicz M, Dobrzyński H, Karkowski G, et al. Septal summit: A narrow epicardial region above the left ventricular summit. Implications for electrophysiological procedures. *Kardiol Pol*. 2022; 80(7-8): 849–852, doi: [10.33963/KP.a2022.0170](https://doi.org/10.33963/KP.a2022.0170), indexed in Pubmed: [35851465](https://pubmed.ncbi.nlm.nih.gov/35851465/).
18. Kuniewicz M, Krupiński M, Gosnell M, et al. Applicability of computed tomography preoperative assessment of the LAA in LV summit ablations. *J Interv Card Electrophysiol*. 2021; 61(2): 357–363, doi: [10.1007/s10840-020-00817-8](https://doi.org/10.1007/s10840-020-00817-8), indexed in Pubmed: [32666410](https://pubmed.ncbi.nlm.nih.gov/32666410/).
19. Liao H, Wei W, Tanager KS, et al. Left ventricular summit arrhythmias with an abrupt V transition: Anatomy of the aortic interleaflet triangle vantage point. *Heart Rhythm*. 2021; 18(1): 10–19, doi: [10.1016/j.hrthm.2020.07.021](https://doi.org/10.1016/j.hrthm.2020.07.021), indexed in Pubmed: [32707175](https://pubmed.ncbi.nlm.nih.gov/32707175/).

20. Mazur M, Hołda M, Koziej M, et al. Morphology of tributaries of coronary sinus in humans - corrosion casting study. *Folia Med Cracov.* 2015; 55(2): 5–13, indexed in Pubmed: [26839238](#).
21. McAlpine WA. *Heart and coronary arteries.* Springer-Verlag, New York, NY 1975.
22. Obel OA, d'Avila A, Neuzil P, et al. Ablation of left ventricular epicardial outflow tract tachycardia from the distal great cardiac vein. *J Am Coll Cardiol.* 2006; 48(9): 1813–1817, doi: [10.1016/j.jacc.2006.06.006](#), indexed in Pubmed: [17084255](#).
23. Pejkovic B, Bogdanovic D. The great cardiac vein. *Surg Radiol Anat.* 1992; 14(1): 23–28, doi: [10.1007/BF01628039](#), indexed in Pubmed: [1589843](#).
24. Petersen HH, Chen X, Pietersen A, et al. Temperature-controlled irrigated tip radiofrequency catheter ablation: comparison of in vivo and in vitro lesion dimensions for standard catheter and irrigated tip catheter with minimal infusion rate. *J Cardiovasc Electrophysiol.* 1998; 9(4): 409–414, doi: [10.1111/j.1540-8167.1998.tb00928.x](#), indexed in Pubmed: [9581956](#).
25. Sacher F, Roberts-Thomson K, Maury P, et al. Epicardial ventricular tachycardia ablation a multicenter safety study. *J Am Coll Cardiol.* 2010; 55(21): 2366–2372, doi: [10.1016/j.jacc.2009.10.084](#), indexed in Pubmed: [20488308](#).
26. Santangeli P, Marchlinski FE, Zado ES, et al. Percutaneous epicardial ablation of ventricular arrhythmias arising from the left ventricular summit: outcomes and electrocardiogram correlates of success. *Circ Arrhythm Electrophysiol.* 2015; 8(2): 337–343, doi: [10.1161/CIRCEP.114.002377](#), indexed in Pubmed: [25637596](#).
27. Whiteman S, Alimi Y, Carrasco M, et al. Anatomy of the cardiac chambers: A review of the left ventricle. *Transl Res Anat.* 2021; 23: 100095, doi: [10.1016/j.tria.2020.100095](#).
28. Słodowska K, Szczepanek E, Dudkiewicz D, et al. Morphology of the left atrial appendage: introduction of a new simplified shape-based classification system. *Heart Lung Circ.* 2021; 30(7): 1014–1022, doi: [10.1016/j.hlc.2020.12.006](#), indexed in Pubmed: [33582020](#).
29. Topaz O, DiSciascio G, Vetrovec GW. Septal perforator arteries: from angiographic-morphologic characteristics to related revascularization options. *Am Heart J.* 1992; 124(3): 810–815, doi: [10.1016/0002-8703\(92\)90304-e](#), indexed in Pubmed: [1514521](#).
30. von Lüdinghausen M. The venous drainage of the human myocardium. *Adv Anat Embryol Cell Biol.* 2003; 168: I–VIII, 1, doi: [10.1007/978-3-642-55623-4](#), indexed in Pubmed: [12645157](#).
31. Wang Y, Di Biase L, Horton RP, et al. Left atrial appendage studied by computed tomography to help planning for appendage closure device placement. *J Cardiovasc Electrophysiol.* 2010; 21(9): 973–982, doi: [10.1111/j.1540-8167.2010.01814.x](#), indexed in Pubmed: [20550614](#).
32. Whiteman S, Saker E, Courant V, et al. An anatomical review of the left atrium. *Transl Res Anat.* 2019; 17: 100052, doi: [10.1016/j.tria.2019.100052](#).
33. Yamada T, McElderry HT, Doppalapudi H, et al. Idiopathic ventricular arrhythmias originating from the left ventricular summit: anatomic concepts relevant to ablation. *Circ Arrhythm Electrophysiol.* 2010; 3(6): 616–623, doi: [10.1161/CIRCEP.110.939744](#), indexed in Pubmed: [20855374](#).

Congenital venous anomalies associated with retrocaval ureter: evaluation using computed tomography

T. Ichikawa¹, S. Ono¹, Y. Nagafuji², M. Kobayashi³, H. Yashiro³, J. Koizumi⁴, F. Uchiyama², Y. Fujii⁵, T. Hasebe⁶, H. Terayama⁷ , J. Hashimoto¹

¹Department of Radiology, Tokai University School of Medicine, Isehara-si, Japan

²Department of Radiology, Ebina General Hospital, Ebina, Japan

³Department of Radiology, Hirastuka City Hospital, Kanagawa, Japan

⁴Department of Radiology, Chiba University, Chiba, Japan

⁵Department of Radiology, Fujisawa City Hospital, Kanagawa, Japan

⁶Department of Radiology, Tokai University Hachioji Hospital, Tokyo, Japan

⁷Department of Anatomy, Tokai University School of Medicine, Kanagawa, Japan

[Received: 1 February 2022; Accepted: 7 March 2022; Early publication date: 5 April 2022]

Background: Retrocaval ureter is a rare congenital anomaly resulting from anomalous development of inferior vena cava (IVC) and not from anomalous of the ureter. The anomaly always occurs on the right side due to regression of right supracardinal vein and persistence of right posterior cardinal vein. Retrocaval ureter tends to be associated with various vena cava anomalies because of the embryogenesis. We aimed to identify the prevalence of associated congenital venous anomalies (CVA) resulting from cardinal vein development in adults with retrocaval ureter using computed tomography (CT) images.

Materials and methods: The study included 22 adults with retrocaval ureter. We evaluated CT findings and determined the incidence of associated CVA using thin slice data sets from CT scanner with 64 or more detectors. We compared the prevalence of CVA in the retrocaval ureter group (mean age: 57 ± 19 years) and in the control group of 6189 adults with normal ureter (mean age: 66 ± 14 years).

Results: In the retrocaval ureter group, 4 (18.2%) adults had CVA including double IVC, right double IVC, preisthmic IVC with horseshoe kidney, and preaortic iliac confluence. One of 2 adults with preaortic iliac confluence had right double right IVC. In the control group, 49 (0.79%) adults had CVA including 37 double IVC, 11 left IVC, and 1 IVC interruption azygos continuation. Fifteen horseshoe kidneys were found. The prevalence of associated CVA in the retrocaval ureter group was higher than that in the control group ($p < 0.001$).

Conclusions: Retrocaval ureter is frequently associated with CVA. Various CVA with retrocaval ureter could happen because of abnormal development of not only the right posterior or supra cardinal vein but also other cardinal veins. (Folia Morphol 2023; 82, 2: 300–306)

Key words: retrocaval ureter, vena cava, congenital venous anomaly

Address for correspondence: Dr. T. Ichikawa, Department of Radiology, Tokai University School of Medicine, 143 Shimokasuya, Isehara, Kanagawa, 259-1193, Japan, tel: 81-463-93-1121, fax: 81-463-93-6827, e-mail: tamaki-i@is.icc.u-tokai.ac.jp

This article is available in open access under Creative Common Attribution-Non-Commercial-No Derivatives 4.0 International (CC BY-NC-ND 4.0) license, allowing to download articles and share them with others as long as they credit the authors and the publisher, but without permission to change them in any way or use them commercially.

INTRODUCTION

Retrocaval ureter, also known as circumcaval ureter, or preureteral vena cava, is a congenital condition characterised by the persistence of the posterior cardinal vein on the right, which causes the proximal ureter to deviate medially, behind the inferior vena cava (IVC), before resuming its natural course anteriorly and laterally [1, 9, 13, 14, 17]. Many authors prefer using the term “preureteral vena cava”, as the cause of this variant is IVC developmental abnormality, and not a ureteral one [9, 13–16, 21]. The prevalence of retrocaval ureter was reported as 0.06–0.27% and the overall prevalence was 0.13% [2, 14]. Males are affected by retrocaval ureter about 3 times more often than females [2, 4]. Bateson and Atkinson distinguished two types of retrocaval ureters: type 1 of low loop (S or ‘fish-hook’ deformity), in which the ureter crosses behind the IVC at the level of the L3 vertebra, and type 2 of high loop (sickle-shaped deformity), in which the renal pelvis and the upper ureter lie horizontally [2]. The low loop type is more common than the high loop type and has a moderate or severe hydronephrosis [2]. From a clinical standpoint, many cases of retrocaval ureter are asymptomatic, and only detected incidentally using imaging techniques [9, 13, 16]. Computed tomography (CT) elegantly depicts the abnormal course of the ureter [13]. When present, the symptoms are usually abdominal pain and haematuria due to ureteral obstruction or urinary infection [1, 2, 13, 16, 26]. Retrocaval ureter has been associated with other local or general congenital abnormalities including horseshoe kidney, right double IVC, contralateral kidney agenesis, preaortic venous confluence [1–3, 7, 9–16, 20, 21, 23, 27, 30]. The associations are related to the development of cardinal veins. A review of the literature by Perimenis et al. [20] revealed that 21% of the cases of retrocaval ureter present with concomitant abnormalities mainly from the cardiovascular system and the genitourinary tract. There are many case reports about congenital association; however, the prevalence of the associated congenital venous anomalies (CVA) and clinical features were not evaluated in case series. The purpose of this article was to identify the prevalence of the associated CVA in patients with retrocaval ureter using CT data, and to emphasize its clinical importance.

MATERIALS AND METHODS

The institutional ethics committee approved this retrospective study and granted a waiver for the requirement of informed consent.

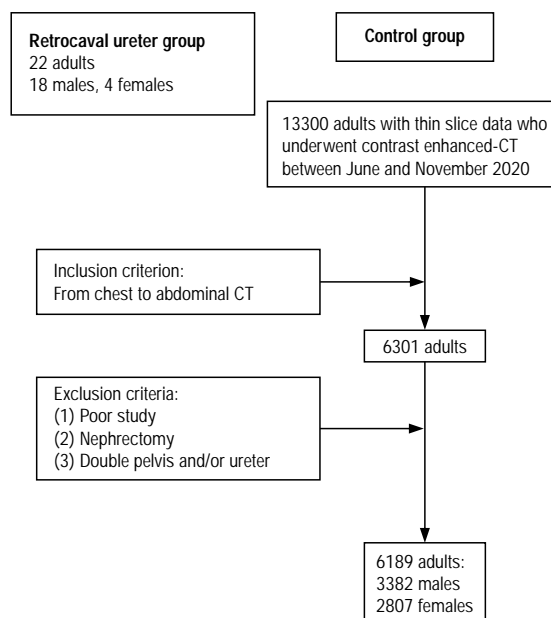


Figure 1. Flow chart shows inclusion and exclusion criteria in the control group; CT — computed tomography.

Our study included 22 adults with retrocaval ureter (18 males and 4 females, mean age: 57 ± 19 years old) and 6189 adults with a normal urinary system (3382 males and 2807 females, mean age: 66 ± 14 years old) in the control group. The control group was selected using the inclusion and exclusion criteria depicted in Figure 1. Cases with retrocaval ureter were searched using the key words “retrocaval ureter”, “circumcaval ureter”, “postcaval ureter” and “preureteral vena cava” among the abdominal CT reports of adults between January 2008 and September 2020 in our university hospital and affiliated hospitals. We excluded cases examined using non-contrast CT. Twenty-two adults with retrocaval ureter underwent contrast enhanced chest-to-abdominal CT between January 2008 and September 2020 in our university hospital and affiliated hospitals. CVA resulting from cardinal vein development and congenital renal anomaly (CRA) were evaluated using CT images (0.5–3 mm) on a picture archiving and communication system (PACS) workstation (SDS viewer, NOBORI Ltd. Tokyo, Japan). For retrocaval ureter group, acquired renal diseases were assessed using CT and medical records. We evaluated side and shape of the retrocaval ureter. We used classification of retrocaval ureter on the shape by Bateson and Atkinson [2].

Computed tomography was performed using a 64- to 128-slice scanner (SOMATOM Force, SOMATOM Definition Flash, SOMATOM Definition Edge, Siemens

AG, Munich, Germany) at a slice thickness of 0.5 mm. The other parameters were as follows: tube voltage, 60–120 kVp; tube current, auto mA; and rotation time: 0.5 s. Contrast-enhanced CT examinations were performed by injecting 2 mL/kg of non-ionic contrast material at a rate of 2 mL/s with scanning delay of 120 s. CT urography was performed with more than 300 s of scanning delay.

Two radiologists with more than 20 years' experience each in CT image interpretation reviewed 1 mm reconstructed axial CT images on a PACS workstation. If needed, additional multiplanar reformations, maximum injection projection and CT urography were used for the evaluations. The radiologists resolved any disagreement through discussion to reach a consensus.

We compared the prevalence of associated CVA and CRA in the retrocaval ureter and control groups using the Mann-Whitney U test. Demographic data in adults with CVA was compared between two groups by chi-square test. Statistical analysis was performed using SPSS version 23 software. P values < 0.05 were considered statistically significant.

RESULTS

In the retrocaval ureter group, 4 adults with CVA and CRA were found: 1 right double IVC (Fig. 2), 1 double IVC, 1 preisthmic IVC with horseshoe kidney (Fig. 3), and 2 cases of preaortic iliac confluence (Fig. 4). An adult with right double IVC had preaortic iliac confluence. In the retrocaval ureter group, the prevalence of CVA and CRA per person was 18.2% (4/22) and 4.5% (1/22).

The adults with CVA and CRA in the control group were 34 males (CVA: 24, CRA: 10) and 30 females (CVA: 25, CRA: 6), and the mean age was 59 ± 21 years old. The control group included 49 adults with CVA. All cases were IVC anomalies: 11 left IVC (8 males, 3 females), 37 double IVC (16 males, 21 females), 1 IVC interruption azygos continuation (1 female). Sixteen adults with CRA were found: 15 horseshoe kidneys (10 males, 5 females) and 1 right renal absence (1 female). One adult with double IVC was associated congenital right renal absence and bicornuate uterus. The prevalence of CVA per person was 0.79% (49/6189), including left IVC (0.18%), double IVC (0.58%), and IVC interruption azygos continuation (0.02%). The prevalence of CRA per person was 0.26% (16/6189).

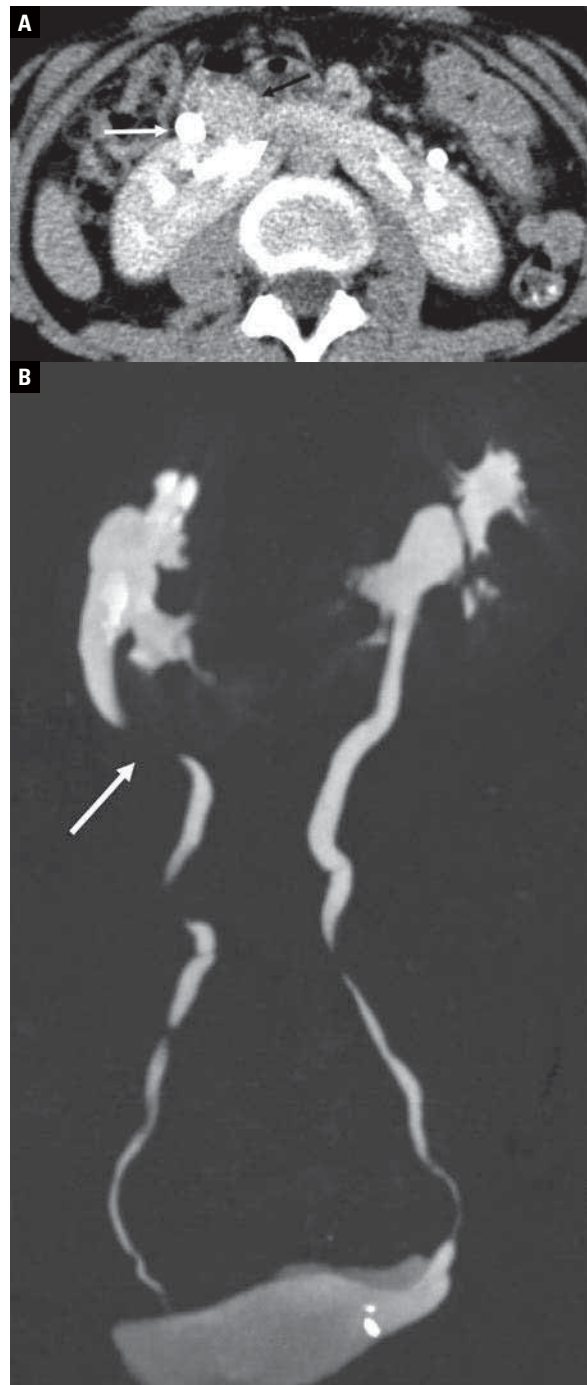


Figure 2. A case of preisthmic inferior vena cava (IVC): **A.** Axial computed tomography image shows preisthmic IVC (white arrow) of horseshoe kidney and retrocaval ureter (black arrow); **B.** Computed tomography urography shows compression of the right retrocaval ureter (white arrow).

The prevalence of CVA and CRA per person in the retrocaval ureter group was higher than that in the control group ($p < 0.001$).

Male ratio associated with CVA in the retrocaval ureter group was higher than that in the control group ($p = 0.009$). There was no significant differ-



Figure 3. A case of right double inferior vena cava; **A.** Axial computed tomography image shows ureter (white arrow) between right sided dorsal (black arrow) and ventral (arrowhead) vena cavae; **B.** Volume rendering image clearly reveals relationship among dorsal (black arrow) and ventral (arrowhead) vena cavae and retrocaval ureter (white arrow). Dotted arrow is left gonadal vein.

ence in age of adults with CVA among two groups ($p = 0.06$).

Five adults with retrocaval ureter were evaluated by CT urography. The clinical and CT findings are shown in Table 1. All retrocaval ureters were on the right side with 14 low loop types and 8 high loop types. Fourteen adults including 4 with CVA in the

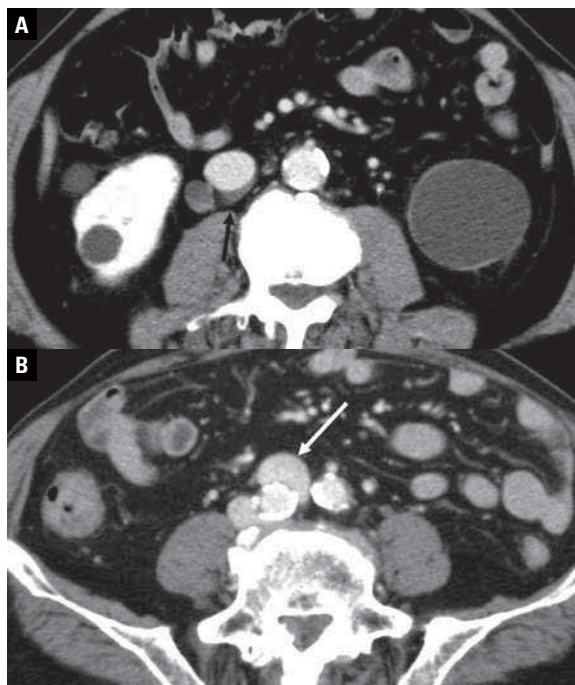


Figure 4. A case of preaortic iliac confluence; **A.** Axial computed tomography image shows retrocaval ureter (black arrow) at lower level of right kidney; **B.** Axial computed tomography image shows left common iliac vein (white arrow) anterior to right common iliac artery.

retrocaval ureter group had asymptomatic and retrocaval ureter associated CVA were found incidentally. Seven adults with hydronephrosis were found and the patients' symptoms were flank pain and haematuria. Eight adults had acquired renal diseases. Three of them treated with surgery, but retroperitoneal laparoscopic approach was not performed. One adult experienced recurrent hydronephrosis with ureter stone after surgery.

DISCUSSION

Retrocaval ureter tends to be associated with IVC anomaly due to the embryological malformation of the cardinal vein [9, 13–16, 21, 27]. Ours is the largest study of associated CVA and CRA in adults with retrocaval ureter using CT data. Our results show that the prevalence of associated CVA was 18.2%. The prevalence of congenital IVC anomalies in the general population was reported as 0.2–3.0% [3–5]. In our study the prevalence was 0.79% and the result was similar to that on previous study. The prevalence of associated CVA and CRA was significantly more frequent in adults with retrocaval ureter than those with a normal ureter. The review of literature by Perimenis et al. [20] revealed that 21% of the cases

Table 1. Summary of clinical and computed tomography (CT) findings

No.	Age	Sex	Cr	CT findings			Clinical findings		
				Side of RCU	Type of RCU	Hydronephrosis	ARD	CRA	CVA
1	60	M	0.7	Right	Low	N	N	N	N
2	24	M	0.8	Right	Low	N	Renal cyst	N	N
3	25	M	1.2	Right	Low	P	Renal cysts	N	N
4	79	M	0.8	Right	High	N	Urolithiasis	N	N
5	38	M	1.1	Right	Low	N	N	N	N
6	40	M	0.8	Right	High	N	N	N	N
7	46	F	0.6	Right	High	N	N	HSK	PIVC
8	46	M	0.8	Right	High	N	N	N	DRIVC, PIC
9	71	M	0.8	Right	High	N	Renal cyst	N	PIC
10	70	F	0.8	Right	High	N	N	N	DIVC
11	50	M	0.7	Right	Low	P	N	N	N
12	55	M	0.9	Right	Low	N	Ureteral cancer	N	N
13	23	M	0.5	Right	Low	N	Urolithiasis	N	N
14	77	M	0.9	Right	Low	N	N	N	N
15	54	M	0.8	Right	Low	N	N	N	N
16	62	M	0.8	Right	Low	P	N	N	N
17	79	M	0.9	Right	High	N	N	N	N
18	73	M	0.8	Right	Low	P	N	N	N
19	60	F	0.8	Right	Low	P	N	N	N
20	74	M	0.6	Right	Low	P	N	N	N
21	76	M	1.41	Right	Low	P	N	N	N
22	77	F	0.65	Right	High	N	Urolithiasis	N	N

Cr — creatinine; CT — computed tomography; RCU — retrocaval ureter; ARD — acquired renal disease; CRA — congenital renal anomaly; CVA — congenital venous anomaly; HSK — horseshoe kidney; IVC — inferior vena cava; PIVC — preisthmic IVC; DRIVC — double right IVC; DIVC — double IVC; PIC — preaortic iliac confluence; M — male; F — female; N — negative; P — positive

of retrocaval ureter present with congenital abnormalities mainly from the cardiovascular system and the genitourinary tract. Present result was similar to that of the review article. However, they did not assess associated congenital cardiovascular diseases in detail [20]. They reported 9 horseshoe kidneys in 352 cases with retrocaval ureter with prevalence of 2.6%, and the prevalence of CRA including renal agenesis was reported as 5.1% [20]. The prevalence of CRA was 4.5% in our study; however, no renal agenesis was found, likely because our sample was small.

Inferior vena cava anomalies in retrocaval ureter patients were left IVC, double IVC, double right IVC and preisthmic IVC with horseshoe kidney [4–7, 10–12, 15, 18, 20–24, 30]. Retrocaval ureter is usually found on the right [1, 2, 9, 13, 14, 16]. All retrocaval ureters found in our study were on the right. Left retrocaval ureter is associated with situs inversus, or duplicated or single left IVC [4, 5, 7, 20, 21, 28, 30]. In double IVC, the retrocaval ureter is present on the

right or left side [4, 5, 7]. The double IVC case in our study had the right retrocaval ureter. Right double IVC is an extremely rare condition, although there are some case reports describing it [5, 6, 11, 23, 24]. Right double IVC is sometimes associated with retrocaval ureter as we observed [6, 11, 23]. In the partial right double IVC, the anomalous ureter crosses thorough IVC split [6, 18].

Preisthmic IVC with retrocaval ureter is the specific finding and associated with horseshoe kidney [10, 12, 20, 29]. Because embryogenesis of the renal parenchyma and its venous drainage in the IVC occur simultaneously, it is plausible that horseshoe kidney and IVC anomalies are consequences of a shared disturbed signal that occurs as these retroperitoneal structures' development [10, 12]. Impairment of renal ascent and rotation may affect the usual venous development [12].

Combined anomaly of retrocaval ureter and preaortic iliac confluence have been rarely report-

ed [6, 9, 24]. In normal development, the posterior aspect forms the iliac venous confluence, but persistence of the subcardinal vein results in preaortic iliac venous confluence [24]. Shin et al. [23] reported a case of right double IVC with combined retrocaval ureter anomalies and preaortic iliac confluence, as we observed.

Congenital IVR anomalies with normal ureter are more than half of left IVC on normal situs and most of them are double IVC, left IVC and IVC interruption azygos continuation [1, 13, 14]. Almost all retrocaval ureter presents on the right side because of the abnormal development of the right posterior cardinal vein. Right retrocaval ureters with double IVC and preaortic iliac confluence such as those in this study have been reported [7, 24]. Various CVA with retrocaval ureter could happen because of abnormal development of not only the right posterior cardinal vein but also other cardinal veins. Variations of associated congenital IVC anomalies were different in patients with normal or retrocaval ureter.

Associated congenital anomalies of the urinary system excluding horseshoe kidney are contralateral renal agenesis, ectopic or malrotated opposite kidney, hypospadias and absence of vas deferens [3, 9]. In our study, we only found a horseshoe kidney.

Retrocaval ureter occurs more often in men, which was confirmed by our results [9]. Retrocaval ureter is usually asymptomatic [9, 20]. In our study, 16 cases were incidentally found in CT examinations (76.2%). When present, symptoms most often begin at ages 30–40 [2, 26]. The mean age of our 5 symptomatic patients was 50 years old. Even though this condition is usually diagnosed in adults, there has been an increased number of case reports in recent years showing symptomatic cases in children [9]. Some patients had abdominal pain and haematuria due to hydronephrosis or urinary infection [1, 9, 13, 14, 16]. Associated urolithiasis and ureteral cancer were reported [8, 19, 25]. Surgical management is needed when the patient is symptomatic with documented subrenal functional obstruction [1, 8, 13, 16, 19, 25]. Surgical treatment should be performed as soon as possible when severe hydronephrosis is present and the upper ureter exhibits obvious dilation that affects the function of the kidney [9]. Patients with recurrent infection, secondary stones, and bleeding require urgent surgical treatment [9]. Surgical treatment involves transection and reloca-

tion of the ureter anterior to IVC [9, 16]. Laparoscopic reconstruction technique is effective and minimally invasive [16, 19, 20].

In our study, 3 patients (2 patients with renal stone and 1 patient with ureteral cancer) were treated with surgery. Two patients with mild hydronephrosis were observed. The main causes for hydronephrosis are stenosis or adhesion of the retrocaval segment and torsion [2]. All our retrocaval ureters associated with CVA were low type and no hydronephrosis was seen. Degree of retrocaval ureter compression in preisthmic IVC is unclear because the anomaly is very rare. Retrocaval ureter compression in the partial right double IVC might be severe because ureter crosses through its narrow slit. Careful observation is necessary for patients with low loop retrocaval ureter because there is marked hydronephrosis in up to 50% of the patients [2]. Caval dilatation due to aging might increase the risk of retrocaval ureter compression. Furthermore, complex anatomy of retrocaval ureter and associated CVA is troublesome on not only urological surgery but also abdominal lymphadenectomy.

Congenital IVC anomalies are one of the risk factors of in the development of deep venous thrombosis [10, 22]. Thrombophlebitis in deep venous thrombosis might be the cause of stenosis and adhesion between retrocaval ureter and IVC. Asymptomatic retrocaval ureter without hydronephrosis is incidentally detected in CT scans. Even though this is a rare condition, high quality CT images with thin slice data reveal the anomaly in detail: CT urography is especially effective (Figs. 1, 4). Understanding of the retrocaval ureter and associated CVA is important, and radiologists should be pointed out the exact anatomy.

Limitations of the study

Our study has some limitations. First, the sample size was too small to evaluate associated diseases. Second, all cases could not be evaluated using CT urography. High loop retrocaval ureter might not be detected at the delayed phase on contrast-enhanced CT. Furthermore, a large study including long-term follow up is necessary to evaluate congenital and acquired disease.

CONCLUSIONS

We identified the prevalence of associated CVA and CRA in patients with retrocaval ureter using CT

data was about 20%. Various CVA with retrocaval ureter were found resulting from abnormal development of not only the right posterior cardinal vein but also other cardinal veins.

Acknowledgements

Authors thank Dr. Shuichi Kawada and Dr. Hiroshi Yamamuro for their technical support.

Conflict of interest: None declared

REFERENCES

- Bass JE, Redwine MD, Kramer LA, et al. Spectrum of congenital anomalies of the inferior vena cava: cross-sectional imaging findings. *Radiographics*. 2000; 20(3): 639–652, doi: [10.1148/radiographics.20.3.g00ma09639](https://doi.org/10.1148/radiographics.20.3.g00ma09639), indexed in Pubmed: [10835118](https://pubmed.ncbi.nlm.nih.gov/10835118/).
- Bateson EM, Atkinson D. Circumcaval ureter: a new classification. *Clin Radiol*. 1969; 20(2): 173–177, doi: [10.1016/S0009-9260\(69\)80166-2](https://doi.org/10.1016/S0009-9260(69)80166-2), indexed in Pubmed: [5771632](https://pubmed.ncbi.nlm.nih.gov/5771632/).
- Cardoza F, Shambhulinga CK, Rajeevan AT. Retrocaval ureter and contra lateral renal agenesis: a case report and review of literature. *Int Braz J Urol*. 2016; 42(4): 842–844, doi: [10.1590/S1677-5538.IBJU.2015.0549](https://doi.org/10.1590/S1677-5538.IBJU.2015.0549), indexed in Pubmed: [27564299](https://pubmed.ncbi.nlm.nih.gov/27564299/).
- Chou CT, Yang AD, Hong YC, et al. Bilateral retrocaval ureters with IVC duplication. *Abdom Imaging*. 2006; 31(5): 596–597, doi: [10.1007/s00261-005-0122-1](https://doi.org/10.1007/s00261-005-0122-1), indexed in Pubmed: [16534551](https://pubmed.ncbi.nlm.nih.gov/16534551/).
- Dudekula A, Prabhu SD. A rare case of right retrocaval ureter with duplication of infrarenal IVC. *Case Rep Radiol*. 2014; 2014: 345712, doi: [10.1155/2014/345712](https://doi.org/10.1155/2014/345712), indexed in Pubmed: [25478276](https://pubmed.ncbi.nlm.nih.gov/25478276/).
- Gong J, Jiang H, Liu Te, et al. Imaging of partial right double vena cava with ureter crossing through its split, confirmed at surgery. *Clin Imaging*. 2011; 35(2): 148–150, doi: [10.1016/j.clinimag.2010.12.001](https://doi.org/10.1016/j.clinimag.2010.12.001), indexed in Pubmed: [21377055](https://pubmed.ncbi.nlm.nih.gov/21377055/).
- Gupta P, Khullar M, Sharma R, et al. A rare presentation of the double inferior vena cava with an anomalous retrocaval right ureter: embryogenesis and clinical implications. *J Clin Diagn Res*. 2013; 7(3): 518–521, doi: [10.7860/JCDR/2013/4576.2810](https://doi.org/10.7860/JCDR/2013/4576.2810), indexed in Pubmed: [23634409](https://pubmed.ncbi.nlm.nih.gov/23634409/).
- Guttilla A, Fiorello M, Fulcoli V, et al. A case of retrograde treatment of a ureteral stone in a retrocaval ureter. *J Endourol Case Rep*. 2018; 4(1): 198–200, doi: [10.1089/cren.2018.0061](https://doi.org/10.1089/cren.2018.0061), indexed in Pubmed: [30671541](https://pubmed.ncbi.nlm.nih.gov/30671541/).
- Hostiuc S, Rusu MC, Negoii I, et al. Retrocaval ureter: a meta-analysis of prevalence. *Surg Radiol Anat*. 2019; 41(11): 1377–1382, doi: [10.1007/s00276-019-02269-w](https://doi.org/10.1007/s00276-019-02269-w), indexed in Pubmed: [31201483](https://pubmed.ncbi.nlm.nih.gov/31201483/).
- Ichikawa T, Kawada S, Koizumi J, et al. Anomalous inferior vena cava associated with horseshoe kidney on multidetector computed tomography. *Clin Imaging*. 2013; 37(5): 889–894, doi: [10.1016/j.clinimag.2013.03.005](https://doi.org/10.1016/j.clinimag.2013.03.005), indexed in Pubmed: [23849103](https://pubmed.ncbi.nlm.nih.gov/23849103/).
- Ichikawa T, Kawada S, Yamashita T, et al. A case of right double inferior vena cava with circumcaval ureter. *Jpn J Radiol*. 2014; 32(7): 421–424, doi: [10.1007/s11604-014-0312-2](https://doi.org/10.1007/s11604-014-0312-2), indexed in Pubmed: [24760202](https://pubmed.ncbi.nlm.nih.gov/24760202/).
- Kehagias DT, Gouliamos AD, Vlahos LJ. Horseshoe kidney associated with anomalous inferior vena cava. *Eur Radiol*. 1999; 9(5): 935–936, doi: [10.1007/s003300050770](https://doi.org/10.1007/s003300050770), indexed in Pubmed: [10369994](https://pubmed.ncbi.nlm.nih.gov/10369994/).
- Kandpal H, Sharma R, Gamangatti S, et al. Imaging the inferior vena cava: a road less traveled. *Radiographics*. 2008; 28(3): 669–689, doi: [10.1148/rg.283075101](https://doi.org/10.1148/rg.283075101), indexed in Pubmed: [18480478](https://pubmed.ncbi.nlm.nih.gov/18480478/).
- Kellman GM, Alpern MB, Sandler MA, et al. Computed tomography of vena caval anomalies with embryologic correlation. *Radiographics*. 1988; 8(3): 533–556, doi: [10.1148/radiographics.8.3.3380993](https://doi.org/10.1148/radiographics.8.3.3380993), indexed in Pubmed: [3380993](https://pubmed.ncbi.nlm.nih.gov/3380993/).
- Lautin EM, Haramati N, Frager D, et al. CT diagnosis of circumcaval ureter. *AJR Am J Roentgenol*. 1988; 150(3): 591–594, doi: [10.2214/ajr.150.3.591](https://doi.org/10.2214/ajr.150.3.591), indexed in Pubmed: [3257616](https://pubmed.ncbi.nlm.nih.gov/3257616/).
- Li HZ, Ma X, Qi L, et al. Retroperitoneal laparoscopic ureteroureterostomy for retrocaval ureter: report of 10 cases and literature review. *Urology*. 2010; 76(4): 873–876, doi: [10.1016/j.urology.2009.12.056](https://doi.org/10.1016/j.urology.2009.12.056), indexed in Pubmed: [20381833](https://pubmed.ncbi.nlm.nih.gov/20381833/).
- Lin HY, Chou YH, Huang SP, et al. Retrocaval ureter: report of two cases and literature review. *Kaohsiung J Med Sci*. 2003; 19(3): 127–131, doi: [10.1016/S1607-551X\(09\)70460-7](https://doi.org/10.1016/S1607-551X(09)70460-7), indexed in Pubmed: [12751873](https://pubmed.ncbi.nlm.nih.gov/12751873/).
- Nagashima T, Lee J, Andoh K, et al. Right double inferior vena cava: Report of 5 cases and literature review. *J Comput Assist Tomogr*. 2006; 30(4): 642–645, doi: [10.1097/00004728-200607000-00014](https://doi.org/10.1097/00004728-200607000-00014), indexed in Pubmed: [16845296](https://pubmed.ncbi.nlm.nih.gov/16845296/).
- Noda Y, Naiki T, Naiki-Ito A, et al. Rare case of carcinoma in situ originated in right retrocaval ureter successfully managed with laparoscopic procedure. *IJU Case Rep*. 2020; 3(4): 128–131, doi: [10.1002/iju.5.12163](https://doi.org/10.1002/iju.5.12163), indexed in Pubmed: [33392470](https://pubmed.ncbi.nlm.nih.gov/33392470/).
- Perimenis P, Gyftopoulos K, Athanasopoulos A, et al. Retrocaval ureter and associated abnormalities. *Int Urol Nephrol*. 2002; 33(1): 19–22, doi: [10.1023/a:1014436432109](https://doi.org/10.1023/a:1014436432109), indexed in Pubmed: [12090330](https://pubmed.ncbi.nlm.nih.gov/12090330/).
- Pierro JA, Soleimanpour M, Bory JL. Left retrocaval ureter associated with left inferior vena cava. *AJR Am J Roentgenol*. 1990; 155(3): 545–546, doi: [10.2214/ajr.155.3.2117354](https://doi.org/10.2214/ajr.155.3.2117354), indexed in Pubmed: [2117354](https://pubmed.ncbi.nlm.nih.gov/2117354/).
- Sakellaris G, Tilemis S, Papakonstantinou O, et al. Deep venous thrombosis in a child associated with an abnormal inferior vena cava. *Acta Paediatr*. 2005; 94(2): 242–244, doi: [10.1111/j.1651-2227.2005.tb01900.x](https://doi.org/10.1111/j.1651-2227.2005.tb01900.x), indexed in Pubmed: [15981763](https://pubmed.ncbi.nlm.nih.gov/15981763/).
- Shin M, Lee JB, Park SB, et al. Right double inferior vena cava associated with retrocaval ureter: computed tomographic findings in two cases. *Clin Imaging*. 2014; 38(3): 353–356, doi: [10.1016/j.clinimag.2013.12.012](https://doi.org/10.1016/j.clinimag.2013.12.012), indexed in Pubmed: [24513316](https://pubmed.ncbi.nlm.nih.gov/24513316/).
- Shindo S, Kobayashi M, Kaga S, et al. Retrocaval ureter and preaortic iliac venous confluence in a patient with an abdominal aortic aneurysm. *Surg Radiol Anat*. 1999; 21(2): 147–149, doi: [10.1007/s00276-999-0147-1](https://doi.org/10.1007/s00276-999-0147-1), indexed in Pubmed: [10399217](https://pubmed.ncbi.nlm.nih.gov/10399217/).
- Simforoosh N, Nouri-Mahdavi K, Tabibi A. Laparoscopic pyelopyelostomy for retrocaval ureter without excision of the retrocaval segment: first report of 6 cases. *J Urol*. 2006; 175(6): 2166–2169, doi: [10.1016/S0022-5347\(06\)00269-2](https://doi.org/10.1016/S0022-5347(06)00269-2), indexed in Pubmed: [16697829](https://pubmed.ncbi.nlm.nih.gov/16697829/).
- Soundappan SVS, Barker AP. Retrocaval ureter in children: a report of two cases. *Pediatr Surg Int*. 2004; 20(2): 158–160, doi: [10.1007/s00383-003-1038-x](https://doi.org/10.1007/s00383-003-1038-x), indexed in Pubmed: [14770320](https://pubmed.ncbi.nlm.nih.gov/14770320/).
- Tamhankar AS, Savalia AJ, Sawant AS, et al. Transperitoneal laparoscopic repair of retrocaval ureter: our experience and review of literature. *Urol Ann*. 2017; 9(4): 324–329, doi: [10.4103/UA.UA_52_17](https://doi.org/10.4103/UA.UA_52_17), indexed in Pubmed: [29118532](https://pubmed.ncbi.nlm.nih.gov/29118532/).
- Thirugnanasambandam V, Nayak P, Mossadeq A. Left retrocaval ureter without situs inversus or inferior vena cava duplication. *Indian J Urol*. 2015; 31(4): 372–373, doi: [10.4103/0970-1591.166481](https://doi.org/10.4103/0970-1591.166481), indexed in Pubmed: [26604455](https://pubmed.ncbi.nlm.nih.gov/26604455/).
- Youssif M. Horseshoe kidney with retrocaval ureter. *Eur Urol*. 1985; 11(1): 61–62, doi: [10.1159/000472452](https://doi.org/10.1159/000472452), indexed in Pubmed: [3987751](https://pubmed.ncbi.nlm.nih.gov/3987751/).
- Watanabe M, Kawamura S, Nakada T, et al. Left preureteral vena cava (retrocaval or circumcaval ureter) associated with partial situs inversus. *J Urol*. 1991; 145(5): 1047–1048, doi: [10.1016/S0022-5347\(17\)38528-2](https://doi.org/10.1016/S0022-5347(17)38528-2), indexed in Pubmed: [2016790](https://pubmed.ncbi.nlm.nih.gov/2016790/).

Quantitative study of the primary ossification centre of the parietal bone in the human fetus

M. Grzonkowska¹, M. Baumgart¹, M. Badura, M. Wiśniewski¹, M. Szpinda

Department of Normal Anatomy, the Ludwik Rydygier Collegium Medicum in Bydgoszcz, the Nicolaus Copernicus University in Torun, Poland

[Received: 22 December 2021; Accepted: 28 January 2022; Early publication date: 28 February 2022]

Background: Detailed morphometric data concentrating on the development of primary ossification centres in human fetuses is critical for the early detection of developmental defects. Thus, an understanding of the growth and development of the parietal bone is crucial in assessing both the normal and pathological development of the calvaria.

Materials and methods: The size of the parietal primary ossification centre in 37 spontaneously aborted human fetuses of both sexes (16 males and 21 females) aged 18–30 weeks was studied by means of computed tomography, digital-image analysis and statistics.

Results: The numerical data of the parietal primary ossification centre in the human fetus displays neither sex nor laterality differences. With relation to fetal age in weeks, the parietal primary ossification centre grew in sagittal diameter according to the quadratic function: $y = 16.322 + 0.0347 \times (\text{age})^2 \pm 1.323$ ($R^2 = 0.96$), in projection surface area according to the cubic function: $y = 284.1895 + 0.051 \times (\text{age})^3 \pm 0.490$, while in both coronal diameter and volume according to the quartic functions: $y = 21.746 + 0.000025 \times (\text{age})^4 \pm 1.256$ and $y = 296.984 + 0.001 \times (\text{age})^4$, respectively.

Conclusions: The obtained morphometric data of the parietal primary ossification centre may be considered age-specific references, and so may contribute to the estimation of gestational ages and be useful in the diagnostics of congenital cranial defects. (Folia Morphol 2023; 82, 2: 307–314)

Key words: parietal bone, bone development, osteogenesis, fetal development

INTRODUCTION

The skull comprises the neurocranium and the viscerocranium or facial skeleton, linked together by sutures, synchondroses and the paired temporomandibular joints [2]. The role of the neurocranium is to protect the brain, while that of the viscerocranium is to protect the sensory and facial organs. The morphogenesis of the bones of calvaria is a long-term

developmental process initiated in the early embryogenesis and terminated at adult age [8]. The bones of the cranial vault develop by membranous ossification, while those of the skull base are formed by endochondral ossification. Their fusion into one functional whole refers to different stages of fetal development and after birth. This interaction ensures that the skull growth mechanism, both sutural and cartilaginous,

Address for correspondence: M. Grzonkowska, MD, Department of Normal Anatomy, the Ludwik Rydygier Collegium Medicum in Bydgoszcz, ul. Łukasiewicza 1, 85–821 Bydgoszcz, Poland, tel: +48 52 585 37 05, e-mail: m.grzonkowska@cm.umk.pl

This article is available in open access under Creative Common Attribution-Non-Commercial-No Derivatives 4.0 International (CC BY-NC-ND 4.0) license, allowing to download articles and share them with others as long as they credit the authors and the publisher, but without permission to change them in any way or use them commercially.

will enable normal growth and development of the brain [9]. The calvaria not only protects the brain, but also constitutes a supportive structure for the face and chewing apparatus functions. However, little is known about mechanical properties and variations of the calvaria [12]. The four borders of the parietal bone are linked to the frontal, temporal, sphenoid, occipital and contralateral parietal bones, thus forming the supero-lateral component of the cranium [11].

The osteogenesis of the cranial vault bones starts with the development of primary ossification centres, specific for each bone. The primary ossification centres appear between weeks 7 and 8 of embryonic life at presumptive bone eminences. Outstandingly, each bone in the calvaria develops from one ossification centre except for the parietal bone. At the very beginning, the parietal bone originates to ossify from two primary ossification centres which subsequently fuse onto single parietal primary ossification centre [10]. The parietal primary ossification centre appears at week 8 of gestational age. Afterwards, the ossification process radiates centrifugally toward peripheries of the parietal bone. By week 14 of gestational age, extensive ossification of bilateral parietal bones occurs, which persists along all borders throughout the fetal life. However, cranial sutures adjacent to the parietal bones are relatively wide, particularly in the parieto-temporal region [8, 11].

In the human, prenatal period is indispensably to assess *in utero* the fetal skull by routine ultrasound. Abnormalities of the parietal bone development may involve the following defects: craniosynostosis, cranium bifidum, fusion of the parietal foramina, congenital absence of the skull roof, anencephaly or exencephaly [4, 5, 10, 13].

Although the timing of ossification of each cranial bone is relatively well-established, no detailed morphometric measurements involving the use of computed tomography (CT) examinations of the parietal primary ossification centres have been reported. To our knowledge, this is the first report in the professional literature to present the morphometric analysis of the parietal primary ossification centre in human fetuses grounded in CT imaging.

In the present study we aimed:

- to perform morphometric analysis of the parietal primary ossification centre in terms of linear, planar and spatial parameters in human fetuses, so as to determine their normative values;
- to examine possible sex differences for all analysed parameters;

- to compute growth dynamics for the analysed parameters, expressed by best-matched mathematical models.

MATERIALS AND METHODS

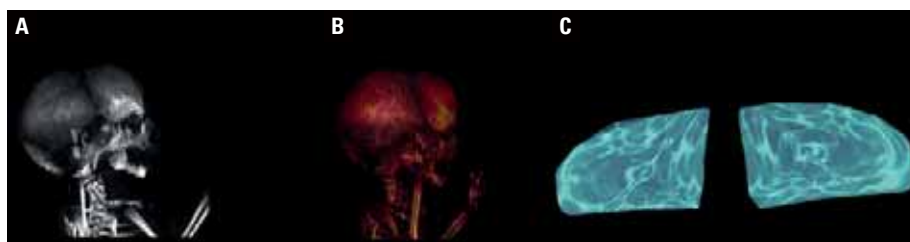
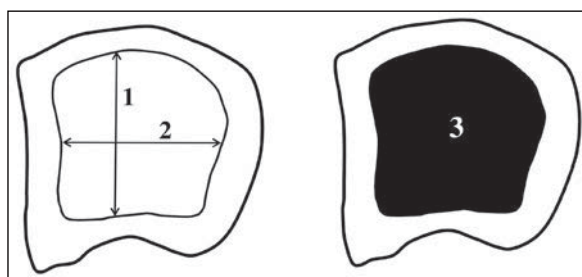
The study material comprised 37 human fetuses of both sexes (16 males and 21 females) aged 18 to 30 weeks of gestation, originating from spontaneous abortions and preterm deliveries. The fetuses were collected before the year 2000 and still remain part of the fetal collection of the Department of Normal Anatomy. The experiment was approved by the Bioethics Committee of Ludwik Rydygier Collegium Medicum in Bydgoszcz (KB 275/2011). The inclusion criteria of investigated fetuses were based on the evaluation of their explicit morphology and statistical cards with the course of pregnancy. Since on macroscopic examination neither internal nor external conspicuous morphological malformations were found, all specimens included in the study were considered normal. Of note, the fetuses did not display any developmental abnormalities of the musculoskeletal system. Fetal ages were determined based on the crown–rump length (CRL) and the known date of the beginning of the last maternal menstrual period. Furthermore, the investigated fetuses could not suffer from growth retardation, as the correlation between the gestational age based on the CRL and that calculated by the last menstruation reached $R = 0.98$ ($p < 0.001$). Table 1 lists the characteristics of the study group, including age, number and sex of the fetuses.

Using the Siemens-Biograph 128 mCT scanner (Siemens Healthcare GmbH, Erlangen, Germany) located at the Department of Positron Emission Tomography and Molecular Imaging (Oncology Centre, the Ludwik Rydygier Collegium Medicum in Bydgoszcz, the Nicolaus Copernicus University Bydgoszcz, Poland), scans of fetuses in DICOM format were attained at 0.4 mm intervals (Fig. 1). The grey scale of the obtained CT images expressed in Hounsfield units (HU) varied from -275 to -134 for minimum, and from $+1165$ to $+1558$ for maximum. Therefore, the window width (WW) varied from 1.404 to 1.692, and the window level (WL) varied from $+463$ to $+712$. The specifics of the imaging protocol were as follows: 60 mAs, 80 kV, pitch: 0.35, field of view: 180, rotational time: 0.5 s, while those of the CT data were: slice thickness: 0.4 mm, image increment: 0.6 mm, and kernel: B45 f-medium. Measurements of the parietal primary ossification centre were done in a specific order (Fig. 2). In each fetus, assessment of the linear pa-

Table 1. Age, number and sex of the fetuses studied

Gestational age	Crown-rump length [mm]				Number of fetuses	Sex	
	Mean	SD	Minimum	Maximum		Men	Women
18	133.33	5.77	130.00	140.00	3	1	2
19	146.50	2.89	143.00	150.00	4	2	2
20	161.00	2.71	159.00	165.00	4	2	2
21	173.67	2.31	171.00	175.00	3	2	1
22	184.67	1.53	183.00	186.00	3	1	2
23	198.67	2.89	197.00	202.00	3	1	2
24	208.00	3.56	205.00	213.00	4	1	3
25	214.00		214.00	214.00	1	0	1
26	229.00	5.66	225.00	233.00	2	1	1
27	240.33	1.15	239.00	241.00	3	3	0
28	249.50	0.71	249.00	250.00	2	0	2
29	253.00	0.00	253.00	253.00	2	0	2
30	262.67	0.58	262.00	263.00	3	2	1
Total					37	16	21

SD — standard deviation

**Figure 1.** A male human fetus aged 20 weeks in the sagittal projection (A), its skeletal reconstruction in the sagittal projection (B), three-dimensional reconstruction of the parietal primary ossification centre (C) using Osirix 3.9 MD.**Figure 2.** Measurement scheme of the parietal primary ossification centre; 1 — coronal diameter; 2 — sagittal diameter; 3 — projection surface area.

rameters, projection surface area and volume of the parietal primary ossification centre was carried out. Despite the cartilaginous stage of development, a morphometric analysis regarding their sagittal diameter and volume was feasible, as the contours of the entire bone were already evidently visible [1, 3].

Measurements of the parietal primary ossification centre included:

- coronal (right and left) diameter, based on the determined distance between its proximal and distal borderlines in the sagittal plane (Fig. 2);
- sagittal (right and left) diameter, based on the determined distance between the anterior and posterior borderlines of the parietal ossification centre in the sagittal plane (Fig. 2);
- projection surface area (right and left), based on the determined contour of the parietal ossification centre in the sagittal plane (Fig. 2);
- volume, calculated using advanced diagnostic imaging tools for three-dimensional reconstruction, taking into account position and the absorption of radiation by a bony tissue (Fig. 1C).

In the present study, to analyse all numerical data, we used the Statistica 12.5 and PQStat 1.6.2.

programmes. Distribution of variables was checked using the Shapiro-Wilk (*W*) test, while homogeneity of variance was checked using Fisher's test. In order to compare the means, Student's *t* test for dependent (left–right) and independent (male–female) variables was used. Afterwards, one-way analysis of variance and Tukey's test were used for post-hoc analysis. If no similarity of variance occurred, the non-parametric Kruskal–Wallis test was used. The characterisation of developmental dynamics of the analysed parameters was based on linear and curvilinear regression analyses. The match between the estimated curves and measurement results was evaluated by coefficients of determination (R^2). Differences were considered

statistically significant at $p < 0.05$. The relationship between variables was also estimated with the Pearson correlation coefficient (*r*).

In an attempt to minimise measurement and observer bias, all measurements were completed by one experienced researcher (M.B.), specialising in image interpretation. Each measurement was reiterated three times under the same conditions but at different times, and then averaged. As shown in Table 2, the intra-class correlation coefficients calculated on the basis of an observer were statistically significant ($p < 0.001$) and of excellent reproducibility.

RESULTS

Mean values and standard deviations of the analysed parameters of the parietal primary ossification centre in human fetuses at analysed gestational stages are presented in Tables 3 and 4.

The statistical analysis revealed neither significant sex nor significant laterality differences, which allowed us to compute one growth curve for each analysed parameter. The growth dynamics expressed in fetal age in weeks were differentiated into quadratic, cubic and quartic functions.

The mean coronal diameter of the parietal primary ossification centre in the gestational age range of 18–30 weeks was between 24.60 ± 0.03 mm and 41.97 ± 0.38 mm on the right, and between 25.51 ± 0.01 mm and 42.13 ± 0.95 mm on the

Table 2. Intra-class correlation coefficients (ICC) values for inter-observer recurrence

Parameter	ICC
Right coronal diameter	0.998*
Left coronal diameter	0.997*
Right sagittal diameter	0.998*
Left sagittal diameter	0.998*
Left projection surface area	0.996*
Right projection surface area	0.995*
Right volume	0.998*
Left volume	0.997*

*Intra-class correlation coefficients marked with asterisk are statistically significant at $p < 0.0001$

Table 3. Coronal and sagittal diameters, projection surface area and volume of the right ossification centre of the parietal bone in human fetuses

Gestational age [weeks]	Number of fetuses	Ossification centre of the right parietal bone							
		Coronal diameter [mm]		Sagittal diameter [mm]		Projection surface area [mm ²]		Volume [mm ³]	
		Mean	SD	Mean	SD	Mean	SD	Mean	SD
18	3	24.60	0.03	28.86	0.05	631.87	1.40	429.67	1.11
19	4	25.40	0.37	29.61	0.34	669.30	17.43	455.15	11.88
20	4	26.10	0.18	30.08	0.07	707.76	15.09	487.58	7.59
21	3	26.51	0.02	30.32	0.12	736.30	9.85	521.34	2.46
22	3	26.67	0.10	31.15	0.57	774.79	20.49	523.27	16.08
23	3	27.00	0.10	33.48	1.26	808.87	7.90	570.68	40.87
24	4	28.08	0.62	35.50	0.39	877.22	28.74	640.37	20.98
25	1	29.10		36.40		932.13		680.46	
26	2	31.45	0.07	38.75	0.07	1048.07	4.27	765.09	3.12
27	3	34.17	0.38	41.47	0.38	1218.51	24.69	865.14	17.53
28	2	38.35	0.21	45.65	0.21	1505.60	15.32	1068.98	10.88
29	2	39.45	0.92	46.65	0.78	1586.45	48.15	1123.93	44.92
30	3	41.97	0.38	47.77	0.35	1721.56	23.30	1224.06	19.51

SD — standard deviation

Table 4. Coronal and sagittal diameters, projection surface area and volume of the left ossification centre of the parietal bone in human fetuses

Gestational age [weeks]	Number of fetuses	Ossification centre of the left parietal bone							
		Coronal diameter [mm]		Sagittal diameter [mm]		Projection surface area [mm ²]		Volume [mm ³]	
		Mean	SD	Mean	SD	Mean	SD	Mean	SD
18	3	25.51	0.01	29.28	0.19	664.68	4.23	451.98	2.88
19	4	26.03	0.41	29.90	0.34	692.59	18.43	470.96	12.53
20	4	26.90	0.17	30.37	0.08	743.36	6.63	524.17	25.62
21	3	27.35	0.12	30.63	0.12	765.16	10.00	550.92	7.20
22	3	27.52	0.09	31.46	0.57	796.55	16.93	549.04	30.35
23	3	27.80	0.12	33.79	1.26	864.49	35.66	561.92	23.18
24	4	28.61	0.65	35.75	0.32	956.52	36.01	621.74	23.41
25	1	29.51		36.24		1005.28		653.43	
26	2	31.17	1.64	37.89	1.63	1060.94	34.68	689.61	22.54
27	3	34.06	1.42	40.77	1.42	1195.58	80.10	760.49	44.17
28	2	37.33	2.55	44.04	2.55	1416.64	78.14	934.98	47.57
29	2	39.58	0.21	46.29	0.21	1575.68	15.67	1118.73	11.12
30	3	42.13	0.95	47.81	0.31	1732.25	48.35	1229.90	34.33

SD — standard deviation

left, following the quartic function: $y = 21.746 + 0.000025 \times (\text{age})^4 \pm 1.256$ ($R^2 = 0.95$) (Fig. 3A).

The mean sagittal diameter of the parietal primary ossification centre in the gestational age range of 18–30 weeks was between 28.86 ± 0.05 mm and 47.77 ± 0.35 mm on the right, and between 29.28 ± 0.19 mm and 47.81 ± 0.31 mm on the left, in accordance with the quadratic function: $y = 16.322 + 0.0347 \times (\text{age})^2 \pm 1.323$ ($R^2 = 0.96$) (Fig. 3B).

The mean projection surface area of the parietal primary ossification centre ranged from 631.87 ± 1.40 mm² at 18 weeks of gestation to 1721.56 ± 23.30 mm² at 30 weeks of gestation on the right, and from 664.68 ± 4.23 mm² to 1732.25 ± 48.35 mm², respectively, on the left, and modelled the cubic function: $y = 284.1895 + 0.051 \times (\text{age})^3 \pm 0.490$ ($R^2 = 0.94$) (Fig. 3C).

The mean volume of the parietal primary ossification centre in the gestational age range of 18–30 weeks was between 429.67 ± 1.11 mm³ and 1224.06 ± 19.51 mm³ on the right, and between 451.98 ± 2.88 mm³ and 1229.90 ± 34.33 mm³ on the left, following the quartic function: $y = 296.984 + 0.001 \times (\text{age})^4 \pm 6.971$ ($R^2 = 0.94$) (Fig. 3D).

DISCUSSION

The ossification process of the parietal bone begins at 7–8 weeks of embryonic life, and is followed by ex-

tensive ossification at week 14, which determines the normal development of the neurocranium until birth. In neonates the neurocranial volume is 60% of adult size, while the viscerocranial volume is 40%. The height of the neurocranium is 60% of the total height of a newborn's skull and 40% of that of an adult's skull [9].

To our knowledge, this paper is the first literature report to quantitatively concentrate on morphometric analysis of the parietal primary ossification centre in human fetuses using CT and, concurrently, its growth dynamics. Previous studies have included only measurements and growth analysis with the development of mathematical growth models for macerated skulls.

Zhang et al. [14] measured the parietal primary ossification centre in 180 human fetuses aged 5 to 38 weeks of gestation and found the parietal ossification to start at week 9 of gestational age from a single ossification centre in the presumptive parietal eminence. According to these authors, in fetuses aged 9–37 weeks its sagittal and coronary diameters ranged from 2.10–3.50 to 83.28–87.07 mm and from 2.10–3.80 to 80.53–84.85 mm, correspondingly. This was modelled by the following linear functions: $y = -20.568 + 2.9676 \times \text{age}$ for sagittal diameter, and $y = -15.709 + 2.7924 \times \text{age}$ for coronary diameter.

In our study, an intensive increase in all parameters tested was observed in the analysed period from 18 to 30 weeks of gestational age, with functions of age

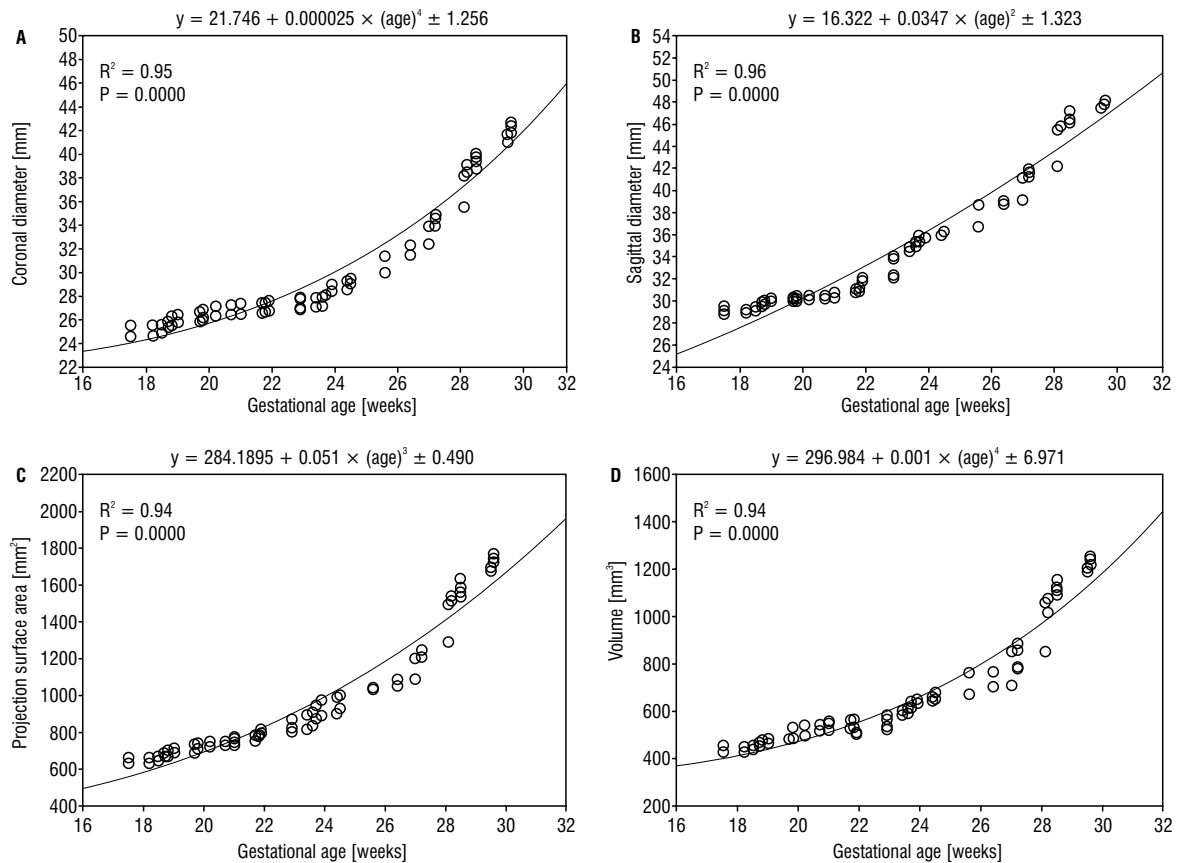


Figure 3. Regression lines for coronal diameter (A), sagittal diameter (B), projection surface area (C), and volume (D) of the parietal primary ossification centre.

from a quadratic function through a cubic function to quartic functions.

The growth dynamics for sagittal diameter displayed the quadratic function: $y = 16.322 + 0.0347 \times (\text{age})^2 \pm 1.323$, while that for projection surface area demonstrated the cubic function: $y = 284.1895 + 0.051 \times (\text{age})^3 \pm 0.490$.

The coronal diameter and volume of the parietal primary ossification centre followed quadratic functions: $y = 21.746 + 0.000025 \times (\text{age})^4 \pm 1.256$ and $y = 296.984 + 0.001 \times (\text{age})^4 \pm 6.971$, respectively.

Our literature review revealed the quantitative assessment of the neurocranial ossification centres using CT to be performed by our team only for the occipital and frontal bones in the fetus.

In our study devoted to the development of the primary ossification centre of the occipital squama in human fetuses, the developmental dynamics of the coronal diameter followed the linear functions: $y = -6.462 + 1.109 \times \text{age} \pm 0.636$ on the right, and $y = -9.395 + 1.243 \times \text{age} \pm 0.577$ on the left. The transverse diameters of the supraoccipital and interparietal

parts as well as projection surface area of the occipital squama ossification centre increased in relation to gestational age expressed in weeks, following the logarithmic functions: $y = -98.232 + 39.663 \times \ln(\text{age}) \pm 0.721$, $y = -79.903 + 32.107 \times \ln(\text{age}) \pm 0.974$, $y = -3062.89 + 1108.98 \times \ln(\text{age}) \pm 29.476$, respectively. The volume of the occipital squama ossification centre increased proportionately to the quadratic function: $y = -330.105 + 1.554 \times \text{age}^2 \pm 32.559$ [7].

Furthermore, in our study of the development of the frontal squama ossification centre in human fetuses, the growth dynamics for its coronal diameter, projection surface area and volume followed the quadratic functions: $y = 13.756 + 0.021 \times \text{age}^2 \pm 0.024$, $y = 38.285 + 0.889 \times \text{age}^2 \pm 0.034$, and $y = -90.020 + 1.375 \times \text{age}^2 \pm 11.441$, respectively. However, the transverse diameter increased proportionately to gestational age alone, following the linear function: $y = 0.956 + 0.956 \times \text{age} \pm 0.823$ [6].

Unfortunately, a lack of numerical data concerning the parietal primary ossification centre in the medical literature limits a more detailed discussion on this topic.

The development of the parietal bone is highly variable. There are reports in the professional literature that the prolonged ossification of the posterior parietal region in the vicinity of the obelion point may lead to the formation of a V-shaped notch named the subsagittal suture of Pozzi and pars obelica. Knowledge of the variability of the parietal bone ossification allows a much better understanding of the formation of the sagittal suture near the obelion point. The formation of the sagittal suture occurs through the closure of three fontanelles, i.e. the anterior fontanelle located between the frontal squama and bilateral parietal bones, the posterior fontanelle sited between the parietal bones and occipital squama and the obelic fontanelle or sagittal fontanelle that occurs in 50–80% of cases and contributes to the formation of unilateral or bilateral parietal foramina. The obelic fontanelle usually closes in the first 2 years of life, and variations in the degree of its closure may result in obelic bones, an accessory parietal emissary foramen, enlarged parietal foramen and the parietal fissure [11].

Understanding the development of the parietal bone in human fetuses is necessary for diagnosing skeletal dysplasias or detecting anomalies of the calvaria. Craniosynostosis is a congenital malformation with its incidence estimated at around 5 per 10,000 live births. It represents a condition, in which a permanent connection among the calvarial bones is formed prematurely. This puts the continued growth of the brain and head in the wrong direction, resulting in deformation, sometimes causing severe damage to the brain due to increased intracranial pressure. Craniosynostosis can be isolated or as a component of various congenital defects, e.g. Apert and Crouzon syndromes [4, 13].

Another aberration is cranium bifidum or “skull cleft”, which forms due to the abnormal closure of the skull in the same way as its medullary counterpart, spina bifida. Cranium bifidum occultum is a rare disease with its incidence of 1–3 per 10,000 births involving delayed ossification of the parietal bone resulting in medially located skull roof foramina, with the scalp, periosteum and dura mater being intact. This is usually the mildest type of neural tube defects because there is no cerebral herniation, and the skull defects often close over time. The disease is generally asymptomatic, but it should be emphasized that the persistent bone defects cause the brain to be unprotected and prone to injuries [10].

Furthermore, cranium bifidum may be accompanied by dysplasias of the viscerocranium, affecting the structure of the medial line of the head and face, such as frontonasal dysplasia [10].

Another set of defects involving the parietal bones is a fusion of parietal foramina, i.e. occurrence of holes in the posterosuperior angles of the parietal bones, by which emissary veins pass through the calvaria. In this defect, the scalp remains intact, and the size of deficiencies decreases as the child ages [10]. Another ossification disturbance in the parietal bone is exemplified by enlarged parietal foramina, occurring due to insufficient ossification around them [5]. Other important defects involving the parietal bone include: cranium bifidum with meningeal or cerebral herniation passing through the hole in the skull, acalvaria — a congenital lack of cranial roof, acrania — a lack of cranial roof and cerebral tissue, and exencephaly — a serious deformation and exposure of the brain which is outside the skull because of the lack of scalp and calvaria [10].

To our opinion, the main limitation of this study is a relatively narrow gestational age group, ranging from 18 to 30 weeks, and a small number of cases, including 37 human fetuses.

CONCLUSIONS

The morphometric parameters of the parietal primary ossification centre display neither sex nor laterality differences.

With relation to fetal age in weeks, the parietal primary ossification centre grows in sagittal diameter according to a quadratic function, in projection surface area according to a cubic function, while in both coronal diameter and volume according to quartic functions.

The obtained morphometric data of the parietal primary ossification centre may be considered age-specific references, and so may contribute to the estimation of gestational ages and be useful in the diagnostics of congenital cranial defects.

Conflict of interest: None declared

REFERENCES

1. Chano T, Matsumoto K, Ishizawa M, et al. Analysis of the presence of osteocalcin, S-100 protein, and proliferating cell nuclear antigen in cells of various types of osteosarcomas. *Eur J Histochem.* 1996; 40(3): 189–198, indexed in Pubmed: [8922947](#).
2. Chmielewski PP. *New Terminologia Anatomica: cranium and extracranial bones of the head.* *Folia Morphol.* 2021; 80(3): 477–486, doi: [10.5603/FM.a2019.0129](#), indexed in Pubmed: [31802475](#).
3. Duarte WR, Shibata T, Takenaga K, et al. S100A4: a novel negative regulator of mineralization and osteoblast differentiation. *J Bone Miner Res.* 2003; 18(3): 493–501,

- doi: [10.1359/jbmr.2003.18.3.493](https://doi.org/10.1359/jbmr.2003.18.3.493), indexed in Pubmed: [12619934](https://pubmed.ncbi.nlm.nih.gov/12619934/).
4. Esteve-Altava B, Vallès-Català T, Guimerà R, et al. Bone fusion in normal and pathological development is constrained by the network architecture of the human skull. *Sci Rep.* 2017; 7(1): 3376, doi: [10.1038/s41598-017-03196-9](https://doi.org/10.1038/s41598-017-03196-9), indexed in Pubmed: [28611422](https://pubmed.ncbi.nlm.nih.gov/28611422/).
 5. Griessenauer CJ, Veith P, Mortazavi MM, et al. Enlarged parietal foramina: a review of genetics, prognosis, radiology, and treatment. *Childs Nerv Syst.* 2013; 29(4): 543–547, doi: [10.1007/s00381-012-1982-7](https://doi.org/10.1007/s00381-012-1982-7), indexed in Pubmed: [23207976](https://pubmed.ncbi.nlm.nih.gov/23207976/).
 6. Grzonkowska M, Baumgart M, Badura M, et al. Morphometric study of the primary ossification center of the frontal squama in the human fetus. *Surg Radiol Anat.* 2020; 42(7): 733–740, doi: [10.1007/s00276-020-02425-7](https://doi.org/10.1007/s00276-020-02425-7), indexed in Pubmed: [32025797](https://pubmed.ncbi.nlm.nih.gov/32025797/).
 7. Grzonkowska M, Baumgart M, Badura M, et al. Quantitative anatomy of the fused ossification center of the occipital squama in the human fetus. *PLoS One.* 2021; 16(2): e0247601, doi: [10.1371/journal.pone.0247601](https://doi.org/10.1371/journal.pone.0247601), indexed in Pubmed: [33621236](https://pubmed.ncbi.nlm.nih.gov/33621236/).
 8. Jin SW, Sim KB, Kim SD. Development and Growth of the Normal Cranial Vault : An Embryologic Review. *J Korean Neurosurg Soc.* 2016; 59(3): 192–196, doi: [10.3340/jkns.2016.59.3.192](https://doi.org/10.3340/jkns.2016.59.3.192), indexed in Pubmed: [27226848](https://pubmed.ncbi.nlm.nih.gov/27226848/).
 9. Kulewicz M. Craniofacial growth and development. *Acta Clinica.* 2002; 2(2): 168–178.
 10. Moreno V, Río M, Coruña M, et al. Cranium bifidum occipitale with severe hypoplasia of parietal bones associate to corpus callosum agenesis and seizures. *J Med Res.* 2017; 3(4): 180–182, doi: [10.31254/jmr.2017.3404](https://doi.org/10.31254/jmr.2017.3404).
 11. Murlimanju BV, Saralaya VV, Somesh MS, et al. Morphology and topography of the parietal emissary foramina in South Indians: an anatomical study. *Anat Cell Biol.* 2015; 48(4): 292–298, doi: [10.5115/acb.2015.48.4.292](https://doi.org/10.5115/acb.2015.48.4.292), indexed in Pubmed: [26770881](https://pubmed.ncbi.nlm.nih.gov/26770881/).
 12. Peterson J, Dechow PC. Material properties of the inner and outer cortical tables of the human parietal bone. *Anat Rec.* 2002; 268(1): 7–15, doi: [10.1002/ar.10131](https://doi.org/10.1002/ar.10131), indexed in Pubmed: [12209560](https://pubmed.ncbi.nlm.nih.gov/12209560/).
 13. Rice DPC, Rice R, Thesleff I. Molecular mechanisms in calvarial bone and suture development, and their relation to craniosynostosis. *Eur J Orthod.* 2003; 25(2): 139–148, doi: [10.1093/ejo/25.2.139](https://doi.org/10.1093/ejo/25.2.139), indexed in Pubmed: [12737212](https://pubmed.ncbi.nlm.nih.gov/12737212/).
 14. Zhang W, Wang J, Wang W. Development and measurement of fetal parital ossification. *Adv Comp Sci Res.* 2015, doi: [10.2991/iccse-15.2015.75](https://doi.org/10.2991/iccse-15.2015.75).

A new classification system of trifold mandibular canal derived from Malaysian population

S.Y.A. Al-Siweedi¹, W.C. Ngeow¹, P. Nambiar^{1,2}, M.I. Abu-Hassan³, R. Ahmad³, M.K Asif⁴, W.L. Chai⁵

¹Department of Oral and Maxillofacial Clinical Sciences, Faculty of Dentistry, University of Malaya, Kuala Lumpur, Malaysia

²Faculty of Dentistry, MAHSA University, Jln SP 2, Bandar Saujana Putra, Jenjarum, Selangor, Malaysia

³Centre of Studies for Restorative Dentistry, Faculty of Dentistry, Universiti Teknologi MARA, Sg Buloh, Malaysia

⁴Department of Research and Forensic Odontology, Shifa College of Dentistry, Shifa Tameer-e-Millat University, Islamabad, Pakistan

⁵Department of Restorative Dentistry, Faculty of Dentistry, University of Malaya, Kuala Lumpur, Malaysia

[Received: 25 January 2022; Accepted: 23 February 2022; Early publication date: 8 March 2022]

Background: The purpose of this study was to identify and classify the anatomic variation of mandibular canal among Malaysians of three ethnicities.

Materials and methods: The courses of the mandibular canal in 202 cone-beam computed tomography scanned images of healthy Malaysians were evaluated, and trifold mandibular canal (TMC) when present, were recorded and studied in detail by categorizing them to a new classification (comprising of 12 types). The diameter and length of canals were also measured, and their shape determined.

Results: Trifold mandibular canals were observed in 12 (5.9%) subjects or 16 (4.0%) hemi-mandibles. There were 10 obvious categories out the 12 types of TMCs listed. All TMCs (except one) were observed in patients older than 30 years. The prevalence according to ethnicity was 6 in Malays, 5 in Chinese and 1 in Indian. Four (33.3%) patients had bilateral TMCs, which was not seen in the Indian subject. More than half (56.3%) of the accessory canals were located above the main mandibular canal. Their mean diameter was 1.32 mm and 1.26 mm for the first and second accessory canal, and the corresponding lengths were 20.42 mm and 21.60 mm, respectively. Most (62.5%) canals had irregularly shaped lumen; there were more irregularly shaped canals in the second accessory canal than the first branch. None of the second accessory canal was oval (in shape).

Conclusions: This new classification can be applied for the variations in the branching pattern, length and shape of TMCs for better clinical description. (Folia Morphol 2023; 82, 2: 315–324)

Key words: accessory canal, mandibular canal, trifold mandibular canal, cone-beam computed tomography, Malaysians

INTRODUCTION

The mandibular canal is nowadays acknowledged as a main canal with multiple smaller canals running roughly parallel to it [16]. These canals are termed

accessory, bifid or trifold canals depending on the size, configuration, and number of canals present. The term “accessory canal” has been used by Kaufmann et al. [12] to denote multiple branches that are

Address for correspondence: Prof. Dr. W. L. Chai, Department of Restorative Dentistry, Faculty of Dentistry, University of Malaya, 50603 Kuala Lumpur, Malaysia, tel: 603-79674548, fax: 603-79674534, e-mail: chaiwl@um.edu.my

This article is available in open access under Creative Common Attribution-Non-Commercial-No Derivatives 4.0 International (CC BY-NC-ND 4.0) license, allowing to download articles and share them with others as long as they credit the authors and the publisher, but without permission to change them in any way or use them commercially.

short, i.e. less than 15 mm in length. The accessory canals are usually detected as incidental findings by means of radiography as they do not have any clinical landmark [16].

The presence of accessory canals has been attributed to the embryonic development of the three branches of the inferior alveolar nerve that innervate three groups of mandibular teeth, namely the incisors, deciduous molars (and their permanent successors) and permanent molars [9]. During this development process, one single main trunk is expected to form. Accessory branching with various patterns however, forms as a result of incomplete fusion of any of these nerve branches [9]. In accordance to this branching, ossification around the nerves results in the formation of accessory canals. Specific variants of these accessory canals, namely the bifid canals have been reported since the 1970s [13, 26]; while the trifid canals, since 2005 [4].

The trifid mandibular canals (TMC) are considered as the second most reported mandibular canal variant in the literature after bifid canals [20]. The first case of TMC was reported in 2005 as an incidental finding adjacent to an impacted lower left third molar, noticed during a pre-orthodontic screening [4]. Computed tomography (CT) scan was used to confirm the initial finding. Most other cases reported since then were case reports [1, 5, 6, 17, 18, 29]. Recently, Aljunid et al. [3] reported a unique case where one of the accessory canals in a patient with TMC became impinged following implant insertion. This case illustrated how injury to a branch of the accessory canals can inflict injury as severe as if the main mandibular canal is affected.

Currently, there are multiple studies that reported on the presence/prevalence of TMC [1, 3–6, 17, 18, 29]. However, the objectives of these studies were not to solely study TMC; instead, all researchers were studying the presence of various types of accessory canals in the mandible. Bogdán et al. [7] in studying dry mandibles found 1 case of TMC out of 46 mandibles examined. This gives a prevalence of 2.2% for the presence of TMC. One other study used digital panoramic images, while the remaining five research groups conducted their study using cone-beam computed tomography (CBCT). The advantage of using CBCT is that it can provide multiplanar images without the presence of a ghost image and the false appearance of the accessory canal. Using CBCT, Okumus and Dumlu [24] reported a prevalence of 2.4% in the

Turkish population, almost similar to that reported by Bogdán et al. [7]. Rashuren et al. [27] reported a prevalence of 1.4% of TMC in 500 patients studied. Yang et al. [30] reported a prevalence of 1.1% among Han Chinese residing in Shanghai. These TMC involved 2 cases of forward canal and 1 case showing a combination of forward canal and retromolar canal. In comparison, Afza and Rahmati [2] reported observing accessory branches (canals) in 40.5% of cases with 8 of them being trifid, i.e. giving a prevalence of 6.9%. De Castro et al. [10] reportedly found 15 patients with TMC (mostly bilateral with one being unilateral) from 700 CBCT scans. This gives an estimated prevalence of 4.12%. Strangely, Fuentes et al. [11] found no evidence of TMC in 925 digital panoramic images examined. This is most probably because of the limitation of a two-dimensional imaging modality.

Currently, only Rashuren et al. [27] have proposed classifying TMC into five subtypes, namely:

- A: two accessory canals of the retromolar type;
- B: two accessory canals of one retromolar and one dental type;
- C: two accessory canals of the dental type;
- D: two accessory canals of one dental and one forward type;
- E: two accessory canals of the retromolar type with two mandibular foramina.

This classification appears to have derived from the classification of bifid mandibular canal proposed by Naitoh et al. [19], except for the description involving two mandibular foramina. It is believed that Rashuren et al. [27] came out with this classification to fit the seven TMC they found in their study.

The purpose of this current study was to investigate the prevalence and the types of TMC present in Malaysian population that consisted of three different ethnic groups, namely Malays, Chinese and Indians, by using CBCT scanned data. As there is currently an inadequate classification system available to define TMC, the authors would like to propose a different classification system that is believed to be more accurate for clinical and academic communication. This study also determined the diameter, shape, and length of the TMC as such information is currently limited.

MATERIALS AND METHOD

Ethical approval

This study received the Faculty Ethical Committee's approval prior to commencement (Ethical approval:

DF DP1303/0014 [P]). The committee was aware that this was a retrospective study and that it was undertaken using patients' data and scanned images. As this is a teaching institution, all patients seeking treatment from the Faculty of Dentistry are informed of the need that all forms of their records may be used for teaching and research purposes, and verbal consent is taken (for imaging purposes) with the assurance that their identity will remain anonymous.

Sample selection

Castro et al. [8] in a review of the literature regarding the classification of the mandibular canal branching reported that the sample size of three-dimensional (3D) classifications used included an average of 187 CT examinations. Therefore, the authors set out to include at least 200 CBCT scans. Following a thorough screening of 850 CBCT scans stored at the database of the Oral Radiology Division of the Faculty of Dentistry, University of Malaya, CBCT scans of 202 subjects (93 male and 109 female) were included in the study based on the inclusion and exclusion criteria. These patients attended the division to obtain scans for various other conditions affecting the upper and/or lower jaws. Each CBCT dataset of the patients that had a complete image of either the right or the left side, or a combination of both sides of the mandible were examined.

Inclusion criteria

- Subjects of both genders from the three main ethnic groups in Malaysia, namely the Malay, Chinese and Indian, were selected.
- Healthy subjects with no mandibular deformity, or medical conditions that affects skeletal growth.
- Accessory canal cortication when present, can be seen and drawn in all aspects of CBCT images.
- Accessory canal must be connected to the mandibular canal.

Exclusion criteria

- Patients with a history of having undergone surgery to the mandible due to trauma or pathology.
- Patients with existing pathological disorder in the mandible such as cyst, tumour, osteomyelitis, fibrous dysplasia, or invasion of cancer that will alter the appearance of the mandible radiographically.
- Syndromic patients and patients with congenital disorders that affect the size and shape of the jaw bones.

- Patients with severe malocclusion that affect the size and shape of the jaw bones.
- Patients with a history of surgical intervention to the body of the mandible i.e. orthognathic surgery, or reconstructive surgery.
- The reformatted CBCT images, which appear distorted or blurred due to patients' movements.

Image acquisition

These patients were subjected to I-CAT Imaging System (Imaging Sciences International, Hatfield, USA), following a standardized protocol for patient positioning and exposure parameter setting (120 kVp, 3–7 mA), with an extended field of view equal to 13 × 16 cm, 0.3 mm voxel, and 20 s of exposure time. As the main clinical reasoning for the examinations arose from the purpose of confirming the diagnosis of a lesion elsewhere in the head and neck region, the CBCTs included had a large field of view and a voxel size of 0.3 mm. The patients were placed in a vertical position and stabilized with custom made head bands and chin support.

Processing of images

The axial slices retrieved from scanning were reformatted according to the protocols advocated by Materialise Dental (Leuven, Belgium). The axial images were elaborately cleaned off from irrelevant anatomies such as the spinal cord, opposing teeth and metal scatterings, in a process called "masking". During this procedure all non-important data were meticulously removed and an exact full-colour 3D reconstruction of the jaw was prepared, as described by Nikzad et al. [21]. The reformatted and cleaned data were rendered to a special implant-planning software programme, SimPlant™ (SimPlant 3-D Pro version 13.1, Materialise Dental, Leuven, Belgium), dedicated for this purpose.

The presence of multiple mandibular canals is documented by first opening the file using Simplant™. The visibility rating and dimensional measurements were performed by only one researcher (first author) who is trained in the interpretation of oral and maxillofacial images. Some questionable CBCT images were re-evaluated by one principle oral and maxillofacial radiologist and one oral and maxillofacial surgeon. The SimPlant™ software allows the viewing of axial, cross-sectional, panoramic and 3D visualisation of the jaw on the same screen. Changing the position of reformatted images makes it possible to trace the

Table 1. Proposed classification for trifold mandibular canal

Type	Description
1A	Retromolar canal ending in bone
1B	Retromolar canal ending in foramen
2A	Dental canal originating from one mandibular foramen
2B	Dental canal originating from multiple mandibular foramina
2C	Dental canal originating from the mandibular canal in the ramus
2D	Dental canal originating from the mandibular canal in the body
3A	Forward canal originating from one mandibular foramen
3B	Forward canal originating from multiple mandibular foramina
3C	Forward canal originating from the mandibular canal and ending in bone
3D	Forward canal originating from the mandibular canal and ending in foramina
4A	Buccolingual canal ending in bone
4B	Buccolingual canal ending in multiple foramina

course of the mandibular canal precisely and draw the exact pathway of the nerve and its branches.

The course of the mandibular canal was marked and determined by firstly identifying the mandibular foramen and mental foramen followed by outlining it by marking in orange using the SimPlant™ software. The location of the mandibular foramen was recorded as being positioned at any of the nine quadrants reported by Lim et al. [15]. Then, the accessory canals/TMCs, when observed, were drawn, and marked in white to distinguish them from the main mandibular canal. The accessory canals were based on their superior-inferior relationship to the main mandibular canal and whether it terminates buccolingually in the bone/foramen or even multiple foramina. Their patterns were firstly recorded, and later they were entered into any of the following classification patterns (Table 1, Figs. 1, 2), which is an expansion of the original classification proposed by Naitoh et al. [19] for bifid mandibular canal. This proposed classification incorporates the origin and ending of the TMC.

The length of TMC was then measured either in the sagittal or panoramic reconstructed CBCT images using the SimPlant™ software as it allows one to measure straight or curved structures. The length of the accessory canals was measured from the starting point of separation of the main canal to an end point that resides in the mandible or at its ending at a foramen.

The diameter of the first and second accessory canals was measured immediately after separation

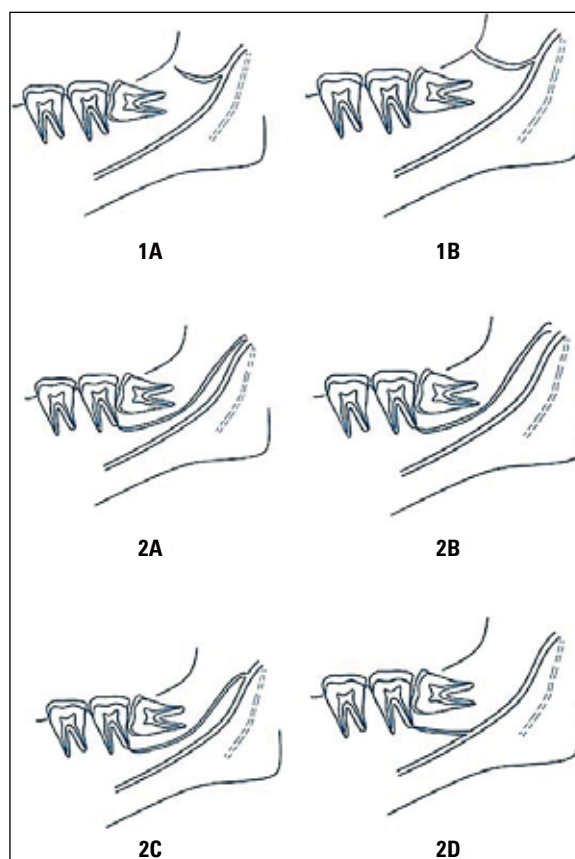


Figure 1. Diagrammatic representation of trifold mandibular canal (type 1A, 1B, 2A, 2B, 2C, 2D) according to our classification system.

on cross-sectional image at the widest portion of the canals. The shape of the lumen of the accessory canal was recorded as either being circular, oval, or irregular.

Intra-observer reliability was performed by analysing 32 randomly selected CBCTs with 2 months intervals between each evaluation. Cohen's Kappa k was used to confirm categorical subclass agreement. Intraclass correlation coefficient (ICC), p was used to assess agreement of length and diameter of the TMC and mandibular canal. The ICC finding was confirmed using Bland-Altman analysis, by applying the following formula:

$$\text{Mean difference} = \frac{\text{Result 1} - \text{Result 2}}{(\text{Result 1} + \text{Result 2})/2} \times 100\%$$

In general, the lower the difference in percentage, the more accurate is the result.

Statistical analysis

All data were gathered, entered, and analysed using SPSS 12.1 (SPSS Inc., Chicago, USA) software programme. Descriptions of parameters were reported as mean \pm standard deviation (SD), and minimum

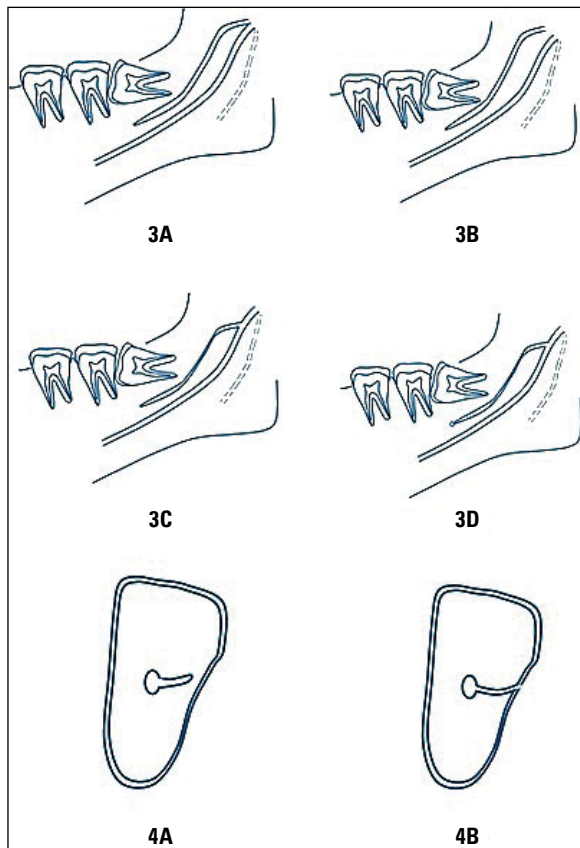


Figure 2. Diagrammatic representation of trifid mandibular canal (type 3A, 3B, 3C, 3D, 4A, 4B) according to our classification system.

and maximum values. The 95% confidence interval (CI) was also determined. Chi-square test was used to determine if any significant differences was present in the prevalence of different types of TMC with respect to ethnicity, gender, and age-group of the subjects. The significant differences in the mean length and diameter of the trifid canal among gender was investigated using independent *t*-test. One-way analysis of variance (ANOVA) with post-hoc Tukey's analysis was used to determine the significant differences between the mean length and diameter of TMC in the subjects of different ethnicity and age-groups. Differences were considered significant when the *p*-value < 0.05.

RESULTS

Measurement of agreement

A total number of 32 records (16% of total sample) were included in the agreement test and retest. All relevant data were measured again after 2 months by using the same methods described earlier. Regarding the assessment of intraexaminer agreement, all parameters showed optimal agreement. Cohen's

Kappa *k* was used for the categorical subclass agreement; the reliability of observing TMC ($k = 0.84$; $p < 0.001$), vertical positioning of canal ($k = 1.00$; $p < 0.001$), lumen shape ($k = 0.73$; $p < 0.001$) and pattern of canal ($k = 0.84$; $p < 0.001$) were between good and excellent.

Intraclass correlation coefficient, *p* was used for the assessments of the length and diameter of the TMC and mandibular canal. The reliability in measuring the length of TMC (ICC = 0.996; $p < 0.001$), diameter of TMC (ICC = 0.763; $p = 0.009$) and diameter of mandibular canal (ICC = 0.923; $p = 0.001$) were between good and excellent. The ICC finding was confirmed using Bland-Altman analysis. The differences in measuring the length of TMC (0.21%), diameter of TMC (2.19%) and diameter of mandibular canal (0.87%) were small, resulting in an average of 0.87% difference being observed.

Prevalence of TMC

Two hundred two scans of the mandibles of patients from three different ethnic groups were studied in this research. Ninety-three of them were Malays, 72 were of Chinese and the remaining 37 were Indians. Their mean age was 48.29 ± 16.9 years (range 11–80 years).

Twelve patients were found to have two accessory canals present in at least one side of the mandible, giving a prevalence of 5.9%. Additionally, the TMC were observed in 16 (4.0%) hemi-mandibles. The mean age of the patients was 53.4 ± 11.4 years (range: 22–76 years). They were observed in 5 males and 7 females and 4 patients presented with bilateral TMCs with the remaining two-third being unilateral presence TMC. Interestingly, 7 of these unilateral TMC patients showed the presence of bifid canals on the contralateral sides. An example of the TMC is shown in Figure 3.

Ethnicity appears to influence the prevalence of TMC. Only 1 Indian presented with TMC as compared to 6 Malays and 5 Chinese subjects. Bilateral TMC was seen in Malays and Chinese but not in the sole Indian subject with TMC. The gender distribution for all subjects with TMC is shown in Figure 4.

Except for one subject (who happened to be the Indian), all TMCs were observed in subjects above the age of 30 years. The average age of Malay, Chinese and Indian subjects were 51.0 years, 56.7 years, and 26 years, respectively. Amongst males, three-quarter of subjects presenting with TMC were found to fall



Figure 3. Trifid mandibular canal (white arrow); main mandibular canal (black arrow). Coronal view (A) and panoramic view (B) of cone-beam computed tomography image improved with SimPlant.

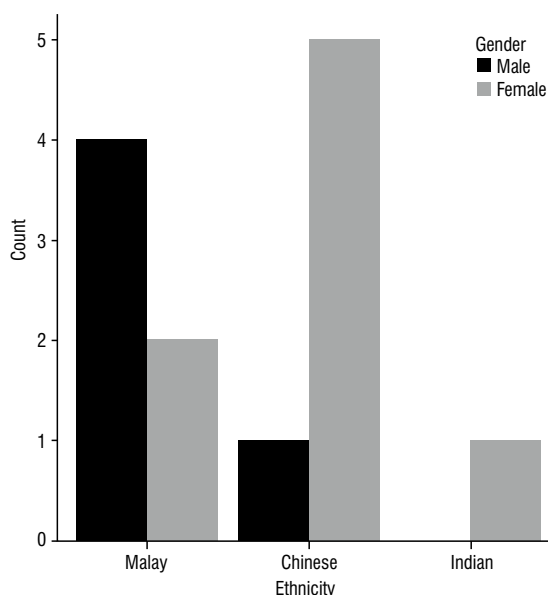


Figure 4. The distribution of trifid mandibular canal found in all subjects of both genders.

within the age of 51 and 80 years old. In females, those between the age of 41 and 50 years made up 57.1% of the subjects, and together with those between the age of 51 and 70 years, they made up of 85.7% of subjects. In summary, it appears that TMC was more commonly seen in female subjects below 50 years, but for the male subjects, the prevalence was higher among those older than 50 years old.

Types of TMCs

Table 2 shows the distribution of various types of TMC according to the classification system proposed in Materials and Methods.

Table 2. Types of trifid mandibular canal according to our classification system

Classification	Number (%)		
	1 st Accessory canal	2 nd Accessory canal	Total
Type 1A	2 (12.5%)	2 (12.5%)	4 (12.5%)
Type 1B	8 (50%)	2 (12.5%)	10 (31.25%)
Type 2A	–	4 (25%)	4 (12.5%)
Type 2B	1 (6.25%)	3 (18.75%)	4 (12.5%)
Type 2C	2 (12.5%)	3 (18.75%)	5 (15.6%)
Type 2D	–	–	–
Type 3A	–	1 (6.25%)	1 (3.12%)
Type 3B	1 (6.25%)	–	1 (3.12%)
Type 3C	–	1 (6.25%)	1 (3.12%)
Type 3D	1 (6.25%)	–	1 (3.12%)
Type 4A	–	–	–
Type 4B	1 (6.25%)	–	1 (3.12%)
Total	16 (100%)	16 (100%)	32 (100%)

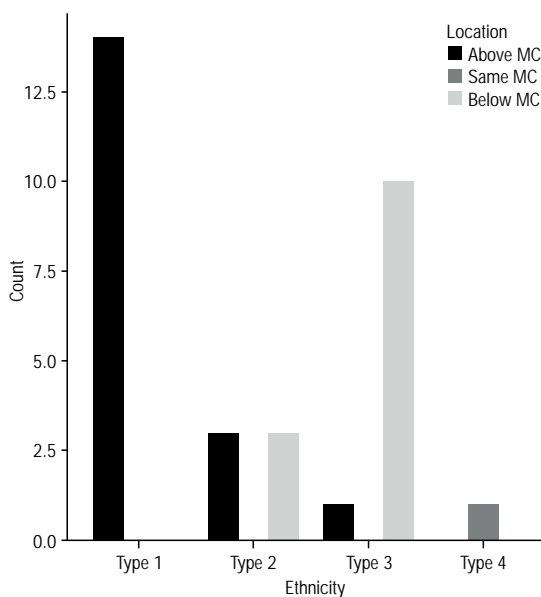
The retromolar canal type (type 1) was observed to be the most common type, dominating 43.8% of TMC observed. The majority (71.4%) of them ended at multiple foramina (type 1B). The dental canal was the second most common type of TMC, making up of 40.6% of TMC. They were almost equally distributed between those originating from one mandibular foramen (type 2A), multiple mandibular foramina (type 2B), and the mandibular canal in the ramus (type 2C). No type 2D dental canal was observed. Four sites presented with each subtype of type 3 canal. Type 4 canal was only present at one site, and it was a buccolingual canal ending in multiple foramina (type 4B). In summary Types 2D and 4A were not observed in our samples.

The vertical position of the accessory canals was classified into three types: above, same or below the main mandibular canal. The majority of the TMC (n = 18) were located above the main mandibular canal. Only one canal was located at the same level with main mandibular canal while the remaining 13 canals were located below the main mandibular canal (Table 3). It appears that most of the first accessory canals were located above the main mandibular canal while the majority of the second accessory canals were most often located below the main mandibular canal.

Figure 5 shows the distribution of four different types of accessory canal according to the three superior-inferior locations. As can be seen, all type 1 canals were located above the main mandibular canal. For type 2 canals, they were equally distributed between

Table 3. Location of trifid mandibular canal (MC) in relation to the main MC

Location	Number (%)	
	1 st Accessory canal	2 nd Accessory canal
Above main MC	14 (87.5%)	4 (25%)
Same level with MC	1 (6.25%)	–
Below main MC	1 (6.25%)	12 (75%)
Total	16 (100%)	16 (100%)

**Figure 5.** The distribution of four different types of accessory branch according to three different locations; MC — mandibular canal.

being located above and below the main mandibular canal. In contrast, most type 3 canals (90.9%) were located below the main mandibular canal. The only type 4 canal present was located at the same level with the main mandibular canal.

Morphometrics of TMC

Diameter of the TMC

One subject had two accessory canals that were larger than the main mandibular canal. Otherwise, all accessory canals were significantly smaller than the main mandibular canal (Table 4). The diameter of the accessory canal was greater than or equal to 50% size of the main canal in 18 (50%) of the cases and lesser than 50% in the remaining 18 (50%) canals.

The overall mean diameter of the accessory canals was 1.29 ± 0.24 mm. The mean diameter of the first accessory canal was 1.32 ± 0.24 mm (range:

0.94–1.89 mm; 95% CI: 1.19 to 1.45 mm) and that of the second accessory canal was slightly smaller at 1.26 ± 0.24 mm (range: 0.93–1.67 mm; 95% CI: 1.14 to 1.39 mm) (Table 3). In comparison, the diameter of the main mandibular canal was 2.40 ± 0.39 mm (range: 1.46–2.89 mm; 95% CI: 2.20 to 2.61 mm). Table 3 outlines the diameter of the main and two accessory mandibular canals in the three ethnic groups, according to their gender.

Although the diameter of the accessory canal appeared different between gender, the average diameter at 1.36 ± 0.24 mm in male was not significantly larger than those observed for female, which averaged at 1.25 ± 0.23 mm (Independent t-test; $p = 0.216$). Malay subjects appeared to have a slightly larger accessory canal (1.31 mm) when compared to Chinese (1.28 mm) and Indian (1.24 mm) subjects although this difference was not statistically significant (ANOVA; $p = 0.888$).

There was no difference in the canal diameter between all four types of canals (ANOVA; $p > 0.05$). Their diameters were 1.35 ± 0.25 mm for type 1, 1.28 ± 0.16 mm for type 2, 1.24 ± 0.23 mm for type 3 and 0.94 for type 4.

Shape of the lumen of the TMC

Three types of lumen shape were identified in this study. The majority of the accessory canals had irregular lumen shape, as observed in 20 (62.5%) hemimandibles. The next most common shape was the circular lumen, accounting for 31.3% ($n = 10$) of cases. Oval shaped lumen was seen in only two (6.3%) cases. Irregularly shaped canal also made up the majority of the first accessory canal (50%) and second accessory canal (75%). All three types of canals can be observed in subjects of both genders, again with the irregularly shaped canal being the most common (male: 66.7%; female: 60.0%).

Length of the TMC

The overall mean length of the accessory canals was 21.01 ± 14.23 mm. The mean length of the first accessory canal was 20.42 ± 13.11 mm (95% CI: 13.44 to 27.41 mm) and that of the second accessory canal was slightly longer at 21.60 ± 15.69 mm (95% CI: 13.23 to 30.00 mm). However, it was observed that there was a wide range in the length of both accessory canals. The first accessory canal ranged from as low 5.00 mm to as high as 52.00 mm. The second accessory canal ranged from as low 7.46 mm

Table 4. The diameter of the main and accessory mandibular canals in the three ethnicities

Ethnic/Gender	Diameter of anatomy structures [mm]			
	Accessory canal 1	Accessory canal 2	Both accessory canals	Main mandibular canal
Malay				
Male	1.48 ± 0.27 mm	1.20 ± 0.18 mm	1.34 ± 0.36 mm	2.45 ± 0.37 mm
Female	1.09 ± 0.18 mm	1.43 ± 0.41 mm	1.26 ± 0.26 mm	2.52 ± 0.45 mm
Both	1.33 ± 0.31 mm	1.29 ± 0.21 mm	1.31 ± 0.25 mm	2.48 ± 0.37 mm
Chinese				
Male	1.45 mm	1.45 mm	1.45 mm	2.60 mm
Female	1.26 ± 0.20 mm	1.23 ± 0.30 mm	1.25 ± 0.24 mm	2.31 ± 0.47 mm
Both	1.29 ± 0.19 mm	1.26 ± 0.28 mm	1.28 ± 0.23 mm	2.35 ± 0.44 mm
Indian				
Female	1.42 mm	1.06 mm	1.24 mm	2.19 mm

Table 5. The length of the main and accessory mandibular canals in the three ethnicities

Ethnic/Gender	Diameter of anatomy structures [mm]		
	Accessory canal 1	Accessory canal 2	Both accessory canals
Malay			
Male	23.51 ± 13.98 mm	13.61 ± 8.47 mm	18.56 ± 12.08 mm
Female	12.34 ± 1.59 mm	15.79 ± 10.58 mm	14.06 ± 7.02 mm
Both	19.32 ± 12.07 mm	14.43 ± 8.61 mm	16.87 ± 10.44 mm
Chinese			
Male	50.00 mm	50.00 mm	27.50 ± 31.82 mm
Female	14.09 ± 5.18 mm	35.05 ± 16.45 mm	24.57 ± 15.97 mm
Both	19.22 ± 14.37 mm	30.76 ± 18.83 mm	24.99 ± 17.17 mm
Indian			
Female	37.68 mm	14.79 mm	26.24 mm

to as high as 50.00 mm. Table 5 outlines the length of both accessory mandibular canals in 3 ethnic stocks, according to their gender.

The average length of accessory canal in the male was 20.05 ± 14.95 mm. This was slightly less than the 21.59 ± 14.15 mm seen in female and this difference was however not statistically significant (Independent *t*-test; *p* = 0.772). There was also no significant difference in the average length of both accessory canals between subjects of three ethnic groups. Malay subjects appeared to have the shortest average length for accessory canals at 16.87 mm, when compared to Chinese and the Indian subject whose TMC measured at 24.99 mm and 26.23 mm respectively (ANOVA; *p* = 0.265).

Trifid mandibular canal type 3 had the longest canal at 36.80 ± 11.64 mm while type 4 was the shortest at 5.85 mm. The mean lengths of type 1 and

type 2 canals were 11.56 ± 4.09 mm and 15.26 ± 9.66 mm, respectively.

DISCUSSION

The prevalence of TMC reported in the current study (5.9%) is within those reported by other studies which ranged from 0% to 6.9% [2, 7, 10, 11, 24, 27, 30]. Ethnic-wise, the Malays presented with the highest percentage of subjects with TMC, followed by the Chinese while the Indians had the lowest prevalence. The prevalence for the Malaysian Chinese group was recorded at 6.9% and this is almost 7× higher than those observed in Shanghainese Chinese (1.1%) [30]. More important is the fact that bilateral TMC was seen in 40.0% of Chinese, 33.3% of Malays but was not observed in the sole Indian subject. This finding has not been reported elsewhere. It must be stated here that the Indian presentation of a single finding

might not be correct as the sample size was only 37 Indians. The authors had difficulty finding CBCT of Indian subjects as they make up only about 7% of the 32 million populations in Malaysia.

Studies in bifid mandibular canal have shown that the length of this accessory canal ranges from 1.6 mm to 35.2 mm [19, 25], while its diameter measured between 0.91 and 2.2 mm [27]. Afsa and Rahmati [2] recently studied the accessory branches of the mandibular canal and reported their length and diameter as 13.61 mm (range: 3.90 to 48.50 mm) and 1.12 mm (range: 0.40 to 3.60 mm), respectively, without distinguishing the types of branching. Rashsuren et al. [27] also reported an average of 16.9 mm in length and 2.2 mm in diameter in 113 subjects with multiple accessory branches. A recalculation of their results provided an average length of 20.1 mm and the diameter of 2.07 mm. Hence, the finding of an average length of 21.01 mm and diameter of 1.29 mm in our TMC cases fit well into the description of accessory canals observed in cases of bifid canals and TMC.

Studies in bifid mandibular canal reported of the difficulty to fit bifid accessory canals into several classification systems even though they are established systems and one of them has even been used for more than four decades [16, 28]. They are the ones proposed by Nortje et al. [22, 23] and Langlais et al. [14] based on panoramic radiographs and the one proposed by Naitoh et al. [19] based on CT/CBCT examinations. Current reports on the prevalence of TMC by several authors did not attempt to categorize the TMC observed [2, 7, 10, 11, 24, 27, 30]. Because of this short coming, the authors had decided to come up with a classification system for TMC from the outset of this study. This current proposed classification system took into consideration the features observed by Nortje et al. [22, 23], Langlais et al. [14] and Naitoh et al. [19], hence retaining some features such as the origin and end of the canal (mandibular foramen, mandibular canal and mental foramina) and the location and orientation of the canal (retromolar, dental, forward and buccolingual canal). It is hope that this classification system will make it easier to communicate the different types of TMC seen in future studies or clinical practice.

This is indeed a significant study done on the scanned images of life patients with CBCT and 3D simulation and it clearly showed accessory canals related with mandibular canal. As the sample size is limited, efforts must be taken to increase the num-

ber of subjects, especially the Indians. In addition, As CBCT uses ionizing radiation and is considered invasive, future research with high resolution magnetic resonance imaging must be encouraged. These imaging modalities do not use ionizing radiation and are considered non-invasive.

CONCLUSIONS

In summary, there are great variations in the pattern, size, and shape of TMC which can be classified into four main types with 12 subtypes. Ten subtypes of TMC were observed in this study.

Trifid mandibular canals were observed in 5.9% of subjects or 4.0% of hemi-mandibles. One-third of these patients had bilateral TMC with more than half (56.3%) of the accessory canals being located above the main mandibular canal. The majority (62.5%) of canals had irregularly shaped lumen; there were more irregularly shaped lumen in the second accessory canal (75%) than the first one (50.0%). None of the second accessory canal was oval (in shape).

Acknowledgements

This project was supported by the University of Malaya's High Impact Research Grant UM.C/625/1/ /HIR/MOHE/05.

Conflict of interest: None declared

REFERENCES

1. Adisen M, Misirlioglu M, Yilmaz S. Trifid mandibular nerve canal. *J Oral Maxillofac Radiol.* 2013; 1(2): 67, doi: [10.4103/2321-3841.120119](https://doi.org/10.4103/2321-3841.120119).
2. Afsa M, Rahmati H. Branching of mandibular canal on cone beam computed tomography images. *Singapore Dent J.* 2017; 38: 21–25, doi: [10.1016/j.sdj.2016.10.005](https://doi.org/10.1016/j.sdj.2016.10.005), indexed in Pubmed: [29229071](https://pubmed.ncbi.nlm.nih.gov/29229071/).
3. Aljunid S, AlSiweedi S, Nambiar P, et al. The management of persistent pain from a branch of the trifid mandibular canal due to implant impingement. *J Oral Implantol.* 2016; 42(4): 349–352, doi: [10.1563/aaid-joi-D-16-00011](https://doi.org/10.1563/aaid-joi-D-16-00011), indexed in Pubmed: [27078072](https://pubmed.ncbi.nlm.nih.gov/27078072/).
4. Auluck A, Ahsan A, Pai KM, et al. Anatomical variations in developing mandibular nerve canal: a report of three cases. *Neuroanatomy.* 2005; 4: 28–30.
5. Auluck A, Pai KM, Mupparapu M. Multiple mandibular nerve canals: radiographic observations and clinical relevance. Report of 6 cases. *Quintessence Int.* 2007; 38(9): 781–787, indexed in Pubmed: [17873985](https://pubmed.ncbi.nlm.nih.gov/17873985/).
6. Auluck A, Pai KM. Trifid mandibular nerve canal. *Dentomaxillofac Radiol.* 2005; 34(4): 259, doi: [10.1259/dmfr/57994569](https://doi.org/10.1259/dmfr/57994569), indexed in Pubmed: [15961604](https://pubmed.ncbi.nlm.nih.gov/15961604/).
7. Bogdán S, Pataky L, Barabás J, et al. Atypical courses of the mandibular canal: comparative examination of dry mandibles and x-rays. *J Craniofac Surg.* 2006; 17(3):

- 487–491, doi: [10.1097/00001665-200605000-00017](https://doi.org/10.1097/00001665-200605000-00017), indexed in Pubmed: [16770186](https://pubmed.ncbi.nlm.nih.gov/16770186/).
8. Castro MA, Lagravere-Vich MO, Amaral TM, et al. Classifications of mandibular canal branching: A review of literature. *World J Radiol.* 2015; 7(12): 531–537, doi: [10.4329/wjr.v7.i12.531](https://doi.org/10.4329/wjr.v7.i12.531), indexed in Pubmed: [26753068](https://pubmed.ncbi.nlm.nih.gov/26753068/).
 9. Chávez-Lomeli ME, Mansilla Lory J, Pompa JA, et al. The human mandibular canal arises from three separate canals innervating different tooth groups. *J Dent Res.* 1996; 75(8): 1540–1544, doi: [10.1177/00220345960750080401](https://doi.org/10.1177/00220345960750080401), indexed in Pubmed: [8906121](https://pubmed.ncbi.nlm.nih.gov/8906121/).
 10. de Castro MA, Barra SG, Vich MO, et al. Mandibular canal branching assessed with cone beam computed tomography. *Radiol Med.* 2018; 123(8): 601–608, doi: [10.1007/s11547-018-0886-3](https://doi.org/10.1007/s11547-018-0886-3), indexed in Pubmed: [29663186](https://pubmed.ncbi.nlm.nih.gov/29663186/).
 11. Fuentes R, Arias A, Farfán C, et al. Morphological variations of the mandibular canal in digital panoramic radiographs: a retrospective study in a Chilean population. *Folia Morphol.* 2019; 78(1): 163–170, doi: [10.5603/FM.a2018.0058](https://doi.org/10.5603/FM.a2018.0058), indexed in Pubmed: [30009366](https://pubmed.ncbi.nlm.nih.gov/30009366/).
 12. Kaufman E, Serman NJ, Wang PD. Bilateral mandibular accessory foramina and canals: a case report and review of the literature. *Dentomaxillofac Radiol.* 2000; 29(3): 170–175, doi: [10.1038/sj/dmfr/4600526](https://doi.org/10.1038/sj/dmfr/4600526), indexed in Pubmed: [10849544](https://pubmed.ncbi.nlm.nih.gov/10849544/).
 13. Kiersch TA, Jordan JE. Duplication of the mandibular canal. *Oral Surg Oral Med Oral Pathol.* 1973; 35(1): 133–134, doi: [10.1016/0030-4220\(73\)90107-2](https://doi.org/10.1016/0030-4220(73)90107-2), indexed in Pubmed: [4508836](https://pubmed.ncbi.nlm.nih.gov/4508836/).
 14. Langlais RP, Broadus R, Glass BJ. Bifid mandibular canals in panoramic radiographs. *J Am Dent Assoc.* 1985; 110(6): 923–926, doi: [10.14219/jada.archive.1985.0033](https://doi.org/10.14219/jada.archive.1985.0033), indexed in Pubmed: [3860553](https://pubmed.ncbi.nlm.nih.gov/3860553/).
 15. Lim MY, Lim WW, Rajan S, et al. Age-related changes in the location of the mandibular and mental foramen in children with Mongoloid skeletal pattern. *Eur Arch Paediatr Dent.* 2015; 16(5): 397–407, doi: [10.1007/s40368-015-0184-x](https://doi.org/10.1007/s40368-015-0184-x), indexed in Pubmed: [25894248](https://pubmed.ncbi.nlm.nih.gov/25894248/).
 16. Luangchana P, Pornprasertsuk-Damrongsri S, Kitisubkanchana J, et al. Branching patterns of the inferior alveolar canal in a Thai population: a novel classification using cone beam computed tomography. *Quintessence Int.* 2019; 50: 224–231.
 17. Mizbah K, Gerlach N, Maal TJ, et al. [Bifid and trifid mandibular canal. A coincidental finding]. *Ned Tijdschr Tandheelkd.* 2010; 117(12): 616–618, doi: [10.5177/ntvt.2010.12.10155](https://doi.org/10.5177/ntvt.2010.12.10155), indexed in Pubmed: [21298889](https://pubmed.ncbi.nlm.nih.gov/21298889/).
 18. Mizbah K, Gerlach N, Maal TJ, et al. The clinical relevance of bifid and trifid mandibular canals. *Oral Maxillofac Surg.* 2012; 16(1): 147–151, doi: [10.1007/s10006-011-0278-5](https://doi.org/10.1007/s10006-011-0278-5), indexed in Pubmed: [21698363](https://pubmed.ncbi.nlm.nih.gov/21698363/).
 19. Naitoh M, Hiraiwa Y, Aimiya H, et al. Observation of bifid mandibular canal using cone-beam computerized tomography. *Int J Oral Maxillofac Implants.* 2009; 24(1): 155–159, indexed in Pubmed: [19344041](https://pubmed.ncbi.nlm.nih.gov/19344041/).
 20. Ngeow WC, Chai WL, Ngeow WC, et al. The clinical anatomy of accessory mandibular canal in dentistry. *Clin Anat.* 2020; 33(8): 1214–1227, doi: [10.1002/ca.23567](https://doi.org/10.1002/ca.23567), indexed in Pubmed: [31943382](https://pubmed.ncbi.nlm.nih.gov/31943382/).
 21. Nikzad S, Azari A, Sabouri S. Double mandibular foramina and canal: report of a case with interactive CT-based planning software. *Iran J Radiol.* 2008; 5: 83–86.
 22. Nortjé CJ, Farman AG, Grotepass FW. Variations in the normal anatomy of the inferior dental (mandibular) canal: a retrospective study of panoramic radiographs from 3612 routine dental patients. *Br J Oral Surg.* 1977; 15(1): 55–63, doi: [10.1016/0007-117x\(77\)90008-7](https://doi.org/10.1016/0007-117x(77)90008-7), indexed in Pubmed: [268217](https://pubmed.ncbi.nlm.nih.gov/268217/).
 23. Nortjé CJ, Farman AG, de V Joubert JJ. The radiographic appearance of the inferior dental canal: an additional variation. *Br J Oral Surg.* 1977; 15(2): 171–172, doi: [10.1016/0007-117x\(77\)90050-6](https://doi.org/10.1016/0007-117x(77)90050-6), indexed in Pubmed: [271020](https://pubmed.ncbi.nlm.nih.gov/271020/).
 24. Okumuş Ö, Dumlu A. Prevalence of bifid mandibular canal according to gender, type and side. *J Dent Sci.* 2019; 14(2): 126–133, doi: [10.1016/j.jds.2019.03.009](https://doi.org/10.1016/j.jds.2019.03.009), indexed in Pubmed: [31210887](https://pubmed.ncbi.nlm.nih.gov/31210887/).
 25. Orhan K, Aksoy S, Bilecenoglu B, et al. Evaluation of bifid mandibular canals with cone-beam computed tomography in a Turkish adult population: a retrospective study. *Surg Radiol Anat.* 2011; 33(6): 501–507, doi: [10.1007/s00276-010-0761-y](https://doi.org/10.1007/s00276-010-0761-y), indexed in Pubmed: [21161224](https://pubmed.ncbi.nlm.nih.gov/21161224/).
 26. Patterson JE, Funke FW. Bifid inferior alveolar canal. *Oral Surg Oral Med Oral Pathol.* 1973; 36(2): 287–288, doi: [10.1016/0030-4220\(73\)90251-x](https://doi.org/10.1016/0030-4220(73)90251-x), indexed in Pubmed: [4515763](https://pubmed.ncbi.nlm.nih.gov/4515763/).
 27. Rashsuren O, Choi JW, Han WJ, et al. Assessment of bifid and trifid mandibular canals using cone-beam computed tomography. *Imaging Sci Dent.* 2014; 44(3): 229–236, doi: [10.5624/isd.2014.44.3.229](https://doi.org/10.5624/isd.2014.44.3.229), indexed in Pubmed: [25279344](https://pubmed.ncbi.nlm.nih.gov/25279344/).
 28. Shen EC, Fu E, Fu MMJ, et al. Configuration and corticalization of the mandibular bifid canal in a Taiwanese adult population: a computed tomography study. *Int J Oral Maxillofac Implants.* 2014; 29(4): 893–897, doi: [10.11607/jomi.3435](https://doi.org/10.11607/jomi.3435), indexed in Pubmed: [25032769](https://pubmed.ncbi.nlm.nih.gov/25032769/).
 29. Wadhvani P, Mathur RM, Kohli M, et al. Mandibular canal variant: a case report. *J Oral Pathol Med.* 2008; 37(2): 122–124, doi: [10.1111/j.1600-0714.2007.00573.x](https://doi.org/10.1111/j.1600-0714.2007.00573.x), indexed in Pubmed: [18197857](https://pubmed.ncbi.nlm.nih.gov/18197857/).
 30. Yang X, Lyu C, Zou D. Bifid mandibular canals incidence and anatomical variations in the population of shanghai area by cone beam computed tomography. *J Comput Assist Tomogr.* 2017; 41(4): 535–540, doi: [10.1097/RCT.0000000000000561](https://doi.org/10.1097/RCT.0000000000000561), indexed in Pubmed: [28722697](https://pubmed.ncbi.nlm.nih.gov/28722697/).

Morphological classification and measurement of the glenoid cavity using three-dimensional reconstruction in a Chinese population

Y. Chen^{1*}, J. Xiong^{2*}, W. Chen^{1*}, D. Xie^{1*}, Y. Zhang¹, Y. Mo¹, X. Gu¹, L. Zhang^{3–6}

¹Department of Orthopaedics, Chinese and Western Medicine Hospital of Yibing, Yibing, China

²School of Clinical Medicine, Southwest Medical University, Luzhou, China

³Department of Orthopaedics, The Affiliated Traditional Chinese Medicine Hospital of Southwest Medical University, Luzhou, China

⁴Centre for Orthopaedic Diseases Research, Affiliated Traditional Chinese Medicine Hospital of Southwest Medical University, Luzhou, China

⁵Expert Workstation in Luzhou, Luzhou, China

⁶Clinical Base of Affiliated Traditional Chinese Medicine Hospital of Southwest Medical University, Guangdong Province Medical 3D Printing Application Transformation Engineering Technology Research Centre, Luzhou, China

[Received: 30 November 2021; Accepted: 3 February 2022; Early publication date: 17 February 2022]

Background: The purpose of this study was to examine the various shapes and record the morphometric data of the glenoid cavity in a Chinese population.

Materials and methods: A total of 501 scapulae, 247 left and 254 right, were analysed. We classified the shape of the glenoid cavity as type I (pear-shaped), type II (oval-shaped), type III (teardrop-shaped), type IV (calabash-shaped) or type V (inverted comma-shaped). Four defined parameters, the superior-inferior glenoid diameter (AB), upper anterior-posterior glenoid diameter (CD), lower anterior-posterior glenoid diameter (EF) and glenoid index (GI), were measured, and five shapes were classified via three-dimensional reconstruction.

Results: The mean AB, CD, EF and GI values of the glenoid were 3.51 ± 0.41 cm, 1.95 ± 0.28 cm, 2.60 ± 0.34 cm, and 1.35 ± 0.12 cm, respectively. The AB value of type II glenoid cavities was significantly smaller than that of type I and III glenoid cavities ($p < 0.05$), but the GI value of type II glenoid cavities was larger than that of type III cavities ($p < 0.05$). The CD value showed a difference between type I and type III glenoid cavities ($p < 0.05$). For the EF parameter, the values of type III glenoid cavities were significantly larger than those of type I and II glenoid cavities ($p < 0.05$).

Conclusions: Measuring and observing the variety of shapes and sizes of the glenoid cavity in Chinese people is conducive to for better understand its morphological features. This information can also guide surgeons in the design and selection of suitable prostheses for total shoulder arthroplasty in the Chinese population in order to reduce postoperative complications. (Folia Morphol 2023; 82, 2: 325–331)

Key words: glenoid cavity, anatomic variation, classification, morphology, three-dimensional reconstruction, glenoid notch

Address for correspondence: Dr. X. Gu, Department of Orthopaedics, Chinese and Western Medicine Hospital of Yibing, e-mail: nxgkx123@163.com; Dr. L. Zhang, Affiliated Traditional Chinese Medicine Hospital of Southwest Medical University, Luzhou, China, 646000, e-mail: zhanglei870722@126.com

*These authors contributed equally to this work. Y. Chen, J. Xiong, W. Chen, D. Xie are the co-first authors.

This article is available in open access under Creative Common Attribution-Non-Commercial-No Derivatives 4.0 International (CC BY-NC-ND 4.0) license, allowing to download articles and share them with others as long as they credit the authors and the publisher, but without permission to change them in any way or use them commercially.

INTRODUCTION

The shoulder joint, which consists of the eminence of the humerus and the glenoid cavity of the scapula, is one of the most flexible but unstable joints of the human body. Once the shoulder joint or scapula is damaged, the glenoid cavity might become injured as well. Hence, the diagnosis and treatment of many shoulder diseases are related to the glenoid cavity. Numerous studies have established that understanding the anatomical characteristics of the glenoid cavity is conducive to choosing the proper therapies for shoulder dislocation, scapular fractures and glenohumeral arthritis [7–9, 20] and especially for improving the surgical treatment for Bankart injury or anterior shoulder dislocation [13]. The morphology of the glenoid cavity should be considered when selecting the ideal anchor insertion angle for a Bankart repair [10]. The morphological structure of the glenoid cavity affects some common shoulder operative methods, such as total shoulder arthroplasty, in addition to associated diseases [1, 11, 14, 16]. This structure can guide orthopaedic surgeons to ensure the appropriate shape and size, as well as the individual placement of prosthetic components [23]. Therefore, it is important to investigate the anatomical morphology of the glenoid cavity in clinical practice.

To date, many papers have documented the anatomical characteristics and physiology of the glenoid cavity. Mamatha et al. [15] reported several anatomical parameters used to define the shape and dimensions of the glenoid cavity that were beneficial for designing glenoid prostheses in the South Indian population. Rajput et al. [20] not only described the anatomy of the glenoid cavity but also created a classification based on its shape. In terms of the classification, most of the traditional anatomical standards have described the shape of the glenoid cavity as pear-shaped, round, or oval or as having an inverted comma shape. Then, some researchers incorporated the glenoid notch into one criterion for categorization [12, 19]. Prescher and Klumpen [19] explained how this notch would influence the shape of the glenoid cavity. They indicated that when the notch was present, the shape could be described as pear- or inverted-comma-shaped. When the notch was absent, the cavity was round or oval in shape. However, in general, most studies describing the morphological classification of the glenoid cavity have only focused on a single point, such as observing the glenoid notch, or have merely measured the anatomical parameters. Few studies have combined anatomical measurements and the glenoid notch to

form the glenoid cavity, which can completely and quantitatively identify the certain morphology. Moreover, no studies have reported the morphological classification among Chinese people.

This study was performed to define a new morphological classification of the glenoid cavity in the Chinese population using three-dimensional (3D) reconstruction in order to better manage and promote relevant knowledge of shoulder diseases and surgical techniques.

MATERIALS AND METHODS

Patients

A total of 501 patients who underwent computed tomography (CT) scans of the unilateral shoulder in the period from 2017 to 2020 at the Department of Orthopaedics, Chinese and Western Medicine Hospital of Yibing were identified (mean age 49.04 ± 16.13 years). This study strictly adhered to the inclusion criteria and exclusion criteria. The study included 254 patients with scans of the right side (mean age 49.05 ± 16.30 years, 114 females and 140 males), and the remaining patients had scans of the left side (mean age 49.02 ± 15.99 years, 110 females and 137 males), with no significant difference in between the left and right side. Inclusion criteria: (1) The glenoid cavity was clear on each scan. Only normal CT images were used. (2) The basic information and imaging data were complete. Exclusion criteria: (1) Any patient with a history of posterior or multidirectional instability, prior surgery, or glenohumeral arthritis. (2) Patients who had contraindications for CT.

3D reconstruction of the scapula

All measurements were carried out at the Radiology Department of the Department of Orthopaedics, Chinese and Western Medicine Hospital of Yibing. A spiral CT scanner (Somatom Emotion; Siemens AG, Munich, Germany) was used, with a scanning voltage of 120 kV, tube current of 120 mAs, and pitch of 0.8. Then, scanned images with 0.75-mm thickness were reconstructed, with a reconstruction interval of 0.75 mm. Next, 3D reconstructions were generated after CT scanning by the Glenosys software (Imascap; Brest; France) which is an automated segmentation process [3]. All 3D images were stored in the Picture Archiving Communication System (PACS; DJ Health Union Systems Corporation, Shanghai, China).

Measurement of the glenoid cavity

After acquiring the 3D reconstruction models, measurements were made by 2 researchers, also re-

ferred to as observers, who had been engaged in the field of radiology for more than 3 years. These researchers independently obtained measurements, and each measurement was repeated 3 times; next, an average of the three values was obtained. In the case of any differences in the results, a third medical practitioner was consulted.

Using the 3D reconstructed scapulae, three experienced researchers used the Glensys software to manually extract the contour of the glenoid articular surface and points. This software could automatically recognise the morphological structure of the proximal humerus, scapula and glenoid. The superior point (highest point on the glenoid articular surface) and the inferior point (lowest point on the glenoid articular surface) were chosen by the Glensys software programme. Based on these extracted points, the glenoid articular surface was defined for each scapula. The first scapular coordinate system was defined by a centre and three orthogonal vectors. The centre (centre of gravity of the glenoid articular surface) was automatically calculated. The three vectors were the vertical axis formed by the intersection of the scapula plane and the glenoid plane (oriented from lower to upper), the sagittal axis oriented back to front and perpendicular to the scapular plane, and the frontal axis oriented medial to lateral and perpendicular to the other two vectors. The second scapular coordinate system was similar to the first system. However, two vectors, the frontal axis oriented medial to lateral and perpendicular to the glenoid plane and the sagittal axis oriented back to front and perpendicular to the other two vectors were different. The scapular coordinate system was used to calculate height, width, height at max width and best-fit sphere by the Glensys software programme.

The following parameters were defined and measured (accurate to 0.1 mm) in the 3D reconstruction models (Fig. 1):

- A: the most prominent point on the upper edge of the glenoid cavity;
- B: the lowest point of the glenoid cavity;
- C: in the upper part of the glenoid cavity, the posterior intersection of the longest line perpendicular to the line defining AB and the glenoid rim;
- D: in the upper part of the glenoid cavity, the anterior intersection of the longest line perpendicular to the line defining AB and the glenoid rim;
- E: in the lower part of the glenoid cavity, the posterior intersection of the longest line perpendicular to the line defining AB and the glenoid rim;

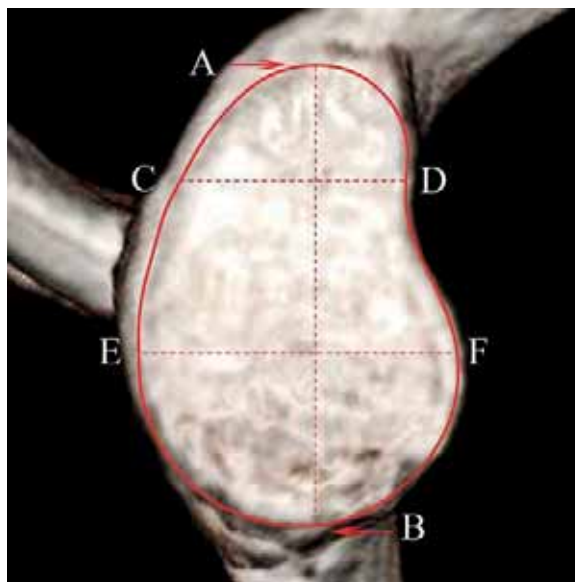


Figure 1. Schematic diagram showing diameters of the glenoid cavity. AB — represents the superior-inferior glenoid diameter; CD — represents the upper anterior-posterior glenoid diameter; EF — represents the lower anterior-posterior glenoid diameter.

- F: in the lower part of the glenoid cavity, the anterior intersection of the longest line perpendicular to the line defining AB and the glenoid rim;
- AB: represents the superior-inferior glenoid diameter (the line formed by A points connected to B points);
- CD: represents the upper anterior-posterior glenoid diameter (the line formed by C points connected to D points);
- EF: represents the lower anterior-posterior glenoid diameter (the line formed by E points connected to F points);
- GI: represents the height-to-width ratio of the glenoid cavity (the ratio of AB to EF).

Compliance with ethical standards

All procedures were allowed by Department of Orthopaedics, Chinese and Western Medicine Hospital of Yibing with the following reference number: KY2020056.

Statistical analysis

All data were collected based on body side, sex and morphology. Morphological data are presented as the mean \pm standard deviation (SD). Statistical analysis was performed using SPSS 20.0 software (IBM Corp, Armonk, NY, USA). The significance level was set at $p = 0.05$.

Statistically significant differences in body side and sex were assessed using independent sample

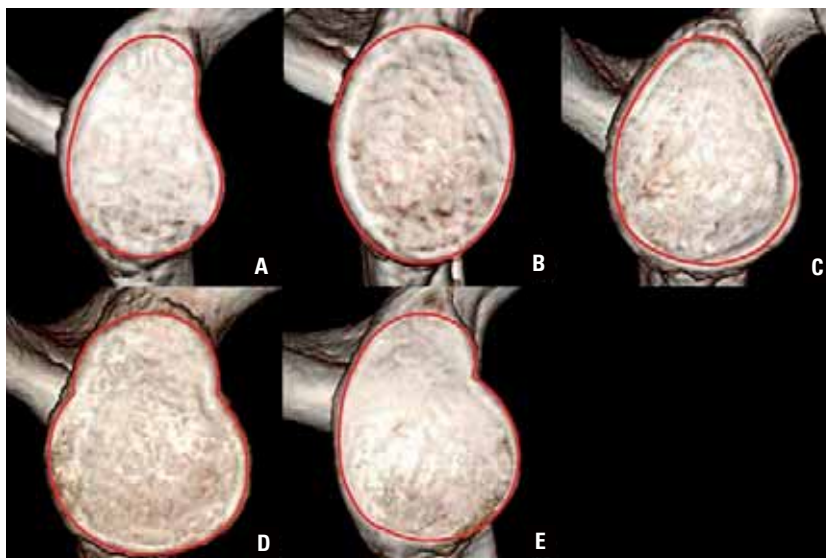


Figure 2. Classification of glenoid cavity; **A.** Type I is pear shaped; **B.** Type II means is oval shaped; **C.** Type III is teardrop shaped; **D.** Type IV is calabash shaped; **E.** Type V is inverted comma shaped.

t-tests and Chi-square tests. Two-way ANOVA and Games-Howell tests were applied to analyse differences in the anatomic parameters of the glenoid cavity among sides, sexes and classifications.

RESULTS

Morphological classification of the glenoid cavity

The glenoid morphology was classified into five types based on the anatomical measurements and the shapes identified in previous literature; the shape was determined by the slightly raised rim of the glenoid cavity (Fig. 2).

According to a previous study, two criteria were used for this classification: one was the presence of the glenoid notch (located approximately somewhat above the middle of the anterior margin of the cavity) and the other was the comparison of the diameters of the upper and lower parts of the glenoid cavity (CD and EF). In addition, according to Prescher and Klumpen [19], we recognised different types of notches were identified. The specific definitions of the five types are as follows:

- type I: pear-shaped glenoid cavities (CD was less than EF, with a shallow notch at the anterior glenoid rim of the upper part of the glenoid cavity);
- type II: oval-shaped glenoid cavities (CD was approximately equal to EF, without a notch);
- type III: teardrop-shaped glenoid cavities (CD was less than EF, without a notch);
- type IV: calabash-shaped glenoid cavities (CD was less than EF, with two notches at the anterior and

posterior glenoid rims of the upper part of the glenoid cavity);

- type V: inverted-comma-shaped glenoid cavities (CD was less than EF, with a prominent notch at the anterior glenoid rim of the upper part of the glenoid cavity).

Of the 501 patients, 53.29% exhibited type I; 24.15% exhibited type II and type III, type IV and type V were exhibited by 17.96%, 2.60% and 2.00%, respectively. The incidence of type I (pear-shaped) cavities was the highest (53.29%) among the total sample ($n = 501$), while the incidence of type IV (inverted-comma-shaped) was the lowest (2.00%). There was no significant difference with regard to body side or sex ($p > 0.05$). The constituent ratios of the classifications by body side and sex are displayed in Table 1.

Morphological parameters of the glenoid cavity

The parameters obtained were not significantly different in terms of body side, except for the average CD value (the right side was 1.99 ± 0.28 cm, and the left side was 1.91 ± 0.28 cm, $p = 0.001$). The significance of the mean values by sex was not surprising; all the average values, except for the glenoid index (GI) value, were larger in males than in females ($p = 0.000$).

Moreover, the parameters exhibited apparent differences among various glenoid cavity types. The AB and EF values of type II cavities (3.40 ± 0.45 cm; 2.50 ± 0.38 cm) were the shortest when compared to the other four types, but the GI value (1.37 ± 0.40 cm) was the longest. A statistically significant differ-

Table 1. Sample size and constituent ratio of the glenoid cavity based on classification [n (%)]

Classification	Side		Gender		Total
	Right ^a	Left	Male ^b	Female	
Type I	133 (52.36%)	134 (54.25%)	144 (51.99%)	123 (54.91%)	267 (53.29%)
Type II	69 (27.17%)	52 (21.05%)	65 (23.47%)	56 (25.00%)	121 (24.15%)
Type III	43 (16.93%)	47 (19.03%)	55 (19.85%)	35 (15.63%)	90 (17.96%)
Type IV	4 (1.57%)	9 (3.64%)	7 (2.52%)	6 (2.68%)	13 (2.60%)
Type V	5 (1.97%)	5 (2.03%)	6 (2.17%)	4 (1.78%)	10 (2.00%)

^aP > 0.05 vs. left, ^bP > 0.05 vs. female

Table 2. Mean values of the glenoid diameters (mean ± standard deviation)

Parameters		AB [cm]	CD [cm]	EF [cm]	GI [cm]
Side	Right	3.53 ± 0.39	1.99 ± 0.28 ^a	2.62 ± 0.33	1.35 ± 0.11
	Left	3.49 ± 0.43	1.91 ± 0.28	2.58 ± 0.34	1.36 ± 0.12
	P	0.298	0.001	0.25	0.772
Gender	Male	3.71 ± 0.38 ^b	2.06 ± 0.26 ^b	2.76 ± 0.31 ^b	1.35 ± 0.12
	Female	3.25 ± 0.28	1.81 ± 0.23	2.40 ± 0.25	1.36 ± 0.11
	P	0.000	0.000	0.000	0.270
Classification	Type I	3.52 ± 0.40 ^c	1.92 ± 0.29 ^d	2.61 ± 0.33 ^{cd}	1.36 ± 0.40
	Type II	3.40 ± 0.45	1.96 ± 0.30	2.50 ± 0.38	1.37 ± 0.12
	Type III	3.60 ± 0.36 ^c	2.02 ± 0.23	2.72 ± 0.26 ^c	1.33 ± 0.10 ^c
	Type IV	3.46 ± 0.29	1.89 ± 0.23	2.60 ± 0.37	1.34 ± 0.13
	Type V	3.68 ± 0.37 ^c	1.87 ± 0.23	2.71 ± 0.34	1.36 ± 0.09
Total		3.51 ± 0.41	1.95 ± 0.28	2.60 ± 0.34	1.35 ± 0.12

^aP < 0.05 vs. right; ^bP < 0.001 vs. female; ^cP < 0.05 vs. type II; ^dP < 0.05 vs. type III; AB — superior-inferior glenoid diameter; CD — upper anterior-posterior glenoid diameter; EF — lower anterior-posterior glenoid diameter; GI — glenoid index

ence was found between type II and type III cavities (p = 0.005). The average CD value of type III cavities (2.02 ± 0.23 cm) was greater than that of type I cavities (1.92 ± 0.29 cm), which was considered statistically significant (p = 0.005) (Table 2).

DISCUSSION

This study analysed the morphological features of the glenoid cavity using some defined anatomical parameters and five types of shapes to reveal the physiological characteristics of the glenoid cavity in the Chinese population. In particular, we found the calabash shape to be a new classification, which illustrates the differences between Chinese people and other populations. This is an improvement from previous studies in which similar measurements were made in other populations. On the one hand, when assessing a variety of shoulder diseases involving the glenoid cavity, our results can assist surgeons in formulating the appropriate treatment for native patients. The glenoid cavity has variations which

means that some compensational mechanism must exist. However, the biomechanical mechanisms and anatomical parameters probably provide this compensation [5]. For total shoulder arthroplasty in the Chinese population, the calabash shape of the glenoid cavity may have to be taken into consideration when designing and fitting components.

Shoulder instability is a common problem in the general population and can be caused by multiple factors, including damage or dysfunction of the glenohumeral articulation, labrum, and glenohumeral ligaments [22]. The glenoid cavity is one of the most critical parts of the shoulder joint. Prescher and Klumpen [19] proposed that the shape of the glenoid cavity impacts the attachment of the glenoid labrum. Furthermore, the design and placement of prostheses are related to the anatomic parameters of the glenoid cavity, such as its height, width, and shape [21]. Therefore, it is important to accurately understand the morphological classification and morphometrical data of the glenoid cavity.

Various studies have classified the glenoid cavity based on the presence of a notch in the anterior rim of the glenoid cavity. Anetzberger and Putz [2] divided the glenoid cavity into teardrop-shaped (types Ia and Ib, with and without a notch) and elongated oval-shaped (type II) cavities, but descriptions of these shapes are rare. Prescher and Klumpen [19] classified the glenoid cavity as pear-shaped (55%) (type I with a distinct glenoid notch and type 2 with a slight notch) and oval-shaped (45%) cavities. Subsequently, a glenoid cavity with a distinct notch and an inverted-comma shaped was proposed separately. A majority of studies classified the shape of the glenoid cavity as pear-shaped, inverted-comma-shaped or oval-shaped cavity [2, 15, 20]. However, we found that there still existed another shape existed, a calabash-shaped cavity, in addition to the four shapes mentioned above. The key point for distinguishing this type of shape is the difference between it and common shapes. With common shape, a notch is either present or absent in the anterior rim of the glenoid cavity, while calabash-shaped cavities have two notches in the anterior and posterior glenoid rims.

The five types of glenoid cavities that our study described are based on the Chinese population. Type I (pear-shaped) cavities exhibited the maximum frequency of 53.29% in all cases, but type IV (inverted comma-shaped) cavities exhibited the minimum frequency of 2.00%. In terms of other populations, many studies have also shown that pear-shaped cavities are the most common [4, 6, 19]. However, Mamatha et al. [15] and Rajput et al. [20] who studied the Indian population, proposed that oval-shaped glenoid cavities oval in shape occurred less frequently than those with other shapes, which was different from the results of our study. Nevertheless, the types of glenoid cavities in the Egyptian population according to El-Din and Ali [6] were consistent with the types found in our study. Additionally, we analysed the average values of the glenoid cavity in terms of body side and sex. According to our results, the values of the right glenoid cavity, except for the CD value were higher than those of the left glenoid cavity, but the difference was not statistically significant ($p = 0.250$); this finding shows that the size of the right glenoid cavity is likely similar to that of the left glenoid cavity. The average values of both the right and left glenoid cavities were larger in our study than in the studies by Mamatha et al. [15] and Rajput et al. [20] but were smaller than the results of El-Din and Ali [6]. In addition, the significance of the mean values in terms of sex was similar to that of other

studies; all measurements except the GI value were larger in males than in females. We also considered the mean values of the glenoid cavity among the different classifications and found that the AB value was the shortest in type II but the GI value was the largest among the other four types. A statistically significant difference was only found between type II and type III glenoid cavities. Owens et al. [18] found that tall and thin glenoid cavities were associated with a higher risk of anterior instability than short and wide glenoid cavities, indicating that type II glenoid cavities might more frequently lead to anterior instability more frequently than type III glenoid cavities. For type III glenoid cavities, the CD value was the largest and the EF value was the widest among the five types. These differences indicate that the shape and size of the glenoid cavity are associated with geographic region and race, and that understanding these features is conducive to the individualisation of surgical treatment.

The present study provides a comprehensive classification of the glenoid cavity in the Chinese population. One of the main contributions of the study is the proposal of a new classification in terms of the calabash shape. To our knowledge, many studies have focused on glenoid classifications in different populations, but few have focused on glenoid classifications in the Chinese population. Furthermore, previous studies have mostly used dry specimens, which are smaller in size, have an unknown sex and have a higher number of defects [2, 15], to investigate the glenoid classification of the glenoid cavity, and these factors may influence the conclusion. Thus, to solve these problems, our study included a large samples size ($n = 501$) and used CT scans in order to reduce the experimental error caused by an insufficient sample size. In addition, knowledge of the sex of the included patients was beneficial for analysing sex differences. Moreover, use of 3D reconstruction in research can accurately reflect the actual anatomy of the glenoid cavity [17].

Limitations of the study

This study has some limitations. Osteoarthritic glenoid cavities were not examined, and thus, the ideal prosthesis size was not determined. In addition, the height of the patients was not recorded, which is associated to the dimensions of the scapula. Although 3D models were reconstructed, these parameters were only measured on 2D images. Descriptive parameters were researched but the variability and seek for volumes or forms were not shown.

CONCLUSIONS

By measuring and observing the shape of the glenoid cavity in Chinese people, the present study divided the shape into five types, including a new classification of calabash-shaped cavity. These anatomical parameters and classifications will help to better understand the morphological features of the glenoid, design and select suitable prostheses for total shoulder arthroplasty in the Chinese population.

Acknowledgements

The authors would like to thank all patients who agreed to participate in this study and the Department of Orthopaedics, Chinese and Western Medicine Hospital of Yibing for providing the PACS CT system.

Funding

This study was supported by Yibin Scientific Research and Technology Bureau Project, grant number 2020SF005; Yibin Municipal Health Commission Research Project, grant number 2020YW007.

Conflict of interest: None declared

REFERENCES

- Alentorn-Geli E, Samitier G, Torrens C, et al. Reverse shoulder arthroplasty. Part 2: Systematic review of reoperations, revisions, problems, and complications. *Int J Shoulder Surg.* 2015; 9(2): 60–67, doi: [10.4103/0973-6042.154771](https://doi.org/10.4103/0973-6042.154771), indexed in Pubmed: [25937717](https://pubmed.ncbi.nlm.nih.gov/25937717/).
- Anetzberger H, Putz R. The scapula: principles of construction and stress. *Acta Anat (Basel).* 1997; 156(1): 70–80, doi: [10.1159/000147830](https://doi.org/10.1159/000147830), indexed in Pubmed: [8960301](https://pubmed.ncbi.nlm.nih.gov/8960301/).
- Boileau P, Gauci MO, Wagner ER, et al. The reverse shoulder arthroplasty angle: a new measurement of glenoid inclination for reverse shoulder arthroplasty. *J Shoulder Elbow Surg.* 2019; 28(7): 1281–1290, doi: [10.1016/j.jse.2018.11.074](https://doi.org/10.1016/j.jse.2018.11.074), indexed in Pubmed: [30935825](https://pubmed.ncbi.nlm.nih.gov/30935825/).
- Checroun AJ, Hawkins C, Kummer FJ, et al. Fit of current glenoid component designs: an anatomic cadaver study. *J Shoulder Elbow Surg.* 2002; 11(6): 614–617, doi: [10.1067/mse.2002.126099](https://doi.org/10.1067/mse.2002.126099), indexed in Pubmed: [12469089](https://pubmed.ncbi.nlm.nih.gov/12469089/).
- De Wilde LF. CORR Insights®: The Muscle Cross-sectional Area on MRI of the Shoulder Can Predict Muscle Volume: An MRI Study in Cadavers. *Clin Orthop Relat Res.* 2020; 478(4): 884–885, doi: [10.1097/CORR.0000000000001103](https://doi.org/10.1097/CORR.0000000000001103), indexed in Pubmed: [31860547](https://pubmed.ncbi.nlm.nih.gov/31860547/).
- El-Din WA, Ali MH. A morphometric study of the patterns and variations of the acromion and glenoid cavity of the scapulae in Egyptian population. *J Clin Diagn Res.* 2015; 9(8): AC08–AC11, doi: [10.7860/JCDR/2015/14362.6386](https://doi.org/10.7860/JCDR/2015/14362.6386), indexed in Pubmed: [26435934](https://pubmed.ncbi.nlm.nih.gov/26435934/).
- Friedman RJ, Hawthorne KB, Genes BM. The use of computerized tomography in the measurement of glenoid version. *J Bone Joint Surg Am.* 1992; 74(7): 1032–1037, indexed in Pubmed: [1522089](https://pubmed.ncbi.nlm.nih.gov/1522089/).
- Fulin P, Kysilko M, Pokorny D, et al. Study of the variability of scapular inclination and the glenoid version — considerations for preoperative planning: clinical-radiological study. *BMC Musculoskelet Disord.* 2017; 18(1): 16, doi: [10.1186/s12891-016-1381-4](https://doi.org/10.1186/s12891-016-1381-4), indexed in Pubmed: [28088244](https://pubmed.ncbi.nlm.nih.gov/28088244/).
- Gilbert F, Eden L, Meffert R, et al. Intra- and interobserver reliability of glenoid fracture classifications by Ideberg, Euler and AO. *BMC Musculoskelet Disord.* 2018; 19(1): 89, doi: [10.1186/s12891-018-2016-8](https://doi.org/10.1186/s12891-018-2016-8), indexed in Pubmed: [29580228](https://pubmed.ncbi.nlm.nih.gov/29580228/).
- Grieshaber JA, Palmer JE, Kim H, et al. Comparison of curved and straight anchor insertion for bankart repair. *Orthopedics.* 2019; 42(2): e242–e246, doi: [10.3928/01477447-20190125-04](https://doi.org/10.3928/01477447-20190125-04), indexed in Pubmed: [30707238](https://pubmed.ncbi.nlm.nih.gov/30707238/).
- Hawi N, Reinhold A, Suero EM, et al. The anatomic basis for the arthroscopic Latarjet procedure: a cadaveric study. *Am J Sports Med.* 2016; 44(2): 497–503, doi: [10.1177/0363546515614320](https://doi.org/10.1177/0363546515614320), indexed in Pubmed: [26657260](https://pubmed.ncbi.nlm.nih.gov/26657260/).
- Huber CE. Zur Form und Größe der Cavitas glenoidalis. *Anatomischer Anzeiger.* 1991; 172: 137–142.
- Klemm C, Toderita D, Nolte D, et al. The critical size of a defect in the glenoid causing anterior instability of the shoulder after a Bankart repair, under physiological joint loading. *Bone Joint J.* 2019; 101-B(1): 68–74, doi: [10.1302/0301-620X.101B1.BJJ-2018-0974.R1](https://doi.org/10.1302/0301-620X.101B1.BJJ-2018-0974.R1), indexed in Pubmed: [30601049](https://pubmed.ncbi.nlm.nih.gov/30601049/).
- Longo UG, Petrillo S, Berton A, et al. Reverse total shoulder arthroplasty for the management of fractures of the proximal humerus: a systematic review. *Musculoskelet Surg.* 2016; 100(2): 83–91, doi: [10.1007/s12306-016-0409-0](https://doi.org/10.1007/s12306-016-0409-0), indexed in Pubmed: [27316439](https://pubmed.ncbi.nlm.nih.gov/27316439/).
- Mamatha T, Pai SR, Murlimanju BV, et al. Morphometry of glenoid cavity. *Online J Health Allied Scs.* 2011; 10.
- Merkle TP, Beckmann N, Bruckner T, et al. Shoulder joint replacement can improve quality of life and outcome in patients with dysmelia: a case series. *BMC Musculoskelet Disord.* 2016; 17: 185, doi: [10.1186/s12891-016-1031-x](https://doi.org/10.1186/s12891-016-1031-x), indexed in Pubmed: [27117810](https://pubmed.ncbi.nlm.nih.gov/27117810/).
- Moineau G, Levigne C, Boileau P, et al. Three-dimensional measurement method of arthritic glenoid cavity morphology: feasibility and reproducibility. *Orthop Traumatol Surg Res.* 2012; 98(6 Suppl): S139–S145, doi: [10.1016/j.otsr.2012.06.007](https://doi.org/10.1016/j.otsr.2012.06.007), indexed in Pubmed: [22964089](https://pubmed.ncbi.nlm.nih.gov/22964089/).
- Owens BD, Campbell SE, Cameron KL. Risk factors for anterior glenohumeral instability. *Am J Sports Med.* 2014; 42(11): 2591–2596, doi: [10.1177/0363546514551149](https://doi.org/10.1177/0363546514551149), indexed in Pubmed: [25248922](https://pubmed.ncbi.nlm.nih.gov/25248922/).
- Prescher A, Klumpen T. The glenoid notch and its relation to the shape of the glenoid cavity of the scapula. *J Anat.* 1997; 190(Pt 3): 457–460, doi: [10.1046/j.1469-7580.1997.19030457.x](https://doi.org/10.1046/j.1469-7580.1997.19030457.x), indexed in Pubmed: [9147231](https://pubmed.ncbi.nlm.nih.gov/9147231/).
- Rajput HB, Vyas KK, Shroff BD. A study of morphological patterns of glenoid cavity of scapula. *National J Med Res.* 2012; 2: 504–507.
- Schrumpf M, Maak T, Hammoud S, et al. The glenoid in total shoulder arthroplasty. *Curr Rev Musculoskelet Med.* 2011; 4(4): 191–199, doi: [10.1007/s12178-011-9096-5](https://doi.org/10.1007/s12178-011-9096-5), indexed in Pubmed: [21826432](https://pubmed.ncbi.nlm.nih.gov/21826432/).
- Vezeridis PS, Ishmael CR, Jones KJ, et al. Glenohumeral dislocation arthropathy: etiology, diagnosis, and management. *J Am Acad Orthop Surg.* 2019; 27(7): 227–235, doi: [10.5435/JAAOS-D-17-00056](https://doi.org/10.5435/JAAOS-D-17-00056), indexed in Pubmed: [30278009](https://pubmed.ncbi.nlm.nih.gov/30278009/).
- Zumstein V, Kraljević M, Hoedel S, et al. The glenohumeral joint — a mismatching system? A morphological analysis of the cartilaginous and osseous curvature of the humeral head and the glenoid cavity. *J Orthop Surg Res.* 2014; 9: 34–39, doi: [10.1186/1749-799X-9-34](https://doi.org/10.1186/1749-799X-9-34), indexed in Pubmed: [24886613](https://pubmed.ncbi.nlm.nih.gov/24886613/).

Cavitation processes in a space filled with loose mesenchymal tissues: a comparison between the retrosternal space and the middle ear tympanic cavity in human fetuses

S. Hayashi¹ , J.H. Kim² , Z.-W. Jin³ , G. Murakami⁴ , J.F. Rodríguez-Vázquez⁵ , S. Abe⁶ 

¹Department of Anatomy, Division of Basic Medicine, Tokai University School of Medicine, Isehara, Japan

²Department of Anatomy, Jeonbuk National University Medical School, Jeonju, Korea

³Department of Anatomy, Wuxi School of Medicine, Jiangnan University, Wuxi, Jiangsu, China

⁴Division of Internal Medicine, Cupid Clinic, Iwamizawa, Japan

⁵Department of Anatomy and Embryology, School of Medicine, Complutense University, Madrid, Spain

⁶Department of Anatomy, Tokyo Dental College, Tokyo, Japan

[Received: 5 January 2022; Accepted: 28 February 2022; Early publication date: 8 March 2022]

Background: During the expansion of the pleural cavity in early fetuses, a thick sheet of loose mesenchymal tissue (SLMT) appears between the lung bud and body wall. Subsequently, the growing lung bud invades into the SLMT and the latter becomes fragmented to disappear. To compare this with the tympanic cavity filled with loose mesenchymal tissues, the present study aimed to demonstrate the development, establishment, and breaking of the SLMT in the retrosternal space.

Materials and methods: Although the retrosternal tissue was almost absent or very thin at 7 weeks, the SLMT appeared behind the manubrium sterni at 8 weeks. Accordingly, at 9–10 weeks, cavitation occurred in the SLMT to expand the pleural cavity. Therefore, the volume of SLMT was not determined by the adjacent structures such as the pericardium and sternum. Likewise, mesenchymal tissues filling the middle ear disappeared after 26 weeks.

Results: There were considerable individual variations in the timing of beginning and location of the tympanic cavitation. However, in contrast to the retrosternal SLMT, the volume of the future tympanic cavity is determined by the adjacent hard tissue and tympanic membrane much earlier than the cavitation. The mesenchymal tissue carried abundant vessels in the middle ear but none or few veins in the retrosternal SLMT.

Conclusions: The concept that the lung bud invades into the splanchnic mesoderm to expand the pleural cavity seems oversimplified. Mechanical stresses from the pleural cavity might induce retrosternal cavitation, while a loss in blood supply might cause tympanic cavitation. (Folia Morphol 2023; 82, 2: 332–338)

Key words: cavitation, retrosternal space, pleural cavity, middle ear, tympanic cavity, human fetuses

Address for correspondence: S. Hayashi, MD, PhD, Department of Anatomy, Division of Basic Medical Science, Tokai University School of Medicine, 143 Shimokasuya, Isehara-shi, Kanagawa 259-1193, Japan, tel: +81-463-93-1121, fax: +81-463-93-1517, e-mail: sho5-884@umin.ac.jp

This article is available in open access under Creative Common Attribution-Non-Commercial-No Derivatives 4.0 International (CC BY-NC-ND 4.0) license, allowing to download articles and share them with others as long as they credit the authors and the publisher, but without permission to change them in any way or use them commercially.

INTRODUCTION

According to Gray's Anatomy [4], pleural cavity expansion is related to lung growth and invasion into the splanchnic mesoderm. However, a previous study [7] showed that the process of the pleural expansion is not simple; during the early development of the lung (at 5–6 weeks or stages of 11–23 mm crown-rump length [CRL]), morphology changes drastically in and along the inner aspect of the lateral and posterior thoracic wall. First, the lung bud attaches to the rib, intercostal muscle, and mesonephros with no or little pleural space. A thick sheet of loose mesenchymal tissue (SLMT) then appears between the lung bud and body wall. Finally, the growing lung bud invades into the SLMT, causing fragmentation to disappearance of the SLMT. The coelomic mesothelium or initial pleura lines covers the SLMT in the second phase. Although transient, the SLMT is not a splanchnic mesoderm itself, but a highly derived structure. Furthermore, contrary to literature [11], the bilateral bottoms of the initial pleural cavity alongside the adrenal do not correspond to the pneumatointeric recess of the lesser sac [7].

Due to the large increase in the adrenal volume at 5–6 weeks, the transient appearance of the SLMT seemed difficult to be identified in the posterolateral thoracic cavity. In contrast, connective tissue growth of the anterior thoracic wall can be easily compared between the different stages. The lung anterior parts (segments III and VIII) extend anteriorly into a thin retrosternal space between the sternum and pericardium in early fetuses [3]. This study first aimed to clearly demonstrate the transient SLMT behind the sternum.

Cavitation in a space filled with loose mesenchymal tissues is not a limited morphology in the SLMT along the growing pleural cavity. It is well known that the ear ossicles and their joints are embedded in loose mesenchymal tissues. However, there might be no clear description of when the mesenchymal tissue disappears in the tympanic cavity. According to Bast and Anson [1, 2], restricted cavitation occurs near the tympanic membrane at 18–21 weeks, and the mesenchymal packing disappears except for recesses of the tympanic cavity by 24 weeks. However, Rodríguez-Vázquez et al. [14] showed that the mesenchymal tissues around the incudomalleolar joint disappear around 34 weeks. This study also aimed to revisit the tympanic cavitation and compare it with the retrosternal space. This comparison would provide better understanding of possible heterogeneity

in the cavitation process since, in contrast to the middle ear, the retrosternal space seems to have no definite marginal structures except for the sternum. This comparison would provide better understanding of possible heterogeneity in the cavitation process since, in contrast to the middle ear, the retrosternal space seems to have no definite marginal structures except for the sternum.

MATERIALS AND METHODS

The study was performed in accordance with the provisions of the Declaration of Helsinki 1995 (as revised in 2013). For observations of the retrosternal space, we used histological sections from 24 human fetuses (7–11 weeks; CRL, 25–61 mm); 10 fetuses of CRL 25–35 mm (7–9 weeks) and 14 fetuses of CRL 46–61 mm (10–11 weeks). Most sections (15 fetuses) were sagittal to visualise the entire length of the sternum. For observations of the tympanic cavitation, we used sagittal sections from 14 human fetus heads (16–37 weeks; CRL 125–310 mm) similar to that used in a recent study [12].

All the aforementioned sections (paraffin-embedded) were part of the large collection kept at the Department of Anatomy of the Universidad Complutense, Madrid, and the embryos were obtained from miscarriages and ectopic pregnancies from the Department of Obstetrics of the University. No information was available on the genetic background of the embryos and/or abortion. The sections were stained with haematoxylin and eosin, Azan or silver impregnation. This study was approved by the Ethics Committee of Complutense University (B08/374). Development of the sternum in early fetuses [13] and sagittal section morphology of the thoracic region [8, 9] are previously reported.

Most images of histology were taken with a Nikon Eclipse 80, whereas photographs at ultra-low magnification (objective lens $< 1\times$) were obtained using a high-grade flat scanner with translucent illumination (Epson scanner GTX970).

RESULTS

Observations of the retrosternal space and pleural cavity

The length and width of the retrosternal mesenchymal tissues are shown in sagittal (Figs. 1, 2) and horizontal (Fig. 3) sections, respectively. At 7 weeks, the retrosternal space or loose tissue was very thin and limited to bilateral sites around the

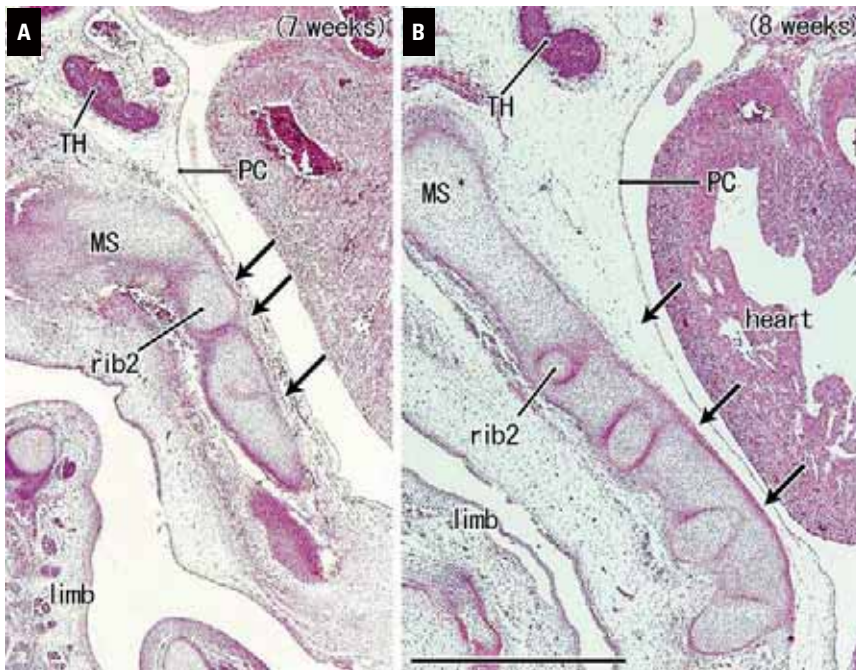


Figure 1. A, B. Retrosternal space observed in sagittal sections. Haematoxylin and eosin staining. Left side of the manubrium sterni (MS) and thymus (TH); **A.** A fetus of 28 mm crown-rump length (7 weeks); **B.** 35 mm crown-rump length (8 weeks). A thin tissue layer (arrows) is compressed between the sternum and pericardium (PC). These sections are medial to the course of the internal thoracic artery. Panels A and B were prepared at the same magnification (scale bar in panel B, 1 mm).

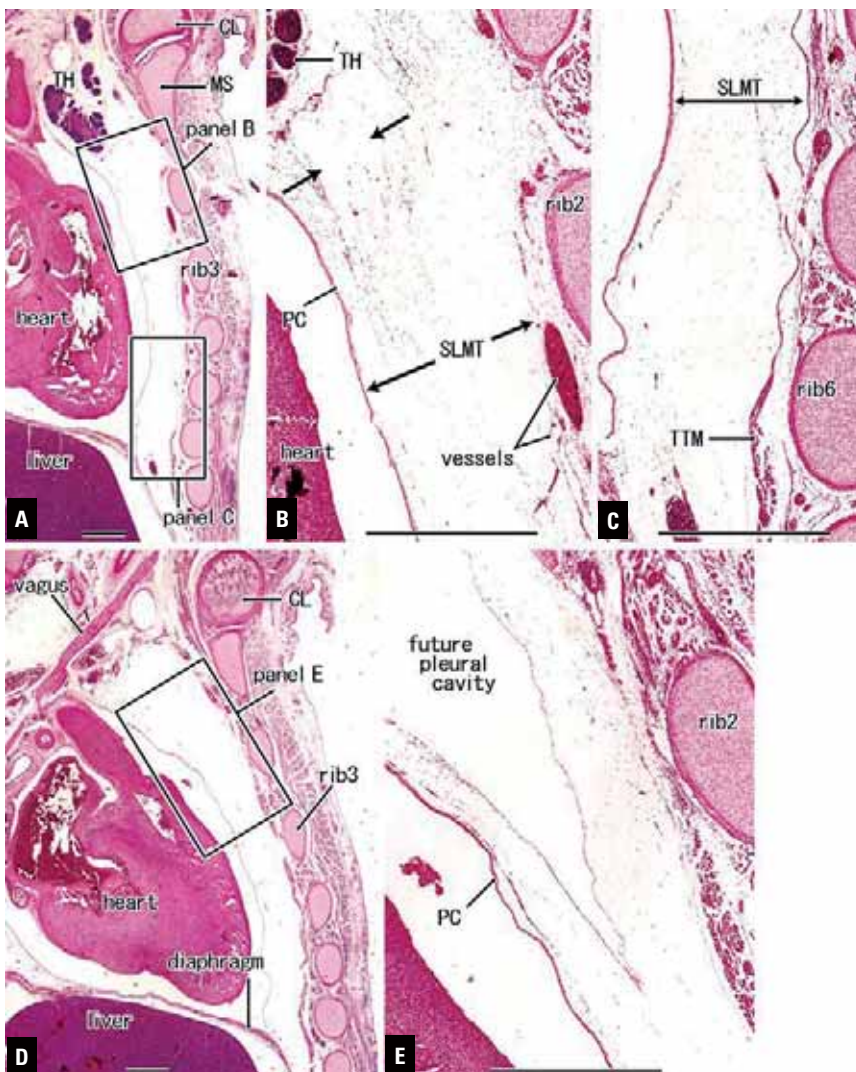


Figure 2. A–E. Thick mesenchymal tissues behind the sternum. Haematoxylin and eosin staining. A fetus of 59 mm crown-rump length (10 weeks). Sagittal sections containing the thymus (TH) and right sternoclavicular joint. Panel A is 0.6 mm medial to panel D. Panels B and C (or panel E) show higher magnification views of squares in panel A (or panel D). A thick sheet-like mesenchymal tissue (SMLT) is sandwiched between the rib and pericardium (PC). Arrows in panel B indicate a small space suggesting the cavitation for the future pleural cavity. Likewise, panel E exhibits a definite space enclosed by a fascia in the anterior side of the right vagus nerve (vagus); CL — clavicle; MS — manubrium sterni; TTM — transversus thoracic muscle. Panels A and D were prepared at the same magnification (all scale bars, 1 mm).

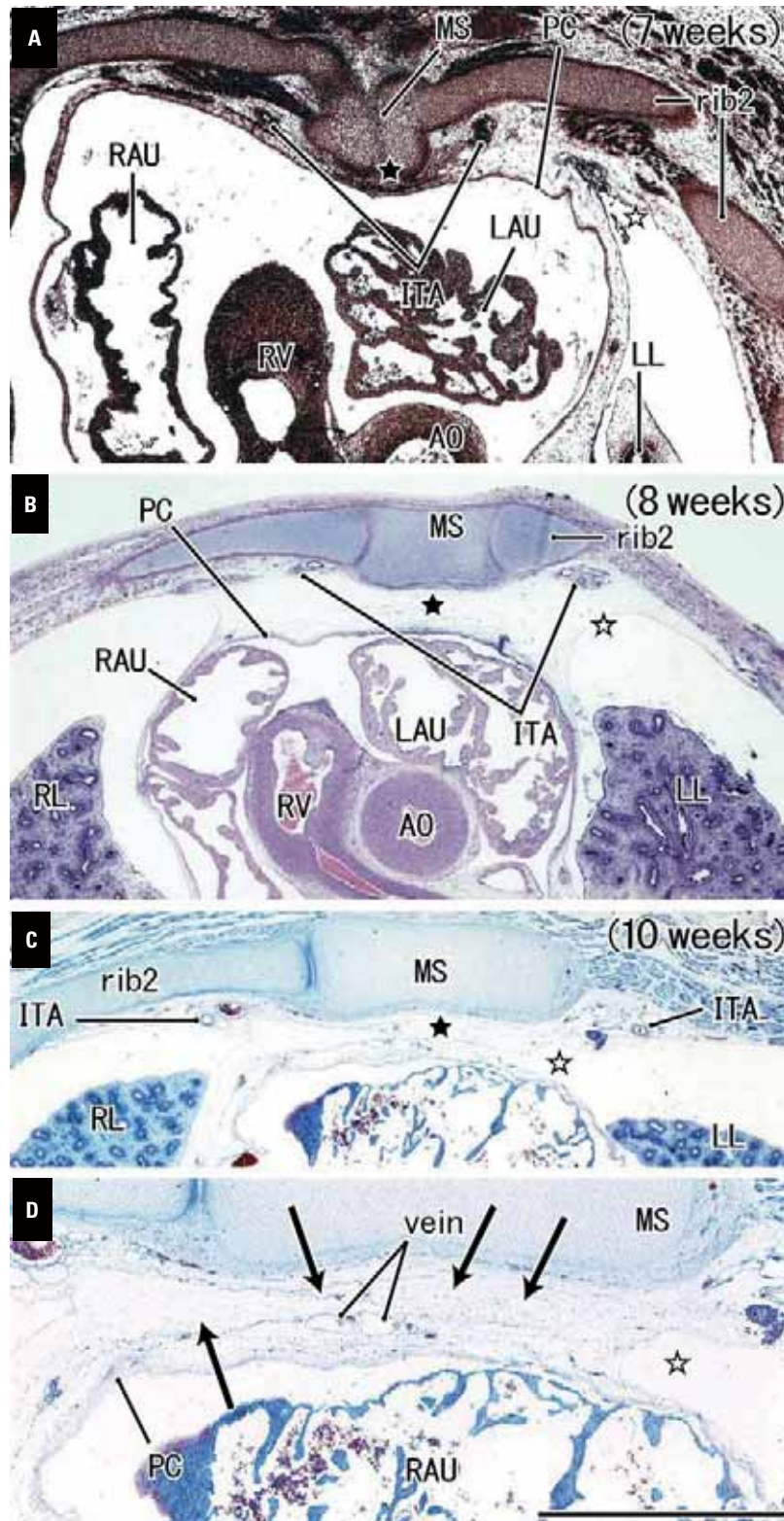


Figure 3. A–D. Change in thickness of the retrosternal mesenchymal tissue observed in horizontal sections at the level of the second rib. Panel A (silver impregnation), a fetus of 26 mm crown-rump length (7 weeks); panel B (haematoxylin and eosin staining), 35 mm crown-rump length (8 weeks); panels C and D (Azan staining), 64 mm crown-rump length (10 weeks). The mesenchymal tissue (black star) behind the manubrium sterni (MS) is thin in panel A, but thick in panels B and C. The anterior end of the left pleural cavity (open star) migrates medially from panel A to panel C. Panel D is a higher magnification view of the central part in panel C. In the retrosternal mesenchymal tissue, fasciae enclose four spaces suggesting the future cavity (arrows in panel D). Panels A–C were prepared at the same magnification (scale bars in panel A and D, 1 mm); AO — ascending aorta; ITA — internal thoracic artery; LL — left lung; PC — pericardium; RAU — right auricle; RL — right lung; RV — right ventricle.

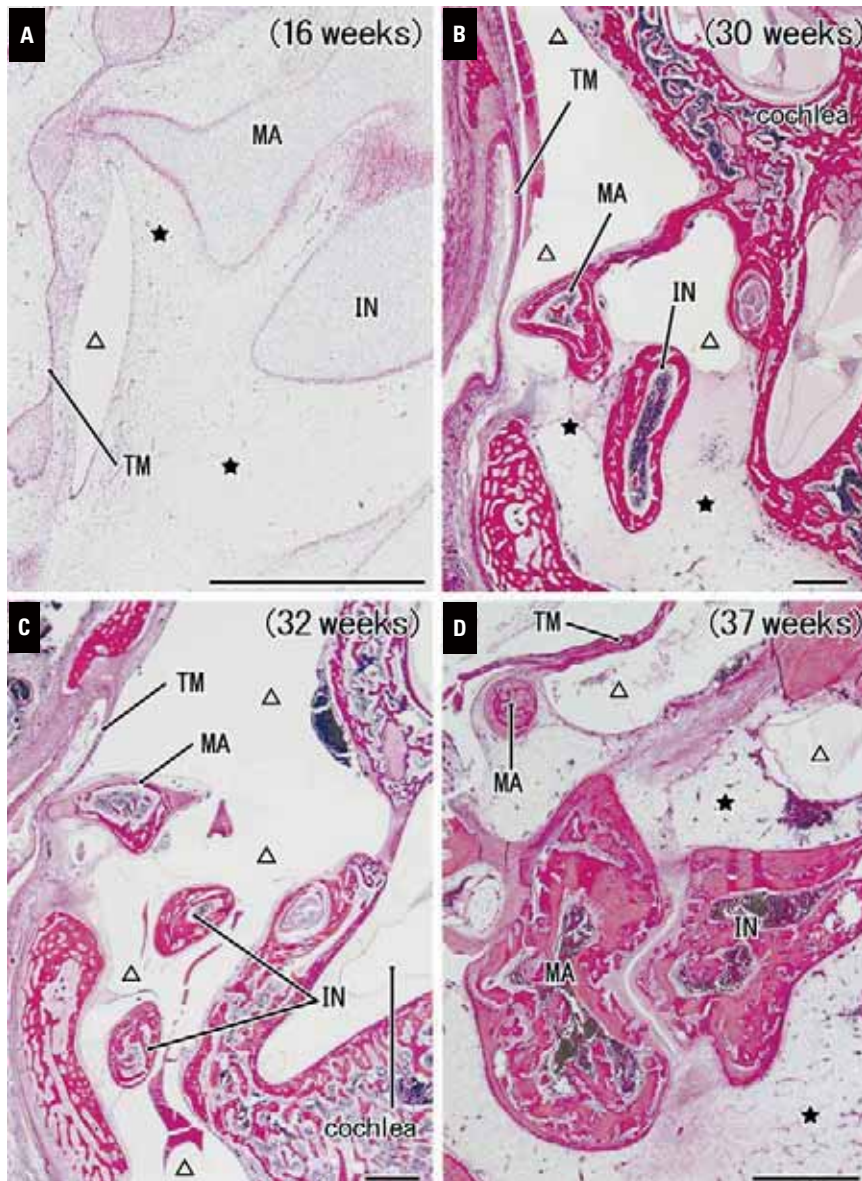


Figure 4. A–D. Cavitation in the middle ear for comparison with the retrosternal space. Haematoxylin and eosin staining. Panel A, a fetus of 125 mm crown-rump length (16 weeks); panel B, 256 mm crown-rump length (30 weeks); panel C, 272 mm crown-rump length (32 weeks); panel D, 310 mm (37 weeks). At 16 weeks, the middle ear is filled with mesenchymal tissues (stars) except for a slender cavity (triangle) near the tympanic membrane (TM). In panel B, the cavitation (triangles) reached half of the middle ear, but the presumed lateral recess is filled with mesenchymal tissues (stars). In panel C, the cavitation (triangles) reached most parts of the middle ear. In panel D showing the largest specimen in this figure, the malleus (MA) and incus (IN) are still embedded in mesenchymal tissues (stars). All scale bars, 1 mm.

internal thoracic vessels (Figs. 1A; 3A). Thus, the pericardium appeared attached to the sternum. The anterior end of the lung did not reach a site in the medial side of the right atrium. However, at 8 weeks (Figs. 1B; 3B), the retrosternal space was identified as the SLMT. The thickening of the SLMT most likely started at the upper site near the thymus and progressed to the lower site near the diaphragm. At 9–10 weeks (Figs. 2; 3C), a cavitation occurred in the upper and lateral parts of the SLMT and connected with the pleural cavity. The cavitation was identified as small or large, multiple fascial spaces (Figs. 2B, E; 3D). Simultaneously, the anterior end of the lung approached the sternum but it did not reach the SLMT or manubrium sterni. Therefore, the lung did not expel mesenchymal tissues of the SLMT from the retrosternal space. The

retrosternal SLMT rarely contained vessels except for the internal thoracic artery and vein. The pericardium was thick behind the sternum in contrast to the thin pleura at the anteromedial end.

Observation of a mesenchymal packing in the middle ear

The middle ear was filled with loose mesenchymal tissues except for a site near the tympanic membrane in 5 fetuses at 16–25 weeks (Fig. 4A). In a fetus of 210 mm CRL (26 weeks), the mesenchymal tissue was restricted to the lateral recess of the tympanic cavity. However, the residual 8 fetuses at 27–37 weeks exhibited variations; the cavitation finished at 32 weeks (Fig. 4C), while the incudomalleolar joint was embedded in the loose tissue at 37 weeks (Fig. 4D).

Furthermore, the lateral recess was filled with loose mesenchymal tissues (Fig. 4B), while the incudomalleolar joint tended to be surrounded by the loose tissue. The mesenchymal tissue contained abundant capillaries. The mesenchymal tissues in the middle ear were always delimited by the bones, cartilages, and tympanic membrane. Therefore, a shape of the future tympanic cavity was established much earlier than the cavitation.

DISCUSSION

It is well known that the proliferated epithelial cells temporally obliterate the lumen of the duodenum during cavitation or recanalization [6]. Similarly, even in late-term fetuses, the laryngeal cavity is temporally obliterated by the proliferated epithelial cells before recanalisation for switching of the airway [15]. In the duodenum and larynx, the outer margin of the proliferated epithelia is determined by the duodenal and laryngeal walls, respectively. The definite walls contain muscles and are delimited by the thick basal lamina. In both the middle ear and retrosternal space, the cavitation does not occur in the proliferated epithelial cell mass but occurs in a packing of loose mesenchymal tissues. Moreover, the process seemed to be significantly different between the middle ear and retrosternal space (see below).

Any margins of the future tympanic cavity, i.e., the bones, cartilages, and the tympanic membrane, were fully developed until the cavitation occurs. Thus, the shape of the future tympanic cavity was determined in the middle ear. Indeed, the retrosternal space was also determined by a space between the sternum and pericardium. Since the latter was not a hard tissue, the mesenchymal tissue or SLMT became drastically thick at 7–8 weeks, possibly due to a mechanical stress imposed by the anteriorly expanding lung. The thickness of the SLMT might be adjusted to the future thickness of the retrosternal pleural cavity. The mechanical stress might induce cell death in the SLMT to provide multiple fascial space inside. Therefore, the concept that the lung bud invades into the splanchnic mesoderm to expand the pleural cavity seems an oversimplification. In fact, the growing lung neither invades a thin mesenchymal tissue along the body wall nor the SLMT. Moreover, the interpretation that the lung determines the size of the SLMT also seems erroneous. The SLMT along the base of the lung was not as thick as that in the retrosternal space and the former receives an inferior edge of the pleura.

Hence, the size of the SLMT might not depend on the marginal shape and thickness of the pleural cavity.

Overall, before cavitation, the middle ear mesenchymal packing was delimited by hard tissues, whereas the SLMT had a variable size and shape depending on the stage. In contrast to the middle ear mesenchyme, none or few vessels developed in the SLMT; the former contributes to blood supply to the contents (ear ossicles and nerves), but the SLMT does not seem to have a role in blood supply except in the internal thoracic artery and vein. A mechanical stress from the expanding pleural cavity (not from the lung itself) might induce retrosternal cavitation, while blood supply loss might cause tympanic cavitation. The SLMT was somewhat similar to a mass of loose mesenchymal tissues around the developing kidney [5, 10]; however, the loose tissues led to the development of a thick renal fascia that surrounds the kidney. Therefore, the perirenal space was quite different from the pleural cavity in the development. Finally, the present study demonstrates a significant individual variation in the establishment of cavitation in the middle ear; the disappearance of the mesenchymal tissue packing was likely to be delayed after birth.

With or without definite marginal structures like bones or muscular walls, there seemed to be different triggers, processes and end-stage morphologies in the cavitation. Recent techniques to identify cell death would reveal a difference in signal transduction between the suggested two-types of triggers for cavitation: a mechanical stress in the retrosternal space and a possible ischaemia in the middle ear.

CONCLUSIONS

The concept that the lung bud invades into the splanchnic mesoderm to expand the pleural cavity seems oversimplified. Mechanical stresses from the pleural cavity might induce retrosternal cavitation, while a loss in blood supply might cause tympanic cavitation.

Conflict of interest: None declared

REFERENCES

1. Bast TH, Anson BJ. The development of the cochlear fenestra, fossula and secondary tympanic membrane. *Q Bull Northwest Univ Med Sch.* 1952; 26(4): 344–373, indexed in Pubmed: [13004246](#).
2. Bast TH, Anson BJ. *The temporal bone and the ear.* 3rd ed. Charles C Thomas, Springfield 1949.
3. Cai P, You Y, Jin ZW, et al. Three-dimensional analysis of the segmental arrangement of lower lung lobes in

- human fetuses: is this arrangement a miniature version of adult morphology? *J Anat.* 2020; 236(6): 1021–1034, doi: [10.1111/joa.13157](https://doi.org/10.1111/joa.13157), indexed in Pubmed: [32023665](https://pubmed.ncbi.nlm.nih.gov/32023665/).
4. Collins P. Development of the trachea, lungs and diaphragm. In: Gray's Anatomy. Standring S eds. 39th ed. Elsevier Churchill Livingstone, London 2005: 1092–1093.
 5. Fukuoka K, Wilting J, Rodríguez-Vázquez JF, et al. The embryonic ascent of the kidney revisited. *Anat Rec.* 2019; 302(2): 278–287, doi: [10.1002/ar.23930](https://doi.org/10.1002/ar.23930), indexed in Pubmed: [30290083](https://pubmed.ncbi.nlm.nih.gov/30290083/).
 6. Hamilton WJ, Mossman HW. Hamilton's human embryology. 4th ed. Williams & Wilkins, London 1976.
 7. Hayashi S, Fukuzawa Y, Rodríguez-Vázquez JF, et al. Pleuroperitoneal canal closure and the fetal adrenal gland. *Anat Rec.* 2011; 294(4): 633–644, doi: [10.1002/ar.21351](https://doi.org/10.1002/ar.21351), indexed in Pubmed: [21370493](https://pubmed.ncbi.nlm.nih.gov/21370493/).
 8. Jin ZW, Yamamoto M, Kim JH, et al. Changes in topographical relation between the ductus arteriosus and left subclavian artery in human embryos: a study using serial sagittal sections. *Folia Morphol.* 2019; 78(4): 720–728, doi: [10.5603/FM.a2019.0028](https://doi.org/10.5603/FM.a2019.0028), indexed in Pubmed: [30835337](https://pubmed.ncbi.nlm.nih.gov/30835337/).
 9. Kim JiH, Hwang SiE, Rodríguez-Vázquez JF, et al. Upper terminal of the inferior vena cava and development of the heart atriums: a study using human embryos. *Anat Cell Biol.* 2014; 47(4): 236–243, doi: [10.5115/acb.2014.47.4.236](https://doi.org/10.5115/acb.2014.47.4.236), indexed in Pubmed: [25548721](https://pubmed.ncbi.nlm.nih.gov/25548721/).
 10. Matsubara A, Murakami G, Niikura H, et al. Development of the human retroperitoneal fasciae. *Cells Tissues Organs.* 2009; 190(5): 286–296, doi: [10.1159/000209231](https://doi.org/10.1159/000209231), indexed in Pubmed: [19321993](https://pubmed.ncbi.nlm.nih.gov/19321993/).
 11. O'Rahilly R, Müller F. Human embryology and teratology. 2nd ed. Wiley-Liss, New York 1996: 246–251.
 12. Rodríguez-Vázquez JF, Iglesias-Moreno MC, Poch A, et al. Fetal development and growth of the fissula ante fenestram in the human ear. *Anat Rec.* 2022; 305(2): 424–435, doi: [10.1002/ar.24711](https://doi.org/10.1002/ar.24711), indexed in Pubmed: [34240820](https://pubmed.ncbi.nlm.nih.gov/34240820/).
 13. Rodríguez-Vázquez JF, Verdugo-López S, Garrido JM, et al. Morphogenesis of the manubrium of sternum in human embryos: a new concept. *Anat Rec.* 2013; 296(2): 279–289, doi: [10.1002/ar.22623](https://doi.org/10.1002/ar.22623), indexed in Pubmed: [23165944](https://pubmed.ncbi.nlm.nih.gov/23165944/).
 14. Rodríguez-Vázquez JF, Yamamoto M, Kim JiH, et al. The incudopetrosal joint of the human middle ear: a transient morphology in fetuses. *J Anat.* 2020; 237(1): 176–187, doi: [10.1111/joa.13181](https://doi.org/10.1111/joa.13181), indexed in Pubmed: [32159229](https://pubmed.ncbi.nlm.nih.gov/32159229/).
 15. Yamamoto M, Honkura Y, Rodríguez-Vázquez JF, et al. Switching of the laryngeal cavity from the respiratory diverticulum to the vestibular recess: a study using serial sagittal sections of human embryos and fetuses. *J Voice.* 2016; 30(3): 263–271, doi: [10.1016/j.jvoice.2015.05.003](https://doi.org/10.1016/j.jvoice.2015.05.003), indexed in Pubmed: [26154762](https://pubmed.ncbi.nlm.nih.gov/26154762/).

Morphometric variants of the paranasal sinuses in a Mexican population: expected changes according to age and gender

N.G. Jasso-Ramírez^{1*}, R.E. Elizondo-Omaña^{1*}, J.L. Treviño-González², A. Quiroga-Garza^{1,3}, I.A. Garza-Rico⁴, K. Aguilar-Morales¹, G. Elizondo-Riojas⁴, S. Guzmán-López¹

¹Universidad Autónoma de Nuevo León, School of Medicine, Human Anatomy Department, Monterrey, Nuevo León, Mexico

²Universidad Autónoma de Nuevo León, University Hospital “Dr. José Eleuterio González”, Otorhinolaryngology Department, Monterrey, Nuevo León, Mexico

³Intituto Mexicano del Seguro Social, Delegación de Nuevo León, General Sugery, Monterrey, Nuevo León, Mexico

⁴Universidad Autónoma de Nuevo León, University Hospital “Dr. José Eleuterio González”, Radiology and Imaging Department, Monterrey, Nuevo León, Mexico

[Received: 18 January 2022; Accepted: 12 March 2022; Early publication date: 29 March 2022]

Background: There are developmental variations in the paranasal sinuses. Our objective was to determine their dimensions and volume stratified by age and sex and define the expected growth pattern.

Materials and methods: A retrospective, observational study was performed including computed tomography (CT) of patients between 1 and 20 years of age. The volumes of the frontal, sphenoid, and maxillary sinuses were obtained.

Results: A total of 210 CT were included with a mean age of 10 ± 6.1 years, 106 (50.5%) were female. Groups were categorised in ranges of 5 years. Spearman correlation coefficients between the right and left sides were 0.843, 0.711, 0.916 for the frontal, sphenoid and maxillary sinuses. Post-hoc for the categorical age groups demonstrated statistically significant differences with values of $p < 0.01$, except between age groups 11–15 against ≥ 16 years of age ($p = 0.8$). Gender-related differences were evident with a higher air volume in girls in the 5–10-year-old group, while boys predominated in the rest of the groups.

Conclusions: Computed tomography is ideal for pre-surgical sinus assessment. The maximum volume of paranasal sinuses is reached at the age of 15. There is a clear volumetric difference between age and gender groups. There is a direct relationship between a volume and its contralateral counterpart. (Folia Morphol 2023; 82, 2: 339–345)

Key words: paranasal sinuses, paediatrics, morphology, age groups, gender

Address for correspondence: J.L. Treviño-González, MD, or S. Guzman-Lopez, MD, PhD, Departamento de Otorinolarinología, Hospital Universitario “Dr. Jose E. Gonzalez”, Universidad Autónoma de Nuevo León, Francisco I. Madero and Jose E. Gonzalez sin número, Colonia Mitras Centro Monterrey, Nuevo León, México, 64460, tel: +52 8183332917, e-mail: jose.trevinog@uanl.mx or dr.santos.anato@gmail.com

*Both authors participated equally in the study, and are both in the position of first author.

This article is available in open access under Creative Common Attribution-Non-Commercial-No Derivatives 4.0 International (CC BY-NC-ND 4.0) license, allowing to download articles and share them with others as long as they credit the authors and the publisher, but without permission to change them in any way or use them commercially.

INTRODUCTION

The paranasal sinuses (PNS) are hollow cavities lodged inside the facial bones. The size of the sinuses is variable and depends particularly on the age and gender of the individual [28]. Their function is controversial [18]. Most believe the PNS support respiratory function and resonance, however, because they constitute the largest viscerocranial cavity, the air space it occupies is the most important anatomical feature [17, 19].

Sadler reports the frontal sinus does not develop before the age of 3, but reaches its maximum development between the ages of 4 and 8 years and continues its growth until 14–16 years [29]. The ethmoidal sinus has a faster development in the anterior ethmoid region and a complete development around 12 years of age with increased convexity of its lateral and middle walls in the last phases [34]. The sphenoid sinus begins to be pneumatized around the age of 2, progresses anterior-posteriorly around the age of 5, and completes its development at the age of 15 in half of the cases, with the other half continuing until the age of 30 [43]. The maxillary sinus initially grows in a transverse pattern (> 2 years of age) and then vertically (0–2 years and 7–10 years) reaching the level of the nasal passages, the nasolacrimal duct, and the zygomatic recess at the age of 12 [33, 43]. All sinuses are usually asymmetrical to their contralateral pair [29].

Knowledge of the variations in the development of the PNS is a clinically relevant issue [37]. Genetic diseases, environmental conditions, and infections can affect its structure and variations [6, 10, 35, 40]. Understanding age-related changes in their dimensions and volume can aid in radiographs and computed tomography (CT) assessment for the identification of pathology [20, 21, 35]. Examples include hypoplasia (incomplete development) and sinus atelectasis (known as silent sinus syndrome, which is a rare finding in general but found in the majority of patients with orbital floor fracture [38], usually seen on CT as an opacified sinus with retraction of its walls towards light and associated loss of volume [31]. For these instances, it is helpful to have normal range values and clinical morphometric parameters in the diagnostic approach of pathologies such as sinusitis or sinus dysmorphism [3]. Morphometric parameters are also important in the preoperative evaluation for functional endoscopic sinus surgery (FESS) as this procedure can jeopardize the anatomical variations of vital structures adjacent to the sinuses [3, 27].

Currently, nasosinus endoscopic surgery has become the surgical procedure of choice to resolve chronic and recurrent nasosinus inflammatory pathologies that do not respond to medical treatment. These minimally invasive techniques allow clear visualization of the sinuses and successful surgical treatment [11, 12, 42].

Previous studies have calculated PNS volume using dry skulls [1], cadaveric specimens [39], CT images [32, 44], and magnetic resonance imaging [21]. The use of CT scan instead of simple radiography for PNS evaluation was introduced by Zinreich et al. [44] in 1987.

Due to the craniofacial variations between populations, our objective is to establish morphometric parameters stratified by age and gender in our population as a guide for endoscopic surgery and a reference for a specific pathology approach.

MATERIALS AND METHODS

A retrospective, descriptive, observational, and cross-sectional study was performed. PNS morphometrics were obtained from CTs of patients between 0 and 20 years of age, from the database of the Radiology and Imaging Department of the University Hospital. Exclusion criteria included those patients with injury or pathology of the PNS or a history of PNS surgery. CTs with poor technical quality were eliminated.

The images were acquired using a helical tomography (Light Speed Plus CT, GE Medical Systems) with collimation of 0.625 mm, a table speed of 15.0 mm per second, a cutting interval of 1.25 mm parallel to the temporal bone with 50 mA and 120 kV and a 512 × 512 matrix. Volume operations were performed with multiplanar reformatting using Centricity Universal Viewer. The studies were assessed separately by two expert head and neck radiologists.

Bilateral measurements were made for frontal, sphenoid, and maxillary sinuses' volume (Figs. 1–3). Data were registered in a database and stratified by age, gender, and laterality. Age groups were categorised in ranges of 5 years of age. Patients less than 1-year-old were included quantifiable as 0 years.

Statistical analysis

The database was analysed using the SPSS statistical package version 20 programme (IBM, Armonk, NY, USA), for Windows 7. Normality tests were applied with Kolmogorov-Smirnoff and for each of the



Figure 1. Three-dimensional reconstruction of aerial structures of the skull of a 4-year-old patient. Scale with marks for each centimetre.

groups, the mean \pm standard deviation for each measurement parameter was determined independently. The Mann-Whitney U test was used to determine the significance of the differences between men and women for each morphometric parameter. Kruskal-Wallis tests were performed to compare the results of each measurement parameter for the different age groups, interpreting a value of $p \leq 0.05$ as significant. The results are presented in Tables 1 and 2.

Ethical considerations

The study was previously reviewed and approved by the University's Ethics and Research Committees, receiving the registration number AH16-00005, making sure it adheres to the Helsinki declaration and national and international standards of research. The

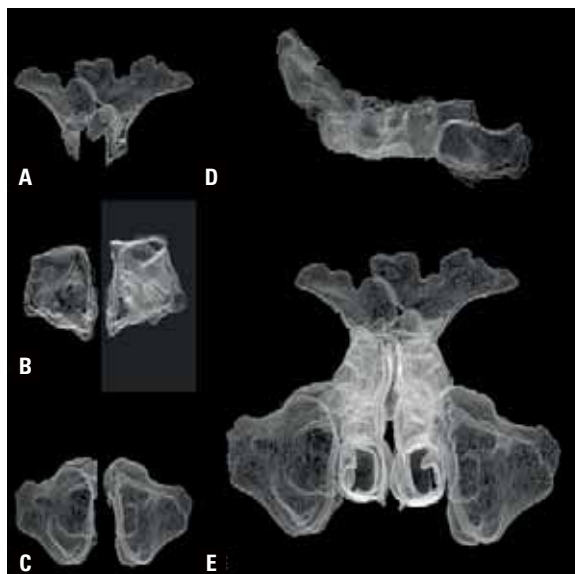


Figure 3. Aerial reconstruction of paranasal sinuses; **A.** Frontal sinuses; **B.** Sphenoidal sinuses; **C.** Maxillary sinuses; **D.** Lateral view of frontal, ethmoidal cells and sphenoidal sinuses (left to right); **E.** Anterior view of frontal sinuses, ethmoidal cells, maxillary sinuses, and nasal turbinates. All images correspond to a fully grown young woman of 18 years of age. Scale with marks for each centimetre.

authors declare no financial or commercial gain for the realisation of this study. Also, the authors declare no conflict of interest. None of the imaging studies were performed for the purposes of this study.

RESULTS

A total of 210 axial head and neck CT scans were included, with similar distribution in gender (104 [49.5%] male, 106 [50.5%] female). The mean age was 10 ± 6.06 years.

The mean volumes and lengths stratified by gender are reported in Table 1 and by age in Table 2. In

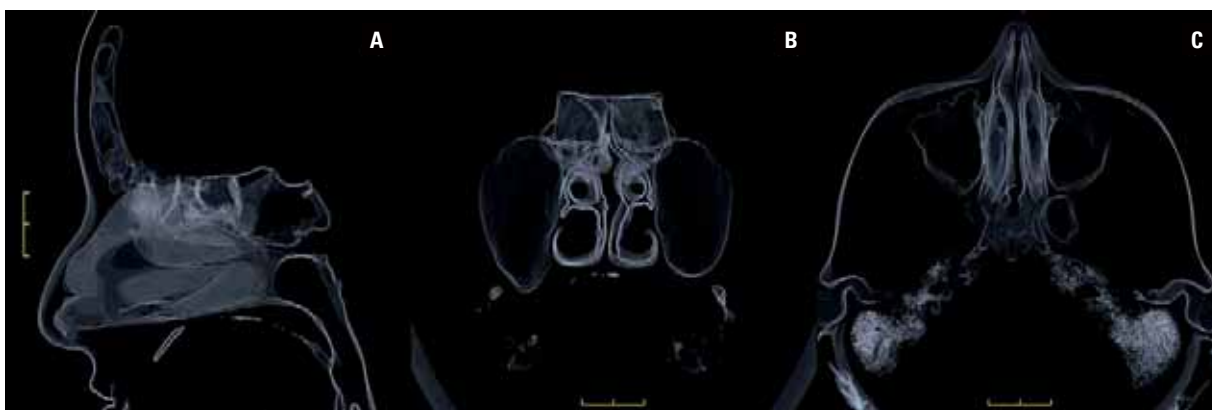


Figure 2. Three-dimensional reconstruction of paranasal sinuses of a 10-year-old patient; **A.** Lateral view in a sagittal slice; **B.** Frontal view with a coronal slice; **C.** Superior view in a transverse slice. Scale with marks for each centimetre.

Table 1. Paranasal sinuses morphometrics stratified by laterality and gender

Volume [cm ³]		Mean	Total (n = 210)	P-value	Males (n = 104)	Females (n = 106)	P-value
Frontal	Right	7.460	6.77 ± 6.70	0.0843	7.76 ± 7.49	5.80 ± 5.71	0.096
	Left		8.14 ± 10.82		8.81 ± 10.08	7.50 ± 11.52	0.243
Sphenoid	Right	8.796	8.38 ± 7.08	0.711	8.52 ± 7.39	8.25 ± 6.8	0.832
	Left		9.21 ± 8.58		9.81 ± 8.41	8.62 ± 8.74	0.181
Maxillary	Right	27.572	27.24 ± 13.79	0.916	28.73 ± 14.37	25.78 ± 13.11	0.179
	Left		27.90 ± 10.20		28.50 ± 14.62	27.31 ± 13.83	0.716

Values reported according to their parameter ± standard deviation. Statistical difference was obtained using the U Mann-Whitney between genders and a Spearman's correlation coefficient for laterality

Table 2. Difference between categorical age between the parameters of volume and length of the paranasal sinuses

Volume [cm ³]		Categorical age			
		< 5 (n = 60, 28.6%)	6–10 (n = 50, 23.8%)	11–15 (n = 50, 23.8%)	> 16 (n = 50, 23.8%)
Frontal	Right	0.79 ± 1.41	3.94 ± 3.30	10.18 ± 4.96	13.38 ± 6.75
	Left	1.14 ± 2.26	4.59 ± 4.37	12.22 ± 6.52	16.05 ± 16.68
Sphenoid	Right	2.65 ± 4.19	6.29 ± 4.69	11.19 ± 6.67	14.54 ± 5.93
	Left	2.84 ± 3.25	7.08 ± 5.84	13.34 ± 10.01	14.87 ± 7.91
Maxillary	Right	12.33 ± 7.66	23.88 ± 8.27	35.95 ± 9.50	39.80 ± 7.76
	Left	12.74 ± 7.84	23.82 ± 7.07	35.51 ± 9.09	42.57 ± 8.79

Values reported according to their parameter ± standard deviation. Statistical difference was obtained using the Kruskal-Wallis formula; All results were statistically significant (p < 0.001)

the post-hoc analysis for non-parametric tests for categorical age groups, all groups were statistically significant with values of p < 0.01, with the exception of the group aged 11 to 15 years with the group over 16 years of age. Significance among the volume means groups having a value of p > 0.8 in all the variables compared between the groups.

DISCUSSION

There has been a continued interest in the sinuses and nasal passages to correlate with the ideal approach for paranasal sinus surgery and surgical approach of associated structures. Computed tomographies are considered the gold standard for the evaluation of PNS due to the invasiveness of an endoscopic approach and its possible complications such as infection, bleeding, perforation, among others [15].

Although a higher time consumption was involved, for this study, manual segmentation was used to create three-dimensional models based on the aerial reconstruction of the PNS, to better identify and delimit each structure. This allows non-invasive visualisation, simulation, and precise quantitative measurements of internal body structures. The PNS

volumes are the most important index due to the large differences shown between the individuals [15].

Several authors (Table 3) have categorized their population using different age groups. Karakas and Kavakli [16] divided their population into 5-year age groups (total five groups) starting at the age of 5 years. Wolf et al. [43] evaluated the development of the sinuses in 102 cadaverous specimens and divided them into four age groups: newborn, 1 to 4 years old, 4 to 8 years old, and 8 to 12 years old. In this study ventrodorsal, cephalocaudal, and mediolateral length measurements were performed, however without differentiating between genders. The group of newborns showed anterior and posterior ethmoid cells almost completely developed in number and a spherical or pyramidal shape for the maxillary sinus. Lorkiewicz-Muszyńska et al. [21] studied their population individually by age and also reported the maxillary sinus was present at birth. They observed the ethmoidal and maxillary region expanding rapidly in the first few years, and similar to our results, they identified frontal and sphenoid sinuses pneumatization. Sadler described, frontal sinuses are always absent at birth, but evident in boys by the age of 2, and until the age of 4 in girls [29].

Table 3. Differences in paranasal sinuses volume between populations

Author, Year, Reference, Country	Imaging method	Sample size (men, women)	Gender	Age groups	Mean volume [cm ³] (men, women)		
					Maxillary	Frontal	Sphenoid
Ariji et al., 1993 [2] Japan	CT	230 (116, 114)	116	4–84	4.56	–	–
			114	6–96	4.76	–	–
Barghouth et al., 2002 [3] Switzerland	MRI	179 (103, 76)		< 1	0.14	–	0.01
				2	1.6	–	0.17
				4	4.1	–	0.57
				8	10.1	–	1.77
				12	17.1	–	3.44
			16	25.9	–	5.82	
Jun et al., 2005 [14] Korea	CT	173 (84, 89)	15 (11, 4)	0–10	8.94, 4.23	–	–
			26 (17, 9)	11–20	19.45, 9.06	–	–
			22 (8, 14)	21–30	2.40, 15.85	–	–
			25 (14, 11)	31–40	22.28, 13.97	–	–
			35 (15, 20)	41–50	18.39, 11.94	–	–
			17 (8, 9)	51–60	19.42, 13.32	–	–
			22 (9, 13)	61–70	14.29, 13.69	–	–
	11 (2, 9)	71–80	20.26, 12.03	–	–		
Karakas and Kavakli, 2005 [16] Turkey	CT	91 (47, 44)	18 (9, 9)	5–10	6.02, 6.81	1.19, 1.23	2.96, 3.14
			19 (10, 9)	11–15	11.17, 9.8	4.20, 1.75	5.40, 4.85
			17 (8, 8)	16–20	14.64, 14.03	7.57, 3.54	7.50, 5.43
			18 (10, 9)	21–25	15.98, 10.90	8.83, 3.51	9.68, 8.71
			19 (10, 9)	> 25	15.50, 11.33	8.41, 3.50	7.88, 1.14
Emirzeoglu et al., 2007 [9] Turkey	CT	77 (39, 38)	39	18–72	19.8	7.5	7.7
			38		16.0	4.1	6.1
Sahlstrand-Johnson et al., 2011 [30] Sweden	CT	60 (28, 32)	20	18–32	14.4	–	–
			20	33–49	16.6	–	–
			20	50–65	15.2	–	–
Masri et al., 2013 [23] Malaysia	CT	144		0–6	1.81, 2.81	–	–
				7–12	10.2, 9.26	–	–
				13–20	17.3, 13.5	–	–
				21–30	19.75, 14.5	–	–
Degermenci et al., 2016 [7] Turkey	CT*	361 (18, 180)	100 (50, 50)	< 5	3.23, 2.89	–	–
			100 (50, 50)	6–10	3.61, 7.18	–	–
			101 (51, 50)	11–15	11.03, 10.40	–	–
			60 (30, 30)	> 16	14.46, 12.58	–	–
Lorkiewicz-Muszyńska et al., 2015 [21] Poland	CT	170	40	0–4	1.97, 2.25	–	–
			30	4–8	5.48, 4.92	–	–
			100	8–17	12.15, 11.35	–	–
Marino et al., 2016 [22] USA	CT	20 (6, 14)	6,14	28–66	27.99	5.61	9.33
Cohen et al., 2018 [5] Israel	CT	201 (101, 100)	100 (50, 50)	25–64	15.7, 13.9	4.9, 3.7	3.7, 2.4
			100 (51, 50)	> 65	13.1, 10.5	3.8, 2.4	3.9, 2.5
Özer et al., 2018 [26] Turkey	CT	144 (89, 55)		–	–	–	10.24, 8.33
Jasso-Ramirez et al., 2020 Mexico	CT	210 (104, 106)	59 (28, 31)	< 5	14.12, 11.04	1.38, 0.56	3.59, 1.95
			51 (25, 26)	6–10	22.25, 25.45	3.55, 4.97	6.27, 7.08
			50 (26, 24)	11–15	36.72, 34.64	12.76, 9.50	13.15, 11.30
			50 (25, 25)	> 16	43.41, 38.95	16.21, 13.2	14.20, 15.18

*Ellipsoid formula vs. Stereological method; CT — computed tomography; MRI — magnetic resonance imaging; cm³ — cubic centimetres

Most studies focus on the maxillary sinuses, lacking data on the sphenoid and frontal sinuses. The sphenoid sinus is considered the most variable cavity in the human body and is of great relevance for optimal surgical access to the pituitary gland [36]. In addition, its' pneumatization may provide access to other parts of the skull base [41]. We report it present at birth, with a continued volume growth throughout all age groups. The degree and direction of pneumatization play a crucial role in the planning of surgical procedures.

According to Wolf et al. [43] at 8 years, pneumatization has progressed considerably and the nasal cavity and sinuses have almost completed their development and reached adult proportions. Karakas and Kavakli [16] reported the volume increased in both sexes up until the age of 25, then progressively decreased thereafter.

In the maxillary sinuses, we report maximum volumes reached at the age of 16–20, similar to that reported by Jun et al. [14] and Lorkiewicz-Muszyńska et al. [21]. Like the maxilla, the frontal sinus has also taken a tetrahedral shape and the sphenoid sinus has reached its permanent size, but its shape is still developing. We determine the greatest change in volume was between the ages of 11 and 15, a contrast to the results of Arijji et al. [2] who reported PNS volumes continued increasing until the age of 20 and then decreased. Similarly, Karakas and Kavakli [16] found the highest means for PNS volumes in the 21-to-25-year age group in men, and in the 16-to-20-year age group for the maxillary sinuses of women. Masri et al. [23] evaluated maxillary sinus and reported sizes and volume increased from birth until 30 years of age; men also exhibited larger maxillary sinus volume than women in 7–12 ($p < 0.01$) and 21–30 ($p < 0.01$) age groups. Size sexual dimorphism was evident in most age groups for the maxillary sinus.

Emirzeglou et al. [9] reported the PNS is typically larger in men than in women. Cohen et al. [5] also demonstrated larger sinus volumes for men. The means for adult PNS were 12.75cc, 4.00cc, and 2.92cc for the maxillary, sphenoid and frontal sinuses, respectively. These compare much smaller than our mean in a paediatric population with 27.57cc, 8.79cc, and 7.46cc, respectively for the same PNS (Table 3).

Laterality dysmorphism was not evident in the vertical, horizontal, and anteroposterior axes of our measurements. However, gender-related differences were evident in the 5-to-10-year-old group, in which

girls had higher volumes than boys. Other studies observed no statistically significant correlation between the measured volumes with age, gender, or side [2, 7, 9, 30]. In our categorical age groups, boys tended to have higher air volumes, agreeing with Cohen et al. [5] that the difference noted could not be solely explained by the general difference in skull size between genders, which has also been demonstrated in other studies [8, 24–26]. Marino et al. [22] consider the postnatal development of the frontal and sphenoid sinuses as a predisposing factor for greater variation in its development and final volumes.

It's important to evaluate the characteristics of the PNS, to correlate with rhinosinusitis diseases, and other bone defects [4, 6, 13]. Our study is the first to evaluate morphometrics in a Latino population, resulting in significantly higher volumes than other populations. However, it is limited by the lack of mastoid cells measurement due to the difficulty and inaccuracy when assessment.

CONCLUSIONS

The use of automated three-dimensional volume reconstructions is a precise tool for PNS morphometrics and accurate knowledge of their anatomy. The CT allows not only a full evaluation of the sinuses and the adjacent anatomical structures but also for the planning of the FESS.

Our results evidence higher volumes at a younger age, than reported in other populations. There is a clear volumetric difference with respect to categorized age groups and gender. The correlation between a volume and its contralateral counterpart is also demonstrated. Head and neck surgeons must consider the PNS differences in size and shape in paediatric patients, from those found in adults. It is important to understand that each age has a specific anatomical characteristic directly related to the development of the facial part of the skull and teething. The size and the disparity in the location of the floor of the nose and the floor of the maxillary sinus in children predispose them to more complications than expected in adults.

Conflict of interest: None declared

REFERENCES

1. Anagnostopoulou S, Venieratos D, Spyropoulos N. Classification of human maxillar sinuses according to their geometric features. *Anat Anz.* 1991; 173(3): 121–130, indexed in Pubmed: [1789468](#).
2. Arijji Y, Kuroki T, Moriguchi S, et al. Age changes in the volume of the human maxillary sinus: a study using computed tomography.

- Dentomaxillofac Radiol. 1994; 23(3): 163–168, doi: [10.1259/dmfr.23.3.7835518](https://doi.org/10.1259/dmfr.23.3.7835518), indexed in Pubmed: [7835518](https://pubmed.ncbi.nlm.nih.gov/7835518/).
3. Barghouth G, Prior JO, Lepori D, et al. Paranasal sinuses in children: size evaluation of maxillary, sphenoid, and frontal sinuses by magnetic resonance imaging and proposal of volume index percentile curves. *Eur Radiol.* 2002; 12(6): 1451–1458, doi: [10.1007/s00330-001-1218-9](https://doi.org/10.1007/s00330-001-1218-9), indexed in Pubmed: [12042953](https://pubmed.ncbi.nlm.nih.gov/12042953/).
 4. Beahm E, Teresi L, Lufkin R, et al. MR of the paranasal sinuses. *Surg Radiol Anat.* 1990; 12(3): 203–208, doi: [10.1007/BF01624524](https://doi.org/10.1007/BF01624524), indexed in Pubmed: [2287986](https://pubmed.ncbi.nlm.nih.gov/2287986/).
 5. Cohen O, Warman M, Fried M, et al. Volumetric analysis of the maxillary, sphenoid and frontal sinuses: A comparative computerized tomography based study. *Auris Nasus Larynx.* 2018; 45(1): 96–102, doi: [10.1016/j.anl.2017.03.003](https://doi.org/10.1016/j.anl.2017.03.003), indexed in Pubmed: [28341352](https://pubmed.ncbi.nlm.nih.gov/28341352/).
 6. de Oliveira AG, dos Santos Silveira O, Francio LA, et al. Anatomic variations of paranasal sinuses: clinical case report. *Surg Radiol Anat.* 2013; 35(6): 535–538, doi: [10.1007/s00276-012-1060-6](https://doi.org/10.1007/s00276-012-1060-6), indexed in Pubmed: [23262557](https://pubmed.ncbi.nlm.nih.gov/23262557/).
 7. Değermenci M, Ertekin T, Ülger H, et al. The age-related development of maxillary sinus in children. *J Craniofac Surg.* 2016; 27(1): e38–e44, doi: [10.1097/SCS.0000000000002304](https://doi.org/10.1097/SCS.0000000000002304), indexed in Pubmed: [26703070](https://pubmed.ncbi.nlm.nih.gov/26703070/).
 8. Elizondo-Omaña R, Muñoz-Leija M, Quiroga-Garza A, et al. Anatomical variations of the ethmoidal roof: differences between men and women. *FASEB J.* 2018; 32(S1), doi: [10.1096/fasebj.2018.32.1_supplement.515.1](https://doi.org/10.1096/fasebj.2018.32.1_supplement.515.1).
 9. Emirzeoglu M, Sahin B, Bilgic S, et al. Volumetric evaluation of the paranasal sinuses in normal subjects using computer tomography images: a stereological study. *Auris Nasus Larynx.* 2007; 34(2): 191–195, doi: [10.1016/j.anl.2006.09.003](https://doi.org/10.1016/j.anl.2006.09.003), indexed in Pubmed: [17084569](https://pubmed.ncbi.nlm.nih.gov/17084569/).
 10. Fahrioglu SL, Andaloro C. Anatomy, head and neck, sinus function and development. StatPearls Publishing 2018.
 11. Gencer ZK, Ozkırış M, Okur A, et al. The effect of nasal septal deviation on maxillary sinus volumes and development of maxillary sinusitis. *Eur Arch Otorhinolaryngol.* 2013; 270(12): 3069–3073, doi: [10.1007/s00405-013-2435-y](https://doi.org/10.1007/s00405-013-2435-y), indexed in Pubmed: [23512432](https://pubmed.ncbi.nlm.nih.gov/23512432/).
 12. Gunkel AR, Freysinger W, Thumfart WF. 3D anatomo-radiological basis of endoscopic surgery of the paranasal sinuses. *Surg Radiol Anat.* 1997; 19(1): 7–10, doi: [10.1007/BF01627727](https://doi.org/10.1007/BF01627727), indexed in Pubmed: [9060110](https://pubmed.ncbi.nlm.nih.gov/9060110/).
 13. Hernandez-Trejo AF, Cuellar-Calderon KP, Treviño-Gonzalez JL, et al. Prevalence of facial canal dehiscence and other bone defects by computed tomography. *Eur Arch Otorhinolaryngol.* 2020; 277(10): 2681–2686, doi: [10.1007/s00405-020-06013-8](https://doi.org/10.1007/s00405-020-06013-8), indexed in Pubmed: [32383094](https://pubmed.ncbi.nlm.nih.gov/32383094/).
 14. Jun BC, Song SW, Park CS, et al. The analysis of maxillary sinus aeration according to aging process; volume assessment by 3-dimensional reconstruction by high-resolution CT scanning. *Otolaryngol Head Neck Surg.* 2005; 132(3): 429–434, doi: [10.1016/j.otohns.2004.11.012](https://doi.org/10.1016/j.otohns.2004.11.012), indexed in Pubmed: [15746857](https://pubmed.ncbi.nlm.nih.gov/15746857/).
 15. Kapakin S. The paranasal sinuses: three-dimensional reconstruction, photo-realistic imaging, and virtual endoscopy. *Folia Morphol.* 2016; 75(3): 326–333, doi: [10.5603/FM.a2016.0006](https://doi.org/10.5603/FM.a2016.0006), indexed in Pubmed: [26916200](https://pubmed.ncbi.nlm.nih.gov/26916200/).
 16. Karakas S, Kavakli A. Morphometric examination of the paranasal sinuses and mastoid air cells using computed tomography. *Ann Saudi Med.* 2005; 25(1): 41–45, doi: [10.5144/0256-4947.2005.41](https://doi.org/10.5144/0256-4947.2005.41), indexed in Pubmed: [15822493](https://pubmed.ncbi.nlm.nih.gov/15822493/).
 17. Kwarai Y, Fukushima K, Ogawa T, et al. Volume quantification of healthy paranasal cavity by three-dimensional CT imaging. *Acta Oto-Laryngologica Suppl.* 1999; 119(540): 45–49, doi: [10.1080/00016489950181198](https://doi.org/10.1080/00016489950181198).
 18. Keir J. Why do we have paranasal sinuses? *J Laryngol Otol.* 2009; 123(1): 4–8, doi: [10.1017/S0022215108003976](https://doi.org/10.1017/S0022215108003976), indexed in Pubmed: [18957158](https://pubmed.ncbi.nlm.nih.gov/18957158/).
 19. Kubal WS. Sinonasal anatomy. *Neuroimaging Clin N Am.* 1998; 8(1): 143–156, indexed in Pubmed: [9449757](https://pubmed.ncbi.nlm.nih.gov/9449757/).
 20. Lee SJ. The relationship of the medial roof and the posterior wall of the maxillary sinus to the sphenoid sinus: a radiologic study. *Braz J Otorhinolaryngol.* 2017; 83(4): 375–380, doi: [10.1016/j.bjorl.2016.04.007](https://doi.org/10.1016/j.bjorl.2016.04.007), indexed in Pubmed: [27210820](https://pubmed.ncbi.nlm.nih.gov/27210820/).
 21. Lorkiewicz-Muszyńska D, Kociemba W, Rewekant A, et al. Development of the maxillary sinus from birth to age 18. Postnatal growth pattern. *Int J Pediatr Otorhinolaryngol.* 2015; 79(9): 1393–1400, doi: [10.1016/j.ijporl.2015.05.032](https://doi.org/10.1016/j.ijporl.2015.05.032), indexed in Pubmed: [26162781](https://pubmed.ncbi.nlm.nih.gov/26162781/).
 22. Marino MJ, Riley CA, Kessler RH, et al. Clinician assessment of paranasal sinus pneumatization is correlated with total sinus volume. *Int Forum Allergy Rhinol.* 2016; 6(10): 1088–1093, doi: [10.1002/alr.21779](https://doi.org/10.1002/alr.21779), indexed in Pubmed: [27159784](https://pubmed.ncbi.nlm.nih.gov/27159784/).
 23. Masri AA, Yusof A, Hassan RA. Three dimensional computed tomography (3D-CT): a study of maxillary sinus in malays. *Can J Basic Appl Sci.* 2013; 1(2): 125–134.
 24. Muñoz-Leija MA, Ordóñez Rivas FO, Barrera-Flores FJ, et al. A proposed extension to the elongated styloid process definition: A morphological study with high-resolution tomography computer. *Morphologie.* 2020; 104(345): 117–124, doi: [10.1016/j.morpho.2020.01.005](https://doi.org/10.1016/j.morpho.2020.01.005), indexed in Pubmed: [32070640](https://pubmed.ncbi.nlm.nih.gov/32070640/).
 25. Muñoz-Leija MA, Yamamoto-Ramos M, Barrera-Flores FJ, et al. Anatomical variations of the ethmoidal roof: differences between men and women. *Eur Arch Otorhinolaryngol.* 2018; 275(7): 1831–1836, doi: [10.1007/s00405-018-4992-6](https://doi.org/10.1007/s00405-018-4992-6), indexed in Pubmed: [29744636](https://pubmed.ncbi.nlm.nih.gov/29744636/).
 26. Özer CM, Atalar K, Öz İI, et al. Sphenoid sinus in relation to age, gender, and cephalometric indices. *J Craniofac Surg.* 2018; 29(8): 2319–2326, doi: [10.1097/SCS.0000000000004869](https://doi.org/10.1097/SCS.0000000000004869), indexed in Pubmed: [30320684](https://pubmed.ncbi.nlm.nih.gov/30320684/).
 27. Rahmati A, Ghafari R, AnjomShoa M. Normal variations of sphenoid sinus and the adjacent structures detected in cone beam computed tomography. *J Dent (Shiraz).* 2016; 17(1): 32–37, indexed in Pubmed: [26966706](https://pubmed.ncbi.nlm.nih.gov/26966706/).
 28. Raspall G. Cirugía Maxilofacial: Patología Quirúrgica de la cara, boca, cabeza y cuello. 1st ed. Ergon, Barcelona 2018: 150.
 29. Sadler TW, Langman J. Langman's Essential Medical Embryology. Lippincott, Philadelphia, PA 2005: 53.
 30. Sahlstrand-Johnson P, Jannert M, Strömbeck A, et al. Computed tomography measurements of different dimensions of maxillary and frontal sinuses. *BMC Med Imaging.* 2011; 11: 8, doi: [10.1186/1471-2342-11-8](https://doi.org/10.1186/1471-2342-11-8), indexed in Pubmed: [21466703](https://pubmed.ncbi.nlm.nih.gov/21466703/).
 31. Saldanha M, Bhat V, Bhandary B, et al. Silent sinus syndrome: a case report and review of literature. *Clin Rhinol.* 2013; 6(3): 144–148, doi: [10.5005/jp-journals-10013-1176](https://doi.org/10.5005/jp-journals-10013-1176).
 32. Sánchez Fernández JM, Anta Escuredo JA, Sánchez Del Rey A, et al. Morphometric study of the paranasal sinuses in normal and pathological conditions. *Acta Otolaryngol.* 2000; 120(2): 273–278, doi: [10.1080/000164800750001080](https://doi.org/10.1080/000164800750001080), indexed in Pubmed: [11603789](https://pubmed.ncbi.nlm.nih.gov/11603789/).
 33. Scuderi AJ, Harnsberger HR, Boyer RS. Pneumatization of the paranasal sinuses: normal features of importance to the accurate interpretation of CT scans and MR images. *Am J Roentgenol.* 1993; 160(5): 1101–1104, doi: [10.2214/ajr.160.5.8470585](https://doi.org/10.2214/ajr.160.5.8470585), indexed in Pubmed: [8470585](https://pubmed.ncbi.nlm.nih.gov/8470585/).
 34. Shah RK, Dhingra JK, Carter BL, et al. Paranasal sinus development: a radiographic study. *Laryngoscope.* 2003; 113(2): 205–209, doi: [10.1097/00005537-200302000-00002](https://doi.org/10.1097/00005537-200302000-00002), indexed in Pubmed: [12567069](https://pubmed.ncbi.nlm.nih.gov/12567069/).
 35. Sivasli E, Sirikçi A, Bayazıt YA, et al. Anatomic variations of the paranasal sinus area in pediatric patients with chronic sinusitis. *Surg Radiol Anat.* 2003; 24(6): 400–405, doi: [10.1007/s00276-002-0074-x](https://doi.org/10.1007/s00276-002-0074-x), indexed in Pubmed: [12652368](https://pubmed.ncbi.nlm.nih.gov/12652368/).
 36. Simonetti G, Meloni F, Teatini G, et al. Computed tomography of the ethmoid labyrinth and adjacent structures. *Ann Otol Rhinol Laryngol.* 1987; 96(3 Pt 1): 239–250, doi: [10.1177/000348948709600301](https://doi.org/10.1177/000348948709600301), indexed in Pubmed: [3605945](https://pubmed.ncbi.nlm.nih.gov/3605945/).
 37. Spaeth J, Krügelstein U, Schlöndorff G. The paranasal sinuses in CT-imaging: development from birth to age 25. *Int J Pediatr Otorhinolaryngol.* 1997; 39(1): 25–40, doi: [10.1016/S0165-5876\(96\)01458-9](https://doi.org/10.1016/S0165-5876(96)01458-9), indexed in Pubmed: [9051437](https://pubmed.ncbi.nlm.nih.gov/9051437/).
 38. Trueba R, Pallante A, Buzzi AE. Síndrome del seno silente. *Rev Arg Radiol.* 2008; 72(1): 51–53.
 39. Uchida Y, Goto M, Katsuki T, et al. A cadaveric study of maxillary sinus size as an aid in bone grafting of the maxillary sinus floor. *J Oral Maxillofac Surg.* 1998; 56(10): 1158–1163, doi: [10.1016/s0278-2391\(98\)90761-3](https://doi.org/10.1016/s0278-2391(98)90761-3), indexed in Pubmed: [9766541](https://pubmed.ncbi.nlm.nih.gov/9766541/).
 40. Virapongse C, Sarwar M, Bhimani S, et al. Computed tomography of temporal bone pneumatization: 1. Normal pattern and morphology. *AJR Am J Roentgenol.* 1985; 145(3): 473–481, doi: [10.2214/ajr.145.3.473](https://doi.org/10.2214/ajr.145.3.473), indexed in Pubmed: [3875250](https://pubmed.ncbi.nlm.nih.gov/3875250/).
 41. Wang J, Bidari S, Inoue K, et al. Extensions of the sphenoid sinus: a new classification. *Neurosurgery.* 2010; 66(4): 797–816, doi: [10.1227/01.NEU.0000367619.24800.B1](https://doi.org/10.1227/01.NEU.0000367619.24800.B1), indexed in Pubmed: [20305499](https://pubmed.ncbi.nlm.nih.gov/20305499/).
 42. Wigand, Malte Erik HI. Endoscopic Surgery of the Paranasal Sinuses and Anterior Skull Base. 2nd ed. Auflage editor, Thieme Publishing Group 2008.
 43. Wolf G, Anderhuber W, Kuhn F. Development of the paranasal sinuses in children: implications for paranasal sinus surgery. *Ann Otol Rhinol Laryngol.* 1993; 102(9): 705–711, doi: [10.1177/000348949310200911](https://doi.org/10.1177/000348949310200911), indexed in Pubmed: [8373095](https://pubmed.ncbi.nlm.nih.gov/8373095/).
 44. Zinreich SJ, Kennedy DW, Rosenbaum AE, et al. Paranasal sinuses: CT imaging requirements for endoscopic surgery. *Radiology.* 1987; 163(3): 769–775, doi: [10.1148/radiology.163.3.3575731](https://doi.org/10.1148/radiology.163.3.3575731), indexed in Pubmed: [3575731](https://pubmed.ncbi.nlm.nih.gov/3575731/).

Demirjian method and Willems method to study the dental age of adolescents in Shanghai before and after 10 years

K. Kwon¹, J. Pan¹, Y. Guo¹, Q. Ren¹, Z. Yang¹, J. Tao², F. Ji¹

¹Department of Orthodontics, Ninth People's Hospital, Shanghai Jiao Tong University School of Medicine, Shanghai, China

²Department of General Dentistry, Ninth People's Hospital, Shanghai Jiao Tong University School of Medicine, Shanghai, China

[Received: 3 February 2022; Accepted: 23 February 2022; Early publication date: 8 March 2022]

Background: The aim of this study was to assess whether the difference in dental ages between 2009 to 2011 and 2021 is affected by environmental factors such as environmental pollution, floating population, and dietary habits.

Materials and methods: Demirjian and Willems dental age estimation methods were conducted for a Han population of children aged 8 to 14 in Shanghai, China. A total of 1259 digital panoramic radiographs of children aged 8.00–14.99 were estimated. All digital panoramic radiographs were estimated using the Demirjian and Willems methods. Data collected in 2009 to 2011 and 2021 were statistically analysed by paired *t*-tests.

Results: The results show that the Demirjian method overestimates 2009 to 2011 and underestimates 2021 the children's chronological age. When using the Willems method, the age of males was overestimated and the age of females was underestimated from 2009 to 2011, and it was underestimated for both genders in 2021.

Conclusions: In conclusion, the difference in dental ages between 2009 to 2011 and 2021 was statistically significant. Factors such as environment and dietary habits have been found to be affected by dental development. However, there are disputes among some researchers about the exact factors, so it is suggested to further study the effects of environmental factors on tooth development. (Folia Morphol 2023; 82, 2: 346–358)

Key words: dental age estimation, environmental factors, Demirjian method, Willems method

INTRODUCTION

The study of dental age is of great significance for the confirmation of individual age, especially for adolescents, in all kinds of civil and criminal cases [1]. For example, some people, such as illegal immigrants from Southeast Asia or Africa and some adopted teenagers and undocumented individuals are unable

to verify their true identity, which makes it impossible for the judicial authorities to investigate, verify and determine their true age [5, 22, 23]. In addition, due to age-related doubts or failure to provide effective relevant certificates, children's admission, marriage, retirement, employment, sports events graded according to age, international political asylum appli-

Address for correspondence: Dr. F. Ji, Department of Orthodontics, Ninth People's Hospital, Shanghai Jiao Tong University School of Medicine, No. 500, Quxi Road, Huangpu District, 20020 Shanghai, China, e-mail: smilefang98@163.com

This article is available in open access under Creative Common Attribution-Non-Commercial-No Derivatives 4.0 International (CC BY-NC-ND 4.0) license, allowing to download articles and share them with others as long as they credit the authors and the publisher, but without permission to change them in any way or use them commercially.

cations, and other situations [10, 14, 26], it is often necessary to seek effective means to estimate the real age. In these events, age estimation plays an irreplaceable role.

In the treatment of adolescents with malocclusion, the most important thing is the correct evaluation of personal development, the determination of optimum treatment time, and a long-term treatment plan [12]. Considering the degree of development is also of great significance for treatment results and prognosis [11]. The consideration of treatment plan is mainly based on craniofacial growth potential. Therefore, the evaluation of development is of great significance for diagnosis, the goal of treatment, treatment plan, and the final result of orthodontic treatment. This method of evaluating growth and development can be roughly divided into actual age and developmental age. The actual age refers to the biological age. Even at the same age, it will show different physical maturity due to individual differences. Therefore, the actual age is not suitable as an indicator of individual growth and development [11]. On the contrary, developmental age is a biological index to evaluate individual maturity and an evaluation method that can reflect the individuality and variability of growth [11].

However, unlike the dental age, bone age is greatly affected by nutrition and heredity, and there are still some subjectivity and experience in inferring age from bones, and there are great variations in inferring physiological age [24]. Therefore, the difference due to changes in the external environment can be identified by dental age.

The results of different researchers estimating dental age showed that there were some differences in the dental age between different regions and even the same region. Some researchers believed that the reason may be due to other environmental factors such as socio-economic conditions, nutrition and dietary habits, and lifestyle [6, 26, 28]. In the study by Wang et al. [26], the Demirjian method underestimated chronological age and the Willems method underestimated chronological age overall. Therefore, it was concluded that the Demirjian method was more accurate than the Willems method. However, this was contrary to Ye et al.'s [30] research in the same region of China. Wang et al. [26] thought that environmental factors such as pollution, nutrition, dietary habits, and lifestyle could explain this difference.

Different environments, such as environmental pollution and dietary habits, affect the growth, development, and morphology of teeth [18]. The development of an industrialized economy due to the rapid

development of China's economy has brought about serious environmental pollution and changes in people's daily eating structure. Children and adolescents have more opportunities to be exposed to foreign diets and get into a habit than before. Furthermore, most of the diets we consume these days are processed foods that almost do not need to be chewed, which may cause growth and development problems. Since the human chewing masticatory system gradually deteriorates, it can cause a malocclusion, microdontia, and hypodontia [16]. As it was said in previous studies, environment and dietary habits affect dental age, but the exact cause is not known now.

Studies by several researchers concluded that different races have different dental ages [10]. Therefore, to reduce the error in this experiment, the study population consisted of persons of the same race, the Han population of China. To preliminarily explore the relationship between dental age and environmental factors, considering the great changes in China's economy, politics, environment, and dietary habits in the past decade, this is the first study to compare the differences in dental age and chronological age of Han children in Shanghai 10 years ago and 10 years later.

Therefore, this study aimed to measure the dental age of the Han population of Chinese children 10 years ago and 10 years later by the Demirjian method and the Willems method to find out the accuracy of the chronological age. Furthermore, this study also aimed to compare the dental age 10 years ago and 10 years later to explore the correlation between dental age and environmental factors.

MATERIALS AND METHODS

Samples

The samples were digital panoramic radiographs produced by Kodak 8000C-8000C X-ray equipment. These were randomly selected panoramic radiographs of 3237 patients between 8 to 14 years old who visited the Shanghai Ninth People's Hospital affiliated to Shanghai Jiao Tong University from 2009 to 2011 and in 2021. According to the literature data source [19], the standard deviation of the interpolation between the male groups' dental age and the chronological age is 1.39 years, the female groups' dental age and the chronological age is 1.50 years, and the allowable error is preset as 0.5 years, $\alpha = 0.05$. After calculation, it was concluded that the sample size of the male groups needed 30 panoramic radiographs, a total of 210 panoramic radiographs, and the female

Table 1. Age distribution of two sexes by age group — 2009–2011

Age group [years]	Female	Male
8.00–8.99	44	44
9.00–9.99	45	44
10.00–10.99	46	46
11.00–11.99	46	47
12.00–12.99	45	46
13.00–13.99	47	46
14.00–14.99	41	42
Total	314	315

Table 2. Age distribution of two sexes by age group — 2021

Age group [years]	Female	Male
8.00–8.99	39	45
9.00–9.99	40	46
10.00–10.99	46	45
11.00–11.99	46	46
12.00–12.99	47	45
13.00–13.99	47	47
14.00–14.99	46	45
Total	311	319

groups needed 35 panoramic radiographs, a total of 245 panoramic radiographs. Sample size calculation: the calculation formula is $n = (\mu \alpha / 2\sigma/\delta)^2$. Panoramic radiographs of 319 males and 311 females obtained from 2009 to 2011 were evaluated. Also, 2021 panoramic radiographs of 315 males and 314 females were evaluated. A total of 1259 digital panoramic radiographs were selected by inclusion and exclusion criteria shown below, then evaluated between 8.00 and 14.99 years old (Tables 1, 2). These samples were divided into 12 age groups each. The chronological age of each subject was calculated by converting the two dates to decimal age and then subtracting the date of birth from the date of digital panorama acquisition. The research was authorized by the Independent Ethics Committee of the Shanghai Ninth People’s Hospital affiliated with Shanghai Jiao Tong University, School of Medicine (SH9H-2019-T75-1).

The inclusion criteria were as follows:

- Han nationality of Chinese population;
- chronological age from 8.00 to 14.99 years old;
- no effect on the mineralization and eruption of the permanent teeth;
- identify the morphology of root, crown, and tooth germ in the digital panoramic radiographs (Fig. 1).



Figure 1. The example of the clear digital panoramic radiographs.



Figure 2. The example of the excluded (loss of teeth) digital panoramic radiographs.



Figure 3. The example of the excluded (history of diseases) digital panoramic radiographs.

The exclusion criteria were as follows:

- loss of teeth (except the third molar) in both sides of the mandible (Fig. 2);
- history of diseases affecting jaw development, such as cleft lip and palate, jaw tumour, craniomaxillo-facial malformation, and systemic diseases (Fig. 3);

- history of dental treatment that affects the normal development of tooth roots, such as endodontic treatment and root canal treatment;
- abnormal tooth morphology, such as fused teeth, microdontia, etc.;
- supernumerary teeth;
- position anomalies;
- hereditary and genetic anomalies.

Methods

At present, there are a variety of dental age estimation methods based on digital panoramic radiographs in the world, among which the Demirjian et al. [7] and Willems et al. [27] methods are widely used to infer the dental age of adolescents. Dental age was estimated on the basis of the development of teeth apical shape in the digital panoramic radiographs. Dental maturity was divided into eight development stages (A–H) of teeth apical closure and tooth mineralisation of each of the seven teeth in the left mandible (from the left lower incisor to the left lower second permanent molar). Firstly, the development stage of each tooth in the male and female groups was converted to a score. Secondly, the total maturity score was the sum of the scores of all seven teeth. Lastly, the total maturity score was transformed to dental age according to the tables designed by Demirjian et al. [7].

The Willems method is a modified new dental age estimation method based on the Demirjian method. Every tooth's maturity classification (A–H) is converted to scores according to the Willems method, and the final dental age is the sum of seven teeth's scores.

To avoid bias, two examiners did not know the personal identification details of the subjects. They have re-examined 60 randomly selected digital panoramic radiographs 3 weeks later. Cohen's Kappa test was measured the intra-observer and inter-observer reproducibility.

Statistical analysis

All the data were statistically analysed by SPSS version 22.0 for windows (IBM, Armonk, NY) and Excel (Microsoft Office) systems. 2010. Descriptive statistics (the mean and standard deviation) were tested using the paired t-test and the Wilcoxon Signed-Rank test was used of discrepancies between 2009 to 2011 and 2021 dental ages in each age and sex group. The mean absolute error (MAE) was used for the accuracy of the two methods. $P \leq 0.05$ was statistically significant.

RESULTS

The Cohen's Kappa values were calculated for intra-observer and inter-observer agreement. The results of the values were 0.729 and 0.753, which revealed no statistically significant intra and inter-observer differences.

The mean chronological age of children from 2009 to 2011 was 11.51 ± 1.99 years for male and 11.62 ± 1.95 years for female patients. The mean chronological age of children from 2021 was 11.42 ± 1.99 years for male and 11.43 ± 1.99 years for female patients. The distribution of the 1259 samples by age and sex is shown in Tables 1 and 2.

Results of 2009 to 2011 years

The tables in which Demirjian and Willems dental ages (DA) were compared with chronological age (CA) in 2009 to 2011 years are shown in Tables 3, 4, 5, and 6, respectively, as male and female groups. The Demirjian mean age difference was 0.65 ± 0.97 years for males and 0.48 ± 1.04 years for females. It was demonstrated that the Demirjian method in MAE in 2009 to 2011 generally overestimated for both sexes, except for male and female groups aged from 14.00 to 14.99 years. The MAE was roughly 0.5–1.4 years in most age groups for both genders, with a mean of 0.87 years for both sexes. The most often monitored age difference was -0.65 to -0.20 years for males and -0.56 to -0.03 years for females (Figs. 4, 5). The Willems mean age difference was 0.19 ± 1.00 years for males and -0.08 ± 0.98 years for females. It was demonstrated that the Willems method in MAE in 2009 to 2011 generally overestimated for males, except those aged from 13.00 to 13.99 years and 14.00 to 14.99 years. On the other hand, DAE generally underestimated chronological age for female groups, except those aged from 10.00 to 10.99 and 11.00 to 11.99 years. The MAE was roughly 0.4 to 1.2 years in most age groups for both genders, with a mean of 0.72 years for males and 0.77 years for females. The most often monitored age difference was -0.12 to 0.38 years for males and -0.01 to 0.49 years for females (Figs. 6, 7).

Results of 2021 years

The table comparing chronological age and dental age in 2021 with the Demirjian and Willems methods is divided into male and female, respectively, and is shown in Tables 7, 8, 9, and 10. The mean age difference between the Demirjian dental age and the chronological age is -0.51 ± 0.73 years for males and

Table 3. Comparison of the chronological age of 2009 to 2011 and Demirjian dental age in male groups

Age group [years]	N	Mean (SD) [years]			95% CI of CA-DA [years]		P	MAE [years]
		CA	DA	CA-DA	Lower	Upper		
8.00–8.99	45	8.54 (0.31)	9.30 (1.05)	0.77 (1.08)	-1.09	-0.44	0.000	0.84
9.00–9.99	46	9.48 (0.32)	10.20 (1.04)	0.72 (1.07)	-1.04	-0.40	0.000	0.91
10.00–10.99	45	10.50 (0.27)	11.72 (0.89)	1.22 (0.83)	-1.47	-0.97	0.000	1.22
11.00–11.99	46	11.59 (0.26)	12.67 (0.93)	1.08 (0.90)	-1.34	-0.81	0.000	1.09
12.00–12.99	45	12.51 (0.24)	13.35 (0.65)	0.84 (0.71)	-1.05	-0.63	0.000	0.88
13.00–13.99	47	13.47 (0.26)	13.64 (0.71)	0.17 (0.70)	-0.37	0.04	0.106	0.57
14.00–14.99	45	14.40 (0.31)	14.19 (0.70)	-0.22 (0.64)	0.03	0.41	0.028	0.56
total	319	11.51 (1.99)	12.16 (1.90)	0.65 (0.97)	-0.76	-0.54	0.000	0.87

N — numbers; SD — standard deviation; CA-DA — chronological age minus dental age; CI — confidence interval; P — the p value of the paired-t test; MAE — mean absolute error

Table 4. Comparison of the chronological age of 2009 to 2011 and Willems dental age in male groups

Age group [years]	N	Mean (SD) [years]			95% CI of CA-DA [years]		P	MAE [years]
		CA	DA	CA-DA	Lower	Upper		
8.00–8.99	45	8.54 (0.31)	9.21 (1.06)	0.68 (1.09)	-1.00	-0.35	0.000	0.81
9.00–9.99	46	9.48 (0.32)	9.96 (1.05)	0.48 (1.07)	-0.8	-0.16	0.004	0.72
10.00–10.99	45	10.50 (0.27)	11.17 (0.97)	0.67 (0.91)	-0.94	-0.40	0.000	0.80
11.00–11.99	46	11.59 (0.26)	12.16 (0.85)	0.57 (0.81)	-0.81	-0.33	0.000	0.77
12.00–12.99	45	12.51 (0.24)	12.75 (0.48)	0.24 (0.54)	-0.41	-0.08	0.004	0.48
13.00–13.99	47	13.47 (0.26)	13.06 (0.67)	-0.41 (0.64)	0.22	0.60	0.000	0.58
14.00–14.99	45	14.40 (0.31)	13.55 (0.69)	-0.86 (0.65)	0.66	1.05	0.000	0.91
Total	319	11.51 (1.99)	11.70 (1.73)	0.19 (1.00)	-0.30	-0.08	0.001	0.72

N — numbers; SD — standard deviation; CA-DA — chronological age minus dental age; CI — confidence interval; P — the p value of the paired-t test; MAE — mean absolute error

Table 5. Comparison of the chronological age of 2009 to 2011 and Demirjian dental age in female groups

Age group [years]	N	Mean (SD) [years]			95% CI of CA-DA [years]		P	MAE [years]
		CA	DA	CA-DA	Lower	Upper		
8.00–8.99	39	8.49 (0.31)	8.87 (0.71)	0.37 (0.63)	-0.58	-0.17	0.001	0.58
9.00–9.99	40	9.51 (0.33)	10.07 (0.92)	0.56 (0.89)	-0.84	-0.27	0.000	0.83
10.00–10.99	46	10.60 (0.25)	11.84 (0.89)	1.23 (0.97)	-1.52	-0.94	0.000	1.28
11.00–11.99	46	11.52 (0.26)	12.92 (0.71)	1.40 (0.77)	-1.63	-1.17	0.000	1.40
12.00–12.99	47	12.59 (0.25)	12.79 (0.95)	0.21 (0.98)	-0.50	0.08	0.158	0.67
13.00–13.99	47	13.40 (0.28)	13.63 (0.71)	0.24 (0.71)	-0.44	-0.03	0.026	0.55
14.00–14.99	46	14.41 (0.27)	13.79 (0.71)	-0.62 (0.76)	0.4	0.85	0.000	0.76
Total	311	11.62 (1.95)	12.10 (1.86)	0.48 (1.04)	-0.60	-0.37	0.000	0.87

N — numbers; SD — standard deviation; CA-DA — chronological age minus dental age; CI — confidence interval; P — the p value of the paired-t test; MAE — mean absolute error

-0.48 ± 0.80 years for females. The MAE of the Demirjian method in 2021 was generally underestimated for both genders except for the age of 10.00 to 10.99 and 11.00 to 11.99 in female groups. In most age groups in both genders, MAEs were approximately 0.3 to 1.4, with a mean of 0.7 years for males and

0.77 years for females. The age difference between -0.55 and -0.18 years for males and -0.57 to 0.16 years for females was the most often observed age difference (Figs. 8, 9). The mean age difference between the Willems dental age and the chronological age was -0.80 ± 0.71 years for males and -0.82 ±

Table 6. Comparison of the chronological age of 2009 to 2011 and Willems dental age in female groups

Age group [years]	N	Mean (SD) [years]			95% CI of CA-DA [years]		P	MAE [years]
		CA	DA	CA-DA	Lower	Upper		
8.00–8.99	39	8.50 (0.31)	8.44 (0.54)	-0.05 (0.54)	-0.12	0.23	0.534	0.44
9.00–9.99	40	9.51 (0.33)	9.39 (0.89)	-0.12 (0.86)	-1.45	0.18	0.368	0.66
10.00–10.99	46	10.60 (0.25)	11.15 (0.97)	0.55 (1.04)	-0.86	-0.24	0.001	0.95
11.00–11.99	46	11.52 (0.26)	12.36 (0.62)	0.84 (0.68)	-1.04	-0.63	0.000	0.88
12.00–12.99	47	12.59 (0.25)	12.33 (0.74)	-0.26 (0.77)	0.03	0.48	0.027	0.65
13.00–13.99	47	13.40 (0.28)	13.05 (0.76)	-0.34 (0.73)	0.13	0.56	0.002	0.68
14.00–14.99	46	14.41 (0.27)	13.32 (0.71)	-1.09 (0.74)	0.87	1.31	0.000	1.12
Total	311	11.62 (1.95)	11.55 (1.85)	-0.08 (0.98)	-0.04	0.18	0.207	0.77

N — numbers; SD — standard deviation; CA-DA — chronological age minus dental age; CI — confidence interval; P — the p value of the paired-t test; MAE — mean absolute error

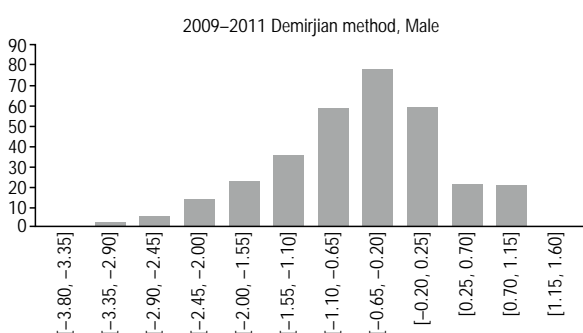


Figure 4. Histogram of the difference between Demirjian dental age and chronological age in male groups in 2009 to 2011.

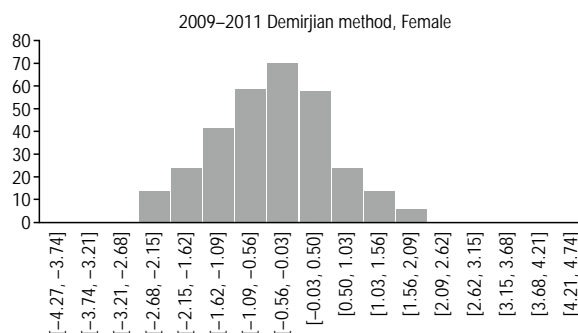


Figure 5. Histogram of the difference between Demirjian dental age and chronological age in female groups in 2009 to 2011.

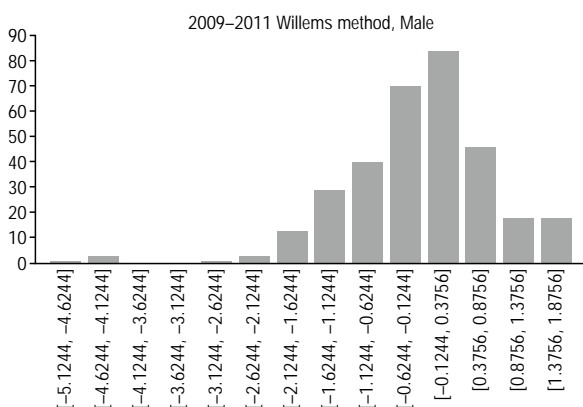


Figure 6. Histogram of the difference between Willems dental age and chronological age in male groups in 2009 to 2011.

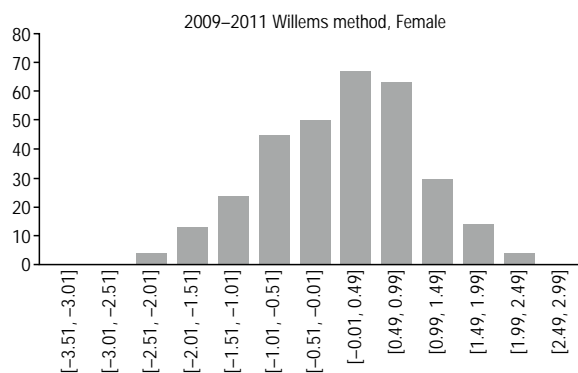


Figure 7. Histogram of the difference between Willems dental age and chronological age in female groups in 2009 to 2011.

± 0.87 years for females. The MAE of the Willems method in 2021 was generally underestimated for both genders. In most age groups in both genders, MAEs were approximately 0.4 to 1.8 years, with a mean of 0.88 years for males and 0.99 years for females. The age difference between -0.97 and -0.61 years for males and -0.97 to 0.53 years for females was the most often observed age difference (Figs. 10, 11).

Comparison of 2009 to 2011 and 2021 years

The results of the comparison of the Demirjian methods for males from 2009 to 2011 and 2021

Table 11 presented the dental age differences of the Demirjian methods between 2009 to 2011 and 2021 in the male group (Fig. 12). Generally, the dental age of the 2009 to 2011 males estimated by the Demirjian method was overestimated compared to the

Table 7. Comparison of the chronological age of 2021 and Demirjian dental age in male groups

Age group [years]	N	Mean (SD) [years]			95% CI of CA-DA [years]		P	MAE [years]
		CA	DA	CA-DA	Lower	Upper		
8.00–8.99	44	8.39 (0.25)	8.19 (0.26)	-0.20 (0.33)	0.10	0.30	0.000	0.31
9.00–9.99	44	9.50 (0.27)	8.76 (0.41)	-0.74 (0.43)	0.61	0.87	0.000	0.75
10.00–10.99	46	10.49 (0.29)	10.29 (0.63)	-0.21 (0.65)	0.01	0.40	0.039	0.55
11.00–11.99	47	11.40 (0.28)	11.03 (0.93)	-0.38 (0.91)	0.11	0.64	0.006	0.77
12.00–12.99	46	12.36 (0.25)	12.07 (0.74)	-0.30 (0.76)	0.07	0.52	0.011	0.57
13.00–13.99	46	13.44(0.30)	12.94 (0.65)	-0.51 (0.66)	0.31	0.7	0.000	0.71
14.00–14.99	42	14.45 (0.34)	13.19 (0.63)	-1.26 (0.56)	1.09	1.44	0.000	1.26
Total	315	11.42 (1.99)	10.92 (1.91)	-0.51 (0.73)	0.42	0.58	0.000	0.70

N — numbers; SD — standard deviation; CA-DA — chronological age minus dental age; CI — confidence interval; P — the p value of the paired-t test; MAE — mean absolute error

Table 8. Comparison of the chronological age of 2021 and Willems dental age in male groups

Age group [years]	N	Mean (SD) [years]			95% CI of CA-DA [years]		P	MAE [years]
		CA	DA	CA-DA	Lower	Upper		
8.00–8.99	44	8.39 (0.25)	8.10 (0.34)	-0.28 (0.39)	0.16	0.40	0.000	0.39
9.00–9.99	44	9.50 (0.27)	8.90 (0.57)	-0.60 (0.53)	0.44	0.76	0.000	0.65
10.00–10.99	46	10.49 (0.29)	9.96 (0.45)	-0.53 (0.48)	0.39	0.68	0.000	0.56
11.00–11.99	47	11.40 (0.28)	10.69 (0.94)	-0.71 (0.92)	0.44	0.98	0.000	0.95
12.00–12.99	46	12.36 (0.25)	11.73 (0.67)	-0.63 (0.69)	0.42	0.83	0.000	0.94
13.00–13.99	46	13.45 (0.30)	12.56 (0.41)	-0.90 (0.45)	0.76	1.03	0.000	0.91
14.00–14.99	42	14.45 (0.34)	12.72 (0.39)	-1.73 (0.40)	1.61	1.85	0.000	1.73
Total	315	11.43 (1.99)	10.67 (1.74)	-0.80 (0.71)	0.68	0.84	0.000	0.88

N — numbers; SD — standard deviation; CA-DA — chronological age minus dental age; CI — confidence interval; P — the p value of the paired-t test; MAE — mean absolute error

Table 9. Comparison of the chronological age of 2021 and Demirjian dental age in female groups

Age group [years]	N	Mean (SD) [years]			95% CI of CA-DA [years]		P	MAE [years]
		CA	DA	CA-DA	Lower	Upper		
8.00–8.99	44	8.47 (0.28)	8.15(0.30)	-0.32 (0.39)	0.20	0.44	0.000	0.43
9.00–9.99	45	9.49 (0.31)	9.03 (0.51)	-0.46 (0.54)	0.30	0.63	0.000	0.57
10.00–10.99	46	10.40 (0.33)	10.65 (0.98)	0.25 (0.90)	-0.52	0.02	0.067	0.79
11.00–11.99	46	11.52 (0.27)	11.54 (0.65)	0.02 (0.61)	-0.20	0.16	0.853	0.50
12.00–12.99	45	12.36 (0.25)	11.98 (0.59)	-0.38 (0.62)	0.19	0.57	0.000	0.60
13.00–13.99	47	13.49 (0.30)	12.45 (0.50)	-1.04 (0.40)	0.92	1.16	0.000	1.04
14.00–14.99	41	14.42 (0.31)	12.99 (0.55)	-1.43 (0.61)	1.24	1.62	0.000	1.43
total	314	11.43 (1.99)	10.96 (1.76)	-0.48 (0.80)	0.38	0.56	0.000	0.77

N — numbers; SD — standard deviation; CA-DA — chronological age minus dental age; CI — confidence interval; P — the p value of the paired-t test; MAE — mean absolute error

chronological age. According to the provided information, only in the groups of 14.00–14.99 years can we observe the underestimation values. As a whole, the dental age of the 2021 males estimated by the Demirjian method was underestimated compared to the chronological age. The most accurate estimation periods belonged to 13.00–13.99 years in 2009 to

2011 and 8.00–8.99 years in 2021 with the Demirjian method, respectively. The values of age difference in 10.00–10.99 and 14.00–14.99 were the largest among all age groups between the ages of 2009 to 2011 and 2021, respectively. Overall, the males that measured in 2021 were found to be slightly more accurate compared to 2009 to 2011.

Table 10. Comparison of the chronological age of 2021 and Willems dental age in female groups

Age group [years]	N	Mean (SD) [years]			95% CI of CA-DA [years]		P	MAE [years]
		CA	DA	CA-DA	Lower	Upper		
8.00–8.99	44	8.47 (0.28)	8.16 (0.54)	-0.32 (0.59)	0.14	0.50	0.001	0.57
9.00–9.99	45	9.49 (0.31)	9.16 (0.64)	-0.33 (0.62)	0.15	0.52	0.001	0.56
10.00–10.99	46	10.40 (0.33)	10.02 (0.94)	-0.38 (0.86)	0.13	0.64	0.004	0.78
11.00–11.99	46	11.52 (0.27)	11.1 (0.78)	-0.42 (0.71)	0.21	0.63	0.000	0.63
12.00–12.99	45	12.36 (0.25)	11.30 (0.71)	-1.06 (0.72)	0.85	1.28	0.000	1.09
13.00–13.99	47	13.49 (0.30)	12.09 (0.56)	-1.40 (0.52)	1.25	1.55	0.000	1.43
14.00–14.99	41	14.42 (0.31)	12.61 (0.59)	-1.81 (0.68)	1.6	2.02	0.000	1.84
Total	314	11.43 (1.99)	10.62 (1.62)	-0.82 (0.87)	0.71	0.91	0.000	0.99

N — numbers; SD — standard deviation; CA-DA — chronological age minus dental age; CI — confidence interval; P — the p value of the paired-t test; MAE — mean absolute error

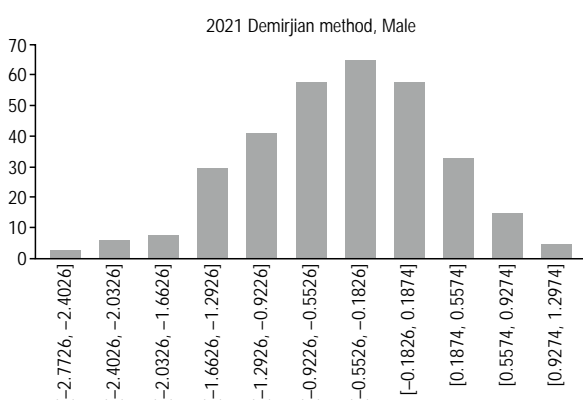


Figure 8. Histogram of the difference between Demirjian dental age and chronological age in male groups in 2021.

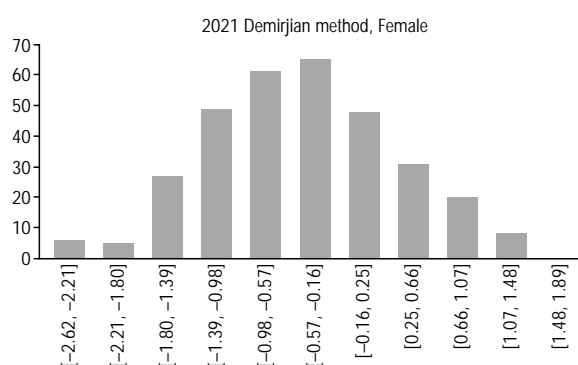


Figure 9. Histogram of the difference between Demirjian dental age and chronological age in female groups in 2021.

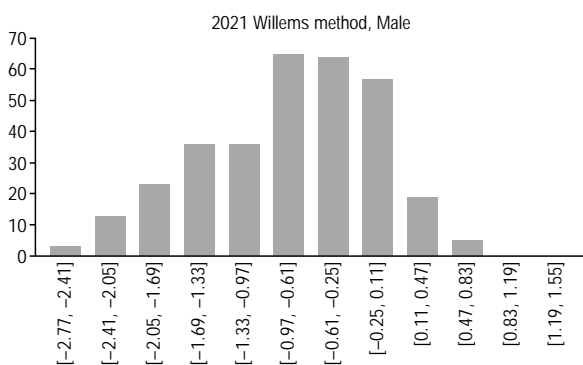


Figure 10. Histogram of the difference between Willems dental age and chronological age in male groups in 2021.

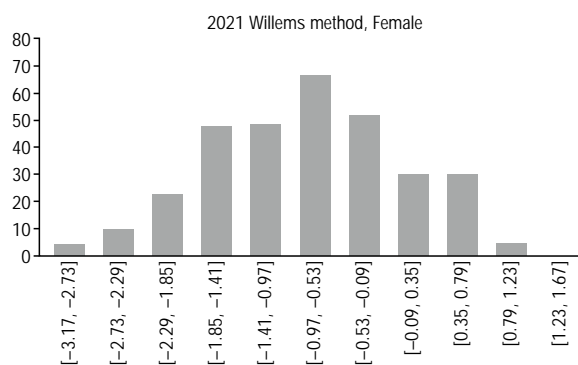


Figure 11. Histogram of the difference between Willems dental age and chronological age in female groups in 2021.

The results of the comparison of the Willems methods for males from 2009 to 2011 and 2021

Table 12 shows the difference in dental ages between 2009 to 2011 years and 2021 years by the Willems method with males' groups (Fig. 13). Compared with chronological age, the dental age of the males Williams method from CA 2009 to 2011 years

was generally overestimated. According to Table 12, underestimation values can be observed only in the age group of 13.00–14.99 years. The dental age of the Willems method for males in 2021 was generally underestimated compared to its chronological age. In the estimation results using the Willems method, the most accurate estimation age was 12.00–12.99

Table 11. Comparison of Demirjian dental age of 2009–2011 and 2021 in male groups

Age group [years]	N	Mean (SD) [years]			95% CI of CA-DA [years]		P	MAE [years]
		2009–2011	2021	(2009–2011)–2021	Lower	Upper		
8.00–8.99	44	9.26 (1.01)	8.19 (0.26)	1.07 (1.12)	0.73	1.41	0.000	1.08
9.00–9.99	44	10.26 (1.03)	8.76 (0.41)	1.50 (1.09)	1.17	1.83	0.000	1.52
10.00–10.99	45	11.72 (0.89)	10.29 (0.63)	1.42 (1.07)	1.10	1.74	0.000	1.48
11.00–11.99	46	12.67 (0.93)	11.02 (0.94)	1.64 (1.38)	1.23	2.05	0.000	1.70
12.00–12.99	45	13.35 (0.65)	12.06 (0.75)	1.29 (0.96)	1.01	1.58	0.000	1.30
13.00–13.99	46	13.63 (0.71)	12.94 (0.65)	0.69 (0.97)	0.41	0.98	0.000	0.93
14.00–14.99	42	14.24 (0.68)	13.19 (0.63)	1.05 (0.89)	0.77	1.32	0.000	1.14
Total	312	12.16 (1.90)	10.92 (1.92)	1.24 (1.11)	1.12	1.36	0.000	1.31

N — numbers; SD — standard deviation; CA-DA — chronological age minus dental age; CI — confidence interval; P — the p value of the paired-t test; MAE — mean absolute error

Table 12. Comparison of Willems dental age of 2009–2011 and 2021 in male groups.

Age group [years]	N	Mean (SD) [years]			95% CI of CA-DA (years)		P	MAE [years]
		2009–2011	2021	(2009–2011)–2021	Lower	Upper		
8.00–8.99	44	9.23 (1.07)	8.10 (0.34)	1.13 (1.17)	0.77	1.48	0.000	1.18
9.00–9.99	44	9.99 (1.06)	8.90 (0.57)	1.09 (1.24)	0.71	1.47	0.000	1.16
10.00–10.99	45	11.17 (0.97)	9.97 (0.45)	1.20 (1.02)	0.89	1.51	0.000	1.23
11.00–11.99	46	12.16 (0.85)	10.68 (0.95)	1.48 (1.27)	1.10	1.86	0.000	1.57
12.00–12.99	45	12.75 (0.48)	11.73 (0.68)	1.03 (0.78)	0.79	1.26	0.000	1.06
13.00–13.99	46	13.06 (0.67)	12.56 (0.41)	0.50 (0.78)	0.27	0.73	0.000	0.69
14.00–14.99	42	13.60 (0.69)	12.72 (0.39)	0.88 (0.79)	0.63	1.12	0.000	0.99
Total	312	11.71 (1.73)	10.67 (1.74)	1.04 (1.06)	0.93	1.16	0.000	1.13

N — numbers; SD — standard deviation; CA-DA — chronological age minus dental age; CI — confidence interval; P — the p value of the paired-t test; MAE — mean absolute error

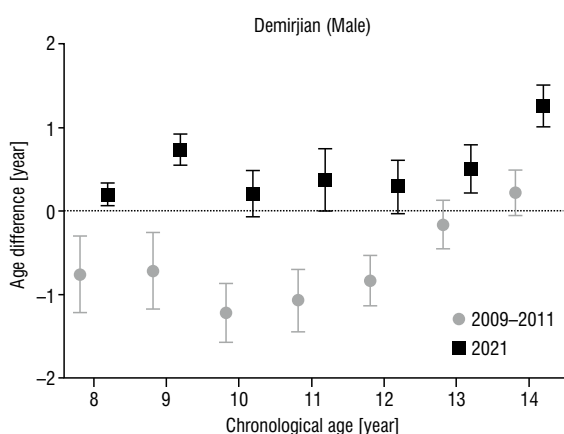


Figure 12. The dental age difference between 2009 to 2011 and 2021 by Demirjian method in the male groups.

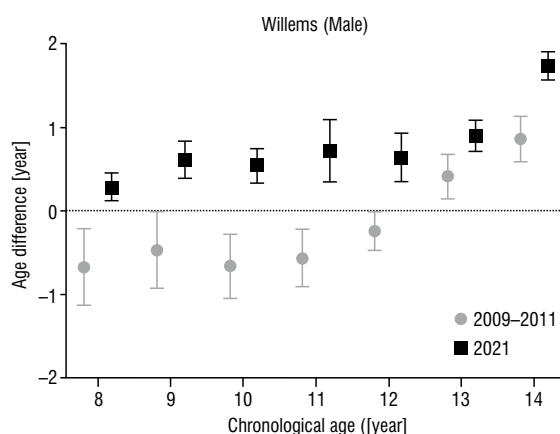


Figure 13. The dental age difference between 2009 to 2011 and 2021 by Willems method in the male groups.

years from 2009 to 2011 and 8.00–12.99 years from 2021. In both 2009 to 2011 and 2021, 14.00–14.99 years had the largest age difference among all age groups. The males that measured from 2009 to 2011 are generally more accurate than in 2021.

The results of the comparison of the Demirjian methods for females from 2009 to 2011 and 2021

Table 13 shows the difference in dental ages of female groups measured by the Demirjian method from 2009 to 2011 and 2021 (Fig. 14). The den-

Table 13. Comparison of Demirjian dental age of 2009–2011 and 2021 in female groups

Age group [years]	N	Mean (SD) [years]			95% CI of CA-DA [years]		P	MAE [years]
		2009-2011	2021	(2009-2011)-2021	Lower	Upper		
8.00–8.99	39	8.87 (0.71)	8.16 (0.29)	0.71 (0.74)	0.47	0.95	0.000	0.81
9.00–9.99	40	10.07 (0.92)	9.08 (0.51)	1.00 (1.00)	0.68	1.32	0.000	1.20
10.00–10.99	46	11.84 (0.89)	10.65 (0.98)	1.18 (1.28)	0.80	1.56	0.000	1.41
11.00–11.99	46	12.92 (0.71)	11.54 (0.65)	1.38 (0.99)	1.09	1.67	0.000	1.39
12.00–12.99	45	12.78 (0.97)	11.98 (0.59)	0.79 (1.12)	0.46	1.13	0.000	1.05
13.00–13.99	47	13.63 (0.71)	12.45 (0.50)	1.19 (0.81)	0.95	1.43	0.000	1.20
14.00–14.99	41	13.78 (0.72)	12.99 (0.55)	0.79 (0.88)	0.51	1.06	0.000	0.99
Total	304	12.07 (1.86)	11.05 (1.72)	1.02 (1.01)	0.90	1.13	0.000	1.15

N — numbers; SD — standard deviation; CA-DA — chronological age minus dental age; CI — confidence interval; P — the p value of the paired-t test; MAE — mean absolute error

Table 14. Comparison of Willems dental age of 2009–2011 and 2021 in female groups

Age group [years]	N	Mean (SD) [years]			95% CI of CA-DA (years)		P	MAE [years]
		2009-2011	2021	(2009-2011)-2021	Lower	Upper		
8.00–8.99	39	8.44 (0.54)	8.17 (0.56)	0.27 (0.77)	0.02	0.52	0.033	0.66
9.00–9.99	40	9.39 (0.89)	9.22 (0.64)	0.17 (0.97)	-0.13	0.48	0.269	0.81
10.00–10.99	46	11.15 (0.97)	10.02 (0.94)	1.14 (1.43)	0.71	1.56	0.000	1.51
11.00–11.99	46	12.36 (0.62)	11.10 (0.78)	1.26 (1.09)	0.94	1.59	0.000	1.34
12.00–12.99	45	12.33 (0.76)	11.30 (0.71)	1.03 (1.04)	0.72	1.35	0.000	1.14
13.00–13.99	47	13.05 (0.76)	12.09 (0.56)	0.96 (0.86)	0.71	1.22	0.000	0.98
14.00–14.99	41	13.32 (0.74)	12.61 (0.59)	0.71 (0.91)	0.42	1.00	0.000	0.98
Total	304	11.52 (1.85)	10.70 (1.59)	0.82 (1.10)	0.69	0.94	0.000	1.06

N — numbers; SD — standard deviation; CA-DA — chronological age minus dental age; CI — confidence interval; P — the p value of the paired-t test; MAE — mean absolute error

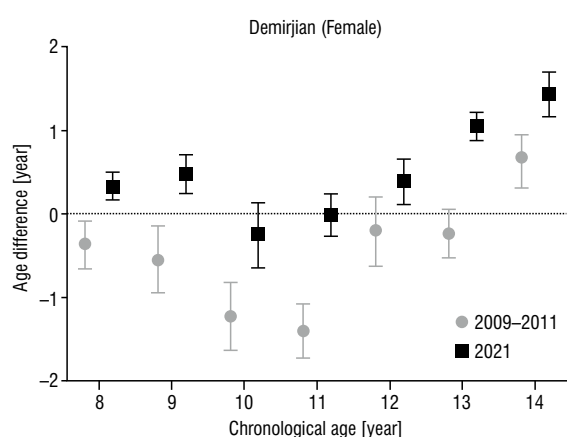


Figure 14. The dental age difference between 2009 to 2011 and 2021 by Demirjian method in the female groups.

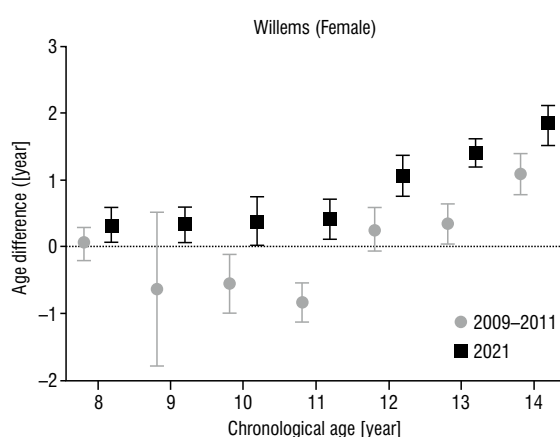


Figure 15. The dental age difference between 2009 to 2011 and 2021 by Willems method in the female groups.

tal age measured by the Demirjian method from 2009 to 2011 was generally overestimated than the chronological age. According to the measured results, underestimation can be observed only in the group from 14.00–14.99. In 2021, half was overestimated

compared to the chronological age, and a half was underestimated compared to the chronological age. The most accurate estimation age of the Demirjian method was 12.00–12.99 years from 2009 to 2011 and 11.00–11.99 years from 2021. The age difference

between 11.00–11.99 years in 2009 to 2011 and 14.00–14.99 years in 2021 was the largest among all age groups. Compared to 2009 to 2011, 2021 measured the dental age of girls more accurately.

The results of the comparison of the Willems methods for females from 2009 to 2011 and 2021

The age difference of girls' dental ages measured by the Willems method from 2009 to 2011 and 2021 can be seen in Table 14 (Fig. 15). The dental age of the Willems method from 2009 to 2011 was underestimated compared to most actual ages. In general, the dental age of the Willems method of female groups from 2009 to 2011 was underestimated compared to their chronological age. The measurement results show that only females aged 10.00–11.99 can observe overestimation. The dental age of the 2021 girls with the Willems method was measured as an overall underestimation compared to the chronological age. The most accurate estimation period is 8.00–8.99 years old from 2009 to 2011 and 2021. Of all age groups from 2009 to 2011 and 2021, measured by the Willems method, the age difference between 14.00–14.99 is the largest. Compared to 2021, the results of females' estimations of 2009 to 2011 are more accurate overall.

DISCUSSION

The dental age estimation method using digital panoramic radiation proposed by Demirjian et al. [7] and Willems et al. [27] is currently the most widely applied method due to its rationality, convenience, and objectivity [20]. Moreover, it has already been established that both the Demirjian method and the Willems method are suitable for use in dental age estimation in Chinese [29]. Several previous studies have found that there are differences in dental age depending on race and region [10]. However, since this study is not a study on the difference in dental age according to race and region, but a study on the difference in dental age according to the environment and dietary habits, the race was unified into the Han population of China. Therefore, the results of this study are not differences in dental age according to changes in species, but differences in dental age according to changes in the environment and dietary habits. This study measured the dental age of males and females in 2009 to 2011 and 2021 using these two methods. A total of 1259 panoramic radiographs of children aged 8.00–14.99 were finally selected to find out the differences in dental age estimations

between 2009 to 2011 and 2021. The reason why this study did not include panoramic radiographs of children under the age of 8.00 is that they rarely take panoramic radiographs. It is also noteworthy that all panoramic radiographs used in the study are mainly used for diagnostic purposes and are used in treatment programs for various dental conditions. In the current study, these panoramic radiographs were used again. In this study, the sample sizes of the Han population of Chinese in 2009 to 2011 and 2021 were similar, and thus the results of this study are obtained.

Although there was a study measuring the difference in dental age between races [2, 15, 21], this is the first study to compare dental development by the Demirjian method and the Willems method in a huge sample from the Han population of Chinese from 2009 to 2011 and 2021. Among this study, only the Willems method for females in 2009 to 2011 showed that the dental age was underestimated in relation to the chronological age, and all the rest showed that the dental age was overestimated in relation to the chronological age. Moreover, both Chinese males and females in 2021 showed that their dental age was underestimated in relation to their chronological age. Shanghai has a large floating population from other regions or even foreign countries. However, since the difference in dental age in 2009 to 2011 and 2021 shown in this study unified the race into the Han population of China, the difference between dental age and races can be excluded from this study. Therefore, dental age could be related to environmental factors such as air pollution, water pollution, soil pollution, dietary habits, floating population, and internationalisation of cities.

In some studies, changes in dental development between populations have been reported [17, 25]. Although the reasons for the change in dental development between populations are not fully understood, it remains to be discussed whether genetic and environmental factors have population differences in dental development [13]. The main factors affecting dental growth and development include hereditary factors and environmental factors, mainly environmental factors [3]. Hereditary factors include family history, race, and even gender. Ethnic evolution is one of the congenital factors affecting dental growth and development. Environmental factors, such as nutritional status, virus infection, drug stimulation, dietary habits, environmental pollution, X-ray radiation, and bad habits, may indirectly cause dental dysplasia, dental

morphology, or malocclusion [3]. There are some differences in water source, soil, dietary habits, and other conditions in different regions, which will indirectly affect the mineral absorption, nutritional conditions, and trace element intake of the human body, to affect the mineralisation and development of tooth roots.

Some researchers have already found that there are differences in dental development by geographically similar races or other races. Australians have significantly delayed dental development by 0.82 years compared to the British [21]. Likewise, there was a marked difference in tooth development among children in Saudi Arabia and Australia [2]. And in another study, dental maturity was 0.40 years faster for Hong Kong Chinese than for the UK Caucasians [15]. As they become globalized, the characteristics of the populations have changed significantly, and their physical conditions have also changed. Dental parameters continue to evolve, which may be related to a marked change in nutritional status, socioeconomic conditions, and genetic. Accordingly, the standards for dental growth and development of the population are expected to change over time.

Controversy continues over whether nutrition, environment, dietary habits, chronic diseases, or infectious diseases affect dental development [15]. Some researchers observed that malnutrition did not affect dental development [4, 8, 9], but other researchers reported that malnutrition delays dental development. The difference in these reports shows that it is not easy to investigate the difference in the timing of dental maturity. The Demirjian method and the Willems method are used to estimating dental age, and whether there is a difference in dental age estimation of digital panoramic radiographs between 2009 to 2011 and 2021. The Demirjian method overestimated the dental age by 0.65 for males and 0.48 for females in 2009–2011. The Willems method overestimated by 0.19 for males and underestimated by –0.08 for females in 2009–2011. The Demirjian method underestimated by –0.51 for males and –0.48 for females in 2021. The Willems method underestimated by –0.80 for males and –0.82 for females in 2021.

It shows the consistency of studies with differences in dental age estimates between different regions or within the same region. The reason for this difference is probably that changes in China's environment and dietary habits have affected dental age.

With the rapid development of China's society and economy, the problem of environmental pollution

caused by human activities is becoming more and more serious. As the mode of economic development is still dominated by industry, the relatively rough economic structure has brought serious environmental problems, such as air pollution, water pollution, soil pollution, and so on. Researchers in several fields have found that many common environmental factors can affect the growth of children and adolescents [28]. In different environments, such as environmental pollution and dietary habits, it will affect the growth, development, and morphology of teeth [18].

Recently, with the increasingly frequent foreign exchanges and the popularity of western food in China, parents tend to reward their children with fast food. Western fast food has become a common diet. In addition, nowadays, the industrialisation era has contributed to the popularity of processed foods. About 95% of processed foods, even oatmeal, avocado, whole wheat bread, and vegetable soup, which are considered to be healthy foods, are very delicate and soft, and almost do not need to be chewed. With the change of food from raw to cooked, from coarse to fine, and from hard to soft, human chewing masticatory also gradually degenerates, and teeth become smaller and fewer. These phenomena cause a malocclusion, microdontia, and hypodontia. Furthermore, these findings provide solid evidence for the exploration of the aetiology of malocclusion [16].

The difference in dental age from 2009 to 2011 and 2021 in this study indicates that changes in the period of dental development may be affected by environmental and dietary factors. However, since there is a lot of debate among researchers now, we need to take a step further on the effects of nutrition, environment, floating population, and dietary habits on dental development.

CONCLUSIONS

This is the first study including a large sample of the Han population of Chinese from 2009 to 2011 and 2021, comparing dental development with the Demirjian method and the Willems method. In conclusion, according to the results of this study, the dental ages determined using the Demirjian method and the Willems method from 2009 to 2011 and 2021 showed a significant difference. It appears that there is a relationship between dental development and the environmental factors such as nutrition and dietary habits. However, since the results of this study are samples limited to Shanghai, further studies are

recommended to obtain more accurate results for other races and geographic regions.

Acknowledgements

This work was supported by the Interdisciplinary Programme of SJTU, Shanghai, China (No. YG2019Z-DA07); and Science and Technology Commission of Shanghai "The mechanism of circ-rpl41 regulating Beclin1 and Runx1 to promote odontoblast differentiation of human dental pulp stem cells" (20ZR1431300).

Conflict of interest: None declared

REFERENCES

- Akkaya N, Yılançı HÖ, Boyacıoğlu H, et al. Accuracy of the use of radiographic visibility of root pulp in the mandibular third molar as a maturity marker at age thresholds of 18 and 21. *Int J Legal Med.* 2019; 133(5): 1507–1515, doi: [10.1007/s00414-019-02036-x](https://doi.org/10.1007/s00414-019-02036-x), indexed in Pubmed: [30864070](https://pubmed.ncbi.nlm.nih.gov/30864070/).
- Al-Tuwirqi A, Holcombe T, Seow WK. A study of dental development in a Caucasian population compared with a non-Caucasian population. *Eur Arch Paediatr Dent.* 2011; 12(1): 26–30, doi: [10.1007/BF03262775](https://doi.org/10.1007/BF03262775), indexed in Pubmed: [21299942](https://pubmed.ncbi.nlm.nih.gov/21299942/).
- Brook AH, Fearné JM, Smith JM. Environmental causes of enamel defects. *Ciba Found Symp.* 1997; 205: 212–221, doi: [10.1002/9780470515303.ch15](https://doi.org/10.1002/9780470515303.ch15), indexed in Pubmed: [9189627](https://pubmed.ncbi.nlm.nih.gov/9189627/).
- Cameriere R, Flores-Mir C, Mauricio F, et al. Effects of nutrition on timing of mineralization in teeth in a Peruvian sample by the Cameriere and Demirjian methods. *Ann Hum Biol.* 2007; 34(5): 547–556, doi: [10.1080/03014460701556296](https://doi.org/10.1080/03014460701556296), indexed in Pubmed: [17786590](https://pubmed.ncbi.nlm.nih.gov/17786590/).
- Cameriere R, Pacifici A, Pacifici L, et al. Age estimation in children by measurement of open apices in teeth with Bayesian calibration approach. *Forensic Sci Int.* 2016; 258: 50–54, doi: [10.1016/j.forsciint.2015.11.005](https://doi.org/10.1016/j.forsciint.2015.11.005), indexed in Pubmed: [26650061](https://pubmed.ncbi.nlm.nih.gov/26650061/).
- De Donno A, Angrisani C, Mele F, et al. Dental age estimation: Demirjian's versus the other methods in different populations. A literature review. *Med Sci Law.* 2021; 61(1_suppl): 125–129, doi: [10.1177/0025802420934253](https://doi.org/10.1177/0025802420934253), indexed in Pubmed: [33591866](https://pubmed.ncbi.nlm.nih.gov/33591866/).
- Demirjian A, Goldstein H, Tanner JM. A new system of dental age assessment. *Hum Biol.* 1973; 45(2): 211–227, indexed in Pubmed: [4714564](https://pubmed.ncbi.nlm.nih.gov/4714564/).
- Eid RMR, Simi R, Friggi MNP, et al. Assessment of dental maturity of Brazilian children aged 6 to 14 years using Demirjian's method. *Int J Paediatr Dent.* 2002; 12(6): 423–428, doi: [10.1046/j.1365-263x.2002.00403.x](https://doi.org/10.1046/j.1365-263x.2002.00403.x), indexed in Pubmed: [12452984](https://pubmed.ncbi.nlm.nih.gov/12452984/).
- Elamin F, Liversidge HM. Malnutrition has no effect on the timing of human tooth formation. *PLoS One.* 2013; 8(8): e72274, doi: [10.1371/journal.pone.0072274](https://doi.org/10.1371/journal.pone.0072274), indexed in Pubmed: [24023614](https://pubmed.ncbi.nlm.nih.gov/24023614/).
- Esan TA, Yengopal V, Schepartz LA. The Demirjian versus the Willems method for dental age estimation in different populations: A meta-analysis of published studies. *PLoS One.* 2017; 12(11): e0186682, doi: [10.1371/journal.pone.0186682](https://doi.org/10.1371/journal.pone.0186682), indexed in Pubmed: [29117240](https://pubmed.ncbi.nlm.nih.gov/29117240/).
- Fishman LS. Radiographic evaluation of skeletal maturation. A clinically oriented method based on hand-wrist films. *Angle Orthod.* 1982; 52(2): 88–112, doi: [10.1043/0003-3219\(1982\)052<0088:REOSM>2.0.CO;2](https://doi.org/10.1043/0003-3219(1982)052<0088:REOSM>2.0.CO;2), indexed in Pubmed: [6980608](https://pubmed.ncbi.nlm.nih.gov/6980608/).
- Fisherman LS. Maturation patterns and prediction during adolescence. *Angle Orthod.* 1987; 57: 178–193.
- Garn SM, Lewis AB, Kerewsky RS. Genetic, nutritional, and maturational correlates of dental development. *J Dent Res.* 1965; 44: 228–242, doi: [10.1177/00220345650440011901](https://doi.org/10.1177/00220345650440011901), indexed in Pubmed: [14242327](https://pubmed.ncbi.nlm.nih.gov/14242327/).
- Gupta S, Mehendiratta M, Rehani S, et al. Age estimation in Indian children and adolescents in the NCR region of Haryana: A comparative study. *J Forensic Dent Sci.* 2015; 7(3): 253–258, doi: [10.4103/0975-1475.172453](https://doi.org/10.4103/0975-1475.172453), indexed in Pubmed: [26814053](https://pubmed.ncbi.nlm.nih.gov/26814053/).
- Jayaraman J, Roberts GJ. Comparison of dental maturation in Hong Kong Chinese and United Kingdom Caucasian populations. *Forensic Sci Int.* 2018; 292: 61–70, doi: [10.1016/j.forsciint.2018.09.005](https://doi.org/10.1016/j.forsciint.2018.09.005), indexed in Pubmed: [30269046](https://pubmed.ncbi.nlm.nih.gov/30269046/).
- Kono K, Tanikawa C, Yanagita T, et al. A novel method to detect 3D mandibular changes related to soft-diet feeding. *Front Physiol.* 2017; 8: 567, doi: [10.3389/fphys.2017.00567](https://doi.org/10.3389/fphys.2017.00567), indexed in Pubmed: [28855872](https://pubmed.ncbi.nlm.nih.gov/28855872/).
- Liversidge HM, Chaillet N, Mörnstad H, et al. Timing of Demirjian's tooth formation stages. *Ann Hum Biol.* 2009; 33(4): 454–470, doi: [10.1080/03014460600802387](https://doi.org/10.1080/03014460600802387).
- Nayak B, Roy MM, Chakraborti D. Dental fluorosis. *Clin Toxicol (Phila).* 2009; 47(4): 355, doi: [10.1080/15563650802660356](https://doi.org/10.1080/15563650802660356), indexed in Pubmed: [19274507](https://pubmed.ncbi.nlm.nih.gov/19274507/).
- Park H, Zhou Z, Tao J, et al. A comparative study on estimating dental age of adolescents in Shanghai. *J Oral Mat Instr.* 2019; 28(1): 16–22.
- Patnana AK, Vabbalareddy RS, V Vanga NR. Evaluating the reliability of three different dental age estimation methods in visakhapatnam children. *Int J Clin Pediatr Dent.* 2014; 7(3): 186–191, doi: [10.5005/jp-journals-10005-1262](https://doi.org/10.5005/jp-journals-10005-1262), indexed in Pubmed: [25709299](https://pubmed.ncbi.nlm.nih.gov/25709299/).
- Peiris TS, Roberts GJ, Prabhu N. Dental Age Assessment: a comparison of 4- to 24-year-olds in the United Kingdom and an Australian population. *Int J Paediatr Dent.* 2009; 19(5): 367–376, doi: [10.1111/j.1365-263X.2009.00984.x](https://doi.org/10.1111/j.1365-263X.2009.00984.x), indexed in Pubmed: [19486370](https://pubmed.ncbi.nlm.nih.gov/19486370/).
- Ritz-Timme S, Cattaneo C, Collins MJ, et al. Age estimation: the state of the art in relation to the specific demands of forensic practise. *Int J Legal Med.* 2000; 113(3): 129–136, doi: [10.1007/s004140050283](https://doi.org/10.1007/s004140050283), indexed in Pubmed: [10876982](https://pubmed.ncbi.nlm.nih.gov/10876982/).
- Rózyło-Kalinowska I, Kiworkowa-Raczkowska E, Kalinowski P. Dental age in Central Poland. *Forensic Sci Int.* 2008; 174(2-3): 207–216, doi: [10.1016/j.forsciint.2007.04.219](https://doi.org/10.1016/j.forsciint.2007.04.219), indexed in Pubmed: [17540524](https://pubmed.ncbi.nlm.nih.gov/17540524/).
- Rózyło-Kalinowska I, Kolasa-Rączka A, Kalinowski P. Relationship between dental age according to Demirjian and cervical vertebrae maturity in Polish children. *Eur J Orthod.* 2011; 33(1): 75–83, doi: [10.1093/ejo/cjq031](https://doi.org/10.1093/ejo/cjq031), indexed in Pubmed: [20558591](https://pubmed.ncbi.nlm.nih.gov/20558591/).
- Tunc ES, Koyuturk AE. Dental age assessment using Demirjian's method on northern Turkish children. *Forensic Sci Int.* 2008; 175(1): 23–26, doi: [10.1016/j.forsciint.2007.04.228](https://doi.org/10.1016/j.forsciint.2007.04.228), indexed in Pubmed: [17560060](https://pubmed.ncbi.nlm.nih.gov/17560060/).
- Wang J, Bai X, Wang M, et al. Applicability and accuracy of Demirjian and Willems methods in a population of Eastern Chinese subadults. *Forensic Sci Int.* 2018; 292: 90–96, doi: [10.1016/j.forsciint.2018.09.006](https://doi.org/10.1016/j.forsciint.2018.09.006), indexed in Pubmed: [30286341](https://pubmed.ncbi.nlm.nih.gov/30286341/).
- Willems G, Van Olmen A, Spiessens B, et al. Dental age estimation in Belgian children: Demirjian's technique revisited. *J Forensic Sci.* 2001; 46(4): 893–895, indexed in Pubmed: [11451073](https://pubmed.ncbi.nlm.nih.gov/11451073/).
- Xi HJ, Li WH. Analysis of environmental factors influencing on growth and development of plateau children and adolescents in China. *Acta Anatomica Sinica.* 2018; 49(6): 770–781.
- Yang Z, Geng K, Liu Y, et al. Accuracy of the Demirjian and Willems methods of dental age estimation for children from central southern China. *Int J Legal Med.* 2019; 133(2): 593–601, doi: [10.1007/s00414-018-1924-3](https://doi.org/10.1007/s00414-018-1924-3), indexed in Pubmed: [30206691](https://pubmed.ncbi.nlm.nih.gov/30206691/).
- Ye X, Jiang F, Sheng X, et al. Dental age assessment in 7-14-year-old Chinese children: comparison of Demirjian and Willems methods. *Forensic Sci Int.* 2014; 244: 36–41, doi: [10.1016/j.forsciint.2014.07.027](https://doi.org/10.1016/j.forsciint.2014.07.027), indexed in Pubmed: [25195126](https://pubmed.ncbi.nlm.nih.gov/25195126/).

Anatomical variations of the biceps brachii insertion: a proposal for a new classification

B. Szewczyk¹, F. Paulsen^{2,3}, R.F. LaPrade⁴, A. Borowski⁵, N. Zielinska¹, Ł. Olewnik¹

¹Department of Anatomical Dissection and Donation, Medical University of Lodz, Poland

²Institute of Functional and Clinical Anatomy, Erlangen, Germany

³Department of Topographic Anatomy and Operative Surgery, Sechenov University, Moscow, Russia

⁴Twin Cities Orthopaedics, Edina, Minnesota, United States

⁵Clinic of Orthopaedic and Paediatric Orthopaedics, Medical University of Lodz, Poland

[Received: 2 October 2021; Accepted: 17 January 2022; Early publication date: 28 February 2022]

Background: The biceps brachii (BB) muscle is one of the three muscles located in the anterior compartment of the arm. Its insertion consists of two parts. The first part — main tendon — attached in the radial tuberosity and the second part — lacertus fibrosus (LF) — in the fascia of the forearm flexors. The intention of research was to reveal the morphological diversity of the insertion of this muscle. Thanks to the results of this work, have been created a classification of the distal attachment of BB. The results of that research can be used to further develop surgical procedures in the given region.

Materials and methods: Eighty (40 left, and 40 right, 42 female, 38 male) upper limbs fixed in 10% formalin solution were examined.

Results: We observed three types of the insertion of the BB. Type I was characterised by a single tendon and occurred most frequently in 78.75% of the examined limbs. The second most common type was type II which was characterised by a double tendon and was observed in 13.75% of all the limbs. The last and least common was type III which was characterised by three tendons and occurred in 7.5% of the examined limbs. Additionally, the type of LF was analysed. In 8 (10%) specimens it was absent, i.e. in 2 specimens with type II insertion and 6 specimens with type III ($p = 0.0001$). Therefore, it may be deduced that type III BB insertion tendon predisposes to LF deficiency.

Conclusions: The BB tendon is characterised by high morphological variability. The new classification proposes three types of distal attachment: type I — one tendon; type II — two separated band-shaped tendons; type III — three separated band-shaped tendons. The presence of type III BB tendon predisposes to a lack of LF. (Folia Morphol 2023; 82, 2: 359–367)

Key words: biceps brachii, biceps brachii tendon, lacertus fibrosus, bicipital aponeurosis, new classification

Address for correspondence: Ł. Olewnik, DPT, PhD, Ass. Prof., Department of Anatomical Dissection and Donation, Medical University of Lodz, ul. Żeligowskiego 7/9, 90–136 Łódź, Poland, e-mail: lukasz.olewnik@umed.lodz.pl

This article is available in open access under Creative Common Attribution-Non-Commercial-No Derivatives 4.0 International (CC BY-NC-ND 4.0) license, allowing to download articles and share them with others as long as they credit the authors and the publisher, but without permission to change them in any way or use them commercially.

INTRODUCTION

The anterior compartment of the arm consists of three muscles: the biceps brachii (BB), brachialis and coracobrachialis muscle. The BB usually consists of two heads: long and short [29]. The short head of the BB, together with the coracobrachialis muscle, originates from the apex of the coracoid process of the scapula, whereas the long head of the BB originates from the supra-glenoid tubercle of the scapula [29]. The proximal tendons belong to long head of BB and short head of BB transform in to muscle tissue that form two muscle bellies. In the distal part, those separated muscle bellies connect together [3, 6, 7].

Insertion of BB consists of two components. One of it is a tendon attached into the radial tuberosity, and the second component being the lacertus fibrosus (LF) which fuses with the fascia of the forearm flexors [6, 7].

The primary functions of the BB are flexion of the elbow and supination of the forearm. In fact, the BB is the prime supinator of the forearm. Since it crosses the glenohumeral joint, it also assists in the shoulder flexion. Depending on the angle of the elbow, the BB performs different actions to cause movements of the upper limb. For example, if the elbow is extended, the BB is a pure elbow flexor until it reaches 90-degree flexion, while at 90 degrees flexion and with the forearm supinated, it produces elbow flexion most efficiently. Also, at 90-degree flexion and with the forearm pronated, the BB becomes the primary forearm supinator [38]. The lacertus fibrosus, on the other hand, has a more complicated function. It is believed that it increases the tension of the main tendon of the BB; it also protects the median nerve and brachial artery running posteriorly [8, 11, 24, 40]. In addition, it plays a significant role in the reinforcement of the antebrachial fascia [24, 38].

The BB is characterised by morphological variability, both in the number of muscle bellies [1, 5, 11, 17, 19, 22, 23], proximal attachments [3, 15, 20, 38, 44], and the variability of its distal attachment, which is much less frequently described in the literature [8, 24, 40].

Studies based on the variability in the types of BB bellies have a significant impact over this research. It could be said whether the number of bellies indicate amount of insertion parts. Also imaging research, e.g. in case of BB insertion rupture/tear, are essential for ongoing research. When imaging, the damaged tendon can be felt superficially (palpation). Examination

of the anatomical variant in detail will allow for more accurate imaging studies [2, 17].

The previous studies of the insertion of the BB assess, for example, the arrangement of the distal portion of BB and the points of reference, this serves in research of relationship between heads of BB and its insertion. It would have a potential clinical value to clarify the particular arrangement of the muscle bellies and tendon fibres. May affect the forces exerted on the distal tendon of insertion. Another work, tries to test the tendon footprint. Decreased radial tuberosity height effectively reduces the biceps supination of forearm, thereby limiting the peak supination torque and ability of the biceps to do work [17].

As a result of the analysis of the available studies on the distal attachment of the BB muscle, there were no measurements such as width, length, thickness according to direct type of insertion: one band, two bands, three bands. Also there was lack information about any correlation between the type of insertion and the superficial LF layer shown in results of measurement as width, length, thickness. Whether there are relationships between the type of trailer and gender or body side? Will any of the types show clearly different dimensions (width, thickness, length) from the others? This study remedies these gaps.

The BB muscle is exposed to frequent overloads. This leads to consecutive micro-injuries, which in turn trigger inflammation and subsequent biceps tendinopathy. A significant occurrence of loads on this muscle may be indicated by the fact that the rupture of the tendon of the head of a long biceps can happen at any age. Many sports aimed at using the strength of the upper limbs lead to a significant load on the work of the BB muscle. In the first place may be one-handed disciplines such as badminton, arm wrestling and two-handed such as ice hockey, tennis. In second place were sports involving throwing, e.g. American football, baseball [15, 20, 38]. Distal tendon ruptures are diagnosed less frequently [26].

Injury to the distal BB tendon is very common in the fourth to sixth decade of life. It usually occurs in the dominant arm of men [25, 27]. The most common cause of such damage is a sudden exertion of an eccentric force on the supinated forearm at the moment when the BB muscle is tense or partially tense [27, 28]. In addition, the irregularity of the radial tuberosity can lead to damage to the attachment of the distal biceps muscle [39].

Examination and anatomical classification of this area due to the multiplicity of damage and the subsequent necessity to perform insertion reconstruction treatments will help in better preparation for the repair plan [28, 39].

The main objective of this study is to provide the measurements that were mentioned in the previous paragraphs and answer the questions. This information could potentially assist in detecting a predisposition to developing tendon injury, if such a relationship were established. Also the purpose of the present study was to characterise the possible variations in the morphology of the distal attachments of the BB and to draw relevant conclusions with regard to an accurate classification of the area that can be useful for improved evaluation of imaging and for planning surgical procedures in the region.

The hypothesis was that there would be variation in the distal BB morphology and that a classification system could be developed. The clinical importance of BB muscle gives us motivation to carry out this research with an aim to determine variation of BB insertion.

MATERIALS AND METHODS

An electronic digital calliper was used for all measurements (Mitutoyo Corporation, Kawasaki-shi, Kanagawa, Japan), and each measurement was performed twice with an accuracy of up to 0.1 mm. The Bioethics Committee of the Medical University of Lodz (resolution RNN/1337/20/KE) approved the study protocol. All methods and techniques used during carrying out the research were in accordance with the protocol approved above. The cadavers belonged to the Department of Anatomical Dissection and Donation of the Medical University of Lodz, Poland.

Eighty (40 left, and 40 right; 42 female, 38 male) upper limbs fixed in 10% formalin solution were examined. The mean age of the cadavers at death was 77.9 years (standard deviation [SD] = 22.5) (53–95) (Central European population). The cadavers were the property of the Department of Anatomical Dissection and Donation, Medical University of Lodz, Poland, having been obtained as donation to the university anatomy programme. Any upper limbs with evidence of surgical intervention in the dissected area were excluded. All dissection procedures in the shoulder and arm area were performed in accordance with a pre-established protocol [30, 31, 33–36, 45, 46].

Dissection began with the removal of the skin and superficial fascia from the area of the shoulder

and anterior and medial side of the arm and the anterior side of the forearm. The next stage included visualisation of the lateral, medial and posterior cords of the brachial plexus, and visualisation of both BB, coracobrachialis, and brachialis muscles. Then, the site of the lacerum was carefully checked. After checking and measuring the lacerum, the muscles of the anterior forearm group were delaminated to locate and check as well as to measure the tendons and examine their insertion. Next, all the structures were thoroughly cleaned [32, 38, 41].

Upon dissection, the following morphological features of the BB were assessed:

- the morphology of the BB lacerum:
 - (proximal) width and thickness at the beginning at the point of detachment from the terminal tendon line;
 - (distal) width and thickness at the end of lacertum fibrosum, the type of BB insertion (indicated by number of tendons);
- morphometric measurements of the BB:
 - (distal) width and thickness at the point of attachment to radial tuberosity;
 - length from attachment radial tuberosity till start of muscle belly.

The procedure of BB dissection was performed in accordance with the following principles:

- when clearing the BB, attention should be paid to the presence of its accessory heads;
- when checking the BB, the distal part should be carefully studied for the presence of coracobrachialis longus muscle and for the relationships between the median nerve and musculocutaneous nerve.

Ethical approval and consent to participate

The Bioethics Committee of the Medical University of Lodz (resolution RNN/1337/20/KE) approved the study protocol. The cadavers belonged to the Department of Anatomical Dissection and Donation of the Medical University of Lodz, Poland. Informed consents were obtained from all participants before they died.

Statistical analysis

A χ^2 test were used to compare differences in insertion types between genders, sides of the body. The Shapiro-Wilk test was used to check the normality of the data. The Manny-Whitney test and the Wilcoxon test were used to compare data on gender and sides of the body. In order to compare data on



Figure 1. Type I of biceps brachii insertion; shBB — short head of the biceps brachii; lhBB — long head of the biceps brachii; R — radius bone.

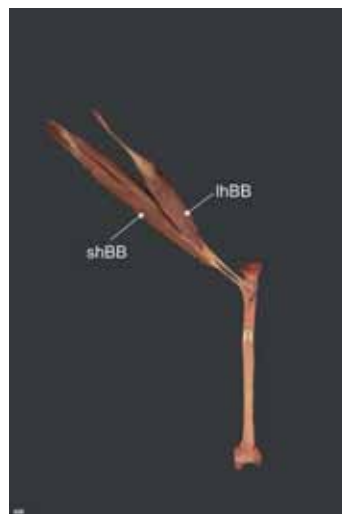


Figure 2. Type II of the biceps brachii insertion; shBB — short head of the biceps brachii; lhBB — long head of the biceps brachii; R — radius bone.

measurements of the indicated types of insertion, we used the Mann-Whitney test and the Kruskal-Wallis test with the appropriate *post hoc* test.

For analysis, Statistica 13.1 was employed. We considered that p-value lower than 0.05 was statistically significant. In addition, Bonferroni correction was used for multiple comparisons.

RESULTS

Anatomic study

In all 80 limbs, the BB insertion was present and suitable for morphological analysis. Based on a morphological analysis, the following types of BB insertion were differentiated:

- type I — was characterised by a single tendon and insertion into the radial tuberosity of the radius. This type was found in 63 upper limbs (78.75%) (34 females, 29 males; 32 right and 31 left) (Fig. 1);
- type II — was characterized by a double tendon and insertion into the radial tuberosity of the radius. This type was observed in 11 limbs (13.75%) (2 females, 9 males; 5 right and 6 left) (Fig. 2);
- type III — was characterised by a triple tendon and insertion into the radial tuberosity. This type was recognised in 6 upper limbs (7.5%) (6 females, 0 males; 3 right and 3 left) (Fig. 3).

Type II was significantly more common in males, whereas type III in females ($p = 0.0013$). There was no significant difference in the frequency of type occurrence between side of the body ($p = 0.9479$).



Figure 3. Type III of biceps brachii insertion; shBB — short head of the biceps brachii; lhBB — long head of the biceps brachii; R — radius bone.

Additionally, the type of LF was analysed (Fig. 4). In 8 specimens it was absent (10%; 8 females, 0 males, $p = 0.2686$; 4 right and 4 left; in 2 specimens with type II insertion and 6 specimens with type III, $p = 0.0001$).

Comparison of morphological data between genders and side of the body is presented in Table 1. Table 2 demonstrates data on insertion types.

According to a post-hoc analysis, the length of tendon I in type I and III is almost equal and its higher than in type II, while tendon I width was greater in type I than in types II and III.



Figure 4. Lacertus fibrosus; lhBB — long head of the biceps brachii; shBB — short head of the biceps brachii; MN — median nerve; BA — brachial artery; BRM — brachioradialis muscle; LF — lacertus fibrosus.

DISCUSSION

The BB muscle probably arises from a common pre-muscle mass with coracobrachialis, and brachialis. All three muscles in very early stages are intimately fused together. The origins of the long and short head of the BB at this early prenatal life are close to each other, and later growth of the scapula will separate them. The distal insertion of the common muscle mass varies at the later time than the proximal [6, 7].

In most cases the distal BB tendon is described as easily divided into two components; an anterior layer linked to the short head, and a posterior layer linked to the long head [7].

The key value of the work is presentation of a new systematic classification of the distal BB insertion based on anatomical dissection. It should be emphasized that this is the first classification of this type that is necessary for orthopaedists and surgeons operating in this area. It can also be useful for physiotherapists when planning rehabilitation procedures and radiologist for imaging analysis [6, 7].

Many studies are focused on the measurement of the tendon and lacertus fibrosus [11, 40]. Eames et al. [13] and also Snoeck et al. [40] observed that LF superficial layer was present in all tested limbs. In the present study, the absence of LF superficial layer was observed in 10%.

In the present study, we have noticed that LF originates both from the long and short head of BB, extends over the pronator teres and connects to the fascia of the forearm, as described earlier by other researchers [3, 6, 7, 40]. The finding that the short and long head in the myotendinous junction was the origin of the LFs was crucial as it identified LF as an important landmark that allows identification of the short head of the tendon and, therefore, correct orientation of the entire distal biceps' tendon during surgical repair [40].

Table 1. Morphometric parameters according to gender and side of the body

Parameter	Sex		P value	Side of the body		P value
	Females	Males		Right	Left	
Tendon I length	66.08 (12.08)	65.92 (12.30)	0.7396	66.08 (12.09)	65.93 (12.28)	0.9037
Tendon I width	7.83 (3.94)	6.04 (2.25)	0.0313	7.01 (3.38)	6.94 (3.36)	0.2736
Tendon I thickness	2.52 (0.65)	2.54 (0.67)	0.9539	2.54 (0.67)	2.52 (0.65)	0.8945
Tendon II length	59.92 (9.74)	55.78 (2.76)	0.0922	58.22 (7.26)	57.29 (7.29)	0.4008
Tendon II width	2.53 (0.55)	3.98 (0.58)	0.0012	3.32 (1.09)	3.27 (0.83)	0.7353
Tendon II thickness	1.78 (0.20)	2.33 (0.38)	0.0006	2.06 (0.45)	2.09 (0.40)	0.8886
Tendon III length	66.46 (3.21)			66.37 (3.59)	66.55 (3.58)	1.0000
Tendon III width	1.91 (0.30)			1.76 (0.22)	2.06 (0.33)	0.1088
Tendon III thickness	1.39 (0.12)			1.35 (0.12)	1.43 (0.11)	0.1088
Lacertus fibrosus length	38.58 (8.76)	36.83 (10.19)	0.4272	37.49 (9.63)	37.91 (9.45)	0.0218
Lacertus fibrosus width proximal	7.62 (3.98)	6.41 (3.27)	0.2281	6.93 (3.64)	7.10 (3.74)	0.3419
Lacertus fibrosus thickness proximal	1.15 (0.63)	1.11 (0.41)	0.9551	1.13 (0.53)	1.12 (0.54)	0.5043
Lacertus fibrosus width distal	12.39 (6.80)	12.26 (10.05)	0.3054	12.59 (8.83)	12.07 (8.32)	0.9249
Lacertus fibrosus thickness distal	1.67 (0.70)	1.58 (0.40)	0.7269	1.60 (0.55)	1.64 (0.60)	0.3339

Table 2. Morphometric parameters according to insertion types

Parameter	Insertion types			P value
	I	II	III	
Tendon I length	68.76 (11.72)	51.83 (5.30)	63.09 (3.27)	0.0001
Tendon I width	7.93 (3.10)	3.91 (1.24)	2.60 (0.10)	0.0001
Tendon I thickness	2.62 (0.65)	2.23 (0.72)	2.09 (0.12)	0.001
Tendon II length		53.77 (5.12)	65.00 (3.04)	0.0011
Tendon II width		3.87 (0.58)	2.24 (0.19)	0.0011
Tendon II thickness		2.18 (0.48)	1.87 (0.10)	0.0392
Tendon III length			66.46 (3.21)	
Tendon III width			1.91 (0.30)	
Tendon III thickness			1.39 (0.12)	
Lacertus fibrosus length	39.07 (9.05)	28.09 (6.61)		0.0003
Lacertus fibrosus width proximal	7.17 (3.88)	5.96 (1.16)		0.8782
Lacertus fibrosus thickness proximal	1.13 (0.56)	1.13 (0.15)		0.7143
Lacertus fibrosus width distal	12.90 (8.91)	8.33 (2.97)		0.3852
Lacertus fibrosus thickness distal	1.60 (0.57)	1.79 (0.55)		0.4641

Athwal et al. [2] describe that the short head of biceps brachii is the starting point of LF. On the other hand, Dirim et al. [12] describe formation of the LF by combining superficial tendon-type fibres arising from both heads of the biceps muscle of the arm. In presented research LF was described same as Dirim did.

The most thorough examination was carried out by Eames et al. [13] who pointed out that LF is formed by the combination of three layers. The long head from its radial side forms the first and thickest layer. The second layer is the middle layer. It is formed by the combination of aponeurosis and a short head. It has the form of loose tissue [13]. The third layer starts as in the case of the first layer only deeper. In addition, it is strengthened by a superficial layer of aponeurosis [13].

Compare presented research to the work of Snoeck et al, the measurement of the LF length was made as a central dimension (according to the manuscript of Snoeck et al. [40]) and it appear no significant statistical differences. Lacertus fibrosus did not show significant variations related to gender, Same result occurred in research of Forthman et al. [16].

Unfortunately width and thickness are unable to be compared. Measuring equipment and measurement procedures may have differed between studies. Most research on the distal part of the BB is limited to performing narrowed morphometric measurements of the tendon as well as describing the LF and the relationship between the BB and LF tendons [8, 11, 13, 21, 26].

Athwal et al. [2] described that it is possible to “separate” the tendon fibres belonging to the short or long head of BB. They specified two attachment sites on the radial tuberosity of the radius. The superior aspect is occupied by the long head of BB and the inferior aspect is occupied by the short head of BB [2]. Also Forthman et al. [16] examined radial tuberosity for the extent of insertion of biceps brachii. The biceps tendon footprint lies over the apex of the tuberosity, with the geometric centre of the tendon inserting in less pronation [2].

Unlike Athwal et al. [2], we did not observe the possibility of “separating” tendons from each other. We strongly believe that the division into the superior and inferior aspect of insertion of the short and long head of BB is not exceptionally reliable, due to the fact that subsequent tests should be based on the possibility of checking the distal attachment, e.g. for BB with three, four and e.g. five heads.

In the present study we observed three types of BB tendon insertions. Therefore we proposed a 3-folded classification. Type I is characterised by a single tendon and occurred most frequently (in 78.75%) in the examined limbs. This type was commonly described by many other researchers [2, 5, 6, 12]. The second most common type is type II which was characterised by a double tendon and was observed in 13.75% of all the limbs. Also this type was already mentioned in other researches [23, 25]. The last and rarest one was type III which was characterised by three tendons and

occurred in 7.5% of the examined limbs. Apart from the information about its rare occurrence, no one has described this type before.

Additionally, the type of LF was analysed. Therefore, it may be deduced that type III BB insertion tendon predisposes to LF deficiency. No one ever before described such comparison. Statistical differences were also observed in the study, e.g. the length of tendon I in type I and III is almost equal and its higher than in type II, while tendon I width was greater in type I than in types II and III. Thus, it can be speculated that type I BB tendon insertions are least likely to be affected by rupture or fiberisation as compared to types II and III.

Knowledge of the anatomical variant of BB insertion will allow for a more accurate diagnostic examination of the case [11–13, 27]. Such as:

- tendon rupture (can be complete or partial);
- disinsertion of the tendon (tendon detachment from its insertion may be partial or complete);
- tendinopathy (it causes loss of the fibrillar aspect of the tendon, the structure of which appears disorganised and accompanied by diffuse, heterogeneous thickening);
- enthesopathy (associated with hypoechoic swelling that involves one or all of the tendons that insert on the radial tuberosity);
- bursitis (distention and inflammation of the tendon bursa, which allows the tendon to roll around radial tuberosity);
- peritendinopathy (chronic pain have tendon sheath effusions that are not associated with tendon anomalies).

Unfortunately, we do not have information about side of limb domination, it would be interesting comparison. However, an anatomical comparison of left to right also seems valid. We assume in advance that men exhibit a greater muscle mass of the BB muscle, so it is interesting which type will be dominant depending on gender. It could be assumed that it will be the most durable type.

Women have naturally smaller muscle tissue, so it can be assumed that the muscle naturally causes less stress on the insertion, so a softer (weaker) attachment is enough for effective work. So it appears that type III is the weakest among those three.

An important piece of information for better planning of surgical procedures for repairing the ruptures of the distal attachment of the BB tendon is knowledge of its size and location. Skilfully idling the

course and orientation of this attachment will support surgeons in determining the size of the partial tear in the thickness of this tendon and indicating the associated muscles. Nowadays, surgical procedures to repair the detachment of the biceps tendon are performed on a daily basis. Tendon fracture repair procedures are performed using the technique of one incision (usually suture anchors are used here) or the technique of two cuts [42, 43].

Broken tendons are subject to several treatment techniques: one cut technique (use of seam anchors), two-cut technique (using bone tunnels), biotendinosis screw for fixation and endobuttons [4, 9, 10, 18, 28, 42, 43]. Different methods of double incision (standard and modified) are characterised by a different dimension of showing the ulnar periosteum. The Morrey technique (muscle splitting technique) reduces the possibility of synostosis [14, 37]. It turned out that against the induction of nerve palsy (radial or lateral antebrachial cutaneous nerve) nor the heterotopic ossification does not protect the anterior small incision of the cubital fossa with the execution of muscle splitting technique [43].

Limitations of the study

Our research is not without its limitations. In the first place, it would be necessary to indicate the non-uniform nature of the classification, which is influenced by morphological details, such as shape or surface of the insertion. In the second place, we should mention that as the results of anatomical research we are able to present a jumble of inconsistencies and the continuation of this work should be studies checking the probable value of using ultrasound and magnetic resonance imaging to image and map the area that has been studied in our work. Performing a biomechanical test of each type of tendon would allow to confirm the indication of which of the types is stronger and whether the differences in the range of morphometric measurements are significant. The study also lacked indications of tendon belonging to muscle heads in type 2 and type 3. Another weakness of these studies is the failure to assess the deep LF layers. Despite the indicated limitations, this work brings with it knowledge that allows for a more accurate definition of search in this area of research/treatment. It also indicates a uniform classification and nomenclature, helping in the work of future researchers or surgeons moving in this region.

CONCLUSIONS

The BB tendon is characterised by high morphological and topographical variability. Its insertion can be affected by different types of lesions, some of which are frequently misdiagnosed on the basis of the clinical examination. Therefore it seems very important to develop the new BB insertion classification. It proposes three types of distal attachment (I–III). Additionally, an equally important piece of information is lack of lacertus fibrosus in presence of type III BB tendon.

Acknowledgements

The authors sincerely thank those who donated their bodies to science so that anatomical research could be performed. Results from such research can potentially increase mankind's overall knowledge that can then improve patient care. Therefore, these donors and their families deserve our highest gratitude.

Conflict of interest: Friedrich Paulsen receives royalties from Elsevier for the 24th Ed. of the anatomy atlas "Sobotta" and the 'Sobotta Textbook of Anatomy' 2nd Ed. The authors declare that they have no competing interests.

REFERENCES

- Al-Kushi G. Anatomical study of the third head of biceps brachii muscle and its innervation by median nerve in human dissection. *J Clin Med Res.* 2013; 5(4): 47–52, doi: [10.5897/jcmr12.017](https://doi.org/10.5897/jcmr12.017).
- Athwal GS, Steinmann SP, Rispoli DM. The distal biceps tendon: footprint and relevant clinical anatomy. *J Hand Surg Am.* 2007; 32(8): 1225–1229, doi: [10.1016/j.jhsa.2007.05.027](https://doi.org/10.1016/j.jhsa.2007.05.027), indexed in Pubmed: [17923307](https://pubmed.ncbi.nlm.nih.gov/17923307/).
- Audenaert EA, Barbaix EJ, Van Hoonacker P, et al. Extra-articular variants of the long head of the biceps brachii: a reminder of embryology. *J Shoulder Elbow Surg.* 2008; 17(1 Suppl): 1145–1175, doi: [10.1016/j.jse.2007.06.014](https://doi.org/10.1016/j.jse.2007.06.014), indexed in Pubmed: [18078764](https://pubmed.ncbi.nlm.nih.gov/18078764/).
- Balabaud L, Ruiz C, Nonnenmacher J, et al. Repair of distal biceps tendon ruptures using a suture anchor and an anterior approach. *J Hand Surg Br.* 2004; 29(2): 178–182, doi: [10.1016/j.jhsb.2003.07.002](https://doi.org/10.1016/j.jhsb.2003.07.002), indexed in Pubmed: [15010168](https://pubmed.ncbi.nlm.nih.gov/15010168/).
- Ballesteros LE, Forero PL, Buitrago ER. Evaluation of additional head of biceps brachii: a study with autopsy material. *Folia Morphol.* 2014; 73(2): 193–198, doi: [10.5603/FM.2014.0028](https://doi.org/10.5603/FM.2014.0028), indexed in Pubmed: [24902098](https://pubmed.ncbi.nlm.nih.gov/24902098/).
- Bardeen C. Studies of the development of the human skeleton. *Am J Anat.* 1905: 265–302.
- Bardeen C. Development and variation of the nerves and the musculature of the inferior extremity and of the neighboring regions of the trunk in man. *Am J Anat.* 2005; 6(1): 259–390, doi: [10.1002/aja.1000060108](https://doi.org/10.1002/aja.1000060108).
- Blasi M, de la Fuente J, Martinoli C, et al. Multidisciplinary approach to the persistent double distal tendon of the biceps brachii. *Surg Radiol Anat.* 2014; 36(1): 17–24, doi: [10.1007/s00276-013-1136-y](https://doi.org/10.1007/s00276-013-1136-y), indexed in Pubmed: [23708377](https://pubmed.ncbi.nlm.nih.gov/23708377/).
- Camp CL, Voleti PB, Corpus KT, et al. Single-Incision technique for repair of distal biceps tendon avulsions with intramedullary cortical button. *Arthrosc Tech.* 2016; 5(2): e303–e307, doi: [10.1016/j.eats.2016.01.002](https://doi.org/10.1016/j.eats.2016.01.002), indexed in Pubmed: [27330947](https://pubmed.ncbi.nlm.nih.gov/27330947/).
- Citak M, Backhaus M, Seybold D, et al. Surgical repair of the distal biceps brachii tendon: a comparative study of three surgical fixation techniques. *Knee Surg Sports Traumatol Arthrosc.* 2011; 19(11): 1936–1941, doi: [10.1007/s00167-011-1591-0](https://doi.org/10.1007/s00167-011-1591-0), indexed in Pubmed: [21713413](https://pubmed.ncbi.nlm.nih.gov/21713413/).
- Cucca YY, McLay SVB, Okamoto T, et al. The biceps brachii muscle and its distal insertion: observations of surgical and evolutionary relevance. *Surg Radiol Anat.* 2010; 32(4): 371–375, doi: [10.1007/s00276-009-0575-y](https://doi.org/10.1007/s00276-009-0575-y), indexed in Pubmed: [19847376](https://pubmed.ncbi.nlm.nih.gov/19847376/).
- Dirim B, Brouha SS, Pretterklieber ML, et al. Terminal bifurcation of the biceps brachii muscle and tendon: anatomic considerations and clinical implications. *AJR Am J Roentgenol.* 2008; 191(6): W248–W255, doi: [10.2214/AJR.08.1048](https://doi.org/10.2214/AJR.08.1048), indexed in Pubmed: [19020211](https://pubmed.ncbi.nlm.nih.gov/19020211/).
- Eames MHA, Bain GI, Fogg QA, et al. Distal biceps tendon anatomy: a cadaveric study. *J Bone Joint Surg Am.* 2007; 89(5): 1044–1049, doi: [10.2106/JBJS.D.02992](https://doi.org/10.2106/JBJS.D.02992), indexed in Pubmed: [17473142](https://pubmed.ncbi.nlm.nih.gov/17473142/).
- Eardley WGP, Odak S, Adesina TS, et al. Bioabsorbable interference screw fixation of distal biceps ruptures through a single anterior incision: a single-surgeon case series and review of the literature. *Arch Orthop Trauma Surg.* 2010; 130(7): 875–881, doi: [10.1007/s00402-009-0974-x](https://doi.org/10.1007/s00402-009-0974-x), indexed in Pubmed: [19787360](https://pubmed.ncbi.nlm.nih.gov/19787360/).
- Enad JG. Bifurcate origin of the long head of the biceps tendon. *Arthroscopy.* 2004; 20(10): 1081–1083, doi: [10.1016/j.arthro.2004.09.003](https://doi.org/10.1016/j.arthro.2004.09.003), indexed in Pubmed: [15592239](https://pubmed.ncbi.nlm.nih.gov/15592239/).
- Forthman C, Zimmerman R, Sullivan M, et al. Cross-sectional anatomy of the bicipital tuberosity and biceps brachii tendon insertion: Relevance to anatomic tendon repair. *J Shoulder Elbow Surg.* 2008; 17(3): 522–526, doi: [10.1016/j.jse.2007.11.002](https://doi.org/10.1016/j.jse.2007.11.002).
- Greig HW, Anson BJ, Budinger JM. Variations in the form and attachments of the biceps brachii muscle. *Q Bull Northwest Univ Med Sch.* 1952; 26(3): 241–244, indexed in Pubmed: [14957982](https://pubmed.ncbi.nlm.nih.gov/14957982/).
- Gupta RK, Bither N, Singh H, et al. Repair of the torn distal biceps tendon by endobutton fixation. *Indian J Orthop.* 2012; 46(1): 71–76, doi: [10.4103/0019-5413.91638](https://doi.org/10.4103/0019-5413.91638), indexed in Pubmed: [22345810](https://pubmed.ncbi.nlm.nih.gov/22345810/).
- Ilayperuma I, Nanayakkara G, Palahepitiya N. Incidence of Humeral Head of Biceps Brachii Muscle: Anatomical Insight. *Int J Morphol.* 2011; 29(1): 221–225, doi: [10.4067/s0717-95022011000100037](https://doi.org/10.4067/s0717-95022011000100037).
- Jeong JY, Park SM, Park YE, et al. Morphological classification of anatomical variants of the intra-articular portion of the long head of the biceps brachii tendon and analysis of the incidence and the relationship with shoulder disease for each subtype. *J Orthop Surg (Hong Kong).* 2017; 25(3): 2309499017742207, doi: [10.1177/2309499017742207](https://doi.org/10.1177/2309499017742207), indexed in Pubmed: [29157108](https://pubmed.ncbi.nlm.nih.gov/29157108/).

21. Joshi SD, Yogesh AS, Mittal PS, et al. Morphology of the bicipital aponeurosis: a cadaveric study. *Folia Morphol.* 2014; 73(1): 79–83, doi: [10.5603/FM.2014.0011](https://doi.org/10.5603/FM.2014.0011), indexed in Pubmed: [24590527](https://pubmed.ncbi.nlm.nih.gov/24590527/).
22. Kopuz C, Sancak B, Ozbenli S. On the incidence of third head of biceps brachii in Turkish neonates and adults. *Kaibogaku Zasshi.* 1999; 74(3): 301–305, indexed in Pubmed: [10429374](https://pubmed.ncbi.nlm.nih.gov/10429374/).
23. Kosugi K, Shibata S, Yamashita H. Supernumerary head of biceps brachii and branching pattern of the musculocutaneous nerve in Japanese. *Surg Radiol Anat.* 1992; 14(2): 175–185, doi: [10.1007/BF01794898](https://doi.org/10.1007/BF01794898), indexed in Pubmed: [1641744](https://pubmed.ncbi.nlm.nih.gov/1641744/).
24. Landa J, Bhandari S, Strauss EJ, et al. The effect of repair of the lacertus fibrosus on distal biceps tendon repairs: a biomechanical, functional, and anatomic study. *Am J Sports Med.* 2009; 37(1): 120–123, doi: [10.1177/0363546508324694](https://doi.org/10.1177/0363546508324694), indexed in Pubmed: [19029314](https://pubmed.ncbi.nlm.nih.gov/19029314/).
25. Lee SE, Jung C, Ahn KY, et al. Bilateral asymmetric supernumerary heads of biceps brachii. *Anat Cell Biol.* 2011; 44(3): 238–240, doi: [10.5115/acb.2011.44.3.238](https://doi.org/10.5115/acb.2011.44.3.238), indexed in Pubmed: [22025976](https://pubmed.ncbi.nlm.nih.gov/22025976/).
26. Mazzocca AD, Cohen M, Berkson E, et al. The anatomy of the bicipital tuberosity and distal biceps tendon. *J Shoulder Elbow Surg.* 2007; 16(1): 122–127, doi: [10.1016/j.jse.2006.04.012](https://doi.org/10.1016/j.jse.2006.04.012), indexed in Pubmed: [17055747](https://pubmed.ncbi.nlm.nih.gov/17055747/).
27. McDonald LS, Dewing CB, Shupe PG, et al. Disorders of the proximal and distal aspects of the biceps muscle. *J Bone Joint Surg Am.* 2013; 95(13): 1235–1245, doi: [10.2106/JBJS.L.00221](https://doi.org/10.2106/JBJS.L.00221), indexed in Pubmed: [23824393](https://pubmed.ncbi.nlm.nih.gov/23824393/).
28. Miyazaki AN, Fregoneze M, Santos PD, et al. Functional evaluation of patients with injury of the distal insertion of the biceps brachii muscle treated surgically. *Rev Bras Ortop.* 2014; 49(2): 129–133, doi: [10.1016/j.rboe.2014.03.015](https://doi.org/10.1016/j.rboe.2014.03.015), indexed in Pubmed: [26229788](https://pubmed.ncbi.nlm.nih.gov/26229788/).
29. Moore K, Arthur F, Dalley I, Agur AM. *Clinically Oriented Anatomy.* 7th ed. Lippincott Williams & Wilkins 2013.
30. Olewnik Ł. Is there a relationship between the occurrence of frenular ligaments and the type of fibularis longus tendon insertion? *Ann Anat.* 2019; 224: 47–53, doi: [10.1016/j.aanat.2019.03.002](https://doi.org/10.1016/j.aanat.2019.03.002), indexed in Pubmed: [30930196](https://pubmed.ncbi.nlm.nih.gov/30930196/).
31. Olewnik Ł, Gonera B, Kurtys K, et al. A proposal for a new classification of the fibular (lateral) collateral ligament based on morphological variations. *Ann Anat.* 2019; 222: 1–11, doi: [10.1016/j.aanat.2018.10.009](https://doi.org/10.1016/j.aanat.2018.10.009), indexed in Pubmed: [30408521](https://pubmed.ncbi.nlm.nih.gov/30408521/).
32. Olewnik Ł, Karauda P, Gonera B, et al. Impact of plantaris ligamentous tendon. *Sci Rep.* 2021; 11(1): 4550, doi: [10.1038/s41598-021-84186-w](https://doi.org/10.1038/s41598-021-84186-w), indexed in Pubmed: [33633305](https://pubmed.ncbi.nlm.nih.gov/33633305/).
33. Olewnik Ł, Kurtys K, Gonera B, et al. Proposal for a new classification of plantaris muscle origin and its potential effect on the knee joint. *Ann Anat.* 2020; 231: 151506, doi: [10.1016/j.aanat.2020.151506](https://doi.org/10.1016/j.aanat.2020.151506), indexed in Pubmed: [32173563](https://pubmed.ncbi.nlm.nih.gov/32173563/).
34. Olewnik Ł, Paulsen F, Tubbs RS, et al. Potential compression of the musculocutaneous, median and ulnar nerves by a very rare variant of the coracobrachialis longus muscle. *Folia Morphol.* 2021; 80(3): 707–713, doi: [10.5603/FM.a2020.0085](https://doi.org/10.5603/FM.a2020.0085), indexed in Pubmed: [32844391](https://pubmed.ncbi.nlm.nih.gov/32844391/).
35. Olewnik Ł, Zielinska N, Karuda P, et al. The co-occurrence of a four headed coracobrachialis muscle, split coracoid process and tunnel for the median and musculocutaneous nerve: the potential clinical relevance of a very rare variation. *Surg Radiol Anat.* 2021; 43(5): 661–669, doi: [10.1007/s00276-020-02580-x](https://doi.org/10.1007/s00276-020-02580-x), indexed in Pubmed: [32979058](https://pubmed.ncbi.nlm.nih.gov/32979058/).
36. Olewnik Ł, Zielinska N, Paulsen F, et al. A proposal for a new classification of soleus muscle morphology. *Ann Anat.* 2020; 232: 151584, doi: [10.1016/j.aanat.2020.151584](https://doi.org/10.1016/j.aanat.2020.151584), indexed in Pubmed: [32810614](https://pubmed.ncbi.nlm.nih.gov/32810614/).
37. Olsen JR, Shields E, Williams RB, et al. A comparison of cortical button with interference screw versus suture anchor techniques for distal biceps brachii tendon repairs. *J Shoulder Elbow Surg.* 2014; 23(11): 1607–1611, doi: [10.1016/j.jse.2014.06.049](https://doi.org/10.1016/j.jse.2014.06.049), indexed in Pubmed: [25219472](https://pubmed.ncbi.nlm.nih.gov/25219472/).
38. Podgórski M, Olewnik Ł, Rusinek M, et al. 'Superior biceps aponeurosis' — Morphological characteristics of the origin of the short head of the biceps brachii muscle. *Ann Anat.* 2019; 223: 85–89, doi: [10.1016/j.aanat.2019.01.014](https://doi.org/10.1016/j.aanat.2019.01.014), indexed in Pubmed: [30797975](https://pubmed.ncbi.nlm.nih.gov/30797975/).
39. Seiler JG, Parker LM, Chamberland PD, et al. The distal biceps tendon. Two potential mechanisms involved in its rupture: arterial supply and mechanical impingement. *J Shoulder Elbow Surg.* 1995; 4(3): 149–156, doi: [10.1016/s1058-2746\(05\)80044-8](https://doi.org/10.1016/s1058-2746(05)80044-8), indexed in Pubmed: [7552670](https://pubmed.ncbi.nlm.nih.gov/7552670/).
40. Snoeck O, Lefèvre P, Sprio E, et al. The lacertus fibrosus of the biceps brachii muscle: an anatomical study. *Surg Radiol Anat.* 2014; 36(7): 713–719, doi: [10.1007/s00276-013-1254-6](https://doi.org/10.1007/s00276-013-1254-6), indexed in Pubmed: [24414231](https://pubmed.ncbi.nlm.nih.gov/24414231/).
41. Szewczyk B, Paulsen F, Duparc F, et al. A proposal for a new classification of coracobrachialis muscle morphology. *Surg Radiol Anat.* 2021; 43(5): 679–688, doi: [10.1007/s00276-021-02700-1](https://doi.org/10.1007/s00276-021-02700-1), indexed in Pubmed: [33564931](https://pubmed.ncbi.nlm.nih.gov/33564931/).
42. Tarallo L, Mugnai R, Zambianchi F, et al. Distal biceps tendon rupture reconstruction using muscle-splitting double-incision approach. *World J Clin Cases.* 2014; 2(8): 357–361, doi: [10.12998/wjcc.v2.i8.357](https://doi.org/10.12998/wjcc.v2.i8.357), indexed in Pubmed: [25133147](https://pubmed.ncbi.nlm.nih.gov/25133147/).
43. Tarallo L, Lombardi M, Zambianchi F, et al. Distal biceps tendon rupture: advantages and drawbacks of the anatomical reinsertion with a modified double incision approach. *BMC Musculoskelet Disord.* 2018; 19(1): 364, doi: [10.1186/s12891-018-2278-1](https://doi.org/10.1186/s12891-018-2278-1), indexed in Pubmed: [30305070](https://pubmed.ncbi.nlm.nih.gov/30305070/).
44. Vangsnest CT, Jorgenson SS, Watson T, et al. The origin of the long head of the biceps from the scapula and glenoid labrum. An anatomical study of 100 shoulders. *J Bone Joint Surg. British Vol.* 1994; 76-B(6): 951–954, doi: [10.1302/0301-620x.76b6.7983126](https://doi.org/10.1302/0301-620x.76b6.7983126).
45. Zielinska N, Olewnik Ł, Karauda P, et al. A very rare case of an accessory subscapularis muscle and its potential clinical significance. *Surg Radiol Anat.* 2021; 43(1): 19–25, doi: [10.1007/s00276-020-02531-6](https://doi.org/10.1007/s00276-020-02531-6), indexed in Pubmed: [32656573](https://pubmed.ncbi.nlm.nih.gov/32656573/).
46. Zielinska N, Tubbs RS, Podgórski M, et al. The subscapularis tendon: A proposed classification system. *Ann Anat.* 2021; 233: 151615, doi: [10.1016/j.aanat.2020.151615](https://doi.org/10.1016/j.aanat.2020.151615), indexed in Pubmed: [33068734](https://pubmed.ncbi.nlm.nih.gov/33068734/).

Venous supply of horseshoe kidneys and normal kidneys: an angio-multislice computed tomography-based study

M. Majos¹, M. Polguy², L. Stefańczyk¹, A. Majos³

¹Department of Radiology, Barlicki University Hospital, Medical University of Lodz, Poland

²Department of Normal and Clinical Anatomy, Chair of Anatomy and Histology, Medical University of Lodz, Poland

³Department of Radiological and Isotopic Diagnosis and Therapy, Medical University of Lodz, Poland

[Received: 27 August 2021; Accepted: 14 September 2021; Early publication date: 5 April 2022]

Background: Horseshoe kidney (HSK) is a common developmental anomaly which can be associated with many atypical anatomical variants of blood supply. The aim of this study was to identify the anatomical variants of renal veins supplying HSK, with particular emphasis on their relationship with the arterial system.

Materials and methods: The analysis included 94 patients with HSK and 248 persons with normal kidneys (NK). Based on computed tomography-angiography, the number of renal arteries and veins was determined, along with the levels the arteries branched off the aorta and the veins communicated to their parental vessels.

Results: Four hundred and twenty-three renal arteries (4.5 per person) and 364 renal veins (3.78 per persons) were found in HSK group ($p = 0.004$), as compared with 598 arteries (2.41 per person) and 567 veins (2.29 per person) in the NK group ($p = 0.025$). Mean number of renal veins in women with HSK was higher than in men (4.11 vs. 3.72 per patient, $p = 0.03$). In the HSK group, the number of renal arteries correlated significantly with the number of renal veins only among men ($k_s = 0.35$, $p = 0.009$). In patients with NK, significant correlations between the number of renal arteries and renal veins were found both in the whole group and among men and women.

Conclusions: Horseshoe kidneys are drained by a higher number of renal veins than NK, especially in women; this also refers to accessory renal veins. The number of renal veins for HSK is less dependent on the number of corresponding arteries than these for NK. (Folia Morphol 2023; 82, 2: 368–374)

Key words: horseshoe kidney, vascular variations, renal vein

INTRODUCTION

Horseshoe kidney (HSK) is a common developmental anomaly which can be associated with many atypical anatomical variants of blood supply [2, 4]. Knowledge of these variants is clinically relevant whenever pathological changes are present in the

kidney or adjacent organs. Blood supply of HSK requires a careful and comprehensive assessment before a planned surgical procedure, such as nephrectomy, transplantation or management of aortic aneurysms [3, 12, 26]. Furthermore, the presence of the atypical anatomical variants of blood supply can be associated

Address for correspondence: Prof. M. Polguy, Department of Normal and Clinical Anatomy, Chair of Anatomy and Histology, Medical University of Lodz, ul. Żeligowskiego 7/9, 90–752 Łódź, Poland, e-mail: michal.polguy@umed.lodz.pl

This article is available in open access under Creative Common Attribution-Non-Commercial-No Derivatives 4.0 International (CC BY-NC-ND 4.0) license, allowing to download articles and share them with others as long as they credit the authors and the publisher, but without permission to change them in any way or use them commercially.

with nephrolithiasis and compression syndromes, such as nutcracker syndrome [8, 17].

The vascular system of kidneys and as well as HSK itself was considerably studied but most of the literature was concerned with arterial blood supply system omitting venous one. Never-the-less, patients with HSK usually do not present any clinical symptoms, the untypical development of the organ provoke preserving vascular system existing for fetal period which can cause complications during either invasive treatment or morbid processes. Up to now the authors have noticed the relation between HSK and anatomical variants of both kidney veins as well as inferior vena cava but the studies were limited in number and usually based on modest sum of participants [9–11, 16]. We found it profitable to deepen the knowledge of this field and decided to plan a study to identify anatomical variants of renal veins supplying HSK, with particular emphasis on their relationship with the arterial system.

MATERIALS AND METHODS

The protocol of the study was approved by the Local Bioethics Committee at the Medical University of Lodz, Poland (decision no. RNN/132/17/KE of 11 April 2017).

The study material consisted of images from all consecutive patients in whom computed tomography (CT)-angiography of the abdominal aorta and minor pelvis demonstrated the presence of HSK (images taken between January 2006 and February 2019) or normal kidneys (NK) (images taken between March 2016 and January 2017). The images were extracted from the PACS archiving system at the Department of Radiology, University Clinical Hospital No. 1 in Lodz, Poland.

The only inclusion criterion for the HSK group was the presence of a single HSK, whereas the control group included only the images from patients who presented with two typically located and NK. The patients were excluded from the study if they underwent partial or complete resection of the kidney, received kidney transplant, their CT angiographic images were incomplete or had inadequate technical quality (lack of all kidney components on the image, insufficient contrast enhancement, motor artifacts or other artifacts hindering full evaluation of renal vessels, e.g. metallic hardware in the spine or barium contrast in the intestines).

Eventually, the HSK group included 94 patients (37 women and 57 men) aged between 15 and 96

years (mean 66.4 ± 15.93 years). The median age of the HSK group was 65.5 years and lower and upper quartile corresponded to 58 and 81 years, respectively. Control group was comprised of 248 patients (122 men and 126 women) with two typically located and NK. Mean age of the controls was 66.4 ± 15.01 years, with the range between 24 and 94 years, a median of 68 years, and lower and upper quartile of 58 and 78 years, respectively.

Computed tomography-angiography was performed with GE Light Speed 64 VCT scanner (GE Healthcare, Milwaukee, WI, US; 120 kV, 10 mA, mAs — dynamic), with 0.625-mm layer width and 0.6-mm pitch, after intravenous administration of 80–100 mL of Ultravist 370 contrast agent (BAYER Schering Pharma AG, Germany) with an automatic syringe at a flow rate of 4.5–4.2 mL/s. The data were acquired for 6 s after achieving a 150 jH contrast enhancement at the level of the aortic bifurcation. Transverse, sagittal and frontal CT angiographic images were evaluated at a doctor's console with the aid of AW 4.0 GE software. The number of renal arteries and veins was determined, along with the level at which the arteries branched off the aorta and the level at which the veins connected to their parental vessels. The number of arteries and veins was calculated as a sum of all vessels supplying the HSK or two NK. This approach was chosen to prevent problems with distinguishing between the vessels supplying the right lateral and the left lateral part of the HSK.

Both groups of patients, with HSK and NK, were divided into subgroups depending on the level at which the renal arteries and veins connected to their parental vessels:

- level I — patients with veins draining to the inferior vena cava and arteries branching off the aorta;
- level II — patients with veins draining to the common iliac vein and arteries branching off the common iliac arteries;
- level III — patients with veins draining to the internal and external iliac veins and arteries branching off the internal and external iliac arteries.

Patients with HSK or NK who did not satisfy any of the criteria mentioned above were not included in this part of the analysis.

Moreover, the number of patients who represented various anatomical variants of renal venous drainage included in the classification proposed by Koc et al. [13], i.e. single renal vein (variant I + II) and accessory renal veins (variant III), was determined.

Table 1. Frequency of additional renal veins in relation to its anatomical variant

	Horseshoe kidneys			Normal kidneys		
	Whole group	Women	Men	Whole group	Women	Men
Variant I + II	10 (10.64%)	1 (2.70%)	9 (16.67%)	189 (76.21%)	95 (77.87%)	94 (74.60%)
Variant III	84 (89.36%)	36 (97.30%)	48 (83.33%)	59 (23.79%)	27 (22.13%)	32 (25.40%)

Furthermore, the topography of the left renal vein was analysed

Statistical analysis

Statistical characteristics of quantitative variables were presented as means, standard deviations (SD), medians, minimum and maximum values, and quartiles. Before the between-group comparison of values of a given quantitative variable, normality of its distribution within the groups was verified with the Shapiro-Wilk test. As the distributions of analysed variables in the study groups were not normal, the significance of between-group differences was verified with a non-parametric Mann-Whitney U-test, and relationships between pairs of selected variables were determined based on the Spearman's coefficients of rank correlation.

The figures were created with syngo.via (Siemens Healthineers, Erlangen, Germany) and Microsoft Paint 3D (Microsoft, Albuquerque, New Mexico, United States of America).

RESULTS

A total of 423 renal arteries and 364 renal veins were found in the group of patients with HSK, as compared with 598 renal arteries and 567 renal veins in patients with NK. The between-group differences in the number of renal arteries and renal veins were statistically significant ($p < 0.001$). Detailed data, including classification of the patients into the anatomical variants proposed by Koc et al. [13] are presented in Table 1.

The identified anatomical variants of the left renal vein included circumaortic renal vein and retroaortic renal vein. In patients with HSK, circumaortic renal vein was found in 2 (2.20%) cases and retroaortic renal vein in 12 (6.59%) (Fig. 1). Circumaortic (Fig. 2) and retroaortic left renal veins were also identified in 7 (2.82%) and 12 (4.8%) patients with NK, respectively. The between-group differences in the occurrence of the circumaortic and retroaortic variants were statistically significant ($p < 0.001$ and $p = 0.008$, respectively).

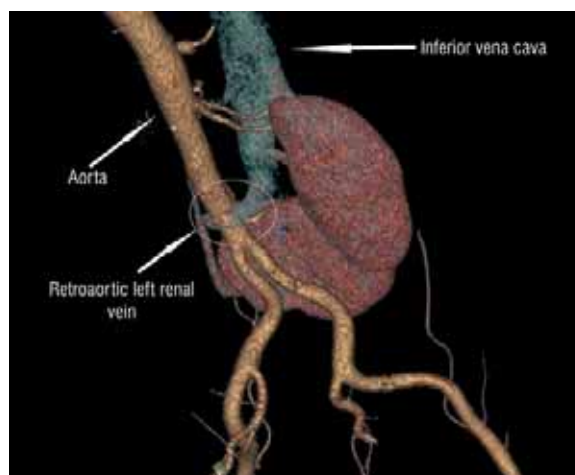


Figure 1. Horseshoe kidney. Left renal vein presents retroaortic variant.

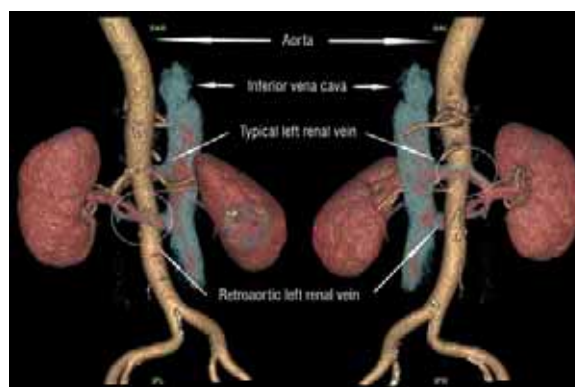


Figure 2. Two normal kidneys. Left kidney is drained by two renal veins creating circumaortic variant.

Relationship between the number of renal veins and patient sex

The mean number of renal veins was stratified according to patient sex. In the HSK group, women presented with a significantly higher number of renal veins than men, 4.11 vs. 3.72 per patient, respectively ($p = 0.03$). In contrast, no significant relationship between patient sex and the mean number of renal veins was found in the group with NK (Table 2).

Table 2. Mean numbers of renal arteries and veins in patients with horseshoe kidneys (HSK) and in patients with normal kidneys (NK)

	Whole group		Group of women		Group of men	
	Veins	Arteries	Veins	Arteries	Veins	Arteries
HSK group	3.87	4.5	4.11	4.24	3.72	4.67
NK group	2.29	2.41	2.24	2.34	2.29	2.50

Mean number of renal veins in women with HSK was 4.11 as compared with 2.24 in women with NK; the between-group difference was statistically significant ($p < 0.001$).

Also, among men, patients with HSK presented with a significantly higher mean number of renal veins than those with NK (3.72 vs. 2.29, $p < 0.001$) (Table 2).

Relationship between the number of renal veins and renal arteries

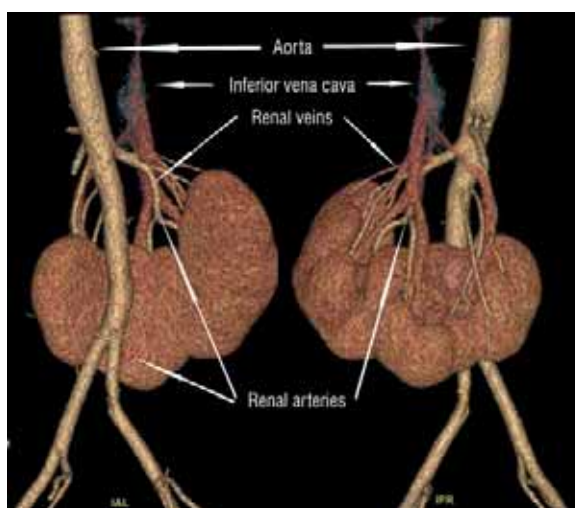
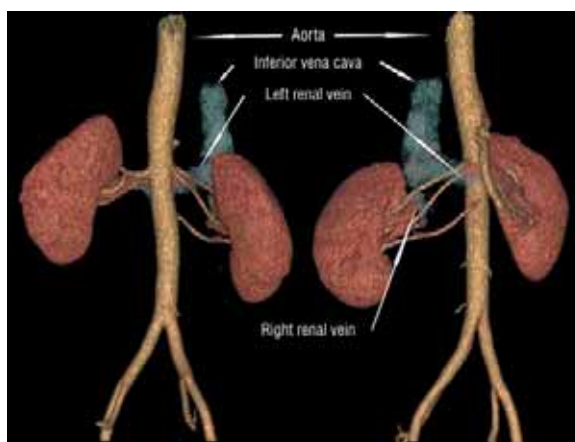
Mean numbers of renal veins and renal arteries in the HSK group were 3.78 and 4.50 per patient, respectively; the difference was statistically significant ($p = 0.004$) (Fig. 3). When the results were stratified according to patient sex, men with HSK presented with 3.72 renal veins and 4.67 renal arteries on average ($p < 0.001$), whereas the mean number of renal veins and renal arteries in women with HSK was 4.11 and 4.24 per patient, respectively ($p = 0.77$)

In patients with NK, the difference between the number of renal veins and renal arteries was statistically significant in the whole group (2.29 vs. 2.41, $p = 0.025$) and among men (2.29 vs. 2.50, $p = 0.016$) (Fig. 4). However, no statistically significant difference was found between the number of renal veins and renal arteries in women with normal kidneys ($p = 0.52$) (Table 2).

Correlations between the number of renal veins and the number of renal arteries

No statistically significant correlations between the number of renal veins and renal arteries were observed in the whole HSK group and among women with this developmental anomaly. However, a moderately strong correlation between the number of renal veins and renal arteries was found in male patients with HSK ($k_s = 0.35$, $p = 0.009$).

The patients with HSK were also stratified according to the level at which the renal veins and renal arteries communicated to their parental vessels. After stratifying the patients according to this criterion, statistically significant correlations between the number

**Figure 3.** Horseshoe kidney supplied by 5 renal artery and drained by 3 renal veins.**Figure 4.** Two normal kidneys supplied by 5 renal arteries and 2 renal veins.

of renal veins and renal arteries were found at level II in the whole study group ($k_s = 0.28$, $p = 0.006$) and at the level I among men ($k_s = 0.27$, $p = 0.04$) (Table 3).

In patients with NK, significant correlations between the number of renal veins and renal arteries were found both in the whole group and among women and men (Table 4). We did not analyse correlations between the number of renal veins and renal arteries communicating to their parental vessels at

Table 3. Correlation between number of renal veins and arteries in a group of patients with horseshoe kidneys depending on vessel level

	Whole group		Group of women		Group of men	
	k_s	p	k_s	p	k_s	p
Level I	0.13	0.203	-0.04	0.834	0.27	0.040
Level II	0.28	0.006	0.44	0.086	0.12	0.673

Table 4. Correlations in between number of renal arteries and veins depending on anatomical variant of a kidney

	Normal kidneys group		Horseshoe kidneys group	
	k_s	p	k_s	p
Whole group	0.25	< 0.001	0.16	0.150
Group of women	0.22	0.014	-0.08	0.634
Group of men	0.26	0.003	0.35	0.009

various levels due to a too small number of vessels representing levels II and III in the group with NK.

DISCUSSION

Arterial supply of the kidneys can be quite heterogeneous. Renal arteries may differ in terms of their number, division patterns and origins [7, 14, 15, 23]. As this problem is clinically recognised, especially with regards to the accessory arteries, it has been frequently analysed in postmortem studies, as well as antemortem, using various imaging techniques, such as ultrasonography, magnetic resonance, but most of all, multislice computed tomography [1, 6, 19, 25]. However, the knowledge of renal venous supply is also important from a clinical perspective, as the atypical venous pattern may pose a threat during surgical procedures involving the kidneys and adjacent organs. The awareness of various anatomical variants of venous supply and careful preoperative assessment thereof may prevent inadvertent damage of blood vessels during the procedure [5, 9, 20]. This is particularly important considering that venous bleeding is markedly more difficult to control than the arterial bleeding.

Blood supply of HSK is particularly important from both research and clinical perspective. Horseshoe kidney is the most common congenital anomaly occurring with a frequency of 1 per 400–800 live births [21, 23]. Only a few published studies analysed the arterial supply of HSK and the reports on venous supply of this structure are even rarer. This justifies comprehensive research on the anatomy of venous supply in this type of kidney.

A total number of renal veins supplying HSK in our material was 353, which corresponded to 3.88 veins per patient; in turn, the overall number of veins for NK was 567, which corresponded to 2.29 veins per person. The difference turned out to be statistically significant. Moreover, a significant difference was found in the overall number of renal arteries and veins supplying HSK and NK ($p < 0.001$ and $p < 0.001$).

The number of veins supplying HSK in women turned out to be significantly higher than in men. In contrast, no significant sex-related difference was found in the number of renal veins for NK.

We also verified whether HSK were supplied with the accessory renal veins more often than the NK. To the best of our knowledge, the occurrence of accessory veins for HSK has not been studied thus far. The proportion of accessory renal veins supplying NK in our control group was similar as in previous studies in which it has been estimated at 8.0–18.8%.

In the case of both HSK and NK, the number of renal arteries was significantly higher than the number of renal veins ($p = 0.004$ and $p = 0.025$). This observation is consistent with the results of a postmortem study of American patients conducted by Pollak et al. [18] and an angio-CT-based study of NK carried out by Staśkiewicz et al. [22]. In both these studies, the number of renal arteries was higher than the number of renal veins, but none of the authors specified whether the difference was statistically significant.

Interestingly, when the results were stratified according to patient sex, the number of renal arteries was significantly higher than the number of renal veins among men, but not in women. A significant difference in the number of renal arteries and renal veins was found neither in female patients with HSK nor in women with NK.

Moreover, we observed a weak, albeit significant correlation between the number of renal arteries and renal veins supplying the NK ($p < 0.001$). The significant correlation was found both in the whole group of patients with NK and after stratifying the results according to sex. While also Staśkiewicz et

al. [22] reported a similar association between the number of renal arteries and renal veins for the NK, they found a significant correlation only for the right kidneys. We did not observe a significant correlation between the number of renal arteries and renal veins supplying HSK in the whole group and among female patients. However, a significant correlation between the number of renal arteries and renal veins was found in men with this developmental anomaly ($p = 0.003$).

During the next stage of the study, we analysed a relationship between the origins of renal arteries and renal veins for HSK. As only three veins represented variant III of renal venous drainage according to the classification proposed by Koc et al. [13], no statistical analysis was carried out for level III, which included this variant. We found a weak correlation between the origins of renal arteries and renal veins at level II in the whole HSK group ($p = 0.006$) and at the level I in men ($p = 0.04$). The relationships between the origins of renal arteries and renal veins were not analysed in patients with NK as none of the renal arteries in this group branched off the aorta below its bifurcation and none of the renal veins connected to other vessels than the inferior vena cava.

From a clinical perspective, particularly important are the circumaortic and retroaortic variants of the left renal vein [3, 24]. Our observation that the retroaortic variant was more common than the circumaortic variant is consistent with the results published by several other authors, but it needs to be stressed that their studies included patients with NK. Surprisingly, comparative analysis of patients with HSK and NK demonstrated that these were the latter who significantly more often presented with the circumaortic variant.

Our study had few limitations: the group of patients with HSK was relatively smaller than in typical anatomical analyses, and we did not compare the CT findings with the results of other imaging studies or postoperative protocols. Moreover, men outnumbered women in the HSK group.

CONCLUSIONS

Venous supply of HSK differs substantially from the supply of NK and does not follow any pattern included in the commonly used classification systems. Horseshoe kidneys are drained by a higher number of renal veins than NK, especially in women; this also

refers to accessory renal veins. The number of renal veins for HSK is less dependent on the number of corresponding arteries. The venous system of HSK is characterised by the lack of correlation or only a weak association between the levels at which the renal veins and renal arteries connect to their parental vessels, as well as by atypical frequency of various anatomical variants of the left renal vein.

These findings justify a comprehensive individualised diagnostic evaluation of both arterial and venous supply in each patient with HSK qualified for a surgical procedure involving the area of this organ.

Funding

The investigation was supported by grant no. 502-03/1-136-01/502-14-357-18 from the Medical University of Lodz, Poland.

Conflict of interest: None declared

REFERENCES

1. Aytac SK, Yigit H, Sancak T, et al. Correlation between the diameter of the main renal artery and the presence of an accessory renal artery: sonographic and angiographic evaluation. *J Ultrasound Med.* 2003; 22(5): 433–439; quiz 440, doi: [10.7863/jum.2003.22.5.433](https://doi.org/10.7863/jum.2003.22.5.433), indexed in Pubmed: [12751854](https://pubmed.ncbi.nlm.nih.gov/12751854/).
2. Boatman DL, Cornell SH, Kölln CP. The arterial supply of horseshoe kidneys. *Am J Roentgenol Radium Ther Nucl Med.* 1971; 113(3): 447–451, doi: [10.2214/ajr.113.3.447](https://doi.org/10.2214/ajr.113.3.447), indexed in Pubmed: [5127705](https://pubmed.ncbi.nlm.nih.gov/5127705/).
3. Bozgeyik Z, Ozdemir H, Orhan I, et al. Pseudoaneurysm and renal arteriovenous fistula after nephrectomy: two cases treated by transcatheter coil embolization. *Emerg Radiol.* 2008; 15(2): 119–122, doi: [10.1007/s10140-007-0646-5](https://doi.org/10.1007/s10140-007-0646-5), indexed in Pubmed: [17593408](https://pubmed.ncbi.nlm.nih.gov/17593408/).
4. Eisendrath DN, Phifer FM, Culver HB. Horseshoe kidney. *Ann Surg.* 1925; 82(5): 735–764, doi: [10.1097/0000658-192511010-00009](https://doi.org/10.1097/0000658-192511010-00009), indexed in Pubmed: [17865363](https://pubmed.ncbi.nlm.nih.gov/17865363/).
5. Glodny B, Petersen J, Hofmann KJ, et al. Kidney fusion anomalies revisited: clinical and radiological analysis of 209 cases of crossed fused ectopia and horseshoe kidney. *BJU Int.* 2009; 103(2): 224–235, doi: [10.1111/j.1464-410X.2008.07912.x](https://doi.org/10.1111/j.1464-410X.2008.07912.x), indexed in Pubmed: [18710445](https://pubmed.ncbi.nlm.nih.gov/18710445/).
6. Gluecker TM, Mayr M, Schwarz J, et al. Comparison of CT angiography with MR angiography in the preoperative assessment of living kidney donors. *Transplantation.* 2008; 86(9): 1249–1256, doi: [10.1097/TP.0b013e3181890810](https://doi.org/10.1097/TP.0b013e3181890810), indexed in Pubmed: [19005407](https://pubmed.ncbi.nlm.nih.gov/19005407/).
7. Gulas E, Wysiadecki G, Cecot T, et al. Accessory (multiple) renal arteries: Differences in frequency according to population, visualizing techniques and stage of morphological development. *Vascular.* 2016; 24(5): 531–537, doi: [10.1177/1708538116631223](https://doi.org/10.1177/1708538116631223), indexed in Pubmed: [26945775](https://pubmed.ncbi.nlm.nih.gov/26945775/).

8. Guvendi B, Ogul H. Left renal vein compression and horseshoe kidney: an extraordinary association. *Med Princ Pract.* 2016; 25(5): 494–496, doi: [10.1159/000447594](https://doi.org/10.1159/000447594), indexed in Pubmed: [27304675](https://pubmed.ncbi.nlm.nih.gov/27304675/).
9. Ichikawa T, Kawada S, Koizumi J, et al. Major venous anomalies are frequently associated with horseshoe kidneys. *Circ J.* 2011; 75(12): 2872–2877, doi: [10.1253/circj.cj-11-0613](https://doi.org/10.1253/circj.cj-11-0613), indexed in Pubmed: [22001291](https://pubmed.ncbi.nlm.nih.gov/22001291/).
10. Ichikawa T, Sekiguchi T, Kawada S, et al. Study of the association between an anomalous superior vena cava and horseshoe kidney. *Circ J.* 2012; 76(5): 1253–1258, doi: [10.1253/circj.cj-11-0874](https://doi.org/10.1253/circj.cj-11-0874), indexed in Pubmed: [22343193](https://pubmed.ncbi.nlm.nih.gov/22343193/).
11. Imura A, Oguchi T, Shibata M, et al. Morphological observation of the horseshoe kidney with circumaortic venous ring. *Okajimas Folia Anat Jpn.* 2012; 89(3): 67–74, doi: [10.2535/ofaj.89.67](https://doi.org/10.2535/ofaj.89.67), indexed in Pubmed: [23429051](https://pubmed.ncbi.nlm.nih.gov/23429051/).
12. Kawamoto S, Lawler LP, Fishman EK. Evaluation of the renal venous system on late arterial and venous phase images with MDCT angiography in potential living laparoscopic renal donors. *AJR Am J Roentgenol.* 2005; 184(2): 539–545, doi: [10.2214/ajr.184.2.01840539](https://doi.org/10.2214/ajr.184.2.01840539), indexed in Pubmed: [15671376](https://pubmed.ncbi.nlm.nih.gov/15671376/).
13. Koc Z, Ulsan S, Oguzkurt L, et al. Venous variants and anomalies on routine abdominal multi-detector row CT. *Eur J Radiol.* 2007; 61(2): 267–278, doi: [10.1016/j.ejrad.2006.09.008](https://doi.org/10.1016/j.ejrad.2006.09.008), indexed in Pubmed: [17049792](https://pubmed.ncbi.nlm.nih.gov/17049792/).
14. Majos M, Polguy M, Szemraj-Rogucka Z, et al. The level of origin of renal arteries in horseshoe kidney vs. in separated kidneys: CT-based study. *Surg Radiol Anat.* 2018; 40(10): 1185–1191, doi: [10.1007/s00276-018-2071-8](https://doi.org/10.1007/s00276-018-2071-8), indexed in Pubmed: [30043151](https://pubmed.ncbi.nlm.nih.gov/30043151/).
15. Majos M, Majos A, Polguy M, et al. Diameters of arteries supplying horseshoe kidneys and the level they branch off their parental vessels: a CT-angiographic study. *J Clin Med.* 2019; 8(4), doi: [10.3390/jcm8040464](https://doi.org/10.3390/jcm8040464), indexed in Pubmed: [30959826](https://pubmed.ncbi.nlm.nih.gov/30959826/).
16. Monzen Y, Mori H, Wakisaka M, et al. Hydronephrosis caused by a left renal vein in a patient with horseshoe kidney: a case report. *Radiat Med.* 1993; 11(3): 95–97, indexed in Pubmed: [8372244](https://pubmed.ncbi.nlm.nih.gov/8372244/).
17. Pawar AS, Thongprayoon C, Cheungpasitporn W, et al. Incidence and characteristics of kidney stones in patients with horseshoe kidney: a systematic review and meta-analysis. *Urol Ann.* 2018; 10(1): 87–93, doi: [10.4103/UA.UA_76_17](https://doi.org/10.4103/UA.UA_76_17), indexed in Pubmed: [29416282](https://pubmed.ncbi.nlm.nih.gov/29416282/).
18. Pollak R, Prusak BF, Mozes MF. Anatomic abnormalities of cadaver kidneys procured for purposes of transplantation. *Am Surg.* 1986; 52(5): 233–235, indexed in Pubmed: [3518559](https://pubmed.ncbi.nlm.nih.gov/3518559/).
19. Sampaio FJ, Passos MA. Renal arteries: anatomic study for surgical and radiological practice. *Surg Radiol Anat.* 1992; 14(2): 113–117, doi: [10.1007/BF01794885](https://doi.org/10.1007/BF01794885), indexed in Pubmed: [1641734](https://pubmed.ncbi.nlm.nih.gov/1641734/).
20. Satyapal KS. Classification of the drainage patterns of the renal veins. *J Anat.* 1995; 186 (Pt 2): 329–333, indexed in Pubmed: [7649831](https://pubmed.ncbi.nlm.nih.gov/7649831/).
21. Stroomsma O, Kooystra G, Schurink GWH. Management of aortic aneurysm in the presence of a horseshoe kidney. *Br J Surg.* 2001; 88: 500–509.
22. Staśkiewicz G, Jajko K, Torres K, et al. Supernumerary renal vessels: analysis of frequency and configuration in 996 computed tomography studies. *Folia Morphol.* 2016; 75(2): 245–250, doi: [10.5603/FM.a2015.0085](https://doi.org/10.5603/FM.a2015.0085), indexed in Pubmed: [26383508](https://pubmed.ncbi.nlm.nih.gov/26383508/).
23. Taghavi K, Kirkpatrick J, Mirjalili SA. The horseshoe kidney: surgical anatomy and embryology. *J Pediatr Urol.* 2016; 12(5): 275–280, doi: [10.1016/j.jpuro.2016.04.033](https://doi.org/10.1016/j.jpuro.2016.04.033), indexed in Pubmed: [27324557](https://pubmed.ncbi.nlm.nih.gov/27324557/).
24. Tatarano S, Enokida H, Yamada Y, et al. Anatomical variations of the left renal vein during laparoscopic donor nephrectomy. *Transplant Proc.* 2019; 51(5): 1311–1313, doi: [10.1016/j.transproceed.2019.01.132](https://doi.org/10.1016/j.transproceed.2019.01.132), indexed in Pubmed: [31036354](https://pubmed.ncbi.nlm.nih.gov/31036354/).
25. Trigaux JP, Vandrogenbroek S, De Wispelaere JF, et al. Congenital anomalies of the inferior vena cava and left renal vein: evaluation with spiral CT. *J Vasc Interv Radiol.* 1998; 9(2): 339–345, doi: [10.1016/s1051-0443\(98\)70278-7](https://doi.org/10.1016/s1051-0443(98)70278-7), indexed in Pubmed: [9540920](https://pubmed.ncbi.nlm.nih.gov/9540920/).
26. Uehara A, Suzuki T, Hase S, et al. Kidney autotransplantation for the treatment of renal artery occlusion after endovascular aortic repair: a case report. *BMC Nephrol.* 2019; 20(1): 160, doi: [10.1186/s12882-019-1353-7](https://doi.org/10.1186/s12882-019-1353-7), indexed in Pubmed: [31088385](https://pubmed.ncbi.nlm.nih.gov/31088385/).

Bihemispheric posterior inferior cerebellar artery in a cadaver with Chiari I malformation

N. Boggio¹, M. Mathkour², Ł. Olewnik³, J. Iwanaga^{1,4}, C.J. Bui⁵, E.E. Biro⁵, R.S. Tubbs^{1,4–9}

¹Department of Neurosurgery, Tulane Centre for Clinical Neurosciences, Tulane University School of Medicine, New Orleans, LA, United States

²Tulane University and Ochsner Clinic Neurosurgery Programme, Tulane University School of Medicine, New Orleans, LA, United States

³Department of Anatomical Dissection and Donation, Medical University of Lodz, Poland

⁴Department of Neurology, Tulane University School of Medicine, New Orleans, LA, United States

⁵Department of Neurosurgery, Ochsner Health System, New Orleans, LA, United States

⁶Department of Structural and Cellular Biology, Tulane University School of Medicine, New Orleans, LA, United States

⁷Department of Anatomical Sciences, St. George's University, St. George's, Grenada, West Indies

⁸Department of Surgery, Tulane University School of Medicine, New Orleans, LA, United States

⁹University of Queensland, Brisbane, Australia

[Received: 3 November 2021; Accepted: 8 December 2021; Early publication date: 5 April 2022]

Typically, patients with Chiari I malformations (CM I) do not have other intracranial anatomical variations, especially vascular derailments. Here, we report the findings of a cadaveric specimen found to have CM I and cerebellar tonsils supplied by a single posterior inferior cerebellar artery (PICA) i.e., a bihemispheric PICA. An adult male cadaver was found to have CM I. It was also noted that the left PICA descended inferiorly to the level of C1 and that there was absence of the right PICA. The territory of the right PICA was supplied by the left PICA. The tonsillar component of the left PICA gave rise to a branch that crossed to the right inferior cerebellum and herniated cerebellar tonsil. A bihemispheric PICA is very rare. To our knowledge, this is the first report of this vascular variation in combination with CM I. Such a variation should be kept in mind, especially during posterior fossa decompression for symptomatic CM I as unilateral PICA injury could have catastrophic results. (Folia Morphol 2023; 82, 2: 375–381)

Key words: hindbrain herniation, vertebrobasilar system, posterior cranial fossa, tonsillar ectopia, variation

INTRODUCTION

Chiari malformations are congenital hindbrain anomalies originally described during the 1890s by Hans Chiari [13, 14]. While Chiari's traditional classification system comprised four types of malformations, more recent and specific systems recognise eight classes: Chiari 0, Chiari I, Chiari 1.5, Chiari II, Chiari III, Chiari 3.5, Chiari IV, and Chiari V [8, 42].

Chiari type I malformation (CM I) involves a caudal herniation of the cerebellar tonsils greater than 5 mm inferior to the plane of the foramen magnum [1, 5, 40]. In 2004, Tubbs et al. [40] found that 96% of CM I patients exhibit asymmetric tonsillar herniation. The herniated tonsils often undergo chronic compression, often succeeded by atrophy and the loss of their folia, which can make them smooth in appearance.

Address for correspondence: J. Iwanaga, DDS, PhD, Department of Neurosurgery, Tulane Centre for Clinical Neurosciences, 131 S. Robertson St. Suite 1300, New Orleans, LA 70112, United States, tel: 5049885565, fax: 5049885793, e-mail: iwanagajoea@gmail.com

This article is available in open access under Creative Commons Attribution-Non-Commercial-No Derivatives 4.0 International (CC BY-NC-ND 4.0) license, allowing to download articles and share them with others as long as they credit the authors and the publisher, but without permission to change them in any way or use them commercially.

However, Cesmebasi et al. [12] noted that apart from the herniated cerebellar tonsils, the brain of a CM I patient is generally normal.

The most common symptom of CM I is pain, occurring in 60–70% of patients, often in the occipital or upper cervical regions [29]. Exacerbated by Valsalva manoeuvres such as laughing, coughing, or sneezing, Chiari-like headaches, which are posteriorly located and short in duration, have also been described [4]. Tubbs et al. (2004) [40] and Cesmebasi et al. (2015) [12] reviewed associated anatomical findings often seen in CM I patients involving the skull, spine, meninges, and spinal cord. Common skull-related findings include occipital bone dysplasia, and basilar skull and craniocervical junction anomalies such as a large foramen magnum, a short clivus, and a shallow posterior cranial fossa [26, 28, 35, 38, 39, 43]. Spinal symptoms commonly associated with CM I include the Klippel-Feil deformity; atlantoaxial assimilation; and scoliosis, often a levoscoliosis [29, 37, 43]. More specifically, the incidence of scoliosis in CM I patients could be as high as 30%, and up to 70% if syringomyelia is also present [32]. If it is caused by syringomyelia, levoscoliosis of the thoracic vertebrae can present as abnormal abdominal reflexes, desensitisation to pain and temperature, or non-specific, non-dermatomal flank or back pain [12]. CM I patients often exhibit symptoms in the meninges such as an elevated slope of the tentorium cerebelli, thickening of the arachnoid mater at the level of the foramen magnum, and/or arachnoid veils obstructing the outlets of the fourth ventricle [12]. Among CM I patients, 50–75% present with a syrinx, usually located in the upper thoracic or lower cervical spine [3, 7, 9, 11, 12, 26]. Other symptoms commonly associated with CM I include weakness or numbness, unsteadiness, ophthalmological or otological disturbances, atrophy, hyperreflexia, ataxia, and lower cranial nerve dysfunction [29].

Currently, decompression surgery of the posterior cranial fossa is widely accepted as the only effective treatment option for patients with symptomatic CM I [7, 12]. The aim of the surgery is to alleviate symptoms and inhibit progressive deterioration by enlarging the posterior fossa region and restoring cerebrospinal fluid flow from the fourth ventricle to the cervical subarachnoid space [29].

Here, we report the findings of a cadaveric specimen found to have CM I and cerebellar tonsils supplied by a single posterior inferior cerebellar artery (PICA).

CASE REPORT

During the routine dissection of the posterior cranial fossa and upper cervical spine in an 89-year-old at death male cadaver, a CM I was identified (Fig. 1). The left cerebellar tonsil was 5 mm inferior to the foramen magnum and the right cerebellar tonsil was 10 mm inferior to the foramen magnum at the level of the C2 nerves rootlets. It was also noted that the left PICA descended inferiorly to the level of C1 and that there was absence of the right PICA. The territory of the right PICA was supplied by the left PICA (Fig. 1). The left PICA arose from the V4 segment of the vertebral artery. The vessel took a normal course by the medulla oblongata and as mentioned above, its tonsillar segment, which hugged the inferior aspect of the left herniated cerebellar tonsil was descended to the level of C1. Small branches supplied the left cerebellar tonsil and inferior surface of the cerebellum. The tonsillar component of the left PICA then, at the midline, gave rise to a branch that crossed to the right inferior cerebellum and herniated cerebellar tonsil although this branch did not course around the caudal pole of the tonsil but over its posterior upper surface (Fig. 1). The posterior spinal artery was contributed to by the left PICA and a contralateral branch of this vessel deep to the right cerebellar tonsil. No other vascular or other intracranial anatomical variations were noted. No intracranial pathology such as haemorrhage, obvious ischaemic changes, or hydrocephalus were found. The cause of death in the cadaver donor was myocardial infarction.

DISCUSSION

The arterial supply to the cerebellum typically involves three sets of paired arteries arising from the vertebrobasilar system: the superior cerebellar artery, the anterior inferior cerebellar artery (AICA), and the PICA. The PICA is most relevant to a discussion of cerebellar tonsil herniation. Along its tortuous course, this artery supplies the lower medulla oblongata, choroid plexus, dura of the posterior cranial fossa, fourth ventricle, cerebellar tonsils, vermis, and inferolateral hemisphere. The PICA most commonly originates as the largest branch of the bilateral intracranial vertebral arteries, often near the vertebrobasilar junction. Although its origin and course are highly variable, the PICA trunk is often divided into five segments as it travels inferiorly toward the foramen magnum: anterior medullary, lateral medullary, tonsillomedullary, telovelotonsillar, and cortical (Fig. 2) [17, 23, 27, 33, 41].

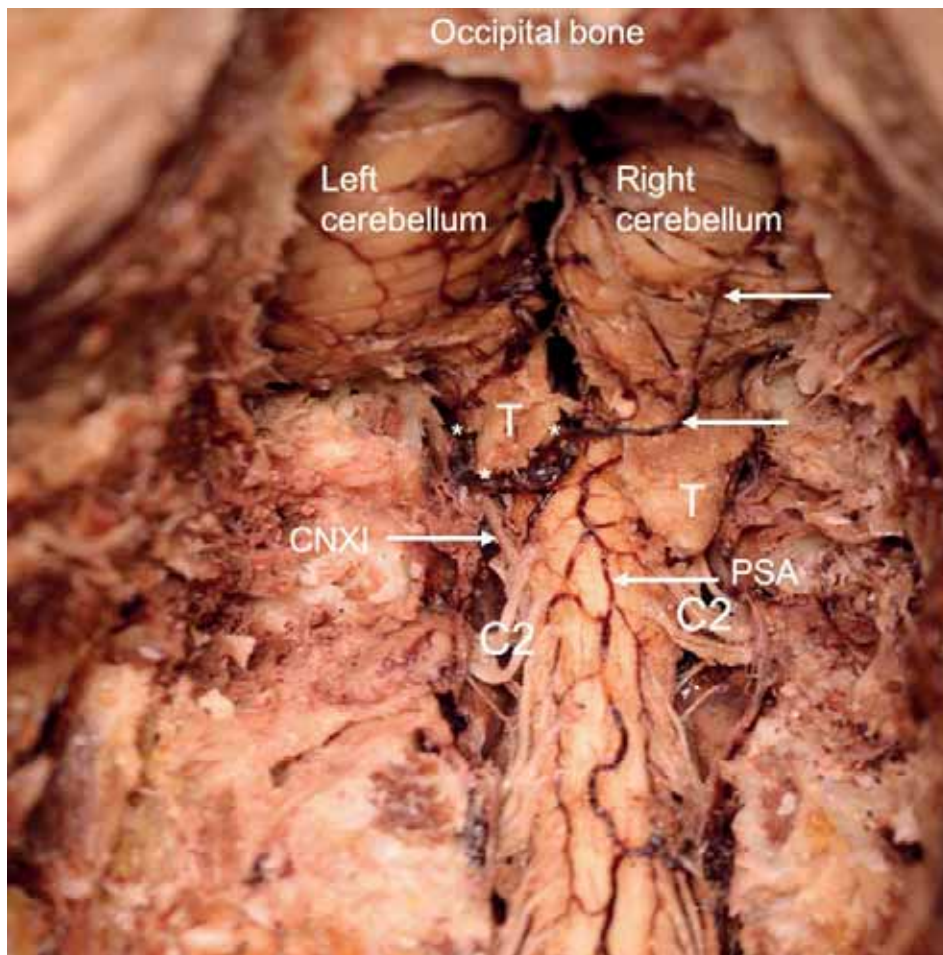


Figure 1. Posterior view of the exposed craniocervical junction in the case described herein. Note the herniated left and right cerebellar tonsils (T), C2 dorsal nerve roots, posterior spinal artery (PSA), and left spinal accessory nerve (CNXI). The left posterior inferior cerebellar artery (PICA) is seen at the asterisk (*). The contralateral branch of the left PICA is seen at the arrows.

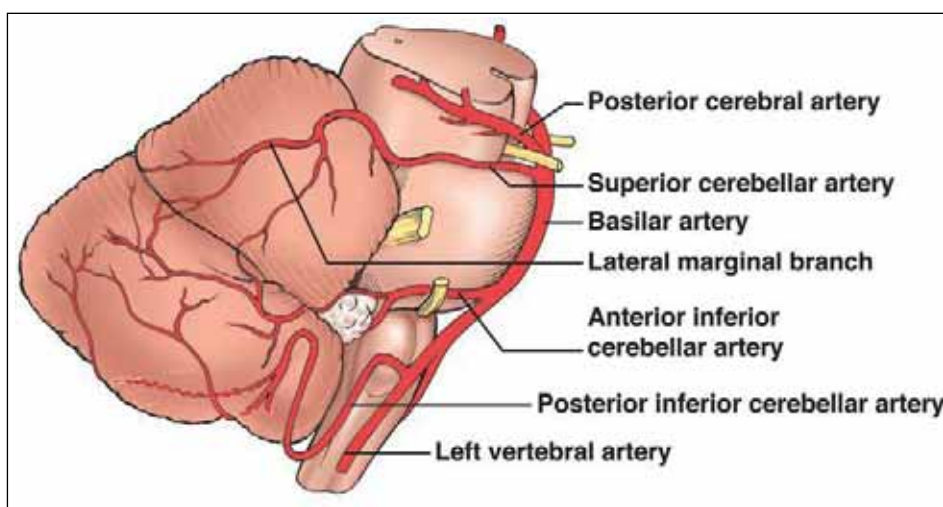


Figure 2. Schematic drawing of the normal course of the left posterior inferior cerebellar artery.

These authors, among others, described those segments as follows. The initial segment, the anterior

medullary segment (1), starts at the origin of the PICA, courses by the anterior medulla, and ends at the me-

dial edge of the inferior olive. From there, the lateral medullary segment (2) extends towards the origins of the lower cranial nerves (CNs IX, X, and XI) at the lateral edge of the inferior olive. Continuing as the tonsillomedullary (posterior medullary) segment (3), the PICA descends to the inferior pole of the cerebellar tonsil and then ascends to the midpoint of the tonsil on its medial surface, forming its caudal loop. The telovelotonsillar (supratonsillar) segment (4) begins at the midportion of the tonsil and continues the ascent of the PICA to the roof of the fourth ventricle before it recurs to form the cranial loop, which contains the choroidal point, then descends posteriorly to the fissures between the tonsil, vermis, and cerebellar hemisphere. The final segment (5), the cortical segment, arises from the tonsillobiventral fissure and often bifurcates in its course around the tonsil into a medial (vermian) trunk, giving off vermian branches, and a lateral (tonsillohemispheric) trunk, giving off tonsillar and hemispheric branches [23].

Major variants of the PICA

As mentioned, the origin and course of the PICA often vary. Miao et al. (2020) [27] reviewed the literature thoroughly and detailed the variations of the PICA as follows. Although this artery most commonly originates from the intradural vertebral artery near the vertebrobasilar junction, its origin has been observed at all points along the intracranial vertebral artery and from every direction [2, 23]. Additional variations in the location of its origin include: the extradural vertebral artery (0.4–20.8% of cases) [23, 24, 30, 31], the basilar artery (6–11% of cases) [16], an AICA-PICA common trunk off the basilar artery, and, less commonly, from other arteries such as the internal carotid, primitive hypoglossal, primitive trigeminal, and posterior meningeal [27]. Several variations relating to the manner in which the PICA arises and its subsequent course have also been described. For example, in 2.8–7% of reported cases, the vertebral artery continued as the [31]. A duplicated origin of the PICA (two distinct arteries without convergence) has been observed in 2–6% of hemispheres [16, 23, 36], and a double origin (two distinct origins with distal convergence) in approximately 1.45% of cases [22]. A fenestrated PICA is very rare, occurring in only about 0.3% of cases (Pekcevik and Pekcevik, 2014 [31]). A hypoplastic PICA has a reported prevalence of 15–32% [16, 20]. Significantly, the PICA has been

reported unilaterally absent in 6–26% of cases and bilaterally absent in 2–3.6% [6, 19, 23, 31, 34, 44].

The distal portion of the PICA is also very variable. While its cortical segment most commonly bifurcates into a medial (vermian) and a lateral (tonsillohemispheric) trunk as it courses over the posterior surface of the tonsil, the locations of both the bifurcation and the division of branches can vary [23, 25]. For example, the tonsillar branches can arise from the medial trunk with the vermian branches, rather than from the lateral trunk [41]. Lister et al. (1982) [23] noted “a reciprocal relationship with frequent overlap in the areas supplied by the tonsillar, hemispheric, and vermian branches” (p. 193). The tonsillar branches were most often observed supplying the medial, posterior, inferior, and a portion of the anterior surface of the tonsil. The number of tonsillar branches arising from a single PICA ranged from 0 to 5 (average 1.6), with 6 out of 50 cerebellar hemispheres having 0 tonsillar branches. In such cases, the adjacent hemispheric and vermian branches supplied the cerebellar tonsils [23].

PICA and Chiari I malformation

In some instances, such as cases of hindbrain herniation seen in CM I, the PICA extends extracranially as seen in the present case report [41]. Margolis and Newton (1971) [25] posited that despite significant variation in the sites at which the lateral trunk gives rise to tonsillar and hemispheric branches, it is because of their common origin that the branches are affected by hindbrain herniation. Moreover, in CM I, it is the caudal herniation of the cerebellar tonsils that pulls on the lateral trunk and ultimately stretches both the tonsillar and hemispheric branches inferiorly. Angiographic visualisation of these caudally displaced branches below the level of the foramen magnum has previously assisted in the diagnosis of Chiari malformations, particularly Chiari II malformation, in which the cerebellar vermis, brainstem, and fourth ventricle are also displaced through the foramen magnum [18, 42]. Some authors have described a stretched-out, hairpin caudal loop of the PICA below the level of the foramen magnum associated with CM I, though the diagnostic value of this has been questioned owing to the immense variability of the course of the PICA [18, 25].

Bihemispheric PICA

Upon further analysis of the AICA and PICA blood supply, Fujii et al. (1980) [16] posited that there is

an inverse relationship between these two arteries with respect to both their diameters and the areas they supply. Furthermore, in cases where one PICA is hypoplastic or absent, the ipsilateral AICA or the contralateral PICA is larger and supplies the area that it would normally have supplied. The authors noted an example in which the left PICA was hypoplastic and the large right PICA travelled across the midline to give rise to the left tonsillohemispheric trunk and send choroidal branches to the choroid plexus. This “extensive type” of PICA, which forms an arterial bridge as it crosses the midline to give branches to the other side of the vermis and occasionally extends over the opposite hemisphere, was observed in 14% of the 50 adult cadaveric cerebellar hemispheres that Fujii et al. [16] examined. Cullen et al. (2005) [15] described a very similar PICA variation in which, when one PICA was hypoplastic or absent, as in our case, the contralateral PICA crossed the midline to supply both cerebellar hemispheres; they termed this a “bihemispheric PICA”. The authors detailed four cases of a bihemispheric PICA, each of which originated from the dominant vertebral artery and gave rise to vermian branches distal to the choroidal point, and then crossed the midline along the dorsal aspect of the vermis and extended onwards to supply the contralateral hemisphere. Cullen et al. [15] posited two subtypes, the true bihemispheric PICA, supplying both cerebellar hemispheres from a single trunk, and the vermian variant, providing the only bilateral supply to the vermis from a single trunk. Three potential mechanisms of development of these types of variations are: a midline bridging of a pial network of vessels; the development of a midline structure, such as the vermis, which could influence a vessel to cross; or fusion with a midline structure such as the basilar artery [10, 15]. In 2005, Cullen et al. [15] suggested the bihemispheric PICA to be extremely rare, less than 0.1%, but in 2013 they proposed a much higher prevalence, closer to 3%. Upon examination of 11 cases of bihemispheric PICAs, Carlson et al. [10] observed true bihemispheric PICAs to be 4 times more common than the vermian variant. Each of the true bihemispheric PICAs were observed in conjunction with contralateral PICA aplasia, whereas the vermian variants were found with a normal contralateral PICA. Regardless of the subtype, all 11 cases involved the PICA crossing the midline near its cortical segment bifurcation into medial and lateral trunks. It is important to note that a true bihemispheric PICA is different from

a ‘PICA communicating artery’ in that no anastomotic connections are formed, as the contralateral PICA is aplastic. Since the incidence is higher than previously recognized, the possibility of a bihemispheric PICA in patients is of clinical relevance. This is particularly true in instances of posterior cranial fossa cerebrovascular disease, such as cerebellar arteriovenous malformation, aneurysm, and stroke and ischemic syndromes. If the problem involves a bihemispheric PICA, the risk of complications such as bilateral cerebellar infarction must be considered [10, 15].

CONCLUSIONS

A bihemispheric PICA is very rare. To our knowledge, this is the first report of this vascular variation in combination with CM I. Such a variation should be kept in mind, especially during posterior fossa decompression for symptomatic CM I as unilateral PICA injury could have catastrophic results.

Acknowledgements

The authors sincerely thank those who donated their bodies to science so that anatomical research could be performed. Results from such research can potentially increase mankind’s overall knowledge that can then improve patient care. Therefore, these donors and their families deserve our highest gratitude [21].

Conflict of interest: None declared

REFERENCES

1. Aboulezz AO, Sartor K, Geyer CA, et al. Position of cerebellar tonsils in the normal population and in patients with Chiari malformation: a quantitative approach with MR imaging. *J Comput Assist Tomogr.* 1985; 9(6): 1033–1036, doi: [10.1097/00004728-198511000-00005](https://doi.org/10.1097/00004728-198511000-00005), indexed in Pubmed: [4056132](https://pubmed.ncbi.nlm.nih.gov/4056132/).
2. Akar ZC, Dujovny M, Slavin KV, et al. Microsurgical anatomy of the intracranial part of the vertebral artery. *Neurol Res.* 1994; 16(3): 171–180, doi: [10.1080/01616412.1994.11740221](https://doi.org/10.1080/01616412.1994.11740221), indexed in Pubmed: [7936084](https://pubmed.ncbi.nlm.nih.gov/7936084/).
3. Alai A, Reddy CG, Amrami KK, et al. Charcot arthropathy of the shoulder associated with typical and atypical findings. *Clin Anat.* 2013; 26(8): 1017–1023, doi: [10.1002/ca.22110](https://doi.org/10.1002/ca.22110), indexed in Pubmed: [22696209](https://pubmed.ncbi.nlm.nih.gov/22696209/).
4. Azahraa Haddad F, Qaisi I, Joudeh N, et al. The newer classifications of the chiari malformations with clarifications: An anatomical review. *Clin Anat.* 2018; 31(3): 314–322, doi: [10.1002/ca.23051](https://doi.org/10.1002/ca.23051), indexed in Pubmed: [29344999](https://pubmed.ncbi.nlm.nih.gov/29344999/).
5. Barkovich AJ, Wippold FJ, Sherman JL, et al. Significance of cerebellar tonsillar position on MR. *Am J Neuroradiol.* 1986; 7(5): 795–799, indexed in Pubmed: [3096099](https://pubmed.ncbi.nlm.nih.gov/3096099/).

6. Bebin J. The cerebellopontile angle, the blood supply of the brain stem and the reticular formation. Anatomical and functional correlations relevant to surgery of acoustic tumors. *Henry Ford Hosp Med J.* 1968; 16(1): 61–86, indexed in Pubmed: [4868296](#).
7. Bindal AK, Dunsker SB, Tew JM. Chiari I malformation: classification and management. *Neurosurgery.* 1995; 37(6): 1069–1074, doi: [10.1227/00006123-199512000-00005](#), indexed in Pubmed: [8584146](#).
8. Bordes S, Jenkins S, Tubbs RS. Defining, diagnosing, clarifying, and classifying the Chiari I malformations. *Childs Nerv Syst.* 2019; 35(10): 1785–1792, doi: [10.1007/s00381-019-04172-6](#), indexed in Pubmed: [31049667](#).
9. Cahan LD, Bentson JR. Considerations in the diagnosis and treatment of syringomyelia and the Chiari malformation. *J Neurosurg.* 1982; 57(1): 24–31, doi: [10.3171/jns.1982.57.1.0024](#), indexed in Pubmed: [7086497](#).
10. Carlson AP, Alaraj A, Dashti R, et al. The bihemispheric posterior inferior cerebellar artery: anatomic variations and clinical relevance in 11 cases. *J Neurointerv Surg.* 2013; 5(6): 601–604, doi: [10.1136/neurintsurg-2012-010527](#), indexed in Pubmed: [23172540](#).
11. Carmel PW, Markesbery WR. Early descriptions of the Arnold-Chiari malformation. The contribution of John Cleland. *J Neurosurg.* 1972; 37(5): 543–547, doi: [10.3171/jns.1972.37.5.0543](#), indexed in Pubmed: [4563792](#).
12. Cesmebasi A, Loukas M, Hogan E, et al. The Chiari malformations: a review with emphasis on anatomical traits. *Clin Anat.* 2015; 28(2): 184–194, doi: [10.1002/ca.22442](#), indexed in Pubmed: [25065525](#).
13. UeberVeränderungen des Kleinhirnsinfolge von Hydrocephalie des Grosshirns. *Med Wochenschr.* 1891; 17: 1172–1175.
14. Chiari H. UeberVeränderungen des Kleinhirns, des Pons und der Medulla oblongata Infolge von congenitalerHydrocephalie des Grosshirns. *Denkschriften Kais Akad Wiss.* 1895; 63: 71–116.
15. Cullen SP, Ozanne A, Alvarez H, et al. The bihemispheric posterior inferior cerebellar artery. *Neuroradiology.* 2005; 47(11): 809–812, doi: [10.1007/s00234-005-1427-z](#), indexed in Pubmed: [16160817](#).
16. Fujii K, Lenkey C, Rhoton AL. Microsurgical anatomy of the choroidal arteries. Fourth ventricle and cerebellopontine angles. *J Neurosurg.* 1980; 52(4): 504–524, doi: [10.3171/jns.1980.52.4.0504](#), indexed in Pubmed: [6966327](#).
17. Fusco MR, Ogilvy CS. Microsurgery of Vertebral Artery and Posterior Inferior Cerebellar Artery. In: Winn HR, Youmans JR (eds.), *Youmans and Winn Neurological Surgery.* 7th ed. Elsevier 2017: 3343–3350.
18. Gabrielsen TO, Seeger JF, Amundsen P. Some new angiographic observations in patients with Chiari type I and II malformations. *Radiology.* 1975; 115(3): 627–634, doi: [10.1148/15.3.627](#), indexed in Pubmed: [1129475](#).
19. Hagenah R, Kosak M, Freckmann N. Anatomic topographical relationship of the intraspinal accessory root to the upper cervical roots and to the vessels of the cranial cervical region. *Acta Anat (Basel).* 1983; 115(2): 158–167, doi: [10.1159/000145686](#), indexed in Pubmed: [6837260](#).
20. Icardo JM, Ojeda JL, Garcia-Porrero JA, et al. The cerebellar arteries: cortical patterns and vascularization of the cerebellar nuclei. *Acta Anat (Basel).* 1982; 113(2): 108–116, doi: [10.1159/000145545](#), indexed in Pubmed: [7124324](#).
21. Iwanaga J, Singh V, Ohtsuka A, et al. Acknowledging the use of human cadaveric tissues in research papers: Recommendations from anatomical journal editors. *Clin Anat.* 2021; 34(1): 2–4, doi: [10.1002/ca.23671](#), indexed in Pubmed: [32808702](#).
22. Lesley WS, Rajab MH, Case RS. Double origin of the posterior inferior cerebellar artery: association with intracranial aneurysm on catheter angiography. *AJR Am J Roentgenol.* 2007; 189(4): 893–897, doi: [10.2214/AJR.07.2453](#), indexed in Pubmed: [17885063](#).
23. Lister JR, Rhoton AL, Matsushima T, et al. Microsurgical anatomy of the posterior inferior cerebellar artery. *Neurosurgery.* 1982; 10(2): 170–199.
24. Magklara EP, Pantelia ET, Solia E, et al. Vertebral artery variations revised: origin, course, branches and embryonic development. *Folia Morphol.* 2021; 80(1): 1–12, doi: [10.5603/FM.a2020.0022](#), indexed in Pubmed: [32073130](#).
25. Margolis MT, Newton TH. An angiographic sign of cerebellar tonsillar herniation. *Neuroradiology.* 1971; 2(1): 3–8, doi: [10.1007/BF00345864](#), indexed in Pubmed: [5164208](#).
26. Menezes AH. Chiari I malformations and hydromyelia-complications. *Pediatr Neurosurg.* 1991; 17(3): 146–154, doi: [10.1159/000120586](#), indexed in Pubmed: [1819330](#).
27. Miao HL, Zhang DY, Wang T, et al. Clinical importance of the posterior inferior cerebellar artery: a review of the literature. *Int J Med Sci.* 2020; 17(18): 3005–3019, doi: [10.7150/ijms.49137](#), indexed in Pubmed: [33173421](#).
28. Oakes WJ, Tubbs ST. Chiari Malformations. In: Winn HR, Youmans JR (eds.), *Youmans and Winn Neurological Surgery.* 2nd ed. Elsevier 2004: 1531–1540.
29. Oakes WJ. Treatment of the Pediatric Chiari I Malformation. In: Tubbs RS, Turgut M, Oakes W (eds.), *The Chiari Malformations.* 2nd ed. Springer, Cham 2020: 437–441.
30. O'Donnell CM, Child ZA, Nguyen Q, et al. Vertebral artery anomalies at the craniovertebral junction in the US population. *Spine (Phila Pa 1976).* 2014; 39(18): E1053–E1057, doi: [10.1097/BRS.0000000000000447](#), indexed in Pubmed: [24979141](#).
31. Pekcevik Y, Pekcevik R. Variations of the cerebellar arteries at CT angiography. *Surg Radiol Anat.* 2014; 36(5): 455–461, doi: [10.1007/s00276-013-1208-z](#), indexed in Pubmed: [24061702](#).
32. Ravindra VM, Brockmeyer DL. Chiari and Scoliosis. In: Tubbs RS, Turgut M, Oakes W (eds.), *The Chiari Malformations.* 2nd ed. Springer, Cham 2020: 219–224.
33. Rodríguez-Hernández A, Rhoton AL, Lawton MT. Segmental anatomy of cerebellar arteries: a proposed nomenclature. Laboratory investigation. *J Neurosurg.* 2011; 115(2): 387–397, doi: [10.3171/2011.3.JNS101413](#), indexed in Pubmed: [21548748](#).
34. Scialfa G, Bank W, Megret M, et al. The arteries of the roof of the fourth ventricle. *Neuroradiology.* 1976; 11(2): 69–71, doi: [10.1007/BF00345015](#), indexed in Pubmed: [948362](#).
35. Sgouros S, Kountouri M, Natarajan K. Skull base growth in children with Chiari malformation Type I. *J Neurosurg.* 2007; 107(3 Suppl): 188–192, doi: [10.3171/PED-07/09/188](#), indexed in Pubmed: [17918522](#).

36. Sharifi M, Ungier E, Ciszek B. Double posterior inferior cerebellar artery. *Surg Radiol Anat.* 2010; 32(1): 87–89, doi: [10.1007/s00276-009-0512-0](https://doi.org/10.1007/s00276-009-0512-0), indexed in Pubmed: [19421705](https://pubmed.ncbi.nlm.nih.gov/19421705/).
37. Shoja MM, Johal J, Oakes WJ, et al. Embryology and pathophysiology of the Chiari I and II malformations: A comprehensive review. *Clin Anat.* 2018; 31(2): 202–215, doi: [10.1002/ca.22939](https://doi.org/10.1002/ca.22939), indexed in Pubmed: [28612426](https://pubmed.ncbi.nlm.nih.gov/28612426/).
38. Shoja MM, Ramdhan R, Jensen CJ, et al. Embryology of the craniocervical junction and posterior cranial fossa, part I: Development of the upper vertebrae and skull. *Clin Anat.* 2018; 31(4): 466–487, doi: [10.1002/ca.23049](https://doi.org/10.1002/ca.23049), indexed in Pubmed: [29345006](https://pubmed.ncbi.nlm.nih.gov/29345006/).
39. Shoja MM, Ramdhan R, Jensen CJ, et al. Embryology of the craniocervical junction and posterior cranial fossa, part II: Embryogenesis of the hindbrain. *Clin Anat.* 2018; 31(4): 488–500, doi: [10.1002/ca.23048](https://doi.org/10.1002/ca.23048), indexed in Pubmed: [29344994](https://pubmed.ncbi.nlm.nih.gov/29344994/).
40. Tubbs RS, Iskandar BJ, Bartolucci AA, et al. A critical analysis of the Chiari 1.5 malformation. *J Neurosurg.* 2004; 101(2 Suppl): 179–183, doi: [10.3171/ped.2004.101.2.0179](https://doi.org/10.3171/ped.2004.101.2.0179), indexed in Pubmed: [15835105](https://pubmed.ncbi.nlm.nih.gov/15835105/).
41. Tubbs ST. Surgical Anatomy of the Craniocervical Junction Relevant to Chiari Malformations. In: Tubbs RS, Turgut M, Oakes W (eds.), *The Chiari Malformations*. 2nd ed. Springer, Cham 2020: 21–39.
42. Tubbs RS, Turgut M. Defining the Chiari Malformations: Past and Newer Classifications. In: Tubbs RS, Turgut M, Oakes W (eds.), *The Chiari Malformations*. 2nd ed. Springer, Cham 2020: 21–39.
43. Wellons JC, Tubbs RS, Oakes WJ. Chiari Malformations and Syringohydromyelia. In: Rengachary SS, Ellenbogen RG (eds.), *Principles of Neurosurgery*. Elsevier, Edinburgh 2005: 181–195.
44. Wollschlaeger G, Wollschlaeger PB, Lucas FV, et al. Experience and result with postmortem cerebral angiography performed as routine procedure of the autopsy. *Am J Roentgenol Radium Ther Nucl Med.* 1967; 101(1): 68–87, doi: [10.2214/ajr.101.1.68](https://doi.org/10.2214/ajr.101.1.68), indexed in Pubmed: [6037344](https://pubmed.ncbi.nlm.nih.gov/6037344/).

Connection between V2 and V3 parts of the trigeminal nerve at the internal cranial base

S. McDonough¹, Ł. Olewnik², J. Iwanaga^{3,4}, A.S. Dumont³, R.S. Tubbs³⁻⁹

¹Tulane University School of Medicine, New Orleans, LA, United States

²Department of Anatomical Dissection and Donation, Medical University of Lodz, Poland

³Department of Neurosurgery, Tulane Centre for Clinical Neurosciences, Tulane University School of Medicine, New Orleans, LA, United States

⁴Department of Neurology, Tulane Centre for Clinical Neurosciences, Tulane University School of Medicine, New Orleans, LA, United States

⁵Department of Anatomical Sciences, St. George's University, St. George's, Grenada, West Indies

⁶Department of Structural and Cellular Biology, Tulane University School of Medicine, New Orleans, LA, United States

⁷Department of Surgery, Tulane University School of Medicine, New Orleans, LA, United States

⁸Department of Neurosurgery and Ochsner Neuroscience Institute, Ochsner Health System, New Orleans, LA, United States

⁹University of Queensland, Brisbane, Australia

[Received: 5 January 2022; Accepted: 12 March 2022; Early publication date: 29 March 2022]

Anatomical variations can occasionally result in unexpected findings on physical examination. Here, we report two cases of seemingly unique connections between V2 and V3 parts of the trigeminal nerve. In these two cadaveric specimens, at the foramen ovale, small neural connections, confirmed with histology, were identified joining V2 to specifically, the motor root of V3. The findings of these two cadaveric specimens and the potential clinical ramifications are discussed. (Folia Morphol 2023; 82, 2: 382–385)

Key words: skull base, anatomy, surgery, trigeminal nerve, interconnections, complications

INTRODUCTION

The fifth cranial nerve, also referred to as the trigeminal nerve (TGN), is the largest cranial nerve. It is a mixed nerve that provides motor input to the muscles of mastication and carries sensory input from the face, the oral and nasal cavities, and a large portion of the scalp [7]. Its peripheral portion is divided into three divisions: ophthalmic (V1), maxillary (V2), and mandibular (V3) [1]. V1 travels anteriorly through the cavernous sinus before exiting the skull through the superior orbital fissure and conveys sensory fibres from various anatomical locations including the orbit, paranasal sinuses, and upper face [7]. V2 travels alongside V1 through the cavernous sinus, exits the

skull through the foramen rotundum, and enters the pterygopalatine fossa. This branch transmits sensory information from primarily the middle third of the face and the upper teeth [7]. V1 and V2 join V3 posteriorly in Meckel's cave after traveling through the cavernous sinus [1]. V3 carries both sensory and motor fibres. Its sensory branches coalesce just below the skull base. These merged sensory branches, the largest division of the TGN, are now considered the V3 trunk, which enters Meckel's cave via the foramen ovale [1]. V1, V2, and the sensory portion of V3 merge to form the trigeminal or Gasserian ganglion within Meckel's cave. V3 brings sensory input from the lower face and the anterior two thirds of the tongue, jaw,

Address for correspondence: J. Iwanaga, DDS, PhD, Department of Neurosurgery, Tulane Centre for Clinical Neurosciences, 131 S. Robertson St. Suite 1300, New Orleans, LA 70112, United States, tel: 5049885565, fax: 5049885793, e-mail: iwanagajoea@gmail.com

This article is available in open access under Creative Commons Attribution-Non-Commercial-No Derivatives 4.0 International (CC BY-NC-ND 4.0) license, allowing to download articles and share them with others as long as they credit the authors and the publisher, but without permission to change them in any way or use them commercially.

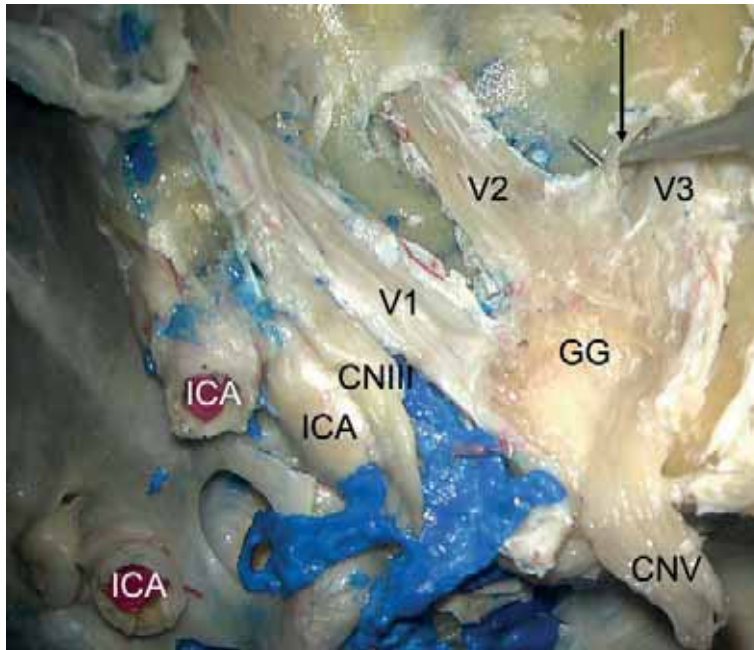


Figure 1. Right-sided cadaveric dissection noting the connecting nerve (under the hook and at the arrow) between V2 and V3. Also, note V1, the oculomotor nerve (CNIII), internal carotid arteries (ICA), Gasserian ganglion (GG), and trigeminal nerve (CNV).

and lower teeth. The motor portion of V3 originates from the motor nucleus in the floor of the fourth ventricle. It travels medially to meet the sensory portion of V3 and enters Meckel's cave, where its fibres bypass the trigeminal ganglion [1]. The motor and sensory portions of V3 coalesce at the internal cranial base. In addition to its sensory innervation, V3 supplies motor innervation to the mylohyoid muscle, muscles of mastication, the anterior belly of the digastric muscle, the tensor tympani muscle, and the tensor veli palatini muscle [4].

Adjacent peripheral nerves, including cranial nerves, are known to often and sometimes normally have intercommunicating branches. Although the exact role of such communicating branches is often unknown, some (e.g., Martin-Gruber connections in the forearm) have found that these connections can serve a functional role [2]. Cranial nerves, especially the lower cranial nerves, have known intercommunicating branches that occur both intra- and extracranially [6]. Therefore, knowledge of such interconnections is important to the clinician who finds unusual findings on physical examination of their patients and to surgeons who encounter these fibres at surgery. Here, we report the unusual finding of cadaveric specimens found to have connections between V2 and V3 prior to the two nerves exiting the internal cranial base. This anatomy and related literature are reviewed.

CASE REPORT

During the routine dissection of the skull bases in a 78-year-old male cadaver and a 67-year-old at death male cadaver, a connection was identified between the V2 and V3 parts of the right TGN. A surgical microscope (Zeiss, Germany) was used to perform the dissections. Both connections between V2 and V3 were identified on right sides. In the first specimen (Fig. 1), the connection was 11 mm long and 1.59 mm wide. The fibres connected V2 at its origin from the Gasserian ganglion to the motor root of V3 just inferior to the foramen ovale. In the second specimen, a similar band that was 5.4 mm long by 1.7 mm wide joined V2 to V3, and again, specifically to its motor root, just at the foramen ovale (Fig. 2). Both connections were submitted for histological analysis (H&E, Masson trichrome, Nissl) and reviewed using a microscope. Both histological samples revealed normal nerve tissue, and due to the size of the nerve fibres, these were consistent with sensory nerve fibres (Fig. 3). No additional gross anatomical variations were noted on ipsilateral or contralateral sides of the two specimens.

DISCUSSION

Fibres of the TGN have been shown to mix at the brainstem level. Two separate groups of rootlets contribute to its motor portion. One of these groups

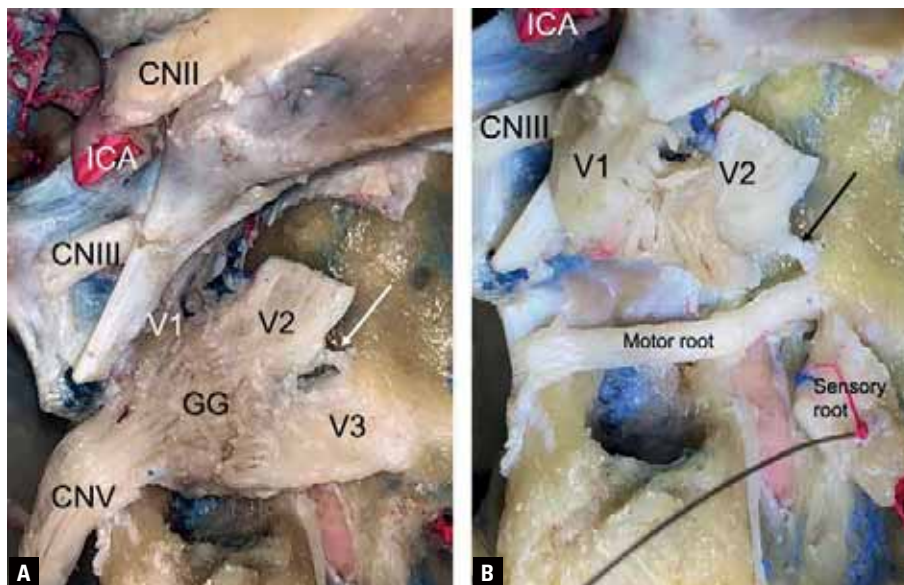


Figure 2. Right-sided cadaveric dissection noting the connecting nerve (arrow) between V2 and V3: **A.** In normal position, note the optic nerve (CNII), oculomotor nerve (CNIII), V1, internal carotid artery (ICA), Gasserian ganglion (GG), and trigeminal nerve (CNV); **B.** Following reflection of the Gasserian ganglion and showing the motor and sensory roots of V3 and the nerve connection (arrow) between V2 and the motor root of V3.

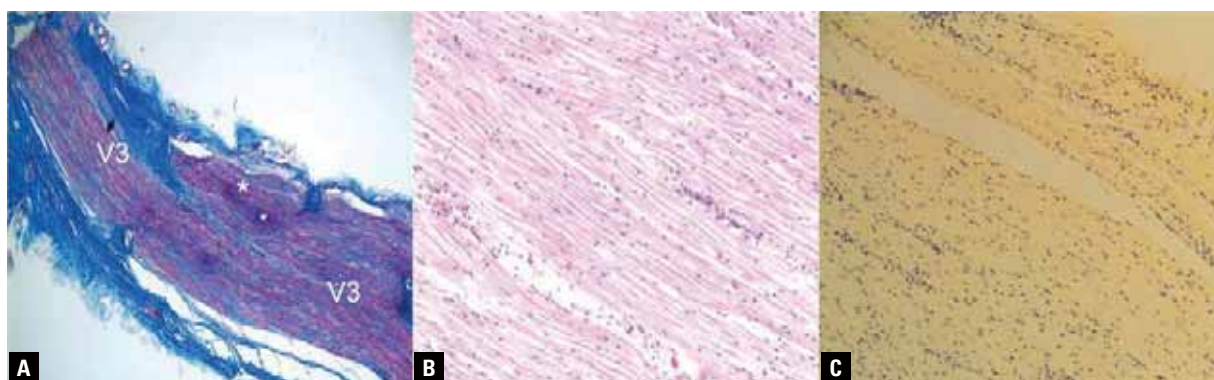


Figure 3. Histological sections of the nerve connections between V2 and V3. The left image (**A**, Masson trichrome 40×) shows the connecting nerve (*) joining V3. The blue stained connective tissue sheaths of the nerves are visible. The middle (**B**, H&E 200×) and right images (**C**, Nissl 200×) verify the nerve quality of the connecting branch.

is superior and the other inferior to the main sensory root [6]. The superior group is considered the origin of the motor root, as it is consistently located in an isolated position superior to the main sensory root. The origin of the inferior rootlets usually contacts the inferior anterior aspect of the main sensory root. The cadaveric study of Saunders and Sachs [5] also revealed several anastomoses between the inferior rootlets and the main sensory root. The superior and inferior rootlets followed the expected course of the motor root of the TGN. They merged within 1 cm of the pons before continuing through Meckel's cave and exiting through the foramen ovale. It was

hypothesized that these so-called inferior rootlets are accessory rootlets carrying sensory fibres to the motor root.

Such anatomical findings such as those of Saunders and Sachs [5] suggest some mixing of sensory and motor fibres within the motor tract of the TGN. The two case reports presented herein further strengthen the mixing of fibres and in these cases, at the skull base and not near the brainstem. This becomes clinically significant in view of reports of people who maintain facial sensation after complete sensory root dissection at the pons, which spares the small motor rootlets [5]. A different

study showed that 12–20% of the fibres in the motor root of TGN are unmyelinated [8]. It is likely that these unmyelinated fibres are afferent and that they originate in sensory ganglion cells in the Gasserian ganglion. The sensory and motor root fibres are likely to merge at these accessory trigeminal fibres [8]. Again, this notion is supported by persistent trigeminal neuralgia after a complete trigeminal rhizotomy. These unique findings associated with the nerve pathways and the clinical scenarios strongly suggest that there are afferent fibres among the TGN motor root.

We previously published a comprehensive review regarding the intercommunications between the cranial nerves with one of these focused on such neural connections between the trigeminal, facial and vestibulocochlear nerves [6]. In this review, all previously reported neural interconnections of the TGN were reported peripherally and primarily between it and adjacent facial nerve branches. Intracranial connections between two parts of the TGN and specifically, its divisions, has, to our knowledge, not been previously reported. Future anatomical and clinical studies will be necessary to further elucidate such connections and their functions.

CONCLUSIONS

We report two cases illustrating gross anatomical connections between V2 and V3 at the skull base, specifically between V2 and the motor root of V3. Such connections should be appreciated during physical examination of patients with unexpected findings and during surgical approaches to the middle cranial fossa near the foramen ovale.

Acknowledgements

The authors sincerely thank those who donated their bodies to science so that anatomical research

could be performed. Results from such research can potentially increase mankind's overall knowledge that can then improve patient care. Therefore, these donors and their families deserve our highest gratitude [3].

Conflict of interest: None declared

REFERENCES

1. Bathla G, Hegde AN. The trigeminal nerve: an illustrated review of its imaging anatomy and pathology. *Clin Radiol.* 2013; 68(2): 203–213, doi: [10.1016/j.crad.2012.05.019](https://doi.org/10.1016/j.crad.2012.05.019), indexed in Pubmed: [22889460](https://pubmed.ncbi.nlm.nih.gov/22889460/).
2. Diz-Díaz J, Gómez-Muñoz E, Sañudo J, et al. Which is the function of a martin-gruber connection? *Clin Anat.* 2019; 32(4): 501–508, doi: [10.1002/ca.23339](https://doi.org/10.1002/ca.23339), indexed in Pubmed: [30664256](https://pubmed.ncbi.nlm.nih.gov/30664256/).
3. Iwanaga J, Singh V, Takeda S, et al. Acknowledging the use of human cadaveric tissues in research papers: Recommendations from anatomical journal editors. *Clin Anat.* 2021; 34(1): 2–4, doi: [10.1002/ca.23671](https://doi.org/10.1002/ca.23671), indexed in Pubmed: [32808702](https://pubmed.ncbi.nlm.nih.gov/32808702/).
4. Joo W, Yoshioka F, Funaki T, et al. Microsurgical anatomy of the trigeminal nerve. *Clin Anat.* 2014; 27(1): 61–88, doi: [10.1002/ca.22330](https://doi.org/10.1002/ca.22330), indexed in Pubmed: [24323792](https://pubmed.ncbi.nlm.nih.gov/24323792/).
5. Saunders RL, Sachs E. Relation of the accessory rootlets of the trigeminal nerve to its motor root. A microsurgical autopsy study. *J Neurosurg.* 1970; 33(3): 317–324, doi: [10.3171/jns.1970.33.3.0317](https://doi.org/10.3171/jns.1970.33.3.0317), indexed in Pubmed: [5457643](https://pubmed.ncbi.nlm.nih.gov/5457643/).
6. Shoja MM, Oyesiku NM, Griessenauer CJ, et al. Anastomoses between lower cranial and upper cervical nerves: a comprehensive review with potential significance during skull base and neck operations, part I: trigeminal, facial, and vestibulocochlear nerves. *Clin Anat.* 2014; 27(1): 118–130, doi: [10.1002/ca.22340](https://doi.org/10.1002/ca.22340), indexed in Pubmed: [24272859](https://pubmed.ncbi.nlm.nih.gov/24272859/).
7. Woolfall P, Coulthard A. Pictorial review: Trigeminal nerve: anatomy and pathology. *Br J Radiol.* 2001; 74(881): 458–467, doi: [10.1259/bjr.74.881.740458](https://doi.org/10.1259/bjr.74.881.740458), indexed in Pubmed: [11388997](https://pubmed.ncbi.nlm.nih.gov/11388997/).
8. Young RF. Unmyelinated fibers in the trigeminal motor root. Possible relationship to the results of trigeminal rhizotomy. *J Neurosurg.* 1978; 49(4): 538–543, doi: [10.3171/jns.1978.49.4.0538](https://doi.org/10.3171/jns.1978.49.4.0538), indexed in Pubmed: [690682](https://pubmed.ncbi.nlm.nih.gov/690682/).

The first histological observation of a C1 posterior arch defect

Y. Fang¹, T. Saga², J. Iwanaga^{3–6}, A.S. Dumont³, R.S. Tubbs^{3, 4, 6–10}

¹Tulane University School of Medicine, New Orleans, LA, United States

²Domain of Anatomy, Kurume University School of Nursing, Kurume, Fukuoka, Japan

³Department of Neurosurgery, Tulane Centre for Clinical Neurosciences, Tulane University School of Medicine, New Orleans, LA, United States

⁴Department of Neurology, Tulane Centre for Clinical Neurosciences, Tulane University School of Medicine, New Orleans, LA, United States

⁵Division of Gross and Clinical Anatomy, Department of Anatomy, Kurume University School of Medicine, Kurume, Fukuoka, Japan

⁶Department of Structural and Cellular Biology, Tulane University School of Medicine, New Orleans, LA, United States

⁷Department of Anatomical Sciences, St. George's University, St. George's, Grenada, West Indies

⁸Department of Surgery, Tulane University School of Medicine, New Orleans, LA, United States

⁹Department of Neurosurgery and Ochsner Neuroscience Institute, Ochsner Health System, New Orleans, LA, United States

¹⁰Department of Anatomy, University of Warmia and Mazury, Olsztyn, Poland

[Received: 8 March 2022; Accepted: 15 March 2022; Early publication date: 29 March 2022]

Deficiencies in the posterior arch of C1 have been well-studied with incidences ranging from 5.65% to 3% and five different classifications. Unfortunately, there is a paucity of information describing the detailed anatomy, muscle attachments, and histology of cases with a C1 posterior arch deficiency. We found a case of an isolated unilateral posterior arch defect in the 83-year-old male cadaver. Histology revealed that the posterior arch defect was filled with collagen fibres and fibrocartilaginous tissue without muscle or bony tissues. This is the first report detailing the histological findings of a posterior arch defect of C1. (Folia Morphol 2023; 82, 2: 386–390)

Key words: posterior arch, atlas, cervical vertebra, anatomy, histology

INTRODUCTION

Deficiencies in the posterior arch of C1 have been well-studied with incidences ranging from 5.65% to 3% and five different classifications [4, 6]. Posterior arch deficiencies are known to be variable in clinical presentation, ranging from neck and head pain or neurologic deficiencies, but most commonly are an incidental radiologic finding [4]. Cases have often been diagnosed following trauma to the cervical spine [11]. As a result, these deficiencies are known to be difficult to diagnose, and may be confused with

fractures following trauma [10, 12, 13]. Patients with a posterior arch defect may be advised to reduce recreational activities or return to normal activity. As complications of C1 posterior arch deficiencies are not well known, there are currently no guidelines for return to activity following diagnosis [2].

Unfortunately, there is a paucity of information describing the detailed anatomy, muscle attachments, and histology of cases with a C1 posterior arch deficiency. We present a case report of an isolated unilateral posterior arch defect in order to further elucidate

Address for correspondence: J. Iwanaga, DDS, PhD, Department of Neurosurgery, Tulane Centre for Clinical Neurosciences, 131 S. Robertson St. Suite 1300, New Orleans, LA 70112, United States, tel: 5049885565, fax: 5049885793, e-mail: iwanagajoea@gmail.com

This article is available in open access under Creative Commons Attribution-Non-Commercial-No Derivatives 4.0 International (CC BY-NC-ND 4.0) license, allowing to download articles and share them with others as long as they credit the authors and the publisher, but without permission to change them in any way or use them commercially.

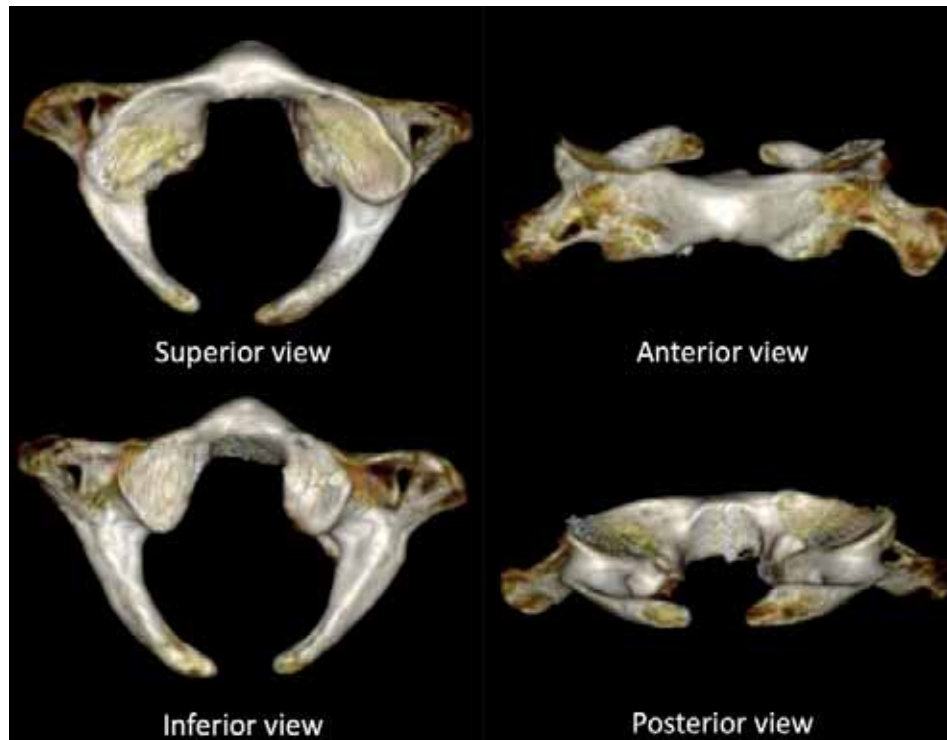


Figure 1. Computed tomographic images of the C1 posterior arch defect.

the specific anatomy and histology of posterior arch defects, allowing for better recognition during surgery of the surgical spine and to improve diagnosis and understanding of C1 posterior arch defects.

CASE REPORT

Prior to a neck dissection of the fresh-frozen cadaver, computed tomographic (CT) images were taken. The specimen was a Caucasian fresh-frozen male cadaver whose age at death was 83-year-old. Incidentally, a posterior arch defect (PAD) of the atlas was noted during predissection CT examination of the specimen (Fig. 1). The defect was mostly on the left side and approximately 10 mm wide. The specimen was then dissected to see the relationship between the PAD and the left rectus capitis posterior minor (RCPm) muscle origin. Once the RCPm on both sides were found, the posterior arch of C1 was palpated and defect of the posterior arch on the left RCPm origin was found. The left RCPm originated from the fibrous connective tissue that filled the defect (Figs. 2, 3).

The tissue in the PAD was then harvested with attached posterior arch for histological evaluation. The sagittal sections of both the PAD on the left and posterior arch on the right were obtained with 5 μ m slices and stained with Masson trichrome staining.

The slides were observed with a light microscope. Histology revealed that the PAD was filled with collagen fibres and fibrocartilaginous tissue without muscle or bony tissues (Fig. 4). The present study was performed in accordance with the requirements of the Declaration of Helsinki (64th WMA General Assembly, Fortaleza, Brazil, October 2013).

DISCUSSION

Curriano et al. [4] previously published five classes of posterior arch deficiencies: type A, a midline defect in the posterior arch, type B, a unilateral defect in the posterior arch, type C, bilateral defects, type D, absence of the posterior arch with an isolated persistent posterior tubercle, and type E, complete absence of the posterior arch. Type B most closely correlates to the posterior arch defect described in the present case study. A radiographic study by Hyun et al. [6] studied 3273 skulls in an effort to categorize the prevalence of each type, finding 181 skulls with some type of posterior arch deficiency. Type A was the most common, making up 151/181 of skulls with defects (81.6%) [6]. Type B, presented in this case study, was found to make up 15/181 cases (8.1%), with an overall prevalence of 0.46% [6]. Senoglu et al. [14] evaluated 1354 cases including 1104 patients, 166 dried bones,

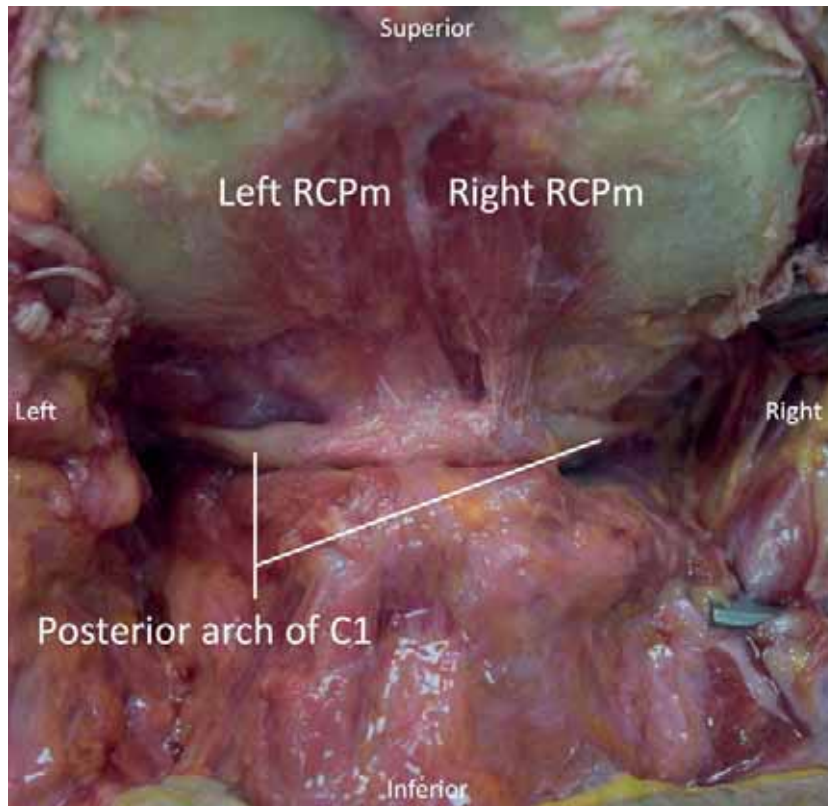


Figure 2. Anatomical exposure of the posterior arch defect. Both the right and left rectus capitis posterior minor (RCPm) muscles are shown.

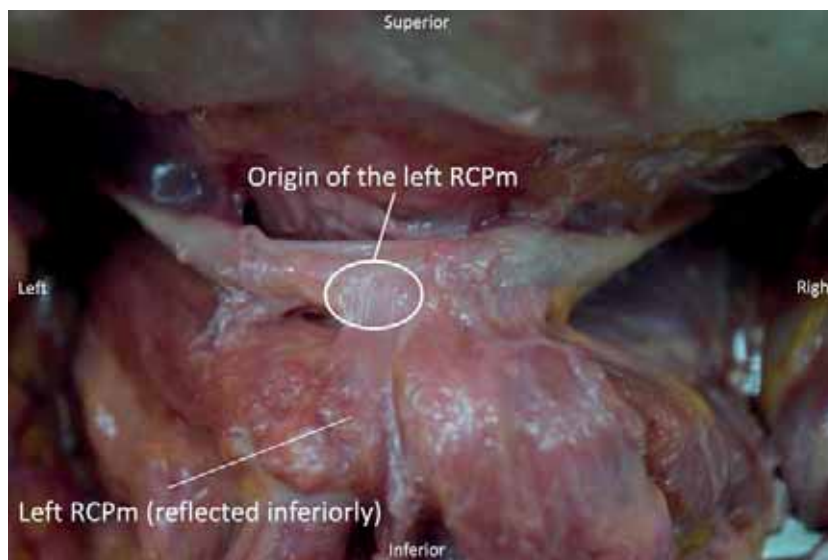


Figure 3. Both right and left rectus capitis posterior minor (RCPm) muscles are turned inferiorly to see their origins.

and 84 fresh cadavers and found 2.95% (40/1354) had the C1 posterior arch deficiency.

Previous studies have reported that patients with a C1 posterior arch deficiency probably have stable cervical spines despite the defect, likely due to the development of a dense fibrous membrane across the

width of the defect, spanning then entire posterior in patients with completely absent posterior arches [2, 4]. Studies on autopsy and surgical specimens have demonstrated these variants were bridged by connective tissue rather than cartilage, and a study by Geipel [5] surveying "anterior" arch defects of C1

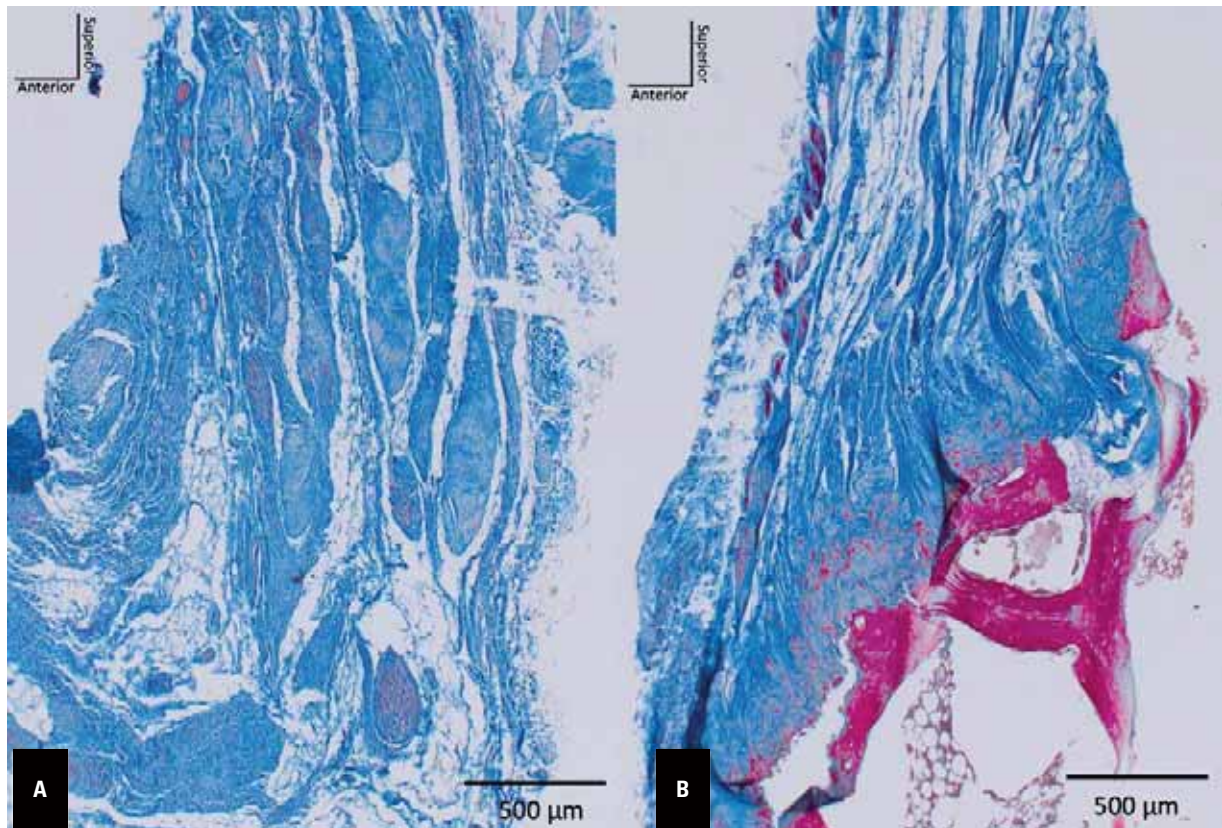


Figure 4. Masson-trichrome stain of the posterior arch of C1. Note that the posterior arch defect of C1 is filled with collagen fibres and fibrocartilaginous tissue (A) and the posterior arch of C1, slightly right of centre, is shown for comparison (B).

reported histological findings of a fibrocartilaginous bridge [8]. In the event of an absent posterior tubercle, the rectus capitis posterior minor and interspinalis cervicis may instead attach to the spinous process of C2, resulting in a compensatory hypertrophy and enlargement of the spinous process [4].

Historically, posterior arch defects have been difficult to distinguish from traumatic injuries such as Jefferson fractures [2, 10, 12, 13]. Arch defects can be differentiated by looking for smooth well-corticated margins on CT with no soft tissue swelling or stranding on CT or magnetic resonance imaging [2, 6, 10]. Lack of fracture callus performed on post-mortem anatomical studies may also help differentiate between a congenital defect, particularly in rare cases such as type B arch defects which may more closely mimic a traumatic event [13].

Embryology and development

The embryology of the spine begins with gastrulation and formation of somatic mesoderm and the notochord, condensation into somites, formation of dermatomes and sclerotomes, and then formation

of membranous somites and resegmentation into vertebrae, ending with chondrification of vertebrae and subsequent ossification [3]. Defects in the C1 posterior arch are generally thought to be due to errors in chondrification, rather than ossification [4, 6]. The atlas normally develops from three primary ossification centres: one midline centre that later develops into the anterior arch of C1, and two lateral masses that extend posteromedially to form the posterior arch of C1 [3, 9]. By the seventh gestational week, the lateral centres have formed the posterior arch, fusing completely by year four [3, 5, 9]. Failure of fusion of these two ossification centres is responsible for the development of defects in the posterior arch [9].

Another developmental cause is found in cases of a dystopic *os odontoideum*. In these patients, the tip of the odontoid process separates from the remaining portion of C2, fusing with the clivus near the foramen magnum [1]. This has been seen to result in hypoplasia of the posterior arch and hypertrophy of the anterior arch, similar to previously reported cases of posterior arch defects [1, 4, 6]. Notably, it is unclear if this variant is congenital or due to trauma [1].

Rarely, an anterior arch defect of C1 may be present in addition to a posterior arch defect, forming a bipartite atlas [2, 4, 6]. Development of this anterior arch defect is thought to be related to posterior arch defects, due to isolated anterior arch defects having a much lower prevalence than a bipartite atlas [6]. The current consensus is that the development of this anterior arch defect is due to biomechanical changes that occur with posterior arch defects, although the exact cause is debatable. One proposed mechanism by Allam et al. [2] states the anterior arch defect occurs due to subclinical fracture of the anterior arch due to the posterior arch anomaly. One study by Hyun et al. [6] found that trauma was unlikely to form a major role due to the lack of correlation between anterior arch defects and patient age, instead suggesting that absence of the posterior arch affects increased axial load of the anterior arch, affecting development as it ossifies later in childhood. Other studies have found that patients with posterior arch variations may have hypertrophy of the anterior arch, suggesting that defects in the posterior arch does affect the development of the anterior arch [4].

Analysis of anatomical variations can contribute to obtaining an actual, not idealised image of the inside of the human body, which is of crucial importance in everyday clinical practice [15].

CONCLUSIONS

This is the first report detailing the histological findings of a posterior arch defect of C1.

Acknowledgements

The authors sincerely thank those who donated their bodies to science so that anatomical research could be performed. Results from such research can potentially increase mankind's overall knowledge that can then improve patient care. Therefore, these donors and their families deserve our highest gratitude [7].

Conflict of interest: None declared

REFERENCES

- Akobo S, Rizk E, Loukas M, et al. The odontoid process: a comprehensive review of its anatomy, embryology, and variations. *Childs Nerv Syst.* 2015; 31(11): 2025–2034, doi: [10.1007/s00381-015-2866-4](https://doi.org/10.1007/s00381-015-2866-4), indexed in Pubmed: [26254085](https://pubmed.ncbi.nlm.nih.gov/26254085/).
- Allam E, Zhou Y. Bipartite atlas or jefferson fracture? A case series and literature review. *Spine (Phila Pa 1976).* 2015; 40(11): E661–E664, doi: [10.1097/BRS.0000000000000874](https://doi.org/10.1097/BRS.0000000000000874), indexed in Pubmed: [26091159](https://pubmed.ncbi.nlm.nih.gov/26091159/).
- Chaturvedi A, Klionsky NB, Nadarajah U, et al. Malformed vertebrae: a clinical and imaging review. *Insights Imaging.* 2018; 9(3): 343–355, doi: [10.1007/s13244-018-0598-1](https://doi.org/10.1007/s13244-018-0598-1), indexed in Pubmed: [29616497](https://pubmed.ncbi.nlm.nih.gov/29616497/).
- Currarino G, Rollins N, Diehl JT. Congenital defects of the posterior arch of the atlas: a report of seven cases including an affected mother and son. *AJNR Am J Neuroradiol.* 1994; 15(2): 249–254. Erratum in: *AJNR Am J Neuroradiol.* 1994; 15(6): A9, indexed in Pubmed: [8192068](https://pubmed.ncbi.nlm.nih.gov/8192068/).
- Geipel P. Zur Kenntnis der Spaltbildung des Atlas und Epistropheus. IV. Teil [Studies on the fissure formation of the atlas and epistropheus. IV]. *Zentralbl Allg Pathol.* 1955; 94(1-2): 19–84, indexed in Pubmed: [13282406](https://pubmed.ncbi.nlm.nih.gov/13282406/).
- Hyun G, Allam E, Sander P, et al. The prevalence of congenital C1 arch anomalies. *Eur Spine J.* 2018; 27(6): 1266–1271, doi: [10.1007/s00586-017-5283-4](https://doi.org/10.1007/s00586-017-5283-4), indexed in Pubmed: [28849400](https://pubmed.ncbi.nlm.nih.gov/28849400/).
- Iwanaga J, Singh V, Ohtsuka A, et al. Acknowledging the use of human cadaveric tissues in research papers: Recommendations from anatomical journal editors. *Clin Anat.* 2021; 34(1): 2–4, doi: [10.1002/ca.23671](https://doi.org/10.1002/ca.23671), indexed in Pubmed: [32808702](https://pubmed.ncbi.nlm.nih.gov/32808702/).
- Logan WW, Stuard ID. Absent posterior arch of the atlas. *Am J Roentgenol Radium Ther Nucl Med.* 1973; 118(2): 431–434, doi: [10.2214/ajr.118.2.431](https://doi.org/10.2214/ajr.118.2.431), indexed in Pubmed: [4354561](https://pubmed.ncbi.nlm.nih.gov/4354561/).
- Park JS, Eun JP, Lee HO. Anteroposterior spondyloschisis of atlas with bilateral cleft defect of posterior arch: a case report. *Spine (Phila Pa 1976).* 2011; 36(2): E144–E147, doi: [10.1097/BRS.0b013e3181efa320](https://doi.org/10.1097/BRS.0b013e3181efa320), indexed in Pubmed: [21228693](https://pubmed.ncbi.nlm.nih.gov/21228693/).
- Park Y, Kim SM, Lee YT, et al. Congenital anomaly of the atlas misdiagnosed as posterior arch fracture of the atlas and atlantoaxial subluxation. *Clin Orthop Surg.* 2014; 6(1): 96–100, doi: [10.4055/cios.2014.6.1.96](https://doi.org/10.4055/cios.2014.6.1.96), indexed in Pubmed: [24605195](https://pubmed.ncbi.nlm.nih.gov/24605195/).
- Petraglia AL, Childs SM, Walker CT, et al. Bipartite atlas in a collegiate football player: Not necessarily a contraindication for return-to-play: A case report and review of the literature. *Surg Neurol Int.* 2012; 3: 126, doi: [10.4103/2152-7806.102351](https://doi.org/10.4103/2152-7806.102351), indexed in Pubmed: [23227431](https://pubmed.ncbi.nlm.nih.gov/23227431/).
- Petre BM, Karp JE, Riley LH. Athletic cervical spine injury in the setting of fusion failure of the anterior and posterior atlas. *Orthopedics.* 2012; 35(9): e1449–e1452, doi: [10.3928/01477447-20120822-39](https://doi.org/10.3928/01477447-20120822-39), indexed in Pubmed: [22955419](https://pubmed.ncbi.nlm.nih.gov/22955419/).
- Sanchis-Gimeno JA, Blanco-Perez E, Aparicio L, et al. Difficulties in distinguishing between an atlas fracture and a congenital posterior atlas arch defect in postmortem analysis. *Forensic Sci Int.* 2014; 242: e1–e5, doi: [10.1016/j.forsciint.2014.06.016](https://doi.org/10.1016/j.forsciint.2014.06.016), indexed in Pubmed: [25037687](https://pubmed.ncbi.nlm.nih.gov/25037687/).
- Senoglu M, Safavi-Abbasi S, Theodore N, et al. The frequency and clinical significance of congenital defects of the posterior and anterior arch of the atlas. *J Neurosurg Spine.* 2007; 7(4): 399–402, doi: [10.3171/SPI-07/10/399](https://doi.org/10.3171/SPI-07/10/399), indexed in Pubmed: [17933313](https://pubmed.ncbi.nlm.nih.gov/17933313/).
- Żytkowski A, Tubbs R, Iwanaga J, et al. Anatomical normality and variability: Historical perspective and methodological considerations. *Trans Res Anat.* 2021; 23: 100105, doi: [10.1016/j.tria.2020.100105](https://doi.org/10.1016/j.tria.2020.100105).

An atypical radiographic appearance of a cardiac myxoma: case report and review of the literature

R. Antoniak¹, M. Kompa¹, R. Burdach¹, L. Grabowska-Derlatka¹, A. Słowikowska², O. Rowiński¹

¹2nd Department of Clinical Radiology, University Clinical Centre of Medical University of Warsaw, Poland

²Department of Cardiac Surgery, University Clinical Centre of Medical University of Warsaw, Poland

[Received: 7 January 2022; Accepted: 7 March 2022; Early publication date: 5 April 2022]

Cardiac myxomas are the most common primary cardiac tumours in adults. They usually present as a solitary, solid mass in the left atrium. Their most common radiographic appearance is that of a hypodense lesion on computed tomography (CT) and inhomogeneous lesion (hypo to isointense on T1 sequences and hyperintense on T2 sequences) on magnetic resonance (MR) with some contrast enhancement. However, different patterns are recognized due to secondary changes within the tumour. We present a case of a 60-year-old man with a hypervascular myxoma. The lesion was a sessile mass located in the left atrium and rigidly attached to the interatrial septum. On CT and MR, it showed vivid contrast enhancement due to intratumoural flush of arterial blood from branches of dominant left circumflex artery and a possible fistula to the left atrium. Furthermore, we review the literature for different atypical radiographic appearances of myxomas. (Folia Morphol 2023; 82, 2: 391–395)

Key words: cardiac tumour, radiology, computed tomography, magnetic resonance

CASE REPORT

A 60-year-old man was referred to our institution with a diagnosis of a cardiac tumour. The patient complained of itching chest pain after exertion. Otherwise, his past medical history was unremarkable. The primary work-up was performed outside our institution. As far as diagnostic imaging is concerned, these investigations consisted of coronary angiogram, transthoracic and transoesophageal echocardiography. The coronary angiogram showed no significant stenotic lesions, but demonstrated atypical branches of the dominant left circumflex artery converging to the interatrial septum. Transthoracic and transoesophageal echocardiography revealed a sessile

mass located in the left atrium and attached to the interatrial septum. The lesion contained calcifications, had a visible blood flow on colour Doppler imaging, and measured 35 × 45 mm. No other significant abnormalities were noted. Chest radiograph showed no abnormalities.

On admission the patient was asymptomatic, and his vital signs (heart rate, blood pressure, blood oxygen saturation level, temperature) were within normal limits. Physical examination revealed systolic murmur in the second right intercostal space. Basic metabolic panel showed slight elevation of alanine aminotransferase level (95 U/L, normal range 7–56 U/L).

Address for correspondence: Dr. R. Antoniak, 2nd Department of Clinical Radiology, Medical University of Warsaw, ul. Banacha 1a, 02–097 Warszawa, Poland, tel: +48 22 599 23 00, e-mail: ro.antoniak@gmail.com

This article is available in open access under Creative Common Attribution-Non-Commercial-No Derivatives 4.0 International (CC BY-NC-ND 4.0) license, allowing to download articles and share them with others as long as they credit the authors and the publisher, but without permission to change them in any way or use them commercially.

Otherwise, his physical, laboratory and electrocardiographic examinations were unremarkable.

Cardiac computed tomography (CT) and magnetic resonance (MR) were performed to better characterise the mass. CT was performed using a 320-row dynamic volume CT scanner (Aquilion One, Toshiba Medical Systems, Ottawara, Japan) with administration of contrast agent (Iomeron-400; Bracco, Milan, Italy). The protocol consisted of electrocardiogram-gated non-contrast, arterial and delayed phases. Arterial phase was triggered when a contrast enhancement threshold of 180 HU was exceeded in the descending aorta followed by a 5 s delay. Delayed phase was acquired 60 s after contrast administration. A four-phasic intravenous injection regimen was used: 5 mL of saline + 60 mL of contrast agent + 30 mL of 50% contrast agent and 50% saline + 40 mL saline chaser at a flow rate of 6 mL/s. The detailed parameters of CT imaging are presented in Table 1. MR was performed using a 1.5 T clinical whole-body MR system (MAGNETOM Avanto; Siemens AG, Erlangen, Germany) with administration of contrast agent as a bolus dose of 0.1 mmol/kg of gadobutrol (Gadovist, Bayer Schering, Berlin, Germany) followed by a 20 mL saline flush at a flow rate of 3 mL/s. The cardiac MR imaging protocol contained HASTE, SSFP CINE, T2-TIRM, T1, T1FS, perfusion and DE-PSIR sequences in several planes (typical cardiac 2CH, 3CH, 4CH and SA as well as specifically adjusted to transect the lesion). The

Table 1. Computed tomography acquisition parameters

Parameter	Non-contrast + contrast-enhanced phases
Tube voltage [kV]	120
Tube current [mA]	Smart mA
Rotation time [s]	0.275
D-FOV [mm]	220.0
Focus	Small
Slice thickness/interval [mm]	0.5/0.25

FOV — field of view

detailed parameters of MR images sequences are summarised in Table 2.

On native CT the lesion was slightly hypodense, with some calcifications (Fig. 1). Arterial phase showed flush of the contrast medium from at least two branches of dominant left circumflex artery to the centre of the mass and a possible narrow connection with the left atrium cavity suggestive of a fistula (Figs. 2, 3). It also confirmed no significant coronary artery disease. On delayed images it was hard to depict any contrast enhancement of the mass beyond the vascular part (Fig. 1). On MR the lesion was inhomogeneous, hypo- to isointense on T1 sequences and hyperintense with some hypointense foci on T2 sequences (Fig. 4). Perfusion images showed the already known flush of arterial blood in the centre of the mass. Delayed images demonstrated weak, heterogeneous enhancement of its remaining part

Table 2. Magnetic resonance sequences' parameters

Parameter	HASTE	SSFP CINE	T2-TIRM	T1 + T1FS	PERFUSION	DE-PSIR
Plane	Axial	2CH, 3CH, 4CH, SA	SA, specific	Specific	Specific	SA, specific
Repetition time [ms]	800	42,3 (2,3CH); 40,05 (4CH); 57,86 (SA)	664	740	160.76	700
Echo time [ms]	40	1.12	47	30	1.05	1.21
Flip angle [°]	160	80 (2,3,4CH); 79 (SA)	180	180	12	45
iPAT factor	2	2	-	2	2	2
Number of signal averages	1	1	1	1	1	1
FOV [mm]	370	340 (2,3CH,SA); 380 (4CH)	360	340	360	340
FOV phase [%]	75	80.4 (2,3,4CH); 81.3 (SA)	81.3	81.3	75	68.8
Breath-hold	No	Yes	Yes	Yes	Yes	Yes
Resolution [mm]	2.4 × 1.4 × 8	1.5 × 1.5 × 6 (2,3CH); 1.7 × 1.7 × 6 (4CH); 2.5 × 1.4 × 8 (SA)	1.9 × 1.4 × 8	2.2 × 1.3 × 5	2.8 × 2.3 × 10	2.5 × 1.8 × 8

HASTE — half-Fourier acquisition single-shot turbo spin-echo; SSFP CINE — steady-state free-precession cine; TIRM — turbo inversion recovery magnitude; FS — fat saturation; DE-PSIR — delayed enhancement phase-sensitive inversion recovery; 2,3,4CH — two, three, four chamber plane; SA — short axis plane; iPAT — integrated parallel acquisition techniques; FOV — field of view

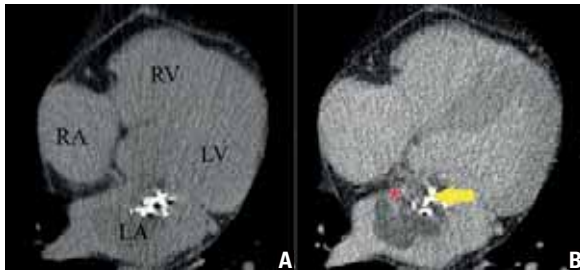


Figure 1. A. Axial non-contrast computed tomography image; **B.** Axial delayed phase contrast-enhanced computed tomography image. Images demonstrate a hypodense mass measuring 35×45 mm in the left atrium. The lesion contains calcifications (yellow arrow on image B) and contrast-enhancing vascular part (red asterisk on image B). Size of cardiac chambers is within normal limits. There are no other cardiovascular abnormalities; RA — right atrium; RV — right ventricle; LA — left atrium; LV — left ventricle.

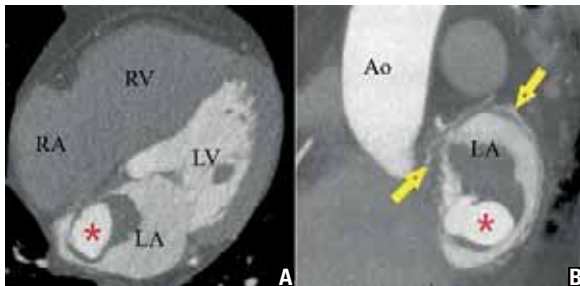


Figure 2. A. Axial arterial phase computed tomography image; **B.** Maximum intensity projection reconstruction of sagittal arterial phase computed tomography images. Images demonstrate the mass measuring 35×45 mm in the left atrium with its vascular and non-vascular components. They present enlarged, tortuous feeding vessels (yellow arrows on image B) and flush of arterial blood in the vascular nidus of the tumour (red asterisks on both images). The non-vascular part of the mass remains hypodense. Size of cardiac chambers is within normal limits. There are no other cardiovascular abnormalities; RA — right atrium; RV — right ventricle; LA — left atrium; LV — left ventricle; Ao — aorta.

(Fig. 5). Both studies were suggestive of a myxoma with an intratumoural fistula between branches of circumflex artery and left atrium.

The patient underwent successful resection of the tumour. The postoperative period was uneventful. The histopathological examination confirmed the diagnosis of a myxoma.

DISCUSSION

We present a case of an atypical radiographic appearance of a cardiac myxoma. Myxomas are the most common primary cardiac tumours in adults accounting for about 50% of cases [3]. They are usually found in the middle-aged population (mean age of about 50) with female predominance [7].

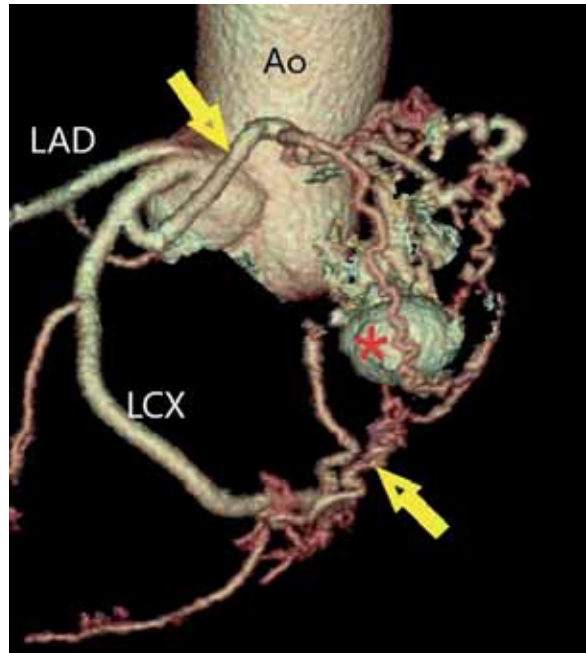


Figure 3. Coronary computed tomography reconstruction. Image shows ascending aorta and coronary tree. It presents domination of left coronary artery and separate origins of left anterior descending (LAD) and left circumflex (LCX) arteries from the left aortic sinus. Two enlarged branches of LCX (yellow arrows) feed the vascular part of the mass (red asterisk). No significant coronary artery disease is noted; Ao — aorta.

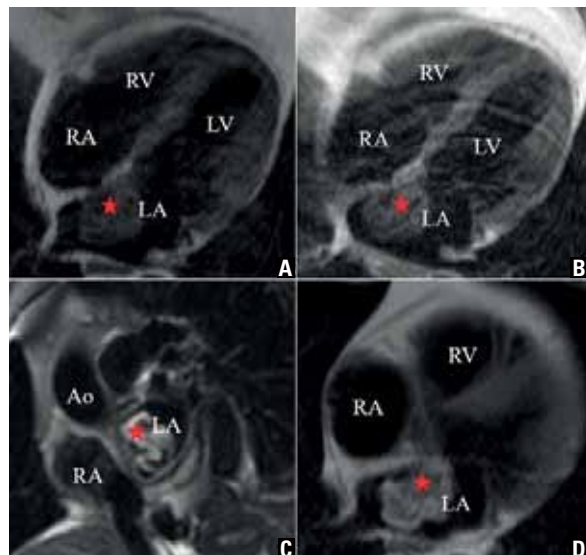


Figure 4. A. Four-chamber T1 image; **B.** Four-chamber T1 fat-saturated image; **C.** Short axis T2 fat-saturated image; **D.** Axial HASTE image. Images demonstrate heterogeneity of the mass (red asterisk) on magnetic resonance. Secondary changes within the tumour (i.e., calcifications and vascular component) are responsible for the hypointense foci on T2 weighted sequences (image C). The lesion contains no fat as it has similar signal intensity on T1 weighted sequences with and without fat saturation (images A and B). Size of cardiac chambers is within normal limits. There are no other cardiovascular abnormalities; RA — right atrium; RV — right ventricle; LA — left atrium; LV — left ventricle.

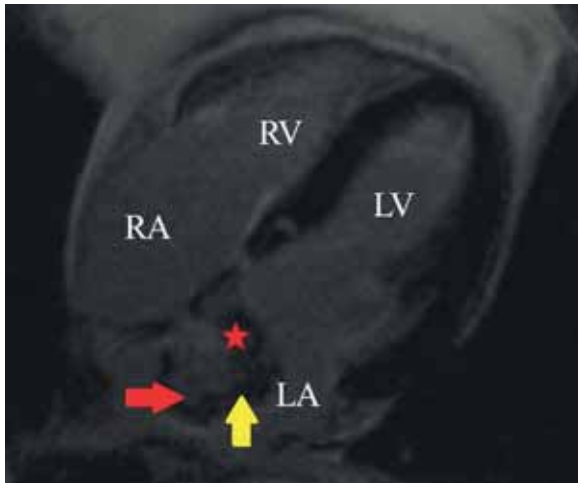


Figure 5. Four-chamber T1 delayed post-contrast image. Image reveals contrast enhancement of both myxoid and vascular parts of the mass (red asterisk). The vascular component follows signal intensity and contrast enhancement of blood on all magnetic resonance sequences. The myxoid part shows some contrast enhancement (red arrow) and a non-enhancing cap (yellow arrow) on delayed imaging. Size of cardiac chambers is within normal limits. There are no other cardiovascular abnormalities; RA — right atrium; RV — right ventricle; LA — left atrium; LV — left ventricle.

The typical appearance is that of a solitary mass in the left atrium, attached to the interatrial septum, with narrow attachment base, lobulated contours, and a diameter of 3–4 cm [3]. On CT myxomas present as hypodense lesions with a very weak contrast enhancement and calcifications in about 10–20% of cases. On MR they are inhomogeneous, hypo- to isointense on T1 sequences, hyperintense on T2 sequences, with heterogeneous contrast enhancement. Myxoid matrix shows very high signal intensity on T2 sequences. Secondary changes within the tumour (e.g., calcifications, fibrosis, cysts, and various stages of haemorrhage) are responsible for their heterogeneity on both T1 and T2 sequences.

However, many atypical radiographic patterns are found in the literature. As mentioned before, the vast majority of myxomas are solitary lesions located in the left atrium, with attachment to the interatrial septum. Multiple lesions occur very rarely and are usually associated with genetic syndromes. The best-known connection is Carney complex described in 1980s [2], a multiple endocrine neoplasia syndrome including skin pigmentation, cardiac and extracardiac myxomas, pituitary adenoma, psammomatous melanotic schwannoma, testicular tumours and osteochondromyxoma. Seldomly, multiple lesions occur

without a known genetic predisposing factor [4]. As far as multiplicity of myxomas is concerned, they have a well-established potential to metastasize. The most common site of metastases is brain [12]. In the literature there are found cases of myxomas' metastases to many other organs including pancreas, kidneys, stomach, bones and even skin [11]. Location of myxomas in other parts of left atrium or in other cardiac chambers is also very rare. It occurs more often in multiple lesions in genetic syndromes. There are published cases of myxomas in all cardiac chambers — right atrium, biatrial, left ventricle, right ventricle, right ventricle outflow tract [5] and even pulmonary artery [1].

Neither width of attachment to the interatrial septum nor contour of the tumour's surface is a discriminating factor. Some tumours are mobile, pedunculated, with a narrow attachment base, while others are non-mobile, sessile, and rigidly attached to the cavity wall. The length of the stalk in pedunculated lesions determines mobility of the mass. The longer the stalk, the more mobile the lesion and more probable to cause obstruction of the atrio-ventricular tract. Surface of the tumours vary from smooth, through lobulated, to even very irregular. Furthermore, the tumour may be covered with a thrombus, which most often occurs in the irregular type. Tumour size and its growth rate are variable. At presentation tumours measure usually 3–4 cm (ranging from 1 up to 15 cm). Their reported mean growth rate is 4–5 mm per year. Some remain stable for several years, while others grow fast mimicking malignant tumours [3].

Myxomas may contain variable portions of postnecrotic and posthaemorrhagic calcifications and cysts. Likewise, vascularisation of these tumours is highly variable. Calcifications are present in about 10–20% of myxomas [3]. Some lesions are highly calcified with myxomatous tissue undetectable by means of diagnostic imaging [6]. In these cases, preoperative differential diagnosis with calcified amorphous tumour, thrombi, vegetations or caseous calcification of mitral annulus may be impossible. Cystic components are far less common. Multiplicity and size of the cysts are variable. Some lesions resemble a single cyst with only a small solid nodule [8] and some have a multicystic appearance [9]. Differential diagnosis of cystic myxomas include hydatid cyst, bronchogenic cyst, interatrial septum aneurysm, varices, and foramen ovale cyst. The vast majority of myxomas are hypovascular

Table 3. Atypical patterns of cardiac myxomas

Feature	Atypical finding		Report
Multiplicity	Intracardiac	Genetic	Carney JA, 1985 [2]
		Non-genetic	Kataoka S, 2016 [4]
	Extracardiac metastases	Wan Y, 2019 [12] Terata Y, 2000 [11]	
Location	Cardiac chambers besides left atrium		Katiyar G, 2020 [5] Baris V, 2016 [1]
Secondary changes within the tumour	Large degree of calcifications		López-Marco A, 2014 [6]
	Cysts	Single	Park JK, 2013 [8]
		Multiple	Singhal A, 2017 [9]
	Hypervascularity		Stiver K, 2015 [10]

and enhance weak after contrast agent administration. Some lesions may show no contrast uptake and simulate a thrombus. Differentiation between myxoma and a thrombus may be even more challenging as they may coexist. MR post-contrast T1 sequences with high inversion times (500–600 ms) are helpful in the differential diagnosis. They are very specific for thrombi, which show no signal intensity. On the other hand, some myxomas are highly vascular or contain a fistula between coronary arteries and cardiac chambers. Stiver et al. [10] presented a case of a myxoma with a well-documented myocardial ischaemia due to myxoma's steal phenomenon. We present a similar case of a patient with an exertion chest pain and a highly vascular cardiac myxoma with a possible fistula between branches of the left circumflex artery and left atrium. The symptoms of our patient cannot be directly correlated with the presence of a highly vascular myxoma. These symptoms did not meet the criteria of typical angina and we have not performed a stress test to confirm the association. Follow-up studies will reveal whether these symptoms pass or remain, and the tumour was only an incidental finding.

CONCLUSIONS

We present a case of an atypical radiographic appearance of a highly vascular myxoma. Additionally, we review the literature for other atypical radiological patterns of these tumours. The summary is presented in Table 3. When dealing with cardiac tumour one should keep in mind the possibility of atypically located, multiple and metastasizing myxomas. These tumours may contain variable portions of calcifications, cystic and vascular components and thus, simulate other masses.

Conflict of interest: None declared

REFERENCES

1. Baris VO, Uslu A, Gerede DM, et al. Rare cause of dyspnoea: pulmonary artery myxoma. *Eur Heart J Cardiovasc Imaging*. 2016; 17(8): 946, doi: [10.1093/ehjci/jew089](https://doi.org/10.1093/ehjci/jew089), indexed in Pubmed: [27126320](https://pubmed.ncbi.nlm.nih.gov/27126320/).
2. Carney JA, Gordon H, Carpenter PC, et al. The complex of myxomas, spotty pigmentation, and endocrine overactivity. *Medicine (Baltimore)*. 1985; 64(4): 270–283, doi: [10.1097/00005792-198507000-00007](https://doi.org/10.1097/00005792-198507000-00007), indexed in Pubmed: [4010501](https://pubmed.ncbi.nlm.nih.gov/4010501/).
3. Colin GC, Gerber BL, Amzulescu M, et al. Cardiac myxoma: a contemporary multimodality imaging review. *Int J Cardiovasc Imaging*. 2018; 34(11): 1789–1808, doi: [10.1007/s10554-018-1396-z](https://doi.org/10.1007/s10554-018-1396-z), indexed in Pubmed: [29974293](https://pubmed.ncbi.nlm.nih.gov/29974293/).
4. Kataoka S, Otsuka M, Goto M, et al. Primary multiple cardiac myxomas in a patient without the Carney complex. *J Cardiovasc Ultrasound*. 2016; 24(1): 71–74, doi: [10.4250/jcu.2016.24.1.71](https://doi.org/10.4250/jcu.2016.24.1.71), indexed in Pubmed: [27081449](https://pubmed.ncbi.nlm.nih.gov/27081449/).
5. Katiyar G, Vernekar JA, Lawande A, et al. Cardiac MRI in right ventricular outflow tract myxoma: Case report with review of literature. *J Cardiol Cases*. 2020; 22(3): 128–131, doi: [10.1016/j.jccase.2020.05.007](https://doi.org/10.1016/j.jccase.2020.05.007), indexed in Pubmed: [32884595](https://pubmed.ncbi.nlm.nih.gov/32884595/).
6. López-Marco A, BinEsmael T, Rowlands G, et al. Complete calcification of right atrial myxoma. *Eur J Cardiothorac Surg*. 2015; 48(1): 171, doi: [10.1093/ejcts/ezu399](https://doi.org/10.1093/ejcts/ezu399), indexed in Pubmed: [25344923](https://pubmed.ncbi.nlm.nih.gov/25344923/).
7. McAllister BJ. Multi modality imaging features of cardiac myxoma. *J Cardiovasc Imaging*. 2020; 28(4): 235–243, doi: [10.4250/jcvi.2020.0027](https://doi.org/10.4250/jcvi.2020.0027), indexed in Pubmed: [32462832](https://pubmed.ncbi.nlm.nih.gov/32462832/).
8. Park KJ, Woo JS, Park JY. Left atrial myxoma presenting with unusual cystic form. *Korean J Thorac Cardiovasc Surg*. 2013; 46(5): 362–364, doi: [10.5090/kjtc.2013.46.5.362](https://doi.org/10.5090/kjtc.2013.46.5.362), indexed in Pubmed: [24175272](https://pubmed.ncbi.nlm.nih.gov/24175272/).
9. Singhal A, Gupta P, Mani S, et al. A rare cystic degeneration of myxoma. *Indian Heart J*. 2017; 1(1): 39–41, doi: [10.1016/j.ihjccr.2017.04.003](https://doi.org/10.1016/j.ihjccr.2017.04.003).
10. Stiver K, Bittenbender P, Whitson BA, et al. Left atrial myxoma causing coronary steal: an atypical cause of angina. *Tex Heart Inst J*. 2015; 42(3): 270–272, doi: [10.14503/THIJ-14-4220](https://doi.org/10.14503/THIJ-14-4220), indexed in Pubmed: [26175646](https://pubmed.ncbi.nlm.nih.gov/26175646/).
11. Terada Y, Wanibuchi Y, Noguchi M, et al. Metastatic atrial myxoma to the skin at 15 years after surgical resection. *Ann Thorac Surg*. 2000; 69(1): 283–284, doi: [10.1016/s0003-4975\(99\)01112-1](https://doi.org/10.1016/s0003-4975(99)01112-1), indexed in Pubmed: [10654539](https://pubmed.ncbi.nlm.nih.gov/10654539/).
12. Wan Y, Du H, Zhang L, et al. Multiple cerebral metastases and metastatic aneurysms in patients with left atrial Myxoma: a case report. *BMC Neurol*. 2019; 19(1): 249, doi: [10.1186/s12883-019-1474-4](https://doi.org/10.1186/s12883-019-1474-4), indexed in Pubmed: [31646971](https://pubmed.ncbi.nlm.nih.gov/31646971/).

Two cases of variations in inferior thyroid arterial pattern and their clinical implications

S.S. Novakov¹, S.D. Delchev¹

Department of Human Anatomy, Histology and Embryology, Medical University, Plovdiv, Bulgaria

[Received: 8 February 2022; Accepted: 14 March 2022; Early publication date: 29 March 2022]

Vascular variations are the most common ones in humans. Inferior thyroid artery arises from the thyrocervical trunk in 90.5%, from subclavian in 7.5%, and very rarely from the common carotid, aortic arch, brachiocephalic, internal thoracic, pericardiacophrenic, or vertebral. Thyroid ima artery is more common variety found in up to 12.2% of the population. Two cadavers dissected in the anatomy department are presented with variations in the blood supply of the thyroid gland. The first case was a 61-year-old man with middle thymothyroid artery arising from the common carotid on the right side and inferior thyroid as a branch of the common carotid on the left. The second case was an 85-year-old female without inferior thyroid arteries bilaterally, replaced by thyroid ima arising from brachiocephalic artery. The awareness of such arterial pattern is crucial for the specialists in imaging and preoperative diagnosing and escaping eventual iatrogenic complications of thyroid gland. (Folia Morphol 2023; 82, 2: 396–399)

Key words: middle thymothyroid artery, thyroid ima artery, human anatomy variations

INTRODUCTION

The human anatomy variations are part of the human anatomy science from its dawn till nowadays and are still an essential part of the gross anatomy research. The main significance of that type of evidence is for the invasive medical procedures and especially surgery [5]. The thyroid gland is an endocrine cervical gland which is well vascularised. Arterial supply comprises 2 superior thyroid arteries (STAs) originating from the external carotid arteries and 2 inferior thyroid arteries (ITAs) originating from the thyrocervical trunk, branch of the subclavian arteries [3, 6, 9]. Occasionally there is an accessory artery termed thyroid ima (TIA), which when present (0.4–12.2%), originates from the brachiocephalic trunk (43.3–86.7%), from the common carotid artery (CCA) (2–50%) or aortic arch (0–66.7%) [11, 13]. Though

rare in humans, middle thyroid artery is found in some animals, such as guinea pig and rabbit [10] and avian species like budgerigar [8]. The awareness of the anatomic variations in the blood supply of thyroid gland are of crucial significance when planning a surgical approach in the infrahyoid region. Knowledge of variability in thyroid vascularisation will facilitate the surgical procedure itself, make it safer and minimise the risk of haemorrhage [5].

CASE REPORT

Case 1

Formalin/ethanol-embalmed cadavers were used for dissection during the anatomy lessons. The length and diameter of the structures were measured by callipers.

A 61-year-old male cadaver was dissected in the department of anatomy and multiple variations in

Address for correspondence: S.S. Novakov, Associate Professor, Department of Anatomy, Histology and Embryology, Medical University, 15A V. Aprilov bul., 4002 Plovdiv, Bulgaria, e-mail: stoyan.novakov@mu-plovdiv.bg

This article is available in open access under Creative Common Attribution-Non-Commercial-No Derivatives 4.0 International (CC BY-NC-ND 4.0) license, allowing to download articles and share them with others as long as they credit the authors and the publisher, but without permission to change them in any way or use them commercially.

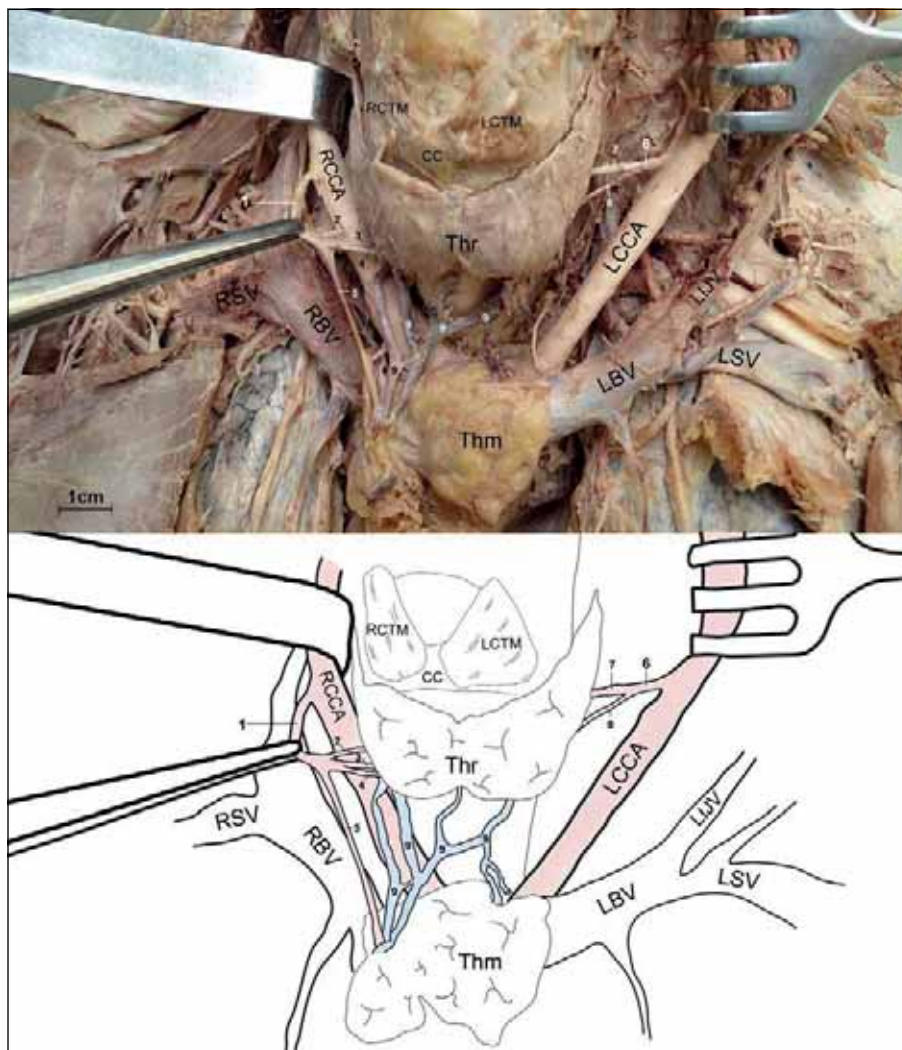


Figure 1. Middle thymothyroid artery on the right side and atypical origin of inferior thyroid artery on the left side; RCTM/LCTM — right/left cricothyroid muscle; CC — cricoid cartilage; Thr — thyroid gland; Thm — thymus; RCCA/LCCA — right/left common carotid artery; RBV/LBV — right/left brachiocephalic vein; RSV/LSV — right/left subclavian vein; LIJV — left internal jugular vein; 1 — middle thymothyroid artery; 2 — upper thyroid branch; 3 — middle thyroid branch; 4 — lower thyroid branch; 5 — thymic branch; 6 — inferior thyroid artery; 7 — superior branch of inferior thyroid artery; 8 — inferior branch of inferior thyroid artery; 9 — inferior thyroid veins.

the bilateral arterial blood supply of the thyroid gland were registered. An accessory artery supplying both thyroid and thymic glands was found on the right side. We agreed with previous authors and named it middle thymothyroid artery [1]. That was a spatial variation also belonging to the category of consistency [12]. It originated from the CCA 48 mm proximal to its bifurcation. The diameter of the CCA was 8 mm and the length of the unusual branch was 17 mm till its division into 3 thyroid branches (upper, middle and lower). The diameter of the middle thymothyroid artery was 2.5 mm and its length with its longest branch as it enters thyroid gland was 63 mm. The continuation of the artery to the thymus (thymic branch) was 1.5 mm in diameter. The STA

and ITA had their standard origin and position. On the left side of the same cadaver the ITA had rare origin from the CCA. The former started at 50 mm from the bifurcation of CCA, which was 6 mm wide. The length of the variable ITA to the release of its branches was 8 mm and its superior branch, which directly continued to the gland was 10 mm long and 1.5 mm wide, while the inferior one was 16 mm long and 0.8 mm wide. The diameter of the ITA was 2.5 mm. The rest of the structures on this side were with standard topography (Fig. 1).

Case 2

During the same semester another variation was found in 85-year-old female cadaver. The routine

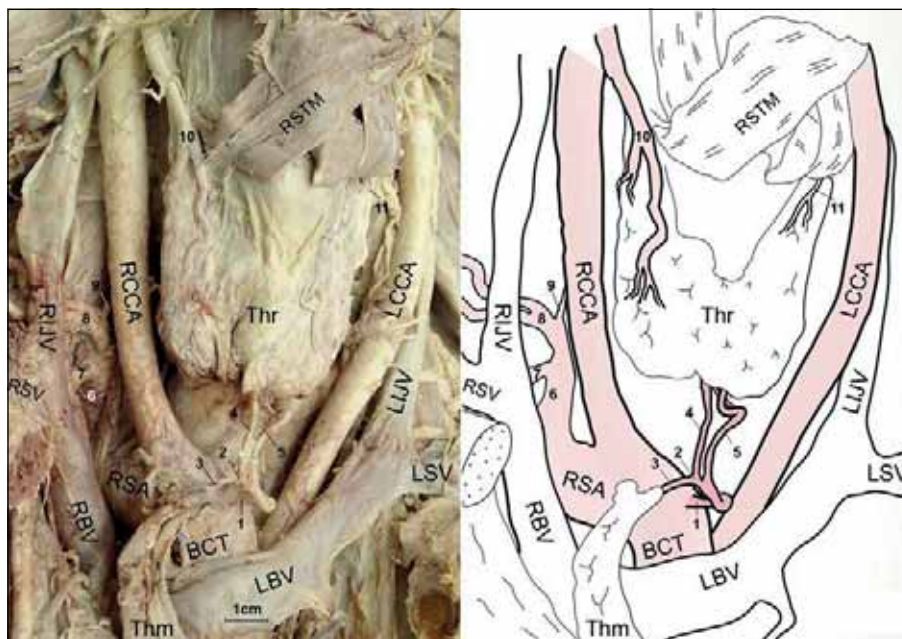


Figure 2. Thyroid ima artery replacing missing inferior thyroid arteries; RSTM — right sternothyroid muscle; Thr — thyroid gland; Thm — thymus; RCCA/LCCA — right/left common carotid artery; RSA — right subclavian artery; BCT — brachiocephalic trunk; RIJ/LIJ — right/left internal jugular vein; RSV/LSV — right/left subclavian vein; RBV/LBV — right/left brachiocephalic vein; 1 — thyroid ima artery; 2 — right branch; 3 — thymic artery; 4 — right inferior thyroid branch; 5 — left inferior thyroid branch; 6 — thyrocervical trunk; 7 — suprascapular artery; 8 — transverse cervical artery; 9 — ascending cervical artery; 10 — right superior thyroid artery; 11 — left superior thyroid artery.

dissection of the neck exposed bilateral absence of the ITAs. The arterial blood supply was compensated by the presence of relatively larger STAs, especially the one on the right side, and prominent TIA arising from the innominate artery. The TIA emerged in the midline 28 mm from the origin of the brachiocephalic trunk measured along its left border. It had a spiral course and diameter of 4 mm as well as a length of 21 mm to its division into: 1. Right branch — 3 mm long and 2 mm wide common trunk, which divides into thymic artery and right ITA; 2. Left branch — it was a continuation of the main artery as left ITA (2 mm in width), which climbed to the left lobe of the thyroid gland and before reaching it released a small branch for the isthmus of the gland. The rest of the topographical anatomy of the neck was standard (Fig. 2).

DISCUSSION

The origin of the ITA from CCA is very rare. Therefore, finding it in the gross anatomy dissecting lab is worth presenting it. The Case 1 of this report describes bilateral variants of the blood supply of the thyroid gland, which are both rare aberrant origins of ITA from CCA (about 1%) [5]. There is an embryological basis of such variations as they are associated

with time and stages of the development of the neck arteries by the aortic arches and the appearance and migration of the thyroid gland. That period between the 3rd and 7th week of development is when the formation of the aortic arch branches and the synchronous descend of the thyroid gland occur and it is not unreasonable to presume that the vascularisation of the gland would occasionally come from other vessels such as the subclavian, the vertebral or the CCA [4, 5]. The thyroid ima found in Case 2 is more common (up to 12.2%) but not usual which makes it an obstacle in thyroid surgery. Phylogenetically, the origin of this variable artery is supposed to appear from the original vascular network which connects brachiocephalic, aortic arch and carotids. During the later development the primary vessels disappearing by fusion may either supplement or substitute the regular blood supply of the thyroid gland, namely the superior and inferior thyroid arteries as the thyroid ima [7].

Though very rare the ITA arising from CCA exposes two major risks for surgical intervention in the area: haemorrhage by injuring this artery when on unusual position and increased possibility of injuring recurrent laryngeal nerve [2, 6].

Carotid endarterectomy as an established procedure for stroke prevention is also related to the

above-mentioned arterial pattern of the CCA, which uniqueness could be crucial for successful removal of the atherosclerotic plaque and the avoidance of postoperative complications [5].

Interventional radiology procedures like endovascular aneurysm reconstruction, chemoembolisation techniques like tumour embolisation, and arterial embolisation for the treatment of thyroid conditions requiring ablation might be affected in case of such variations [2, 5].

CONCLUSIONS

The role of anatomy science on variations and especially those of the vascular system and in the neck region is essential. Surgeons and interventional radiologists might come upon such rare variations during procedures in the neck area and any preceding awareness will be valuable to limit the incidence of possible iatrogenic complications.

Acknowledgements

The authors would like to thank the people who donated their bodies for teaching students and scientific studies, and the technical staff of the Anatomy, Histology and Embryology Department for their support.

Conflict of interest: None declared

REFERENCES

1. Banneheka S, Chiba S, Fukazawa M, et al. Middle thyromyoid artery arising from the common carotid artery: case report of a rare variation. *Anat Sci Int.* 2010; 85(4): 241–244, doi: [10.1007/s12565-009-0055-9](https://doi.org/10.1007/s12565-009-0055-9), indexed in Pubmed: [19680744](https://pubmed.ncbi.nlm.nih.gov/19680744/).
2. Branca JJV, Lascialfari Bruschi A, Pilia AM, et al. The thyroid gland: a revision study on its vascularization and surgical implications. *Medicina (Kaunas).* 2022; 58(1), doi: [10.3390/medicina58010137](https://doi.org/10.3390/medicina58010137), indexed in Pubmed: [35056445](https://pubmed.ncbi.nlm.nih.gov/35056445/).
3. Burlakoti A, Massy-Westropp N. Bilateral variant thyroid arteries. *Int J Anat Var.* 2015; 8: 43–46.
4. Cigali BS, Ulucam E, Bozer C. Accessory inferior thyroid artery and internal thoracic artery originating from the thyrocervical trunk. *Anat Sci Int.* 2008; 83(4): 283–285, doi: [10.1111/j.1447-073X.2007.00206.x](https://doi.org/10.1111/j.1447-073X.2007.00206.x), indexed in Pubmed: [19159360](https://pubmed.ncbi.nlm.nih.gov/19159360/).
5. Mariolis-Sapsakos T, Kalles V, Papapanagiotou I, et al. Bilateral aberrant origin of the inferior thyroid artery from the common carotid artery. *Surg Radiol Anat.* 2014; 36(3): 295–297, doi: [10.1007/s00276-013-1153-x](https://doi.org/10.1007/s00276-013-1153-x), indexed in Pubmed: [23783369](https://pubmed.ncbi.nlm.nih.gov/23783369/).
6. Ngo Nyeki AR, Peloni G, Karenovics W, et al. Aberrant origin of the inferior thyroid artery from the common carotid artery: a rare anatomical variation. *Gland Surg.* 2016; 5(6): 644–646, doi: [10.21037/gs.2016.12.03](https://doi.org/10.21037/gs.2016.12.03), indexed in Pubmed: [28149813](https://pubmed.ncbi.nlm.nih.gov/28149813/).
7. Jayaraju R, Mohiyuddin A, Merchant S, et al. Thyroidea ima artery: a report of two cases. *Int J Head Neck Surg.* 2014; 5(2): 89–90, doi: [10.5005/jp-journals-10001-1188](https://doi.org/10.5005/jp-journals-10001-1188).
8. Radek T, Piasecki T. The topographical anatomy and arterial supply of the thyroid and parathyroid glands in the budgerigar (*Melopsittacus undulatus*). *Folia Morphol.* 2004; 63(2): 163–171, indexed in Pubmed: [15232771](https://pubmed.ncbi.nlm.nih.gov/15232771/).
9. Standring S. *Gray's Anatomy: The Anatomical Basis of Clinical Practice.* 40th Ed. Churchill Livingstone, Spain 2008: 462.
10. Won HS, Han SH, Oh CS, et al. Superior and middle thyroid arteries arising from the common carotid artery. *Surg Radiol Anat.* 2011; 33(7): 645–647, doi: [10.1007/s00276-011-0781-2](https://doi.org/10.1007/s00276-011-0781-2), indexed in Pubmed: [21279355](https://pubmed.ncbi.nlm.nih.gov/21279355/).
11. Yalcin B. Thyroid gland. In: Tubbs RS, Shoja MM, Loukas M (eds.) *Bergman's comprehensive encyclopedia of human anatomic variation.* 1st ed. Wiley-Blackwell, New Jersey 2016: 1199–1200.
12. Yammine K. Evidence-based anatomy. *Clin Anat.* 2014; 27(6): 847–852, doi: [10.1002/ca.22397](https://doi.org/10.1002/ca.22397).
13. Yohannan DG, Rajan R, Chandran AB, et al. An unusual origin and course of the thyroidea ima artery, with absence of inferior thyroid artery bilaterally. *Surg Radiol Anat.* 2019; 41(2): 235–237, doi: [10.1007/s00276-018-2122-1](https://doi.org/10.1007/s00276-018-2122-1), indexed in Pubmed: [30361839](https://pubmed.ncbi.nlm.nih.gov/30361839/).

A left circumflex aorta with a displaced thoracic duct in a 94-year-old male cadaver: a case report with discussion on embryology

P. Ostrowski¹, S. Popovchenko¹, M. Bonczar¹, T. Mroczek², J.A. Walocha¹, M.P. Zarzecki¹ 

¹Department of Anatomy, Jagiellonian University Medical College, Krakow, Poland

²Department of Paediatric Cardiac Surgery, Jagiellonian University Medical College, Krakow, Poland

[Received: 23 February 2022; Accepted: 29 March July 2022; Early publication date: 20 April 2022]

A left circumflex aorta (LCA) is an extremely rare variation of the thoracic aorta. It is distinguished by a retroesophageal descending aorta that subsequently travels down the right side of the thoracic vertebrae towards the aortic hiatus. Nonetheless, its embryological origin ought not to be overly generalised, but each case should be considered individually due to its unique vascular patterns.

This study presents a description of a LCA in a 94-year-old male cadaver. The dissection revealed the descending aorta posteriorly from the trachea and oesophagus and then laterally on the right from the thoracic vertebral bodies. The branching pattern of the aortic arch was typical, so was the course of the left and right recurrent laryngeal nerves. However, the thoracic duct was placed on the right, and drained into the right internal carotid vein. Due to the normal appearance of the ascending part and the arch of the aorta, it is safe to presume that the variation originated from the persistent right dorsal aorta, with the retroesophageal part from the persistent left dorsal aorta.

Detailed understanding of the variations of the thoracic aorta, and the anomalies associated with the LCA, can help to improve management of these conditions, and with that, improve patients' overall outcomes. Patients with a LCA, or another vascular ring, can either be asymptomatic or present with oesophageal and/or tracheal compression symptoms. Management of this anomaly consists namely of ligation of the patent ductus arteriosus/ligamentum arteriosum and aortic uncrossing. (Folia Morphol 2023; 82, 2: 400–406)

Key words: left circumflex aorta, thoracic duct, anatomy, embryology, anatomical variation

INTRODUCTION

A left circumflex aorta (LCA) is an uncommon congenital variation of the cardiovascular anatomy. A circumflex aorta is distinguished by a retroesophageal thoracic aorta that crosses contralaterally to the ascending aorta. The circumflex retroesophageal variation of the aorta was first described by D'Cruz et

al. in 1966 [6]. However, a case of a left aortic arch and a right descending aorta was presented by Paul et al. in 1948 [16], matching the description of the LCA presented in this case study.

Anomalies of the aortic arch are quite rare in the general population, with their prevalence ranging from 1% to 2% [4]. A right circumflex aorta (RCA)

Address for correspondence: Dr. M.P. Zarzecki, MD, Department of Anatomy, Jagiellonian University Medical College, ul. Kopernika 12, 31–034 Kraków, Poland, tel: +48 12 422 95 11, e-mail: michal.zarzecki96@gmail.com

This article is available in open access under Creative Commons Attribution-Non-Commercial-No Derivatives 4.0 International (CC BY-NC-ND 4.0) license, allowing to download articles and share them with others as long as they credit the authors and the publisher, but without permission to change them in any way or use them commercially.

occurs less frequently than a double aortic arch, or right aortic arch with an aberrant left subclavian artery with a Kommerell's diverticulum. A LCA is even less common than the aforementioned anomalies [7].

Anomalies of the aortic arch are often associated with the formation of a vascular ring, with the circumflex aorta being an extreme example of the latter [9]. The circumflex aorta is divided into two groups; an RCA, and an LCA. The RCA can occur with, or without an aberrant left subclavian artery. On the other hand, the LCA can appear with, or without an aberrant right subclavian artery. In many cases, a patent ductus arteriosus/ligamentum arteriosum together with a left, or right, circumflex aorta develops a true vascular ring [9].

Unfortunately, the embryological origin of the circumflex aorta is oftentimes confused and has a tangled description in the available literature. The main reason behind this fact is the uniqueness of the found thoracic aorta vascular patterns that ought not to be generalised for the whole population. Instead, it is prudent for the medical professionals to carefully examine each case individually and hence attempt to delineate the possible embryological mechanisms involved.

Many other anomalies of the cardiovascular system can occur in individuals with an LCA. These consist namely of formation of a vascular ring and an aberrant right subclavian artery, amongst others [9, 25]. Furthermore, the prevalence of additional cardiac anomalies in patients with a circumflex aorta is 50% to 60% [21].

Knowledge regarding the different anomalies associated with the circumflex aorta might help increase the overall efficiency of their management, and therefore, aid in attaining better outcomes for the patients.

The following study aimed to present a thorough description of a LCA case, its branches and relation to the surrounding anatomical entities. Moreover, the embryology of the circumflex aorta, its symptoms, management, and associated anomalies were comprehensively discussed.

CASE REPORT

During a routine dissection of a 94-year-old male formalin fixed cadaver, anomalies of the thoracic aorta were observed. No pathology that could distort the thoracic cavity was neither noticed upon the dissection, nor was it found in the available medical record of the donor. Two prosectors S.P. and P.O. performed the dissection under close supervision by M.P.Z. and J.A.W.

The cadaver's thorax was opened with the help of an oscillating saw. The cuts were made at the level of the sternal angle, underneath the clavicles and anteriorly to the long thoracic nerve. Having opened the rib cage and released the connective tissue adhesions, the heart was identified as shifted towards the left lung, compressing it. The left lung was located in the vertebral column segments Th1 to Th8. The segments 3, 4, and 5 of the said lung were enlarged and positioned behind the heart, reaching to the right midclavicular line. The right lung was significantly larger than the left lung. The bronchopulmonary segments 3 and 5 of the right lung were partly positioned on the surface of the heart, reaching the left parasternal line.

Both lungs were excised and revealed the presence of the LCA in the posterior inferior mediastinum. Its branches and surrounding structures were carefully dissected, and documented photographically. The external diameters of the aorta and its branches were measured by using a digital calliper (Lux tools, China), and presented as an average of three independent measurements. Figures 1–4 present the various view-points of the variant, whereas Figure 5 is a schematic depiction of the anomaly in relation to the nearby neurovascular structures.

The aorta drained the left ventricle in the usual manner. The ascending aorta was oval in shape, instead of round, hence two dimensions were measured, these were 43.2 mm and 19.8 mm, respectively. The aorta ascended from the base of the left ventricle at approximately the Th3 vertebral body, passing to the left of the Th2 vertebral body (where its apex was found), and then turning sharply to the right. The descending aorta began at the Th2–Th3 intervertebral disc level, coursed posteriorly to the trachea and oesophagus, and descended on the right side of the thoracic vertebral bodies, laterally from the oesophagus. The branches of the aortic arch from both its convex and concave side arose in the classical manner. Going namely proximal to distal: the brachiocephalic trunk was the first branch originating from the aortic arch, giving rise to the right common carotid and right subclavian arteries. The external diameter of the brachiocephalic trunk at its origin was measured at 21.6 mm, and at its branching point 21.6 mm. The next branches of the aortic arch were the left common carotid, and left subclavian arteries. They had an external diameter of 11.6 mm and 15.3 mm, respectively.

The ligamentum arteriosum was a thick band of connective tissue connecting the aortic arch with the superior part of the left pulmonary artery. The left

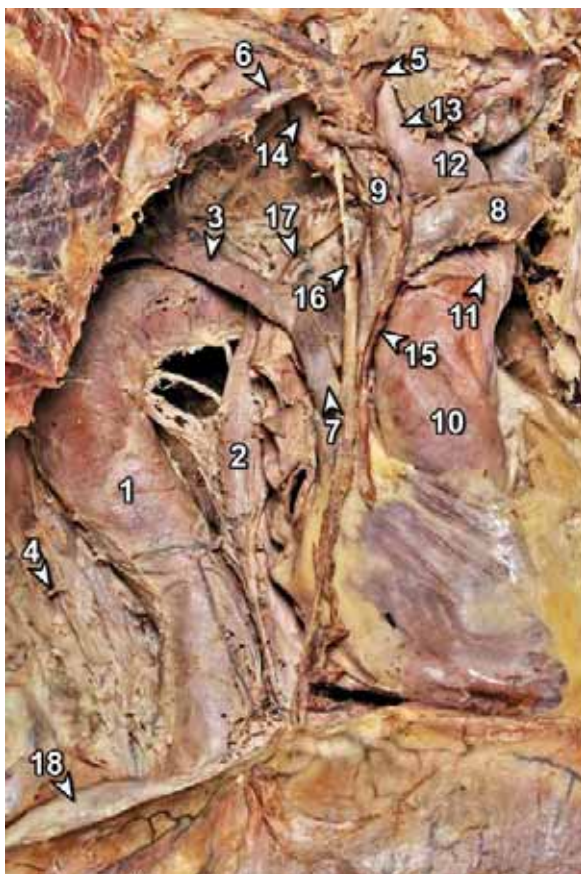


Figure 1. A right-sided view on the posterior mediastinum; 1 — descending aorta; 2 — oesophagus; 3 — azygos vein; 4 — thoracic duct; 5 — right internal jugular vein; 6 — right subclavian vein; 7 — superior vena cava; 8 — left brachiocephalic vein; 9 — right brachiocephalic vein; 10 — ascending aorta; 11 — arch of aorta; 12 — brachiocephalic trunk; 13 — right common carotid artery; 14 — right subclavian artery; 15 — right internal thoracic artery; 16 — right phrenic nerve and pericardiophrenic vessels; 17 — right vagus nerve; 18 — diaphragm.

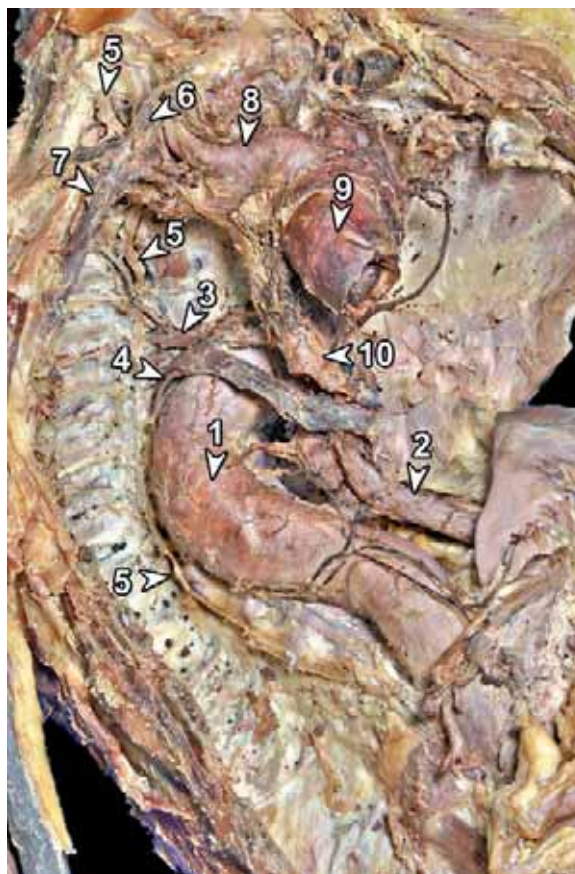


Figure 2. A right-sided view on the posterior mediastinum with the heart removed; 1 — descending aorta; 2 — oesophagus; 3 — right superior intercostal vein; 4 — azygos vein; 5 — thoracic duct; 6 — right internal jugular vein; 7 — right subclavian vein; 8 — brachiocephalic trunk; 9 — ascending aorta; 10 — right main bronchus.

recurrent laryngeal nerve passed inferiorly to the ligamentum arteriosum and the aortic arch; however, the right recurrent laryngeal nerve passed underneath the brachiocephalic trunk (instead of the right subclavian artery as classically described). The bronchial arteries were also observed, with the left one originating from the arch of aorta, and the right one originating from the descending aorta.

After giving off the left subclavian artery, the aorta passed the trachea and oesophagus posteriorly, and descended in the thoracic cavity leaving a significant impression on the right lung. The aorta was dilated at the point where it crossed the oesophagus, with an external diameter of 34.3 mm. At the approximate Th3–Th4 intervertebral disc level (where it was placed laterally on the right of the vertebral bodies), the descending aorta had an external diameter of 29.6 mm.



Figure 3. An enlarged view on the left recurrent laryngeal nerve; 1 — arch of aorta; 2 — left vagus nerve; 3 — left recurrent laryngeal nerve; 4 — left phrenic nerve; 5 — left pericardiophrenic vessels.

The external diameter remained unchanged as it passed through the aortic hiatus in the diaphragm, which was in close proximity to the oesophageal hiatus. All the measurements concerning the exter-



Figure 4. A right enlarged view on the posterior mediastinum; 1 — ascending aorta; 2 — brachiocephalic trunk; 3 — right common carotid artery; 4 — right subclavian artery; 5 — right vagus nerve; 6 — right recurrent laryngeal nerve; 7 — right internal thoracic artery.

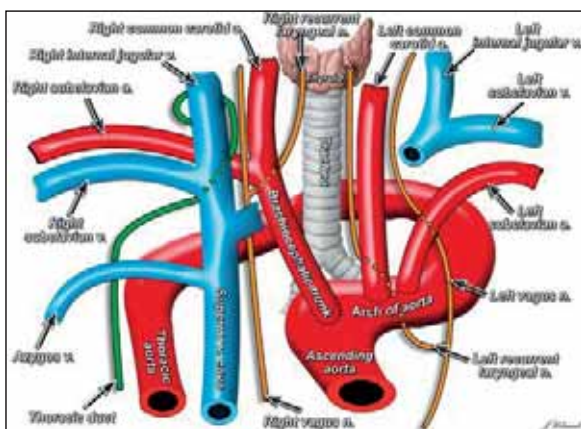


Figure 5. A sketch of the left circumflex aorta and its surrounding structures.

nal diameter of the aorta and its major branches are presented in Table 1. The descending aorta had a winding course in the thoracic cavity, lying anteriorly to the right scoliotic vertebral column.

Table 1. The external diameter of the aorta and its major branches

The measurement point	External diameter [mm]
Ascending aorta — at origin (oval in shape)	43.2 and 19.8
Aorta — at the junction with oesophagus	34.3
Descending aorta — at Th3/Th4 intervertebral disc	29.6
Brachiocephalic trunk — at origin	21.6
Brachiocephalic trunk — at the branching point	21.6
Left common carotid artery — at origin	11.6
Left subclavian artery — at origin	15.3

The azygos vein ascended on the right side of the thoracic cavity, coursing between the vertebral column and the descending aorta. It looped around the aorta, and drained directly into the superior vena cava. The remaining venous tributaries of the thorax were anatomically normal.

The thoracic duct was displaced by the descending aorta to the right side of the vertebral column, and drained into the right internal jugular vein. No vessel draining into the left venous angle was visualised by macroscopic dissection. Moreover, the bronchopulmonary lymph nodes were enlarged and calcified.

Macroscopic evaluation of the heart revealed no visible structural abnormalities except for a small patent foramen ovale that was on average 2.1 mm in diameter. The origin of both right and left coronary arteries was typical, as well as their course and main branching pattern. The patient did not present any other visible vascular abnormalities neither within the thorax, nor the abdomen. Unfortunately, due to the unavailability of the donor’s medical records no conclusions could have been made regarding the presence or absence of any clinical symptoms in vivo, associated with the present variant.

Ethical concern

All procedures performed in studies involving human participants were in accordance with the ethical standards of the institutional and/or national research committee and with the 1964 Helsinki declaration and its later amendments or comparable ethical standards. The material used for this research was obtained from a body donation programme.

DISCUSSION

The above-mentioned case presents a description of a LCA with typical aortic arch branching pattern. The thoracic duct found in the described specimen

was displaced to the right side, draining into the right internal jugular vein. To the best knowledge of the authors, this is the first case of a right sided thoracic duct accompanying a LCA in the available literature.

There are numerous descriptions regarding the embryology of the systemic arterial system in the available literature. Following Sadler's description [18], the ascending aorta arises as the distal (cranial) part of the truncus arteriosus. It gives rise to two ventral aorta, from which the pharyngeal arch arteries (PAA) emerge. As the development process continues, they are brought closer together to form the aortic arch and its major branches, as well as the pulmonary trunk. The arteries in question are related to the 3rd, 4th and 6th pharyngeal arches. Going right to left, the brachiocephalic trunk arises from the right horn of the aortic sac, whereas the proximal aspect of the aortic arch from the left horn. Next, the right common carotid artery has its origin in the third right PAA and the right subclavian artery in its proximal portion from the fourth right PAA (its distal segment comes from the right seventh intersegmental artery). The left third PAA forms the left common carotid, whereas the left fourth PAA is responsible for the creation of the aortic arch between the left common carotid and the left subclavian arteries. Next, the left subclavian artery sprouts from the left seventh intersegmental artery. Lastly, the sixth PAAs give rise to the right and left pulmonary arteries, respectively, as well as the ductus arteriosus on the left. The remaining part of the thoracic aorta originates from the fusion of both right and left dorsal aorta [18].

If one of the PAAs fails to regress, a vascular ring encircling the trachea and oesophagus may develop [2]. A vascular ring is a rare congenital cardiovascular anomaly, which can be formed as a consequence of a variety of embryological defects, such as a double aortic arch, a right aortic arch with left ductus arteriosus, a retroesophageal aberrant left subclavian artery, and others [26]. Vascular rings represent approximately 1% of cardiovascular congenital anomalies [13].

Notwithstanding, in the case described herein the ascending aorta and the aortic arch with its major branches were formed in the typically described manner. Henceforth, it is the authors' understanding that no abnormality in the failed regression of the PAAs could have been involved. The only variation found was the abnormal course of the descending aorta, crossing both the trachea and oesophagus posteriorly, to then descend laterally on the right from the thoracic vertebrae. Therefore, bearing in mind the

aforementioned appropriate anatomy of the remaining parts of the thoracic aorta, it is safe to presume that the variation encountered in this case originated from the persistent right dorsal aorta below the right seventh intersegmental artery. The retroesophageal portion of the descending aorta was most probably a remnant of the left dorsal aorta that has involuted in the lower thoracic segments, leaving room for the dominance of the right dorsal aorta. It has also occurred to the authors that the displacement of the descending aorta could have resulted from the scoliosis that the patient also presented. Severe scoliosis can result in major arterial dislocation due to the disruption in the normal anatomy and proportions of the thorax; however, it would not explain the completely retroesophageal course of the aorta. Henceforth, the authors believe that the variation found was inborn.

Circumflex aortas can be associated with various abnormalities, a prime example being the aberrant subclavian artery. Depending on its branching off point from the aorta, its embryological origin might differ between the patients. The aberrant right subclavian artery, when not accompanied by the circumflex aortic variation, is one of the most common congenital aortic arch anomalies, with a prevalence ranging from 0.16% to 4.4% in the general population [15]. Patients with an aberrant right subclavian artery, when it has a retroesophageal course, can give symptoms of oesophageal and/or tracheal compression, and thus will need to be surgically managed [1]. Notwithstanding, the patient in the current paper did not present this variation, but instead the right subclavian artery originated from the brachiocephalic trunk in the typical manner.

Another example may be the Kommerell's diverticulum, or Kommerell's aneurysm, that is a persistent remnant of the fourth primitive dorsal arch due to its failed regression. It can occur in both left and right sided aortic arches. In a case of the left aortic arch with this anomaly, the right dorsal aorta involutes proximal to the right subclavian artery, and leaves the subclavian artery attached to the left descending aorta via the distal portion of the right dorsal aorta. Individuals with aberrant right or left subclavian arteries are in 20–60% of the cases associated with Kommerell's diverticulum [22]. Management of this condition can be obtained by either open or endovascular procedures. Some of the open procedures are diverticulum resections, interposition, patch repairs, and more. The endovascular procedure for the

management of Kommerell's diverticulum is thoracic endovascular aortic repair using stent grafting [24]. However, in the present case, the LCA had a typical branching pattern without a Kommerell's aneurysm.

Various findings in individual cases make it troublesome for the clinical practitioners to assign a single, unified embryological defect responsible for the creation of the LCA. The description of the LCA's origin provided by Hanneman et al. [8] and Haranal et al. [9] with absent variant right subclavian artery resulting from the involution of the right aortic arch in its part between the right subclavian and the ductus arteriosus most certainly does not pertain to the current case. For that variation to occur, the typical left aortic arch would not be present, contrary to the present findings. The authors would like to acknowledge Sánchez Torres and Roldán Conesa [19], as their case seems to resemble a very similar clinical picture to the one presented in this study, hence likewise we would like to propose and reiterate that the embryological origin of the encountered here variation is the regression of the left dorsal aorta. Henceforth, the authors would like to urge caution whilst overly generalising the embryological origin of the encountered diversity of the thoracic aorta and rather use an individual approach to a single case to discern its true meaning.

A circumflex thoracic aorta can impede the respiratory pathways, resulting in severe respiratory symptoms and recurrent pulmonary infection [11]. It can also give oesophageal compression symptoms with dysphagia being the most common one [12]. The development of a complete vascular ring from a LCA undoubtedly depends on the position of the ductus or ligamentum arteriosum. If the ductus or ligamentum arteriosum is present on the right side, connecting the right sided descending aorta with the right pulmonary artery, a complete vascular ring develops [21]. However, if the ductus or ligamentum arteriosum is located on the left side, the vascular ring is incomplete [9], as found in the present case. Even though a LCA with a left patent ductus arteriosus does not form a complete vascular ring, it can still cause severe respiratory compression, as shown by Sheth et al. [20] in a case of a 2-month-old patient whose left main bronchus was obstructed. In patients aged two years old or less, the symptoms of a vascular ring are typically respiratory in nature, whereas older children and adults suffer mostly from dysphagia, less frequently the former [25].

The external diameters of the aorta and its branches described herein were higher than average. An example of this is the external diameter of the brachiocephalic trunk, which has an average diameter of 8.3–15.5 mm in females and in males 9.1–14.5 mm [14]. However, the brachiocephalic trunk in the specimen presented in the current study, had an external diameter measured at 21.6 mm at its origin, and 21.6 mm at its branching point. The aortic arch had a dilation at the point where it passed the oesophagus, with an external diameter of 34.3 mm. Ectasia at this point could have given symptoms of oesophageal compression [23].

Indisputably, symptomatic patients require fast and adequate management of the LCA, so as to prevent the most serious complications that could potentially include death. Blanco Pampin et al. [3] described a case of a 26-days-old neonate in whom the LCA was present (with obliterated left ductus arteriosus) who suddenly passed away overnight. The said case contrasts greatly with the current 94-year-old patient, pointing out to the vastly divergent clinical picture of the discussed variation.

There is constant need for advancements in the management of the circumflex aorta due to the fact that a simple ligation of the ligamentum/ductus arteriosus may not necessarily relieve the respiratory or swallowing compressive symptoms associated with it [9]. The first available description of the aortic uncrossing procedure comes from 1984 provided by Planche and LaCoeur-Gayet [17]. The said authors operated on patients who presented with postoperative respiratory and/or swallowing obstructive syndromes following the previously undertaken ligamentum/ductus arteriosus ligations [17]. The aortic uncrossing is a major procedure during which the retroesophageal aorta is transected, mobilised, and reconnected to the ascending aorta on the same side of the airway as the descending aorta, relieving the tracheal and/or oesophageal external constriction. Nonetheless, the surgery does not resolve the problem of cartilage malformation and tracheal stenosis, nor the tracheobronchomalacia that could have resulted from the previous compression [11], hence those issues ought to be addressed by different techniques.

Lastly, it is crucial to bear in mind possible variations of the thoracic duct, which as in the case reported herein can drain into the right sided vessels instead of the typically acknowledged left venous angle. In a report by Cerfolio et al. [5], chylothorax was a complication of 0.42% of general thoracic proce-

dures (47 cases out of 11,315). An unanticipated high level of liquid drainage from the thoracic cavity (not necessarily milky in nature as chylomicrons and triglycerides might be of lower concentrations due to patients not receiving normal diets) might be indicative of thoracic duct's iatrogenic injury [5]. Henceforth, its anatomy and closeness to the major vessels ought to be always taken into account during a thoracic surgery in furtherance of avoiding complications.

CONCLUSIONS

The above-mentioned study presents a case of a LCA, a rare anatomical variant of the cardiovascular system. A circumflex retroesophageal arch is distinguished by an aortic arch which crosses the midline posteriorly to the oesophagus, approximately at the level of the carina, and descends on the contralateral side of the spine [9]. Special caution ought to be in place when examining the available literature for the embryological origin of the LCA, as presence of additional variants and thorough description of the course of the aorta can oftentimes shed light onto a completely different mechanism than previously described. The LCA could be associated with many anomalies, especially those of the cardiovascular system. Henceforth, an extensive knowledge regarding the different variations of the LCA, and the anomalies associated with it, is surely of great importance upon encountering this rare variant to provide the patient with adequate care.

Acknowledgements

The authors are beholden to Mr Jacenty Urbaniak for the technical support and graphical depiction of this variation. "The authors wish to sincerely thank those who donated their bodies to science so that anatomical research could be performed. Results from such research can potentially improve patient care and increase mankind's overall knowledge. Therefore, these donors and their families deserve our highest gratitude" [10].

Conflict of interest: None declared

REFERENCES

- Amore D, Casazza D, Casalino A, et al. Symptomatic aberrant right subclavian artery: advantages of a less invasive surgical approach. *Ann Thorac Cardiovasc Surg.* 2020; 26(2): 104–107, doi: [10.5761/atcs.nm.19-00206](#), indexed in Pubmed: [32023569](#).
- Arazińska A, Polguj M, Szymczyk K, et al. Right aortic arch analysis: anatomical variant or serious vascular defect? *BMC Cardiovasc Disord.* 2017; 17(1): 102, doi: [10.1186/s12872-017-0536-z](#), indexed in Pubmed: [28420337](#).
- Blanco Pampin J, Garcia Rivero A, Morte Tamayo N, et al. Left aortic arch with right-sided descending aorta associated with sudden neonatal death: a case report. *Med Sci Law.* 2003; 43(4): 353–356, doi: [10.1258/rsmmsl.43.4.353](#), indexed in Pubmed: [14655967](#).
- Bravo C, Gámez F, Pérez R, et al. Fetal Aortic Arch Anomalies: Key Sonographic Views for Their Differential Diagnosis and Clinical Implications Using the Cardiovascular System Sonographic Evaluation Protocol. *J Ultrasound Med.* 2016; 35(2): 237–251, doi: [10.7863/ultra.15.02063](#), indexed in Pubmed: [26715656](#).
- Cerfolio RJ, Allen MS, Deschamps C, et al. Postoperative chylothorax. *J Thorac Cardiovasc Surg.* 1996; 112(5): 1361–1365, doi: [10.1016/S0022-5223\(96\)70152-6](#), indexed in Pubmed: [8911335](#).
- D'Cruz IA, Cantez T, Namin EP, et al. Right-sided aorta. I. Occurrence of right aortic arch in various types of congenital heart disease. II. Right aortic arch, right descending aorta, and associated anomalies. *Br Heart J.* 1996; 28(6): 722–739, doi: [10.1136/hrt.28.6.722](#), indexed in Pubmed: [5332779](#).
- Gould SW, Rigsby CK, Donnelly LF, et al. Useful signs for the assessment of vascular rings on cross-sectional imaging. *Pediatr Radiol.* 2015; 45(13): 2004–16; quiz 2002, doi: [10.1007/s00247-015-3424-7](#), indexed in Pubmed: [26260202](#).
- Hanneman K, Newman B, Chan F. Congenital variants and anomalies of the aortic arch. *Radiographics.* 2017; 37(1): 32–51, doi: [10.1148/rg.2017160033](#), indexed in Pubmed: [27860551](#).
- Haranal M, Srimurugan B, Sivalingam S. Circumflex aorta: An uncharted territory. *Asian Cardiovasc Thorac Ann.* 2022; 30(2): 217–225, doi: [10.1177/02184923211015092](#), indexed in Pubmed: [33957784](#).
- Iwanaga J, Singh V, Takeda S, et al. Acknowledging the use of human cadaveric tissues in research papers: recommendations from anatomical journal editors. *Clin Anat.* 2021; 34(1): 2–4, doi: [10.1002/ca.23671](#), indexed in Pubmed: [32808702](#).
- Kamran A, Friedman KG, Jennings RW, et al. Aortic uncrossing and tracheobronchopexy corrects tracheal compression and tracheobronchomalacia associated with circumflex aortic arch. *J Thorac Cardiovasc Surg.* 2020; 160(3): 796–804, doi: [10.1016/j.jtcvs.2020.03.158](#), indexed in Pubmed: [32616349](#).
- Konstantinov IE, Puga FJ. Surgical treatment of persistent esophageal compression by an unusual form of right aortic arch. *Ann Thorac Surg.* 2001; 72(6): 2121–2123, doi: [10.1016/s0003-4975\(01\)02667-4](#), indexed in Pubmed: [11789810](#).
- Licari A, Manca E, Rispoli GA, et al. Congenital vascular rings: a clinical challenge for the pediatrician. *Pediatr Pulmonol.* 2015; 50(5): 511–524, doi: [10.1002/ppul.23152](#), indexed in Pubmed: [25604054](#).
- Manole AM, Iliescu DM, Rusali A, et al. Morphometry of the aortic arch and its branches. *ARS Medica Tomitana.* 2013; 19(3): 154–159, doi: [10.2478/arsm-2013-0027](#).
- Natsis K, Didagelos M, Gkiouliava A, et al. The aberrant right subclavian artery: cadaveric study and literature review. *Surg Radiol Anat.* 2017; 39(5): 559–565, doi: [10.1007/s00276-016-1796-5](#), indexed in Pubmed: [27999944](#).
- Paul RN. A new anomaly of the aorta; left aortic arch with right descending aorta. *J Pediatr.* 1948; 32(1): 19–29, doi: [10.1016/s0022-3476\(48\)80125-3](#), indexed in Pubmed: [18920568](#).
- Planché C, Lacour-Gayet F. [Aortic uncrossing for compressive circumflex aorta. 3 cases]. *Presse Med.* 1984; 13(21): 1331–1332, indexed in Pubmed: [6233555](#).
- Sadler TW. Vascular development. In: Langman's medical embryology, 14th ed. Wolters Kluwer, Philadelphia 2019: 206–222.
- Sánchez Torres G, Roldán Conesa D. [Left aortic arch without a circumflex segment and a right descending aorta: a hypothetical case and a real example]. *Arch Inst Cardiol Mex.* 1989; 59(2): 125–131, indexed in Pubmed: [2764632](#).
- Sheth R, Varghese R, Sivakumar K. Left aortic arch with right descending aorta and severe coarctation: an unusual "vascular clamp" with airway compression. *Cardiol Young.* 2018; 28(8): 1056–1058, doi: [10.1017/S1047951118000665](#), indexed in Pubmed: [29895337](#).
- Smith BM, Lu JC, Dorfman AL, et al. Rings and slings revisited. *Magn Reson Imaging Clin N Am.* 2015; 23(1): 127–135, doi: [10.1016/j.mric.2014.09.011](#), indexed in Pubmed: [25476681](#).
- Tanaka A, Milner R, Ota T. Kommerell's diverticulum in the current era: a comprehensive review. *Gen Thorac Cardiovasc Surg.* 2015; 63(5): 245–259, doi: [10.1007/s11748-015-0521-3](#), indexed in Pubmed: [25636900](#).
- Türkvtan A, Büyükbayraktar FG, Olçer T, et al. Congenital anomalies of the aortic arch: evaluation with the use of multidetector computed tomography. *Korean J Radiol.* 2009; 10(2): 176–184, doi: [10.3348/kjr.2009.10.2.176](#), indexed in Pubmed: [19270864](#).
- Vinnakota A, Idrees JJ, Rosinski BF, et al. Outcomes of Repair of Kommerell Diverticulum. *Ann Thorac Surg.* 2019; 108(6): 1745–1750, doi: [10.1016/j.athoracsur.2019.04.122](#), indexed in Pubmed: [31254511](#).
- Weinberg PM. Aortic arch anomalies. *J Cardiovasc Magn Reson.* 2006; 8(4): 633–643, doi: [10.1080/10976640600713756](#), indexed in Pubmed: [16869315](#).
- Yoshimura N, Fukahara K, Yamashita A, et al. Congenital vascular ring. *Surg Today.* 2020; 50(10): 1151–1158, doi: [10.1007/s00595-019-01907-5](#), indexed in Pubmed: [31676999](#).

A unique bilateral accessory forearm flexor muscle

R.K. Fernandez¹, S. Ramakrishnan¹, T.T. Sukumaran¹, N. Kilarkaje², M. Pillay¹

¹Department of Anatomy, Amrita School of Medicine, Amrita Institute of Medical Sciences, Amrita Vishwa Vidyapeetham, Kochi, Kerala, India

²Department of Anatomy, Faculty of Medicine, Kuwait University, Kuwait

[Received: 3 March 2022; Accepted: 23 March 2022; Early publication date: 5 April 2022]

Muscular and neurovascular variations in the upper extremity are of utmost clinical significance. Here we report a unique bilateral accessory muscle in the forearm and palm of an 89-year-old male cadaver. The accessory muscle presented two bellies on the right side, one in the forearm, innervated by the anterior interosseous nerve, and the other in the palm, innervated by a branch of the median nerve. A long tendon interconnected the two bellies. On the left side, the muscle had a single belly in the palm, which began at the end of a long tendon that extended from the forearm. However, on both sides, the muscle originated from the posterior surface of the flexor digitorum superficialis belly and inserted along with the first lumbrical muscle into the dorsal digital expansion of the index finger. The proximal parts of the variant muscles were sandwiched between the flexor digitorum muscles. The palmar bellies coursed distally through the carpal canal and lay deep to the superficial palmar arch, and superficial to the first lumbrical, between the thenar muscles and the lateral-most tendon of the flexor digitorum superficialis. Arguably, the accessory muscle might be a variant of a lumbrical muscle, as reported before, but innervation of the proximal belly by the anterior interosseous nerve suggests that the muscle may well be a deep accessory muscle at the forearm, probably appeared as a diverted part of the flexor digitorum profundus. Its space-occupying course through the forearm and palm, especially through the carpal canal, might be clinically significant as it might contribute to nerve compression pathologies in the upper extremity. This accessory muscle also indicates the complex nature of individual muscle formation and evolution of the upper extremity with constant changes in the morphology of muscles based on their changing functions. (Folia Morphol 2023; 82, 2: 407–411)

Key words: anatomical variations, accessory muscle, first lumbrical muscle, forearm, flexor digitorum superficialis muscle, median nerve

INTRODUCTION

Accessory muscles of the flexor compartment of the forearm are not uncommon, and when present, they may cause nerve compression syndromes or

simulate soft tissue tumours [4]. Numerous variations of flexor digitorum superficialis (FDS) have been reported in literature, often consisting of one or more accessory bellies associated with a varying number

Address for correspondence: Prof. M. Pillay, PhD, Department of Anatomy, Amrita School of Medicine, Amrita Institute of Medical Sciences, Amrita Vishwa Vidyapeetham, Kochi 682041, Kerala, India, tel: 0091-484 2858101 (office), 0091-9895511577 (mobile), fax: 0091-484 2802020, e-mail: minniepillay@aims.amrita.edu; pillayminnieanat@gmail.com

This article is available in open access under Creative Common Attribution-Non-Commercial-No Derivatives 4.0 International (CC BY-NC-ND 4.0) license, allowing to download articles and share them with others as long as they credit the authors and the publisher, but without permission to change them in any way or use them commercially.

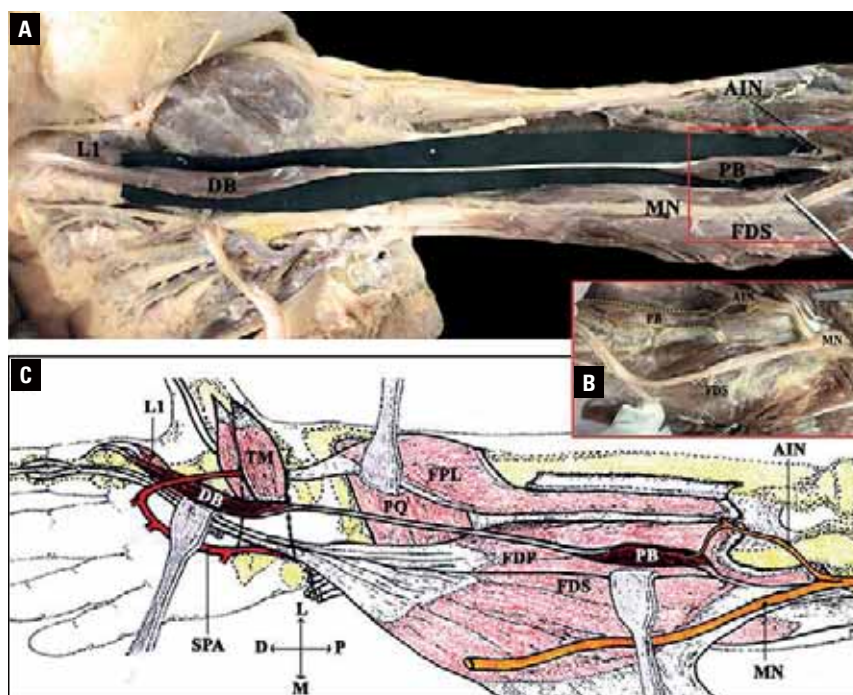


Figure 1. The accessory digastric muscle on the right forearm and hand of an 89-year-old male; **A.** The forearm (on the right side of the figure) showing the proximal belly (PB), innervated by the anterior interosseous nerve (AIN), originating from the deeper aspect of proximal flexor digitorum superficialis (FDS). The tendon of the PB extends distally to connect the distal belly (DB), which accompanies the first lumbrical (L1) for a common insertion in the hand (shown on the left side of the figure); **B.** An enlarged view of the boxed area in panel A showing a twig arising from the thick AIN innervating the PB (confined to the area bounded by broken line) from its lateral side. Note that the median nerve (MN) along with FDS has been deflected to the ulnar side; **C.** A diagrammatic representation of the accessory muscle, its PB and DB. The description of the muscle given in panels A and B are clearly depicted. Note the relationships of the muscle with the FDS, flexor digitorum profundus (FDP), pronator quadratus (PQ), flexor pollicis longus (FPL), thenar muscles (TM), and the superficial palmar arch (SPA); Compass: P — proximal; D — distal; M — medial; L — lateral.

of tendons. They were categorised into five classes by Elliot et al. [6] depending on their location and attachments. They may remain confined to the forearm [3, 23, 25] or extend for varying distances in the palm [11, 13, 19, 21]. Such anomalies of FDS or its tendons, especially to the index finger, presenting as masses or pseudo-tumours within the palm, have gained importance in recent years due to the clinical problems caused by them that require surgery [6, 21]. Of these, one that bears slight resemblance to the present case only by virtue of its 'digastricism' is that reported by Caetano et al. [2]; it was, however, a small variant confined purely to the forearm, being placed close to the FDS and inserting rather unusually, into the medial epicondyle of the humerus. Abundant literature also exists documenting different types of variant lumbricals, especially the lateral two [12, 14, 15, 24]. Rarer variations, such as those associated with flexor carpi ulnaris (FCU) [4, 18] and flexor pollicis longus (FPL) [8] have also been reported.

We report a unique bilateral case of a supernumerary muscle spanning remarkable portion of both

forearm and palm, originating from FDS and sharing a common insertion with the first lumbrical into the dorsal digital expansion of the index finger. Innervation of the proximal belly of the right aberrant muscle by the anterior interosseous nerve and its antebrachial origin proximal to the flexor retinaculum suggest that the present case does not fit into either of the two commonest muscular variations of the upper limb. In fact, the palmar bellies of both the muscles by virtue of their location and innervation, are suggestive of an atavistic trait seen normally in amphibians [24].

CASE REPORT

During routine dissection of upper extremities at our medical school, a distinct bilateral variation was noted in the forearms of a male cadaver aged 89 years. A digastric muscle was observed on the right side, consisting of proximal and distal bellies connected by a long tendon (Fig. 1A, C). The proximal belly, about 7.5 cm long, took origin from the posterior surface of FDS by a short tendon, and then continued in the forearm as a long tendon of 12 cm length.

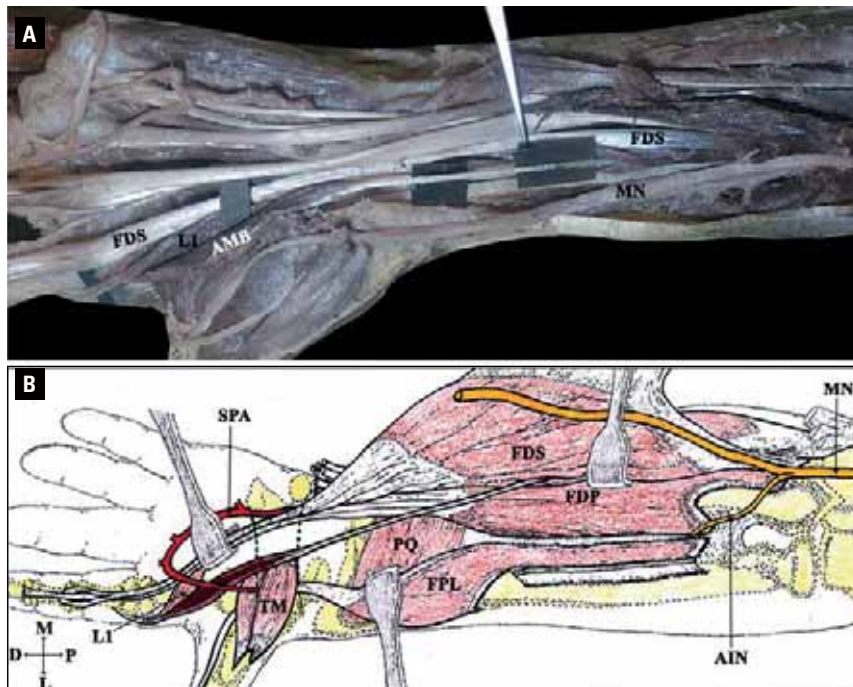


Figure 2. The accessory muscle (AM) on the left forearm (shown on the right side of the image) and hand (shown on the left side of the image) of an 89-year-old male; **A.** The AM took a tendinous origin from the middle of the deeper aspect of the flexor digitorum superficialis (FDS) and coursed distally through the carpal canal to join a muscle belly which we called accessory muscle belly (AMB), which similar to that on the right side, joined the first lumbrical (L1). The median nerve (MN) innervated the AM; **B.** A diagrammatic representation of the AM depicting its relationships with other structures in the vicinity such as the anterior interosseous nerve (AIN), flexor digitorum profundus (PDP), pronator quadratus (PQ), thenar muscles (TM), and the superficial palmar arch (SPA); Compass: P — proximal; D — distal; M — medial; L — lateral.

On reaching the wrist, the tendon transformed into a slightly longer distal belly about 8 cm, which entered the palm through the carpal canal on the radial side of FDS tendon for the index finger and was inserted by a short tendon with the first lumbrical to the radial side of the dorsal digital expansion of the extensor tendon of the index finger (Fig. 1A, C). On the left side, the accessory muscle took origin from the middle of the length of the fleshy belly of FDS muscle by a thin tendon, about 8 cm long, which continued distally as a fusiform muscle belly, 7 cm in length, traversing the carpal canal, and joining the first lumbrical in a common insertion similar to its counterpart on the right (Fig. 2A, B).

On both sides, the original FDS and flexor digitorum profundus (FDP) tendons for the index finger had normal insertion. The proximal belly of the right accessory muscle was innervated by a branch of the anterior interosseous nerve (Fig. 1B). The innervation of palmar bellies on both sides was by the median nerve.

The proximal belly of the muscle on the right side and the tendons on both sides were superficial to the FDP and deep to the FDS. The FPL formed the lateral

relation of the proximal parts in both forearms. On both palms, the palmar belly passed through the carpal tunnel and more distally, lay deep to the superficial palmar arch and immediately superficial to the first lumbrical, with which it shared a common insertion. The tendon of the FDS to the index finger was medial to the muscle throughout its course.

DISCUSSION

Variant morphology of FDS has been listed by Bergman et al. [1] and reported by several others [5, 11], but an accessory muscle belly taking origin from the dorsal surface of the FDS and inserting with the first lumbrical, though does find mention in literature, is rare [9, 10]. Elliot et al. [6] had classified FDS into five types (I–V), based on variations reported between 1866 and 1999. Though the variant described in the present case share some similarities with types III and IV described by him, it is a separate accessory muscle present bilaterally, with origin from the FDS, but insertion independent of FDS tendon for the index finger.

Though the concept of atavism is no longer considered relevant, the fact that the same anomalies recur regularly is difficult to explain as purely by chance [2].

The palmar bellies reported in this case closely resemble the unilateral variant reported by Wesser et al. [24] both by virtue of their location and innervation, but they may well be atavistic structures representing intrinsic flexors of the hand seen in amphibians and most reptiles, where forearm flexors act on the wrist, never inserting distal to metacarpals [6]. Their digits are flexed by superficial and deep groups of intrinsic flexors in the palm. The mammalian musculature appears to have evolved by the forearm muscle bellies retreating proximally from the carpus, while their insertions became parts of long flexor tendons passing through the carpal canal into the palm. The superficial short muscles either disappeared or became parts of superficialis tendons in the palm, while lumbricals developed from the central part of the deep short flexor muscles [2, 3]. Some authors project accessory muscle bellies observed in the forearm attached to the FDS to be anomalous lumbrical muscles with abnormally proximal origins [12, 15, 22]. Koizumi et al. [12] reported a case of a bilateral anomalous muscle quite similar to this case. The author performed nerve tracing analysis and concluded that the aberrant muscles have a close relationship to the first lumbrical muscle owing to similar innervation. Subsequently, many authors who reported similar findings also quoted the same hypothesis [22].

The FDP and pronator quadratus are believed to represent the deeper layer of forearm muscles of amphibians [6, 10]. In the present case, the proximal belly of the right variant, however, was remarkably distant from the palm and gained innervation from the anterior interosseous nerve. It is, therefore, quite unlikely to be an accessory lumbrical, but could rather be a remnant of the primitive deep group of forearm muscles which gained attachment to FDS. Alternatively, it could be part of FDP which did not fuse with the main muscle during phase 3 of muscle ontogenesis, when muscle primordia from different layers fuse to form a single muscle, or it could be part of muscle primordia that normally disappear, but persisted and, later differentiated into an accessory belly [3–5, 7]. The former explanation is more likely as suggested by its innervation. The palmar bellies of the variants could be remnants of the deep group of palmar intrinsic muscles, which perhaps became attached to a separated part of FDP tendon.

Analysis of anatomical variations can contribute to obtaining an actual, not idealized image of the inside of the human body, which is of crucial importance

in everyday clinical practice [26]. Accessory or variant muscles of the forearm and palm are of interest to clinicians. They often appear as abnormal swellings, especially palmar bellies commonly manifesting as painful or painless masses [6, 9, 19], that may be misdiagnosed as lipomas, ganglia, vascular malformations, or tendon sheath tumours [13, 21].

In many studies, anatomical variations of the upper limb correlate with nerve entrapment and such compressions are frequently attributed to some type of accessory muscle [16]. Hence it is important to know the normal anatomy and the possible variations of the structures concerned so as to avoid non-specific differential diagnosis of such conditions [16]. Carpal tunnel syndrome is the most common peripheral nerve entrapment encountered worldwide [17]. Although aetiology of carpal tunnel syndrome can vary, ranging from muscle hypertrophy [17] to persistent median artery [17, 20], when forming a content of the carpal tunnel or Guyon's canal, the supernumerary muscles like the ones reported here, are likely to cause compression of neurovascular structures, most commonly, the median or ulnar nerves [9]. According to Elliot et al. [6] symptoms of nerve compression could be intermittent, manifesting only during proper flexion, when muscle bellies move proximally. The possibility of an aberrant muscle belly should be considered when any abnormal mass detected is soft, in line with a digit, or when it shows increased firmness on active contraction against resistance [9]. Diagnosis of such conditions necessitates confirmation through electrophysiological testing and/or imaging techniques to decide whether or not more invasive surgical intervention is required [17]. While radiographs are of little value in such diagnosis, MRI scanning proves to be of greater use in addition to thorough history and physical examination [21]. Ultrasonography is another useful and more affordable option that has the added advantage of capturing movements of potential aberrant muscles [21]. The palmar bellies reported here were considerably long, traversing the entire span of the carpal canal but as to whether symptoms of nerve compression were present in the person concerned could not be ascertained, as this was an incidental finding observed during dissection, with no clinical history available.

CONCLUSIONS

This is a unique case of bilateral variant musculature of upper extremity. Not only does it add a new

facet to the evolutionary pattern of limb musculature but also warrants diligent investigation of such unprecedented variations for accurate diagnosis and suitable therapy in case of clinical conditions involving them. The need for surgical excision will depend on diagnosis and symptoms.

Acknowledgements

The authors gratefully acknowledge the technical assistance of Mr. Mayilswami and Mr. Anandhu Umeshan in dissection procedures, and Mr. Varghese MM in formatting figures for the manuscript.

Conflict of interest: None declared

REFERENCES

- Bergman RA, Afifi AK, Miyauchi R Opus I: Muscular System: Alphabetical Listing of Muscles: F, Flexor Digitorum Profundus. In: Bergman RA, Afifi AF, Miyauchi R, editors. Illustrated Encyclopedia of Human Anatomic Variation. URL: <http://www.anatomyatlases.org/AnatomicVariants/MuscularSystem/Text/F/16Flexor.shtml> and <https://www.anatomyatlases.org/AnatomicVariants/Images/0138.shtml>.
- Caetano EB, Sabongi Neto JJ, Ribas LA, et al. Accessory muscle of the flexor digitorum superficialis and its clinical implications. *Rev Bras Ortop.* 2017; 52(6): 731–734, doi: [10.1016/j.rboe.2017.10.004](https://doi.org/10.1016/j.rboe.2017.10.004), indexed in Pubmed: [29234659](https://pubmed.ncbi.nlm.nih.gov/29234659/).
- Choudhary U, Patil S, GM M, et al. Accessory belly of flexor digitorum superficialis — case report of a rare variant. *Int J Res Med Sci.* 2015; 3(2): 488, doi: [10.5455/2320-6012.ijrms20150220](https://doi.org/10.5455/2320-6012.ijrms20150220).
- Ciftçioğlu E, Kopuz C, Corumlu U, et al. Accessory muscle in the forearm: a clinical and embryological approach. *Anat Cell Biol.* 2011; 44(2): 160–163, doi: [10.5115/acb.2011.44.2.160](https://doi.org/10.5115/acb.2011.44.2.160), indexed in Pubmed: [21829760](https://pubmed.ncbi.nlm.nih.gov/21829760/).
- Cihák R. Ontogenesis of the skeleton and intrinsic muscles of the human hand and foot. *Ergeb Anat Entwicklungs-gesch.* 1972; 46(1): 5–194, indexed in Pubmed: [5043313](https://pubmed.ncbi.nlm.nih.gov/5043313/).
- Elliot D, Khandwala AR, Kulkarni M. Anomalies of the flexor digitorum superficialis muscle. *J Hand Surg Br.* 1999; 24(5): 570–574, doi: [10.1054/jhsb.1999.0237](https://doi.org/10.1054/jhsb.1999.0237).
- Grim M. Ultrastructure of the ulnar portion of the contrahent muscle layer in the embryonic human hand. *Folia Morphol.* 1972; 20(2): 113–115, indexed in Pubmed: [5021666](https://pubmed.ncbi.nlm.nih.gov/5021666/).
- Hafez S. A report on the accessory head of flexor pollicis longus and variations of forearm musculature. *J Morphol Sci.* 2018; 34(02): 098–106, doi: [10.4322/jms.103616](https://doi.org/10.4322/jms.103616).
- Honing ML, Ritt MJ, Bos KE. An anomalous flexor digitorum superficialis to the index finger. *Surg Radiol Anat.* 1995; 17(4): 339–341, doi: [10.1007/BF01795194](https://doi.org/10.1007/BF01795194), indexed in Pubmed: [8896155](https://pubmed.ncbi.nlm.nih.gov/8896155/).
- Jones FW. The morphology of the extrinsic muscles. The Principles of Anatomy as Seen in the Hand. 2nd ed. Bailliere, London 1944: 243–255.
- Kerasnoudis A. Elongated muscle belly of the flexor digitorum superficial causing carpal tunnel syndrome. *Hand (NY).* 2012; 7(3): 333–334, doi: [10.1007/s11552-012-9435-z](https://doi.org/10.1007/s11552-012-9435-z), indexed in Pubmed: [23997744](https://pubmed.ncbi.nlm.nih.gov/23997744/).
- Koizumi M, Kawai K, Honma S, et al. Anomalous lumbrical muscles arising from the deep surface of flexor digitorum superficialis muscles in man. *Ann Anat.* 2002; 184(4): 387–392, doi: [10.1016/S0940-9602\(02\)80062-0](https://doi.org/10.1016/S0940-9602(02)80062-0), indexed in Pubmed: [12201049](https://pubmed.ncbi.nlm.nih.gov/12201049/).
- Kostakoğlu N, Borman H, Keçik A. Anomalous flexor digitorum superficialis muscle belly: an unusual case of mass in the palm. *Br J Plast Surg.* 1997; 50(8): 654–656, doi: [10.1016/s0007-1226\(97\)90515-4](https://doi.org/10.1016/s0007-1226(97)90515-4), indexed in Pubmed: [9613412](https://pubmed.ncbi.nlm.nih.gov/9613412/).
- Mallikarjun A, Pramod R. Accessory belly of the first lumbrical – a case report. *Int J Anat Var.* 2011; 4: 20–21.
- Nayak SR, Rathan R, Chauhan R, et al. An additional muscle belly of the first lumbrical muscle. *Cases J.* 2008; 1(1): 103, doi: [10.1186/1757-1626-1-103](https://doi.org/10.1186/1757-1626-1-103), indexed in Pubmed: [18710552](https://pubmed.ncbi.nlm.nih.gov/18710552/).
- Orellana-Donoso M, Valenzuela-Fuenzalida J, Gold-Semmler M, et al. Neural entrapments associated with musculoskeletal anatomical variations of the upper limb: Literature review. *Transl Res Anat.* 2021; 22: 100094, doi: [10.1016/j.tria.2020.100094](https://doi.org/10.1016/j.tria.2020.100094).
- Osiak K, Elnazir P, Walocha JA, et al. Carpal tunnel syndrome: state-of-the-art review. *Folia Morphol.* 2022; 81(4): 851–862, doi: [10.5603/FM.a2021.0121](https://doi.org/10.5603/FM.a2021.0121), indexed in Pubmed: [34783004](https://pubmed.ncbi.nlm.nih.gov/34783004/).
- Saxena A, Agarwal KK, Das AR. Developmentally and clinically defined rare anomalous muscles in brachium and antebrachium. *Int J Anatradiol Surg.* 2018; 7(1): AC01–AC03, doi: [10.7860/IJARS/2018/34300:2350](https://doi.org/10.7860/IJARS/2018/34300:2350).
- Smith RJ. Anomalous muscle belly of the flexor digitorum superficialis causing carpal-tunnel syndrome. Report of a case. *J Bone Joint Surg Am.* 1971; 53(6): 1215–1216, indexed in Pubmed: [5092807](https://pubmed.ncbi.nlm.nih.gov/5092807/).
- Solewski B, Lis M, Pękala JR, et al. The persistent median artery and its vascular patterns: a meta-analysis of 10,394 subjects. *Clin Anat.* 2021; 34(8): 1173–1185, doi: [10.1002/ca.23770](https://doi.org/10.1002/ca.23770), indexed in Pubmed: [34371525](https://pubmed.ncbi.nlm.nih.gov/34371525/).
- Stephens N, Marques E, Livingston C. Anomalous flexor digitorum superficialis muscle belly presenting as a mass within the palm. *Can J Plast Surg.* 2007; 15(1): 44–46, doi: [10.1177/229255030701500103](https://doi.org/10.1177/229255030701500103), indexed in Pubmed: [19554131](https://pubmed.ncbi.nlm.nih.gov/19554131/).
- Trivedi S, Satapathy BC, Rathore M, et al. A rare case of anomalous origin of first lumbrical from the tendon of flexor digitorum superficialis to index finger. *J Clin Diagn Res.* 2016; 10(11): AD03–AD04, doi: [10.7860/JCDR/2016/23358.8801](https://doi.org/10.7860/JCDR/2016/23358.8801), indexed in Pubmed: [28050355](https://pubmed.ncbi.nlm.nih.gov/28050355/).
- Vasavi RG, Potu B, Jetti R, et al. Rare origin of two accessory bellies from the undersurface of the flexor digitorum superficialis muscle. *Eur J Gen Med.* 2009; 6(1): 57–59, doi: [10.29333/ejgm/82640](https://doi.org/10.29333/ejgm/82640).
- Wesser DR, Calostypis F, Hoffman S. The evolutionary significance of an aberrant flexor superficialis muscle in the human palm. *J Bone Joint Surg Am.* 1969; 51(2): 396–398, indexed in Pubmed: [5767330](https://pubmed.ncbi.nlm.nih.gov/5767330/).
- Yesilada AK, Tatlıdede HS, Çakmak E, et al. Anomalous large unique muscle belly of flexor digitorum superficialis and the absence of palmaris longus in the forearm. *J Plast Reconstr Aesthet Surg.* 2013; 66(1): 137–139, doi: [10.1016/j.bjps.2012.04.044](https://doi.org/10.1016/j.bjps.2012.04.044), indexed in Pubmed: [22652291](https://pubmed.ncbi.nlm.nih.gov/22652291/).
- Żytkowski A, Tubbs R, Iwanaga J, et al. Anatomical normality and variability: Historical perspective and methodological considerations. *Transl Res Anat.* 2021; 23: 100105, doi: [10.1016/j.tria.2020.100105](https://doi.org/10.1016/j.tria.2020.100105).

Anatomical variation of quadratus plantae in relation to flexor hallucis longus and flexor digitorum longus: a rare case

S. Haratizadeh, S. Seyyedin, S.N. Nematollahi-mahani

Department of Anatomical Sciences, Kerman University of Medical Sciences, Kerman, Iran

[Received: 13 February 2022; Accepted: 14 March 2022; Early publication date: 29 March 2022]

The quadratus plantae (QP) is considered as a part of the plantar intrinsic foot muscles. This muscle has two lateral and medial heads of origin, both of which arise from the plantar surface of calcaneus, and insert into the tendon of flexor digitorum longus (FDL). Various functions have been attributed to the QP muscle, which includes assisting the plantar flexion of the lateral four toes, straightening the oblique pull of FDL and etc. Several anatomical variations of the QP muscle have been reported in the literature. During a routine dissection in the Department of Anatomy at Kerman University of Medical Sciences, a variant plantar muscle was observed in a 40-year-old male cadaver. In the present case, we report a rare variation associated with the insertion pattern of this muscle, which is reported for the first time in Iran. The tendinous end of the QP muscle was divided into three tendons and were then inserted to the inferior surface of 2nd, 3rd and 4th tendons of FDL. Also, a slim tendinous interconnection was also observed between the QP and flexor hallucis longus (FHL). The lack of connection between the FDL and FHL tendons was the other rare variation of this case. Exact knowledge of the possible variations of the QP muscle is of utmost importance to foot surgeons, clinicians and also anatomists. (Folia Morphol 2023; 82, 2: 412–415)

Key words: quadratus plantae, flexor digitorum longus, flexor hallucis longus, foot, tendon

INTRODUCTION

The quadratus plantae (QP) muscle is located in the second layer of the plantar muscles of the foot [4]. "Massae carnae", "caro plantae pedis", "caro quadrata", "pronator pedis" and "flexor accessorius" are the names which have been attributed to this muscle so far [16].

The QP has no equivalent muscle in the hand. This muscle originates by two heads which are inserted to the plantar surface of calcaneus. They are separated at their origin by the long plantar ligament [4]. The

lateral head is smaller and originates from lateral border of the plantar surface of the calcaneus and the long plantar ligament, while the larger medial head arises from the medial concave surface of the calcaneus [4]. The medial head is only found in man, but the lateral head is presented in the other mammals [16]. These heads attach to the posterolateral surface of flexor digitorum longus (FDL) tendons by a flattened end [8].

In terms of comparative anatomy, the equine, bovine, ovine and porcine species do not possess the QP

Address for correspondence: Dr. S. Seyyedin, Prof. S.N. Nematollahi-mahani, Department of Anatomical Sciences, Kerman University of Medical Sciences, Kerman, Zip code: 0098, Iran, tel: +989137581242, +989131409249, e-mail: s.seyyedin@kmu.ac.ir; nnematollahi@kmu.ac.ir

This article is available in open access under Creative Common Attribution-Non-Commercial-No Derivatives 4.0 International (CC BY-NC-ND 4.0) license, allowing to download articles and share them with others as long as they credit the authors and the publisher, but without permission to change them in any way or use them commercially.

muscle; however, this muscle is presented in the canine and feline species and also in some primates [13, 16].

The QP muscle has several functions, such as assisting the FDL in plantar flexion of the lateral four toes [6], pronation of the foot and supporting the medial and lateral longitudinal arches of the foot [7]. Another important action of this muscle is straightening the oblique pull of FDL [11]. Despite the wide number of proposed functions, the exact role of this muscle has been remained unexplained [15].

The QP muscle is subjected to great variations in human. These variations include the sites of origin, the type of insertion and also the number of heads of this muscle [1, 9, 18]. It may be also completely absent which is a rare exception [13].

Here, we present a rare variation in QP muscle associated with an unusual type of insertion which to our knowledge, is reported for the first time in Iran.

CASE REPORT

During a routine dissection in the Department of Anatomy at Kerman University of Medical Sciences, a variant plantar muscle was observed in a 40-year-old male cadaver. After dissecting and retracting the skin and subcutaneous tissues, the plantar aponeurosis and the flexor digitorum brevis tendons were cut from the first layer of the foot at the metatarsophalangeal joints to expose the second layer of the foot. During this step, the medial and lateral plantar nerves and vessels were revealed. Then, a relationship in the distal end of the QP with the flexor hallucis longus (FHL) and FDL tendons was observed in both feet (Fig. 1). For accurate assessment of this connection, the FHL and FDL tendons were followed and the flexor retinaculum was dissected. The tibial nerve was diagnosed, and the tendons were then cut at the ankle joint proximally and at the metatarsophalangeal joints distally. The abnormal insertion of QP was then studied carefully and photographed (Fig. 2).

In the current case, origin of the medial and lateral heads was the calcaneus (normal origin) and QP was innervated by lateral plantar nerve. At the insertion point, this muscle had a tendinous end which was divided into three tendons and were then inserted to the inferior surface of 2nd, 3rd and 4th tendons of FDL (with the same thickness as the FDL tendons). Also, the tendinous part was connected to the FHL tendon with a slim tendinous connection (about one-third of the thickness of FHL tendon, Fig. 2) [3, 6]. It should



Figure 1. Photograph of foot dissection, the quadratus plantae tendons beneath the flexor digitorum longus and the tendinous interconnection between quadratus plantae and flexor hallucis longus are shown; FDLT — flexor digitorum longus tendon; FHLT — flexor hallucis longus tendon; FDB — flexor digitorum brevis; QP — quadratus plantae; QPT — quadratus plantae tendons; L — lumbrical; black arrowhead — tendinous interconnection; white arrowhead — medial plantar nerve.

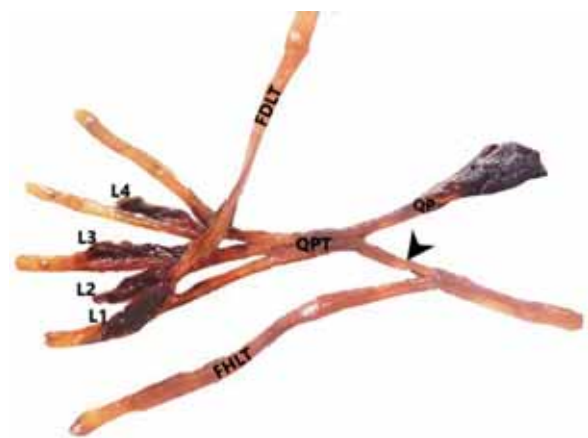


Figure 2. The arrangement pattern of tendons; FDLT — flexor digitorum longus tendon; FHLT — flexor hallucis longus tendon; QP — quadratus plantae; QPT — quadratus plantae tendons; L1 — first lumbrical; L2 — second lumbrical; L3 — third lumbrical; L4 — fourth lumbrical.

be noted that no connection was seen between the FHL and FDL tendons in this case.

DISCUSSION

Understanding the high variability of QP muscle is of great importance to surgeons who perform foot reconstructive surgery. This is due to the fact that this muscle might get injured in hindfoot traumas such as fractures of calcaneus or it may cross the operation field used for the treatment of various deformities

and diseases such as congenital clubfoot, diabetic foot, etc. [13, 17].

Several variations of QP including its insertion pattern and also the tendinous interconnection between the QP and FHL have been reported in the literature [9, 10, 13, 14, 17, 18]. According to the type of insertion, the QP muscles can be categorised into three groups: muscular, tendinous and aponeurotic [13]. In the present case, the QP had only the tendinous insertion pattern, and also its tendon was divided into three slips which were then inserted into the flexor tendons of the second, third and fourth toes. The QP acts as the medial stabilizer of FDL tendons but since it has not been attached to the posterolateral side of FDL in this case, it seems that it lacks the function of medial stabilization of FDL tendons [11].

In the present case, a tendinous interconnection was observed between the QP and FHL. Nasir has shown that this type of interconnection may be responsible for straightening the line of pull of FHL and therefore facilitates the role of first toe during take-off. However, such variation does not lead to any clinical disorders since it does not cause the entrapment of any vessels and nerves [10].

The interconnections between the FDL and FHL can be classified into four types: type I (a connecting slip from the FHL to FDL tendons), type II (a slip from FDL tendons to FHL), type III (crossed slips between FDL and FHL) and type IV (no attachment between FDL and FHL) [12]. Pretterklieber [14] reported a summary of previous studies on connections between the FHL and the FDL in which the percentages of different types of interconnections were 75%, > 1%, 23% and 2% for types I, II, III and IV, respectively. Based on the previous studies, it has been stated that a connection between the FHL and the FDL is regarded as the regular case [6, 9, 18]. For instance, Le Double [9] has shown that the slip from the FHL to the 2nd and 3rd tendon of FDL is the regular condition. However, in the current case, no connection was observed between the FDL and FHL tendons which is considered as a rare variation compared to the other studies. Treatment of posterior tibial tendon dysfunction and also Achilles tendon rupture, requires tendon transfer of either FDL or FHL. In order to perform this surgical procedure in the best possible way, exact knowledge of the variations of FDL, FHL and the QP, and also their connections are essential to foot surgeons [2, 5].

CONCLUSIONS

The rare variation in the QP insertion which was reported in the present case give us more understanding of the possible variations of the QP muscle which is important for anatomists, and useful for various surgical procedures in the foot region and also the imaging and biomechanical studies.

Acknowledgements

We are thankful to the generous body donors whose cadavers formed the basis of this study.

Conflict of interest: None declared

REFERENCES

1. Athavale SA, Geetha GN, Swathi N. Morphology of flexor digitorum accessorius muscle. *Surg Radiol Anat.* 2012; 34(4): 367–372, doi: [10.1007/s00276-011-0909-4](https://doi.org/10.1007/s00276-011-0909-4), indexed in Pubmed: [22139394](https://pubmed.ncbi.nlm.nih.gov/22139394/).
2. Chadwick C, Whitehouse SL, Saxby TS. Long-term follow-up of flexor digitorum longus transfer and calcaneal osteotomy for stage II posterior tibial tendon dysfunction. *Bone Joint J.* 2015; 97-B(3): 346–352, doi: [10.1302/0301-620X.97B3.34386](https://doi.org/10.1302/0301-620X.97B3.34386), indexed in Pubmed: [25737518](https://pubmed.ncbi.nlm.nih.gov/25737518/).
3. Cunningham DJ, Koshi R. *Cunningham's manual of practical anatomy.* 16th ed. Oxford, New York 2017.
4. Gray H, Standring S. *Gray's Anatomy: the anatomical basis of clinical practice.* 41st ed. Elsevier, Philadelphia 2016.
5. Hunt KJ, Cohen BE, Davis WH, et al. Surgical treatment of insertional achilles tendinopathy with or without flexor hallucis longus tendon transfer: a prospective, randomized study. *Foot Ankle Int.* 2015; 36(9): 998–1005, doi: [10.1177/1071100715586182](https://doi.org/10.1177/1071100715586182), indexed in Pubmed: [25990545](https://pubmed.ncbi.nlm.nih.gov/25990545/).
6. Hur MS, Kim JH, Woo JS, et al. An anatomic study of the quadratus plantae in relation to tendinous slips of the flexor hallucis longus for gait analysis. *Clin Anat.* 2011; 24(6): 768–773, doi: [10.1002/ca.21170](https://doi.org/10.1002/ca.21170), indexed in Pubmed: [21812033](https://pubmed.ncbi.nlm.nih.gov/21812033/).
7. Kelly LA, Kuitunen S, Racinais S, et al. Recruitment of the plantar intrinsic foot muscles with increasing postural demand. *Clin Biomech (Bristol, Avon).* 2012; 27(1): 46–51, doi: [10.1016/j.clinbiomech.2011.07.013](https://doi.org/10.1016/j.clinbiomech.2011.07.013), indexed in Pubmed: [21864955](https://pubmed.ncbi.nlm.nih.gov/21864955/).
8. Last RJ. *Anatomy: regional and applied.* 7th ed. Churchill Livingstone, Edinburgh 1985.
9. Le Double AF. *Traité des variations du système musculaire de l'homme: et de leur signification au point de vue de l'anthropologie zoologique.* Reinwald, Paris 1897.
10. Nasir N. A rare instance of a tendinous interconnection between flexor hallucis longus and flexor digitorum accessorius. *Int J Anat Var* 2013. 2013; 6(1): 18–19.
11. Neumann D. *Kinesiology of the musculoskeletal system: foundations for rehabilitation.* 3rd ed. Elsevier, St. Louis, Missouri 2017.

12. O'Sullivan E, Carare-Nnadi R, Greenslade J, et al. Clinical significance of variations in the interconnections between flexor digitorum longus and flexor hallucis longus in the region of the knot of Henry. *Clin Anat.* 2005; 18(2): 121–125, doi: [10.1002/ca.20029](https://doi.org/10.1002/ca.20029), indexed in Pubmed: [15696523](https://pubmed.ncbi.nlm.nih.gov/15696523/).
13. Pretterklieber B. Morphological characteristics and variations of the human quadratus plantae muscle. *Ann Anat.* 2018; 216: 9–22, doi: [10.1016/j.aanat.2017.10.006](https://doi.org/10.1016/j.aanat.2017.10.006), indexed in Pubmed: [29166622](https://pubmed.ncbi.nlm.nih.gov/29166622/).
14. Pretterklieber B. The high variability of the chiasma plantare and the long flexor tendons: Anatomical aspects of tendon transfer in foot surgery. *Ann Anat.* 2017; 211: 21–32, doi: [10.1016/j.aanat.2017.01.011](https://doi.org/10.1016/j.aanat.2017.01.011), indexed in Pubmed: [28163203](https://pubmed.ncbi.nlm.nih.gov/28163203/).
15. Schroeder KL, Rosser BW, Kim SY. Fiber type composition of the human quadratus plantae muscle: a comparison of the lateral and medial heads. *J Foot Ankle Res.* 2014; 7(1): 54, doi: [10.1186/s13047-014-0054-5](https://doi.org/10.1186/s13047-014-0054-5), indexed in Pubmed: [25530807](https://pubmed.ncbi.nlm.nih.gov/25530807/).
16. Sooriakumaran P, Sivananthan S. Why does man have a quadratus plantae? A review of its comparative anatomy. *Croat Med J.* 2005; 46(1): 30–35, indexed in Pubmed: [15726673](https://pubmed.ncbi.nlm.nih.gov/15726673/).
17. Talhar SS, Sontakke BR, Wankhede V, et al. A rare variation of flexor digitorum accessorius insole and its phylogenetic significance. *J Mahatma Gandhi Inst Med Sci.* 2017; 22(1): 44, doi: [10.4103/0971-9903.202017](https://doi.org/10.4103/0971-9903.202017).
18. Testut L. *Les anomalies musculaires chez l'homme.* G Masson, Paris 1884.

Bilateral accessory head of the adductor longus muscle: an anatomical case study

T. Kozioł¹, M.P. Zarzecki¹ , W. Przybycień¹, W. Twardokęś², J.A. Walocha¹

¹Department of Anatomy, Jagiellonian University Medical College, Krakow, Poland

²Department of Histology, Cytophysiology and Embryology, Faculty of Medicine in Zabrze, University of Technology in Katowice, Zabrze, Poland

[Received: 5 December 2021; Accepted: 17 January 2022; Early publication date: 17 February 2022]

The adductor longus muscle, with its proximal origin at the pubic bone and distal at the linea aspera, is reported to be one of the most frequently injured groin muscles in contact sports, namely football or ice hockey. Notwithstanding, there is a scarcity of published works regarding the accessory heads of the adductor longus muscle in the existing literature, let alone the clinical significance of the said variant.

The following study is a case report describing bilateral accessory heads of the adductor longus muscle in a 97-year-old female cadaver. A routine cadaveric dissection revealed two accessory heads on the right thigh and one on the left thigh of a donor with no known structural or pathological abnormalities of the proximal lower extremity. The anterior division of the obturator nerve provided nerve supply to the variants on both sides. The deep femoral, superficial external pudendal, femoral vessels were responsible for the vascular supply to the accessory heads of the adductor longus.

Undoubtedly, extensive knowledge regarding the variant anatomy of the hip adductor muscles is of immense importance to physiotherapists and orthopaedists treating patients for their injury or complete tears. Nonetheless, there is little information regarding the accessory heads of the adductor longus in the existing literature (originating mostly from cadaveric studies) that requires further evaluation in vivo to assess whether this variant might have an impact on a patient's everyday life. (Folia Morphol 2023; 82, 2: 416–421)

Key words: adductor longus, anatomical variation, anatomy, orthopaedics, physiotherapy

INTRODUCTION

There are six distinct adductor muscles of the hip, found at the proximal end of the lower extremity in humans that include the adductor longus, adductor magnus, adductor brevis, gracilis, pectineus and obturator externus muscles. The adductor longus muscle has been found to be the most common muscle to be injured, occurring in approximately 62% in a study of

55 cases of groin injuries [15]. The said muscle has its proximal attachment at the pubic bone, inferiorly to the pubic tubercle, travels anteriorly as a fan-shaped muscle covering the adductor brevis and the middle part of the adductor magnus to its distal attachment at the middle third of the linea aspera of the femur [9]. Moreover, the adductor longus forms the posterior wall of the adductor canal (alongside the

Address for correspondence: Dr. M.P. Zarzecki, MD, Department of Anatomy, Jagiellonian University Medical College, ul. Kopernika 12, 31–034 Kraków, Poland, tel/fax: +48 12 422 95 11, e-mail: michal.zarzecki96@gmail.com

This article is available in open access under Creative Common Attribution-Non-Commercial-No Derivatives 4.0 International (CC BY-NC-ND 4.0) license, allowing to download articles and share them with others as long as they credit the authors and the publisher, but without permission to change them in any way or use them commercially.

adductor magnus) through which the femoral artery, femoral vein, and saphenous nerve pass towards the popliteal fossa, as well as nerve to vastus medialis [9]. A branch from the anterior division of the obturator nerve (originating from the L2-L4 levels of the spinal cord) is said to be responsible for its innervation [9].

The obvious function of the adductor longus is to provide adduction of the thigh. Nonetheless, the aforementioned muscle has also been found to play an important role in hip flexion, as well as internal and external rotation on limited flexion angles [12]. A study by Hides et al. [3] has found the adductor magnus muscle to be involved to a greater extent in weight-bearing closed chain exercises compared to the adductor longus. Henceforth, the aforementioned types of exercise would not be beneficial in training the latter muscle. The adductor longus action is best noticeable during flexion of the hip in the hip extension position, whereas the adductor magnus works indifferently to the position of the hip [5].

Injuries to the groin, and especially the hip adductor muscles, occur frequently in athletes and contact sports. Extensive knowledge regarding these muscles and their variant anatomy and function is of immense importance to medical professionals and physiotherapists worldwide, as it may help devise a prevention programme (with appropriately directed exercises to strengthen these muscles) or provide adequate treatment upon injuries [3]. Henceforth, the purpose of this case report was to provide a thorough description of bilateral accessory heads of the adductor longus muscle, encountered during a routine cadaver dissection and to provide an up-to-date overview of the clinical implications pertaining to this muscle.

CASE REPORT

A routine cadaver dissection of a 97-year-old Polish female formalin fixed donor was undertaken at the Department of Anatomy, Jagiellonian University Medical College in Krakow, Poland in November 2021. The procedure was performed on previously untouched lower extremities. Three prosectors (T.K., M.P.Z., J.A.W.) were responsible for the specimen preparation. No visible trauma or other pathology were noted upon their inspection, nor were they found in the available medical records of the patient. Having removed the skin, the subcutaneous tissue and muscular fascia were carefully removed to individually expose the muscles of the thigh. Upon closer inspection of the adductor group of both right and

left lower extremities, there were bilateral variations noted regarding the adductor longus muscle. Measurements of the vascular length were obtained with the help of a digital calliper, averaged from three separate measurements.

On the left lower extremity, the adductor longus comprised two distinct heads. The proximal insertion point of both heads was located close to the pubic tubercle at the inferior pubic ramus, with the typical head attached more medially than the lateral head. The typical head appeared more muscular in its form, with tendinous attachments visible in the close proximity of the inferior pubic ramus, whereas the lateral head had a more tendinous proximal attachment. The distal insertion point for both heads was at the linea aspera of the femur, with the lateral head attached superiorly to the typical head. The saphenous vein crossed both of the heads anteriorly. The lateral head was located posteriorly and laterally from the typical head.

Both of the aforementioned heads of adductor longus muscle were innervated by the anterior division of the left obturator nerve. The vascular supply to both the typical and lateral heads was derived from the deep femoral artery (a single branch for both of them), with its length to the lateral head being 18.87 mm on average, and 25.69 mm to the typical head. The average length of the femoral artery (measured from the femoral canal to the branching off point of the deep femoral artery) was 72.65 mm (Figs. 1, 2).

On the right lower extremity, the adductor longus comprised three distinct heads. All of them had a common origin at the inferior pubic ramus, close to the pubic tubercle. The lateral accessory head had a more tendinous proximal attachment, located most laterally of the three, whereas the middle accessory head, also with a tendinous attachment, was positioned in between the lateral head and the typical head of the accessory longus muscle. The proximal attachment of the typical head appeared to be more muscular in its form, with tendinous attachments visible in the close proximity of the inferior pubic ramus. The distal attachment of all three heads was at the middle 2/3 of the linea aspera of the femur, with the lateral head located most superiorly, and the typical head most inferiorly. The typical and lateral heads were crossed by the saphenous vein anteriorly, whereas the middle head was located deep in between the two other heads. The lateral head was positioned posteriorly and laterally from the typical



Figure 1. A left accessory adductor longus head with its neural supply; 1 — adductor longus; 2 — adductor longus accessory head; 3 — obturator nerve (anterior division); 4 — branch of the obturator nerve to adductor brevis; 5 — branch of the obturator nerve to the adductor longus accessory head; 6 — branch of the obturator nerve to the adductor longus.



Figure 2. A left accessory adductor longus head with its vascular supply; 1 — adductor longus; 2 — adductor longus accessory head; 3 — femoral artery; 4 — branch from the deep femoral artery to the adductor longus and its accessory head.

head, whereas the middle head was located the most posteriorly and in between the two said structures.

All three aforementioned heads were innervated independently by the anterior division of the obturator nerve. The average length of the femoral artery (measured from the femoral canal to the branching off point of the deep femoral artery) was 73.44 mm. The typical head had a dual vascular supply. A branch

of the deep femoral artery to the typical head was 31.48 mm in length and reached the middle part of the muscle, whereas a small branch from the femoral artery 14.69 mm in length supplied the inferior part of the muscle. The middle head obtained its vascular supply also from the deep femoral artery that was 27.67 mm in length. The vascular supply for the typical and middle head originated from the same

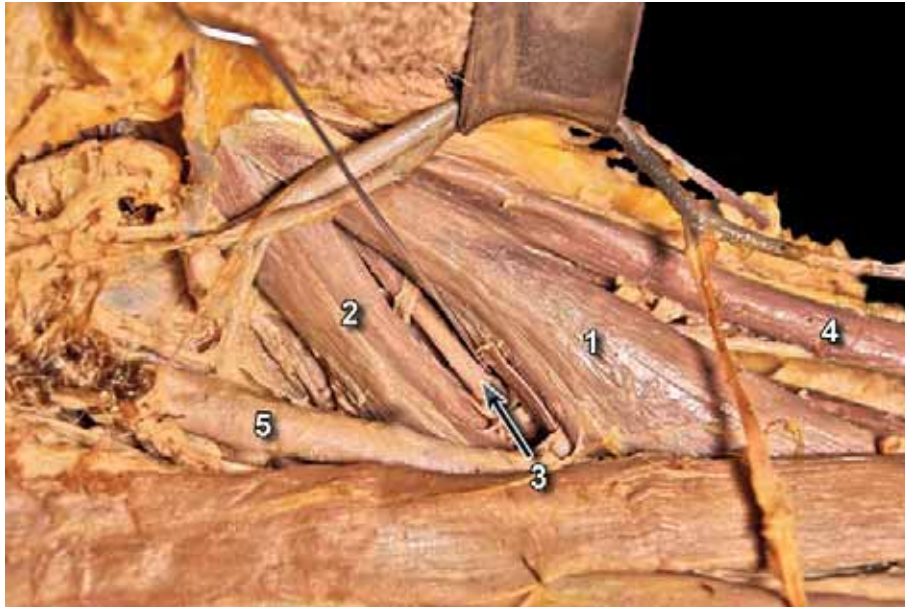


Figure 3. Two right accessory adductor longus heads; 1 — adductor longus; 2 — adductor longus lateral accessory head; 3 — adductor longus middle accessory head; 4 — gracilis muscle; 5 — femoral artery.

branch. The lateral head also had a dual supply. Its superior part was derived from the superficial external pudendal artery and veins that were 40.07 mm in length from their origin point at the external pudendal vessels. The inferior part was supplied by a branch from the deep femoral artery that was 16.59 mm in length, and originated separately from the branch that supplied the typical and middle head (Fig. 3).

Unfortunately, the average lengths of the respective heads on both sides were not measured, as that would require for the surrounding muscles to be excised in order to obtain wide access and reliable measurements from their proximal to their distal insertion points.

DISCUSSION

The current study reports a case of bilateral accessory heads of the adductor longus muscle, two on the right and one on the left. Their vascular supply was chiefly derived from the deep femoral artery, but also from the superficial external pudendal artery and the femoral artery. The available literature of the subject suggests that the adductor longus may also be vascularised by the obturator arteries [13, 14], but the authors have not found any of the said branches in the current study.

There is scarcity of research regarding the accessory heads of the adductor longus muscle in the available literature. Tuite et al. [17] are the only authors

that made a brief mention about bicephalic adductor longus. The study was based on 37 cadaveric observations and investigated variations in the proximal tendinous origin and the typical muscle's length. Most of the described cases had tendinous attachments on the anterior surface, but on the posterior side it was usually muscular in origin [17]. The aforementioned authors also reported other types of anomalies, such as adductor longus muscular origin on the anterior surface or fused proximal tendons of the adductor longus and the gracilis muscles [17].

There are works [11, 14] that noticed the possibility of adductor longus having two distinct parts, however access to the primary source of this information turned out impossible. The second variation also mentioned in several sources is the muscle's length [11, 14]. In some uncommon cases, the adductor longus may even reach as far as the knee and fuse with the adductor magnus tendon [11]. Du Plessis et al. [11] reported that in this situation the tendons of the adductor longus and the adductor magnus can be fused together.

The clinical significance of the adductor longus muscle has been described only in a few case reports. The most frequent condition involving the aforementioned anatomical entity is its total rupture, which occurs mostly in football players [8, 10]. Incomplete tears or strains happen frequently at the more susceptible parts of the muscle, i.e. at its proximal part on

the junction point of muscular and tendinous fibres or else at its insertion on the pubic bone. However, complete muscle tears occur more often at the distal attachment to the femur [15]. Injury to the adductor longus is also common in sports such as ice hockey, horseback riding, skating and hurdling [17].

Nonetheless, sport injuries are not the only disorders associated with the adductor longus muscle. Alimehmeti et al. [1] described an unusual case of saphenous neuropathy due to a hydatid cyst located in the adductor longus, that caused swelling, numbness and pain in the medial part of the right thigh. The cyst was excised and the patient walked independently the next day after the procedure. Another example of a non-traumatic disorder is urinary bladder cancer metastasis to the adductor longus [7]. The 62-year-old male patient in question presented with unusual symptoms in the right thigh, namely pain, swelling of the extremity and struggled with mobility. Unfortunately, the patient died during treatment, hence there is not enough information to estimate how the metastasis would have impacted his gait and muscle activation.

Accessory muscles are usually asymptomatic, but sometimes they may present clinical symptoms [16, 18]. Various cases of supernumerary muscles have previously been reported in the thigh and knee area, e.g. the tensor vastus intermedius [2], accessory sartorius muscle [6], tensor fasciae latae, accessory semimembranosus muscle or accessory popliteus muscle [16, 18]. Accessory muscles can cause nerve entrapment syndromes, vascular compressions or may mimic other pathologies, namely soft tissue tumour or the Baker's cyst [18]. Truly, the clinical symptoms associated with presence of a supernumerary muscle depend on its location and the neighbouring neurovascular entities involved. Clinical deduction derived from cadaveric studies is extremely difficult and poses a high risk of bias, as most often encountering some of the anatomical variations occurs incidentally, without the previous knowledge of the patient or their family of their existence. Therefore, lack of medical history with the description of potential symptoms makes it impossible for cadaveric studies to truly discern the clinical meaning of the finding, hence it remains only as an assumption.

Generally speaking, the adductor longus muscle does not have an extensive description of its anatomy and clinical considerations in the available literature. Most of the publications describe its traumatology, bi-

omechanics and therapeutic management in injuries. The reason behind it may potentially be low clinical importance of anatomical variations in this area. More research, and on a larger scale, regarding the anatomy of the adductor longus is still needed to estimate the prevalence of its accessory heads. The authors in their dissection experience have not encountered the described here variation in the past, regardless of its laterality, hence presume that its prevalence is rare. Both clinical and biomechanical properties of the accessory heads of the adductor longus would be beneficial to ascertain its potential role in the human organism. Nonetheless, the authors would like to acknowledge Żytkowski et al. [19] in saying that although the so-called 'anatomical norm' proves beneficial in everyday medical practice by presenting the most common anatomy of a structure, it is also a double-edged sword as it may also present an overly idealised view.

CONCLUSIONS

Anatomical variations of the adductor longus muscle play a crucial role whilst assessing a groin injury in contact sports, but also in case of cysts and casuistic neoplastic metastasis to the muscle. Undoubtedly, a thorough knowledge is required from medical professionals to adequately diagnose and treat such patients. This is most probably the first study to report bilateral accessory heads of the adductor longus muscle (with two accessory heads on the right thigh) thus adding to the existing literature and pointing to the yet still needed further scientific exploration of the said muscular variation in vivo.

Acknowledgements

The authors are indebted to Mr Jacenty Urbaniak for the technical support. "The authors sincerely thank those who donated their bodies to science so that anatomical research could be performed. Results from such research can potentially increase mankind's overall knowledge that can then improve patient care. Therefore, these donors and their families deserve our highest gratitude" [4].

Conflict of interest: None declared

REFERENCES

1. Alimehmeti R, Seferi A, Rroji A, et al. Saphenous neuropathy due to large hydatid cyst within long adductor muscle: case report and literature review. *J Infect Dev Ctries.*

- 2012; 6(6): 531–535, doi: [10.3855/jidc.1766](https://doi.org/10.3855/jidc.1766), indexed in Pubmed: [22706197](https://pubmed.ncbi.nlm.nih.gov/22706197/).
2. Franchi T. Tensor vastus intermedius: a review of its discovery, morphology and clinical importance. *Folia Morphol.* 2021; 80(4): 792–798, doi: [10.5603/FM.a2020.0123](https://doi.org/10.5603/FM.a2020.0123), indexed in Pubmed: [33084009](https://pubmed.ncbi.nlm.nih.gov/33084009/).
 3. Hides JA, Beall P, Franettovich Smith MM, et al. Activation of the hip adductor muscles varies during a simulated weight-bearing task. *Phys Ther Sport.* 2016; 17: 19–23, doi: [10.1016/j.ptsp.2015.06.001](https://doi.org/10.1016/j.ptsp.2015.06.001), indexed in Pubmed: [26576708](https://pubmed.ncbi.nlm.nih.gov/26576708/).
 4. Iwanaga J, Singh V, Ohtsuka A, et al. Acknowledging the use of human cadaveric tissues in research papers: Recommendations from anatomical journal editors. *Clin Anat.* 2021; 34(1): 2–4, doi: [10.1002/ca.23671](https://doi.org/10.1002/ca.23671), indexed in Pubmed: [32808702](https://pubmed.ncbi.nlm.nih.gov/32808702/).
 5. Kato T, Taniguchi K, Akima H, et al. Effect of hip angle on neuromuscular activation of the adductor longus and adductor magnus muscles during isometric hip flexion and extension. *Eur J Appl Physiol.* 2019; 119(7): 1611–1617, doi: [10.1007/s00421-019-04150-5](https://doi.org/10.1007/s00421-019-04150-5), indexed in Pubmed: [31030295](https://pubmed.ncbi.nlm.nih.gov/31030295/).
 6. Kim J, Lee JH. A unique case of an accessory sartorius muscle. *Surg Radiol Anat.* 2019; 41(3): 323–325, doi: [10.1007/s00276-018-2155-5](https://doi.org/10.1007/s00276-018-2155-5), indexed in Pubmed: [30539207](https://pubmed.ncbi.nlm.nih.gov/30539207/).
 7. Koca I, Ucar M, Bozdog Z, et al. Adductor longus muscle metastasis of transitional cell carcinoma of the urinary bladder. *BMJ Case Rep.* 2014; 2014, doi: [10.1136/bcr-2014-203768](https://doi.org/10.1136/bcr-2014-203768), indexed in Pubmed: [24827659](https://pubmed.ncbi.nlm.nih.gov/24827659/).
 8. Masionis P, Popov K, Kurtinaitis J, et al. Surgical treatment of the adductor longus muscle's distal tendon total rupture in a soccer player. *Orthop Traumatol Surg Res.* 2016; 102(5): 673–676, doi: [10.1016/j.otsr.2016.03.011](https://doi.org/10.1016/j.otsr.2016.03.011), indexed in Pubmed: [27132783](https://pubmed.ncbi.nlm.nih.gov/27132783/).
 9. Moore K, Dalley AI, Agur A. (ed). *Lower limb. Moore Clinically Orientated Anatomy*, 7th ed. Lippincott Williams and Wilkins, Baltimore / Philadelphia 2014: 548–556.
 10. Peterson L, Stener B. Old total rupture of the adductor longus muscle. A report of seven cases. *Acta Orthop Scand.* 1976; 47(6): 653–657, doi: [10.3109/17453677608988754](https://doi.org/10.3109/17453677608988754), indexed in Pubmed: [1015261](https://pubmed.ncbi.nlm.nih.gov/1015261/).
 11. du Plessis M, Loukas M. Thigh muscles. In: Tubbs R, Shoja M, Loukas M (ed.). *Bergman's Comprehensive Encyclopedia of Human Anatomic Variation*, 1st ed. Wiley-Blackwell, Hoboken, NJ, USA 2016: 415.
 12. Pressel T, Lengsfeld M. Functions of hip joint muscles. *Med Eng Phys.* 1998; 20(1): 50–56, doi: [10.1016/s1350-4533\(97\)00040-4](https://doi.org/10.1016/s1350-4533(97)00040-4), indexed in Pubmed: [9664285](https://pubmed.ncbi.nlm.nih.gov/9664285/).
 13. Ransom AL, Sinkler MA, Nallamothu SV. *Anatomy, Bony Pelvis and Lower Limb, Femoral Muscles*. [Updated 2021 Oct 6]. In: StatPearls [Internet]. Treasure Island (FL): StatPearls Publishing. <https://www.ncbi.nlm.nih.gov/books/NBK500008/> (2021 Jan).
 14. Reicher M, Łasiński W. Mięśnie uda. In: Bochenek A (ed.). *Anatomia Człowieka*. Vol. I. 6th ed. Państwowy Zakład Wydawnictw Lekarskich, Warszawa 1990: 875–876.
 15. Renström P, Peterson L. Groin injuries in athletes. *Br J Sports Med.* 1980; 14(1): 30–36, doi: [10.1136/bjism.14.1.30](https://doi.org/10.1136/bjism.14.1.30), indexed in Pubmed: [7378668](https://pubmed.ncbi.nlm.nih.gov/7378668/).
 16. Sookur PA, Naraghi AM, Bleakney RR, et al. Accessory muscles: anatomy, symptoms, and radiologic evaluation. *Radiographics.* 2008; 28(2): 481–499, doi: [10.1148/rg.282075064](https://doi.org/10.1148/rg.282075064), indexed in Pubmed: [18349452](https://pubmed.ncbi.nlm.nih.gov/18349452/).
 17. Tuite DJ, Finegan PJ, Saliaris AP, et al. Anatomy of the proximal musculotendinous junction of the adductor longus muscle. *Knee Surg Sports Traumatol Arthrosc.* 1998; 6(2): 134–137, doi: [10.1007/s001670050086](https://doi.org/10.1007/s001670050086), indexed in Pubmed: [9604200](https://pubmed.ncbi.nlm.nih.gov/9604200/).
 18. Vanhoenacker FM, Desimpel J, Mespreuve M, et al. Accessory muscles of the extremities. *Semin Musculoskelet Radiol.* 2018; 22(3): 275–285, doi: [10.1055/s-0038-1641575](https://doi.org/10.1055/s-0038-1641575), indexed in Pubmed: [29791956](https://pubmed.ncbi.nlm.nih.gov/29791956/).
 19. Żytkowski A, Tubbs R, Iwanaga J, et al. Anatomical normality and variability: Historical perspective and methodological considerations. *Transl Res Anat.* 2021; 23: 100105, doi: [10.1016/j.tria.2020.100105](https://doi.org/10.1016/j.tria.2020.100105).

A rare unreported bilateral thoracic muscle on the inferior and posteromedial aspect of the rib cage: case report and literature review

A. Lee¹, C. Dean¹, K. Labagnara¹, D. Jun Yun¹, A. Pinkas¹, P.L. Mishall^{1, 2}

¹Department of Pathology, Albert Einstein College of Medicine, Bronx, NY, United States

²Department of Ophthalmology and Visual Science, Albert Einstein College of Medicine, Bronx, NY, United States

[Received: 3 February 2022; Accepted: 8 March 2022; Early publication date: 22 March 2022]

Thoracic wall muscles are essential for respiration. Few anatomical variations in thoracic wall muscles have been reported. Such variants must be considered during surgical procedures that involve the thorax muscles. During routine dissection of a 65-year-old male cadaver as part of a fourth-year clinical anatomy elective, additional muscle strips were found in the inner and inferior aspect of the rib cage closer to the posteromedial body wall. The muscle consisted of two strips of narrow muscle fibres originating from the inferior borders of ribs 11 and 12 that radiated to insert on the transverse processes of the T11 and T12 vertebrae. The case report describes an unusual, novel medial thoracic wall muscle that has not been previously described in the literature. Variations in thoracic muscles can affect respiratory function and surgical interventions like chest tube placement and needle therapy for local anaesthesia, therefore, it is important for clinicians to be aware of such variants. (Folia Morphol 2023; 82, 2: 422–423)

Key words: anatomical variations, rare thoracic wall muscle, rib cage, posteromedial wall, T11 and T12 vertebrae

INTRODUCTION

The thoracic wall is composed of 5 muscles that include the external intercostal, internal intercostal, innermost intercostal, subcostal, and transversus thoracis [1]. The intercostal muscles originate from the inferior border of the ribs and insert on the superior border of the inferior ribs. The subcostal muscles are seen in the lower ribs and connect the internal surface of one rib to the superior border of the rib located in two or three intercostal spaces inferiorly. Finally, the transversus thoracis muscles originate from the posterior surface of the lower sternum and insert on the internal surface of the costal cartilage [2]. These muscles are primarily involved in changing

the volume of the thoracic cavity during inspiration and expiration [1]. Posteriorly, the serratus posterior superior and serratus posterior inferior muscles are responsible for elevating the ribs while the levatores costarum muscles depress the ribs [2].

Anatomical variations in the muscles of the thorax have rarely been reported. The most common muscle variant seen in the thoracic region is the sternalis muscle, found in 8% of the population [1]. Clinically, the sternalis muscle can pose diagnostic challenges and lead to surgical malpractice if clinicians remain unaware that such a variant exists [3]. Other thoracic muscle variants have implications for respiratory function and surgical interventions, such as chest tube

Address for correspondence: P.L. Mishall, Associate Professor, Departments of Pathology and Ophthalmology and Visual Sciences, Albert Einstein College of Medicine, 1300 Morris Park Ave, F6205C, Bronx, NY 10461, United States, tel: +1 (718) 430-3423, fax: +1 (718) 430-8996, e-mail: priti.mishall@einsteinmed.edu

This article is available in open access under Creative Commons Attribution-Non-Commercial-No Derivatives 4.0 International (CC BY-NC-ND 4.0) license, allowing to download articles and share them with others as long as they credit the authors and the publisher, but without permission to change them in any way or use them commercially.

placement and needle therapy for either decompression or anaesthesia.

MATERIALS AND METHODS

The thoracic region of a 65-year-old male cadaver was dissected by faculty members to prepare cadaver prosections for a first-year anatomy course. Using a bone saw, a vertical incision was made from ribs two through nine anteriorly and the parietal pleura was dissected. The anterior thoracic wall was reflected inferiorly, exposing the pulmonary cavities and mediastinum. The lungs and heart were removed. The lateral thoracic cavity and posterior intercostal space was cleared of fascial remnants.

RESULTS

Twelve ribs and their corresponding intercostal veins, nerves, and arteries were identified. Within the lateral thoracic cavity, a novel muscle was seen along the posterior aspect of the ribs (Fig. 1). The novel muscle was seen in the inner and inferior aspect of the rib cage closer to the posteromedial body wall. The unusual muscle consisted of two narrow strips of muscle fibres originating from the inferior borders of ribs 11 and 12 and radiating to insert on the transverse processes of the T11 and T12 vertebrae. The novel muscle strips received blood supply from branches of the 11th and 12th intercostal vessels.

DISCUSSION

This case report describes the presence of an unknown and novel muscle seen in the inner aspect and on the posteromedial side of the rib cage. The muscle consists of narrow strips of two sets of fibres originating from the inferior borders of ribs 11 and 12 and radiating to insert on the transverse processes of the T11 and T12 vertebrae. A thorough literature review did not reveal description of a thoracic muscle with similar origin. Moreover, little information is found regarding variations in the muscles of thoracic wall, with the most common variation being the sternalis muscle, which is an anterior chest wall muscle and found in 8% of patients [1]. More specifically, there is a dearth of knowledge regarding muscle variations of the lateral thoracic cavity despite their known roles in regular respiratory function [1]. The authors did not find this muscle described in either contemporary anatomy textbooks or an encyclopaedia of anatomic variations. Thus, it appears that the variation found in this case report

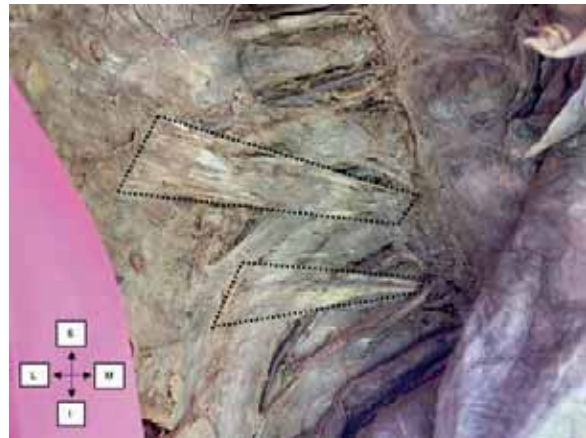


Figure 1. Novel thoracic muscle on the inferior and posteromedial aspect of the rib cage (dotted line); S — superior; M — medial; I — inferior; L — lateral.

is rare, and there has yet to be any reported cases of this novel muscle.

CONCLUSIONS

Thoracic wall muscles play a crucial role in aiding respiration through altering the volume of the chest cavity in regular physiology. As such, there is significant value in recording and being aware of variations that may affect these crucial structures. As this is a novel variation in a muscle group with a clinically important function, there is no current knowledge regarding any functional or clinical effect of this muscle. The unknown function of this novel muscle variant, as well as its possible clinical relevance in diagnosis, common procedures, and surgical outcomes warrants further study in the future.

Acknowledgements

The authors acknowledge and gratefully thank the individual whose body and tissues were used in this study for the advancement of physician education and patient care.

Conflict of interest: None declared

REFERENCES

1. Keith L, Moore AMRA, Dalley AF. *Essential Clinical Anatomy*. 5th ed. Lippincott Williams & Wilkins, Philadelphia 2015.
2. Raikos A, Paraskevas GK, Tzika M, et al. Sternalis muscle: an underestimated anterior chest wall anatomical variant. *J Cardiothorac Surg*. 2011; 6: 73, doi: [10.1186/1749-8090-6-73](https://doi.org/10.1186/1749-8090-6-73), indexed in Pubmed: [21575244](https://pubmed.ncbi.nlm.nih.gov/21575244/).
3. Tang A, Bordoni B. *Anatomy, Thorax, Muscles*. StatPearls, Treasure Island 2021.

The “sand watch” mandible

M.C. Rusu¹, M.D. Stoenescu^{1, 2}, M. Butucescu^{3, 4}, M. Săndulescu⁵

¹Division of Anatomy, Faculty of Dental Medicine, “Carol Davila” University of Medicine and Pharmacy, Bucharest, Romania

²“Carol Davila” Central Military Emergency University Hospital, Bucharest, Romania

³Division of Restorative Odontotherapy, Bucharest, Romania

⁴Faculty of Dental Medicine, “Carol Davila” University of Medicine and Pharmacy, Bucharest, Romania

⁵Division of Implant Prosthetic Therapy, Faculty of Dental Medicine, “Carol Davila” University of Medicine and Pharmacy, Bucharest, Romania

[Received: 26 October 2021; Accepted: 25 January 2022; Early publication date: 31 January 2022]

The lingual surface of the mandible’s body is commonly indicated as presenting the submandibular and sublingual fossae, which are separated by the mylohyoid line. The mylohyoid line attaches to the mylohyoid muscle (MM). Less attention has been paid to the ‘mylohyoid boutonnières’, which allow the ‘sublingual buttons’ to pass through the mylohyoid muscle in the submandibular space. The cone-beam computed tomography files of patients were routinely examined for anatomical studies. Two cases were found with unexpected morphologies of the mandible’s body — the mylohyoid lines were incomplete anteriorly, and herniated sublingual tissue determined an additional fossa inferior to that line in the premolar region. That fossa was termed the ‘accessory submandibular fossa’. It determined on coronal slices a ‘sand watch’ contour of the mandible’s body. With such a peculiar morphology, the mandible is more prone to fracture. Moreover, when inserting endosseous implants, the procedure should be carefully personalised in such rare cases. (Folia Morphol 2023; 82, 2: 424–428)

Key words: mandible, cone-beam computed tomography, mental foramen, premolar teeth, sublingual fossa, endosseous implants

INTRODUCTION

On the internal surface of the mandible’s body is the mylohyoid line, which separates the submandibular and sublingual fossae and normally courses toward the digastric fossa (Fig. 1). The lingual tuberosity (LT) appears as a bony shelf located lingual to the mandibular molars in some individuals, at the posterior extremity of the mylohyoid line [8]. Greatly enlarged LTs prevent the proper denture base extension [8]. Commonly, the LT does not extend on the lingual side of the mandibular premolars. The two fossae are occupied, respectively, by the submandibular and sublingual glands. The mylohyoid line is the origin of the mylohyoid muscle (MM), which is an anterior

suprahyoid muscle separating the submandibular and sublingual spaces [14]. A deficiency or hiatus on the part of the MM could lead to the penetration of the sublingual glands [10]. This was found in up to 42% of 150 cadavers [10, 13].

We hereby report an unexpected morphology for the mandible’s body in which the mylohyoid line was incomplete anteriorly and the herniated sublingual tissue determined an additional fossa inferior to that line, in the premolar region.

MATERIALS AND METHODS

The archived cone-beam computed tomography (CBCT) files of 2 patients, a 56-year-old male and

Address for correspondence: M.C. Rusu, MD, PhD (Med.), PhD (Biol.), Dr. Hab., Prof., “Carol Davila” University of Medicine and Pharmacy, 8 Eroilor Sanitari Blvd., RO-76241, Bucharest, Romania, tel: +40722363705, e-mail: mugurel.rusu@umfcd.ro; anatomon@gmail.com

This article is available in open access under Creative Common Attribution-Non-Commercial-No Derivatives 4.0 International (CC BY-NC-ND 4.0) license, allowing to download articles and share them with others as long as they credit the authors and the publisher, but without permission to change them in any way or use them commercially.



Figure 1. Internal view of a normal right hemimandible. Three-dimensional computed tomography volume rendering; 1 — mylohyoid line; 2 — sublingual fossa; 3 — submandibular fossa; 4 — digastric fossa; 5 — mental spine.

a 61-year-old female were documented for a peculiar morphology of the mandible. The subjects were routinely scanned, according to the manufacturer instructions using an iCat CBCT machine (Imaging Sciences International [Hatfield, PA, USA]) with the settings: resolution 0.250, field of view 130, and image matrix size 640 × 640. The CBCT files were exported as single uncompressed DICOM files, which were analysed with the Planmeca Romexis Viewer 3.5.0.R software, as in other previous studies [17–19]. There were evaluated the 2-dimensional planar cuts as well as 3-dimensional volume renderings. Relevant results were exported as image files (*.tif). The patients have given written informed consents for use of medical data if anonymised. The responsible authorities (2nd affiliation of the 2nd author) approved the study (approval no. 372/18.03.2020).

RESULTS

In the first case, the male (Fig. 2), the mandible was completely dentate. On the inner aspect of each hemimandible, left and right, LTs were found at the level of all molars. The posterior segments of the mylohyoid lines were applied on the LTs. At the level of the molars, the submandibular fossae were identified. However, on each side, the mylohyoid line continued toward the mental spine, not descending toward the digastric fossa. Beneath that line and anterior to the submandibular fossa accessory submandibular fossae, left and right, were identified in the premolar regions. Both mylohyoid lines were indented correspondingly. On each side, the mental foramen was located at the level of the second mandibular premo-

lar. On coronal cuts through the mental foramina, on each side, a “sand watch” contour of the mandible was identified due to the lingual cortical plate of the accessory submandibular fossa, which reached extremely close to the respective mental foramen.

In the second case, the female (Fig. 3), the mandible was partly edentulous. On the right side, the 1st mandibular premolar and all the molars were missing. On the left side, the 2nd premolar and the 3rd molar were missing. The inner side of each hemimandible had an evident mylohyoid line just in the posterior regions, at the level of the molars. At the level of the premolars, on each side, accessory submandibular fossae were found. As in the other case, the coronal cuts revealed a “sand watch” aspect of the mandible’s body. In this case, as in the previous one, the coronal cuts revealed incomplete mandibular attachments of the MMs, allowing protrusions of the sublingual tissues (sublingual buttons) to descend and occupy the accessory submandibular fossae.

DISCUSSION AND CONCLUSIONS

Gaughran (1963) [6] observed, in dissections of the submandibular space, a ‘mass of tissue lying between the mandible laterally and the MM medially’, which was seen ‘to continue through the MM, passing into the paralingual compartment’. He documented the standard gross anatomy textbooks at that time and observed that this anatomical condition was described by Henle (1871), Poirier (1900), Eisler (1912), Quain (1923), Morris (1942), Testut and Latarjet (1948), Pernkopf (1952), Lanz and Wachsmuth (1955), and Meyer (1958) (all quoted in [6]). Gaughran [6] also studied previous reports and found that the first hint regarding a hiatus on the part of the MM belongs to Forget (1870) (quoted in [6]). The following observation on the part of Gaughran, in 1963, is still valid: ‘Looking at the clinical literature concerned with anatomical studies of the submandibular and paralingual regions one obtains the overwhelming impression of a complete mylohyoid barrier between the two compartments.’ When Gaughran studied 162 cadavers (324 half-heads), he found, in 36.1%, ‘distinct masses of tissue resting on the inferior surface of the mylohyoid muscle’, which he termed sublingual buttons located either in the anterior half or in the anterior two thirds of the MM, in the cleft between that muscle and mandible’s body [6]. Therefore, such sublingual buttons can *bona fide* determine the bone accessory submandibular fossae, such as those report-

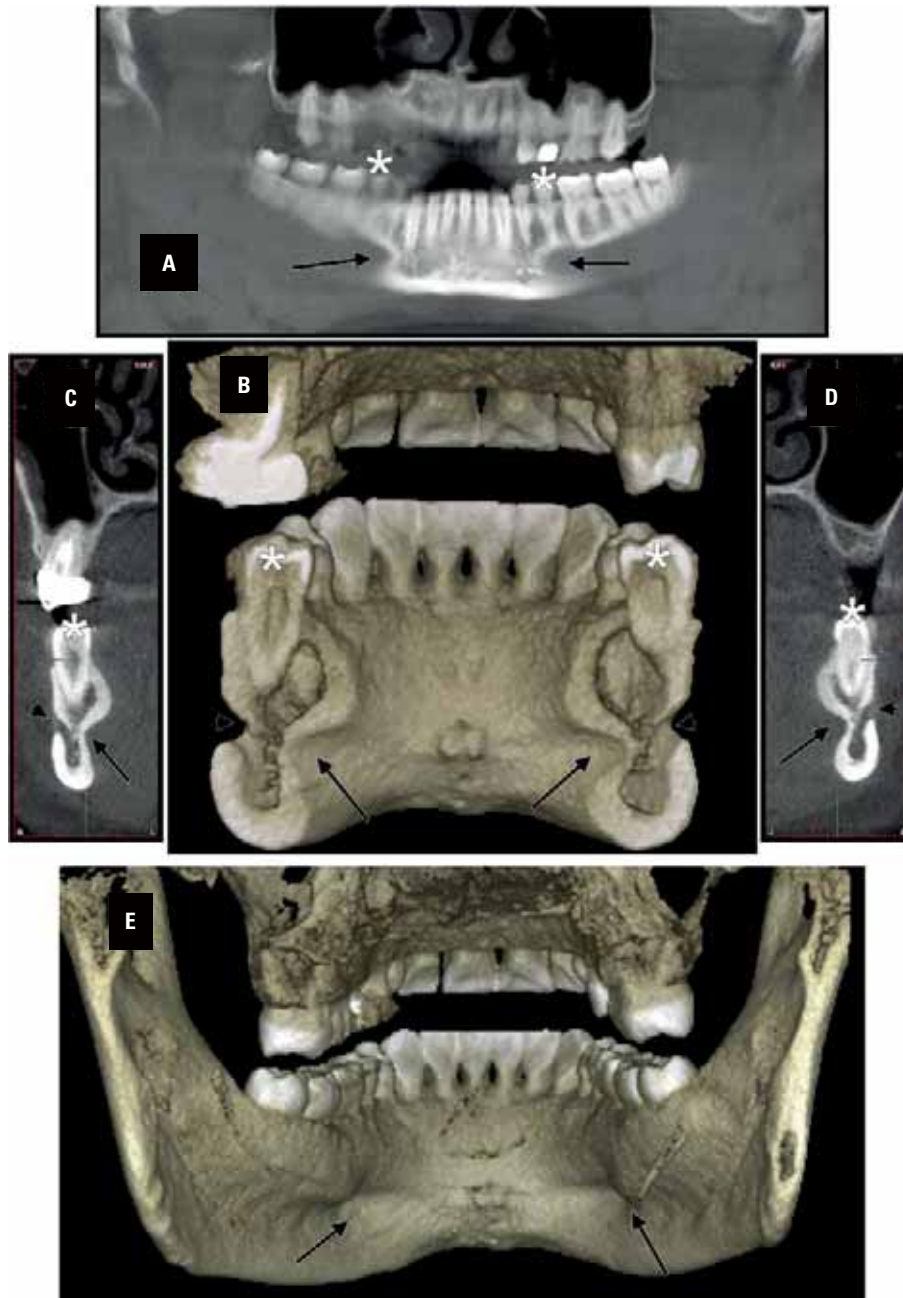


Figure 2. Case 1. The bilateral anomalous morphology of the “sand watch” mandible is documented on digital orthopantomogram (A), coronal cuts, 3-dimensional rendering (B, posterior view) and orthogonal (C, left side; D, right side), and complete 3-dimensional rendering (E, posterior view). The arrowheads indicate the mental foramen, the arrows indicate the deep accessory submandibular fossae beneath the premolar alveoli. The 2nd mandibular premolar is indicated (*).

ed here. Most of these buttons were processes of the sublingual gland, which penetrated the MM through a “mylohyoid boutonnière” and occurred bilaterally in just 19% of cases [6]. Through that boutonnière were also found, exclusively, fat herniations [6]. Branches of the submental vessels were also found within the boutonnière [6, 13, 22]. In just 0.9% of cases, neither glandular tissue nor fat was found within

the boutonnière of the MM [6]. Double sublingual buttons were found, with one being fatty and the other being glandular [5].

The prevalence of the mylohyoid boutonnière was reviewed by Ahmed et al. (2009) [1] and ranged from 30% to 80%. However, Windisch et al. (2004) [21] found herniations and deficiencies of the MM in just 12.2% of 205 cadavers. To our knowledge, sublingual

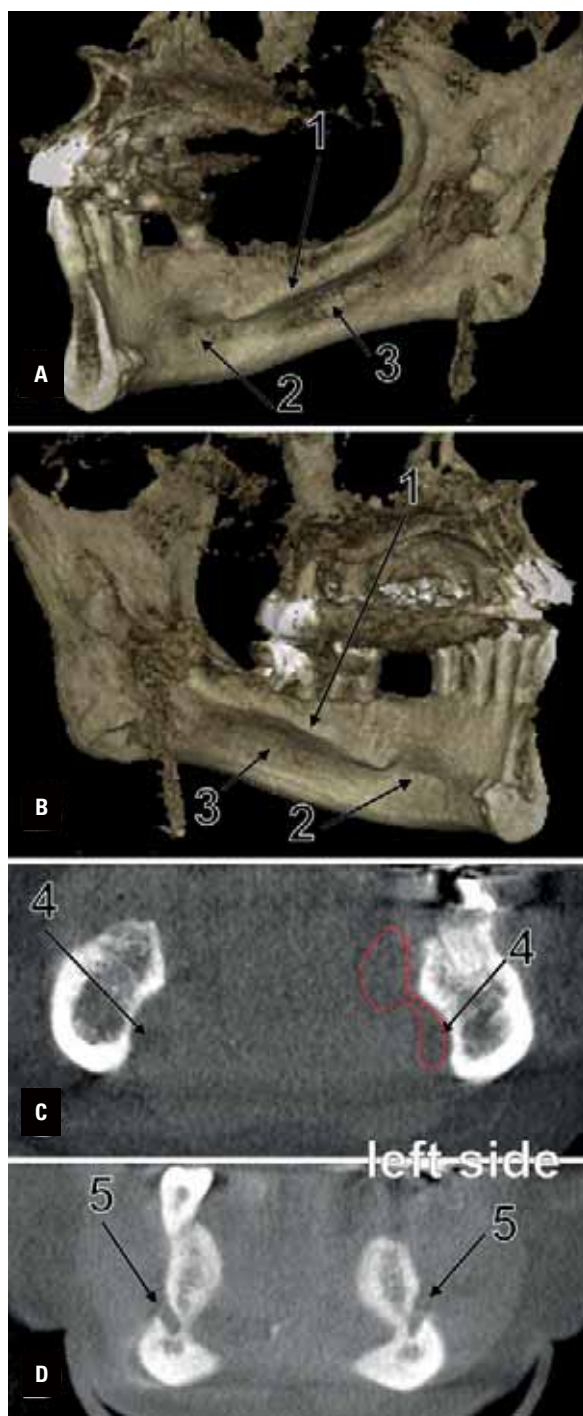


Figure 3. Case 2. Three-dimensional renderings of the right (A) and left (B) hemimandible. Coronal cut through the accessory submandibular fossa (C). Coronal cut at the level of the mental foramina — the “sand watch” aspect of the mandible (D); 1 — mylohyoid line; 2 — submandibular fossa; 3 — accessory submandibular fossa; 4 — bilateral sublingual buttons; 5 — mental foramina.

buttons were not previously observed to determine accessory submandibular fossae on the body of the mandible [13, 20, 21].

The accessory submandibular fossae we found occurred bilaterally. This could be suggestive of developmental symmetry on the part of the mylohyoid boutonnières. Such unexpected fossae of the inner cortical plate of the body of mandible, if unidentified, increase the risks of iatrogenic events during the placement of endosseous implants in the mandible; therefore, the pronounced lingual concavity of the bony plate should be taken into account and correlated with the length and inclination of an implant inserted in the premolar region of the mandible.

The region of the sublingual fossa is highly vulnerable to perforation during implant placement procedures [11]. While perforating the lingual plate of the mandible in the molar region may damage the salivary gland, a perforation in the premolar area carries a much higher risk because the osteotomy drill may damage the arterial plexus formed by the sublingual and submental arteries. There are several cases reported in the literature with a potentially serious risk for the patient [4, 7, 12, 15], and this concavity of the mandible in the premolar area may predispose patients to this kind of accident [3].

Moreover, it is well-known that a severe complication related to endosteal implants is the fracture of the edentulous, resorbed mandible [2, 16]. The fragility of the mandible may increase not only in edentulous mandibles but also in “sand watch” mandibles, such as those reported herein. Overloading such a “sand watch” mandible could also lead to an unexpected fracture during mastication or during a traumatic event, such as violence or an accident. Such mandibular fractures more commonly occur in the weaker areas of the mandible [9].

Clinicians, as well as students and teachers, should pay attention to individual anatomical characteristics [23]. Such “sand watch” mandibles can be identified in CBCT, and the treatment plan for such should be personalised.

Conflict of interest: None declared

REFERENCES

1. Ahmed M, Strauss M, Kassaie A, et al. Bilateral submandibular gland aplasia with clinico-radiological mass due to prolapsing sublingual salivary tissue through mylohyoid boutonniere: a case report and review. *Dentomaxillofac Radiol.* 2009; 38(2): 121–124, doi: [10.1259/dmfr/63254814](https://doi.org/10.1259/dmfr/63254814), indexed in Pubmed: [19176656](https://pubmed.ncbi.nlm.nih.gov/19176656/).
2. Chrcanovic BR, Custódio AL. Mandibular fractures associated with endosteal implants. *Oral Maxillofac Surg.*

- 2009; 13(4): 231–238, doi: [10.1007/s10006-009-0171-7](https://doi.org/10.1007/s10006-009-0171-7), indexed in Pubmed: [19789898](https://pubmed.ncbi.nlm.nih.gov/19789898/).
3. Çitir M, Gunduz K, Kasap P. Investigation the anterior mandibular lingual concavity by using cone-beam computed tomography. *Folia Morphol.* 2021; 80(4): 916–922, doi: [10.5603/FM.a2020.0128](https://doi.org/10.5603/FM.a2020.0128), indexed in Pubmed: [33084005](https://pubmed.ncbi.nlm.nih.gov/33084005/).
 4. Dubois L, de Lange J, Baas E, et al. Excessive bleeding in the floor of the mouth after endosseous implant placement: a report of two cases. *Int J Oral Maxillofac Surg.* 2010; 39(4): 412–415, doi: [10.1016/j.ijom.2009.07.062](https://doi.org/10.1016/j.ijom.2009.07.062), indexed in Pubmed: [20079609](https://pubmed.ncbi.nlm.nih.gov/20079609/).
 5. Engel JD, Harn SD, Cohen DM. Mylohyoid herniation: gross and histologic evaluation with clinical correlation. *Oral Surg Oral Med Oral Pathol.* 1987; 63(1): 55–59, doi: [10.1016/0030-4220\(87\)90340-9](https://doi.org/10.1016/0030-4220(87)90340-9), indexed in Pubmed: [3468466](https://pubmed.ncbi.nlm.nih.gov/3468466/).
 6. Gaughran GR. Mylohyoid boutonnière and sublingual bouton. *J Anat.* 1963; 97: 565–568, indexed in Pubmed: [14064098](https://pubmed.ncbi.nlm.nih.gov/14064098/).
 7. Kalpidis CD, Konstantinidis AB. Critical hemorrhage in the floor of the mouth during implant placement in the first mandibular premolar position: a case report. *Implant Dent.* 2005; 14(2): 117–124, doi: [10.1097/01.id.0000165028.89434.99](https://doi.org/10.1097/01.id.0000165028.89434.99), indexed in Pubmed: [15968182](https://pubmed.ncbi.nlm.nih.gov/15968182/).
 8. Kelly EK. The prosthodontist, the oral surgeon, and the denture-supporting tissues. *J Prosthet Dent.* 1966; 16(3): 464–478, doi: [10.1016/0022-3913\(66\)90051-5](https://doi.org/10.1016/0022-3913(66)90051-5), indexed in Pubmed: [5218889](https://pubmed.ncbi.nlm.nih.gov/5218889/).
 9. Khan AA, Banerjee A, Mbamalu D. Mandibular fracture caused by mastication. *Emerg Med J.* 2009; 26(2): 153, doi: [10.1136/emj.2008.062299](https://doi.org/10.1136/emj.2008.062299), indexed in Pubmed: [19164647](https://pubmed.ncbi.nlm.nih.gov/19164647/).
 10. Kiesler K, Gugatschka M, Friedrich G. Incidence and clinical relevance of herniation of the mylohyoid muscle with penetration of the sublingual gland. *Eur Arch Otorhinolaryngol.* 2007; 264(9): 1071–1074, doi: [10.1007/s00405-007-0321-1](https://doi.org/10.1007/s00405-007-0321-1), indexed in Pubmed: [17479273](https://pubmed.ncbi.nlm.nih.gov/17479273/).
 11. Kusum CK, Mody PV, Nooji D, et al. Interforaminal hemorrhage during anterior mandibular implant placement: An overview. *Dent Res J (Isfahan).* 2015; 12(4): 291–300, doi: [10.4103/1735-3327.161422](https://doi.org/10.4103/1735-3327.161422), indexed in Pubmed: [26288617](https://pubmed.ncbi.nlm.nih.gov/26288617/).
 12. Mordenfeld A, Andersson L, Bergstrom B. Hemorrhage in the floor of the mouth during implant placement in the edentulous mandible: A case report. *Int J Oral Maxillofac Implants.* 1997; 12: 558–561, indexed in Pubmed: [9274086](https://pubmed.ncbi.nlm.nih.gov/9274086/).
 13. Nathan H, Luchansky E. Sublingual gland herniation through the mylohyoid muscle. *Oral Surg Oral Med Oral Pathol.* 1985; 59(1): 21–23, doi: [10.1016/0030-4220\(85\)90109-4](https://doi.org/10.1016/0030-4220(85)90109-4), indexed in Pubmed: [3856203](https://pubmed.ncbi.nlm.nih.gov/3856203/).
 14. Otonari-Yamamoto M, Nakajima K, Tsuji Y, et al. Mylohyoid muscle defects: comparison of CT findings and dissected specimens. *Oral Radiology.* 2011; 27(1): 50–56, doi: [10.1007/s11282-011-0066-9](https://doi.org/10.1007/s11282-011-0066-9).
 15. Pigadas N, Simoes P, Tuffin JR. Massive sublingual haematoma following osseo-integrated implant placement in the anterior mandible. *Br Dent J.* 2009; 206(2): 67–68, doi: [10.1038/sj.bdj.2009.2](https://doi.org/10.1038/sj.bdj.2009.2), indexed in Pubmed: [19165260](https://pubmed.ncbi.nlm.nih.gov/19165260/).
 16. Raghoebar GM, Stellingsma K, Batenburg RH, et al. Etiology and management of mandibular fractures associated with endosteal implants in the atrophic mandible. *Oral Surg Oral Med Oral Pathol Oral Radiol Endod.* 2000; 89(5): 553–559, doi: [10.1067/moe.2000.105237](https://doi.org/10.1067/moe.2000.105237), indexed in Pubmed: [10807710](https://pubmed.ncbi.nlm.nih.gov/10807710/).
 17. Rusu MC, Săndulescu M, Sava CJ, et al. Bifid and secondary superior nasal turbinates. *Folia Morphol.* 2019; 78(1): 199–203, doi: [10.5603/FM.a2018.0047](https://doi.org/10.5603/FM.a2018.0047), indexed in Pubmed: [29802719](https://pubmed.ncbi.nlm.nih.gov/29802719/).
 18. Rusu MC, Sava CJ, Ilie AC, et al. Agger nasi cells versus lacrimal cells and uncinata bullae in cone-beam computed tomography. *Ear Nose Throat J.* 2019; 98(6): 334–339, doi: [10.1177/0145561319840836](https://doi.org/10.1177/0145561319840836), indexed in Pubmed: [31012345](https://pubmed.ncbi.nlm.nih.gov/31012345/).
 19. Sava CJ, Rusu MC, Săndulescu M, et al. Vertical and sagittal combinations of concha bullosa media and paradoxical middle turbinate. *Surg Radiol Anat.* 2018; 40(7): 847–853, doi: [10.1007/s00276-018-1998-0](https://doi.org/10.1007/s00276-018-1998-0), indexed in Pubmed: [29502247](https://pubmed.ncbi.nlm.nih.gov/29502247/).
 20. White DK, Davidson HC, Harnsberger HR, et al. Accessory salivary tissue in the mylohyoid boutonniere: A clinical and radiologic pseudolesion of the oral cavity. *AJNR Am J Neuroradiol.* 2001; 22: 406–412, indexed in Pubmed: [11156791](https://pubmed.ncbi.nlm.nih.gov/11156791/).
 21. Windisch G, Weiglein AH, Kiesler K. Herniation of the mylohyoid muscle. *J Craniofac Surg.* 2004; 15(4): 566–569, doi: [10.1097/00001665-200407000-00007](https://doi.org/10.1097/00001665-200407000-00007), indexed in Pubmed: [15213531](https://pubmed.ncbi.nlm.nih.gov/15213531/).
 22. Zdilla MJ, Bender-Heine AN, Lambert HW, et al. Clinical implications of the submental and sublingual arteries in relation to the mylohyoid boutonniere. *Otolaryngol Head Neck Surg.* 2021; 164(2): 322–327, doi: [10.1177/0194599820939852](https://doi.org/10.1177/0194599820939852), indexed in Pubmed: [32689891](https://pubmed.ncbi.nlm.nih.gov/32689891/).
 23. Żytkowski A, Tubbs R, Iwanaga J, et al. Anatomical normality and variability: Historical perspective and methodological considerations. *Transl Res Anat.* 2021; 23: 100105, doi: [10.1016/j.tria.2020.100105](https://doi.org/10.1016/j.tria.2020.100105).

Case report of the double-headed extensor hallucis longus

K. Ruzik¹ , K. Westrych¹, R.S. Tubbs^{2–5}, Ł. Olewnik¹, P. Łabętowicz⁶, N. Zielinska¹

¹Department of Anatomical Dissection and Donation, Medical University of Lodz, Poland

²Department of Neurosurgery, Tulane University School of Medicine, New Orleans, LA, United States

³Department of Neurosurgery and Ochsner Neuroscience Institute, Ochsner Health System, New Orleans, LA, United States

⁴Department of Anatomical Sciences, St. George's University, Grenada, West Indies

⁵Department of Surgery, Tulane University School of Medicine, New Orleans, LA, United States

⁶Department of Normal and Clinical Anatomy, Medical University of Lodz, Poland

[Received: 28 October 2021; Accepted: 30 November 2021; Early publication date: 17 February 2022]

Background: We present a case report of double-headed extensor hallucis longus (EHL) with potential clinical significance.

Materials and methods: Cadaveric dissection of the right lower limb of a 70-year-old at death female was performed for research and teaching purposes at the Department of Anatomical Dissection and Donation, Medical University of Lodz. The limb was dissected using standard techniques according to a strictly specified protocol. Each head and tendon of the muscle was photographed and subjected to further measurements.

Results: During dissection, an unusual type of EHL muscle was observed. It consisted of two muscle bellies, a main tendon and an accessory tendon. Both muscle bellies were located on anterior surface of the fibula and the interosseous membrane. The main tendon insertion was located on the dorsal aspect of the base of the distal phalanx of the big toe, while the accessory tendon insertion was located medially.

Conclusions: The EHL muscle is highly morphologically variable at both the point of origin and the insertion. Knowledge of its variations is connected to several pathologies such as foot drop, tendonitis, tendon rupture, and anterior compartment syndrome. (Folia Morphol 2023; 82, 2: 429–433)

Key words: extensor hallucis longus, additional muscle belly, anatomical variations, hallux valgus, embryology

INTRODUCTION

The extensor hallucis longus (EHL), in addition to the tibialis anterior and extensor digitorum longus, is part of the anterior compartment of the lower limb [24, 35]. Its origin is located on the anterior surface of the fibula and on the interosseous membrane lateral to the origin of the tibialis anterior and medial to the

origin of the extensor digitorum longus. The EHL is situated in the middle of these muscles and is largely covered by them [17].

The thin muscle belly becomes the tendon situated behind the superior and inferior extensor retinaculum and is then inserted into the dorsal aspect of the base of the distal phalanx of the big toe [38]. The

Address for correspondence: K. Ruzik, MD, Department of Anatomical Dissection and Donation, Medical University of Lodz, ul. Żeligowskiego 7/9, 90–752 Łódź, Poland, e-mail: kacper.ruzik@umed.lodz.pl

This article is available in open access under Creative Common Attribution-Non-Commercial-No Derivatives 4.0 International (CC BY-NC-ND 4.0) license, allowing to download articles and share them with others as long as they credit the authors and the publisher, but without permission to change them in any way or use them commercially.

EHL is innervated by branches originating from the deep fibular nerve and is supplied by branches of the anterior tibial artery [2, 34].

The role of the EHL is to extend the great toe. It is also responsible for dorsiflexion of the foot, adjunct foot eversion and inversion. There are EHL classifications for fetuses and adults, and more recently an exact classification was proposed by Zielinska et al. [1, 7, 17, 22, 26, 27, 38], distinguishing three types of EHL with subtypes. Anatomical variations of the EHL can predispose to hallux valgus deformity, tendonitis and acute compartment syndrome [11, 16, 33].

The present report describes a case of a two-headed EHL. Knowledge of the morphological variability of this muscle is significant for orthopaedic surgeons, physiotherapists and anatomists [17, 27].

CASE REPORT

During a routine dissection performed for research and teaching purposes at the Department of Anatomical Dissection and Donation, Medical University of Lodz, a supernumerary head of the EHL was found (Fig. 1). The dissection was performed using traditional anatomical methods according to a previously described protocol [17, 24, 27]. The subject of the dissection was a 70-year-old at death female cadaver.

The right lower limb was positioned in the supine position on the dissection table. First, all the skin, subcutaneous tissue and superficial fascia were removed up to the crural region and from the area of the foot. Secondly, the crural fascia was then carefully removed. Then the muscle bellies and tendons were cleaned from the medial to lateral side. After that, the muscles of the anterior crural compartment were separated from each other. Finally, the tendons were dissected to identify potential additional tendon bands.

Each head of the muscle and each tendon was photographed and measured using an electronic calliper with an accuracy of up to 0.1 mm (Mitutoyo Corporation, Kawasaki-shi, Kanagawa, Japan), each measurement being performed twice by two researchers.

The dominant muscle belly originated from the anterior surface of the fibula and from the interosseous membrane 208.45 mm above a line drawn between the malleoli. The width and thickness of the muscle were 19.67 mm × 3.55 mm at the origin. The length of the muscle belly was 167.88 mm. The width and thickness of the muscle were 4.27 mm × 1.91 mm upon passing the muscle belly.

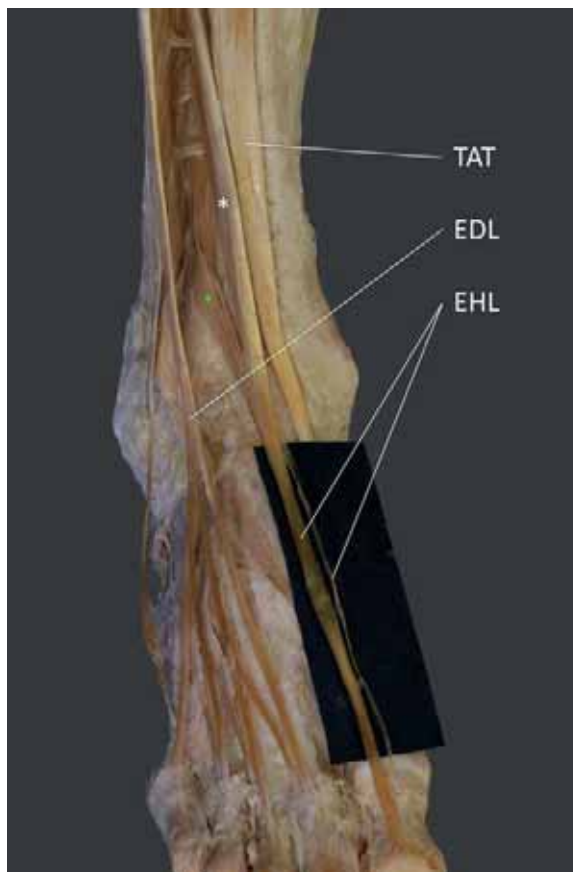


Figure 1. Supernumerary head of the extensor hallucis longus (EHL); EDL — extensor digitorum longus; TAT — tibialis anterior tendon; white star — main muscle belly; green star — additional muscle belly.

The lesser muscle belly appeared from beneath the anterior surface of the fibula and from the interosseous membrane 83.44 mm above a line drawn between the malleoli. The width and thickness of the muscle were 12.55 mm × 2.30 mm at the origin. The length of the muscle belly was 87.02 mm. The width and thickness of the muscle were 3.32 mm × 1.03 mm upon passing the muscle belly.

The type of insertion corresponds to subtype 2B proposed by Zielinska et al. [38]. The main tendon length was 184.60 mm. The width and thickness of the tendon were 5.63 mm × 0.95 mm at the insertion, which was located on the dorsal aspect of the base of the distal phalanx of the big toe. The additional tendon length was 119.59 mm. The width and thickness of the tendon were 2.33 mm × 0.42 mm at the insertion, which was located on the dorsal aspect of the proximal phalanx of the hallux, medial to the insertion of the EHL main tendon.

No extension point (i.e. the point where the tendon begins to expand into its insertional footprint) was observed at any of the described tendons.

Declarations and ethical approval

The cadavers were the property of the Department of Anatomical Dissection and Donation, Medical University of Lodz,

This article describes no studies involving human participants or animals performed by any of the authors.

DISCUSSION

Accessory muscle bellies in the upper and lower limbs have been widely reported. Such anatomical variations are common among large muscles such as the quadriceps femoris, coracobrachialis, biceps brachii, subscapularis and also vestigial muscles such as the plantaris [15, 29, 32, 36, 37]. An accessory muscle head can be related to potential compression of nerves or vessels but can be useful during reconstruction surgery [25, 36]. Whether additional muscle bellies are rare anatomical variations or are more often observed thanks to more carefully performed studies and better embalming of human cadavers is an open question. For example, Olewnik et al. [28] found an additional head of the quadriceps femoris muscle in 68 out of 106 lower limbs and opened the discussion: is it quadriceps or multiceps femoris?

Evolutionary aspect

The EHL, despite the quadratus plantae and plantaris muscles, appeared first in Mammalia [8, 18]. In all hominoids, it originates from the medial aspect of the fibula shaft, and in *Hylobates* and *Pan* there is an additional origin from the lateral condyle of the tibia [6]. In all taxa, insertion is onto the dorsum of the distal phalanx of the hallux. However, Ferrero et al. [12] reported an additional insertion onto the dorsum of the proximal phalanx in a gorilla limb. Origins from the interosseous membrane of the leg have also been demonstrated in the gorilla. Interestingly, Ferrero et al. [12] only reported this type of proximal attachment in a single orangutan limb. It was not described among apes.

Embryological aspect

To understand the complexity of the variations of the EHL insertion, it is necessary to consider its embryological basis. In a 5-week embryo, the limbs start

to form when the mesoderm migrates into the limb bud and anterior and posterior condensations start to generate the musculoskeletal system of the lower limb [3, 4]. The posterior condensation develops into the extensor musculature of the lower limb. The EHL splits from the deep portion of this extension mass, although its tendon remains fused with the extensor digitorum longus, with which it is often fused in later life [13, 20, 21].

Retinoic acid, sonic hedgehog (SHH), HOX genes (Hoxd-9, Hoxd-10, Hoxd-11, Hoxd-12, Hoxd-13), the apical ectodermal ridge, and the zone of polarizing activity are described as factors responsible for forming the lower limb musculature. Aberrant gene expressions can cause malformations of the limbs [5].

Morphological variability

Anatomy textbooks describe the insertion of the EHL into the dorsum of the base of the distal phalanx of the big toe. However, several studies have described variations of this insertion [1, 7, 17, 22, 26, 27].

Al-Saggaf [1] described three types of possible distal attachment. Type I (most common) was characterised as a single tendinous insertion on the dorsal aspect of the base of the distal phalanx of the big toe. In subsequent years, new classifications based on adult cadavers, fetuses and ultrasonography were proposed [1, 7, 9, 17, 22, 26, 27]. The most recent classification proposed by Zielinska et al. [38] summarizes the previously mentioned studies. They proposed three types of EHL insertion.

The proximal attachment of the EHL is less varied than the insertion. Egea et al. [10] described a case report of a double origin of the EHL. In contrast to our study they reported a medial and lateral origin of this muscle; we present upper and lower muscle bellies with separate innervations.

Clinical significance

The EHL tendon has been used in a variety of tendon transfer and tenodesis surgeries to correct iatrogenic hallux varus deformity, equinovarus foot deformity, clawed hallux associated with a cavus foot, and dynamic hyperextension of the hallux though it is usually used to prevent pedal imbalance after transmetatarsal amputation [16, 31].

Importantly, rupture or significant injury to the EHL tendon can result in a dropped hallux, loss of dorsiflexion, resulting in an unpaired gait [11]. This

can be treated surgically by transferring the first slip of the extensor digitorum longus and extensor hallucis brevis to the injured EHL. Rupture of this tendon is a result of laceration [11].

The EHL is also implicated in tendonitis, when the tendon becomes overstressed causing inflammation and pain [23]. Excessive calf muscle tightness, over-extension during exercise, and falling of the foot arch are listed as the most common factors [23]. The condition can be treated with stretching, non-steroidal anti-inflammatory drugs, and walking boots in more severe cases [19].

The anterior compartment of the leg is also the most common site for acute compartment syndrome, which can result from trauma, blunt force injury, or reperfusion after acute interruption of flow to muscles in the crural compartment. Swelling after these insults can lead to muscle ischemia because the muscles in these compartments are highly bound by the tough crural fascia, making it difficult for them to expand in response to injury. When the muscles expand, they can compress the artery, resulting in ischemic injury. Nerves can also be compressed causing loss of neuromuscular function. Importantly, definitive management of acute compartment syndrome is a subcutaneous fasciotomy [33]. There is also chronic compartment syndrome resulting from excessive exercise, causing pain and swelling. The pressure is increased by increases in blood flow and muscle mass from excessive exercise. As a result, arteries can be compressed [33]. It is feasible that an additional muscle belly will aggravate the symptoms of both acute and chronic compartment syndrome and be another anatomical structure that can compress nerves or vessels.

The hallux valgus deformity is a common forefoot pathology. It is characterised by lateral deviation of the great toe (hallux) and medial deviation of the first metatarsal and has several possible causes, the most common being wrongly matched footwear [38]. Other factors include muscle imbalance, genetic predisposition, ligamentous laxity and long-standing work in an upright posture [30]. However, the involvement of the EHL in hallux valgus pathogenesis is unclear. Natsis et al. [22] found that hallux valgus coincided with an accessory tendon of the EHL in 65.4% of the feet examined. If additional tendons predispose to hallux valgus deformity, it seems likely that a second muscle belly also affects the development of this pathology. However, biomechanical research is needed to confirm this prediction.

CONCLUSIONS

The EHL muscle is highly morphologically variable at both the points of origin and insertion. Knowledge of its variations is related to several pathologies such as foot drop, tendonitis, tendon rupture, and anterior compartment syndrome.

Acknowledgements

The authors sincerely thank those who donated their bodies to science so that anatomical research could be performed. Results from such research can potentially increase mankind's overall knowledge that can then improve patient care. Therefore, these donors and their families deserve our highest gratitude [14].

The authors wish to express their gratitude to all those who donated their bodies to medical science.

Conflict of interest: None declared

REFERENCES

1. Al-Saggaf S. Variations in the insertion of the extensor hallucis longus muscle. *Folia Morphol.* 2003; 62(2): 147–155, indexed in Pubmed: [12866676](#).
2. Aragonés P, Rodríguez-Niedenführ M, Quinones S, et al. Popliteal artery: Anatomical study and review of the literature. *Ann Anat.* 2021; 234: 151654, doi: [10.1016/j.aanat.2020.151654](#), indexed in Pubmed: [33278577](#).
3. Bardeen C. Studies of the development of the human skeleton. (A). The development of the lumbab, sacbal and coccygeal vertebwe. (B). The cubves and the pbopobtionate regional lengths of the spinal column during the first thbee months of embbyonic development. (C). The development of the skeleton of the posterior limb. *Am J Anat.* 1905; 4(3): 265–302, doi: [10.1002/aja.1000040302](#).
4. Bardeen C. Development and variation of the nerves and the musculature of the inferior extremity and of the neighboring regions of the trunk in man. *Am J Anat.* 1906; 6(1): 259–390, doi: [10.1002/aja.1000060108](#).
5. Barham G, Clarke NMP. Genetic regulation of embryological limb development with relation to congenital limb deformity in humans. *J Child Orthop.* 2008; 2(1): 1–9, doi: [10.1007/s11832-008-0076-2](#), indexed in Pubmed: [19308596](#).
6. Beddard F. VII. Contributions to the anatomy of the anthropoid apes. *Trans Zool Soc Lndon.* 1893; 13(5): 177–218, doi: [10.1111/j.1096-3642.1893.tb00049.x](#).
7. Bibbo C, Arangio G, Patel DV. The accessory extensor tendon of the first metatarsophalangeal joint. *Foot Ankle Int.* 2004; 25(6): 387–390, doi: [10.1177/107110070402500604](#), indexed in Pubmed: [15215022](#).
8. Boyer E. The musculature of the inferior extremity of the orang-utan *Simia satyrus*. *Am J Anat.* 1935; 56(2): 193–256, doi: [10.1002/aja.1000560203](#).
9. Denk CC, Oznur A, Sürücü HS. Double tendons at the distal attachment of the extensor hallucis longus muscle. *Surg*

- Radiol Anat. 2002; 24(1): 50–52, doi: [10.1007/s00276-002-0016-7](https://doi.org/10.1007/s00276-002-0016-7), indexed in Pubmed: [12197010](https://pubmed.ncbi.nlm.nih.gov/12197010/).
10. Egea JM, Cabeza L, Ortiz R, et al. Double origin of the extensor hallucis longus muscle: a case report. *Surg Radiol Anat.* 2019; 41(12): 1421–1423, doi: [10.1007/s00276-019-02309-5](https://doi.org/10.1007/s00276-019-02309-5), indexed in Pubmed: [31482300](https://pubmed.ncbi.nlm.nih.gov/31482300/).
 11. Fadel GE, Alipour F. Rupture of the extensor hallucis longus tendon caused by talar neck osteophyte. *Foot Ankle Surg.* 2008; 14(2): 100–102, doi: [10.1016/j.fas.2007.11.004](https://doi.org/10.1016/j.fas.2007.11.004), indexed in Pubmed: [19083623](https://pubmed.ncbi.nlm.nih.gov/19083623/).
 12. Ferrero EM, Pastor F, Fernandez F, Barbosa M, Diogo R, Wood B. Comparative anatomy of the lower limb muscles of hominoids: attachments, relative weights, innervation and functional morphology. In: Everett F, Hughes and Medison E. Hill (ed.) *PRIMATES: Classification, Evolution and Behavior*. Nova publishers 2012.
 13. Gros J, Tabin CJ. Vertebrate limb bud formation is initiated by localized epithelial-to-mesenchymal transition. *Science.* 2014; 343(6176): 1253–1256, doi: [10.1126/science.1248228](https://doi.org/10.1126/science.1248228), indexed in Pubmed: [24626928](https://pubmed.ncbi.nlm.nih.gov/24626928/).
 14. Iwanaga J, Singh V, Takeda S, et al. Acknowledging the use of human cadaveric tissues in research papers: Recommendations from anatomical journal editors. *Clin Anat.* 2021; 34(1): 2–4, doi: [10.1002/ca.23671](https://doi.org/10.1002/ca.23671), indexed in Pubmed: [32808702](https://pubmed.ncbi.nlm.nih.gov/32808702/).
 15. Je SS, Park B, Kim J, et al. Five-headed biceps brachii muscle with a rare origin from the tendon of pectoralis major muscle. *Anat Sci Int.* 2016; 91(1): 110–113, doi: [10.1007/s12565-015-0288-8](https://doi.org/10.1007/s12565-015-0288-8), indexed in Pubmed: [26012790](https://pubmed.ncbi.nlm.nih.gov/26012790/).
 16. Johnson KA, Spiegl PV. Extensor hallucis longus transfer for hallux varus deformity. *J Bone Joint Surg Am.* 1984; 66(5): 681–686, indexed in Pubmed: [6725316](https://pubmed.ncbi.nlm.nih.gov/6725316/).
 17. Karauda P, Shane Tubbs R, Polguy M, et al. Morphological variability of the extensor hallucis longus in human fetuses. *Ann Anat.* 2021; 234: 151627, doi: [10.1016/j.aanat.2020.151627](https://doi.org/10.1016/j.aanat.2020.151627), indexed in Pubmed: [33171222](https://pubmed.ncbi.nlm.nih.gov/33171222/).
 18. Lewis OJ. The phylogeny of the cruropedal extensor musculature, with special reference to the primates. *J Anat.* 1966; 100(PT 4): 865–880.
 19. Lezak B, Summers S. *Anatomy, Bony Pelvis and Lower Limb, Extensor Hallucis Longus Muscle*. StatPearls Publishing, Treasure Island (FL) 2021.
 20. Lezak B, Wehrle CJ, Summers S. *Anatomy, Bony Pelvis and Lower Limb, Posterior Tibial Artery*. StatPearls Publishing, Treasure Island (FL) 2020.
 21. Mróz I, Kielczewski S, Pawlicki D, et al. Blood vessels of the shin — anterior tibial artery - anatomy and embryology — own studies and review of the literature. *Folia Med Cracov.* 2016; 56(1): 33–47, indexed in Pubmed: [27513837](https://pubmed.ncbi.nlm.nih.gov/27513837/).
 22. Natsis K, Konstantinidis GA, Symeonidis PD, et al. The accessory tendon of extensor hallucis longus muscle and its correlation to hallux valgus deformity: a cadaveric study. *Surg Radiol Anat.* 2017; 39(12): 1343–1347, doi: [10.1007/s00276-017-1881-4](https://doi.org/10.1007/s00276-017-1881-4), indexed in Pubmed: [28601923](https://pubmed.ncbi.nlm.nih.gov/28601923/).
 23. Ng JM, Rosenberg ZS, Bencardino JT, et al. US and MR imaging of the extensor compartment of the ankle. *Radiographics.* 2013; 33(7): 2047–2064, doi: [10.1148/rg.337125182](https://doi.org/10.1148/rg.337125182), indexed in Pubmed: [24224598](https://pubmed.ncbi.nlm.nih.gov/24224598/).
 24. Olewnik Ł. Fibularis tertius: anatomical study and review of the literature. *Clin Anat.* 2019; 32(8): 1082–1093, doi: [10.1002/ca.23449](https://doi.org/10.1002/ca.23449), indexed in Pubmed: [31408221](https://pubmed.ncbi.nlm.nih.gov/31408221/).
 25. Olewnik Ł, Paulsen F, Tubbs RS, et al. Potential compression of the musculocutaneous, median and ulnar nerves by a very rare variant of the coracobrachialis longus muscle. *Folia Morphol.* 2021; 80(3): 707–713, doi: [10.5603/FM.a2020.0085](https://doi.org/10.5603/FM.a2020.0085), indexed in Pubmed: [32844391](https://pubmed.ncbi.nlm.nih.gov/32844391/).
 26. Olewnik Ł, Podgórski M, Polguy M, et al. Is ultrasound effective in determining variation of the insertion of the extensor hallucis longus tendon? *Clin Anat.* 2020; 33(8): 1235–1239, doi: [10.1002/ca.23572](https://doi.org/10.1002/ca.23572), indexed in Pubmed: [32017249](https://pubmed.ncbi.nlm.nih.gov/32017249/).
 27. Olewnik Ł, Podgórski M, Polguy M, et al. A cadaveric study of the morphology of the extensor hallucis longus: a proposal for a new classification. *BMC Musculoskelet Disord.* 2019; 20(1): 310, doi: [10.1186/s12891-019-2688-8](https://doi.org/10.1186/s12891-019-2688-8), indexed in Pubmed: [31266496](https://pubmed.ncbi.nlm.nih.gov/31266496/).
 28. Olewnik Ł, Tubbs RS, Ruzik K, et al. Quadriceps or multiceps femoris? Cadaveric study. *Clin Anat.* 2021; 34(1): 71–81, doi: [10.1002/ca.23646](https://doi.org/10.1002/ca.23646), indexed in Pubmed: [32644202](https://pubmed.ncbi.nlm.nih.gov/32644202/).
 29. Olewnik Ł, Zielinska N, Karauda P, et al. A three-headed plantaris muscle: evidence that the plantaris is not a vestigial muscle? *Surg Radiol Anat.* 2020; 42(10): 1189–1193, doi: [10.1007/s00276-020-02478-8](https://doi.org/10.1007/s00276-020-02478-8), indexed in Pubmed: [32382814](https://pubmed.ncbi.nlm.nih.gov/32382814/).
 30. Perera AM, Mason L, Stephens MM. The pathogenesis of hallux valgus. *J Bone Joint Surg Am.* 2011; 93(17): 1650–1661, doi: [10.2106/JBJS.H.01630](https://doi.org/10.2106/JBJS.H.01630), indexed in Pubmed: [21915581](https://pubmed.ncbi.nlm.nih.gov/21915581/).
 31. Roukis TS. Flexor hallucis longus and extensor digitorum longus tendon transfers for balancing the foot following transmetatarsal amputation. *J Foot Ankle Surg.* 2009; 48(3): 398–401, doi: [10.1053/j.jfas.2008.12.013](https://doi.org/10.1053/j.jfas.2008.12.013), indexed in Pubmed: [19423046](https://pubmed.ncbi.nlm.nih.gov/19423046/).
 32. Ruzik K, Waśniewska A, Olewnik Ł, et al. Unusual case report of seven-headed quadriceps femoris muscle. *Surg Radiol Anat.* 2020; 42(10): 1225–1229, doi: [10.1007/s00276-020-02472-0](https://doi.org/10.1007/s00276-020-02472-0), indexed in Pubmed: [32318799](https://pubmed.ncbi.nlm.nih.gov/32318799/).
 33. Via AG, Oliva F, Spoliti M, et al. Acute compartment syndrome. *Muscles Ligaments Tendons J.* 2015; 5(1): 18–22, indexed in Pubmed: [25878982](https://pubmed.ncbi.nlm.nih.gov/25878982/).
 34. Vittoria N, Giuseppe M, Ivano D, et al. The innervation of extensor hallucis longus muscle: an anatomical study for selective neurotomy. *Acta Neurochir (Wien).* 2009; 151(10): 1275–1279, doi: [10.1007/s00701-009-0504-1](https://doi.org/10.1007/s00701-009-0504-1), indexed in Pubmed: [19730770](https://pubmed.ncbi.nlm.nih.gov/19730770/).
 35. Zdilla MJ, Paulet JE, Lear JJ, et al. A review of extensor hallucis longus variants featuring a novel extensor primi interodii hallucis muscle merging with extensor hallucis brevis. *J Foot Ankle Surg.* 2018; 57(6): 1218–1220, doi: [10.1053/j.jfas.2018.03.031](https://doi.org/10.1053/j.jfas.2018.03.031), indexed in Pubmed: [30146339](https://pubmed.ncbi.nlm.nih.gov/30146339/).
 36. Zielinska N, Olewnik Ł. Six-headed coracobrachialis muscle. *Folia Morphol.* 2022; 81(3): 809–813, doi: [10.5603/FM.a2021.0082](https://doi.org/10.5603/FM.a2021.0082), indexed in Pubmed: [34608984](https://pubmed.ncbi.nlm.nih.gov/34608984/).
 37. Zielinska N, Olewnik Ł, Karauda P, et al. A very rare case of an accessory subscapularis muscle and its potential clinical significance. *Surg Radiol Anat.* 2021; 43(1): 19–25, doi: [10.1007/s00276-020-02531-6](https://doi.org/10.1007/s00276-020-02531-6), indexed in Pubmed: [32656573](https://pubmed.ncbi.nlm.nih.gov/32656573/).
 38. Zielinska N, Tubbs RS, Ruzik K, et al. Classifications of the extensor hallucis longus tendon variations: Updated and comprehensive narrative review. *Ann Anat.* 2021; 238: 151762, doi: [10.1016/j.aanat.2021.151762](https://doi.org/10.1016/j.aanat.2021.151762), indexed in Pubmed: [33992748](https://pubmed.ncbi.nlm.nih.gov/33992748/).

A unilateral sternopharyngeal branch of the sternocleidomastoid muscle in an aged Caucasian male: a unique cadaveric report

S. Silawal, S. Morgan, L. Ruecker, G. Schulze-Tanzil

Institute of Anatomy and Cell Biology, Paracelsus Medical University, Nuremberg and Salzburg, General Hospital Nuremberg, Nuremberg, Germany

[Received: 6 December 2021; Accepted: 12 January 2022; Early publication date: 17 February 2022]

The sternocleidomastoid muscle (SCM) consists of a sternal and a clavicular head which merge together and inserts distally posterolateral on the mastoid process and superior nuchal line, hence separating the anterior from the posterior triangle of the neck. Many types of structural variations in SCM have already been reported before. A unique variation of this muscle was discovered in an aged Caucasian male cadaver during an anatomical dissection at the Paracelsus Medical University in Nuremberg, Germany.

This study reports a right unilateral accessory muscular branch at the sternal head of the SCM which formed a tendon on the level of omohyoid muscle before dividing into anterior and posterior fascicles. The posterior fascicle attached to the external carotid artery at the site where a common trunk for lingual and facial artery branched off, drawing external carotid artery inferiorly to build an inferior loop, whereas the anterior fascicle passed further superior and broadened to form a muscular belly. This superior muscular belly extended to the posterior and lateral side of the pharynx to ultimately merge into the superior constrictor pharyngeal muscle. Such anatomical variation has never been reported before.

Therefore, we propose the nomenclature of this variational structure as a sternopharyngeal branch of the SCM. This report helps not only to inform the clinicians regarding the possible variation of this muscle during surgical procedures or radiological diagnostics but also encourage developmental researches in the future. (Folia Morphol 2023; 82, 2: 434–438)

Key words: sternopharyngeal, sternocleidomastoid, sternocervical, variation

INTRODUCTION

The sternocleidomastoid muscle (SCM) borders anteriorly the posterior triangle of the neck and limits the anterior triangle of the neck posteriorly. As per the anatomical literature, this muscle consists of a sternal and a clavicular head which merge together

and attaches posterolateral to the mastoid process and the superior nuchal line. Structures like spinal accessory nerve, branches of the cervical plexus, roots and trunks of the brachial plexus, phrenic nerve, subclavian artery, transverse cervical artery, external jugular vein, inferior belly of the omohyoid, scalene

Address for correspondence: Dr. med. S. Silawal, Institute of Anatomy and Cell Biology, Paracelsus Medical University, Salzburg and Nuremberg, Prof. Ernst Nathan Str. 1, 90419 Nuremberg, Germany, tel: +49 – (0)911-398-116771, fax: +49 – (0)911-398-6774, e-mail: sandeep.silawal@pmu.ac.at; sandeep.silawal@klinikum-nuernberg.de

This article is available in open access under Creative Common Attribution-Non-Commercial-No Derivatives 4.0 International (CC BY-NC-ND 4.0) license, allowing to download articles and share them with others as long as they credit the authors and the publisher, but without permission to change them in any way or use them commercially.

muscles, splenius muscle, levator scapulae muscle, occipital supraclavicular lymph nodes etc. lie in a close proximity posterior to the SCM. Submental, submandibular, superior and inferior carotid triangles are the regions in the anterior triangle of the neck. Common carotid artery, branches of the external carotid artery (ECA), the internal jugular vein, vagus nerve, branches of the ansa cervicalis are some of the examples of vital structures that are located in this triangle anterior to the SCM [11]. Anatomical variations of SCM could impact on above neighbouring structures via compression or narrowing of the surrounding space. Also, understanding the relevance of such variations is very important during surgical interventions in the neck area such as neck dissection. Various anomalies in the proximal heads of SCM have been described before [1–4, 6–10, 12, 15, 16, 18, 20, 21, 23]. During the developmental process of the shoulder girdle musculature, SCM and trapezoid muscles derive from the lateral plate mesoderm as a common embryonic source [19, 25]. The splitting of the embryological common trapezius-sternocleidomastoideus muscle system leads to two individual muscles of the neck, where they still share the common innervation of the accessory nerve [5]. This process of separation could result in different forms of muscle variations. Even though the variations in the proximal head are reportedly commonly, the variations described in the insertional end are not that common [13, 24]. A particular muscular variation, the so called cleidocervical or levator claviculae muscle shows that the muscle is attached proximally to the clavicle and distally to different levels of the cervical vertebra [17]. Our study reports a special variation of the SCM where a muscular branch from the sternal side finds non-osseous attachment sites which makes the case report unique.

CASE REPORT

During an anatomical dissection class at the Paracelsus Medical University, we discovered a 0.3 cm thick (maximum thickness) accessory muscular branch of the sternal head of the right SCM in a formalin-fixed 102-year-old Caucasian male (Fig. 1A). The cadavers are registered in the Munich body donation programme and contains written consents of the body donors. This inferior muscular belly deviated medially towards the carotid triangle. 6.5 cm distal from the sternal end, on the level of the crossing of the omohyoid muscle, the tendon of this muscle

was divided into anterior and posterior fascicles (Fig. 1A–C). The posterior fascicle was attached to the ECA (Fig. 1B, C). The insertion of this fascicle was located at a site where a common trunk for lingual and facial artery (cLA/FA) was branched from the ECA (Fig. 1B, C). Grade I kinking of the internal carotid artery was observed (Fig. 1B, C) [14]. The anterior fascicle passed further superior in front of cLA/FA before it broadened to form a superior muscular belly (Fig. 1B–D; #). This muscular belly then passed towards the posterior and lateral side of the pharynx to ultimately merge into the superior constrictor pharyngeal muscle (Fig. 1D). Glossopharyngeal nerve pierced the superior muscular belly at the narrow proximal section before it made a loop towards anterior (Fig. 1D). In comparison, the corresponding left side of the neck was void of this sternopharyngeal muscular variation (Fig. 2).

DISCUSSION

A small morphological study in an Indian population with 18 cadavers showed that 27.8% of the specimens had SCM variations with three unilateral and two bilateral presentations [23]. A different study describes a strap-like muscle originating from the middle third of the clavicle inserting at the transverse process of the C3 vertebra [20]. The level of cervical attachments of these cleidocervical (levator claviculae) muscles can, however, vary from atlas to the 6th cervical vertebra as reported in a literature survey by Obate et al. [17] on 2012. In another study with computed tomography scans, this muscle was identified in 6 subjects out of 300 subjects, which makes the prevalence of this muscle of about 2% [22]. A unique variation has been reported in our study. An accessory muscular branch from the sternal head split into anterior and posterior fascicles. Since the posterior fascicle of this muscular branch was attached to ECA, a muscular contraction during any movement of the head could have possible traction to this artery inferiorly. Any symptomatic consequence to this arterial traction cannot be followed back; however, the inferior looping of ECA was detected which could be a possible anatomical result of continuous traction during the development. The anterior fascicle ran in front of cLA/FA and built another thin muscular belly. This muscle ran upwards towards the posterior and lateral side of the pharynx and merged into the right superior pharyngeal constrictor muscle. Since the glossopharyngeal nerve penetrated this superior belly of the sternopharyngeal muscular branch, we

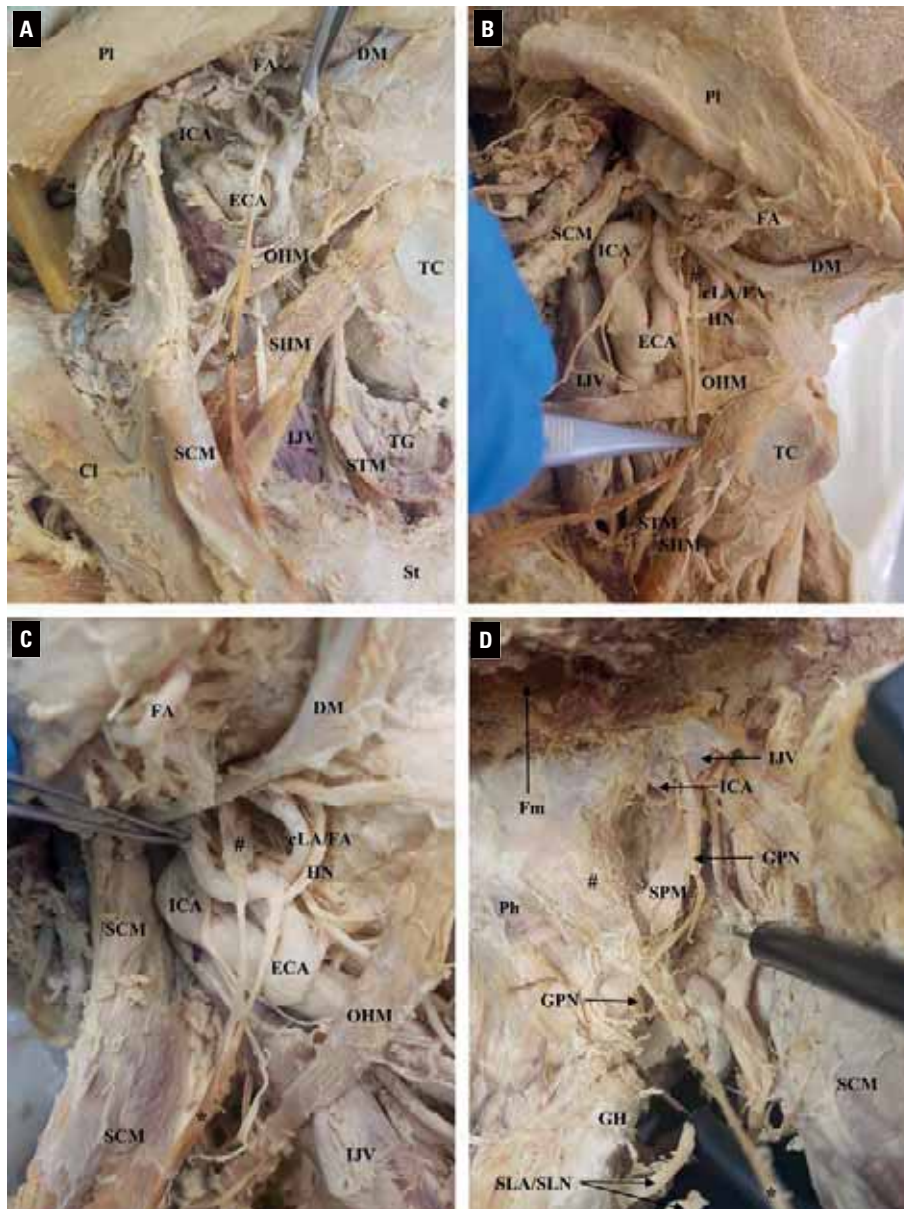


Figure 1. A–D. Chronological stages of dissections of the neck. The digastric sternopharyngeal muscle branch (*) of the sternocleidomastoid muscle (SCM) along the sternal head and the division into anterior and posterior tendinous fascicles. The anterior fascicle continues to form a superior muscular belly (#); **A.** Anterolateral view of the neck. The sternal head of the SCM has been detached and moved to the lateral side. The proximal end of the sternohyoid muscle (SHM) has been folded towards the lateral side; **B.** Lateral view of the neck. The facial vein has been removed. The musculotendinous junction of the sternopharyngeal muscular branch held by forceps with a light pull inferiorly to develop strain in the two tendinous fascicles; **C.** Closer view of the superior carotid triangle. The distal part of the external carotid artery (ECA) has been folded lightly towards the lateral side to show the superior muscular belly (#); **D.** Retropharyngeal view of the right lateral side. Insertion of the superior muscular belly (#) of the sternopharyngeal muscle to form part of the superior constrictor pharyngeal muscle. The muscle pierced by the glossopharyngeal nerve (GPN); CCA — common carotid artery; CI — clavicle; cLA/FA — common branch of lingual and facial artery; DM — digastric muscle; FA — facial artery; Fm — foramen magnum; GH — greater horn of the hyoid bone; HN — hypoglossal nerve; ICA — internal carotid artery; IJV — internal jugular vein; OHM — omohyoid muscle; Ph — pharynx; PI — platysma; SPM — stylopharyngeal muscle; St — sternum; SLA/SLN — superior laryngeal artery/nerve; STM — sternothyroid muscle; TC — thyroid cartilage; TG — thyroid gland.

assume that this nerve should be responsible for the innervation of the superior muscular belly. However, the inferior belly would be rather distant from the glossopharyngeal nerve, hence it would be more

appropriate to be innervated by the accessory nerve. Unfortunately, we cannot prove this hypothesis in this case report. Finally, we propose a proper nomenclature for this variation as a sternopharyngeal



Figure 2. Retropharyngeal overview for the comparison of both sides. Insertion of the superior muscular belly (#) of the sternopharyngeal muscle to form part of the superior constrictor pharyngeal muscle (red triangle). The inferior section of the muscle has been lifted and retracted to the lateral side; Ph — pharynx; GPN — glossopharyngeal nerve; GH — greater horn of the hyoid bone; SPM — stylopharyngeal muscle; Fm — foramen magnum.

branch of the SCM. Even though two fascicles of this muscular branch were observed, we assume that they resulted from splitting of a single muscle during the embryological development. The muscular fibres close to the ECA could have mal-attached to the artery. The pulsating behaviour of the artery could have split the muscle away from its original position. This hypothesis, however, has not been proven yet and would obviously need further investigation.

CONCLUSIONS

This manuscript reports a unique case of right sided unilateral muscular variation derived from the sternal head of the SCM ultimately merging into the right superior constrictor pharyngeal muscle. Such

anatomical variation has never been reported before. Therefore, we propose the nomenclature of this variational structure as a sternopharyngeal branch of the SCM. This novel discovery broadens the spectrum of SCM variations and help surgeons or physicians to understand the possible anatomy of neck while accessing the anterior triangle of the neck for any clinical purposes.

Acknowledgements

We are very thankful to the body donors for their contribution to the academic teaching and research field of anatomy.

Conflict of interest: None declared

REFERENCES

1. Amorim Júnior AA, Lins C, Cardoso A, et al. Variation in clavicular origin of sternocleidomastoid muscle. *Int J Morphol.* 2010; 28(1): 97–98, doi: [10.4067/s0717-95022010000100013](https://doi.org/10.4067/s0717-95022010000100013).
2. Anil A, Yaşar YK, Anil F, et al. Variation of bilateral multi-headed sternocleidomastoid muscle. *Gazi Med J.* 2017; 28(1): 56–57, doi: [10.12996/gmj.2017.17](https://doi.org/10.12996/gmj.2017.17).
3. Arquez HF. Muscular variation in the neck region with narrowing of the minor and major supraclavicular fossa. *Int Arch Med.* 2017; 10, doi: [10.3823/2478](https://doi.org/10.3823/2478).
4. Cherian S, Nayak S. A rare case of unilateral third head of sternocleidomastoid muscle. *Int J Morphol.* 2008; 26(1): 99–101, doi: [10.4067/s0717-95022008000100017](https://doi.org/10.4067/s0717-95022008000100017).
5. Fujita T. The smaller occipital nerve, its topographic relation to the trapezius-sternocleidomastoideus muscle system. A consideration on the factors determining the course of a nerve. *Okajimas Folia Anat Jap.* 1959; 33(4): 217–224, doi: [10.2535/ofaj1936.33.4_217](https://doi.org/10.2535/ofaj1936.33.4_217).
6. Fulmali D, Thute P, Keche H, et al. Variant sternocleidomastoid with extra clavicular head: a case report. *J Evolut Med Dent Sci.* 2020; 9(43): 3258–3260, doi: [10.14260/jemds/2020/715](https://doi.org/10.14260/jemds/2020/715).
7. Fulzele RR, Reddy A. Accessory clavicular head of sternocleidomastoid muscle: a case report. *Sch J Med Case Rep.* 2015; 3(98): 865–867.
8. Heo YR, Kim JW, Lee JH. Variation of the sternocleidomastoid muscle: a case report of three heads and an accessory head. *Surg Radiol Anat.* 2020; 42(6): 711–713, doi: [10.1007/s00276-019-02388-4](https://doi.org/10.1007/s00276-019-02388-4), indexed in Pubmed: [31768700](https://pubmed.ncbi.nlm.nih.gov/31768700/).
9. Kaur D, Jain M, Shukla L. Six heads of origin of sternocleidomastoid muscle: a rare case. *Int J Med Update EJournal.* 2013; 8: 62–64.
10. Kim SY, Jang HB, Kim J, et al. Bilateral four heads of the sternocleidomastoid muscle. *Surg Radiol Anat.* 2015; 37(7): 871–873, doi: [10.1007/s00276-014-1397-0](https://doi.org/10.1007/s00276-014-1397-0), indexed in Pubmed: [25422097](https://pubmed.ncbi.nlm.nih.gov/25422097/).
11. Kohan EJ, Wirth GA. Anatomy of the neck. *Clin Plast Surg.* 2014; 41(1): 1–6, doi: [10.1016/j.cps.2013.09.016](https://doi.org/10.1016/j.cps.2013.09.016), indexed in Pubmed: [24295343](https://pubmed.ncbi.nlm.nih.gov/24295343/).
12. Mansoor SN, Rathore FA. Accessory clavicular sternocleidomastoid causing torticollis in an adult. *Prog Rehabil Med.* 2018; 3: 20180006, doi: [10.2490/prm.20180006](https://doi.org/10.2490/prm.20180006), indexed in Pubmed: [32789231](https://pubmed.ncbi.nlm.nih.gov/32789231/).
13. Mehta V, Arora J, Kumar A, et al. Bipartite clavicular attachment of the sternocleidomastoid muscle: a case report. *Anat Cell Biol.* 2012; 45(1): 66–69, doi: [10.5115/acb.2012.45.1.66](https://doi.org/10.5115/acb.2012.45.1.66), indexed in Pubmed: [22536555](https://pubmed.ncbi.nlm.nih.gov/22536555/).
14. Metz H, Bannister RG, Murray-Leslie RM, et al. Kinking of the internal carotid artery. *Lancet.* 1961; 277(7174): 424–426, doi: [10.1016/s0140-6736\(61\)90004-6](https://doi.org/10.1016/s0140-6736(61)90004-6).
15. Natsis K, Asouchidou I, Vasileiou M, et al. rare case of bilateral supernumerary heads of sternocleidomastoid muscle and its clinical impact. *Folia Morphol.* 2009; 68(1): 52–54, indexed in Pubmed: [19384831](https://pubmed.ncbi.nlm.nih.gov/19384831/).
16. Nayak SR, Krishnamurthy A, Sij MK, et al. A rare case of bilateral sternocleidomastoid muscle variation. *Morphologie.* 2006; 90(291): 203–204, doi: [10.1016/s1286-0115\(06\)74507-6](https://doi.org/10.1016/s1286-0115(06)74507-6), indexed in Pubmed: [17432052](https://pubmed.ncbi.nlm.nih.gov/17432052/).
17. Odate T, Kawai M, Iio K, et al. Anatomy of the levator claviculae, with an overview and a literature survey. *Anat Sci Int.* 2012; 87(4): 203–211, doi: [10.1007/s12565-012-0148-8](https://doi.org/10.1007/s12565-012-0148-8), indexed in Pubmed: [22923186](https://pubmed.ncbi.nlm.nih.gov/22923186/).
18. Oh JS, Kim CE, Kim J, et al. Bilateral supernumerary clavicular heads of sternocleidomastoid muscle in a Korean female cadaver. *Surg Radiol Anat.* 2019; 41(6): 699–702, doi: [10.1007/s00276-019-02227-6](https://doi.org/10.1007/s00276-019-02227-6), indexed in Pubmed: [30919044](https://pubmed.ncbi.nlm.nih.gov/30919044/).
19. Pu Q, Huang R, Brand-Saberi B. Development of the shoulder girdle musculature. *Dev Dyn.* 2016; 245(3): 342–350, doi: [10.1002/dvdy.24378](https://doi.org/10.1002/dvdy.24378), indexed in Pubmed: [26676088](https://pubmed.ncbi.nlm.nih.gov/26676088/).
20. Raikos A, Paraskevas G, Triaridis S, et al. Bilateral supernumerary sternocleidomastoid heads with critical narrowing of the minor and major supraclavicular fossae: clinical and surgical implications. *Int J Morphol.* 2012; 30(3): 927–933, doi: [10.4067/s0717-95022012000300027](https://doi.org/10.4067/s0717-95022012000300027).
21. Ramesh Rao T, Vishnumaya G, Prakashchandra S, et al. Variation in the origin of sternocleidomastoid muscle: a case report. *Int J Morphol.* 2007; 25(3): 621–623, doi: [10.4067/s0717-95022007000300025](https://doi.org/10.4067/s0717-95022007000300025).
22. Rubinstein D, Escott EJ, Hendrick LL. The prevalence and CT appearance of the levator claviculae muscle: a normal variant not to be mistaken for an abnormality. *AJNR Am J Neuroradiol.* 1999; 20(4): 583–586, indexed in Pubmed: [10319965](https://pubmed.ncbi.nlm.nih.gov/10319965/).
23. Saha A, Mandal S, Chakraborty S, et al. Morphological study of the attachment of sternocleidomastoid muscle. *Singapore Med J.* 2014; 55(1): 45–47, doi: [10.11622/smedj.2013215](https://doi.org/10.11622/smedj.2013215), indexed in Pubmed: [24241357](https://pubmed.ncbi.nlm.nih.gov/24241357/).
24. Sarikcioglu L, Donmez BO, Ozkan O. Cleidooccipital muscle: an anomalous muscle in the neck region. *Folia Morphol.* 2001; 60(4): 347–349, indexed in Pubmed: [11770348](https://pubmed.ncbi.nlm.nih.gov/11770348/).
25. Theis S, Patel K, Valasek P, et al. The occipital lateral plate mesoderm is a novel source for vertebrate neck musculature. *Development.* 2010; 137(17): 2961–2971, doi: [10.1242/dev.049726](https://doi.org/10.1242/dev.049726), indexed in Pubmed: [20699298](https://pubmed.ncbi.nlm.nih.gov/20699298/).

A new type of the coracobrachialis muscle

N. Zielinska¹, P. Aragonés^{2, 3}, J.R. Sañudo³, P. Łabętowicz¹, R.S. Tubbs^{4–9}, Ł. Olewnik¹ 

¹Department of Anatomical Dissection and Donation, Medical University of Lodz, Poland

²Department of Orthopaedics Surgery, Hospital Santa Cristina, Madrid, Spain

³Department of Human Anatomy and Embryology, Facultad de Medicina, Universidad Complutense de Madrid, Spain

⁴Department of Neurosurgery, Tulane University School of Medicine, New Orleans, LA, United States

⁵Department of Neurosurgery and Ochsner Neuroscience Institute, Ochsner Health System, New Orleans, LA, United States

⁶Department of Anatomical Sciences, St. George's University, Grenada, West Indies

⁷Department of Neurology, Tulane University School of Medicine, New Orleans, LA, United States

⁸Department of Structural and Cellular Biology, Tulane University School of Medicine, New Orleans, LA, United States

⁹Department of Surgery, Tulane University School of Medicine, New Orleans, LA, United States

[Received: 31 October 2021; Accepted: 14 December 2021; Early publication date: 28 February 2022]

The coracobrachialis muscle belongs to the anterior group of the brachial region. Its main functions are flexion and adduction at the glenohumeral joint. It is highly morphologically variable, especially in the number of bellies, place of origin or insertion, and its relationship to the musculocutaneous nerve. Accessory structures associated with the coracobrachialis muscle include the coracobrachialis brevis or coracobrachialis longus muscle. The present case describes a three-headed coracobrachialis muscle with two such additional structures. One of these has a tendinous origin connected to the periosteum and located on the surgical neck of the humerus. Its insertion is fused with the third head of the coracobrachialis muscle. The other has a proximal attachment fused with the capsule of the shoulder joint, and its distal attachment is fused with the third head of the coracobrachialis muscle in place of its connection with the short head of the biceps brachii. This could result in better stabilisation of the glenohumeral joint; on the other hand, it could limit operational access during treatment of subscapularis tears. (Folia Morphol 2023; 82, 2: 439–444)

Key words: coracobrachialis muscle, accessory muscle, case report, coracocapsularis longus, coracobrachialis brevis, morphological variation, embryological development, embryogenesis

INTRODUCTION

The anterior group of the brachial region consists of the coracobrachialis (CBM), biceps brachii, and brachialis muscles. The origin of the CBM is located on the coracoid process, and the short head of the biceps brachii muscle (SHBB) has a proximal attachment in the same place [19, 20, 22]. It is worth mentioning that in some cases these two structures create a common junction [22]. The insertion of the

CBM is located on the medial surface and border of the body of the humerus, usually referred to as an anteromedial surface. Its distal attachment is between the proximal attachments of the triceps brachii and the brachialis muscle. Three parts of the CBM can be distinguished: proximal (from the coracoid process), middle (larger than the first), and distal, the largest and most superficial part [3]. The CBM is supplied by the brachial artery, or more precisely by its muscular

Address for correspondence: Ł. Olewnik, DPT, PhD, Ass. Prof., Department of Anatomical Dissection and Donation, Medical University of Lodz, ul. Żeligowskiego 7/9, 90–136 Łódź, Poland, e-mail: lukasz.olewnik@umed.lodz.pl

This article is available in open access under Creative Common Attribution-Non-Commercial-No Derivatives 4.0 International (CC BY-NC-ND 4.0) license, allowing to download articles and share them with others as long as they credit the authors and the publisher, but without permission to change them in any way or use them commercially.

branches. Innervation is delivered by the musculocutaneous nerve (MCN), which arises from the lateral cord of the brachial plexus [19, 20, 22].

The main functions of this muscle are flexion and adduction at the glenohumeral joint. Its proximal attachment allows it to participate in stabilisation of the humeral head (mainly anterior glenohumeral stability) [19, 22]. The subscapularis muscle has a similar function [26, 27]. The CBM also prevents deviation of the arm from the frontal plane during abduction [22]. This muscle not only fulfils those anatomical functions, it can also be used in procedures such as breast reconstruction after mastectomy or treatment of facial palsy. One of the most important conditions for performing such operations is good vascularisation [8, 11].

The CBM is highly morphologically variable [8–11, 14, 19, 20]. The most interesting variation is the occurrence of additional structures, not only the presence of additional head but also, very rarely, distinct muscles. The literature includes descriptions of structures such as the coracocapsularis muscle [3, 25], the coracobrachialis brevis muscle [1, 3, 17], the minor coracobrachialis muscle of Cruveilhier [6], the coracobrachialis longus muscle [3, 11, 14, 20], and others [11]. They differ in their place of attachment and location in relation to the CBM [11]. Some variations of the CBM are associated with the MCN. Anatomically, this nerve should pierce the CBM, but in some cases it is located close to the muscle without piercing it [7–9, 14, 19, 20, 23]. A very rare morphological variation is fusion of the CBM with the medial surface of the end of the pectoralis major muscle [18].

Some CBM variations can be clinically significant because of possible compression of different nerves or blood vessels [7–9, 19, 20]. Branches of the brachial plexus can potentially be compressed, leading for example to paralysis and hypoesthesia of the flexor group of the forearm [9]. However, the accessory variants of the muscle are not only pathological; as mentioned above, the CBM can be used during breast reconstruction after mastectomy. There should be no objection to using extra muscles such as the coracocapsularis for this procedure [7, 11].

The present report describes a three-headed variant of the CBM, which originated as a common junction with the SHBB from the coracoid process. Moreover, there were two additional structures. One of these had a tendinous origin connected with the periosteum and located on the surgical neck of the

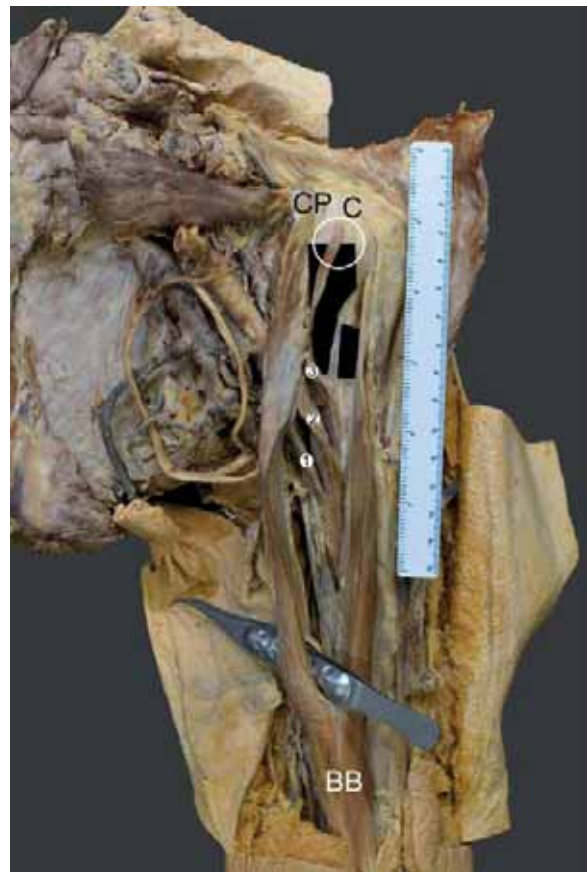


Figure 1. Unrecognized type of the coracobrachialis muscle; CP — coracoid process of the scapula; C — capsule of the humeral joint; BB — biceps brachii; 1 — first head of the coracobrachialis muscle; 2 — second head of the coracobrachialis muscle; 3 — third head of the coracobrachialis muscle.

humerus. Its insertion was fused with the third head of the CBM. The other had a proximal attachment fused with the capsule of the shoulder joint, and its distal attachment was fused with the third head of the CBM in place of its connection with the short head of the biceps brachii. Knowledge of the morphological variability of this muscle is essential for clinicians. To our knowledge, this is the first description of such a case (Fig. 1).

CASE REPORT

A 99-year-old male cadaver was subjected to routine anatomical dissection for research and teaching purposes at the University Complutense of Madrid. Dissection of the left upper limb revealed morphological variations related to the CBM.

In the present case, the CBM consisted of three heads. All three created a common junction with the SHBB, which functioned as a proximal attachment

Table 1. Morphometric measurements of individual parts of the coracobrachialis muscle (CBM)

	1st head of the CBM	2nd head of the CBM	3rd head of the CBM	1st additional structure	2nd additional structure
Length	72.60 mm	138.16 mm	34.81 mm**	65.41 mm*	39.14 mm*
CJ with the SHBB	Involved	Involved	Involved (but not involved in creation of the CJ)	Attached to the SHBB	Not involved
PA	The coracoid process	–	–		
Width	11.11 mm	–	–		
Thickness	5.71 mm	–	–		
PA					
Localization:	From the SHBB capsule of the surgical neck of shoulder joint the humerus				
Width	4.11 mm	8.99 mm	4.34 mm	3.46 mm	1.57 mm
Thickness	1.40 mm	1.89 mm	1.59 mm	1.95 mm	0.35 mm
DA					
Location:	Anteromedial surface of the humerus			Connected with the 3 rd head of the CBM	
Width	6.15 mm	7.81 mm	3.98 mm		
Thickness	1.81 mm	3.46 mm	0.49 mm		

*To the point of division; **From the point of division; SHBB — short head of the biceps brachii muscle; CJ — common junction; PA — proximal attachment; DA — distal attachment

located on the coracoid process. At the point of origin the width was 11.11 mm and the thickness was 5.71 mm. The distal attachment of all the heads of the CBM was located on the anteromedial surface of the humerus; it was 6.15 mm wide and 1.81 mm thick.

As mentioned above, the first head was attached to the SHBB. The length of the first belly was 72.60 mm. At the point of departure from the SHBB the width was 4.11 mm and the thickness 1.40 mm.

The second head could be recognized as a main belly. From the point of the junction with the SHBB its length was 136.16 mm. At the same point it was 8.99 mm wide and 1.89 mm thick.

The third head was really interesting. Its proximal attachment was also represented by a common junction with the SHBB. At the point of connection with the SHBB, the width was 4.64 mm and thickness 1.59 mm. However, this head was connected with two anomalous structures. The length of the third head between the place of division into these two morphological variants and its distal attachment was 34.81 mm.

The first additional structure was represented by a tendinous slip attached to the periosteum in the surgical neck of the humerus. At that location it was 1.57 mm wide and 0.35 mm thick. The distal attachment of this structure was fused with the third head of the CBM, and at this point of division it was 3.98 mm wide and 0.49 mm thick. The length of this

variant muscle from its origin to fusion with the third head was 39.14 mm.

The second structure was a proximal accessory band represented only by a muscular part, which was attached to the capsule of the shoulder joint. Its origin was 3.46 mm wide and 1.95 mm thick. Its distal attachment was fused with the third head of the CBM where it connected with the SHBB. The length from the origin to the fusion with the CBM was 65.41 mm.

An electronic calliper (Mitutoyo Corporation, Kawasaki-shi, Kanagawa, Japan) was used for the measurements. Each measurement was repeated twice with an accuracy of up to 0.1 mm.

No other morphological variabilities were found. Table 1 summarizes the morphometric measurements of the present case.

Ethical approval and consent to participate

The cadaver belonged to the Department of Anatomy and Embryology of the University Complutense of Madrid.

DISCUSSION

The CBM is highly morphologically variable [8–11, 14, 19, 20]. This is best demonstrated in the classification system by Szewczyk et al. [22], who identified three types with subtypes distinguished by different proximal attachments, and two types distinguished by different insertions. There were cases of CBMs

originating by one single belly from the coracoid process. There were also cases of CBMs with two heads, assigned to appropriate subtypes depending on whether both heads started on the coracoid process, or one on the coracoid process and the other from the SHBB. There were also cases of a CBM with three heads, two of which originated from the coracoid process and the third from the SHBB [22].

Two types were distinguished according to the insertion of the CBM. In the first, a single belly was attached to the distal 1/3 of the humerus. The second was characterised by two bellies, one attached to the distal 1/3 of the humerus and the other fused with the medial head of the triceps brachii [22].

The relationship between the CBM and the MCN was also studied. In some cases the MCN pierced the muscle belly, but there were also cases in which it passed between the heads of the CBM [22].

Although the system created by Szewczyk et al. [22] is the latest classification of the CBM, variabilities were observed around 150 years ago. For example, Wood [25] was the first to notice that the CBM can consist of three parts. The origin of the upper part was located on the coracoid process and the insertion was fused with the capsule of the shoulder joint. This structure is usually called the CBM superior, or brevis, or rotator humeri [25]. The middle part was attached to the mid-portion of the humerus and called the CBM proprius or medius. The third and lowest part was attached to the internal condyloid ridge, the internal intermuscular septum, or the trochlea, and it was called the CBM longus. Interestingly, the middle and the lowest part are fused and together to create the CBM; the CBM brevis is rather rare [3, 25].

Kyou-Jouffroy et al. [15] divided the CBM into three portions. All of them had a proximal attachment on the coracoid process, but they differed in the location of their distal attachments. The first part had an insertion on the medial epicondyle of the humerus, and this structure was called the CBM longus or superficialis. The second was attached to the humeral diaphysis and was called the CBM medius. The last was inserted on to the humeral neck and was called the CBM profundus or brevis [15].

The CBM brevis is an interesting structure [3, 25]. Its origin is located on the anterior surface of the coracoid process. It passes downwards and outwards and can insert on to the lesser tubercle or surgical neck of the humerus. In the present case, one of the additional structures was also attached to the surgical

neck of the humerus, but we cannot call it the CBM brevis. The main difference is that the attachment of the CBM brevis on the surgical neck functions as an insertion [3]; in our case it functions as a proximal attachment. The present case also has a tendinous slip passing downwards and fused with the third head of the CBM.

The literature describes another interesting structure called the coracocapsularis muscle [2, 3]. It was recognized as a variation of the CBM brevis, the insertion of which was fused with the capsule of the shoulder joint [2]. In the present case there is an additional structure attached to the capsule, but we cannot name this a coracocapsularis muscle either. The reason is the same as above: the attachment of the coracocapsularis fused with the capsule of the shoulder joint functions as an insertion [2, 3]. In our case, it functions as an origin passing downwards and fusing with the third head of the CBM.

While searching the literature for a structure that could correspond to our muscles, we found many interesting variants related to the CBM. For example, there is the coracobrachialis minor secundus [3], which typically originates from the coracoid process and inserts to the pectoralis major tendon [25]. There are also structures in which the insertion is fused with the tendon of the latissimus dorsi. They are named the CBM brevis s. rotator humeri, le court coracobrachialis, or the minor coracobrachial muscle of Cruveilhier [3, 6]. They all have origins on the coracoid process [3, 6].

Another variation was described by Chouke [5]. It had a proximal accessory band originating from the conoid ligament of the clavicle and inserting on to the medial intermuscular septum [5].

The literature also describes the CBM longus, sometimes named the CBM inferior. It is a very rare variant that can insert to the humerus, medial epicondyle, fibrous band of the medial intramuscular septum, i.e. Struther's ligament, or the tendinous part of the latissimus dorsi [3, 7, 10, 20, 25]. There was also a case of the CBM longus inserted on to the olecranon [20].

Considering all the aforementioned variants of the CBM, we can conclude that there is no special name for the additional structures we present here. We found only a case report by Catli et al. [4] in which the CBM was represented by three heads, two of which had a typical origin on the coracoid process. Their insertion was located on the middle third of the

humerus. The third head had the same point of distal attachment, but its proximal attachment was fused with the capsule of the glenohumeral joint [4]. The course of this head was therefore similar to one of the additional structures in the present case, but in the latter, it was also attached to the third head at the point of its connection with the SHBB.

Coexistence of three heads of the CBM and two additional structures, one of which originated from the surgical head of the humerus and the second from the capsule of the shoulder joint, has not yet been described in the literature. To our knowledge, therefore, this is the first description of such a case.

One question is: what causes such structures to appear? Possible reasons are changes during embryo development. During embryogenesis, the upper limb bud mesenchyme of the lateral plates differentiates into intrinsic muscles. The muscle primordia then fuse and a single muscle mass of the CBM is formed [24]. Not all muscle primordia fuse, but normally disappear through cell death [12]. However, if this process fails, accessory structures such as the coracocapsularis, coracobrachialis brevis, or coracobrachialis longus muscle can result. The structures described in the present case could have arisen in the same manner.

The course of these anomalous structures can have advantages. They can both contribute to better stabilisation of the shoulder joint. The first additional structure, which originated from the surgical neck of the humerus and was fused with the periosteum, could potentially prevent excessive external rotation of the humerus. The second, attached to the capsule and SHBB by the third head of the CBM, could prevent excessive anterior dislocation in the upper limb, allowing the anteroposterior and mediolateral position of the humerus to be maintained. In conclusion, these anomalous structures are involved dynamically and passively in the stability of the glenohumeral joint.

However, better stabilisation could entail some limitation of precise movements. To confirm this, biomechanical studies are needed [27]. Unfortunately, there are difficulties with this, the main one being that such structures are very rare. A solution could be to examine other additional structures that could potentially function in a similar way; for example, an accessory subscapularis muscle. If a case is found in which there is insertion by a tendinous slip attached to the capsule of the shoulder joint as a distinct structure, the superior migration of the humeral head and maintenance of its anteroposterior position could be limited.

Unfortunately, such additional structures could also have disadvantages. An operation is usually needed to treat subscapularis tendon tears [27]. During surgery, arthroscopic repair should be performed [16]. Among patients with full thickness tears less than 50%, one anchor should be made. Among patients with full thickness tears more than 50%, two anchors are necessary [16]. This procedure should be performed very carefully to avoid, for example, completely intersecting the rotator interval tissue and coracohumeral/superior glenohumeral ligaments [21].

In the present case, one of the additional structures was fused with the capsule of the shoulder joint, which anatomically covers the tendinous insertion of the subscapularis muscle. Occurrence of such an anomaly could be related to limitations during an operation, for example because the incision is markedly limited. To facilitate detection of different morphological variations, imaging methods such as ultrasonography or computed tomography can be used. However, there is no certainty that additional structures will be detected among all patients [16].

CONCLUSIONS

The coracobrachialis muscle is highly morphologically variable. This could be because the regression of some muscle primordia is prematurely terminated. The course of the described case could be associated with advantages such as better stabilisation of the glenohumeral joint. On the other hand, such variants can significantly limit operational access during treatment of subscapularis tears.

Acknowledgements

The authors sincerely thank those who donated their bodies to science so that anatomical research could be performed. Results from such research can potentially increase mankind's overall knowledge that can then improve patient care. Therefore, these donors and their families deserve our highest gratitude [13].

Conflict of interest: None declared

REFERENCES

1. Bauones S, Moraux A. The accessory coracobrachialis muscle: ultrasound and MR features. *Skeletal Radiol.* 2015; 44(9): 1273–1278, doi: [10.1007/s00256-015-2153-1](https://doi.org/10.1007/s00256-015-2153-1), indexed in Pubmed: 25924580.
2. Beattie PH. Description of bilateral coraco-brachialis brevis muscle, with a note on its significance. *Anat Rec.* 1947;

- 97(1): 123–126, doi: [10.1002/ar.1090970110](https://doi.org/10.1002/ar.1090970110), indexed in Pubmed: [20286224](https://pubmed.ncbi.nlm.nih.gov/20286224/).
3. Bergman R, Afifi A, Miyauchi R. Illustrated Encyclopedia of Human Anatomic Variations. Anatomy Atlas, 2017.
 4. Catli MM, Ozsoy U, Kaya Y, et al. Four-headed biceps brachii, three-headed coracobrachialis muscles associated with arterial and nervous anomalies in the upper limb. *Anat Cell Biol.* 2012; 45(2): 136–139, doi: [10.5115/acb.2012.45.2.136](https://doi.org/10.5115/acb.2012.45.2.136), indexed in Pubmed: [22822469](https://pubmed.ncbi.nlm.nih.gov/22822469/).
 5. Chouke KS. Variation of the coracobrachialis muscle. *Anat Rec.* 1924; 27(3): 157–163, doi: [10.1002/ar.1090270303](https://doi.org/10.1002/ar.1090270303).
 6. Cruveilhier J. *Traité d'anatomie descriptive I.* Asselin, Paris 1862.
 7. El-Naggar MMA. study on the morphology of the coracobrachialis muscle and its relationship with the musculocutaneous nerve. *Folia Morphol.* 2001; 60: 217–224, indexed in Pubmed: [11552663](https://pubmed.ncbi.nlm.nih.gov/11552663/).
 8. El-Naggar MM, Al-Saggaf S. Variant of the coracobrachialis muscle with a tunnel for the median nerve and brachial artery. *Clin Anat.* 2004; 17(2): 139–143, doi: [10.1002/ca.10213](https://doi.org/10.1002/ca.10213), indexed in Pubmed: [14974102](https://pubmed.ncbi.nlm.nih.gov/14974102/).
 9. Garbelotti SA, Marques SR, Rocha PR, et al. An unusual case of accessory head of coracobrachialis muscle involving lateral cord of brachial plexus and its clinical significance. *Folia Morphol.* 2017; 76(4): 762–765, doi: [10.5603/FM.a2017.0033](https://doi.org/10.5603/FM.a2017.0033), indexed in Pubmed: [28353299](https://pubmed.ncbi.nlm.nih.gov/28353299/).
 10. Georgiev GP, Landzhov B, Tubbs RS. A novel type of coracobrachialis muscle variation and a proposed new classification. *Cureus.* 2017; 9(7): e1466, doi: [10.7759/cureus.1466](https://doi.org/10.7759/cureus.1466), indexed in Pubmed: [28936378](https://pubmed.ncbi.nlm.nih.gov/28936378/).
 11. Georgiev GP, Tubbs RS, Landzhov B. Coracobrachialis longus muscle: humeroepitrochlearis. *Cureus.* 2018; 10(5): e2615, doi: [10.7759/cureus.2615](https://doi.org/10.7759/cureus.2615), indexed in Pubmed: [30027007](https://pubmed.ncbi.nlm.nih.gov/30027007/).
 12. Guha R, Satyanarayana N, Reddy CK, et al. Variant insertion of coracobrachialis muscle-morphological significance, embryological basis and clinical importance. *J Coll Med Sci.* 1970; 6(2): 42–46, doi: [10.3126/jcmsn.v6i2.3616](https://doi.org/10.3126/jcmsn.v6i2.3616).
 13. Iwanaga J, Singh V, Ohtsuka A, et al. Acknowledging the use of human cadaveric tissues in research papers: Recommendations from anatomical journal editors. *Clin Anat.* 2021; 34(1): 2–4, doi: [10.1002/ca.23671](https://doi.org/10.1002/ca.23671), indexed in Pubmed: [32808702](https://pubmed.ncbi.nlm.nih.gov/32808702/).
 14. Kopuz C, İçten N, Yildirim M. A rare accessory coracobrachialis muscle: a review of the literature. *Surg Radiol Anat.* 2003; 24(6): 406–410, doi: [10.1007/s00276-002-0079-5](https://doi.org/10.1007/s00276-002-0079-5), indexed in Pubmed: [12652369](https://pubmed.ncbi.nlm.nih.gov/12652369/).
 15. Kyou-Jouffroy M, Lessertissur J, Saban R, et al. Musculature des membres, membre pectoral, groupe branchial ventral. *Grassé PP.* 1971.
 16. Lenart BA, Ticker JB. Subscapularis tendon tears: Management and arthroscopic repair. *EFORT Open Rev.* 2017; 2(12): 484–495, doi: [10.1302/2058-5241.2.170015](https://doi.org/10.1302/2058-5241.2.170015), indexed in Pubmed: [29387471](https://pubmed.ncbi.nlm.nih.gov/29387471/).
 17. Loukas M, Aqueelah H. Musculocutaneous and median nerve connections within, proximal and distal to the coracobrachialis muscle. *Folia Morphol.* 2005; 64: 101–108, indexed in Pubmed: [16121328](https://pubmed.ncbi.nlm.nih.gov/16121328/).
 18. Mori M. Statistics on the musculature of the Japanese. *Okajimas Folia Anat Jpn.* 1964; 40: 195–300, doi: [10.2535/ofaj1936.40.3_195](https://doi.org/10.2535/ofaj1936.40.3_195), indexed in Pubmed: [14213705](https://pubmed.ncbi.nlm.nih.gov/14213705/).
 19. Olewnik Ł, Zielinska N, Karauda P, et al. The co-occurrence of a four-headed coracobrachialis muscle, split coracoid process and tunnel for the median and musculocutaneous nerves: the potential clinical relevance of a very rare variation. *Surg Radiol Anat.* 2021; 43(5): 661–669, doi: [10.1007/s00276-020-02580-x](https://doi.org/10.1007/s00276-020-02580-x), indexed in Pubmed: [32979058](https://pubmed.ncbi.nlm.nih.gov/32979058/).
 20. Olewnik Ł, Paulsen F, Tubbs RS, et al. Potential compression of the musculocutaneous, median and ulnar nerves by a very rare variant of the coracobrachialis longus muscle. *Folia Morphol.* 2021; 80(3): 707–713, doi: [10.5603/FM.a2020.0085](https://doi.org/10.5603/FM.a2020.0085), indexed in Pubmed: [32844391](https://pubmed.ncbi.nlm.nih.gov/32844391/).
 21. Park YB, Park YE, Koh KH, et al. Subscapularis tendon repair using suture bridge technique. *Arthrosc Tech.* 2015; 4(2): e133–e137, doi: [10.1016/j.eats.2014.11.013](https://doi.org/10.1016/j.eats.2014.11.013), indexed in Pubmed: [26052489](https://pubmed.ncbi.nlm.nih.gov/26052489/).
 22. Szewczyk B, Polgaj M, Paulsen F, et al. A proposal for a new classification of coracobrachialis muscle morphology. *Surg Radiol Anat.* 2021; 43(5): 679–688, doi: [10.1007/s00276-021-02700-1](https://doi.org/10.1007/s00276-021-02700-1), indexed in Pubmed: [33564931](https://pubmed.ncbi.nlm.nih.gov/33564931/).
 23. Tatar I, Brohi R, Sen F, et al. Innervation of the coracobrachialis muscle by a branch from the lateral root of the median nerve. *Folia Morphol.* 2004; 63(4): 503–506, indexed in Pubmed: [15712151](https://pubmed.ncbi.nlm.nih.gov/15712151/).
 24. Vollala VR, Nagabhooshana S, Bhat SM, et al. Multiple accessory structures in the upper limb of a single cadaver. *Singapore Med J.* 2008; 49(9): e254–e258, indexed in Pubmed: [18830534](https://pubmed.ncbi.nlm.nih.gov/18830534/).
 25. Wood J. On human muscular variations and their relation to comparative anatomy. *J Anat Physiol.* 1867: 44–59.
 26. Zielinska N, Olewnik Ł, Karauda P, et al. A very rare case of an accessory subscapularis muscle and its potential clinical significance. *Surg Radiol Anat.* 2021; 43(1): 19–25, doi: [10.1007/s00276-020-02531-6](https://doi.org/10.1007/s00276-020-02531-6), indexed in Pubmed: [32656573](https://pubmed.ncbi.nlm.nih.gov/32656573/).
 27. Zielinska N, Tubbs RS, Podgórski M, et al. The subscapularis tendon: A proposed classification system. *Ann Anat.* 2021; 233: 151615, doi: [10.1016/j.aanat.2020.151615](https://doi.org/10.1016/j.aanat.2020.151615), indexed in Pubmed: [33068734](https://pubmed.ncbi.nlm.nih.gov/33068734/).

Comment on “A left circumflex aorta with a displaced thoracic duct in a 94-year-old male cadaver: a case report with discussion on embryology”

D. Borthakur*, F. George*, R. Dhingra*

All India Institute of Medical Sciences, New Delhi, India

[Received: 21 August 2022; Accepted: 28 September 2022; Early publication date: 14 October 2022]

We read the article “A left circumflex aorta with a displaced thoracic duct in a 94-year-old male cadaver: a case report with discussion on embryology” by Ostrowski et al. [7] with great interest. In fact this article was selected for presentation in the weekly journal club organized by Department of Anatomy at All India Institute of Medical Sciences (AIIMS), New Delhi, India. The meticulous dissection by authors showing the anomalous left circumflex aorta (LCA) and other associated structures was appreciated by the faculty. The article is well written about an interesting case report. The authors discussed their findings in details; however, we wanted to add few additional points. The authors hypothesized that the concomitant presence of scoliosis although apparently seemed to displace the LCA to the right side, but it is more prudent to consider it an anomaly during embryogenesis, specifically regression of the left dorsal aorta and its retro-oesophageal course. Agreeing with the authors and erstwhile observations by Sanchez Torres and Roldan Conesa [9], we also believe that the LCA anomaly is inborn and related to embryological deviation. It is not less than a miracle to witness such an extremely rare anomaly in an individual who lived 94 years without obvious clinical symptoms and surgical procedure, which raises a question here. It also emphasizes the need of modified approach towards the art of eliciting past medical history from the kin at the time of body donation. The aorta is seen significantly larger than average throughout its course,

which can be due to increase in external diameter or aortic wall thickness with simultaneous reduction in elastin density in the tunica media with advancing age. Studies show that the number of elastic lamellae and the physiological circumferential stress per unit area of the circumferential lamellae remains always constant [2]. Therefore some degree of age-related ectasia is expected in the vessel, but significant dilatation without any compressive symptoms is difficult to interpret. Probably histology of the same could have revealed the state of degeneration of elastin fibres, their fibrosis along with elastin fragmentation in the tunica media as well as internal and external elastic laminae [5]. Considering the triad of LCA, scoliosis and aberrant right sided thoracic duct, we want to draw attention to an important gene *TBX1* (T-box DNA binding transcription factor) involved in 22q11 micro deletion syndrome (also known as the Di-George syndrome with multiple congenital defects) and Goldenhar syndrome with pharyngeal arch artery defects [4]. *TBX1* has been shown to be crucial for mesenteric lymphangiogenesis by regulating expression of vascular endothelial growth factor receptor 3 (VEGFR3) in endothelial cells [3]. An important observation was made that in *TBX*-null conditions, lymph angiogenesis did occur but was highly disorganized, which suggests that *TBX1* is not merely crucial for lymph angiogenesis but also important for its maintenance [3]. Thus, *TBX1* is not essential for lymphangiogenesis per se; rather, it is required for the devel-

Address for correspondence: Prof. Dr. R. Dhingra, PhD, Department of Anatomy, All India Institute of Medical Sciences (AIIMS), New Delhi, Ansari Nagar-110029, India, e-mail: renudhingraaiims@gmail.com

*All authors contributed equally to this work.

This article is available in open access under Creative Common Attribution-Non-Commercial-No Derivatives 4.0 International (CC BY-NC-ND 4.0) license, allowing to download articles and share them with others as long as they credit the authors and the publisher, but without permission to change them in any way or use them commercially.

opment of the lymphatic network. This could explain the right sided thoracic duct. *TBX1* is also reported to be extensively expressed in the endothelium of blood vessels [8, 10]. Evidences suggest that genetic variant of *TBX1* is linked with idiopathic scoliosis and optimal expression of *TBX1* is required during pharyngeal arch artery development [1, 6]. Therefore a genetic study investigating the expression *TBX1* gene can be undertaken in similar cases to elucidate the underlying molecular embryonic regulatory mechanism. Also an attempt to explore the lymphatic drainage of left side could also have been done as the authors did not find any lymphatic duct draining into left venous angle (according to Ostrowski et al. [7] “No vessel draining into the left venous angle was visualised by macroscopic dissection.”). A proofreading error which drew our attention is seen in the abstract section where thoracic duct is mentioned to be draining into the right internal carotid vein (according to Ostrowski et al. [7] “However, the thoracic duct was placed on the right, and drained into the right internal carotid vein.”) which might perplex readers. Such an inadvertent error, although minor might confuse the readers. We hope our concerns will be considered and we will appreciate additional clarification in this regard. We are eagerly waiting for author’s further investigative report to solve the molecular mystery of LCA embryogenesis.

Conflict of interest: None declared

REFERENCES

1. Anderson RH, Bamforth SD. Morphogenesis of the mammalian aortic arch arteries. *Front Cell Dev Biol.* 2022; 10: 892900, doi: [10.3389/fcell.2022.892900](https://doi.org/10.3389/fcell.2022.892900), indexed in Pubmed: [35620058](https://pubmed.ncbi.nlm.nih.gov/35620058/).
2. Changes S, Human IN, Aortas T, et al. Mechanical and structural changes in human. *Acta Biomater.* 2020; 103: 172–188, doi: [10.1016/j.actbio.2019.12.024](https://doi.org/10.1016/j.actbio.2019.12.024).
3. Chen Li, Mupo A, Huynh T, et al. *Tbx1* regulates *Vegfr3* and is required for lymphatic vessel development. *J Cell Biol.* 2010; 189(3): 417–424, doi: [10.1083/jcb.200912037](https://doi.org/10.1083/jcb.200912037), indexed in Pubmed: [20439995](https://pubmed.ncbi.nlm.nih.gov/20439995/).
4. Glaeser AB, Santos AS, Diniz BL, et al. Candidate genes of oculo-auriculo-vertebral spectrum in 22q region: A systematic review. *Am J Med Genet A.* 2020; 182(11): 2624–2631, doi: [10.1002/ajmg.a.61841](https://doi.org/10.1002/ajmg.a.61841), indexed in Pubmed: [32893956](https://pubmed.ncbi.nlm.nih.gov/32893956/).
5. Komutrattananont P, Mahakkanukrauh P, Das S. Morphology of the human aorta and age-related changes: anatomical facts. *Anat Cell Biol.* 2019; 52(2): 109–114, doi: [10.5115/acb.2019.52.2.109](https://doi.org/10.5115/acb.2019.52.2.109), indexed in Pubmed: [31338225](https://pubmed.ncbi.nlm.nih.gov/31338225/).
6. Li Y, Wu Z, Xu L, et al. Genetic Variant of *TBX1* Gene Is Functionally Associated With Adolescent Idiopathic Scoliosis in the Chinese Population. *Spine (Phila Pa 1976).* 2021; 46(1): 17–21, doi: [10.1097/BRS.0000000000003700](https://doi.org/10.1097/BRS.0000000000003700), indexed in Pubmed: [32947497](https://pubmed.ncbi.nlm.nih.gov/32947497/).
7. Ostrowski P, Popovchenko S, Bonczar M, et al. A left circumflex aorta with a displaced thoracic duct in a 94-year-old male cadaver: a case report with discussion on embryology. *Folia Morphol.* 2023; 82(2): 400–406, doi: [10.5603/FM.a2022.0043](https://doi.org/10.5603/FM.a2022.0043), indexed in Pubmed: [35481702](https://pubmed.ncbi.nlm.nih.gov/35481702/).
8. Paylor R, Glaser B, Mupo A, et al. *Tbx1* haploinsufficiency is linked to behavioral disorders in mice and humans: implications for 22q11 deletion syndrome. *Proc Natl Acad Sci U S A.* 2006; 103(20): 7729–7734, doi: [10.1073/pnas.0600206103](https://doi.org/10.1073/pnas.0600206103), indexed in Pubmed: [16684884](https://pubmed.ncbi.nlm.nih.gov/16684884/).
9. Sánchez Torres G, Roldán Conesa D. [Left aortic arch without a circumflex segment and a right descending aorta: a hypothetical case and a real example]. *Arch Inst Cardiol Mex.* 1989; 59(2): 125–131, indexed in Pubmed: [2764632](https://pubmed.ncbi.nlm.nih.gov/2764632/).
10. Vitelli F, Morishima M, Taddei I, et al. *Tbx1* mutation causes multiple cardiovascular defects and disrupts neural crest and cranial nerve migratory pathways. *Hum Mol Genet.* 2002; 11(8): 915–922, doi: [10.1093/hmg/11.8.915](https://doi.org/10.1093/hmg/11.8.915), indexed in Pubmed: [11971873](https://pubmed.ncbi.nlm.nih.gov/11971873/).

Unreported bilateral thoracic muscle — is it a new variant or a well-known subcostal muscle?

G.P. Georgiev¹ , Ł. Olewnik² 

¹Department of Orthopaedics and Traumatology, University Hospital Queen Giovanna – ISUL, Medical University of Sofia, Bulgaria

²Department of Anatomical Dissection and Donation, Chair of Anatomy and Histology, Medical University of Lodz, Poland

[Received: 28 March 2022; Accepted: 3 May 2022; Early publication date: 20 May 2022]

We read with interest the article by Lee et al. [2] on a supposedly previously unreported variation — “A rare unreported bilateral thoracic muscle on the inferior and posteromedial aspect of the rib cage: case report and literature review.” The muscle was presented by additional muscle strips that were found in the inner and inferior aspect of the rib cage closer to the posteromedial body wall. The “unreported” muscle consisted of two strips of narrow muscle fibres that originated from the inferior borders of ribs 11 and 12 that radiated to be inserted on the transverse processes of the T11 and T12 vertebrae. According to Lee et al. [2], only a few anatomical variations in thoracic wall muscles have been reported.

However, we do not agree with the author’s claims that this is a novel, previously unreported muscle. This is a classic case of subcostal muscle and is well described elsewhere [5]. This muscle is widely known to anatomists and surgeons, e.g., Bergman et al. [1] — “Illustrated encyclopedia of human anatomic variations”. They also point out that the subcostales are usually better developed on the inner surface of the thorax and are variable in number. During our dissection courses, we frequently observed the presented “unreported” subcostal muscle. We also cannot accept the statement that only a few variations of thoracic wall muscles have been reported in the literature. Numerous variant muscles of the thoracic region have been described in different articles and presented in human atlases and surgical books [1, 3–5]. The reference section of the so-called review is also poorly presented. If the authors pretend that this article present something new and made literature review,

they need to make extensive research in the literature, not only 3 references. Another question exists: how do they accept this muscle as unreported without using the classical old anatomical books? Moreover, why we do not see the other side of the thorax to observe the contralateral “unreported” muscle, and why is there no photograph that clearly presents the attachment of the transverse processes of the T11 and T12 vertebrae to which the novel muscle attached?

In conclusion, we recommend that when the authors accept a novel unreported variation first to check carefully the classical anatomical books, not only quick search in PubMed. This will prevent future miscommunications.

Conflict of interest: None declared

REFERENCES

1. Bergman RA, Afifi AK, Miyauchi R (2022) Subcostalis. In: Illustrated encyclopedia of human anatomic variations. Available via DIALOG. <https://www.anatomyatlases.org/AnatomicVariants/MuscularSystem/Text/S/44Subcostalis.shtml> (Accessed 19 March 2020).
2. Lee A, Dean C, Labagnara K, et al. A rare unreported bilateral thoracic muscle on the inferior and posteromedial aspect of the rib cage: case report and literature review. *Folia Morphol.* 2023; 82(2): 422–423, doi: [10.5603/FM.a2022.0028](https://doi.org/10.5603/FM.a2022.0028), indexed in Pubmed: [35347697](https://pubmed.ncbi.nlm.nih.gov/35347697/).
3. Macalister A. Additional observations on muscular anomalies in human anatomy (third series), with a catalogue of the principal muscular variations hitherto published. *Trans Roy Irish Acad.* 1875; 25: 1–130.
4. Snosek M, Loukas M. Thoracic wall muscles. In: Tubbs RS, Shoja MM, Loukas M (Eds.). *Bergman’s comprehensive encyclopedia of human anatomic variation*. Wiley & Sons, Inc., Hoboken, New Jersey 2016: 335–368.
5. Standing S. *Gray’s Anatomy. The Anatomical Basis of Clinical Practice*. Elsevier, Edinburgh 2020.

Address for correspondence: G.P. Georgiev, MD, PhD, DSc, Department of Orthopaedics and Traumatology, University Hospital Queen Giovanna – ISUL, Medical University of Sofia, 8, Bialo More Str., BG 1527 Sofia, Bulgaria, tel: +359884 493523, e-mail: georgievpp@yahoo.com

This article is available in open access under Creative Common Attribution-Non-Commercial-No Derivatives 4.0 International (CC BY-NC-ND 4.0) license, allowing to download articles and share them with others as long as they credit the authors and the publisher, but without permission to change them in any way or use them commercially.

Morphometric variants of the paranasal sinuses in a Mexican population: expected changes according to age and gender	339
N.G. Jasso-Ramírez, R.E. Elizondo-Omaña, J.L. Treviño-González, A. Quiroga-Garza, I.A. Garza-Rico, K. Aguilar-Morales, G. Elizondo-Riojas, S. Guzmán-López	
Demirjian method and Willems method to study the dental age of adolescents in Shanghai before and after 10 years	346
K. Kwon, J. Pan, Y. Guo, Q. Ren, Z. Yang, J. Tao, F. Ji	
Anatomical variations of the biceps brachii insertion: a proposal for a new classification	359
B. Szewczyk, F. Paulsen, R.F. LaPrade, A. Borowski, N. Zielinska, Ł. Olewnik	
Venous supply of horseshoe kidneys and normal kidneys: an angio-multislice computed tomography-based study	368
M. Majos, M. Polgaj, L. Stefańczyk, A. Majos	
CASE REPORTS	
Bihemispheric posterior inferior cerebellar artery in a cadaver with Chiari I malformation	375
N. Boggio, M. Mathkour, Ł. Olewnik, J. Iwanaga, C.J. Bui, E.E. Biro, R.S. Tubbs	
Connection between V2 and V3 parts of the trigeminal nerve at the internal cranial base	382
S. McDonough, Ł. Olewnik, J. Iwanaga, A.S. Dumont, R.S. Tubbs	
The first histological observation of a C1 posterior arch defect	386
Y. Fang, T. Saga, J. Iwanaga, A.S. Dumont, R.S. Tubbs	
An atypical radiographic appearance of a cardiac myxoma: case report and review of the literature	391
R. Antoniak, M. Kompa, R. Burdach, L. Grabowska-Derlatka, A. Słowikowska, O. Rowiński	
Two cases of variations in inferior thyroid arterial pattern and their clinical implications	396
S.S. Novakov, S.D. Delchev	
A left circumflex aorta with a displaced thoracic duct in a 94-year-old male cadaver: a case report with discussion on embryology	400
P. Ostrowski, S. Popovchenko, M. Bonczar, T. Mroczek, J.A. Walocha, M.P. Zarzecki	
A unique bilateral accessory forearm flexor muscle	407
R.K. Fernandez, S. Ramakrishnan, T.T. Sukumaran, N. Kilarkaje, M. Pillay	
Anatomical variation of quadratus plantae in relation to flexor hallucis longus and flexor digitorum longus: a rare case	412
S. Haratizadeh, S. Seyyedini, S.N. Nematollahi-mahani	
Bilateral accessory head of the adductor longus muscle: an anatomical case study	416
T. Kozioł, M.P. Zarzecki, W. Przybycień, W. Twardokęs, J.A. Walocha	
A rare unreported bilateral thoracic muscle on the inferior and posteromedial aspect of the rib cage: case report and literature review	422
A. Lee, C. Dean, K. Labagnara, D. Jun Yun, A. Pinkas, P.L. Mishall	
The “sand watch” mandible	424
M.C. Rusu, M.D. Stoenescu, M. Butucescu, M. Săndulescu	
Case report of the double-headed extensor hallucis longus	429
K. Ruzik, K. Westrych, R.S. Tubbs, Ł. Olewnik, P. Łabętowicz, N. Zielinska	
A unilateral sternopharyngeal branch of the sternocleidomastoid muscle in an aged Caucasian male: a unique cadaveric report	434
S. Silawal, S. Morgan, L. Ruecker, G. Schulze-Tanzil	
A new type of the coracobrachialis muscle	439
N. Zielinska, P. Aragonés, J.R. Sañudo, P. Łabętowicz, R.S. Tubbs, Ł. Olewnik	
LETTERS TO THE EDITOR	
Comment on “A left circumflex aorta with a displaced thoracic duct in a 94-year-old male cadaver: a case report with discussion on embryology”	445
D. Borthakur, F. George, R. Dhingra	
Unreported bilateral thoracic muscle — is it a new variant or a well-known subcostal muscle?	447
G.P. Georgiev, Ł. Olewnik	

C O N T E N T S

REVIEW ARTICLES

- Variations in the branching pattern of tibial nerve in foot: a review of literature and relevant clinical anatomy 231
A. Priya, S.K. Ghosh, J.A. Walocha, R.S. Tubbs, J. Iwanaga
- Pneumatization of the articular eminence in cone-beam computed tomography: prevalence and characteristics — literature review 242
M. Wrzosek, K. Wilczek, J. Tusiewicz, M. Piskórz, I. Różyło-Kalinowska

ORIGINAL ARTICLES

- Propofol protects rats against intra-cerebroventricular streptozotocin-induced cognitive dysfunction and neuronal damage 248
L. Sun, X. Dou, W. Yang
- The spinal accessory nerve and its entry point into the posterior triangle of the neck 256
S. Ellis, C. Brassett, N. Glibbery, J. Cheema, S. Madenlidou
- The structure of the rostral epidural rete mirabile and caudal epidural rete mirabile of the domestic pig 261
S. Graczyk, M. Zdun
- The relationship between the aggrecan VNTR polymorphism and its content in lumbar intervertebral discs 269
P. Pękala, D. Felkle, K. Dykas, A. Jarosz, P. Elnazir, T. Konopka, J.A. Walocha, J. Dulinska-Litewka
- Multidetector computed tomography evaluation of origin, V2 segment variations and morphology of vertebral artery 274
R. Tasdemir, O.F. Cihan
- Variations of coronary sinus tributaries among patients undergoing cardiac resynchronisation therapy 282
B. Gach-Kuniewicz, G. Goncerz, D. Ali, M. Kacprzyk, M. Zarzecki, M. Loukas, J. Walocha, E. Mizia
- Topographical anatomy of the left ventricular summit: implications for invasive procedures 291
M. Kuniewicz, M. Krupiński, M. Urbańczyk-Zawadzka, M.K. Hołda, R. DeFonseka, T. Wadhwa, N. Cholewa, A. Matuszyk, J. Walocha, H. Dobrzynski
- Congenital venous anomalies associated with retrocaudal ureter: evaluation using computed tomography 300
T. Ichikawa, S. Ono, Y. Nagafuji, M. Kobayashi, H. Yashiro, J. Koizumi, F. Uchiyama, Y. Fujii, T. Hasebe, H. Terayama, J. Hashimoto
- Quantitative study of the primary ossification centre of the parietal bone in the human fetus 307
M. Grzonkowska, M. Baumgart, M. Badura, M. Wiśniewski, M. Szpinda
- A new classification system of trifid mandibular canal derived from Malaysian population 315
S.Y.A. Al-Siweedi, W.C. Ngeow, P. Nambiar, M.I. Abu-Hassan, R. Ahmad, M.K. Asif, W.L. Chai
- Morphological classification and measurement of the glenoid cavity using three-dimensional reconstruction in a Chinese population 325
Y. Chen, J. Xiong, W. Chen, D. Xie, Y. Zhang, Y. Mo, X. Gu, L. Zhang
- Cavitation processes in a space filled with loose mesenchymal tissues: a comparison between the retrosternal space and the middle ear tympanic cavity in human fetuses 332
S. Hayashi, J.H. Kim, Z.-W. Jin, G. Murakami, J.F. Rodríguez-Vázquez, S. Abe



INDEXED in: BIOSIS Previews, CAS, CINAHL, CrossRef, Dental Abstracts, EBSCO, Elsevier BIOBASE, EMBIOLOGY, FMJ, Google Scholar, Index Copernicus (159.83), Index Medicus/MEDLINE, Index Scholar, Polish Ministry of Education and Science (70), NCBI/National Center for Biotechnology Information, Polish Medical Bibliography, Scopus, SJR, Thomson Reuters, Thomson Scientific Products — Biological Abstracts, Ulrich's Periodicals Directory, Veterinary Bulletin, WorldCat and Zoological Record.

Cover picture: An enlarged view on the left recurrent laryngeal nerve; 1 — arch of aorta; 2 — left vagus nerve; 3 — left recurrent laryngeal nerve; 4 — left phrenic nerve; 5 — left pericardiacophrenic vessels. For details see: P. Ostrowski et al., *Folia Morphol* 2023; 82, 2: 400–406.